Nuclide Production and Imaging Applications of ^{225}Ac for Targeted Alpha Therapy

by

Andrew Kyle Henderson Robertson

BSc (Hons.), The University of Victoria, 2013

A THESIS SUBMITTED IN PARTIAL FULFILLMENT OF
THE REQUIREMENTS FOR THE DEGREE OF

DOCTOR OF PHILOSOPHY

in

The Faculty of Graduate and Postdoctoral Studies

(Physics)

THE UNIVERSITY OF BRITISH COLUMBIA

(Vancouver)

December 2020

The following individuals certify that they have read, and recommend to the Faculty of Graduate and Postdoctoral Studies for acceptance, the thesis entitled:

Nuclide Production and Imaging Applications of ^{225}Ac for Targeted Alpha Therapy

submitted by **Andrew Kyle Henderson Robertson** in partial fulfillment of the requirements for
the degree of **Doctor of Philosophy**
in **Physics**

Examining Committee:

Paul Schaffer, Radiology
Co-supervisor

Vesna Sossi, Physics and Astronomy
Co-supervisor

Stefan Reinsberg, Physics and Astronomy
Supervisory Committee Member

Rob Kiefl, Physics and Astronomy
Supervisory Committee Member

Douglas Bryman, Physics and Astronomy
University Examiner

Laurel Schafer, Chemistry
University Examiner

Ken Czerwinksi, University of Washington
External Examiner

Harry Brumer, Chemistry
Chair

Abstract

Targeted alpha therapies using actinium-225 (^{225}Ac, $t_{1/2}$ = 9.9 d) can treat advanced metastatic disease, yet insufficient ^{225}Ac availability limits their development (63 GBq/year is produced globally via ^{229}Th generators). This thesis describes efforts to produce ^{225}Ac and apply multi-nuclide SPECT imaging in preclinical evaluation of ^{225}Ac-radiopharmaceuticals. Initial ^{225}Ac production used $^{\mathrm{Nat}}$U-spallation-produced and mass-separated ion beams, producing up to 8.6 MBq of ^{225}Ra (an ^{225}Ac parent) and 18 MBq of ^{225}Ac. This material helped characterize the performance of ^{225}Ac decay chain imaging on a microSPECT/PET/CT scanner in terms of contrast recovery, spatial resolution, and noise. Larger ^{225}Ac quantities were produced via thorium target irradiation with a 438 MeV, 72 μA proton beam for 36 hours, producing (521 ± 18) MBq of ^{225}Ac and (91 ± 14) MBq of ^{225}Ra. These irradiations enabled ^{232}Th(p,x) cross sections measurements for ^{225}Ac, ^{225}Ra, and ^{227}Ac: (13.3 ± 1.2) mb, (4.2 ± 0.4) mb, and (17.7 ± 1.7) mb, respectively. Thirty-five other cross sections were measured and compared to FLUKA simulations; measured and calculated values generally agree within a factor of two. Ac separation from irradiated thorium and co-produced radioactive by-products used a thorium peroxide precipitation followed by cation exchange and extraction chromatography. Studies showed this method separates Ac from most elements, providing a directly-produced Ac product (^{227,225}Ac†) with measured ^{227}Ac content of (0.15 ± 0.04)%, a hazardous long-lived ($t_{1/2}$ = 21.8 y) impurity with prohibitively low waste disposal limits. A second, indirectly-produced ^{225}Ra/^{225}Ac-generator-derived Ac product (^{225}Ac*) with ^{227}Ac content of $<7.5\times10^{-5}$% was also obtained. The thorium target design, the simulations benchmarked against newly measured cross sections, and the precipitation-based thorium target processing method are separate novel contributions that together form the first demonstration of ^{225}Ac* production technology that can be scaled to useful clinical quantities. This thesis therefore presents the scientific foundation for a new potential ^{225}Ac production paradigm that

could substantially increase production of ^{227}Ac-free ^{225}Ac using accelerator-based methods that are independent of the fixed ^{229}Th quantities available from ^{233}U stockpiles. Such increased ^{225}Ac supplies will be required for the widespread clinical adoption of emerging ^{225}Ac-based targeted alpha therapies to be realized.

Lay Summary

Actinium-225 is an isotope that has shown potential for the treatment of cancer using targeted, alpha-particle-emitting pharmaceuticals. However, global production of actinium-225 is too low to support widespread use or development of these drugs. This thesis demonstrates alternative actinium production methods at TRIUMF, a particle accelerator lab in Vancouver, Canada. Initial efforts used TRIUMF's ISAC facility to produce small actinium-225 quantities that were used in medical imaging experiments related actinium radiopharmaceutical development. Efforts then shifted towards production via scalable methods: accelerated protons travelling 75% the speed of light were collided with thorium targets, resulting in the decomposition of the thorium nuclei into smaller atoms, including actinium-225. A thorium target capable of withstanding the heat deposited by the proton beam was developed, nuclear reaction rates were measured and compared with simulations, and chemical separation methods were developed to purify the actinium-225 from the thorium and other radioactive by-products.

Preface

All of the work presented in this thesis was conducted at TRIUMF or the University of British Columbia's Centre for Comparative Medicine, both located on the University of British Columbia Point Grey campus, with the exception of radioactive ICP-MS analysis conducted by Canadian Nuclear Laboratories (Chalk River, ON).

Chapter 1 was written by me, with contributions to the editing by P. Schaffer. Additional contributions to the editing of Sections 1.3.1, 1.3.2, and 1.3.4 were made by C. Ramogida and V. Radchenko as part of the publication of these sections as *Robertson, A. K. H., Ramogida, C. F., Schaffer, P., and Radchenko, V. (2018). Development of ^{225}Ac Radiopharmaceuticals: TRIUMF Perspectives and Experiences. Current Radiopharmaceuticals 11(3):156-172* [1]. Sections of this publication written by C. Ramogida and V. Radchenko are not included in this thesis. Reuse of this published material in this thesis is permitted under the terms of the Creative Commons Attribution-Non-Commercial 4.0 International Public License (http://creativecommons.org/licenses/by-nc/4.0/).

Chapter 2 was written by me with contributions to the editing by P. Schaffer. Hardware setup of the gamma spectrometer in Section 2.1 was provided by T. Moskven, and hardware setup of the alpha spectrometer in Section 2.2 was provided by P. Kunz. Besides these contributions, I was solely responsible for the remainder of the work described in Sections 2.1 and 2.2, including all data collection, analysis, and presentation. Appendix A provides additional details on Section 2.1 and is entirely my original work. Appendix B provides additional details on Section 2.2 and was written by B. McNeil, an undergraduate student working under my supervision. Data collection and analysis for Appendix B was done by B. McNeil under my direction. A version of Section 2.3.2 was published as *Robertson, A. K. H., Ladouceur, K., Nozar, M., Moskven, L., Ramogida, C. F., D'Auria, J., Sossi, V., and Schaffer, P. (2017). Design and Simulation of a Thorium Target for ^{225}Ac Production. AIP Conference Proceedings 1845(1):020019-1–020019-5* [2]. I ran all FLUKA simulations used in this work, analyzed and presented the results, and wrote the text with editing contributions

from all co-authors. Additionally, M. Nozar provided guidance on how to set up the simulations and also created the FLUKA geometry input based on the thorium oxide prototype target designed by L. Moskven, K. Ladouceur, and J. D'Auria. Supervisory authors for this publication were V. Sossi and P. Schaffer, with concept formation of the thorium irradiation initiative credited to P. Schaffer. This published material is used in this thesis with permission from AIP Publishing.

Chapter 3 was written by me with contributions to the editing by P. Schaffer and C. Ramogida. A version of this chapter was published as part of a larger article in *Ramogida, C. F., Robertson, A. K. H., Jermilova, U., Zhang, C., Yang, H., Kunz, P., Lassen, J., Bratanovic, I., Brown, V., Southcott, L., Rodríguez-Rodríguez, C., Radchenko, V., Bénard, F., Orvig, C., and Schaffer, P. (2019). Evaluation of polydentate picolinic acid chelating ligands and an a-melanocyte-stimulating hormone derivative for targeted alpha therapy using ISOL-produced ^{225}Ac. EJNMMI Radiopharmacy and Chemistry 4(1):21-41* [3]. C. Ramogida and I produced the ^{225}Ac used in this project and these aspects are presented in Chapter 3. The production of ^{225}Ac used for this work relied on the ISAC Implantation Station designed by co-author P. Kunz and the operation of the laser ion source by co-author J. Lassen. Sample preparation required for the data in Table 3.2 was done by U. Jermilova. The remaining co-authors (H. Yang, I. Bratanovic, V. Brown, L. Southcott, C. Rodríguez-Rodríguez, V. Radchenko, F. Bénard, and C. Orvig) contributed to other parts of this publication that are not included in this thesis. Reuse of this published material in this thesis is permitted under the terms of the Creative Commons Attribution 4.0 International License (http://creativecommons.org/licenses/by/4.0/).

Chapter 4 was written by me and published with minor modifications as *Robertson, A. K. H., Ramogida, C. F., Rodríguez-Rodríguez, C., Blinder, S., Kunz, P., Sossi, V., and Schaffer, P. (2017). Multi-isotope SPECT imaging of the ^{225}Ac Decay Chain: Feasibility Studies. Physics in Medicine and Biology 62:4406-4420* [4]. All co-authors contributed to editing of this manuscript. Concept formation was done by supervisory authors P. Schaffer and V. Sossi. Input to experiment design was provided at the conceptual level by V. Sossi, S. Blinder, and me (in particular, the chromatography column concept utilized in Sections 4.2.5 and 4.3.5) with detailed experimental design details finalized by S. Blinder, C. Rodríguez-Rodríguez and me. Guidance on SPECT projection data collection and scanner operation was provided by C. Rodríguez-Rodríguez. The production of ^{225}Ac used for this work relied on the ISAC Implantation Station designed by co-author P. Kunz and the post-irradiation chemistry done by C. Ramogida and me. In

this publication I was responsible for conducting all aspects of the imaging experiments, including SPECT/CT data acquisition, image reconstruction, image analysis, data presentation, and writing of the manuscript. Chapter 4 is included in this thesis under terms of IOP Publishing's Author Rights Policy (subscription articles). This chapter is the Accepted Manuscript version of an article accepted for publication in *Physics in Medicine and Biology*. IOP Publishing Ltd is not responsible for any errors or omissions in this version of the manuscript or any version derived from it. The Version of Record is available online at doi.org/10.1088/1361-6560/aa6a99.

I was the lead investigator for work presented in Chapters 5, 6, and 7 where I was responsible for all major areas of concept formation, hiring and training of undergraduate students, experiment design, and the majority of data collection, analysis, and presentation. I was also the project proponent for these efforts, representing the project at internal design and safety reviews. The extensive radiation safety analysis reports required were written by me and are shown in Appendices C and D.

Chapter 5 was written by me and published with minor modifications as *Robertson, A. K. H., Lobbezoo, A., Moskven, L., Schaffer, P., and Hoehr, C. (2019). Design of a Thorium Metal Target for ^{225}Ac Production at TRIUMF. Instruments 3(1):20-26* [5]. For this effort I was responsible for: project definition and proposal; hiring, training, and supervising of an undergraduate student, A. Lobbezoo; representing the project at internal design and safety reviews; coordination of target manufacturing and irradiation; and the majority of the writing of the manuscript. The final target design was made by A. Lobbezoo, who under my guidance also performed all of the thermal and mechanical simulations that generated the raw data shown in Chapter 5. Co-author L. Moskven reviewed the simulation work. Co-authors C. Hoehr and P. Schaffer were supervisory authors and contributed to editing of the manuscript. I was responsible for the majority of the manuscript writing, but received contributions in the methods sections and figures from A. Lobbezoo. Reuse of this published material in this thesis is permitted under the terms of the Creative Commons Attribution 4.0 International License (http://creativecommons.org/licenses/by/4.0/).

Chapter 6 is my original and independent work and represents an effort that I independently conceived of, proposed, and carried out. An expanded version of Chapter 6, which includes an additional comparison to GEANT4 simulations has been published as *Robertson, A. K. H., Kunz, P., Hoehr, C., and Schaffer, P. (2020). Nuclide Production Cross Sections from Irradiation of Thorium by 438 MeV Protons and a Comparison to FLUKA and GEANT4 Simulations. Physical Review C 102:044613* [6]. Collabora-

tor P. Kunz provided the GEANT4 simulations and C. Hoehr contributed to editing of the manuscript; P. Schaffer was the supervisory author. This published material is reprinted in this thesis with permission from the American Physical Society.

Chapter 7 was written by me and has been published as *Robertson, A. K. H., McNeil, B., Yang, H., Gendron, D. Perron, R., Radchenko, V., Zeisler, S., Causey, P., and Schaffer, P. (2020).* ^{232}*Th-Spallation-Produced* ^{225}*Ac with Reduced* ^{227}*Ac Content. Inorganic Chemistry 59(17):12156-12165* [7]. I was the lead investigator for this effort who proposed the project and carried out the majority of the work. I was responsible for experiment design, chemistry process development, most data collection, and all data analysis and presentation. Co-author B. McNeil prepared all non-radioactive ICP-MS samples used in the creation of Table 7.1 and Figure 7.6. ICP-MS analysis of radioactive samples (Table 7.2 and Figure 7.7) prepared by me was done by collaborators, D. Gendron, R. Perron, and P. Causey, at Canadian Nuclear Laboratories (Chalk River, ON). The publication was written by me, with contributions to the editing from co-authors B. McNeil, H. Yang, D. Gendron, R. Perron, P. Causey, and P. Schaffer. Guidance during the chemistry process development was provided by H. Yang and S. Zeisler. This published material is reprinted (adapted) in this thesis with permission from Robertson *et al* [7]. Copyright (2020) American Chemical Society.

Chapter 8 was written by me, with contributions to the editing by P. Schaffer.

Table of Contents

Appendices

List of Tables

List of Figures

List of Acronyms and Abbreviations

ARIEL	Advanced Rare Isotope Laboratory
BL1A	Beamline 1A
BNL	Brookhaven National Laboratory
Bq (kBq, MBq, etc.)	bequerel (kilobequerel, megabequerel, etc.)
Ci (mCi, etc.)	curie (millicurie, etc.)
CNL	Canadian Nuclear Laboratories
CT	computer tomography
DGA	diglycolamine
DNA	deoxyribonucleic acid
DOE	Department of Energy
DOTA	dodecane tetraacetic acid
EB	electron beam
EOB	end of bombardment
eV (keV, MeV, etc.)	electronvolt (kiloelectronvolt, megaelectronvolt)
EXFOR	Exchange Format
FDG	fluorodeoxyglucose
FLUKA	fluktuierende kaskade
FWHM	full width at half maximum
HEUHR	high-energy ultra high resolution
HPGe	high purity germanium
IAEA	International Atomic Energy Agency
ICP-MS	inductively coupled plasma mass spectroscopy
ICP-OES	inductively coupled plasma optical emission spectroscopy
IIS	ISAC Implantation Station
INR	Institute for Nuclear Research
IPF	Isotope Production Facility
IPPE	Leipunskii Institute for Physics and Power Engineering

ISAC	Isotope Separator and Accelerator
ISOL	isotope separation online
ITU	Institute for Transuranium Elements
LANL	Los Alamos National Laboratory
LET	linear energy transfer
MCA	multi-channel analyzer
MEDICIS	Medical Isotopes Collected from ISOLDE
NIST	National Institute of Standards and Technology
ORNL	Oak Ridge National Laboratory
PET	positron emission tomography
PSMA	prostate specific membrane antigen
RCR1	Radiochemistry Room 1
ROI	region of interest
RPG	Radiation Protection Group
SDD	source-to-detector distance
SI	International System of Units
SPECT	single photon emission computed tomography
SRIM	Stopping Range of Ions in Matter
TAT	targeted alpha therapy
TLC	thin layer chromatography
TRIUMF	Tri-University Meson Facility
TRT	targeted radionuclide therapy
UHS	ultra high sensitivity
UV	ultraviolet
VECTor	versatile emission computed tomography

Acknowledgements

I offer my enduring gratitude to the faculty, staff, and fellow students at TRIUMF and UBC, especially all members of TRIUMF's Life Sciences Division for their support of me and this work and their scientific and technical guidance that made it successful. I owe particular thanks to Dr. Paul Schaffer for providing me with incredible mentorship and countless opportunities to grow as a scientist, individual, and leader.

Special thanks is offered to my parents for supporting me through years of education. Most of all, I would like to thank my life partner for her enduring love, moral support, and sacrifices in time not spent together throughout my graduate studies.

TRIUMF receives funding via a contribution agreement with the National Research Council of Canada. This research was supported by scholarships (NSERC PGS D (518984-2018), IsoSiM CREATE (448110)) and a Discovery Grant (RGPIN 2016-04413) from the Natural Sciences and Engineering Research Council of Canada.

Dedication

To Sarah

1 Introduction

Targeted radionuclide therapy (TRT) combining disease-targeting biomolecules with radionuclides emitting cytotoxic charged particle radiation is used in the treatment of cancers. While beta-particle-emitting nuclides such as ^{177}Lu, ^{131}I, and ^{90}Y have achieved clinical approval [8–10], there is currently a heightened interest in the potential of alpha-particle-emitting radionuclides as a complementary – and possibly more potent – therapeutic approach [11–22]. One non-targeted alpha-emitting radiopharmaceutical containing ^{223}Ra has already received clinical adoption [23, 24]. Due to the higher linear energy transfer and shorter range of alpha-radiation, alpha-emitting nuclides selectively delivered to diseased cells are more potent and damage fewer surrounding healthy cells than beta-emitting nuclides. These advantages have recently been demonstrated by patients who successfully responded to treatment with an alpha-emitting radionuclide after failing to respond to a beta-emitting analog, or not qualifying for treatment with a beta-emitting analog due to the close proximity of metastases to organs at risk [25]. Alpha particles also cause double-stranded DNA breaks, which are more resistant to DNA repair mechanisms [26], and unlike other forms of radiation, the biological response to alpha-radiation has been shown to be independent of dose rate and oxygenation [27]. Sections 1.1.1 through 1.1.4 will discuss TRT in greater detail and introduce key concepts such as radiation therapy, radioactive decay, and radiopharmaceuticals.

Actinium-225 (^{225}Ac, $t_{1/2}$ = 9.92 d) is a promising candidate alpha-emitter for use in TRT due to its suitable half-life, favorable chemistry, and a decay chain that contains four alpha-emissions and no long-lived progeny. The cytotoxic effects of ^{225}Ac were demonstrated decades ago [28], and clinical results have since demonstrated the remarkable ability of this nuclide to treat advanced metastatic disease [25, 29–32]. Sections 1.1.4 and 1.1.5 will describe what makes ^{225}Ac such a suitable alpha-emitter for TRT and summarize clinical data demonstrating its effectiveness.

However, the nature of the ^{225}Ac decay chain (detailed in Section 1.2.1) presents challenges for patient dosimetry, a cornerstone of conventional radiation therapy that is used to correlate the quantity of radiation delivered with resulting biological outcomes. The benefit of the ^{225}Ac decay chain's four alpha emissions requires the retention of both ^{225}Ac and its nuclear progeny at target cells, despite liberation of daughter isotopes after each decay [15]. Individual biodistributions of each nuclide (especially ^{221}Fr and ^{213}Bi) must therefore be determined when assessing the efficacy of ^{225}Ac radiopharmaceuticals. However, this is a quantification problem that is complicated by the half-lives and types of radiation emitted by ^{225}Ac and its progeny.

Additionally, the development of ^{225}Ac-radiopharmaceuticals has been hindered by the limited global ^{225}Ac production capacity [1, 33–35], resulting in an intense global effort to increase ^{225}Ac production by methods other than the typical ^{229}Th/^{225}Ac generators historically derived from decades-old ^{233}U stockpiles [1, 33, 36–40]. Current and alternative methods for ^{225}Ac production will be discussed in Section 1.3.

Section 1.4 will then detail how this thesis aims to address both the production and dosimetry challenges facing the development of ^{225}Ac-radiopharmaceuticals. Before that, Chapter 1 will first introduce key concepts and background information, such as: radiation therapy, radiopharmaceuticals, and targeted alpha therapy with ^{225}Ac (Section 1.1); radioactivity and decay chains, ^{225}Ac properties, and ^{225}Ac decay chain quantification (Section 1.2); and radionuclide production methods, including a review of current and potential ^{225}Ac production methods (Section 1.3).

1.1 Targeted Alpha Therapy and ^{225}Ac

1.1.1 Radiation therapy for cancer treatment

Ionizing radiation has been used in the treatment of cancer since soon after the discovery of the x-ray in 1895 [41, 42]. However, while therapeutic and palliative benefits of radiation therapy were observed, an incomplete knowledge of radiation physics, the biological effects of radiation, the underlying radiobiological mechanisms led to morbidities and misuse of radiation and radioactivity during the beginning of the 20$^{\text{th}}$ century. Our current understanding of the mechanisms through which radiation can provide therapeutic benefit – and how it can also cause harm – was not made possible until the discovery of deoxyribonucleic acid (DNA) and its essential role in life [43], and later, in radiation-induced biological damage.

Cancers are diseases that result from mutations to biological cells. While many different types of mutations can be involved, hallmarks of cancer include: evading growth suppression, inducing angiogenesis, resisting death, sustained proliferative signaling, and evading growth suppression. All cancers are also characterized by some form of uncontrolled and invasive cellular growth. While healthy biological cells will grow, replicate, divide, and die at a controlled rate, cells that grow too quickly become tumours. Tumours that are invasive and grow in a way such that they invade other tissues become cancer. Cancer cells can migrate from the tumour and travel through the cardiovascular or lymphatic systems to invade distant parts of the body, forming metastases. While this rapid cellular division (rapid relative to healthy cells) is part of what makes cancers so harmful, it also provides a mechanism through which the disease is often targeted.

DNA replication is an important step in cell division that allows each new cell to retain a copy of the molecule that ultimately controls all cellular chemistry via the synthesis of proteins. When DNA was discovered, the observation that heredity was a stable process lead to the assumption that DNA itself must be a stable molecule. However, despite its importance, DNA is actually quite unstable. Instead, a number of DNA repair processes have evolved. Multiple DNA repair mechanisms exist for different types of DNA damage, including single-strand breaks (damage to one of the two DNA backbones, which is more common but more easy to repair) and double-strand breaks (damage to both backbones, which is more rare yet more difficult to repair). DNA damage, if not repaired, most often leads to cell death by preventing the cell from functioning or dividing properly. Cells that replicate more frequently are more sensitive to DNA damage because they are more often in DNA replication stages of the cell cycle where DNA repair cannot occur. By damaging DNA, ionizing radiation is more harmful to more rapidly dividing cancerous cells than it is to healthy cells.

Ionizing radiation causes DNA damage induced by ionization of atoms within the cell. This damage can be direct or indirect. More often, damage is indirect and caused by the ionization of another molecule, causing radiolysis and formation of free radicals that then chemically interact with DNA. Since cells are mostly water, these free radicals are typically reactive oxygen species, for example, $^{*}OH$, H_2O_2, H_3O^{+}, OH^{-}, H^{+}, e^{-}_{aq}, etc. The mechanisms through which radiation interacts with matter to cause ionization are further explained in Section 1.1.3.

It is important to keep in mind that while radiation may be more destructive to cancerous tissues, it is harmful to healthy cells as well. The essential challenge in radiation therapy is determining how to deliver radiation to the

cancer while minimizing the dose to nearby healthy tissues. Often, it is the toxicity to nearby healthy organs-at-risk that limits the radiation dose that can be delivered to the tumour. The amount of energy deposited in matter by ionizing radiation is measured by the quantity absorbed dose, which has the SI unit gray (Gy) equivalent to one Joule of absorbed energy per kilogram of matter. Decades of research has shown that absorbed dose distributions are correlated with biological outcomes of both targeted tissues (cancer) and healthy tissues (organs-at-risk), allowing this quantity to be used in radiation therapy treatment planning.

Radiation therapy is most often delivered with an external beam of radiation, including gamma rays (ex. from ^{60}Co sources), bremsstrahlung x-rays (produced by the stopping of electron beams), electron beams, proton beams, or heavy ion beams. Technological advancements over recent decades have increased the precision with which external beam radiation therapy delivers dose, shaping and rotating the beam around the patient to contour the dose to the tumour as tightly as possible. However, dose to healthy tissue is still unavoidable, as the radiation must typically pass through healthy tissue before reaching the tumour. Brachytherapy uses radiation sources that are placed inside the patient's body and near the tumour, either for a short duration or on a permanent basis. Still, such internal sources of radiation may provide dose to nearby healthy tissues. Regardless of the approach taken, the ability to target diseased cells and only diseased cells with radiation can only be as good as the ability of localizing these tissues. Often the boundary between such regions is unclear or the precision with which the radiation can be delivered is limited by diagnostic imaging resolution, the precision of radiation therapy technology, or the movement of patient tissues; this results in margins of error being added to the target region, potentially increasing dose to healthy tissues. The localization and targeting of very small and disseminated metastases with external beam radiation therapy and brachytherapy is also very challenging, meaning these cells may not be seen or treated.

While external beam radiation therapy and brachytherapy are well established treatment options that have been widely used for decades, newer technologies such as targeted radionuclide therapy (TRT) and especially targeted alpha therapy (TAT) aim to overcome some of these dose delivery challenges by targeting disease at the molecular level and delivering radiation sources directly to individual tumour cells. The potential of these treatment options is the main motivation for much of the work in this thesis.

The remainder of Section 1.1 will provide background information as to how TAT works, including an introduction to nuclear medicine and can-

cer targeting in Section 1.1.2 and to radiation interactions with matter in Section 1.1.3. A summary of the clinical data that demonstrates the potential of TAT – and particularly TAT with ^{225}Ac – that currently motivates the heightened interest in ^{225}Ac-radiopharmaceutical development is then presented in Sections 1.1.4 and 1.1.5.

1.1.2 Diagnostic radiopharmaceuticals

Nuclear medicine applies radioactive substances inside the body for the diagnosis or treatment of disease. The internalization of these radiopharmaceuticals results in the preferential distribution of the radionuclide towards the tissues or organs of diagnostic or therapeutic interest. There are multiple modes of decay, each characterized by the type of particle emitted in the process, the most common being alpha decay, beta decay, gamma decay, and electron capture. Alpha decay results in the emission of an alpha particle, a positively charged helium nucleus containing two protons and two neutrons. Beta-minus decay results in the emission of an electron and an antineutrino as a neutron changes into a proton, while beta-plus decay results in emission of a positron and a neutrino as a proton changes into a neutron. Protons can also convert to neutrons via electron capture, in which the nucleus captures an atomic electron and emits a neutrino. More details regarding the physics of radioactive decay are discussed in Section 1.2.1.

The most simple radiopharmaceuticals utilize radionuclides whose elemental chemistry naturally results in the desired biodistribution. Examples include: ^{133}Xe ($t_{1/2} = 5.6$ d), a radioactive noble gas that, when inhaled, can be used to image the lungs and assess pulmonary function; ^{82}Rb ($t_{1/2} = 1.26$ min), a radioactive alkali metal administered intravenously as rubidium chloride that, due to its similar biochemistry to K^+, is rapidly absorbed by cardiac muscle where it participates in sodium-potassium exchange and is used to image cardiac muscle function; and ^{123}I ($t_{1/2} = 13.2$ d), a radioactive halogen administered orally as sodium iodide that is preferentially absorbed by the thyroid (which uses iodine for hormone production) allowing ^{123}I to be used in thyroid imaging. The range of half-lives, chemical properties, methods of internalization, and applications (pulmonology, cardiology, and oncology) provided by these three example radiopharmaceuticals exemplifies the diversity of medical radionuclides and their applications.

The above radiopharmaceutical examples are non-targeting agents, meaning they do not have a molecular structure designed to bind to a specific cellular receptor(s) of the tissues they are used to image. Instead, their elemental chemistry results in the desired preferential uptake in the

tissue of interest. These are the first of four generations of radiopharmaceuticals that have been developed: simple molecules or salts that result in diffusion-based, non-specific imaging. Other examples include [^{99m}Tc]TcO_4, [^{99m}Tc]Tc-methyl diphosphonate, and [^{18}F]F^-.

Second, third, and fourth generation radiopharmaceuticals are targeted compounds that combine radionuclides with a molecular structure that targets specific metabolic processes or binds to cell surface receptors that are over-expressed on cells within the tissues of interest. Second generation radiopharmaceuticals are imaging agents that typically use small molecules that target metabolic functions that are altered by disease. The most common example is the use of ^{18}F ($t_{1/2} = 110$ min) in fluorodeoxyglucose (FDG). [^{18}F]FDG is a radioactive glucose analog that, when administered, results in a preferential uptake of ^{18}F in tissues that require more energy and consume more glucose. This includes rapidly replicating cancer cells that require excess energy to sustain their growth, allowing ^{18}F to be used to image and screen for metastases. Third generation radiopharmaceuticals are diagnostics that use targeting compounds of greater molecular weight, typically peptides or antibodies that preferentially bind to cell surface receptors. These pharmaceuticals also typically contain a chelating moiety that binds the radionuclide to the targeting compound. A more detailed overview of targeted drugs and their structure is beyond the scope of this work; for more, the reader is referred to the text by Knapp and Dash [44]. Fourth generation radiopharmaceuticals are targeted compounds (third generation targeting vectors such as peptides and antibodies) that have therapeutic effects, including the ^{225}Ac-radiopharmaceuticals discussed in Section 1.1.5.

Most nuclear medicine applications involve the use of diagnostic radiopharmaceuticals that use radionuclides emitting gamma rays or positrons that annihilate with nearby electrons, converting their mass-energy into a pair of gamma rays (see Section 1.1.3). These photons originate from the tissues in which the radiopharmaceutical is distributed and travel through tissues, exiting the body where they are then detected by nearby imaging devices that count the number of particles detected and convert this data into an image that is representative of the radiopharmaceutical's biodistribution within the patient. Imaging modalities include planar imaging gamma cameras, SPECT (single photon emission computed tomography), and PET (positron emission computed tomography). The use of these drugs relies on the tracer principle, i.e. that the biological process or function they are imaging is not disturbed or altered during the diagnostic process by the presence of the tracer. Thus the radiation emitted by diagnostic radionuclides allows clinicians to observe tissue function and diagnose disease, while

typically avoiding the delivery of radiation doses that result in destructive and deterministic damage to healthy tissues.

Therapeutic radiopharmaceuticals, in contrast, emit radiation that is comparatively much more destructive to the tissues in which the pharmaceutical is distributed. This radiation is either electrons (resulting either from beta minus decay or Auger electron emission) or alpha particles that are emitted during radioactive decay. Unlike gamma rays used in diagnostic applications, this charged particle radiation travels a shorter distance and does not leave the body. To understand the different effects these types of radiation have on the body and what radiation properties make for good diagnostic or therapeutic radionuclides, we must first discuss the mechanisms through which ionizing radiation interacts with matter that are presented in the following section.

1.1.3 Ionizing radiation interactions with matter

An understanding of ionizing radiation interactions with matter is not only important for understanding how targeted radionuclide therapy work, but also for understanding many aspects of this thesis, including gamma and alpha spectroscopy (Chapter 2), the collection of radioactive ion beams for nuclide production (Chapter 3), nuclear medicine imaging systems (Chapter 4), and proton targets for nuclide production (Chapter 5). This section will summarize the mechanisms through which photons indirectly ionize matter, as well as charged particle interactions that are directly ionizing.

Photon (x-ray and gamma ray) interactions with matter are stochastic. In other terms, a photon passing through a thin layer of material of thickness dl may or may not interact with the material; the probably of interaction is described by the attenuation coefficient, μ. For a beam of photons, the change in flux, I, after passing through the thin layer is therefore described by $dI = -\mu dl$. Similar to the equations for radioactive decay (Equations 1.4 and 1.5 in Section 1.2.1), this leads to the familiar exponential attenuation curve for photons passing through thick materials, specifically

$$I = I_o e^{-\mu x} \tag{1.1}$$

where I is the flux remaining after the initial flux, I_o passes through a material of thickness x. The value of the attenuation coefficient depends on both the material and the energy of the photon. Due to the attenuation coefficient's energy dependence, Equation 1.1 only holds for monoenergetic photon beams. The energy dependence of the attenuation coefficient is explained by the three dominant yet different physical mechanisms through

which photons interact with matter: the photoelectric effect, Compton scattering, and pair production.

The photoelectric effect is the dominant process at low photon energies (i.e. energies below $\sim 10^1$ keV) and involves the ejection of a bound atomic electron from an atom after the destruction of the photon and absorption of the photon's energy by the electron. A small amount of energy goes into overcoming the atomic electron binding energy, though the majority of the photon's energy is converted to kinetic energy of the now free electron. Compton scattering is dominant in the $\sim 10^2$ to $\sim 10^3$ keV range and involves the interaction of a photon with a free (or very loosely bound, and approximately free) electron. This is an inelastic two-body collision where the photon transfers only part of its energy to the electron. Relativistic conservation of energy and momentum can be used to relate the final electron and photon energies to the scattering angle of the photon. Finally, pair production becomes possible above 1022 keV and involves the interaction of a photon with a nuclei's magnetic field that results in the destruction of the photon and the creation of an electron-positron pair. Again, relativistic conservation of momentum and mass-energy dictate the amount of kinetic energy transferred to the electron and positron. The 1022 keV threshold is equal to the sum of the electron and positron rest masses. The positron that is created then soon encounters another electron and undergoes annihilation, an inverse process to pair production whereby the positron and electron are destroyed and their rest masses are converted to energy in the form of – because of conservation of momentum and energy – two 511 keV gamma rays travelling in opposite directions. Regardless of whether a photon interacts with a material via the photoelectric effect, Compton scattering, or pair production, the result is the creation of energetic charged particles that go on to directly ionize the medium via the processes described below for energetic charged particle interactions with matter.

Unlike high-energy photons (x-rays and gamma rays), charged particles (ex. electrons, protons, alpha particles, etc.) interact continuously and non-stochastically with media through which they travel. These interactions can be described by a series of Coulomb interactions between the charged particle and atomic electrons or nuclei within the medium, through which a small fraction of the particle's kinetic energy is lost with each collision. The type of interaction that occurs with an individual atom is determined, in general, by the interaction's impact parameter, defined as the minimum distance between the particle's trajectory and the centre of the atom. When the impact parameter is larger than the atomic radius, Coulomb interactions affect the entire atom and energy is transferred to the atom by ionizing the

atom or by exciting its atomic electrons to higher energy states. When the impact parameter is on the order of the atomic radius, collisions with individual atomic electrons occur, resulting in their ejection from the atom. These energetic secondary electrons, or delta rays, then travel through the medium and result in additional charged particle interactions. For small impact parameters much smaller than the atomic radius, the charged particle interacts with the atomic nucleus; while most of these interactions are elastic, heavy charged particles with sufficient energy can also induce nuclear reactions (see Section 1.3.3).

The large number of discrete interactions together correspond to a process through which the charged particle continuously loses energy while passing through the media; this is known as the "continuous slowing-down approximation". The rate of kinetic energy loss, dE, per unit path length, dx, is called the stopping power, $\frac{-dE}{dx}$, and depends on the type of particle, the particle's energy, and the material and density of the medium. The integral of the stopping power with respect to kinetic energy defines the particle's range (i.e. the expected path length) in the material, a non-stochastic value that is also characteristic of the charged particle radiation and the medium through which it is travelling. For heavy charged particles such as protons and alpha particles, the stopping power in a given medium for a given particle velocity is described by the Bethe-Bloch equation; for more on this topic, the reader is referred to the text by Podgorsak [45].

While knowledge of the amount of energy deposited along a particle's trajectory enables dose calculations (see Section 1.1.1), the creation of energetic delta rays results in the deposition of some of the primary particle's energy away from the primary particle's track. For this reason, the restricted linear energy transfer (LET), L_Δ, is used instead, where

$$L_\Delta = \frac{-dE_\Delta}{dx} \tag{1.2}$$

and where dE_Δ is the energy lost by the primary charged particle, excluding the energy that is transferred to secondary electrons with kinetic energies greater than Δ. In the limit where Δ approaches infinity, the LET and stopping power are equivalent.

These concepts for ionizing radiation interactions with matter are applied in many ways throughout this thesis. For example, differences in LET and range between alpha particles and beta particles (electrons) explain why targeted radionuclide therapy with alpha-emitting radionuclides has advantages over TRT with beta-emitting radionuclides in certain situations (and vice versa), while an understanding of stopping power and heat deposition

plays an important role in the development of proton targets (Chapter 5). Similarly, gamma ray interactions with matter enable gamma spectroscopy, the most widely used analytical technique throughout this work (Section 2.1).

1.1.4 Radionuclide therapy

Like their diagnostic counterparts (Section 1.1.2), therapeutic radiopharmaceuticals preferentially deliver radioactivity to tissues of interest using either non-targeting or targeting compounds. However, unlike diagnostics, therapeutic radionuclides emit radiation that is destructive to the surrounding tissues, specifically, charged particles such as beta or alpha radiation that have a short range and high LET. In this way, therapeutic radiopharmaceuticals deliver radiation dose to the diseased tissue using an internal radiation source that is inside the diseased tissue itself.

Radionuclide therapy was first used in 1941, when a mixture of ^{130}I and ^{131}I produced by the irradiation of tellurium by deuterons was administered to patients diagnosed with hyperthyroidism [46]. Soon after, ^{131}I was also used to treat patients with thyroid cancer [47], in what was also one of the earliest applications of "theranostic" radionucides: the administration of therapeutic quantities of ^{131}I was preceded by the administration of smaller quantities to first verify radioiodide uptake in the metastases. In theranostic applications, diagnostic radiopharmaceuticals are used to predict the biodistribution and dose that will later result from the administration of the therapeutic radiopharmaceutical. The diagnostic radiopharmaceutical can also then be used to assess the patient's response to the treatment. Theranostic radiopharmaceuticals can involve a single radionuclide, such as ^{131}I (which emits both beta-minus radiation that can be used for therapy as well as gamma rays that can be used for diagnosis), or a theranostic pair of radionuclides, such as ^{123}I and ^{131}I (^{123}I cannot be used for therapy, but is able to provide a higher quality diagnostic image than ^{131}I). A key requirement of theranostics is that the diagnostic and therapeutic radiopharmaceuticals are chemically identical, meaning that identical biodistributions within the patient can be assumed.

Other examples of non-targeting beta-emitting radiophamaceuticals include [^{89}Sr]$SrCl_2$ and [^{153}Sm]Sm-EDTMP (ethylendiaminetetramethylene phosphonate), which are preferentially absorbed in areas of bone growth and are used in the palliative treatment of pain resulting from bone metastases. Targeted examples include [^{90}Y]Y-ibritumomab and [^{131}I]-tositumomab, which combine beta-emitters with monoclonal antibodies directed against

the CD20 antigen that is over-expressed in some non-Hodgkin lymphomas. Most recently, [^{177}Lu]Lu-DOTATATE – a somatostatin analog peptide that binds to somatostatin receptors over-expressed on some neuroendocrine tumours – has been approved for the treatment of patients with advanced neuroendocrine tumours of the pancreas or gastrointestinal tract.

Due to physical differences between how alpha and beta particles interact with matter, radionuclide therapy with alpha-emitters has theoretical advantages over radionuclide therapy with beta-emitters. First, the higher LET of alpha particles ($\sim$80 keV/μm, compared to $\sim$0.2 keV/μm for betas) makes alpha particles more destructive, delivering more dose per decay and causing more free radical formation and double-strand DNA breaks that are harder to repair. This higher cytotoxicity also means that fewer alpha particles are required to kill a cell (possibly as low as 1-5, compared to hundreds for beta particles), which is potentially advantageous for radiopharmaceuticals that target cell surface receptors that are specific to the disease but limited in number. Second, the shorter range of alpha particles (40-100 μm, compared to 1-10 mm for beta particles) means that fewer nearby healthy cells are irradiated, reducing dose to nearby organs and enabling the use of radionuclide therapy for metastases in close proximity to organs at risk. The combination of high LET and short range also means that targeted alpha therapy has the potential to destroy very small metastases that would not be similarly affected if using a beta emitter. These advantages of alpha particles have recently been demonstrated by early reports of patients who successfully responded to treatment with an alpha-emitting radionuclide after failing to respond to a beta-emitting analog, or not qualifying for treatment with a beta-emitting analog due to the close proximity of metastases to organs at risk (in this case, bone marrow), which would receive too much dose even from a short-ranged beta-emitter such as ^{177}Lu [25].

Another example of the advantages of alpha-emitters is [^{223}Ra]$RaCl_2$ (Xofigo), which in 2013 became the first clinically approved alpha-emitting radiopharmaceutical and uses the alpha-emitter ^{223}Ra ($t_{1/2} = 11.4$ d). Like previously mentioned beta-emitting radiopharmaceuticals, Xofigo was intended to treat pain resulting from bone metastases, however, clinical trials demonstrated that Xofigo also increased average overall survival by 3 months and delayed the onset of more severe skeletal symptoms [24].

While ^{223}Ra is currently the only clinically approved alpha-emitter, others are also under investigation for their use in radionuclide therapy. However, of the approximately 447 known alpha-emitters on the chart of nuclides, only a handful have properties suitable for medical use. The half-life of a therapeutic nuclide must be long enough such that the radionuclide and

radiopharmaceutical can be produced and administered, resulting in the delivery of the radionuclide to the targeted tissues. This excludes the use of short-lived nuclides with half-lives below the tens of minutes; for example, ^{211}Bi ($t_{1/2}$ = 2.1 min), which is part of the ^{223}Ra decay chain. However, the nuclide's half-life should also not be too long, so as to ensure that the radiation is delivered faster than the disease progression and that residual radioactivity does not remain long after treatment and result in the accumulation of long-lived radioactive waste; this excludes the use of naturally occurring alpha-emitters such as ^{226}Ra ($t_{1/2}$ = 1600 y), ^{232}Th ($t_{1/2}$ = 14 billion y), and ^{238}U ($t_{1/2}$ = 4.5 billion y). In addition to the half-life, one must also consider the decay products of the alpha-emitter, especially since many alpha-emitting nuclides have long decay chains and can have progeny nuclides with unfavourable half-lives or chemical characteristics. A therapeutic alpha-emitter must also have suitable chemical properties that enable its delivery to the targeted tissues. For example, ^{222}Rn ($t_{1/2}$ = 3.8 d) is an alpha-emitter naturally present in the environment, but is not suitable for therapy as it is an inert noble gas. Similarly, while ^{223}Ra is approved as a non-targeting alpha-emitting radiopharmaceutical, it does not have suitable chemical properties that allow it to be chelated and bound to disease targeting biomolecules. Other practical considerations – such as the ease and cost of radionuclide production – must also be considered if a radionuclide is to be used in the widespread treatment of a disease.

The remainder of this section briefly describes the handful of radionuclides that are studied for their use in TAT, ending with ^{225}Ac. The list of nuclides below represents TAT nuclides that have been investigated to the point where they have been used in human patients. Other candidate TAT nuclides that have been proposed by the TAT field are not included (examples include ^{149}Tb, ^{226}Th, and ^{230}U).

^{227}Th

Thorium-227 ($t_{1/2}$ = 18.68 d) decays to stable ^{207}Pb via 5 alpha decays and 2 beta decays. Besides its immediate daughter nuclide, ^{223}Ra ($t_{1/2}$ = 11.4 d), all the radioactive ^{227}Th progeny have half-lives shorter than one hour. ^{227}Th is typically produced via generators containing its parent ^{227}Ac ($t_{1/2}$ = 21.8 y); note that the use of ^{227}Ac/^{227}Th generators is described in Section 7.2.4.2. While clinical results of ^{227}Th-TAT are not yet published, some clinical studies are ongoing; for more, see the review by Frantellizzi *et al* [48].

^{213}Bi

Bismuth-213 ($t_{1/2}$ = 45.6 min) decays to stable ^{209}Bi via one alpha and two beta decays. As part of the ^{225}Ac decay chain, ^{213}Bi is typically produced via ^{225}Ac/^{213}Bi generators [49]. Multiple clinical studies of ^{213}Bi-TAT have been reported for various cancers, including neuroendocrine tumours [50], carcinomas [51], myeloid leukemia [52, 53], gliomas [54, 55], and malignant melanoma [56–58].

^{212}Pb and ^{212}Bi

Lead-212 ($t_{1/2}$ = 10.6 h) decays by beta minus decay to bismuth-212 ($t_{1/2}$ = 60.6 min), which decays to stable ^{208}Pb via one alpha decay and one beta minus decay. Though not technically an alpha emitter, the decay of ^{212}Pb to stable ^{208}Pb results in alpha particle emission and both ^{212}Pb and ^{212}Bi are nuclides with potential applications in TAT radiopharmaceuticals. Both are typically obtained from the generators containing the parent nuclide ^{224}Ra. Reported clinical studies of ^{212}Pb-TAT include treatments for prostate cancers [59] and HER-2 expressing cancers [60, 61].

^{211}At

Astatine-211 ($t_{1/2}$ = 7.2 h) decays to stable ^{207}Pb via one alpha decay and one electron capture decay. ^{211}At is typically produced by irradiating bismuth targets with accelerated alpha particles. Reported clinical studies of ^{211}At-TAT include treatments for brain tumours [62] and ovarian cancer [63, 64]. For more, the reader is directed towards the review by Lindergren *et al* [65].

^{225}Ac

^{225}Ac ($t_{1/2}$ = 9.92 d) is an alpha-emitting radionuclide with properties well-suited for use in targeted alpha therapy. Its half-life is sufficiently long for radionuclides distribution, radiopharmaceutical production, and for the delivery of ^{225}Ac to tumours using large-molecule targeting vectors that, once injected, can take days to accumulate in their targeted tissues. This is useful since it is generally important to match the physical half-life of the radionuclide with the pharmacology of the radiopharmaceutical. For use with faster-localizing small molecules, the ^{225}Ac progeny nuclide, ^{213}Bi ($t_{1/2}$ = 45.6 min), can also be separated from the ^{225}Ac chain (see Section

1.2) and used in TAT if a shorter-lived radionuclide is more pharmacologically desirable. Ac also has – despite a lack of stable isotopes that has limited the study of its chemistry – favourable chemical properties for incorporation into targeting biomolecules. The four alpha emissions in the ^{225}Ac decay chain additionally provide a potentially more potent source of alpha radiation. The availability of the radionuclide, though currently limited, has so far been sufficient and reliable enough to enable the early stage development of many ^{225}Ac-radiopharmaceuticals for TAT.

Together, these properties are part of the reason that ^{225}Ac is currently one of the most widely studied TAT radionuclides. More details on the properties of ^{225}Ac and the ^{225}Ac decay chain can be found in Section 1.2, and the clinical experience is summarized in Section 1.1.5. Additionally, existing methods for ^{225}Ac production are discussed in detail in Section 1.3, including an examination of how limitations in the current production methods and ^{225}Ac availability have limited the development of ^{225}Ac-radiopharmaceuticals.

1.1.5 Clinical uses of ^{225}Ac in targeted alpha therapy

Since the use of ^{225}Ac in TAT was first proposed in 1993 by Geerlings *et al* [38], ^{225}Ac has become the alpha-emitting radionuclide most commonly used in clinical applications of therapeutic radiopharmaceuticals that use disease-targeting biomolecules. While several clinical investigations have explored treatments for neuroendocrine tumours [66, 67], gliomas [68, 69], leukemia [29, 30, 52, 70–73], and prostate cancer [25, 31, 32, 74–77], no ^{225}Ac-radiopharmaceutical compound has yet completed clinical trials and received approval for clinical use. This section summarizes the available literature on clinical applications of ^{225}Ac; for additional details, the reader is directed to recent reviews by Poty *et al* [12], or Morgenstern *et al* [78].

Neuroendocrine tumours

^{225}Ac-DOTATOC has been studied in a small number of patients for the treatment of neuroendocrine tumours. Kratochwil *et al* reported a dose escalation study involving 34 patients with progressive neuroendocrine tumours and found that multiple doses of 25 MBq every 4 months or 18.5 MBq every 2 months were tolerated, up to a cumulative activity of 75 MBq [66]. The study also demonstrated treatment efficacy in various patients that was independent of the fractionation cycle used. Kunikowska *et al* published results from a single patient who showed partial response to ^{225}Ac-DOTATOC,

as demonstrated by ^{68}Ga-DOTATATE PET. The patient received 20 MBq of ^{225}Ac-DOTATOC, followed by an additional 40 MBq of ^{225}Ac-DOTATOC and had previously been treated with beta-emitting radiopharmaceuticals ^{90}Y-DOTATOC and ^{177}Lu-DOTATOC.

Glioblastoma

Krolicki *et al* have studied TAT for treatment of glioblastoma multiforme using both ^{213}Bi and ^{225}Ac [68, 69]. ^{225}Ac studies were limited to 21 patients with a recurrence of glial tumour (grade II-IV) who received 1-6 doses (20-40 MBq) of ^{225}Ac-DOTAGA-SP via an intracranial catheter in 2-month intervals [69]. Details regarding the efficacy are not yet available; the study is ongoing [69]. It will be interesting to see how this work evolves with the inclusion of control groups and the implementation of formal clinical trials.

Leukemia

Jurcic *et al* have studied the use of ^{225}Ac and ^{213}Bi for the treatment of acute myeloid leukemia using the targeting agent lintuzumab, a humanized anti-CD33 monoclonal antibody [29, 30, 52, 70–73]. An initial study with ^{225}Ac-lintuzumab involved 18 patients who received a single dose of 18.5-148 kBq/kg. The maximum tolerable dose was determined to be 111 kBq/kg, based on dose limiting toxicities observed in patients that included death from sepsis in two patients who received 111 kBq/kg and 148 kBq/kg. Reductions in myeloblast counts were observed in 10 of 16 patients (peripheral blasts), and in 10 of 15 patients (bone marrow blasts) [73]. A subsequent Phase I trial investigated the toxicity and response rate of ^{225}Ac-lintuzumab administered in fractionated doses [71, 73]. Patients received two fractions of ^{225}Ac-lintuzumab (18.5-74 kBq/kg/fraction), with 7 days between each fraction. The maximum tolerable dose was not reached as there were no deaths within a month of treatment. Five of 18 patients had complete remission (2 with incomplete platelet recovery and 2 with incomplete blood count recovery); these responses to treatment were only observed for patients receiving $\geq$37 kBq/kg/fraction. Following this, a Phase II trial consisting of 40 patients was conducted [72, 73]. Thirteen and 27 patients were administered ^{225}Ac-lintuzumab doses of 74 kBq/kg/fraction and 55.5 kBq/kg/fraction, respectively. Patients in the 55.5 kBq/kg/fraction group experienced fewer adverse side effects (specifically, prolonged grade 4 thrombocytopenia) at a rate of 30%, compared to a rate of 46% for the 74 kBq/kg/fraction group. However, patients in the lower dose group also experienced a lower rate of

complete remissions (22%) compared to the higher dose group (69%).

Prostate cancer

The majority of clinical applications of ^{225}Ac has been as a last-line treatment for metastatic castration-resistant prostate cancer [25, 31, 32, 74–77]. A recent review by Kratochwil *et al* provides an excellent summary of the history of these treatments, including the preclinical data and a summary of the dosimetry [77]. Most of these treatments used the ^{225}Ac-PSMA-617 compound that combines ^{225}Ac via a DOTA chelator to a peptide that targets the prostate specific membrane antigen (PSMA), which is over-expressed on the surface of most prostate cancer cells. The clinical use of ^{225}Ac-PSMA-617 was first reported in 2016 by Kratochwil *et al* [25], which included results from two patients who had undergone all other available conventional treatments. The first patient, having significant skeletal metastases was contraindicated for treatment with ^{177}Lu-PSMA-617 due to expected bone marrow dose that would result. However, due to the shorter alpha-particle range compared to the beta-emissions from ^{177}Lu, this patient was therefore treated with 100 kBq of ^{225}Ac-PSMA-617 per kilogram of body weight. After two months, PET/CT scans were visually free of PSMA-positive lesions and the patient's PSA levels (a blood indicator of prostate cancer progression) had fallen from 3000 ng/mL to 0.26 ng/mL. A final 6 MBq injection of ^{225}Ac -PSMA-617 resulted in a further PSA reduction to 0.1 ng/mL. The second patient was not contraindicated for ^{177}Lu-PSMA-617, yet did not respond to successive treatments containing 7.4 GBq of ^{177}Lu-PSMA-617. However, after receiving 3 cycles of 6.4 MBq (100 kBq/kg) of ^{225}Ac-PSMA-617 the patient had a complete remission. The remarkable response of these patients to treatment with ^{225}Ac-PSMA-617 came at the expense of the only clinically reported side effect of moderate to severe xerostomia (dry mouth) due to uptake of PSMA-617 in the salivary glands.

Subsequent studies with larger patient cohorts have found that between 10-33% of patients had to stop ^{225}Ac-PSMA-617 treatment due to xerostomia [31, 74]. In 2018, Kratochwil *et al* published results from 40 patients who were treated with three 100 kBq/kg cycles of ^{225}Ac-PSMA-617 [31], and reported a median duration of tumour control of 9 months; 5/40 patients had an sustained treatment response after 2 years. These findings have also been independently confirmed by Bal *et al* [79].

Alternative ^{225}Ac-PSMA-617 treatment regimens applied by Sathekge *et al* used an initial 8 MBq treatment followed by 7, 6, or 4 MBq based on the response to previous doses, with 8 weeks between 2-4 cycles as needed

[32, 76]. This resulted in 85-100% of patients experiencing xerostomia, but none severe enough to discontinue treatment. One study involving 70 patients receiving ^{225}Ac-PSMA-617 as a last-line treatment reported 34/70 patients responding to treatment with a delayed disease progression, a median progression-free survival of 15.2 months, and a median overall survival of 18 months [76]. A second study involving patients who had not previously received chemotherapy included 17 patients, 82% of whom had a $\geq$90% reduction in PSA levels; 41% of patients had undetectable PSA after treatment and remained in remission after 1 year [32]. Combination therapy of ^{225}Ac-PSMA-617 with ^{177}Lu-PSMA-617 has also been explored as a method for reducing salivary gland toxicity [80–82].

While these clinical results for the treatment of end-stage prostate appear to be quite promising and provide remarkable before-and-after patient images that often illustrate a reduction of metastases, it is important to consider the context in which these treatments occurred to date: on an individual patient basis outside of formal clinical trials within jurisdictions permitting compassionate care use. The patients in these studies therefore have heterogenous treatment histories and the studies themselves lack specific inclusion or exclusion criteria for patients. Importantly, there is also an absence of control groups. However, the clinical results with prostate cancer are nevertheless promising and, combined with clinical results for the treatment of neuroendocrine tumours and leukemia, provide a strong motivation for increasing the availability of ^{225}Ac. In fact, increased radionuclide availability may itself help to initiate formal clinical trials.

1.2 Properties of the ^{225}Ac Decay Chain

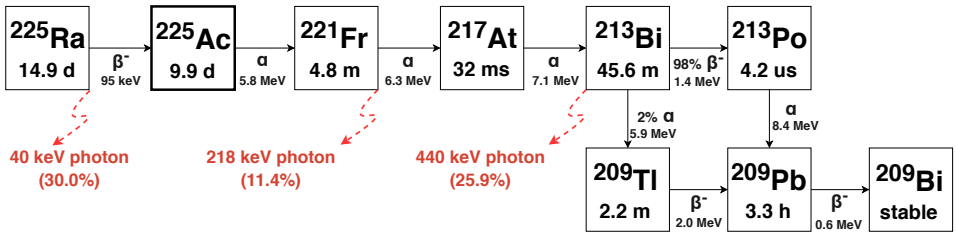

Figure 1.1: The decay chain of ^{225}Ac and its parent, ^{225}Ra, including gamma emissions with high branching ratios that are useful for radioactivity measurements.

^{225}Ac is a radioactive nuclide containing 89 protons ($Z = 89$) and 136

neutrons that decays with a half-life of 9.92 days to stable ^{209}Bi via 4 alpha- and 2 beta-decays. This ^{225}Ac decay chain, shown in Figure 1.1, thus contains 8 nuclei, including ^{225}Ac, the final stable ^{209}Bi state, and 6 radioactive intermediary nuclides that all have half-lives much shorter than ^{225}Ac.

A general understanding of decay chain dynamics combined with specific knowledge of the ^{225}Ac decay chain is essential when working with ^{225}Ac or any of its radioactive progeny. This is especially true when quantification of radioactivity is concerned, since changes in physical and chemical properties of a nucleus as the decay chain progresses can result in time-dependent radioactive emission rates that dictate methods used for radioactivity measurements. An understanding of the dynamics between ^{225}Ac and its parent, ^{225}Ra, is also necessary when discussing ^{225}Ac production.

This section will introduce these concepts, including a discussion of radioactive decay and a generalized formalism of decay chain dynamics (Section and 1.2.1), the relevant physical and chemical properties of the nuclei in the ^{225}Ac decay chain (Section 1.2.2), and the properties of its parent nuclei (Section 1.2.3). The use of these concepts in ^{225}Ac production via ^{225}Ra decay (Section 1.2.3) and in ^{225}Ac quantification (Section 1.2.4) will then be described. The concept of daughter nuclei recoil and its consequences for TAT with ^{225}Ac are then introduced in Section 1.2.5.

1.2.1 Radioactive decay and decay chain dynamics

Radioactive decay is a random process in which a nucleus transitions to a lower energy state, resulting in the emission of radiation. As mentioned in Section 1.1.3, there are multiple modes of decay, each characterized by the type of particle emitted in the process. The most common are alpha decay, beta decay, gamma decay, and electron capture. Other less common forms of decay are also possible (ex. proton decay).

Alpha decay results in the emission of an alpha particle, a positively charged helium nucleus containing two protons and two neutrons. Beta-minus decay results in the emission of an electron and an antineutrino as a neutron changes into a proton, while beta-plus decay results in emission of a positron and a neutrino as a proton changes into a neutron. Protons can also convert to neutrons via electron capture, in which the nucleus captures an atomic electron and emits a neutrino. Since the proton number, Z, changes, these types of decay all result in nuclear transmutation, the conversion of the nucleus into a nucleus of a different element. Of these most-common decay types, only alpha decay results in a change in mass number, A.

Radioactive decay without nuclear transmutation is possible via neutron

emission (in which nuclei that are both neutron-rich and proton-deficient emit a neutron) or isomeric transition decays. Isomeric transitions and gamma decays occur when a nucleus in an excited state transitions to a lower energy state via the emission of a gamma ray. Such decays typically occur after an alpha or beta decay (or other nuclear interaction) creates a residual nucleus in an excited state. (This transition of a nucleus to a lower energy state by gamma-emission is analogous to atomic electron transitions and x-ray emission. Similar to the atomic photoelectric effect, in photonuclear reactions, gamma rays can interact with nuclei to eject protons or neutrons from the nucleus.) If an excited nuclear state is long-lived enough such that its decay can be considered separate from the previous decay that created it (typically, $>10^{-9}$ s), then the nucleus is considered metastable and is referred to as a nuclear isomer of its specific nuclide; isomers can transition to the nuclide's ground state by isomeric transition or undergo other types of decay. In contrast, gamma decays occur promptly (10^{-12} to 10^{-9} s) after creation of the excited nucleus and are thus often included as part of the initial decay process that created the excited nucleus. Multiple gamma decays are often emitted as an excited nucleus decays to its ground state. These emissions are referred to as a gamma cascade and, as far as this thesis is considered, can be considered to occur simultaneously. Interactions of these gamma rays with atomic electrons can also result in ejection of these electrons from the atom, a type of secondary decay radiation called Auger particles. Reconfiguration of the remaining atomic electrons also results in the emission of additional x-rays.

Radioactive nuclei are generally not restricted to a single decay path, with some radionuclides having the possibility to undergo either alpha or beta decay, for example. The probability with which a nuclide decays through a specific process is called its branching ratio, denoted β. The branching ratio can also refer to the probability that a decay will result in a specific radioactive emission.

The type and energy of the radiation emitted by a nuclide, combined with the branching ratios for each of its possible emissions, are characteristic of that specific radioactive nuclide. These radiation signatures enable spectroscopic identification and quantification of radioactive nuclei by techniques such as gamma or alpha spectroscopy (see Sections 2.1 and 2.2, respectively). Databases of characteristic decay data are therefore essential resources. For an example of such a database used extensively throughout this work, the reader is referred to the National Nuclear Data Center maintained by Brookhaven National Laboratory [83].

While there are multiple types of radioactive decay, all are stochastic

processes. While it is not possible to predict when a radioactive nucleus will decay, all nuclides have a specific probability of decaying within a given unit of time. This probability is called the decay constant, λ, which is also characteristic of the specific nuclide. For a large collection of N nuclei of a given radioactive species, the number of decays occurring per unit time, or the radioactivity, A, is described by

$$A = \lambda N \tag{1.3}$$

and the change in the number of radioactive nuclei dN per unit time dt is described by

$$dN = -\lambda N dt \tag{1.4}$$

which has the solution

$$A(t) = A_0 e^{-\lambda t} \tag{1.5}$$

where A_0 denotes the amount of radioactivity present at time $t = 0$. From this wee see that the amount of radioactivity present decreases exponentially. The amount of time it takes for the radioactivity to be reduced by half, called the half-life, $t_{1/2}$, is often used to describe how long-lived a specific nuclide is. Note that the half-life and decay constant are related by

$$t_{1/2} = \frac{\ln(2)}{\lambda} \tag{1.6}$$

Equation 1.5 is an important relation when working with radioactivity because it allows multiple radioactivity measurements taken at different times to be decay corrected to a common point of reference. However, the change in the amount of a nuclide present over time described by Equation 1.5 assumes that none of the nuclide in question is being created – an assumption that does not hold for progeny nuclides in a decay chain.

For a radioactive parent nuclide with activity A_p decaying to a radioactive daughter nuclide with activity A_d, the change in the number of daughter nuclei per unit time is described by

$$dN_d = (\lambda_p N_p - \lambda_d N_d) dt \tag{1.7}$$

which has a general solution

$$A_d(t) = \frac{\lambda_d A_{p_0}}{\lambda_d - \lambda_p} e^{-\lambda_p t} + C e^{-\lambda_d t} \tag{1.8}$$

where $A_{p_0} = A_p(t = 0)$ describes the initial amount of the parent at time $t = 0$, and $C = \frac{A_d(t=0)}{\lambda_d} - \frac{A_p}{\lambda_d - \lambda_p}$ depends on the initial amount of the daughter present. In the case where $A_d(t = 0) = 0$, Equation 1.8 simplifies to

$$A_d(t) = \frac{\lambda_d A_{p_0}}{\lambda_d - \lambda_p}\left(e^{-\lambda_p t} - e^{-\lambda_d t}\right) \tag{1.9}$$

Equations 1.8 and 1.9 are written assuming a branching ratio of $\beta = 1$ for the decay of the parent to the daughter; if $\beta \neq 1$, these equations must be multiplied by the branching ratio.

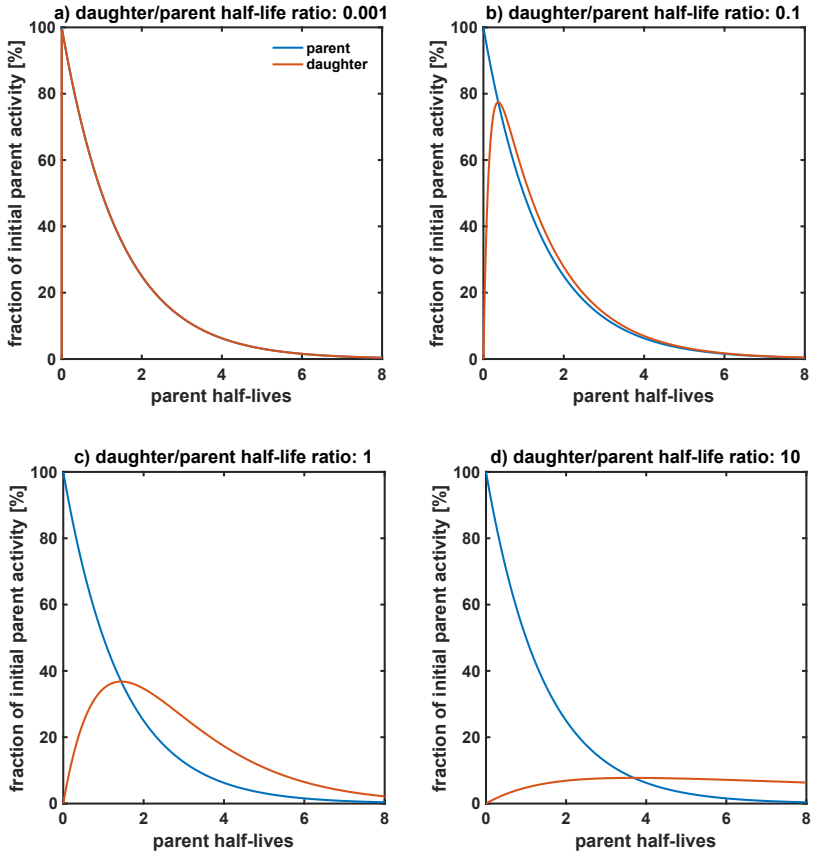

Figure 1.2: Equation 1.9 for different ratios of parent:daughter half-lives, with the number of parent half-lives on the x-axis. The equilibrium cases in plots a) and b) are also shown in Figure 1.3.

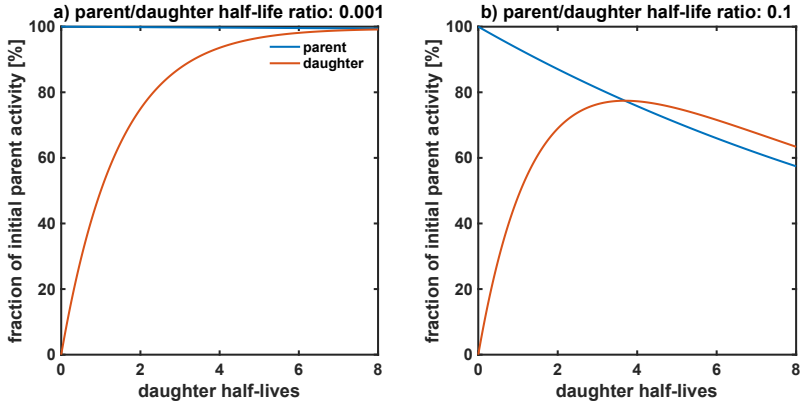

Figure 1.3: Equation 1.9 for different ratios of parent:daughter half-lives, with the number of daughter half-lives on the x-axis. These plots show a daughter nuclide as it comes into secular (a) or transient (b) equilibrium with its parent nuclide.

From Equation 1.9 one can see that the change in daughter activity over time will depend primarily on the difference between the decay constants of the parent and daughter nuclides; examples are shown in Figures 1.2 and 1.3. Two equilibrium cases occur when the parent half-life is at least multiple times greater than the daughter half-life. Secular equilibrium (Figures 1.2a and 1.3a) occurs when the parent is much more longer lived than the daughter, resulting in the daughter activity increasing until it remains constant and equal to the parent activity. In this situation, the daughter activity curve is an inverted exponential decay curve: half of the difference between the initial parent and daughter activities at $t = 0$ is recovered within one daughter half-life. Transient equilibrium (Figures 1.2b and 1.3b) also occurs when the parent is longer lived than the daughter, but when the difference in half-lives is not as great as in secular equilibrium, resulting in the daughter activity increasing until it begins to decay with the ratio between the parent and daughter activity remaining approximately constant. For both secular and transient equilibrium, equilibrium is reached after approximately five daughter half-lives.

The secular and transient equilibrium conditions enable the use of radionuclide generators, in which a parent nuclide is used to create a product that contains its daughter nuclide of interest. Once equilibrium is established, the daughter is chemically separated from the parent and used for its intended purpose. The parent then continues to produce more of the

daughter nuclide, which after a sufficient grow-in period, can be once again chemically separated from the parent.

Equation 1.8 must be used for decay correction of measurements that are affected by parent-daughter effects. This could include the measurement of a parent's activity using a radiation signal emitted by its daughter – in such situations, it is important that equilibrium is established before the measurement, if possible. Another situation could be the measurement of a daughter's activity in a sample that also contains its parent nuclide. In such situations, the amount of the daughter present at $t = 0$ is nonzero – Figure 1.4 shows how the secular equilibrium case changes when the daughter nuclide is present at $t = 0$.

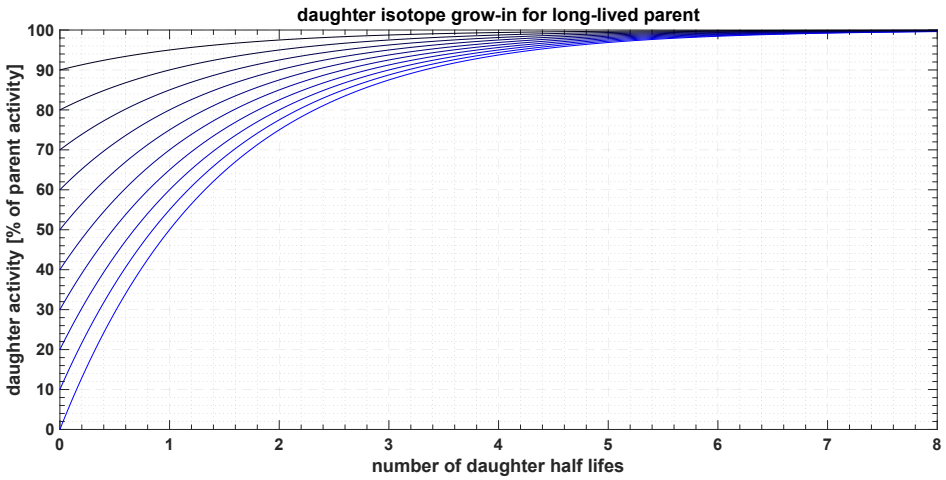

Figure 1.4: In-growth of a daughter nuclide that reaches secular equilibrium with its parent, with individual lines representing a different initial amount of daughter activity (between 0 and 100% of parent activity at time $t = 0$).

For decay chains containing multiple decays and daughter products, Equations 1.7 through 1.9 must be further modified to describe the activities of all daughter products over time. For a decay chain with n decays, the activities of each nuclide are described by

$$\begin{aligned} dN_1 &= -\lambda_1 N_1 dt \\ dN_i &= \big(\lambda_{i-1} N_{i-1} - \lambda_i N_i\big) dt \end{aligned} \tag{1.10}$$

The solution to this series of coupled differential equations can be found using Laplace transformation. The result is a solution known as the Bateman equation [84], which has the following general formula

$$A_n(t) = \lambda_n \sum_{i=1}^{n} \left[N_i(t=0) \times \left(\prod_{j=i}^{n-1} \lambda_j \right) \times \left(\sum_{j=i}^{n} \left(\frac{e^{-\lambda_j t}}{\prod_{p=i,p\neq j}^{n} \left(\lambda_p - \lambda_j\right)} \right) \right) \right] \tag{1.11}$$

1.2.2 ^{225}Ac and its progeny

Measurements of ^{225}Ac and its progeny must combine general principles of radioactive decay (described in Section 1.2.1) with characteristic decay data regarding the nuclides in the ^{225}Ac decay chain. This sections describes relevant details for each of these nuclides, with a summary provided in Table 1.1. A diagram of the ^{225}Ac decay chain is also shown in Figure 1.1.

^{225}Ac

^{225}Ac alpha-decays to ^{221}Fr with a half-life of (9.920 ± 0.003) d [85]; previous measurements reported a 10.0 d half-life [86, 87]. While it is often approximated as a pure alpha-emitter ($\beta_\alpha \approx 1$), ^{225}Ac also decays by cluster emission of a ^{14}C particle with a branching ratio of $\beta_{^{14}C} = (5.3 \pm 1.0) \times 10^{-12}$ [88, 89]; this latter decay mode is considered negligible for this work.

^{225}Ac can decay by emitting alpha-particles with energies between 5021 and 5830 keV, though the most common emissions are either at 5830 keV ($\beta = 0.507$) or near 5792 keV (5791 keV and 5793 keV emissions with branching ratios of $\beta = 0.086$ and $\beta = 0.181$, respectively) [90]. While a number of gamma rays and x-rays are emitted following ^{225}Ac decay, all have branching ratios that are too small to be easily or reliably used for quantification; the most intense gamma emissions are at 99.8 keV ($\beta = 1.00\%$), 150.1 keV ($\beta = 0.60\%$), and 188.0 keV ($\beta = 0.45\%$) [90].

Ac is a metallic element found in the oxidation state +3, and the first in the actinide series. It is chemically similar to lanthanum and other lanthanides. Since Ac has no stable isotopes, lanthanum (La) is often used as an Ac analog when macroscopic quantities are required. This absence of stable Ac isotopes has resulted in limited available data regarding Ac chemistry.

^{221}Fr

^{221}Fr alpha-decays to ^{217}At with a half-life of (4.801 ± 0.006) min [91–93]. It has two dominant alpha-emissions at 6341 keV ($\beta = 0.833$) and 6126

keV ($\beta = 0.151$). ^{221}Fr decay also results in several gamma emissions, of which the 218.0 keV ($\beta = 11.44\%$) and 100.2 keV ($\beta = 0.14\%$) are the most abundant.

All isotopes of francium, an alkali metal, are highly radioactive. The most stable, ^{223}Fr, has a half-life of only 22.8 min.

^{217}At

^{217}At decays to ^{213}Bi by alpha-decay with a half-life of (32.8 ± 3) ms and a branching ratio of 99.993% [92]. ^{217}At is typically approximated as a pure alpha-emitter: the remaining small fraction of decays are beta-decays to ^{217}Rn ($t_{1/2} = 0.54$ ms) followed by an alpha decay to ^{213}Po, where it rejoins the conventional ^{225}Ac decay chain (Figure 1.1). ^{217}At emits a 7067 keV alpha particle ($\beta = 0.9989$); other emissions of alpha particles and gamma rays exist but none are abundant enough to be relevant for most measurements [94]. Like Ac and Fr, At has no stable isotopes, with the longest-lived being ^{210}At ($t_{1/2} = 8.1$ h).

^{213}Bi

^{213}Bi has a half-life of (45.61 ± 0.06) min and decays either by beta-decay to ^{213}Po ($\beta = (97.86 \pm 0.01)\%$) or by alpha-decay to ^{209}Tl ($\beta = (2.140 \pm 0.010)\%$) [95, 96]. ^{213}Bi alpha-emissions either have an energy of 5875 keV ($\beta = 1.96\%$) or 5558 keV ($\beta = 0.18\%$) [95]. While most of its many gamma emissions are not abundant enough to be easily used for quantification, the 440.5 keV line emitted following beta-decay to ^{213}Po is the most abundant gamma emission in the ^{225}Ac decay chain ($\beta = (25.94 \pm 0.15)\%$). Following this, the 292.8 keV ($\beta = 0.43\%$) and 807.4 keV ($\beta = 0.29\%$) emissions are the most abundant [96].

With one (semi)stable isotope, the primordial ^{209}Bi ($t_{1/2} = 2 \times 10^{19}$ y), Bi is the first element in the ^{225}Ac decay chain with well-studied chemical properties. ^{209}Bi is also the final nuclide in the ^{225}Ac decay chain.

As discussed in Section 1.1.5, ^{213}Bi is another nuclide with application in TAT. In this context is it considered a pure alpha-emitter, since the short ^{213}Po half-life (3.7 μs) means that each ^{213}Bi decay will promptly result in the emission of an alpha particle, regardless of whether or not it decays to ^{209}Tl. The production of ^{213}Bi via ^{225}Ac/^{213}Bi generators is thus the most common application for ^{225}Ac outside of its direct use in TAT.

^{213}Po

^{213}Po decays by alpha emission to ^{209}Pb with a half-life of (3.708 ± 0.008) μs [92]. It has a single 8376 keV alpha emission ($\beta = 1$) and no useful gamma emissions (the most abundant is at 779 keV with a branching ratio of 0.004%) [95].

^{209}Tl

^{209}Tl beta-decays to ^{209}Pb with a half-life of (2.162 ± 0.007) min [95]. It has the highest energy gamma emissions in the ^{225}Ac decay (up to 2.3 MeV), most notably its 1567 keV gamma line with a branching ratio of 99.66%. Other abundant emissions include 117 keV ($\beta = 0.76$) and 465 keV ($\beta = 0.95$) [95]. However, because of the low probability of ^{213}Bi decaying to ^{209}Tl, the abundance of these gamma emissions per ^{225}Ac decay is much lower.

^{209}Pb

The final radionuclide in the ^{225}Ac decay chain, ^{209}Pb beta-decays to ^{209}Bi with a half-life of (3.234 ± 0.007) h [95]. Other than its single beta particle, no other radiation is emitted during ^{209}Pb decay.

Table 1.1: Summary decay properties for nuclides in the ^{225}Ac decay chain.

nuclide	$t_{1/2}$	decay mode, branching ratio (%)	prominent α and γ emissions (energy, branching ratio)
^{225}Ac	(9.920 ± 0.003) d	α, ≈ 100	α: 5830 keV, 50.7% γ: 99.8 keV, 1.00%
^{221}Fr	(4.801 ± 0.006) min	α, 100	α: 6341 keV, 83.3% γ: 218 keV, 11.44%
^{217}At	(32.8 ± 3) ms	α, ≈ 100	α: 7067 keV, 99.89%
^{213}Bi	(45.61 ± 0.06) min	β^-, 97.86% α, 2.14%	α: 5875 keV, 1.96% γ: 440.5 keV, 25.94%
^{213}Po	(3.708 ± 0.008) μs	α, 100	α: 8376 keV, 100%
^{209}Tl	(2.162 ± 0.007) min	β^-, 100%	γ: 1567 keV, 99.66%
^{209}Pb	(3.234 ± 0.007) h	β^-, 100%	none

1.2.3 ^{225}Ra, the parent of the ^{225}Ac decay chain

^{225}Ra is an important nuclide in ^{225}Ac production, since ^{225}Ac production methods often produce ^{225}Ac indirectly through ^{225}Ra production and decay (see Section 1.3 for more details). The production of ^{225}Ac via ^{225}Ra decay is especially important to this work, as further detailed and demonstrated in Chapter 7.

^{225}Ra decays primarily by beta-decay ($\beta \approx 1$) to ^{225}Ac with a half-life of (14.9 ± 0.2) d [97]; it also rarely alpha-decays to ^{221}Rn with a branching ratio of 2.6×10^{-5} [98]. A single gamma ray is emitted after ^{225}Ra beta-decay at (40.09 ± 0.05) keV with a branching ratio of $(30.0 \pm 0.07)\%$, providing the only direct signal for ^{225}Ra quantification.

The grow-in of ^{225}Ac from ^{225}Ra as described by Equation 1.9 is shown in Figure 1.5. Equation 1.9 peaks at time $t = \frac{ln\lambda_d/\lambda_p}{\lambda_d - \lambda_p}$, which for ^{225}Ra and ^{225}Ac occurs at 17.4 d, at which point ^{225}Ac activity reaches 44.5% of the initial ^{225}Ra activity. Ra and Ac have different chemical properties that make ^{225}Ra/^{225}Ac separation easy. Ra is an alkaline earth metal with oxidation state +2, and has chemical properties that are well-known through the study of the naturally occurring ^{226}Ra ($t_{1/2} = 1600$ y) [99]. Figure 1.6 shows the ^{225}Ac activity over time for a theoretical ^{225}Ra/^{225}Ac generator that is used on an operational schedule that separates ^{225}Ac every 17.4 d. The total amount of ^{225}Ac that can be obtained from a generator operated on such a schedule is described by a geometric series and is equal to $\frac{1}{1-0.445} - 1 = 0.80$, or 80% of the initial amount of ^{225}Ra.

Other parents of the ^{225}Ac Decay Chain

^{225}Ac also has other parent nuclides that are often ignored since they play minor roles in ^{225}Ac production. ^{229}Pa ($t_{1/2} = 1.50$ d) alpha-decays to ^{225}Ac with a branching ratio of 0.48% [97]. ^{225}Th also decays to ^{225}Ac by electron capture with a branching ratio of 0.1 [97]. These decay pathways are important when considering spallation-based production of ^{225}Ac (see Chapter 6).

1.2.4 Quantification of ^{225}Ac, its parent, and its progeny

Measurements of radioactivity typically involve detecting and counting the amount of radiation emitted from a sample. Combined with knowledge of the efficiency of the detector and sample-detector geometry, the branching ratio of the emitted radiation, and the measurement time, a measure

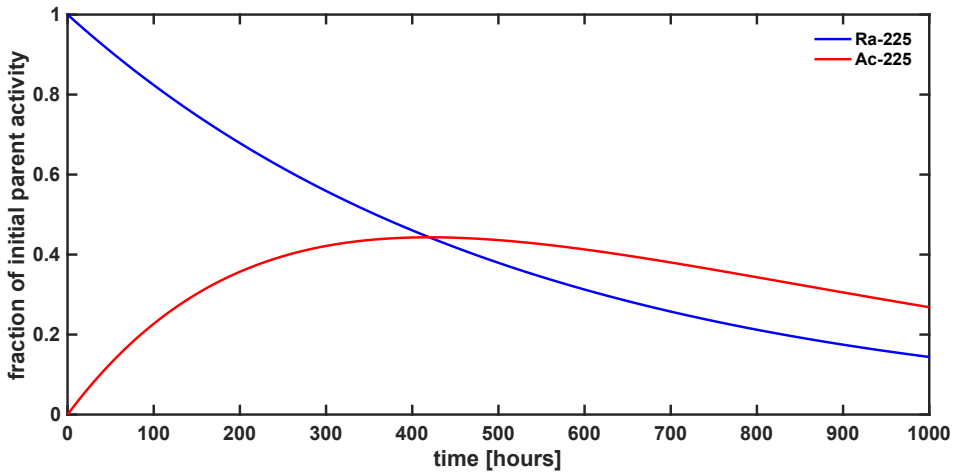

Figure 1.5: In-growth of ^{225}Ac activity from a ^{225}Ra source containing zero ^{225}Ac at time $t = 0$.

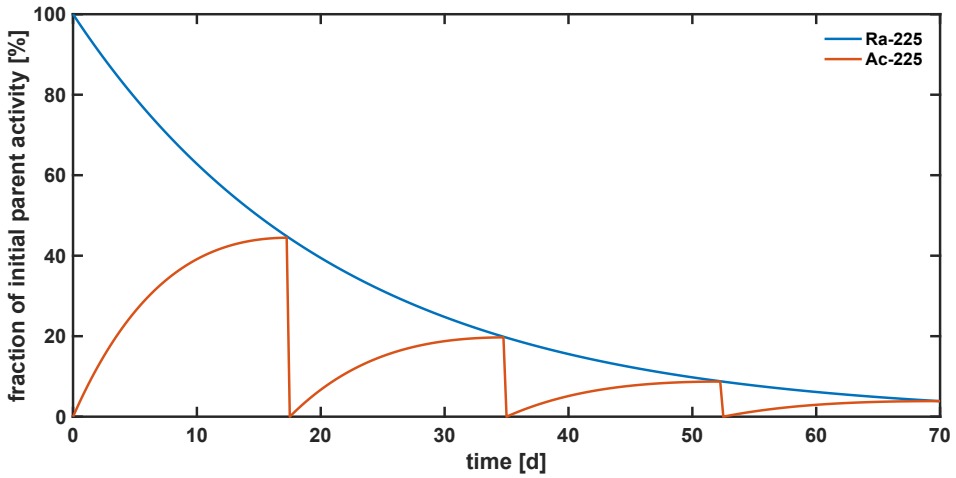

Figure 1.6: In-growth of ^{225}Ac activity from a ^{225}Ra generator, with Ra/Ac separation occurring approximately every 17.4 days.

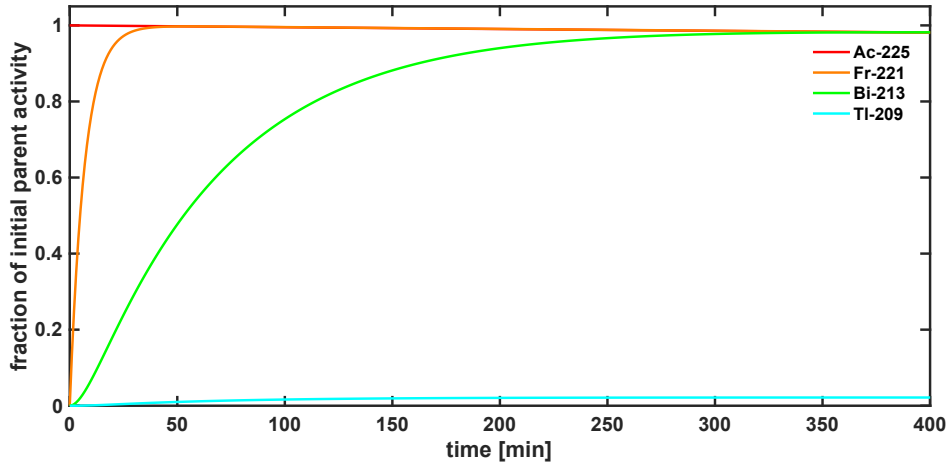

Figure 1.7: In-growth of ^{225}Ac progeny, ^{221}Fr, ^{213}Bi, and ^{209}Tl, from an ^{225}Ac source containing zero ^{225}Ac progeny at time $t = 0$.

of counts can be converted to a radioactivity value. Detection methods can include both spectroscopic and gross counting methods, depending on whether or not the energy of the detected particles is also measured. Only spectroscopic methods can be used to quantify radioactivity in samples containing either: 1) an unknown radionuclide species, or 2) multiple radionuclide species, unless the relative abundance of all nuclides in the sample are known. ^{225}Ac can complicate both these measurement methods since the different chemistry of the various nuclides in the decay chain can lead to physical separation of ^{225}Ac and its progeny, resulting in an unknown time-dependence in the radiation emitted by the sample. This time dependence can be seen in Figure 1.7, which shows the in-growth of ^{225}Ac progeny, as described by Equation 1.11, from a sample that contains no ^{225}Ac progeny at time $t = 0$; similar plots for ^{225}Ra and ^{225}Ac are shown in Figure 1.5. Radioactivity measurements of ^{225}Ra, ^{225}Ac, or any of the ^{225}Ac progeny must account for these effects by considering the state of decay chain at the time of measurement and the amount of time between the time of measurement and the sample time (the time to which radioactivity values will be decay-corrected). The remainder of this section provides examples of such considerations that may need to be applied to measurements of ^{225}Ra, ^{225}Ac, ^{221}Fr, and ^{213}Bi.

Measuring ^{225}Ra

Spectroscopic methods for ^{225}Ra quantification rely on the nuclide's only gamma-emission at 40.0 keV. As the parent nuclide for ^{225}Ac and its decay chain, ^{225}Ra is not subject to parent-daughter effects provided that no ^{229}Th is present in the sample. If necessary, the absence of significant ^{229}Th quantities can be verified by the absence of ^{229}Th gamma lines in the same spectrum. With no parents present, measured ^{225}Ra activities can be decay-corrected using Equation 1.5. However, it should be noted that ^{225}Ra measurements using the low-energy peak at 40 keV are not without challenges, as described in Section 2.1.5.2.

Gross counting methods for ^{225}Ra must occur in the absence of ^{225}Ac, since this parent-daughter pair does not reach an equilibrium state (see Figures 1.2, 1.3, and 1.5). The length of the ^{225}Ac half-life permits this, provided that ^{225}Ra measurements are completed within a couple hours after Ra/Ac separation.

Measuring ^{225}Ac

^{225}Ac can be directly quantified by gamma spectroscopy using its 150 and 188 keV gamma lines. A 100 keV peak may also be used, though can be less reliable due to interferences from the many other gamma and x-ray peaks in this energy range, as well as uncertainties in the efficiency calibration in this energy range. However, the low branching ratio of these gamma lines ($\beta \leq 1\%$) means that ^{225}Ac may not be detected in samples containing small amounts of ^{225}Ac, measurements with low counting times, or spectra containing a high background.

In such situations, ^{225}Ac is better quantified indirectly using the 218 keV ($\beta = 11.44\%$) peak of ^{221}Fr. This requires equilibrium between ^{225}Ac and ^{221}Fr, which as shown in Figure 1.7 occurs relatively quickly: the ^{221}Fr activity is within 95% and 99% of the ^{225}Ac activity within 21 and 31 min, respectively. Note that interferences from the 216 keV peak of ^{225}Ac should be accounted for in the analysis. ^{225}Ac can similarly be measured indirectly via the 440 keV peak of ^{213}Bi, though equilibrium between ^{225}Ac and ^{213}Bi takes longer to establish (^{213}Bi activity is within 95% and 99% of the ^{225}Ac activity within 201 and 292 min, respectively). Both direct and indirect ^{225}Ac measurements can then be decay-corrected using Equation 1.5 or 1.7, depending on the amount of ^{225}Ra present. Gross counting measurements of ^{225}Ac are also possible, but must occur only after the decay chain has reached secular equilibrium and in the absence of other nuclides.

Measuring ^{221}Fr and ^{213}Bi

Due to its short half-life, gamma spectroscopy measurements of ^{221}Fr activity via its 218 keV gamma line must occur promptly, before the sample can decay or, if ^{225}Ac is also present, before additional ^{221}Fr is generated. Even though parent-daughter decay-correction using Equation 1.7 can be applied, the resulting uncertainties in the final radioactivity will increase as the time between sample collection and measurement also increases. Similar considerations apply to ^{213}Bi, though its longer half-life means samples can be counted with less urgency; additional corrections for ^{221}Fr content may need to be applied to ^{213}Bi measurements, though any decay correction for ^{217}At can be neglected due to its short half-life.

1.2.5 Daughter Recoil

A final topic relevant to decay chains and TAT is the daughter recoil effect and its consequences for dosimetry. Alpha particle emission causes recoil of the daughter nucleus to occur after alpha decay because of conservation of momentum. The considerable energy of alpha particles means that the kinetic energy imparted to the daughter nucleus can be substantial. For ^{225}Ac, the emission of a 5.8 MeV alpha particle implies that the ^{221}Fr daughter nucleus will gain approximately 104 keV in kinetic energy and travel a distance on the order of 10-100 nm in water-based media. Since this recoil energy is $\sim 10^3$ times greater than the strength of any chemical bond, the ^{225}Ac progeny will no longer be bound to any targeting vector that delivers ^{225}Ac to the targeted tissue. The ^{225}Ac progeny (especially the longest-lived alpha-emitting progeny, ^{213}Bi) are then, in principle, free to migrate to other parts of the body when they can irradiate non-target tissues (most likely excretory organs such as the kidneys), potentially resulting in dose-limiting toxicity.

While a complete discussion of this topic is beyond the scope of this section, it should be noted that this effect is considered to be one the greatest limitations of TAT using decay chains of multiple alpha-emitters, particularly ^{225}Ac and ^{227}Th. For more information, the reader is directed to the reviews on this topic by de Kruijff *et al* [100] and Poty *et al* [11].

1.3 Current ^{225}Ac Production Challenges

Despite the promising early clinical results for ^{225}Ac-radiopharmaceuticals described in Section 1.1, the development of these drugs has for many years been hindered by the limited global supply of ^{225}Ac – currently only about

63 GBq (1.7 Ci) annually (see Section 1.3.1). Not only is this small supply inadequate to support a widely used and clinically approved drug, it also results in a prohibitively high cost to researchers developing ^{225}Ac-radiopharmaceuticals. This section will provide a detailed overview of existing and potential ^{225}Ac production methods, including relevant background information and literature, while demonstrating the need for increased ^{225}Ac sources and highlighting the potential of TRIUMF's facilities for achieving this goal.

1.3.1 Existing ^{225}Ac supplies

1.3.1.1 ^{229}Th Generators

Current sources of ^{225}Ac are primarily derived from radionuclide generators (see Section 1.2.1) originating from the build-up of ^{229}Th through the decay of ^{233}U stockpiles (see Fig. 1.8 of the ^{233}U decay chain). The majority of this ^{233}U ($t_{1/2} = 1.6 \times 10^5$ y) was produced between 1954 and 1970 via neutron irradiation of ^{232}Th while being investigated for its use in nuclear weapons and reactors that were never fully deployed [39]. Between 1995 and 2005, ^{229}Th ($t_{1/2} = 7340$ y) generated from ^{233}U decay was extracted from stockpiles stored at Oak Ridge National Laboratory (ORNL, Oak Ridge, TN). This ^{229}Th now exists in two sources: one at ORNL ($\sim$5.55 GBq (150 mCi), or $\sim$704 mg) [37] and another (1.7 GBq (46 mCi), or 215 mg) [36] transferred to the Institute for Transuranium Elements (ITU, Karlsruhe, Germany). A third ^{229}Th source (5.55 GBq (150 mCi), 704 mg) obtained from Russia ^{233}U stockpiles exists at the Leipunskii Institute for Physics and Power Engineering (IPPE, Obninsk, Russia) [40]. These three sources serve as generators of ^{225}Ac and its parent ^{225}Ra ($t_{1/2} = 14.9$ d) and act as the world's primary ^{225}Ac sources, producing approximately 26.6 GBq (720 mCi) (ORNL) [34] and 13.1 GBq (350 mCi) (ITU) [36] of ^{225}Ac annually. While the IPPE source contains as much ^{229}Th as the ORNL source, reported values indicate ^{225}Ac production from this source is sporadic [40, 101]. Most recently, a new ^{229}Th generator was developed at Canadian Nuclear Laboratories (Chalk River, ON) that is capable of providing up to 3.7 GBq (100 mCi) of ^{225}Ac per year [102]. Overall, the accepted global annual production from ^{229}Th is 63 GBq (1.7 Ci) [35, 49, 103–105].

While a key advantage of this production method is an ^{225}Ac product free of other actinium isotopes, 63 GBq (1.7 Ci) is insufficient to meet the current global demand for researchers. This supply will be even more inadequate should any ^{225}Ac-radiopharmaceuticals receive clinical approval and

increased use [34]. From research into fundamental ^{225}Ac chemistry to the most promising clinical trials (see Section 1.1.5), the development of ^{225}Ac radiopharmaceuticals is slowed by the small supply and resulting high cost that makes ^{225}Ac inaccessible to many researchers.

1.3.1.2 Leveraging Unique Facilities to Supply ^{225}Ac Research

Due to the high cost of ^{225}Ac, ^{225}Ac-radiopharmaceutical development at TRIUMF started by leveraging the Isotope Separator and Accelerator (ISAC) Facility [106]. This is discussed in detail in Chapter 3. Commissioned in 2000, ISAC produces beams of rare isotopes for experiments primarily studying nuclear structure and nuclear astrophysics. Irradiation of uranium or thorium targets with protons at 480 MeV results in the production of a number of isotopes that are extracted into a heterogeneous ion beam. Isotope Separation On-Line (ISOL) mass-separates these nuclides to produce an isobarically homogeneous ion beam [107]. Isolation of mass 225 produces an ion beam containing ^{225}Ra and ^{225}Ac that is directed onto an aluminum target in which the isotopes are deposited at a depth of 20 nm (as determined by SRIM [108]). Etching of the aluminum post-implantation followed by separation of ^{225}Ra and ^{225}Ac on a solid phase extraction (DGA) resin provides both a primary ^{225}Ac fraction for immediate studies, as well as a number of subsequent ^{225}Ac batches isolated through the decay of ^{225}Ra. When eluted at the peak ^{225}Ac activity (after 17.4 days of grow-in) a ^{225}Ra/^{225}Ac generator theoretically produces ^{225}Ac with an activity equal to 44.4% of the ^{225}Ra activity present at the previous elution[1], as shown in Figures 1.5 and 1.6. Further details on ^{225}Ac production at ISAC can be found in Chapter 3.

Since 2015, ^{225}Ac production at ISAC has enabled radiolabeling and preclinical studies at TRIUMF. Though ISOL provides isotopically pure ^{225}Ac sources, yields remain insignificant compared to quantities available from ^{229}Th generators. At TRIUMF, the maximum measured ISAC beam intensities of 1.3×10^8 ions/s for ^{225}Ac and 1.6×10^8 ions/s for ^{225}Ra could theoretically produce up to 370 MBq (10 mCi) of ^{225}Ac per month[2]. However, ISAC does not operate as a dedicated medical isotope production facility and ^{225}Ac production occurs within the overarching context of the laboratory's research program. Total ^{225}Ac production for 2016 was only 44.4

[1] 1 MBq of ^{225}Ra produces $\frac{1}{1-0.444} - 1 = 0.80$ MBq of ^{225}Ac from the generator if it is eluted every 17.4 days. Calculations in this section convert ^{225}Ra production values to ^{225}Ac production values using this conversion factor.

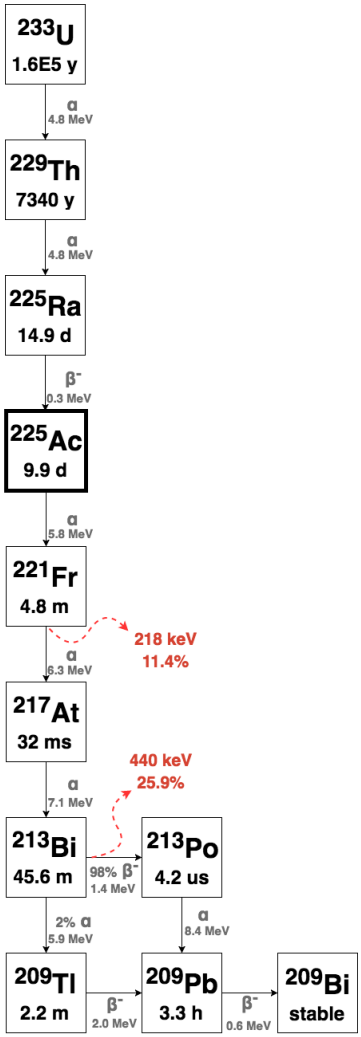

Figure 1.8: Decay schematic showing the decay and generator-based production pathways for ^{225}Ac. Gamma emissions useful for quantification of ^{225}Ac are shown in red.

MBq (1.2 mCi). ISOL methods have also been applied at ISOLDE (CERN, Geneva) to produce ^{225}Ac for radiopharmaceutical development [109].

1.3.2 The need for new ^{225}Ac production methods

Estimates of current demand for ^{225}Ac are less than 185 GBq (5 Ci) per year, however this is likely significantly tempered by both supply constraints and cost. While predicting future demand is difficult, it can be estimated to grow by about 200 to 400 GBq per year (about 5 to 10 Ci per year) for each ^{225}Ac-based therapy that is approved for clinical use[3]. Should efforts to develop ^{213}Bi-radiopharmaceuticals also increase, ^{225}Ac demands will be even higher.

As will be shown in Chapter 3, facilities like ISAC can facilitate radiopharmaceutical development by providing access to medical isotopes that are otherwise challenging to obtain. However, their application will likely remain limited to medical isotopes in the development stages. Even with potential proposed upgrades to the MEDICIS facility that could enable monthly production of up to 1.7 GBq (45 mCi) of ^{225}Ac [109], and potential upgrades to ISAC that could increase yields by a factor of $\sim$1000[4], these facilities are not expected to meet existing ^{225}Ac demand and could not supply enough ^{225}Ac to support wide-spread use of a clinically approved therapy. Such facilities instead have value as research enablers whose utility comes from their ability to provide quick access to a range of high-purity medical isotopes so that the feasibility of a given isotope's applications can be explored before having to build dedicated large-scale isotope-specific production infrastructure.

While harnessing untapped ^{229}Th supplies has the potential to more significantly impact ^{225}Ac availability, in the long term this may also be inadequate if multiple ^{225}Ac-radiopharmaceuticals become clinically approved. Due to the high costs and security issues regarding the storage of ^{233}U, in 2005 the U.S. Congress ordered the Department of Energy (DOE) to cease extraction of ^{229}Th from ^{233}U stockpiles and to instead begin down-blending

[2]For three 10-day implantations, ^{225}Ac yield $= 3 \times [1.3 \times 10^8 (1 - e^{-\lambda_{225\,Ac} \times 10d}) + 0.8 \times 1.6 \times 10^* (1 - e^{-\lambda_{225\,Ra} \times 10d}) = 370$ MBq (10 mCi)

[2]While no specific monthly production estimate is explicitly stated by Dos Santos Augusto *et al* [109], the reported estimated activity from one target is 28 MBq (0.75 mCi) from targets exchanged on a "weekly basis", which is 112 MBq (3 mCi) monthly.

[3]Assuming four rounds of 1 μCi/kg doses [29] for 10 000 patients (each 75 kg) per year per therapy, and one half-life for processing and transport.

[4]10$\times$ from increasing proton beam current from 10 to 100 μA, 6$\times$ from increasing target thickness from 10 to 60 g/cm^2, 2$\times$ more efficient beam extraction, and 8.39$\times$ from replacing uranium carbide targets with thorium targets [110].

(dilution with ^{238}U to a non-weaponizable ^{233}U concentration) and permanent disposal of the two tonnes of stockpiled ^{233}U [39]. Petitions to recover ^{229}Th before ^{233}U disposition were denied [101] until recently in 2019. From the high- and intermediate-purity ^{233}U sources within the inventory [111], this unused material represents the loss of 32.6 g (∼260 GBq or 7 Ci) of ^{229}Th or a potential 1.5 TBq (40.5 Ci) of annual ^{225}Ac production. Other estimates suggest this is a loss of 37 g (∼8 Ci) of ^{229}Th [37] and suggest a loss of 2.2 TBq (60 Ci) of annual ^{225}Ac production [101]. Without new ^{229}Th sources, ^{225}Ac production from current DOE ^{229}Th generators could increase by only 20% if the current milking schedule is optimized for ^{225}Ac production instead of unit cost [34]. Quantities of additional ^{229}Th-containing ^{233}U sources that may exist in other countries (ex. Russia) remain unknown.

Without the existence of significant additional ^{229}Th generators, the use of ^{225}Ac or ^{213}Bi in multiple approved therapies will require the development of new ^{225}Ac production methods. The remainder of this section aims to present a comprehensive list of alternative ^{225}Ac production options. The potential of each method to meet projected ^{225}Ac demand and the practical challenges associated with each method will be discussed. Possible production methods proposed in the literature are summarized in Table 1.2, while Table 1.3 summarizes other nuclear reactions capable of producing ^{225}Ac but that are considered impractical at this time. When not derived from original sources, details of calculations are provided in footnotes.

1.3.3 Nuclear reactions for radionuclide production

This section aims to introduce general nuclear reaction concepts that are relevant to medical radionuclide production. Reactions used for medical radionuclide production typically involve the bombardment of a target made of naturally occurring stable (or very long-lived) nuclei with particles containing few nucleons, such as neutrons, protons, deuterons, or alpha particles; photonuclear interactions (first mentioned in Section 1.2.1) can also be used to remove nucleons from a target nucleus. These reactions all generally result in the production of a residual nucleus (either the radionuclide of interest, or its parent) and other emitted particles. A general description of nuclear reactions can be written as

$$\text{projectile} + \text{target nucleus} \rightarrow \text{residual nucleus} + \text{emitted particle(s)} \quad (1.12)$$

which can also be written as a $T(P,E)R$ reaction, where T denotes the target nucleus at rest ($\text{KE}_T = 0$), P denotes the projectile particle, R the

residual nucleus, and E the sum of the emitted particle(s).

An example reaction is[5]

$$\alpha + {}^{14}\mathrm{N} = {}^{17}\mathrm{O} + p \tag{1.13}$$

which is also written as ${}^{14}\mathrm{N}(\alpha,p){}^{17}\mathrm{O}$.

Nuclear reactions are governed by a number of conservation laws, importantly, conservation of mass-energy and conservation of momentum (for a more complete discussion of conserved quantities in nuclear reactions, the reader is referred to the text by Schieck [113]). Nuclear reactions that result in the formation of new nuclei are inelastic ($Q \neq 0$) and can either be exoergic ($Q > 0$) or endoergic ($Q < 0$), where the Q-value is the difference between the total mass energy of the reactants and the total mass energy of the products, i.e.

$$Q = \big[(m_P + m_T) - (m_R + m_E)\big]c^2 \tag{1.14}$$

where m_i is the mass of particle i. By conservation of energy, Q can also be expressed as the change in kinetic energy during the reaction, i.e.

$$Q = (\mathrm{KE}_R + \mathrm{KE}_E) - (\mathrm{KE}_P + \mathrm{KE}_T) \tag{1.15}$$

Kinetically, reactions are possible provided that $Q + \mathrm{KE}_P > 0$ in the reference frame of the reaction's center of mass. Endoergic reactions, therefore, can only occur if enough kinetic energy is provided by the projectile. This threshold energy, ε_s, is described by

$$\mathrm{KE}_P \geq \varepsilon_s = -Q\frac{m_P + m_T}{m_T} \tag{1.16}$$

in the lab frame ($\varepsilon_s > Q$ because some kinetic energy will always be associated with the center of mass, meaning that not all of KE_P is available for the reaction).

While the threshold energy described by Equation 1.16 is a necessary requirement for a reaction to occur, it is not a sufficient requirement with respect to the projectile energy. For both endoergic and exoergic reactions, other thresholds arise from the repulsive potential the projectile may have to overcome in order to enter the target nucleus. While the complete potential experienced by the incoming projectile is the sum of the attractive nuclear potential, repulsive Coulomb potential, and the effective potential resulting

[5]This reaction is the first nuclear reaction that was observed by Rutherford in 1919 [112–114]

from centrifugal forces, in the context of barriers and threshold energies, we will here consider only the Coulomb potential (for more, see the texts by Loveland *et al* [115] or Konya *et al* [114]).

The Coulomb barrier experienced by a projectile approaching the target is described by

$$V_C = \frac{Z_P Z_T q^2}{R_P + R_T} \tag{1.17}$$

where Z_i and R_i is the proton number and radius of each particle, respectively. Neutrons experience no Coulomb barrier and the threshold energy of exoergic neutron reactions approaches zero and can be on the order of eV. However, charged projectiles must have sufficient kinetic energy to overcome the Coulomb barrier and enter the nucleus in order for reactions to occur.

Once sufficient conditions for a reaction to occur are met, the probability that it will occur is described by the reaction's cross section, σ, a key energy dependent observable of nuclear reactions. Given a flux of projectile particles, Φ, incident on a target containing N_T target nuclei, the reaction rate per unit time, $\phi = \sigma N_T \Phi$. Often, multiple reactions are possible for a given target and projectile, and the total cross section that describes the probability the these particles will interact is given by the sum of cross sections for all possible elastic or inelastic reactions, and can also be thought of as the effective cross sectional area of a single target atom. An additional discussion of cross sections is provided in Section 6.2.1.

Once a projectile enters the target nucleus, various models can be used to describe the interactions that take place, depending on the reactants and energy of the reaction (again, for more see the textbook by Schieck [113]). The most relevant model for medical nuclide production is the compound nucleus reaction model. In this model, the projectile enters the target nucleus and forms a compound nucleus, a short-lived reaction intermediate. The projectile's kinetic energy is distributed among the other nucleons of the compound nucleus and the compound nucleus is then modelled as a hot Fermi gas. The excited compound nucleus then decays by emitting nucleons, which can be modelled as evaporation of nucleons from the Fermi gas: the emitted particles exhibit a Maxwellian energy distribution with a minimum energy equal to the height of the exit barrier (roughly equal to the Coulomb barrier). The result of the interaction is the residual nucleus, R, and the emission of particles, E. The residual nucleus may also be in an excited state, and can decay by gamma emission. The cross section for compound nuclei reactions can be described as the product of the compound nucleus formation cross section and the probability that the compound nucleus will

decay through a given exit channel. An important assumption of this model is that the mode of compound nucleus decay is independent of how the nucleus was formed.

A noticeable trend described by this model is the energy dependence of the cross section for potential reaction exit channels. Considering neutron emission, as the projectile energy increases from the threshold energy, the cross section for evaporation of a single neutron increases until it becomes kinetically possible for emission of two neutrons to occur. As energy further increases, this two-neutron emission will become dominant over the one-neutron emission exit channel and the cross section for this two-neutron process will further increase until the evaporation of three neutrons becomes kinetically possible, and so on.

However, as projectile energy increases beyond approximately some tens of MeV per nucleon, the nuclear reactions are no longer described by the compound nucleus model because projectiles begin to interact with individual nucleons within the target nucleus, instead of with the target nucleus as a whole. This is explained by the decrease in the particle's de Broglie wavelength with energy ($\boldsymbol{\lambda} \propto \mathrm{KE}_P^{-\frac{1}{2}}$). For example, a 10 MeV proton has a wavelength ($\boldsymbol{\lambda} \approx 10^{-12}$cm) approximately equal to the size of a nucleus, while a 1000 MeV ($\boldsymbol{\lambda} \approx 10^{-14}$cm) proton has a wavelength smaller than the typical inter-nucleon spacing within a nucleus. The consequence of this is that the 10 MeV proton will interact with the entire nucleus – the compound nucleus process – while the 1000 MeV proton will undergo a series of two-body projectile-nucleon interactions as it passes through the nucleus – the spallation process.

This series of projectile-nucleon interactions is called an intranuclear cascade, and is only the first step in the spallation process. The intranuclear cascade results in the high-energy ejection of several nucleons from the nucleus (a number that increases with projectile energy), and leaves behind a highly excited nucleus. The remaining energy deposited in the nucleus is distributed evenly among the nucleons, and the excited nucleus decays by evaporation. The evaporation process is similar to that described previously for the compound nucleus process, however, a greater number of exit channels will be available after the more energetic intranuclear cascade, including potential emission of protons, low-energy neutrons, alpha particles, light nuclear fragments, deuterons, etc. For heavy target nuclei, the high-energy fission of the excited nucleus can also occur in competition with the evaporation process. This high-energy fission process differs from the typical low-energy neutron-induced fission process in that the fission product mass

distribution becomes more symmetric with increases in incident particle energy, diminishing nuclear shell effects that make an asymmetric distribution more kinetically favorable in low incident projectile energies. A variety of approaches are used to model the intranuclear cascade, evaporation, and high-energy fission processes of spallation reactions [116].

This concludes a brief introduction to the physical processes typically involved in the production of medical radionuclides. For a more detailed discussion, the reader is directed to the following references [113–116]. The remainder of Section 1.3 will discuss how nuclear reactions can be used for ^{225}Ac production.

1.3.4 Potential alternative ^{225}Ac production methods

1.3.4.1 Potential for ^{225}Ac Production in Nuclear Reactors

While the majority of medical isotopes today are sourced from nuclear reactors [117], the potential for reactor-based ^{225}Ac production is limited. The parent isotope, ^{225}Ra, can be produced in reactors via the ^{226}Ra(n,2n)^{225}Ra reaction, however, this reaction would require an intense source of high (>6.4 MeV) neutrons found only near the tail end of a typical breeder reactor neutron energy spectrum. Given that significantly more lower energy neutrons would be present, these irradiations would be dominated by the co-production of ^{227}Ac, a long-lived ($t_{1/2}$ = 21.8 y) and highly toxic actinium isotope, the presence of which in significant quantities may prevent the clinical approval of a pharmaceutical. To the best of our knowledge, this method has not been investigated experimentally or thoroughly modelled. However, rough estimates suggest this method could produce MBq to GBq (μCi to mCi) amounts of ^{225}Ac per month per gram of ^{226}Ra target material at a single reactor facility[6].

The potential to increase ^{229}Th stocks using reactors has also been investigated [120, 121]. Results suggest the irradiation of ^{226}Ra targets at a single reactor could produce 100 MBq (2.7 mCi) of ^{229}Th per month per gram of ^{226}Ra target material [120]. Other results have suggested this value may be closer to 59 MBq (1.6 mCi) [121]. While larger specific yields were seen when using ^{228}Ra and ^{227}Ac target materials (352 and 600 MBq (9.5 and 16.2 mCi) of ^{229}Th per month per gram, respectively), these isotopes cannot

[6]Assuming two 15-day irradiations per month, 1 gram ^{226}Ra target, average cross-section of 2 barns over the 6.4 to 16.4 MeV range [118], and average neutron flux of 1×10^{12} n/s/cm^2 over the same energy range [119] produces 52 GBq (1.4 Ci) of ^{225}Ra or 44 GBq (1.2) Ci of ^{225}Ac per month.

be supplied in sufficient quantities [120]. The ^{228}Th(n,γ)^{229}Th reaction is impractical for the same reason. For example, 2.5 thousand tonnes of natural thorium would have to be processed to produce a single gram of ^{228}Ra ($t_{1/2}$ = 5.8 y), which could potentially be used to slowly generate ^{228}Th ($t_{1/2}$ = 1.9 y). However, given the challenges and costs associated with safely handling large ^{226}Ra sources (see Section 1.3.4.4) and the resulting low ^{225}Ra or ^{229}Th yields, reactor production of sufficient ^{225}Ac quantities may not be practical.

1.3.4.2 Potential for ^{225}Ac Production Using Electron Accelerators

The use of the ^{226}Ra (γ,n)^{225}Ra reaction for ^{225}Ac production has been explored experimentally [122] and theoretically [123]. These works have explored irradiating old radium needles on electron linear accelerators (linacs) found in many cancer centres. These linacs typically use electron beams incident on tungsten targets to produce bremsstrahlung x-rays for external beam radiation therapy. Experimental results measured the production of 2.44 MBq (66 μCi) of ^{225}Ac after a single-hour irradiation by 18 MV x-rays of a 20 mg of ^{226}Ra source located 12.5 cm from the tungsten target and with incident electron beam of 26 μA average current [122]. This scales to a potential 48 GBq (1.3 Ci) of ^{225}Ac per month for a 1 g ^{226}Ra source, which could be potentially increased by irradiation parameter optimization. This method has the advantage of producing ^{225}Ac without contamination from other actinium isotopes. While co-production of ^{224}Ra occurs for photons above 12 MeV, this should not impact the desired ^{225}Ra/^{225}Ac generator as ^{224}Ra ($t_{1/2}$ = 3.7 d) decays to inert ^{220}Rn and does not result in the production of any Ac isotopes.

While many medical linacs capable of this ^{225}Ac production method may exist, these facilities are used for patient care and, to our knowledge, none are currently equipped with the infrastructure required for safe large-scale isotope production and processing. Again, the 48 GBq (1.3 Ci) of ^{225}Ac per month would likely be cost prohibitive given the challenges (see Section 1.3.4.4) associated with a 1 g ^{226}Ra target. It has been estimated that linac-based ^{225}Ac production could be increased by up to a factor of 16, although accompanied by an increase in target mass [124].

Given this low yield, sufficient ^{225}Ac production via the ^{226}Ra(γ,n)^{225}Ra reaction would require the use of a facility with significantly higher electron beam current. Though none are dedicated medical isotope production facilities, some such facilities exist for which ^{225}Ac production values deter-

mined by scaling experimental medical linac irradiation results by electron beam current can be found in Table 1.2. In addition, TRIUMF's planned Advanced Rare IsotopE Laboratory (ARIEL) facility will use a 50 MeV, 10 mA electron beam to produce intense high-energy x-rays for radioisotope production by photofission [106]. While the ARIEL electron target is intended for operation as an ISOL facility for fundamental research – not a medical isotope production facility – scaling experimental results for ^{225}Ra production on medical linacs to account for the higher current and different irradiation geometry suggests ARIEL could theoretically produce up to 74 TBq (2000 Ci) of ^{225}Ac per month from a 1 g ^{226}Ra target. However, how an isotope production target could survive a 500 kW beam is another unsolved problem. Other lower current electron accelerators, such as the existing 50 MeV, 10 μA ALTO electron accelerator (Orsay, France) [125], could theoretically produce up to 56 GBq (1.5 Ci) per month.

1.3.4.3 Potential for ^{225}Ac Production using Low Energy Proton Accelerators

The promising use of the ^{226}Ra(p,2n)^{225}Ac reaction to produce ^{225}Ac on low-energy proton accelerators was first demonstrated in 2005 by Apostolidis *et al* [126]. This reaction has a high (710 mb) cross-section peak at 16.8 MeV and could thus be performed on the many low energy cyclotrons already in use worldwide for medical isotope production. An estimated >550 of these cyclotrons have an energy over 16 MeV, some of which operate at up to 500 μA [127]. Another advantage of this approach is that it would not coproduce ^{227}Ac. While the (p,n) reaction is expected to produce some ^{226}Ac ($t_{1/2}$ = 29.4 h), measurements of co-production of ^{226}Ac have not been reported from experiments found in the literature [126]. A simple FLUKA [128, 129] simulation approximating the Apostolidis *et al* experiment suggests an ^{226}Ac activity at end of bombardment (EOB) equal to ∼11% the ^{225}Ac activity. However, unlike with ^{227}Ac contaminants, the ratio of expected ^{226}Ac to ^{225}Ac activity would decrease over time due to the differences in half-lives. The co-production of ^{225}Ra via the ^{226}Ra(p,pn)^{225}Ra reaction is expected to be negligible at the optimal energies required for direct ^{225}Ac production [130].

Given the high cross-section, large scale production of ^{225}Ac via the (p,2n) reaction would be capable of meeting long-term demand for ^{225}Ac with only a single production site. Combining available cross-section data [126] with stopping power for ^{226}Ra [108] suggests a single 20 MeV, 500 μA proton beam incident on a ^{226}Ra target (∼1 g) could produce a theoretical

maximum of 4 TBq (108 Ci) of ^{225}Ac per month[7].

The use of low energy proton irradiation of ^{232}Th to produce ^{229}Pa, which decays to ^{229}Th, has also been explored [131]. The peak measured cross-section for this ^{232}Th(p,4n)^{229}Pa reaction is 162 mb for a proton energy of 29.8 MeV. However, yields for this production method are low, with a potential to produce only 7.4 MBq (0.2 mCi) of ^{229}Th per month on a 50 MeV, 500 μA cyclotron.

1.3.4.4 Challenges Associated with ^{226}Ra Targets

Most alternative ^{225}Ac production methods discussed so far have involved the use of ^{226}Ra as a target material. Since irradiations for radionuclide production typically require targets containing macroscopic quantities (>mg) of target material, a stable or naturally occurring and long-lived target material is typically required. The closest such nuclide to ^{225}Ac, ^{226}Ra is one of only a few options – spallation reactions on naturally occurring ^{232}Th and ^{238}U being the only other possibilities for large scale ^{225}Ac production. Other potential target materials such as ^{230}Th, ^{228}Th, ^{228}Ac, and ^{228}Ra are not available in large enough quantities to be of practical use.

Despite its potential, the use of ^{226}Ra targets poses significant challenges due to the availability of the nuclide and safety hazards that complicate the target manufacturing, irradiation, processing, and recycling. Part of the ^{238}U decay chain, ^{226}Ra ultimately decays to stable ^{206}Pb and is typically found in equilibrium with most isotopes in its decay chain. ^{226}Ra was the first radioactive isotope discovered and was produced in large quantities from the 1920s for use in a number of medical and industrial applications until production stopped in 1960 [132]. Due to its high radiotoxicity, reactivity with water and air, and decay to the noble alpha-emitting ^{222}Rn gas, ^{226}Ra sources typically contained radium salts encapsulated in platinum [133]. The internal production of helium from the five alpha decays in the ^{226}Ra chain caused most of these sources to rupture, after which ^{222}Rn gases are released and ^{226}Ra salts can leak out. Even when sealed, the gamma rays emitted by ^{226}Ra progeny present external radiation hazards, with a dose rate of 8.1

[7]Activity produced by a target completely stopping the incident proton beam can be calculated using energy-dependent values for stopping power, $S(E)$, and cross-section, $\sigma(E)$, using the following equation: $A(t) = \rho\phi(1 - e^{-\lambda t}) \int_{E_0}^{0} \frac{\sigma(E)dE}{S(E)}$, given target density ρ, proton fluence ϕ and initial energy E_0, irradiation time time t, and product isotope decay constant λ. For this equation, a ^{226}Ra target density of 5 g/cm^2 was assumed, as well as an irradiation schedule of three 10-day irradiations to get a monthly production value. The integral was performed using fitted data in `MATLAB`.

mSv/h at 1 m from a 37 GBq (1 Ci, 1 g) ^{226}Ra source without shielding. The high energies of some of these gamma rays can also present shielding challenges.

While the use of ^{226}Ra sources declined after the health effects of radiation exposure became known and safer reactor-based isotopes became available, many ^{226}Ra sources remained in storage – primarily in hospitals – for decades. The hazards associated with the presence of ^{226}Ra sources lead many governments to push for the elimination of ^{226}Ra inventories and in 1996 the International Atomic Energy Agency (IAEA) established guidelines for the disposal of ^{226}Ra sources in long term geological repositories [133]. This limits the availability of large ^{226}Ra quantities, with the IAEA estimating only a few kilograms of ^{226}Ra exist among these sources worldwide [133]. Typical medical sources contained <100 mg of ^{226}Ra, with a some industrial sources containing up to 1000 mg quantities. For this reason, calculations in Table 1.2 assume 1 g as a reasonable upper limit on the size of potential ^{226}Ra targets.

New ^{226}Ra sources could be extracted from the waste of current uranium mining operations. Approximately 50 thousand tonnes of uranium ore is mined each year [134], from which ^{226}Ra is separated and disposed of as waste. With potential to extract 257 mg of ^{226}Ra from each tonne of U_3O_8 [123], this amounts to about 12.85 kg of ^{226}Ra waste per year.

Whether obtained using old sources or through uranium mine tailings, the manufacturing of ^{226}Ra targets for ^{225}Ac production would require infrastructure beyond what is typically used to make medical isotope production targets. ^{226}Ra regulatory and safety issues – particularly those associated with ^{222}Rn – would also require additional infrastructure during the target irradiation, processing, and the necessary recycling of irradiated ^{226}Ra material. While ^{226}Ra targets have the greatest potential for ^{225}Ac production per gram of target material, difficulties and costs associated with these targets is a significant disadvantage of the ^{226}Ra(p,2n)^{225}Ac and ^{226}Ra(γ,n)^{225}Ra production methods.

1.3.4.5 Potential for ^{225}Ac Production via High-Energy Proton Spallation of Thorium

An alternative ^{225}Ac production method that avoids the use of ^{226}Ra targets involves the irradiation of natural thorium targets with protons above approximately 70 MeV. This ^{232}Th(p,x)^{225}Ac reaction produces ^{225}Ac through a number of reaction pathways, though the total cross-section peaks ~40 times lower than for ^{226}Ra(p,2n)^{225}Ac production. Thorium metal is the

preferred chemical form for post-irradiation processing of the target, and isolation of MBq to GBq (μCi to mCi) quantities of ^{225}Ac from irradiated thorium metal has been demonstrated by both American and Russian research groups at Brookhaven National Laboratory (BNL, Brookhaven, NY), Los Alamos National Lab (LANL, Los Alamos, NM), and the Institute for Nuclear Research of the Russian Academy of Sciences (INR) [35, 101, 104, 135–142]. Unlike ^{226}Ra (3.7×10^{10} Bq/g, or 1 Ci/g), ^{232}Th (4.1×10^{3} Bq/g, 110 nCi/g) is not prohibitively radioactive, poses fewer radiological hazards and is readily available as a target material. Tens of kilograms are known to exist in stockpiles within a number of countries, and more thorium metal is able to be produced in bulk quantities from thorium oxide or thorium nitrate, hundreds of tonnes of which are produced annually worldwide as a by-product of rare-earth mining [134]. This availability means recycling of irradiated ^{232}Th target material may not be necessary. Another advantage of this method is that facilities already exist with demonstrated ability to perform target fabrication, irradiation, and processing. Examples of accelerator facilities capable of producing large amounts of ^{225}Ac via proton spallation are listed in Table 1.2.

While spallation of naturally occurring ^{238}U will also produce ^{225}Ac, ^{232}Th irradiation is preferred for a number of reasons. The ^{238}U(p,x)^{225}Ac reaction cross-section is $\sim$10 times lower (as modelled using FLUKA), and due to the higher density and lower melting point of uranium, thorium targets could more safely handle the higher heat load induced by higher proton beam currents. The co-production of fissile ^{239}Pu and ^{235}U is also avoided by ^{232}Th irradiation.

The spallation of thorium produces a number of radionuclides other than ^{225}Ac. While this may provide opportunity for recovery of other useful medical radionuclides, it also complicates target processing by requiring the separation of dozens of elements. Concerns also exist in the field that the amount of ^{227}Ac co-produced from thorium spallation will prevent its use as a method for clinical-grade ^{225}Ac production. An ^{227}Ac to ^{225}Ac activity ratio of 0.1-0.3% is typically found in irradiated targets at end of bombardment [136, 138–141, 143]. However, potential exists for current target processing methods to be modified to produce ^{225}Ac quantities that are free of ^{227}Ac by isolation of an radium-actinium generator [2]. Most methods already isolate radium from the irradiated thorium matrix, and if this is done days after EOB, only ^{228}Ra, ^{226}Ra, ^{225}Ra, ^{224}Ra, and ^{223}Ra will be present because of the length of their half-lives ($t_{1/2}$ = 5.7 y, 1600 y, 14.9 d, and 3.6 d, respectively), and ^{223}Ra ($t_{1/2}$ = 11.4 d). Of these, ^{228}Ra and ^{225}Ra beta-decay to actinium isotopes, while the others alpha-decay to

radon isotopes. Use of this mixture as a radium-actinium generator will produce ^{225}Ac free of ^{227}Ac. While ^{228}Ac ($t_{1/2}$ = 6.2 h) will be present after ^{225}Ra/^{225}Ac separation, the ratio of ^{228}Ac to ^{225}Ac activity (∼0.88% at the time of optimal ^{225}Ac elution [2]) will decrease with time. After sufficient ^{228}Ac decay, ^{225}Ac could then be removed from the ^{228}Th ($t_{1/2}$ = 1.9 y) produced by ^{228}Ac decay to obtain a final ^{225}Ac product with significantly reduced radioactive impurities when compared to the directly produce ^{225}Ac fraction. While the total ^{225}Ac yield from this method will be reduced by a factor of about 10, it does not prevent the use of the directly-produced, ^{227}Ac-containing batch of ^{225}Ac from being used for research or for use in ^{225}Ac/^{213}Bi generators.

Only a few existing accelerators can produce proton beams with a current and energy sufficient for large-scale ^{225}Ac production. A list of some of these facilities is given in Table 1.2 along with estimates of the maximum amount of ^{225}Ac each could produce per month. These values only include directly produced ^{225}Ac and exclude ^{225}Ac produced from ^{225}Ra generators that would increase production for each by roughly 10% to 20%. Without knowing details of each institutions's target irradiation facilities, all are compared based on their maximal yield estimates that assume a target station capable of handling a thorium target thick enough to completely stop the proton beam (the same assumption was made for ^{226}Ra (p,2n)^{225}Ac maximal yields)[8]. As a result, practical yields will be lower. For example, while TRIUMF's 500 MeV, 120 μA beam could theoretically produce 11.2 TBq (304 Ci) of ^{225}Ac per month, 3 TBq (82 Ci) of monthly ^{225}Ac production is a more practical limit given the existing target station's size and cooling capacity. Similarly, practical estimates reported for production at BNL and LANL are 165 GBq (4.5 Ci) per month [142].

[8]Calculated using the equation in Footnote 7, using a target density of 11.72 g/cm^2 and three 10-day irradiations. Thorium stopping power was obtained from SRIM [108], thorium spallation cross-sections were obtained from EXFOR [144].

Table 1.2: Summary of current and potential ^{225}Ac production methods. Production values for current sources list current production levels, while values for potential sources list estimates of maximum possible production at sample of existing and operational facilities that have dedicated stations for large-scale medical isotope production. Details of calculations or references to cited values can be found in the text. Values listed for ^{226}Ra targets assume a target mass of 1 g.

	Production Method	**Facility**	**Capabilities**	**Monthly ^{225}Ac Production [GBq (Ci)]**
Current Sources	**^{229}Th generator**	ORNL	0.704 g (150 mCi) of ^{229}Th	2.2 (0.06)
		ITU	0.215 g (46 mCi) of ^{229}Th	1.1 (0.03)
		IPPE	0.704 g (150 mCi) of ^{229}Th	2.2 (0.06)
Potential Future Sources	**^{232}Th(p,x)^{225}Ac**	TRIUMF	500 MeV, 120 μA	11266.5 (304.05)
		BNL	200 MeV, 173 μA	2675.84 (72.32)
		INR	160 MeV, 120 μA	1002.0 (27.08)
		Arronax	70 MeV, 2×375 μA	462.1 (12.49)
		LANL	100 MeV, 250 μA	12.00
		iThemba LABS	66 MeV, 250 μA	127.7 (3.45)
	^{226}Ra(p,2n)^{225}Ac	20 MeV, 500 μA cyclotron		3983.1 (107.65)
		15 MeV, 500 μA cyclotron		1157.4 (31.28)
	ISOL	TRIUMF (existing)		0.37 (0.01)
		TRIUMF (potential upgrades)		190.6 (5.15)
	^{226}Ra(γ,n)^{225}Ra	medical linac	18 MeV, 26 μA	48.1 (1.3)
		ALTO	50 MeV, 10 μA	55.5 (1.5)
	^{226}Ra(n,2n)^{225}Ra	fast breeder reactor		∼37 (1)

Table 1.3: Other methods for ^{225}Ac production.

Production Method	**Comments**
^{226}Ra(p,pn)^{225}Ra	Yields insignificant compared to ^{226}Ra(p, n)^{225}Ac production ($10^5\times$ less according to FLUKA simulation)
^{232}Th(p,4n)^{229}Pa	Low cross-section
^{Nat}U(p,x)^{225}Ac	Produces approx. $10\times$ less ^{225}Ac and ^{225}Ra compared to thorium spallation, creates fissile ^{239}Pu and ^{235}U, can handle less beam current than thorium spallation targets
^{232}Th(n,γ)^{233}U	Would take decades for ^{229}Th to build up
^{230}Th(γ,n)^{229}Th	^{230}Th not available in sufficient quantities
Reactor production of ^{229}Th	Potential target materials ^{228}Ac, ^{228}Ra, ^{228}Th, and ^{230}Th not available in sufficient quantities. Production yields from ^{226}Ra irradiation (110 MBq/month/g, or 3 mCi/month/g) too low considering cost and difficulty of ^{226}Ra source production.

1.4 Thesis Outline

The initial motivations for the research presented in this thesis were to investigate if multi-nuclide imaging of the ^{225}Ac decay chain could be used to quantify individual biodistributions of the decay chain's nuclides, thus potentially providing a more complete understanding of the decay chain's pharmacokinetics during preclinical ^{225}Ac-radiopharmaceutical evaluation. At that time, due to its scarcity and cost, the only potential readily-available source of ^{225}Ac was TRIUMF's ISAC facility (Section 1.3.1.2). Therefore, the development of ^{225}Ac production and collection at ISAC was also a goal of this work. Specifically, these efforts can be framed by the following research questions:

(1) **^{225}Ac production at ISAC:** How can ^{225}Ac be produced at ISAC? How much ^{225}Ac can be produced? Can this ^{225}Ac be used for preclinical ^{225}Ac-radiopharmaceutical development?

(2) **Feasibility of ^{225}Ac decay chain imaging:** Can available preclinical imaging instruments be used to individually quantify distributions of ^{225}Ac progeny nuclides, ^{221}Fr and ^{213}Bi? What is the performance

of the instrumentation for creating separate ^{221}Fr and ^{213}Bi images from simultaneously acquired data?

(3) **Preclinical ^{225}Ac decay chain imaging:** Can these multi-nuclide imaging methods be used to individually image dynamic ^{221}Fr and ^{213}Bi biodistributions in a preclinical model?

Questions (1) and (2) are addressed in Chapters 3 and 4, respectively. However, during the course of this work, it became evident that addressing question (3) would require greater quantities of ^{225}Ac than what could be produced at ISAC. This obstacle motivated a change in research focus towards new methods of ^{225}Ac production using alternative TRIUMF facilities. This new focus, centering on ^{225}Ac production using TRIUMF's 500 MeV Isotope Production Facility (IPF), forms the majority of the research presented herein. These new research questions include:

(4) **IPF targetry:** What are the appropriate design requirements for a thorium-based ^{225}Ac production target at TRIUMF's IPF? What does a target design that meets these requirements look like? What are the proton beam parameters that will allow this target to be safely irradiated? How much ^{225}Ac and ^{225}Ra can be produced in these targets at IPF?

(5) **^{232}Th(p,x) radionuclide production:** What other radionuclides are co-produced in ^{225}Ac production targets at IPF? How accurate are Monte Carlo methods for estimating the resulting radioactive inventory? What are the ^{232}Th(p,x) cross sections for ^{225}Ac and ^{225}Ra production, and for the production of other relevant radionuclides?

(6) **Chemical separation of ^{225}Ac from IPF targets:** How can existing radiochemical separation methods for isolation of Ac from proton irradiated thorium be modified such that they can be applied for IPF targets, using TRIUMF's radiochemistry facilities? Can the production of ^{225}Ra during thorium irradiation be used to chemically isolate a generator-produced Ac product with fewer long-lived impurities (specifically, ^{227}Ac) than the directly-produced Ac product? And, how does the quality of these two Ac products compare to each other?

Questions (4), (5), and (6) are addressed by Chapters 5, 6, and 7, respectively. Each of the research chapters in this thesis (Chapters 3 through 7) have been published in peer-reviewed journals in some similar form to how

they appear herein. Therefore, each chapter is structured to read as a standalone paper and includes background information and methods specific to that chapter. General methods that are employed in multiple research chapters are introduced in Chapter 2. Finally, Chapter 8 provides a summary and overall perspective on these research chapters as a whole.

2 Methods Used for Radioactivity Quantification and Estimation

The quantification of radioactivity is the principle measurement used to generate the majority of the data presented in this thesis and is used in every research chapter (Chapters 3 through 7). While measurement methods that are specific to each chapter are described therein, Chapter 2 describes these radioactivity quantification techniques in general, focusing on aspect of the methods that are applicable to all chapters. The measurement methods presented include gamma spectroscopy (Section 2.1) and alpha spectroscopy (Section 2.2). Section 2.3 then introduces FLUKA simulations, a method used for estimating the radioactive inventories of irradiated materials in situations where empirical measurements (gamma or alpha spectroscopy) are impossible or impractical.

2.1 Gamma Spectroscopy

Gamma spectroscopy was essential throughout the work presented in this thesis and comprises the majority of the data that is presented, especially for Chapters 6 and 7. Therefore, a thorough description of this technique and how it was applied to the research is warranted.

Section 2.1 describes the methods and procedures used to set up, calibrate, commission, and maintain the TRIUMF Life Sciences Division's High-Purity germanium (HPGe) detector, located in the RCR1 lab, which was the gamma-ray spectroscopy workhorse used throughout all chapters of this thesis. The aims of this section are to:

1. Document calibration procedures, operating parameters, and initial performance that may need to be referenced during the detector's lifetime

2. Demonstrate the detector's ability to reliably perform accurate quan-

titative assays of radioactive samples, as well as the limitations of such measurements

3. Provide a reference manual for the many user-created files that are regularly referenced and required for use of the detector

In fulfillment of these objectives, the basic functioning of the detector is outlined, followed by the steps taken for its setup and calibration. The use and location of key files is also described. Experiments used to validate the accuracy of the detector are also presented.

2.1.1 Background

HPGe gamma spectroscopy detectors permit precise, high energy resolution (<1 keV), quantitative measurements of radioactive samples. Gamma rays that interact and deposit energy within the detector's semi-conducting germanium crystal elevate electrons into the conduction band. A high (kV) electric potential accelerates these electrons towards a collecting cathode, creating an electronic pulse with an integrated charge directly proportional to the energy deposited by the gamma ray. This electronic pulse is amplified before being set to a multi-channel analyzer (MCA), which records the integral of the amplified pulse in a histogram. This histogram is referred to as a gamma ray spectrum.

Detectors and samples being measured are typically placed within a thick lead shielding well with a heavy movable lid in order to eliminate signal from other nearby radiation sources. Due to the small conduction band gap of germanium, the crystal must be cooled by liquid nitrogen whenever the high voltage is applied in order to prevent catastrophic damage to the detector. Therefore, the detector is thermally connected by a thick rod to a dewar filled with liquid nitrogen that sits below the shielding well. Since the positioning of samples relative to the detector significantly affects measurements, a 3D printed sample holder is used to provide reproducible detector-sample configurations.

The Genie 2000 software suite (version 3.4, Canberra Industries Inc.) was used to acquire and analyze gamma ray spectra. Two other similar detector systems exist at TRIUMF and are maintained by the Radiation Protection Group (RPG), also operated using the Genie 2000 software suite.

Setup, calibration, commissioning, and routine use of these detectors requires the creation of a number of critical files that must be referenced during data acquisition and analysis, including:

- **MCA Interface Definition (MID) files**, which configure the MCA parameters
- **Energy Calibration files**, which define the energy range of each MCA channel as well as the expected shape (FWHM and low-tail) of gamma peaks
- **Peak-to-Total Calibration files**, which describe ratio of the number of counts in a photopeak to the number of counts in the Compton continuum as a function of photopeak energy, required for use of the Genie 2000 Cascade Correction algorithm
- **Geometry files**, which describe detector-sample geometries for the Genie 2000 Cascade Correction algorithm
- **Efficiency Calibration files**, which describe counting efficiency as a function of energy for a given detector-sample geometry
- **Background Spectra files**, which account for radiation sources within the detector shielding well
- **Library files**, which define radionuclides and their gamma emissions and are used to identify nuclides within a spectrum
- **Certificate files**, which define calibration sources
- **Analysis Sequence files**, which define customizable automated algorithms for analyzing spectra
- **Calibration Spectra files**, the raw data used for calibrating the detector
- and of course, **data files** themselves

Section 2.1 aims to record the creation of these files, and demonstrate that they work both individually and together to permit reliable and quantitatively accurate assays of radioactive samples.

Mixed calibration sources containing ^{133}Ba ($t_{1/2}$ = 10.6 y) and ^{152}Eu ($t_{1/2}$ = 13.5 y) were used for calibrations. These sources were provided by Stuart Hunt & Associates (Mississauga, ON) and have activity concentrations traceable to the National Institute of Standards and Technology (NIST). All values describing physical properties of nuclides (half-lives, gamma ray energies etc.) are taken from the NuDat database maintained by Brookhaven National Laboratory [83].

2.1.1.1 Hardware Setup

The following settings were used when setting up the high voltage unit and amplifier:

- Potential: -3500 V
- Coarse gain: 100
- Fine gain: 6.26
- Pulse shaping: 2 μs

The 2 μs pulse shaping was selected as the value that provided the best energy resolution (see Appendix A.1). This parameter defines the time interval over which pulses are integrated in the detector during detection of events.

The file `GAMMA.mid` defines the the MCA (serial #04049755) parameters and is used by the Genie 2000 Acquisition and Analysis software to communicate with the detector.

2.1.2 Energy and shape calibration

Energy-channel and peak shape calibrations are performed simultaneously in Genie 2000. Since spectra are stored in the MCA as number of counts per MCA channel, it is necessary to perform an energy calibration so that specific energy ranges can be assigned to each of the 8192 channels. Shape calibration, including both peak width and low-tail calibrations, provides useful information when performing fits to measured data, as expected peak widths can be used to restrain fits in multiplets (overlapping peaks), or can indicate if a peak may be a multiplet.

To perform these calibrations, a spectrum was acquired using a source (R-01107a) containing ^{152}Eu (1.5050 $\pm$ 0.04515 kBq) and ^{133}Ba (1.5147 $\pm$ 0.0454 kBq) in a 20 mL vial, positioned at approximately 20 cm above the detector end cap for a 24 hour data acquisition. The analysis sequence `enerCal` is used to analyze spectra before performing an energy and shape calibration. This analysis sequence initiates the Genie 2000 Interactive Peak Fit Tool, and it is critical that the user uses this tool to ensure peaks used in the calibrations have high-quality fits. The fits used in this calibration are illustrated in Appendix A.2. The energy and shape calibrations are then initiated using the certificate file `energyCalibration.ctf`. These fits were then used to perform the energy, FWHM, and low-tail calibrations described

in Sections 2.1.2.1, 2.1.2.2, and 2.1.2.3. Data in these sections are from a calibration performed on 2016-09-24.

2.1.2.1 Energy Calibration

Table 2.1 shows the values used to perform the energy calibration using a 3rd-order polynomial fit. An energy calibration is shown in Figure 2.1 and indicates the energy response is highly linear over the full range of 0.4 to 2001.0 keV.

Table 2.1: Gamma peaks used by the `energyCalibration.ctf` certificate file along with values from an energy calibration performed on 2016-09-24. Peak centroid values were determined using Genie 2000's Interactive Peak Fit Tool. These values are plotted in Figure 2.1.

Centroid Channel	Energy [keV]	Nuclide
216.93 ± 0.02	53.1622 ± 0.0006	^{133}Ba
331.11 ± 0.01	80.9979 ± 0.0011	^{133}Ba
498.19 ± 0.01	121.7817 ± 0.0003	^{152}Eu
1131.08 ± 0.01	276.3989 ± 0.0012	^{133}Ba
1239.35 ± 0.01	302.8508 ± 0.0005	^{133}Ba
1408.90 ± 0.01	344.2785 ± 0.0012	^{152}Eu
1456.92 ± 0.01	356.0129 ± 0.0007	^{133}Ba
1570.83 ± 0.01	383.8485 ± 0.0012	^{133}Ba
3187.68 ± 0.02	778.9045 ± 0.0024	^{152}Eu
3945.18 ± 0.02	964.057 ± 0.005	^{152}Eu
4443.30 ± 0.02	1085.837 ± 0.010	^{152}Eu
4550.76 ± 0.01	1112.076 ± 0.003	^{152}Eu
5762.27 ± 0.03	1408.013 ± 0.003	^{152}Eu

2.1.2.2 Peak Width Calibration

The width of gamma peaks on HPGe detectors is known to be energy dependent. Calibration of the peak FWHM values provides useful information when performing fits to measured data, as expected peak widths can be used to restrain fits in multiplets, or can indicate if multiple gamma rays are present within a peak. Values used for the 2016-09-24 calibration are shown in Table 2.2.

Unlike the energy calibration, Genie 2000 provides no flexibility in the equation used to fit the shape calibration data. The following equation is

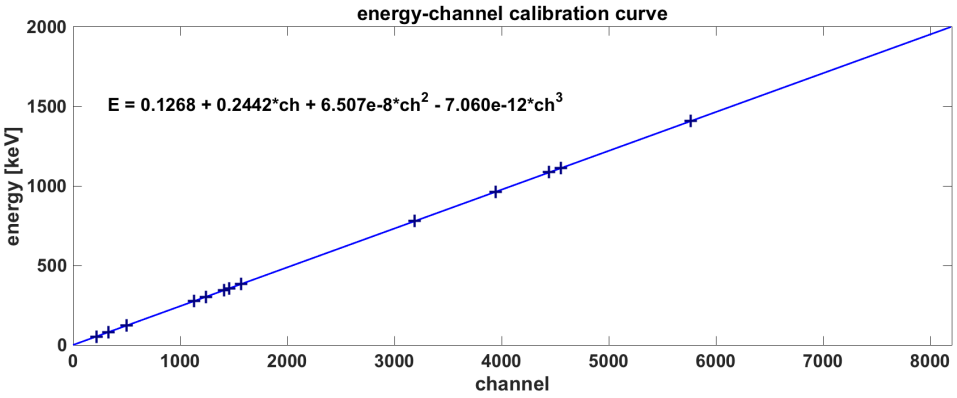

Figure 2.1: Energy calibration curve from 2016-09-24. The uncertainties for each data point are listed in Table 2.1.

used by Genie 2000 for the FWHM calibration:

$$FWHM = a + b * E^{0.5} \tag{2.1}$$

where E is the energy of the peak. The poor suitability of this equation is shown in Figure 2.2. While an accurate width calibration is not essential to the analysis of spectra, the user should keep this in mind when using calibration-based FWHM values during any analysis with Genie 2000. A linear fit to this data is much more appropriate, as shown in Figure 2.2. A table of predicted FWHM values based off of a linear calibration curve is given in Appendix A.3.

The exception to predictable peak widths are annihilation photons, which appear broader than peaks from gamma rays emitted directly by a nucleus, as shown in Figure 2.2. This is a result of the underlying energy distribution of annihilation photons, which occurs since not all positrons annihilate at rest.

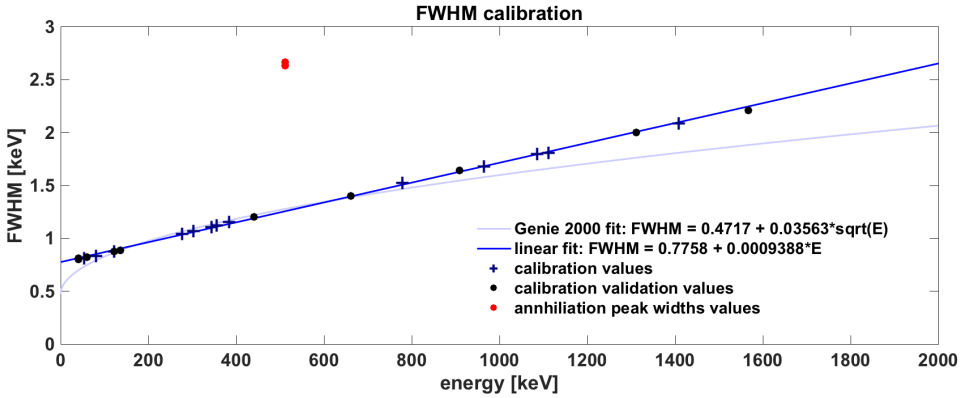

Figure 2.2: Peak width calibration curves determined by Genie 2000 and by a linear fit. The poor agreement of the Genie 2000 calibration curve is evident. This calibration was performed on 2016-09-24. Verification of the calibration was performed on 2016-12-05 using an number of different radionuclides. The broader nature of annihilation photons is also shown.

Table 2.2: Peak shape calibration values determined during an energy calibration on 2016-09-24. The resulting width and tail calibrations are shown in Figures 2.2 and 2.3, respectively.

energy [keV]	**FWHM [keV]**	**low tail [keV]**
53.16	0.813 ± 0.002	0.125 ± 0.007
81.00	0.833 ± 0.001	0.168 ± 0.010
121.78	0.877 ± 0.001	0.227 ± 0.010
276.40	1.040 ± 0.001	0.232 ± 0.012
302.85	1.067 ± 0.001	0.310 ± 0.032
344.28	1.106 ± 0.001	0.315 ± 0.034
356.01	1.121 ± 0.001	0.335 ± 0.017
383.85	1.153 ± 0.002	0.291 ± 0.029
778.90	1.526 ± 0.001	0.327 ± 0.020
964.06	1.680 ± 0.002	0.330 ± 0.015
1085.8	1.800 ± 0.002	0.398 ± 0.027
1112.08	1.807 ± 0.002	0.376 ± 0.015
1408.01	2.085 ± 0.002	0.437 ± 0.017

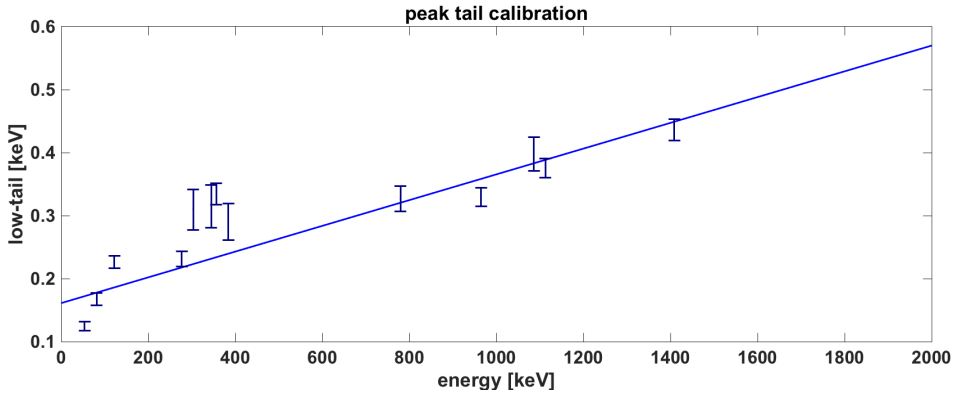

Figure 2.3: Peak low-tail values and the calibration curve determined by Genie 2000 using a linear fit. Values and uncertainties are determined by Genie 2000. This calibration was performed on 2016-09-24.

2.1.2.3 Peak Low-Tail Calibration

Peaks measured with HPGe detectors are known to exhibit a low-energy tail that slightly skews the otherwise Gaussian-shaped peak towards lower energies. The result is peaks that are not symmetrical. For more information on the definition of the low-tail, the reader is referred to p. 252 of *Genie 2000 Customization Tools Manual* [145]. The size of the low tail is also energy dependent and is calibrated along with the FWHM during shape calibrations. Genie 2000 uses a linear fit for the low-tail calibration. Though calibration of this feature has little affect on results, values from a calibration performed on 2016-09-24 are shown in Table 2.2 and are plotted in Figure 2.3.

2.1.3 Background spectra

It is especially important during long (>12 hour) data acquisitions or when assaying samples containing low (∼mBq) levels of radioactivity that the background radiation environment be taken into account during the analysis. Regular assessment of the background is also required to monitor the detector for radioactive contamination that may affect future measurements.

Background correction during data analysis in Genie 2000 is performed by referencing a previously acquired and analyzed background spectrum. The background spectrum should be acquired over a minimum of 24 hours with the sample holder to be used in future measurements empty but in-

side the detector well (in case the sample holder becomes contaminated). The peaks within the background spectrum must be located and their areas determined before the spectrum can be used for background correction. The area of peaks found in the background spectrum are subtracted from any overlapping peaks in the spectrum being analyzed. No subtraction of the Compton scatter continuum is performed – this is done by the peak area algorithms – so only photo*peaks* can affect the background. Photons that make it through the shielding well as scatter will only contribute to the continuum and will not affect the background. Therefore, background gamma-radiation with potential to affect measurements will originate from inside the detector well.

Even if the interior well of the detector is free of user-generated contaminants, a number of peaks will still be present in background spectra from the decay of the naturally occurring, long-lived radionuclides ^{40}K, ^{232}Th , ^{235}U, ^{238}U, and their progeny. The library file `BACKGROUND.NLB` listed in Appendix A.4 contains a list of gamma lines that may be seen in a background spectrum because of these nuclides. The presence of these radionuclides is not significant enough for these peaks to become detectable during data acquisitions shorter than a couple of hours.

It is recommended that a $\geq$24-hour background spectrum be acquired weekly on the detector (preferably over the weekend) to check for contamination and to provide up-to-date information for accurate background correction. Table 2.3 lists peaks typically seen in 24-hour background acquisitions on the RCR1 detector, based on five acquisitions during the fall of 2016. A comparison of these peaks with background spectra acquired from other similar detectors on the TRIUMF site is also provided.

After acquisition of the background spectrum, analysis should be performed using the user-defined `BACKGROUND` sequence. Due to the low signal-to-noise ratio expected in background spectra, this sequence uses a low-sensitivity peak search algorithm to locate peaks at 4-sigma above the continuum. The peaks are then compared to gamma lines from the naturally occurring radioisotopes listed above using the library in Appendix A.4. Any peaks listed as unidentified that are not found in Table 2.3 should be further investigated as a possible source of detector contamination.

Table 2.3: Peaks (>20 keV) seen in typical 24-hour background acquisition on the detector in TRIUMF's RCR1 lab, including a comparison with other detectors at TRIUMF and the naturally-occurring source of the peaks.

energy [keV]	**seen on other detectors?**	**origin**
46.54	✓	^{210}Pb
53.4	✓	unknown
55.6		unknown
63.29	✓	^{232}Th
x-rays (70-100 keV)	✓	multiple sources
139.6	✓	unknown
143.76	✓	possibly ^{235}U
185.71	✓	^{235}U
198.4	✓	unknown
238.63	✓	^{212}Pb
511.00	✓	multiple sources
583.19	✓	^{208}Tl
609.32	✓	^{214}Bi
911.8	✓	unknown
1120.29		^{214}Bi
1460.82	✓	^{40}K

2.1.4 Peak-to-total calibration and cascade correction

2.1.4.1 Cascade Summing Effects

Most nuclear decays result in the emission of multiple gamma rays, typically separated by mere picoseconds or nanoseconds. Compared to the resolving time of the detector (2 μs) these emissions are effectively simultaneous. If one or more of these gamma from a single decay interact with the detector, the sum total of energy deposited in the crystal is recorded instead of the energies of the two (or more) individual gamma rays. These gamma lines are said to be subjected to Cascade Summing Effects. For a detailed overview of the theory of Cascade Summing and Correction, the reader is referred to Appendix D of the Genie 2000 Customization Tools Manual [145]. A brief example from that document is summarized below.

In transition to the daughter nucleus ground state, the nucleus can transition through simultaneous emission of γ_1 and γ_2 or through emission of γ_3, where the energy, E_{γ_3}, of γ_3 is equal to $E_{\gamma_3} = E_{\gamma_1} + E_{\gamma_2}$. If γ_1 and γ_2 both interact with the detector, then the total energy recorded by the detector will be equal to γ_3. A measurement of the activity of the parent nuclide based on γ_1 or γ_2 will therefore be subject to cascade summing *losses*, while a measurement based on γ_3 will be subject to cascade summing *gains*. Similar effects occur when x-rays or annihilation photons are also present.

Since it is also possible for either of γ_1 or γ_2 to deposit only part of their energy in the detector crystal, correction of cascade summing effects requires determination of the *total* efficiency of the detector as a function of energy, in addition to the peak efficiency. These values are typically expressed as a peak-to-total ratio, defined as the number of counts in the photopeak over the number of counts in the entire spectrum, assuming that there is only one peak in the spectrum. A peak-to-total ratio calibration is used by patented Genie 2000 algorithms to correct for cascade summing effects. These algorithms also require a geometry file made using the Genie 2000 Geometry Composer that describes the detector-sample geometry in question.

Nuclear decay and emissions data containing information needed to perform cascade correction for a given isotope is stored in the Genie 2000 True Cascade Summing Library. This library is non-editable and radionuclides not found in the library cannot be corrected for cascades. A list of these nuclides is provided in Appendix A.5. For more information about the library, the reader is referred to the Genie 200 documentation [146].

Table 2.4: Spectra used for the peak-to-total calibration, including the origins of calibration sources used.

energy [keV]	nuclide	side peaks [keV]
40.0	^{225}Ra	n/a
59.4	^{241}Am	n/a
122.0	^{57}Co	136.8
511.0	^{64}Cu	1345.8
661.9	^{137}Cs	n/a
909.7	^{89}Zr	511.0

2.1.4.2 Peak-to-Total Calibration for Cascade Correction

Peak-to-total ratios must be measured using spectra acquired for single-nuclide sources that are free of cascade summing effects. Table 2.4 lists the sources used. This makes sourcing of the calibration sources difficult: only three suitable sources (Table 2.4) were available on site at TRIUMF. Fortunately, the regular production of short-lived isotopes at the TR-13 and the ISAC Implantation Station (IIS) provided access to the other three sources. The geometry-dependence of peak-to-total ratios is known to be negligible, so the geometries of spectra used for the calibration was not kept consistent. Spectra used in the calibration are located in the `CAMFILES\DetectorMaintenance\PTcal` directory.

The spectra in Table 2.4 were first analyzed with the user-defined `p2tcal` analysis sequence, which performs peak location and nuclide identification for only the peaks listed in Table 2.4. Any other located peaks were deleted from the analysis. Since ^{57}Co, ^{64}Cu, and ^{89}Zr spectra each have a second photopeak that will also contribute to the total number of counts in the spectrum, these 'side peaks' were also included in the analysis. Genie 2000 uses an iterative algorithm to correct for the presence of these additional peaks during the peak-to-total calibration. Low-energy noise and x-ray peaks were removed by using an extrapolation channel of 140 (34.3 keV). Nuclide identification via `p2tcal` is performed using the library `PTCAL.nlb`, an editable library provided by the Genie 2000 installation that must be located in the `CAMFILES` directory in order for peak-to-total calibration to be performed. This library had to be edited so that ^{64}Cu, ^{89}Zr, and ^{225}Ra could be included in the calibration. A copy of this updated library is listed in Appendix A.6.

The results of this calibration are shown in Figure 2.4. A spline fit with a cross-over energy of 122 keV was used, as recommended by the Genie 2000 Operations Manual [147]. It is likely that this calibration could be improved

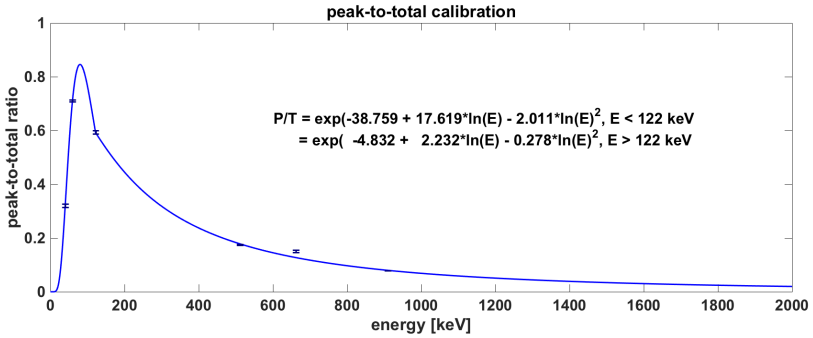

Figure 2.4: Peak-to-Total Calibration performed 2016-12-23. Figure shows the calculated calibration curve as well as the values (including error bars) measured during the calibration.

over time as more sources are made available during work from within the Life Sciences group.

2.1.5 Efficiency calibration

Since the probability of detecting a gamma ray depends on its energy, an energy-efficiency calibration is required for quantitative gamma spectroscopy. The peak efficiency, defined for a given gamma ray as the number of gamma rays of that energy detected over the number emitted, is determined by the source-to-detector distance (SDD), the source shape, the materials between the source and the detector, and the energy-dependent probability of the gamma ray stopping within the detector crystal. Together these features are referred to as a geometry, and an efficiency calibration must be performed for each geometry for which quantitative spectroscopy is desired. While the efficiency decreases at higher energies due to decreased probability of interacting with the detector, it also decreases with low energies as the probability of being attenuated before reaching the detector increases.

The geometry discussed in this section is a 20 mL vial (containing a 20 mL volume) positioned approximately 20 cm above the detector cap. This is the greatest SDD that will allow the 20 mL vial to fit inside the closed shielding well of the detector.

Table 2.5: Expected and measured ratios of individual peak areas within multiplets used in the efficiency calibration, as determined using the Interactive Peak Fit Tool.

peaks in multiplet [keV]	**measured peak area ratio (high/low)**	**expected ratio (high/low)**	**nuclide**
30.63, 30.97	2.11 ± 0.05	1.83 ± 0.08	^{133}Ba
39.52, 40.12	1.90 ± 0.02	1.79 ± 0.06	^{152}Eu
79.61, 81.00	12.15 ± 0.18	12.42 ± 0.26	^{133}Ba

2.1.5.1 Efficiency Calibration for Cascade-Free, Low Sensitivity Geometries

A 20 mL calibration source (R-01107a), containing (30.05 ± 3.0%) kBq of ^{133}Ba and (30.23 ± 3.0%) kBq of ^{152}Eu, was positioned approximately 20 cm from the surface of the detector using the sample holder shown in Figure 2.5. A spectrum was acquired for 12 hours on 2016-09-22. The analysis sequence `effiCal` was used to locate peaks in the spectrum and initiate the Interactive Peak Fit Tool. The Sum/Non-linear LSQ Fit algorithm [145] was used to determine the areas of all singlet and multiplet peaks. Unlike the energy calibration, multiplet peaks were used for the efficiency calibration to provide additional data points in the low-energy, high-slope regions of the efficiency calibration curve. To ensure quality multiplet fits, care was taken to ensure that the fit resulted in individual peaks with nearly equal FWHMs and that the ratios of individual peak areas matched the expected branching ratios of peaks within the multiplet as closely as possible. Measured and expected peak area ratios for peaks in all relevant multiplets are shown in Table 2.5. The fits for all peaks used in efficiency calibration are shown in Appendix A.7.

With all peak areas determined, the efficiency calibration was performed using the certificate file `R01107a.ctf`. Care was taken to ensure the correct peak area from within each multiplet was selected by Genie 2000 during this step of the process, and manually corrected if necessary. Efficiency values determined for each peak are shown in Table 2.6. A spline fit with a crossover energy of 81 keV was used to determine the efficiency calibration curve from these data points, as shown in Figure 2.6.

This calibration is stored in the calibration file `effiCal_20mL_20cm.cal`.

Table 2.6: Measured efficiency values for all peaks used to determine the calibration curve shown in Figure 2.6.

Energy [keV]	**Measured Efficiency**	**Uncertainty [%]**
30.63	0.00140	4.41
39.52	0.00188	3.88
53.16	0.0022	3.72
79.61	0.00231	3.83
81.00	0.00226	3.14
121.78	0.00215	3.06
223.24	0.00144	3.62
244.70	0.00131	3.09
302.85	0.00105	3.11
344.28	0.00091	3.11
356.01	0.00089	3.00
383.85	0.00081	3.14
411.12	0.00076	3.22
778.90	0.00040	3.17
867.38	0.00036	3.77
1085.84	0.00030	3.18
1089.74	0.00030	3.45
1112.08	0.00029	3.19
1299.14	0.00026	4.37
1408.01	0.00023	3.09

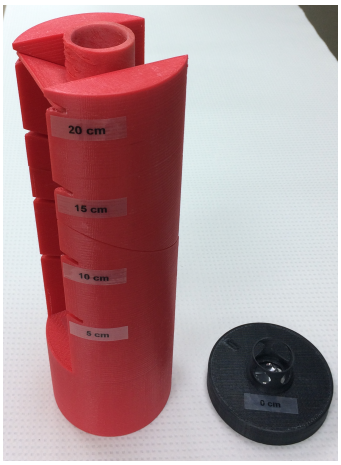

Figure 2.5: 3D printed sample holders used to reproducibly position 20 mL vials at nominal sample-to-detector distances of 5, 10, 15, and 20 cm (left) and 0 cm (right).

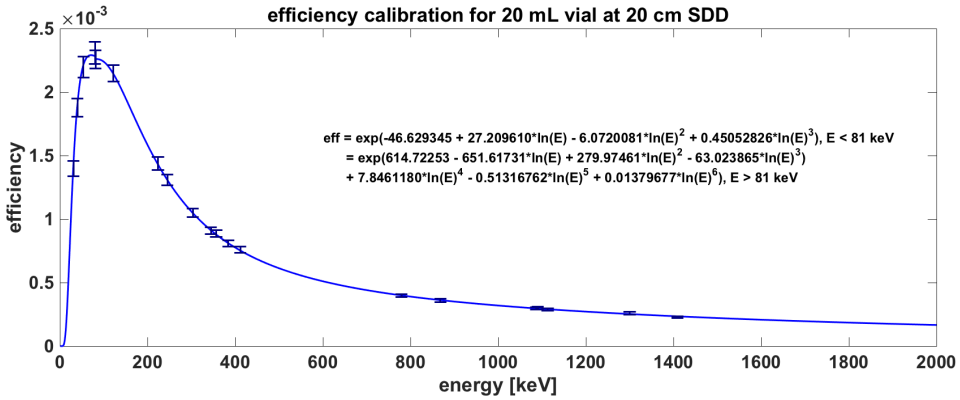

Figure 2.6: Efficiency calibration curve determined for a 20 mL vial with approximately 20 cm SDD. The ^{133}Ba and ^{152}Eu peaks used to fit the curve are also shown. A spline fit with 81 keV crossover is used, dividing the curve into a low and a high energy fit.

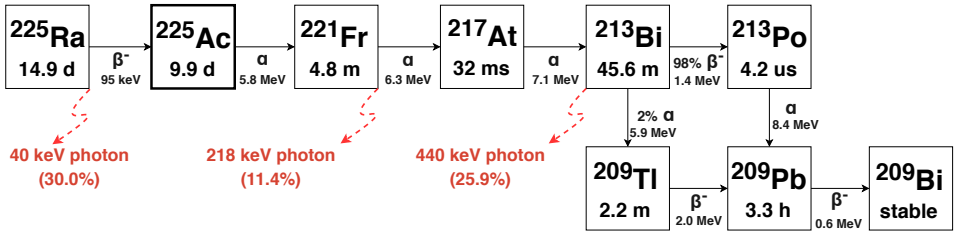

Figure 2.7: ^{225}Ra decay chain, including gamma emissions with high branching ratios.

2.1.5.2 Validation of Efficiency Calibration

An accurate efficiency calibration curve is essential for accurate quantitative gamma spectroscopy. Errors in this calibration are likely to be greatest in the low-energy region where the slope of the curve is high. Unfortunately, many isotopes – such as ^{225}Ra – can only be quantified using a single low-energy peak.

Radioactive decay chains provide a useful way of validating the shape of the efficiency calibration curve, since they can contain a number of different isotopes with known activities at a given point in time. Since these separate isotopes may be quantified via gamma rays of different energies, only an efficiency calibration with correct shape will measure the expected relative amounts of each isotope in the decay chain.

The ^{225}Ra decay chain is shown in Figure 2.7. A 20 mL sample containing ^{225}Ra ($t_{1/2}$ = 14.9 days) was used to validate the efficiency calibration described in Section 2.1.5.1. At $t = 0$ the sample contained ^{225}Ra and only negligible amounts of ^{213}Bi. The sample was counted periodically every few days so as to observe the grow-in of the decay products. ^{225}Ra, ^{221}Fr, and ^{213}Bi activities were measured using 40, 218, and 440 keV gamma lines, respectively. As can be seen from Figure 2.8, the measured activity concentrations match calculated values predicted from the first data point at $t = 0$. This implies that the relative shape of the efficiency calibration curve is accurate, at least in the 40, 218, and 440 keV regions. Small errors in the calibration curve shape may exist in the energy region near the peak of the efficiency curve.

An independent test of the efficiency calibration was performed using a separate 20 mL calibration source (R-01119) provided by RPG. This source's radioactivity is NIST-traceable, containing (1.82 ± 0.06) kBq of ^{133}Ba and (36.79 ± 1.29) kBq of ^{152}Eu. When this source was counted on the RCR1

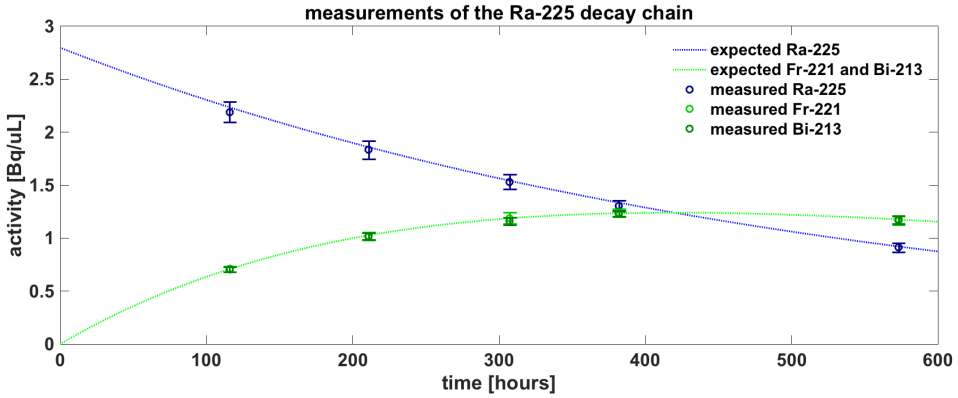

Figure 2.8: Gamma spectroscopy measurements of the ^{225}Ra decay chain of the same sample over time. Dotted lines represent calculated ^{225}Ra , ^{221}Fr , and ^{213}Bi activity concentrations predicted from the first data point at $t = 116h$, and assuming zero ^{225}Ac at $t = 0$, as is usually observed.

detector for 16 hours, (1.79 ± 0.02) kBq of ^{133}Ba and (37.11 ± 0.23) kBq of ^{152}Eu were measured, consistent with values determined by the source manufacturer.

2.1.5.3 Efficiency Calibration for Cascade-Prone, High Sensitivity Geometries

While decreasing SDD results in higher sensitivities and faster measurements of low-activity samples, coincidence summing effects (Section 2.1.4) are also increased. This section describes the effect of coincidence summing on gamma spectroscopy results and provides documentation for an efficiency calibration of a 20 mL vial, 0 cm SDD geometry.

Coincidence summing effects were shown to be negligible for the 20 cm SDD geometry described in Section 2.1.5.1. While an approximately 20-fold increase in counting efficiency is observed when SDD is decreased to 0 cm, as will be shown, coincidence summing effects make these measurements less reliable even when using Genie 2000's Cascade Correction algorithm. Since the ^{133}Ba and ^{152}Eu calibration nuclides have significant cascades, both the efficiency calibration for the geometry *and* measurements acquired with these geometries must be corrected for cascades.

The geometry discussed in this section is a 20 mL vial (containing a 20 mL volume) positioned approximately 0 cm above the detector cap using the sample holder shown in Figure 2.5.

Efficiency Calibration with and without Cascade Correction

A 20 mL calibration source (R-01107b), containing (1.505 ± 3.0%) kBq of ^{133}Ba and (1.515 ± 3.0%) kBq of ^{152}Eu, was positioned approximately 0 cm from the surface of the detector using the sample holder shown in Figure 2.5. A spectrum was acquired for 24 hours on 2016-09-25. The analysis sequence `effiCal` was used to locate peaks in the spectrum and initiate the Interactive Peak Fit Tool. The Sum/Non-linear LSQ Fit algorithm [145] was used to determine the areas of all singlet and multiplet peaks.

With all peak areas determined, the efficiency calibration was performed using the certificate file `R01107b.ctf`. Care was taken to ensure the correct peak area from within each multiplet was selected by Genie 2000 during this step of the process, and manually corrected if necessary. The efficiency calibration was performed both with and without cascade correction of the ^{133}Ba and ^{152}Eu peaks, creating two efficiency calibrations. For cascade correction, the peak-to-total calibration described in Section 2.1.4 was used, as was the geometry file `20mL_0cm.geo`. Efficiency values determined for each peak with and without cascade correction are shown in Table 2.7. Some cascade-corrected values were rejected as the cascade correction resulted in some data points appearing as significant outliers. A spline fit with a crossover energy of 81 keV was used to determine the efficiency calibration curves from these data points, as shown in Figure 2.9.

These calibrations are stored in the calibration files `effiCal_20mL_0cm_noCC.cal` and `effiCal_20mL_0cm_withCC.cal`.

Test of Cascade-Corrected Efficiency Using Cascade-Free Isotopes

The cascade-corrected efficiency calibration can be validated by comparing measurements of cascade-free radionuclides acquired at 0 cm SDD and at 20 cm SDD (where cascade effects are negligible). Table 2.8 shows results of such measurements. Since most of the ^{133}Ba and ^{152}Eu peaks used for the low energy efficiency curve are not subject to cascades, measurements below 81 keV are expected to change little if the efficiency calibration is determined with or without cascade correction. However, for the high energy efficiency curve (>81 keV) ^{133}Ba and ^{152}Eu cascades should affect the efficiency calibration. Though Table 2.8 contains few data points, both these effects are are evident. Results for the cascade-prone geometry are determined both using an efficiency calibration that corrects for ^{133}Ba and ^{152}Eu cascades, and an efficiency calibration performed without cascade correction. Both cascade-corrected and uncorrected results are consistent with the cascade-

Table 2.7: Measured efficiency values for all peaks used to determine the calibration curves shown in Figure 2.9.

energy [keV]	**without cascade correction**		**with cascade correction**	
	measured efficiency	uncertainty [%]	measured efficiency	uncertainty [%]
30.63	0.04491	4.30	0.04491	4.30
39.52	0.05493	3.85	0.05493	3.85
53.16	0.05828	3.45	0.06870	4.13
79.61	0.06736	3.58	0.07830	4.15
81.00	0.06801	3.14	0.07871	3.75
121.78	0.05975	3.06	-	-
244.70	0.03041	3.09	0.03977	4.69
276.40	0.02731	3.12	-	-
302.85	0.02579	3.09	-	-
356.01	0.02274	3.00	-	-
411.12	0.01913	3.13	0.02430	4.47
443.96	0.01809	3.08	0.02477	5.09
778.90	0.01095	3.10	0.01257	3.65
1085.84	0.00839	3.11	0.00827	3.12
1089.74	0.00821	3.23	0.00933	3.70
1299.14	0.00671	3.73	0.00772	4.22
1408.01	0.00563	3.06	0.00601	3.20

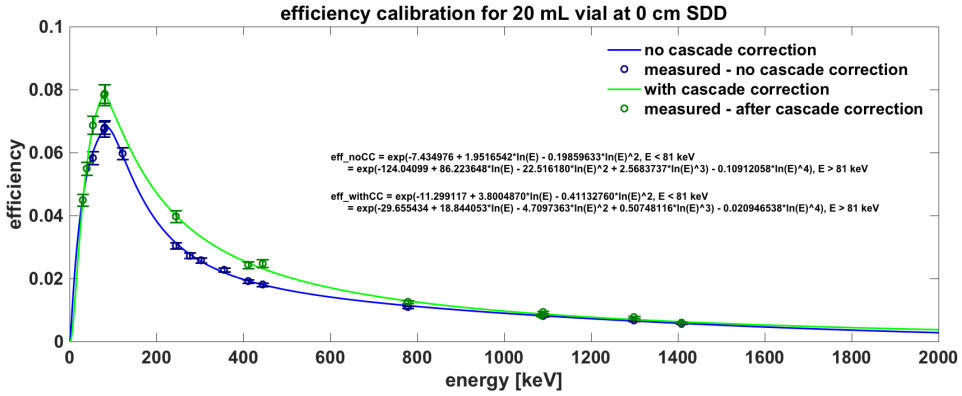

Figure 2.9: Efficiency calibration curves determined for a 20 mL vial with approximately 0 cm SDD, determined both with (green) and without (blue) cascade correction. The ^{133}Ba and ^{152}Eu peaks used to fit the curves are also shown. A spline fit with 81 keV crossover is used, dividing the curve into a low and a high energy fit.

free geometry for the 40 keV region, where ^{133}Ba and ^{152}Eu cascades have little effect on the efficiency. However, for higher energy regions only the cascade-corrected 0 cm SDD geometry agrees with measurements from the 20 cm geometry.

2.1.6 Effect of cascade summing on nuclides with cascades

The nuclides with the most significant cascades that are also readily available include ^{225}Ac, ^{221}Fr, and ^{213}Bi. Table 2.9 includes measurements of

Table 2.8: Measurements of cascade-free isotopes determined using a cascade-negligible geometry (20 cm SDD) and a cascade-prone geometry (0 cm SDD).

		activity [a.u.]		
		20 cm SDD	**0 cm SDD**	
nuclide	energy [keV]	no cascade effects	no cascade correction	with cascade correction
^{89}Zr	511	4.13 ± 0.12	5.03 ± 0.11	4.02 ± 0.14
	909	4.40 ± 0.09	5.02 ± 0.11	4.59 ± 0.11
^{225}Ra	40	1.90 ± 0.08	2.01 ± 0.05	1.85 ± 0.05

Table 2.9: Radioactivity composition of a 20 mL sample containing isotopes with significant cascades, measured using a cascade-negligible geometry (20 cm SDD) and a cascade-prone geometry (0 cm SDD). The decay chain containing ^{225}Ac, ^{221}Fr, and ^{213}Bi was in transient equilibrium at the times of measurement.

	activity [a.u.]		
	20 cm SDD	**0 cm SDD**	
	no cascade effects	no cascade correction	with cascade correction
^{225}Ac	1.02 ± 0.09	1.59 ± 0.04	1.18 ± 0.05
^{221}Fr	1.08 ± 0.04	1.54 ± 0.04	0.97 ± 0.05
^{213}Bi	1.03 ± 0.03	1.25 ± 0.02	0.81 ± 0.02

these isotopes using the efficiencies determined in Section 2.1.5.3 both with and without cascade correction determined, as well as with the 20 cm SDD efficiency determined in Section 2.1.5.1 for which cascade summing effects have been shown to be negligible. The measurements in Table 2.9 were acquired from a single sample containing ^{225}Ac and its progeny isotopes in transient equilibrium (see Figure 2.7). Results for the cascade-prone geometry are determined both using an efficiency calibration that corrects for ^{133}Ba and ^{152}Eu cascades, and an efficiency calibration performed without cascade correction. Cascade correction was performed only on the efficiency, not on the measurements of ^{225}Ac, ^{221}Fr, and ^{213}Bi , since these nuclides are not found in the Cascade Summing Library.

Since the decay chain is in equilibrium, ^{225}Ac, ^{221}Fr, and ^{213}Bi activities should be equal, as seen when using the cascade-negligible geometry (20 cm SDD). Since none of the ^{225}Ac, ^{221}Fr, and ^{213}Bi isotopes are found in the Genie 2000 Cascade Summing Library (Appendix A.5), they cannot be corrected for cascade summing effects, even when using an efficiency created using cascade correction. Therefore, measurements of these isotopes made using efficiencies that did not include cascade correction will be doubly prone to cascade summing effects – this is evident in Table 2.9 as the values determined with cascade corrected efficiencies are in closer agreement to those determined with the cascade-negligible efficiency.

The values in Table 2.9 demonstrate that if cascade correction is not applied to the efficiency calibration nor to measurements of nuclides with significant cascades, errors of over 50% can exist in the results.

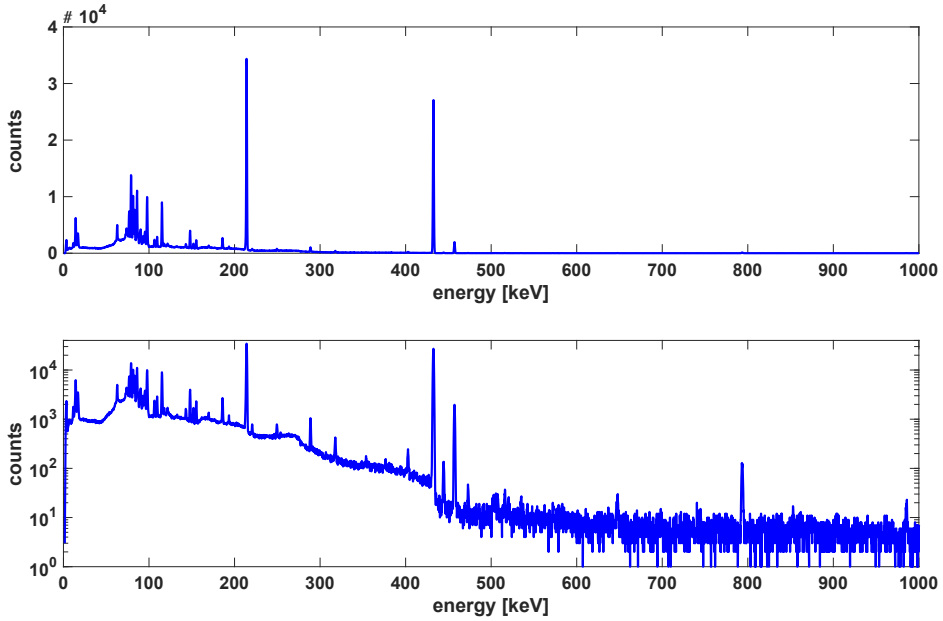

Figure 2.10: Gamma ray spectrum of the ^{225}Ac decay chain in equilibrium, shown with both a linear (top) and log (bottom) y-axis.

2.1.7 Efficiencies calibrations for additional geometries

The purchase of separate stock solutions of ^{133}Ba and ^{152}Eu (100 kBq each) allows for the creation of additional calibration sources for geometries that may be desired in the future. A list of calibration sources made from these solutions is listed in Appendix A.8.

2.1.8 Gamma spectroscopy for ^{225}Ac quantification

A gamma spectrum of the ^{225}Ac decay chain in equilibrium is shown in Figure 2.10. However, as discussed in Section 1.2.4, the equilibrium or non-equilibrium state of the ^{225}Ac decay chain must be considered when applying decay correction during the spectrum analysis. Most often, ^{225}Ac is best quantified via the 218 keV peak of ^{221}Fr under conditions where ^{225}Ac/^{221}Fr equilibrium can be assumed.

2.1.9 Summary

Results from Section 2.1.5.1 demonstrate the reliability of this detector to accurately quantify radionuclides for geometries where cascade summing effects are negligible. Unfortunately, these geometries have a low efficiency, implying that higher activity samples must be used if fast counting is desired. For samples containing very low activities, it would be desirable to have reliable geometries with higher efficiency.

The 0 cm SDD efficiency calibration discussed in Section 2.1.5.3 is subject to cascade summing effects from ^{133}Ba and ^{152}Eu. Though results in Table 2.8 suggest the cascade corrected efficiency calibration may be adequate for cascade-free radionuclides, the number of measurements in this table are insufficient to be definitive. The ability of Genie 2000 to correct for measurements of radionuclides with cascades has not be validated on this detector, since no appropriate samples have been available yet. Though papers exist in the literature demonstrating the reliability of the Genie 2000 Cascade Correction Algorithm to correct for cascade effects [148, 149], this algorithm relies on user-created files (peak-to-total calibration and geometry descriptions) and its performance should therefore be checked for each detector. It is likely that improvements could be made to the peak-to-total calibration (Section 2.1.4) by adding additional data points using additional cascade-free nuclides.

Even with proper setup of the cascade correction, cascading radionuclides not present in the Cascade Summing Library (Appendix A.5), such as ^{225}Ac, ^{221}Fr, and ^{213}Bi, cannot be corrected for cascade summing, as shown in Table 2.9. This library is not user editable and is defined by the manufacturer. Thus reliable measurements of these nuclides must be performed with geometries for which cascade summing effects are negligible.

2.2 Alpha Spectroscopy

Alpha-particle spectroscopy is another technique that can quantify radioactivity and identify radionuclides via the detection of emitted radiation. However, fundamental differences between how gamma-rays and alpha-rays interact with matter lead to marked differences in how these two techniques work and for what applications they can be applied. Alpha spectroscopy has a obvious advantage for detection and quantification of alpha-emitting radionuclides that do not emit sufficient gammas or x-rays to be detected by gamma spectroscopy. However, alpha spectroscopy sample preparation requirements are more time consuming and can introduce additional sources

of uncertainty that make gamma spectroscopy options more favorable when available, as is the case for ^{225}Ac and this work. However, the use of alpha spectroscopy to verify the absence of other alpha-emitters is prudent, if not essential, when producing therapeutic alpha-emitting nuclides. This section will introduce alpha spectroscopy, provide some comparison to gamma spectroscopy, and describe how alpha spectroscopy was used (and why it often was not used) in the work described in this thesis.

Challenges and limitations of alpha spectroscopy arise from the sample preparation requirements. Unlike gamma rays and x-rays that interact stochasticlly with matter, alpha particles lose energy continuously as they pass through matter (see Section 1.1.3). This means any material between the radiation source and the alpha particle detector will degrade the alpha particle energy, resulting in loss of energy resolution in the alpha particle spectrum that can be significant enough to render the spectrum useless. The high alpha particle LET means this effect is significant even for materials with very low density (such as air) or materials that are only micrometres thick (such as a material used to contain or seal the alpha radiation source). This means that alpha spectroscopy sources cannot be sealed radiation sources, nor can they be in the liquid form in which most samples originate.

The preparation of alpha spectroscopy sources from liquid samples is commonly done by microprecipitation and filtration of the radioactivity from the solution. This technique is described in detail in Appendix B, but will be summarized briefly here. A small (μg quantity) cerium carrier is added to the sample and then mixed with concentrated hydrofluoric acid, resulting in the precipitation of cerium fluoride from the solution; most alpha-emitting elements (except gaseous radon) coprecipitate with the cerium fluoride. The solution is then passed through a 100 nm thick filter, depositing the alpha radiation source on the top of the filter. The filter is then placed inside the vacuum chamber of the alpha spectrometer, which is then pumped down to remove air from between the source and the detector.

Detectors used in alpha spectroscopy are most commonly surface barrier detectors, consisting of a p-n semiconductor. A reverse bias applied to the semiconductor creates a depletion region without free charges that faces the radiation source. Alpha particles that enter the depletion region lose energy by creating electron-hole pairs. The bias voltage causes these free electrons to move towards one side of the semiconductor, creating a charged pulse signal that is proportional to the amount of energy deposited in the detector. Much of this is similar to what was described for gamma spectroscopy in Section 2.1, however, because alpha particles can be fully

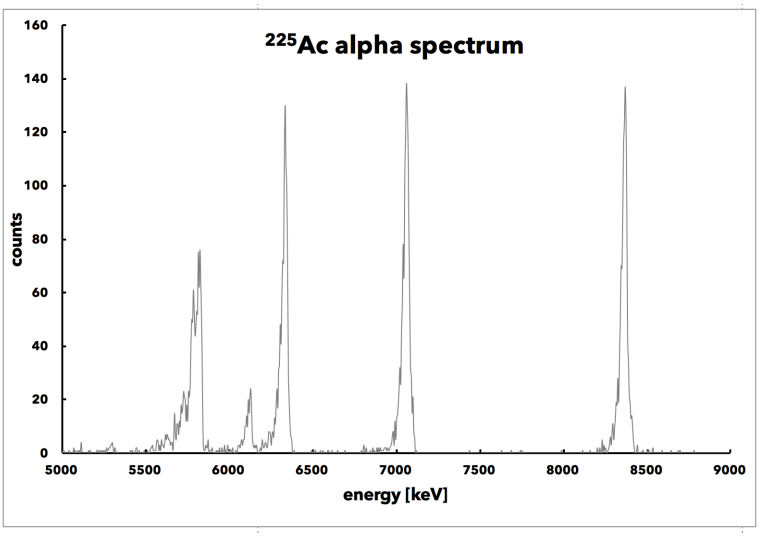

Figure 2.11: An example alpha particle energy spectrum collected from a sample containing ^{225}Ac and its progeny in equilibrium.

stopped within a small amount of material, unlike gamma spectroscopy detectors, the efficiency of an alpha spectrometer is independent of incident particle energy.

An example ^{225}Ac alpha spectrum is shown in Figure 2.11. The alpha spectrum appears more simple than the gamma spectrum (Figure 2.10), with clear distinct peaks associated with the nuclides in the decay chain: the 8.4 MeV ^{213}Po peak, the 7.1 MeV ^{217}At peak, two ^{221}Fr peaks at 6.3 and 6.1 MeV, and two overlapping ^{225}Ac peaks at 5.83 and 5.79 MeV. The absence of a background below and between the peaks means peak areas can be determined by the total counts without any baseline subtraction.

Appendix B describes the collection and analysis of ^{225}Ac spectra. This method is able to determine ^{225}Ac activity to within $<5\%$ of values determined by gamma spectroscopy. However, alpha spectroscopy was not used for ^{225}Ac quantification throughout this work. Gamma spectroscopy is favourable for ^{225}Ac quantification, where available, because the sample preparation and spectrum acquisition are much faster. Gamma spectroscopy is also inherently more safe, since gamma spectroscopy samples can be sealed without interfering with the measurement. The steps (precipitation, filtration, etc.) involved in alpha spectroscopy also introduce additional sources of uncertainties and potential for losses of activity that could go uncounted. While internal standards are often used to account for such losses when

measuring quantities of different nuclides, for Ac there is no such suitable nuclide other than ^{225}Ac.

2.3 FLUKA Simulations

2.3.1 An Introduction to Fluka

While gamma spectroscopy (Section 2.1) and and alpha spectroscopy (Section 2.2) provide empirical radioactivity measurements, situations can arise where such measurements are impractical or incapable of providing a desired radioactivity measurement. For example, a nuclide of interest may not emit sufficient gamma rays or alpha particles for it to be counted, or may be present in quantities too small to detect (because of a radioactivity value that is small either in absolute value or small compared to other nuclides in the sample that create interferences in the spectrum). The sample may also have a form factor that prohibits accurate measurements (ex. the sample is too large to fit into the detector, or a geometry for which an accurate calibration source is unavailable) or have a total activity that is too high to count. Situations may also arise where the number of radionuclides to be analyzed is prohibitively laborious.

All of these above situations – especially the latter – can arise in the case of radioactive samples produced by the high-energy proton irradiations that are a central component of this work. Fortunately, high-energy particle transport codes are able to model such irradiations and provide estimates of the resulting radioactive inventory. Such codes combine various physics models with Monte Carlo methods to simulate the interactions of primary and secondary particles with targets and surrounding materials during an irradiation. FLUKA is one such high-energy transport code with applications in radiation shielding and facility design, dosimetry, detector and target design, medicine, and radionuclide production [128, 129].

A number of publications have demonstrated the accuracy of the results that FLUKA can provide in such applications [150–159]. An assessment of FLUKA's performance for estimating radioactive inventories from the 438 MeV proton irradiation of thorium was one of the primary objectives of Chapter 6, and shows that the estimated activities are generally accurate to within a factor of 2 for most nuclides. Chapter 6 (Section 6.2.7) also contains the most complete description within this thesis of the necessary FLUKA input and settings required for accurate radioactivation simulations.

FLUKA is capable of modelling a variety of different particle interactions over a broad range of energies. For spallation reactions (described in

Section 1.3.3), the specific physics models used to model intranuclear cascades, evaporation, and high-energy fission are described comprehensively elsewhere [116, 128].

FLUKA was used in a number of ways throughout the efforts that resulted in this thesis. Most importantly, FLUKA's predictions of radioactive inventories enabled essential experiment planning by predicting the viability of the ^{225}Ac production approaches and the radiation safety hazards that result. Such pre-experimental safety assessments are crucial for determining the appropriate level of radiation safety precautions that must be taken and for securing necessary internal safety approvals. An example of such safety assessments is provided in Appendices C and D. Appendix C also contains an example list of the full FLUKA-estimated radioactive inventory produced by the proton irradiation of thorium at approximately 450 MeV, as well as a description of the models used to quantify radiation hazards resulting from the irradiation, including internal and external dose estimates. A shorter example of a question FLUKA was used to answer during the planning of this work is provided in Section 2.3.2.

2.3.2 An example Fluka study

The purpose of this section is to provide an example of how FLUKA radioactivity estimates were used in the planning of the work that lead to this thesis. These previously published conference proceedings consider the irradiation of a thorium oxide prototype target and compare the expected impurities in thorium-spallation-derived Ac products produced both directly and by the decay of Ra isotopes [2]. The thorium oxide prototype target described was later irradiated at TRIUMF and demonstrated by gamma spectroscopy measurements that ^{225}Ac production at TRIUMF's IPF facility was viable. While not an ideal target material for routine production, the thorium oxide was irradiated as the first prototype because it was readily available at the time, while procurement of the thorium metal took many months. The conclusion of this FLUKA study that the spallation production of sufficient ^{225}Ac quantities without the presence of ^{227}Ac was possible at the time contributed to the decision to further pursue this production method at TRIUMF (see Chapters 5 through 7).

Background

There has been increasing interest in leveraging TRIUMF's existing infrastructure to produce a large-scale supply of alpha-emitting isotopes useful

for targeted radioimmunotherapy. Nuclides of interest include ^{225}Ra, ^{224}Ra, ^{223}Ra, ^{225}Ac, and ^{213}Bi [15]. The decay chain containing ^{225}Ra, ^{225}Ac, and ^{213}Bi (Figure 1.1) is of particular and current focus. The current annual global supply of ^{225}Ac is less than 1.7 Ci, and desire for new sources is strong [160]. Los Alamos, Oak Ridge, and Brookhaven National Laboratories have recently demonstrated the feasibility of accelerator-production of ^{225}Ac via proton irradiation of thorium above 100 MeV [140]. To this end, TRIUMF's 500 MeV Isotope Production Facility (IPF) could be considered an ideal facility for regular and potent production given the energy (454 MeV), intensity (up to 120 μA), and reliable operation of available beam.

Here we present the initial design of a thorium target that aims to test IPF production of ^{225}Ac , starting at a low level (1130 μA*h) and producing mCi amounts of ^{225}Ac. Included are simulations of expected target production and radiochemical yields for isolated ^{225}Ra and ^{225}Ac products. The proposed radiochemical procedure produces ^{225}Ac both directly and indirectly via a ^{225}Ra generator, the latter containing a significantly reduced fraction of the long-lived and toxic ^{227}Ac within the final product.

Materials and Methods

Target Design

The target was designed to combine the IPF target facility and TRIUMF's existing materials and methods for thorium target manufacturing, previously established for the production of radioactive ion beams at ISAC. To adapt the ISAC ThO_2 foils to fit within the current encapsulated IPF target design, a centering ring assembly is used to hold an encapsulated tantalum target containing 1 g of ThO_2. Additional infrastructure used in the target will be manufactured from Inconel-based alloys. Figure 2.12 provides an overview of this target assembly. The target is housed in a carriage where it is submerged in water flowing at a rate of 14.25 L/min.

FLUKA *Simulation*

FLUKA was used to estimate the radioactive inventory in the irradiated target at end of bombardment (EOB), and one day, one week, and one month after EOB. A 454 MeV proton beam with 90 μA current, and widths in the x- and y-directions of 1.35 and 1.38 cm FWHM, respectively, was simulated for an irradiation lasting 12.56 h. The target was defined as shown in Figure 2.12. A neutron energy cut-off of 10^{-5} eV and a proton

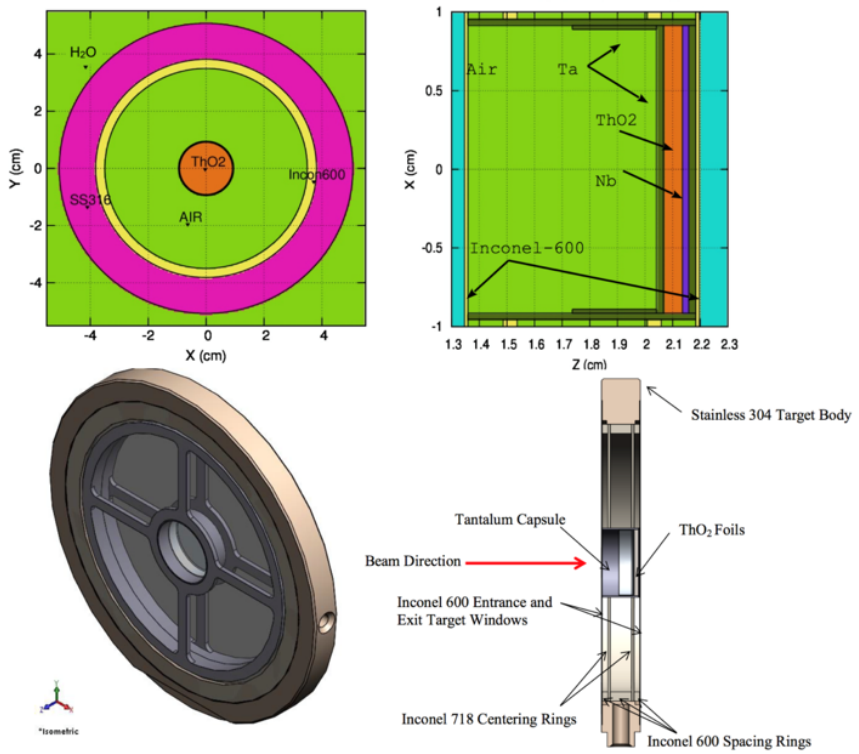

Figure 2.12: Models of the thorium oxide target design made in FLUKA (top) and in SolidWorks (bottom).

cut-off of 100 keV was used.

Potential Radiochemical Separation

While known methods exist for the dissolution of the proposed ThO_2 target material [161], possible redesigns of the target using thorium metal may be required to facilitate easier radiochemical separation. This should not significantly affect FLUKA results if the same amount of thorium is used. While several methods for separating ^{225}Ac from irradiated thorium metal can be found in the literature [104, 139, 141], the method described by Aliev *et al* is one of the more simple methods that separates Ra and Ac, and has also been tested at the mCi level [143]. The method involves the following steps:

1. Dissolution of irradiated thorium using a 50 mL solution containing 8

M HNO_3 and 0.004 M HF.

2. Extraction of Th, Pa, Cd, Zr, Nb products with a solution of HDEHP acid in toluene (final volume 100-150 mL).

3. Separation of Ac and rare earth metals from the remaining products (including Ra) using DGA resin and N,N,N‘,N‘tetroctyldiglioclamide as an extracting phase, and eluting Ac and rare earth elements in 3 mL 0.01 M HNO_3.

4. Separation of Ac from the rare earth metals using TRU resin with octyl(phenyl)-N,N-disobutylcarbomoylmethylphosphine oxide dissolved in tributylphosphate as an extracting phase and eluting pure Ac in 30 mL of 3 M HNO_3.

Aliev *et al* report retention of >99% for Ac and Ra up to step 3, and final Ac yield of 85%. The separation of ^{225}Ra and ^{225}Ac by DGA resin has be replicated recently at TRIUMF with >98% yields.

One drawback of spallation-production of ^{225}Ac is the co-production of other Ac isotopes, most notably the long-lived ^{227}Ac ($t_{1/2} = 21.8$ y). Other potential contaminants are ^{228}Ac ($t_{1/2} = 6.2$ h) and ^{226}Ac ($t_{1/2} = 26.4$ h). In order to create an ^{225}Ac product without these contaminants that is suitable for medical use, we consider producing ^{225}Ac both directly and via a co-produced ^{225}Ra generator. Waiting until one week after EOB to perform the target dissolution will permit the decay of the ^{227}Ac parent isotope, ^{227}Ra ($t_{1/2} = 42$ min), and other short-lived products. The first Ac/Ra separation is then performed, isolating all Ac isotopes present in the target one week after EOB. The separated Ra fraction forms a ^{225}Ac generator, that another 17.5 days later will yield a second batch of generator-produced ^{225}Ac with significantly reduced ^{227}Ac content. ^{228}Ac and ^{226}Ac contaminants from ^{228}Ra and ^{226}Ra in the generator are short-lived and will decay much faster than ^{225}Ac.

Reported yields form the radiochemical separation process were combined with the FLUKA estimation to predict the composition of both directly produced and generator-produced ^{225}Ac products.

Results

Relevant FLUKA simulation results showing the activities of selected Ra and Ac isotopes in the target at EOB and one week EOB are shown in Table 2.10. The yields and impurities for final ^{225}Ac products predicted by FLUKA and

Table 2.10: FLUKA estimation indicating the radioactive inventory of the thorium target immediately and one week after a 1130 μA*h irradiation at 90 μA.

	at EOB		EOB + 1 week	
	Activity [Bq]	Uncertainty [%]	Activity [Bq]	Uncertainty [%]
^{230}Ra	2.50E+07	15.9	0	-
^{228}Ra	1.94E+04	7.9	1.95E+04	7.9
^{227}Ra	1.39E+08	6.6	2.84E-03	0.8
^{226}Ra	1.59E+02	4.5	3.05E+02	2.6
^{225}Ra	**6.87E+06**	**4.8**	**4.96E+06**	**4.8**
^{224}Ra	1.37E+08	1.8	5.14E+07	1.6
^{223}Ra	1.54E+07	3.4	2.48E+07	1.7
^{228}Ac	1.04E+09	2.1	1.95E+04	7.9
^{227}Ac	9.09E+04	1.9	9.14E+04	1.9
^{226}Ac	4.18E+08	2.0	7.96E+06	2.0
^{225}Ac	**7.70E+07**	**1.7**	**4.97E+07**	**1.7**
^{224}Ac	1.56E+09	2.0	3.29E+03	8.3

Table 2.11: Predicted amount of ^{225}Ac produced when the Ra/Ac separation is performed 1 week after EOB. Impurities of other actinium isotopes are expressed as a percent of the ^{225}Ac activity. Due to their short half-lives, ^{228}Ac and ^{226}Ac percent impurities decrease with time.

Time since Ra/Ac isolation	0 days	1 day	5 days
^{225}Ac [MBq]	42.2	39.4	29.9
^{228}Ac/^{225}Ac [%]	0.039	0.003	0.000
^{227}Ac/^{225}Ac [%]	0.185	0.198	0.261
^{226}Ac/^{225}Ac [%]	16.020	9.740	1.330

Table 2.12: Predicted amount of ^{225}Ac and impurities (expressed as activity ratios) produced when the radium fraction (initially separated from actinium in Table 2) is used as an ^{225}Ac generator. ^{227}Ac impurity is significantly reduced from Table 1 due to the short half-life of its parent ^{227}Ra. ^{226}Ac impurities are effectively removed since no radium isotopes decay to ^{226}Ac. ^{228}Ac impurities decrease with time after the Ac is removed from the generator.

Time since Ra/Ac isolation	0 days	2 days
^{225}Ac [MBq]	42.2	39.4
^{228}Ac/^{225}Ac [%]	0.882	0.003
^{227}Ac/^{225}Ac [%]	9.95E-9	1.14E-8
^{226}Ac/^{225}Ac [%]	0	0

the chemical procedure described are shown in Table 2.11 (directly produced ^{225}Ac) and Table 2.12 (^{225}Ac produced via ^{225}Ra decay). These results assume that the target was left to decay for one week before processing began – likely necessary given the current infrastructure for removing the irradiated target from the beamline.

After one week of decay, the target is dissolved and the Ra and Ac isotopes are chemically isolated. At this time, 42.22 MBq (1.14 mCi) of ^{225}Ac is available. The 4.96 MBq (0.13 mCi) of isolated ^{225}Ra forms a generator that produces 2.20 MBq (0.06 mCi) of ^{225}Ac 17.5 days later. As seen in Tables 2.10 and 2.11, the lower yield for the generator produced ^{225}Ac comes with the benefit of higher purity.

Conclusion

Simulated yields suggest production of considerable ^{225}Ac quantities free of significant ^{227}Ac contaminants can be produced at an existing and underutilized TRIUMF facility. A low-level irradiation of 1130 μA*h on a 1 g ThO_2 target is expected to demonstrate this by directly producing 42.22 MBq (1.14 mCi) of ^{225}Ac containing 80 kBq of ^{227}Ac, and indirectly producing 2.20 MBq (0.06 mCi) of ^{227}Ac via a ^{225}Ra generator isolated one week after EOB. The generator-produced ^{225}Ac fraction should contain <1 Bq of ^{227}Ac.

3 ^{225}Ac Production at TRIUMF's ISAC Facility

3.1 Background

^{225}Ac was first produced at TRIUMF using the ISAC Facility's isotope separation on-line (ISOL) technique. This effort provided a source of ^{225}Ac for use in a number of experiments [3, 4, 162–165], including the ^{225}Ac imaging studies described in Chapter 4. However, the small and infrequent quantities of ^{225}Ac available from ISAC were insufficient to reliably progress these studies into ^{225}Ac applications requiring larger amounts of radioactivity; this motivated the desire to focus the rest of this thesis on alternative methods for ^{225}Ac production (Chapters 5, 6, and 7). Despite the small quantity of ^{225}Ac produced, the work presented in this chapter describes TRIUMF's first efforts to produce ^{225}Ac. These efforts allowed TRIUMF to gain valuable experience working with ^{225}Ac before addressing more complex targetry (Chapter 5) and radiochemistry (Chapter 7) challenges associated with ^{225}Ac production via thorium irradiation.

3.2 Methods Used for ^{225}Ac Production at ISAC

Ion beams of ^{225}Ra and ^{225}Ac were created using the ISOL technique at TRIUMF's ISAC facility [106]. Detailed descriptions of the collection of radioactivity from these beams is described elsewhere [1, 3, 164–167]. The ISAC facility produces radioactive ion beams by irradiating a uranium carbide target with 9.8 μA of 480 MeV protons, resulting in spallation and high-energy fission reactions that produce most nuclides lighter than ^{238}U, including ^{225}Ra and ^{225}Ac. Simultaneous ionization of the target under vacuum using surface or resonant laser ionization ionizes the target material and the nuclear reaction products into a secondary particle beam that is accelerated to 30-40 keV and passed through a high-resolution mass separator

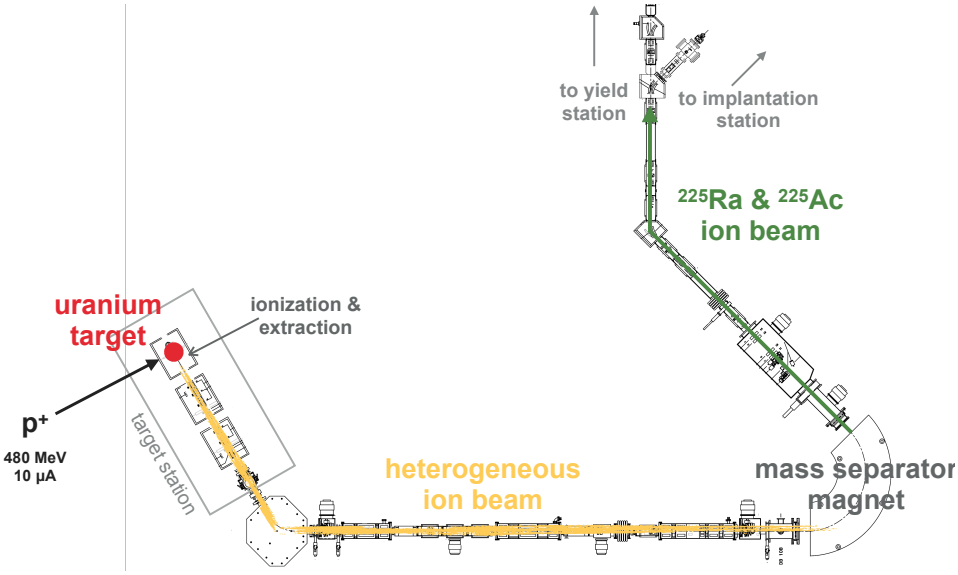

Figure 3.1: Beamlines at TRIUMF's ISAC facility that are relevant for ^{225}Ra and ^{225}Ac production.

before being delivered to various experiments. A diagram of this process is shown in Figure 3.1.

For ^{225}Ac production, selection of mass A=225 results in a beam containing ^{225}Fr, ^{225}Ra, and ^{225}Ac, which is then directed towards an aluminum target into which the radioactive ion beam is directed. Ions that hit the target interact as charged particles moving through a medium and slow down until reaching an expected range within the material (see Section 1.1.3) that can be calculated using SRIM [108]. The aluminum implantation target is housed within a chamber that can be detached from the beamline; the target and implantation chamber are shown in Figure 3.2. After implantation, the aluminum target containing the implanted radioactivity was removed from the beamline and moved to a radiochemistry lab. The ^{225}Ra and ^{225}Ac was retrieved from the aluminum material by etching the surface of the aluminum with HCl (0.1 M) to obtain a final solution containing ^{225}Ra and ^{225}Ac in approximately 0.5 mL. The etching of the aluminum target surface is facilitated by a small cavity (approximately 1 mm deep) on the target's surface (see Figure 3.2).

The purification of ^{225}Ac from ^{225}Ra was adapted from previously reported methods for isolation of ^{225}Ac [36, 104, 168, 169]. The recovered ^{225}Ra/^{225}Ac solution (0.1 M HCl, approximately 0.5 mL) was diluted to

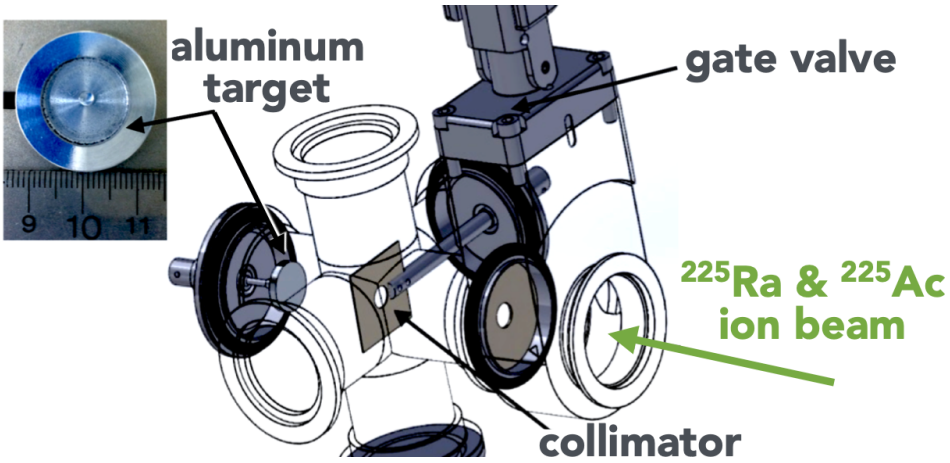

Figure 3.2: Solid model of the ISAC implantation chamber for collection of radioactive ion beams. The inset photograph in the top left corner shows the aluminum target used for ^{225}Ra and ^{225}Ac ion beam collection.

4 M HNO_3 (5 mL), and passed through a DGA column (35-40 mg DGA branched resin in a 6 mm diameter reservoir, preconditioned with H_2O (2 mL), 0.5 M HNO_3 (2 mL), and 4 M HNO_3 (2 mL). Under these conditions, Ac binds to the DGA while Ra passes through. The loaded DGA column was then washed with 4 M HNO_3 (4 mL). After air drying the column, the ^{225}Ac was eluted from the resin using 0.05 M HNO_3 (0.5 mL). The load fraction containing ^{225}Ra was collected and retained for use as an ^{225}Ra/^{225}Ac generator. A diagram of this process is shown in Figure 3.3.

The chemical purity of the ^{225}Ac product was assessed via inductively coupled plasma optical emission spectrometry (ICP-OES) and inductively coupled plasma mass spectrometry (ICP-MS) to quantify the presence of any stable cations that may compete with ^{225}Ac in radiolabeling reactions. Samples of both the initial solution containing ^{225}Ra and ^{225}Ac (before separation via DGA) and the final purified ^{225}Ac solution were analyzed for elemental composition using an Agilent 7700 ICP-MS. All samples were prepared by drying on a hotplate, treated with concentrated HNO_3 and then again dried to convert all salts into the nitrate form. Samples were then diluted with a 1% HNO_3, 0.05% HF solution containing 10 ppb indium as an internal standard. Standard solutions were prepared from both mixed and single-element standards purchased from Inorganic Ventures (Christiansburg, VA, USA). Elements assayed included: Be, Al, Ca, Sc, Ti, Cr, Mn, Fe, Co, Ni, Cu, Zn, Ga, Sr, Y, Zr, Nb, Mo, Sn, W, and Pb.

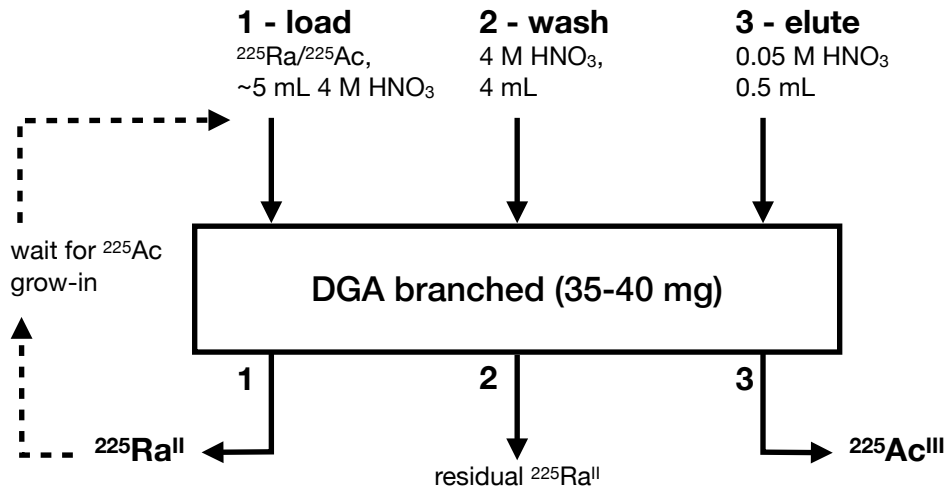

Figure 3.3: ^{225}Ra/^{225}Ac radiochemical separation methods used for purification of ISOL-produced ^{225}Ac.

3.3 Results from ^{225}Ac Production at ISAC

Mass A=225, singly-charged (+1) ion beams produced at TRIUMF's ISAC facility contained ^{225}Ra and ^{225}Ac intensities between 4.0×10^6-1.6×10^8 and 3.8×10^6-1.3×10^8 ions/s, respectively, depending on the state of the extraction electrode and the availability of the laser ionisation source [106]. ^{225}Fr was also present but decayed rapidly to ^{225}Ra. For durations between 13.3 and 80.7 h, the 40 keV ions beams were implanted into an aluminum disk to depth of 10-35 nm as determined by SRIM (see Figure 3.4) [108]. Etching of the radioactivity from the aluminum target post-implantation with 500 μL of 0.1 M HCl resulted in 0.2 to 7.5 MBq of ^{225}Ra and 0.16 to 18.0 MBq of ^{225}Ac. A summary of the production runs is shown in Table 3.1.

Single-column purification of ^{225}Ac from ^{225}Ra on the DGA column reliably yielded a pure ^{225}Ac product, free from parent isotope ^{225}Ra and with isolation yields >90% as determined by gamma ray spectroscopy. A second elution with an additional 0.5 mL of 0.05 M HNO_3 was typically able to recover the remaining ^{225}Ac. The overall purification yield of Ac from the target solution was >98%. Example results from a single separation are shown in Figure 3.5, based on gamma ray spectra similar to those shown in Figures 3.6, 3.7, and 3.8.

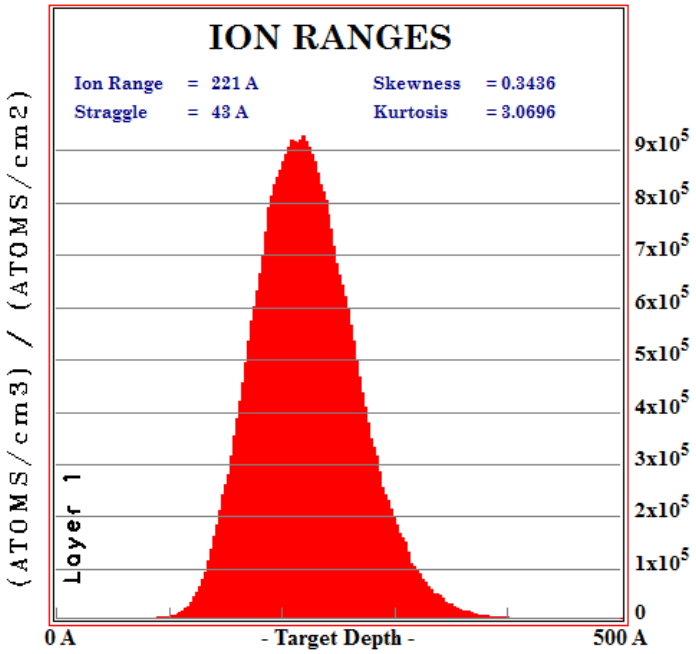

Figure 3.4: SRIM simulation results showing the depth distribution of 40 keV $^{225}Ra^{+}$ ions incident on an aluminum surface.

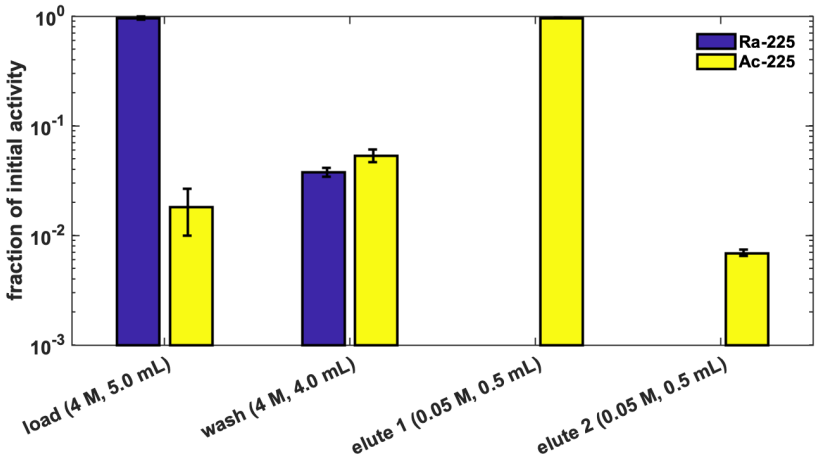

Figure 3.5: Representative elution profile for $^{225}Ra/^{225}Ac$ separation on DGA branched resin in nitric acid media.

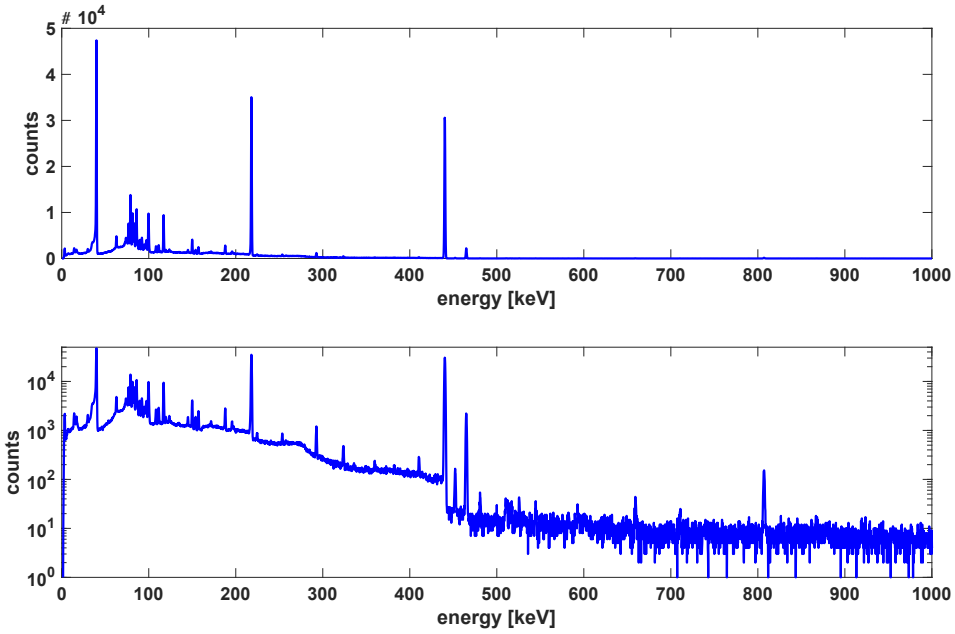

Figure 3.6: Representative gamma ray spectrum of a sample containing both ^{225}Ra and ^{225}Ac, before purification using the procedure shown in Figure 3.3. The spectrum is shown with both a linear (top) and log (bottom) y-axis. Evident is the 40 keV peak used for ^{225}Ra quantification, as well as the 218 keV ^{221}Fr peak and the 440 keV ^{213}Bi peak that can be used for ^{225}Ac quantification under decay chain equilibrium conditions (see Section 1.2.4). The less detectable 100 keV peak of ^{225}Ac can be used for direct quantification provided there are enough counts in the peak to provide a sufficient signal to noise ratio. However, as shown in the figure, this 100 keV peak is located in the energy region with highest background signal (Compton scatter) and near many other potentially overlapping peaks, making it less desirable for ^{225}Ac quantification.

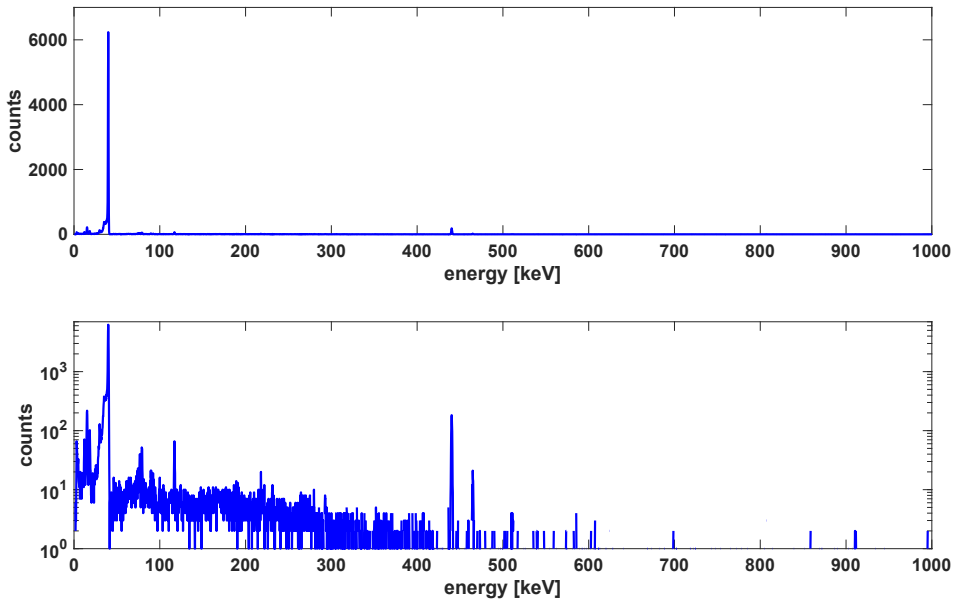

Figure 3.7: Gamma ray spectrum of a sample containing ^{225}Ra and undetectable quantities of ^{225}Ac (fraction 1 of the procedure shown in Figure 3.3). The spectrum is shown with both a linear (top) and log (bottom) y-axis. Evident is the 40 keV peak used for ^{225}Ra quantification. Small amounts of ^{213}Bi are often seen in this fraction as evident from the small 440 keV peak. However, the absence of 218 keV ^{221}Fr peak indicates that this ^{213}Bi does not result from the decay of ^{225}Ac within the purified ^{225}Ra fraction.

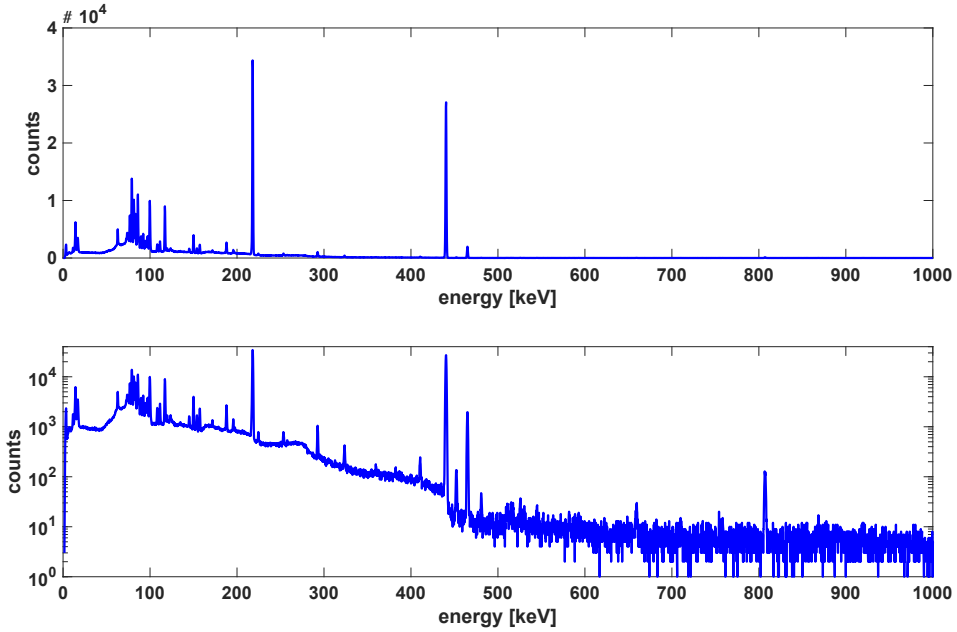

Figure 3.8: Gamma ray spectrum of a sample containing ^{225}Ac and indetectable quantities ^{225}Ra (fraction 3 of the procedure shown in Figure 3.3). The spectrum is shown with both a linear (top) and log (bottom) y-axis.

Table 3.1: Summary of ^{225}Ra and ^{225}Ac production runs at ISAC, TRIUMF's ISOL facility. [a]EE = extraction electrode; [b]LIS = laser ionization source. The values of ^{225}Ra and ^{225}Ac radioactivity produced have uncertainties between 3-5%.

implantation parameters				beam intensity [ions/s]		production [MBq]	
date	time [h]	EE[a]	LIS[b]	^{225}Ra	^{225}Ac	^{225}Ra	^{225}Ac
Dec '15	13.3	off	off	3.20E+07	3.80E+06	0.19	0.16
Apr '16	44.8	off	on	4.00E+06	1.00E+07	0.99	1.4
May '16	48.9	off	on	-	-	1.13	1.35
Aug '16	21.6	on	on	1.60E+08	5.70E+07	7.1	10.5
Dec '16	45	on	on	9.30E+07	1.30E+08	6.8	18
Apr '17	80.7	off	on	9.00E+07	2.80E+06	7.5	1.7
Sept '18	40	on	off	1.00E+08	1.60E+07	8.6	9.4

To quantify the amount of stable metal impurities present in the ^{225}Ac product that could compete with ^{225}Ac during radiolabeling reactions, the chemical purity of the ^{225}Ac was assessed via ICP-OES and ICP-MS. Modest values of aluminum with (7709 ± 1281) and (10175 ± 872) ppb or (3.9 ± 0.6) μg and (5.1 ± 0.4) were present in the first and second eluates, respectively, compared to 166,000 ppb (830 μg) present in the load fraction (see Table 3.2). The 200-fold decrease of Al in the eluate 1 compared to the initial load solution suggests that the DGA resin does a satisfactory job of removing excess Al^{III} from the $^{225}Ac^{III}$ product with a separation factor of $\sim 10^2$. However, an additional washing step may further decrease the amount of metal impurities, which may in turn positively impact radiolabeling yields. Calcium, iron, copper, nickel, and zinc were found in the ^{225}Ac product (elute 1) with amounts of (1392 ± 208), (203 ± 20), (47 ± 12), (19 ± 6), and (137 ± 21) ppb, respectively. If one assumes the entire solution of eluate 1 (0.5 mL) were to contain 10 MBq of ^{225}Ac, the non-radioactive impurities would account for (6970 ± 1158) atoms of aluminum, (847 ± 127) atoms of calcium, (88 ± 9) atoms of iron, (51 ± 8) atoms of zinc, (8 ± 2) atoms of nickel, and (18 ± 5) atoms of copper per atom of actinium. Of concern are the high metal:Ac^{III} ratios of Al^{III}, Fe^{III}, and Ca^{II} in the ^{225}Ac eluate, since the gold standard in actinium chelation, DOTA, also has a strong affinity for these metals [170].

Table 3.2: Trace metal content in ppb (μg/L) determined by ICP-MS (n=2, average ± standard deviation). Values denoted with (*) were determined by ICP-OES (n=1).

	Be	Al	Ca*	Sc	Ti	Cr	Mn
Load	0.055 ± 0.002	166000*	47.4 ± 0.8	0.07 ± 0.02	15 ± 1	46 ± 11	66 ± 11
Wash	0.018 ± 0.001	14000*	63 ± 8	0.061 ± 0.003	15 ± 1	11 ± 3	15 ± 4
Elute 1	0.06 ± 0.02	7709 ± 1281	1392 ± 208	0.5 ± 0.1	77 ± 11	14.9 ± 0.3	4.37 ± 0.02
Elute 2	0.07 ± 0.02	10175 ± 872	745 ± 24	0.9 ± 0.3	101 ± 8	62 ± 63	7 ± 3

	Fe	Co	Ni	Cu	Zn	Ga	Sr
Load	274 ± 45	0.11 ± 0.02	18 ± 15	32 ± 11	57 ± 25	3.1 ± 0.6	1.13 ± 0.1
Wash	94 ± 3	0.04 ± 0.01	76 ± 94	12 ± 5	36 ± 5	0.86 ± 0.03	1.69 ± 0.02
Elute 1	202 ± 20	0.10 ± 0.02	19 ± 6	47 ± 12	137 ± 21	1.8 ± 0.5	20 ± 1
Elute 2	427 ± 192	0.6 ± 0.7	37 ± 17	46 ± 4	134 ± 23	2.1 ± 0.4	11.5 ± 0.6

	Y	Zr	Nb	Mo	Sn	W	Pb
Load	0.19 ± 0.01	7.8 ± 0.7	<dl	0.90 ± 0.05	0.73 ± 0.04	1.0 ± 0.1	2.2 ± 0.6
Wash	0.32 ± 0.01	7.8 ± 0.8	0.022 ± 0.001	1.226 ± 0.004	0.31 ± 0.01	0.6 ± 0.3	8 ± 2
Elute 1	3.6 ± 0.2	40 ± 5	0.21 ± 0.04	5.8 ± 0.8	0.94 ± 0.01	9 ± 5	132 ± 27
Elute 2	3.6 ± 0.3	41 ± 5	0.3 ± 0.1	8.3 ± 1.5	0.9 ± 0.2	12 ± 6	19 ± 1

3.4 Summary

Mass $A = 225$ ion beams containing ^{225}Ra and ^{225}Ac at TRIUMF's ISAC facility were successfully used to produce ^{225}Ac (up to 18.0 MBq). The ^{225}Ac produced was sufficient for use in a number of preclinical experiments [3, 162, 163], and enabled the imaging studies detailed in Chapter 4.

However, the small and infrequent quantities of ^{225}Ac available from ISAC were not sufficient to progress the imaging studies of Chapter 4, and as described in Section 1.3.2, were not sufficient to support development of ^{225}Ac-TAT beyond the preclinical stages. This motivated the transition of the focus of this thesis towards developing an alternative production method that is described further in Chapters 5, 6, and 7.

4 Multi-Nuclide SPECT of the ^{225}Ac Decay Chain

4.1 Background

Due to the high cytotoxicity and short range of alpha radiation, targeted internal radiation therapy using alpha-emitters can potentially treat aggressive cancers by destroying small or single-cell metastases with minimal harm to healthy tissue [171]. The ^{225}Ac decay chain (Fig. 1.8) has considerable potential for use in this therapy due to the relatively long ^{225}Ac half-life ($t_{1/2}$ = 9.9 d) followed by four alpha-emissions [172]. Physical properties of the ^{225}Ac decay chain are summarized in Section 1.2.2.

The advantage gained from multiple alpha-particles is offset by the challenge of retaining both ^{225}Ac and its progeny at the target, as the migration of the daughter products from the target following ^{225}Ac decay reduces therapeutic effect and increases toxicity to non-target and excretion organs [100]. While used in a small number of clinical studies (see Section 1.1.5), the difficulty of targeting cells with the entire decay chain remains a concern for ^{225}Ac pharmaceutical development and is an active area of research [173–176]. As an example from preclinical trials, some targeting vectors exhibit renal toxicity due to ^{213}Bi uptake that limits the amount of ^{225}Ac that can be administered [177, 178].

Performance evaluation of ^{225}Ac pharmaceuticals must therefore separately assess the biodistributions of each alpha-emission in the ^{225}Ac decay chain and the resulting integrated dose to various tissues. Determining this in preclinical studies is currently a challenge since quantitative *ex vivo* assessment is limited by the short half-lives of ^{225}Ac progeny isotopes, ^{221}Fr ($t_{1/2}$ = 4.8 min) and ^{213}Bi ($t_{1/2}$ = 45.6 min).

While quantitative SPECT imaging could assess the pharmacokinetics of radiopharmaceuticals *in vivo*, there are currently no established imaging-based methods capable of separately yet simultaneously imaging the multiple

radionuclides in the ^{225}Ac decay chain. While SPECT images of ^{213}Bi alone have been acquired with a VECTor microSPECT/PET/CT system, neither ^{225}Ac nor ^{221}Fr were present [179]. Qualitative ^{221}Fr SPECT images have been reported in two preclinical cases, as have qualitative clinical images of ^{213}Bi alone [29, 50, 55, 173, 176]. While other imaging modalities such as alpha-cameras [180] or Cherenkov imaging [181] have also been used to image the biodistributions of the ^{225}Ac decay chain or other alpha-emitting medical isotopes, quantitative SPECT has a distinct advantage over these methods. Though alpha-camera spatial resolution is on the order of tens of microns and is superior to SPECT, alpha-cameras are limited to *ex vivo* planar imaging. Advantages of SPECT over Cherenkov imaging of the ^{225}Ac decay chain include higher sensitivity, the ability to produce quantitative and 4D biodistriutions, and the potential to use photon energy discrimination to distinguish between different components of the ^{225}Ac decay chain.

This chapter describes first steps taken towards developing quantitative preclinical imaging tests of ^{225}Ac radiopharmaceuticals via dual-isotope SPECT imaging of ^{225}Ac progeny ^{221}Fr (218 keV) and ^{213}Bi (440 keV) using a VECTor microSPECT/PET/CT system. To the best of our knowledge, we present the first simultaneously acquired quantitative ^{221}Fr and ^{213}Bi images. This study is limited by the small amount of ^{225}Ac that was available at the time. Performance assessment of VECTor for simultaneously imaging ^{221}Fr and ^{213}Bi is presented, and the ability to separately image dynamic ^{221}Fr and ^{213}Bi activity distributions is demonstrated. If used *in vivo*, this technique could provide invaluable information for evaluating the safety and efficacy of ^{225}Ac radiopharmaceuticals under development by assessing the biodistribution of multiple ^{225}Ac decay chain components over time. Ultimately, this could facilitate faster development of ^{225}Ac pharmaceuticals at the preclinical stage, by determining which pharmaceuticals are best suited for larger preclinical therapy studies or clinical trials.

4.2 Materials and Methods

4.2.1 Relevant physical properties, production, and quantification of ^{225}Ac

^{225}Ac decays to stable ^{209}Bi via two beta and four alpha decays (see Section 1.2.2). The alpha-emitting portion of the decay chain effectively encompasses ^{225}Ac through ^{213}Bi, since ^{213}Po decay occurs microseconds after ^{213}Bi decay. Only ^{221}Fr and ^{213}Bi can be imaged, via their 218 keV (11.4%) and 440 keV (25.9%) gamma emissions, respectively. Other gamma emis-

sions are present with branching ratios less than 3% relative to ^{225}Ac decays. While many of these isotopes emit x-rays in the 80 to 100 keV range, these photons cannot provide images representing activity distributions of specific isotopes. As detailed in Section 1.2.1, the short half-lifes of ^{225}Ac progeny relative to the parent causes the decay chain to establish transient equilibrium.

All work presented in this chapter was done using ^{225}Ac produced at TRIUMF's ISAC Facility (see Chapter 3). A total of (3.8 ± 0.30) MBq of ^{225}Ac was available for imaging, free of other radioactive contaminants. The radioactive composition of all samples was determined via gamma spectroscopy using the Genie 2000 software package and a high-purity germanium detector (see Section 2.1). ^{225}Ac quantities were determined indirectly via measurement of ^{221}Fr and ^{213}Bi once transient equilibrium was established. These measurements were experimentally determined to have an uncertainty of 8%.

4.2.2 Data acquisition and image reconstruction

The Versatile Emission Computed Tomography (VECTor) imaging platform (MILabs, Utrecht, Nederlands) is a small-animal, multi-modality scanner capable of quantitatively imaging single photons over a wide energy range (both SPECT and PET isotopes) [182]. The imaging platform combines a CT scanner and a SPECT system with three flat panel NaI detectors in a triangular arrangement. Within the NaI panels is an interchangeable cylindrical collimator containing rings of clustered pinholes. Collimator interchangeability provides versatility, with collimators of varying resolution, sensitivity, and diameter optimized for different photon energies and applications. The field of view is limited to a small region inside the collimator that is visible to all pinholes. Larger volumes are imaged by stepping the bed through multiple bed positions within the collimator.

VECTor uses a 350 keV threshold to distinguish between both high (PET-like, i.e. 511 keV) and low (^{99m}Tc-like, i.e. 140 keV) energy photons. Given the difficulties in obtaining large ^{225}Ac quantities, and since simultaneous ^{221}Fr (218 keV) and ^{213}Bi (440 keV) imaging involves both these high and low energy ranges, two collimators were selected as potential candidates for imaging with VECTor: the ultra-high sensitivity (UHS) collimator [183], and the high-energy ultra-high resolution (HEUHR) collimator [184]. The UHS collimator performs optimally at lower energies and provides higher sensitivity favourable for low-activity imaging. In contrast, the HEUHR collimator offers higher spatial resolution and improved performance over

a broad energy range. When imaging with 140 keV, the collimators yield a sensitivity of approximately 12500 cps/MBq (UHS) and 3000 cps/MBq (HEUHR), and spatial resolutions of 1 and 0.55 mm, respectively. In this study, we characterize VECTor's ability to simultaneously image ^{221}Fr and ^{213}Bi for both HEUHR and UHS collimators.

Despite the low activity available for imaging, the 9.9 day ^{225}Ac half-life permits long data acquisitions, providing sufficient counts for image reconstruction. However, such long acquisitions prohibit *in vivo* imaging. The collimator, duration, bed positions, and counts acquired for each acquisition is reported in Table 4.1. Unless otherwise stated, all data were acquired with the decay chain in equilibrium. Data acquired in list mode were sorted into 512 energy bins of 3.86 keV width; resulting spectra are shown in Fig. 4.1. The system's energy resolution is 9.3% for 140 keV and 8.6% for 511 keV. Two images were reconstructed from each data acquisition: one from data collected in the 218 keV photopeak (^{221}Fr) and another from the data in the 440 keV peak (^{213}Bi). Different system matrices are used to reconstruct low energy (^{221}Fr) and high energy (^{213}Bi) images. A system matrix optimized for 140 keV is used when reconstructing events from energy peaks below 350 keV, while for energies above 350 keV a system matrix calculated for 511 keV photons is used. Data were corrected for decay, and images with 0.4 mm wide cubic voxels were reconstructed using energy windows of 15% width, 4 subsets, and 25 iterations using VECTor's pixel-based ordered subset expectation maximization (POSEM) iterative reconstruction algorithm [185]. This combination of subsets and iterations was chosen based on optimization of contrast-to-noise ratio (CNR) for resolution phantom images (see Section 4.2.4). The number of MLEM-equivalent iterations (number of POSEM subsets times number of iterations) was first determined. 100 MLEM-equivalent iterations was selected as this number yielded the optimal CNR for most images when using different isotope (^{221}Fr vs ^{213}Bi) and collimator (UHS vs HEUHR) combinations. Keeping this number fixed, the number of subsets was varied. Compared to a single-subset reconstruction, no significant differences were observed when data were divided into 4 subsets. Therefore, 4 subsets and 25 iterations was chosen as the best optimization of image quality and reconstruction time. Background and scatter correction is performed by the VECTor image reconstruction software, in this case using a triple energy window method with a high and low energy background window of a 3% width. Co-registration of emission images and the subsequently acquired CT images enabled attenuation correction of the SPECT images. To enable quantitative SPECT reconstruction, calibration factors for each collimator and photopeak were determined from images of

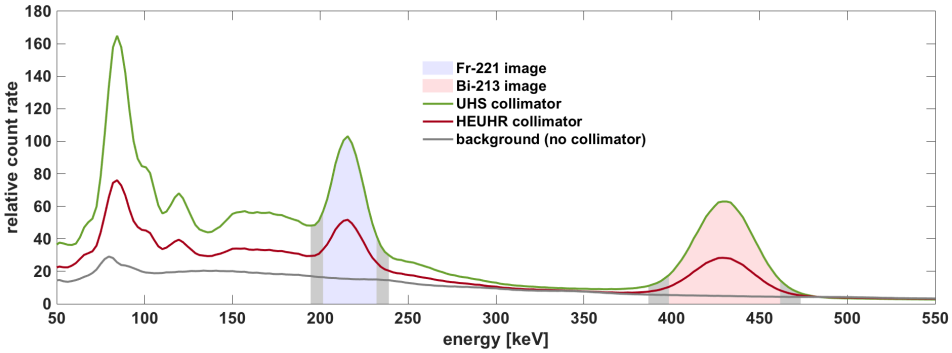

Figure 4.1: Energy spectra, normalized by acquisition time, acquired by the VECTor scanner for both HEUHR (red) and UHS (green) collimators with a comparison to a background spectrum (grey) acquired with no collimator or activity present. Spectra were acquired using a uniform source containing 1.05 MBq (28.3 μCi) of ^{225}Ac. The energy regions used to reconstruct the ^{221}Fr and ^{213}Bi are shown in blue and red, respectively. The adjacent grey regions indicate the energy windows defined for background and scatter correction.

a uniform syringe containing (1.05 $\pm$ 0.08) MBq of ^{225}Ac reconstructed from a 12-hour acquisition. The reconstructed images were analyzed using MATLAB (v. 2015b).

4.2.3 Image contrast and noise

Image contrast and uniformity were assessed using a cylindrical acrylic phantom similar to the NEMA NU-4 micro-PET image quality phantom [186]. The phantom contains one high activity concentration insert ('hot' region) and one activity-free insert ('cold' region), both submerged in a low activity concentration background ('warm' region). These inserts permit contrast measurements similar to *in vivo* conditions, where a small high activity region may be present within a uniform low activity background. The insert-free portion of the warm region was used to measure noise characteristics and the uniformity of the system's response. The hot and warm regions were filled with ^{225}Ac concentrations of (1.56 $\pm$ 0.12) MBq/mL and (0.33 $\pm$ 0.03) MBq/mL, respectively. For contrast and uniformity measurements only, a 1 mm Gaussian filter was applied to the reconstructed images. Contrast measurements were performed using cylindrical ROIs defined within CT images and centred over the hot, warm, and cold regions using diameters equal to

Table 4.1: Activities used, acquisition durations, and counts acquired in each photopeak for all imaging experiments. Values for dynamic scans list the number of counts in the first frame.

Phantom	**Total Activity [MBq]**	**Bed Positions**	**Collimator**	**Time per Bed Position [min]**	**Counts [millions]**
Contrast, Noise, Uniformity	2.77 ± 0.22	36	HEUHR	40	^{221}Fr 4.34 ^{213}Bi 8.37
			UHS	40	^{221}Fr 27.30 ^{213}Bi 101.07
Resolution	1.79 ± 0.14	18	HEUHR	80	^{221}Fr 5.23 ^{213}Bi 9.53
			UHS	40	^{221}Fr 15.98 ^{213}Bi 43.25
Cation column	0.24 ± 0.02	1	HEUHR	60	^{221}Fr 0.15 ^{213}Bi 0.23

80% of the physical diameter of each volume (ROI placement is visualized in Fig. 4.2a). Definitions of contrast recovery as defined by the NEMA NU 2-2007 standard were used [187]. Contrast recovery between the hot and warm regions was therefore defined as:

$$CR_{h-w} = \frac{I_h/I_w - 1}{a_h/a_w - 1} * 100\% \tag{4.1}$$

and contrast recovery between the warm and cold (activity-free) regions was defined as:

$$CR_{w-c} = (1 - \frac{I_c}{I_w}) * 100\% \tag{4.2}$$

where I_h, I_w, and I_c represent mean activity concentrations measured within the hot, warm and cold ROIs, and a_h and a_c represent activity concentrations independently determined by gamma spectroscopy. Profiles across the hot and cold regions were also measured on a single image plane.

Image uniformity can be assessed using radial profiles through uniform regions containing high activity concentrations. Due to the low activity concentration within our phantom and the resulting noise, images were averaged over 4 mm in the axial direction before measuring radial uniformity profiles.

Within this uniform region of the phantom, image noise was also assessed using two metrics. To assess the variability in the response to a uniform radioactivity concentration, noise was assessed by measuring the coefficient of variation (COV) within the warm ROI across 45 (7.6 mm) adjacent planes. In a method similar to that described by Tong *et al* [188], background variability was measured using 9 ROIs located within the uniform region of the phantom and having diameters equal to those of the hot and cold inserts. The placement of these ROIs is shown in Fig. 4.2b, and was done using 5 non-adjacent image slices 2 mm apart for a total of 45 ROIs. The coefficient of variation of ROI mean values was taken as the final measure of background variability.

4.2.4 Image resolution and limit of detection

An acrylic phantom containing groups of cylindrical holes of diameters 1.70, 1.50, 1.30, 1.10, 0.95, and 0.85 mm was used to assess the ability to resolve small objects that may be present in future *in vivo* studies. All but the 0.85 mm holes were filled with (4.66 ± 0.37) MBq/mL of ^{225}Ac. Attempts to get as much of the available activity as possible into the phantom resulted in the smallest holes not filling with the solution. The resulting images were

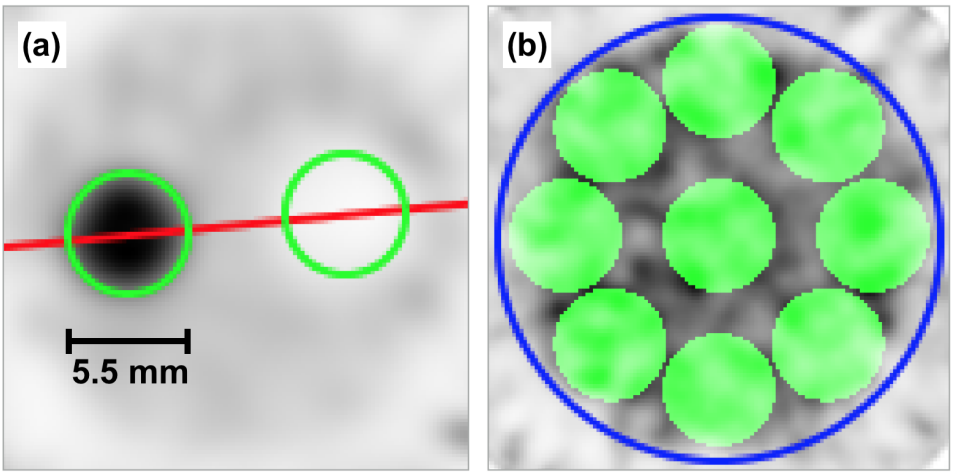

Figure 4.2: (a) SPECT cross section of the phantom's contrast region, with green circles indicating the location of ROIs used to determine contrast measurements, and the red line showing the location of the measured profiles. (b) SPECT cross section of the phantom's uniform region, with blue circle indicating the location of the ROI used for the 'warm' region, and green circles indicating the ROIs used for noise measurements.

analyzed by measuring inter-rod contrast as defined by Walker *et al* [189]. This metric measures inter-rod contrast between ROIs centered inside and in between rods of a given size. ROIs were defined using known dimensions of the phantom and positioned using CT images. The ideal value for this metric is 100%, with 20% defined as the minimum threshold for resolvability.

To assess the ability to accurately quantify the activity concentration within small objects, the recovery coefficient (RC) was measured for each rod using ROIs with diameters 80% of the physical rod diameter. The RC has an ideal value of one and is defined as:

$$RC = \frac{\overline{h_d}}{h_o} \tag{4.3}$$

where h_o is the known activity concentration and $\overline{h_d}$ is the apparent activity concentration within the ROI.

To parameterize the quantitative accuracy of images at lower activity concentrations, inter-rod contrast and RC measurements were repeated for images reconstructed using 20%, 5%, and 1% of the total counts, simulating data acquired with activity concentrations of 0.93, 0.23, and 0.05 MBq/mL.

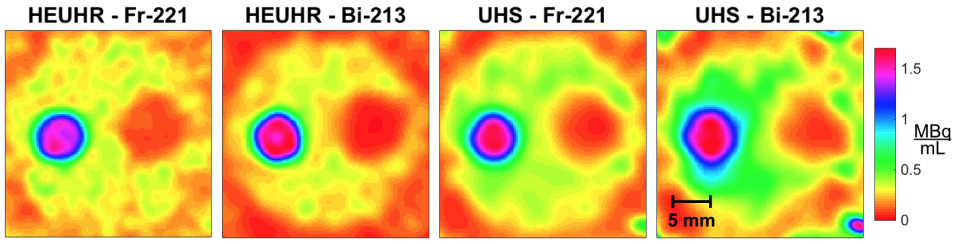

Figure 4.3: ^{221}Fr and ^{213}Bi images of the contrast phantom acquired with both the HEUHR and UHS collimators and filtered with a 1mm 3D Gaussian filter.

4.2.5 Dynamic imaging of differing ^{221}Fr and ^{213}Bi distributions

To demonstrate the ability to image dynamic ^{221}Fr and ^{213}Bi activity distributions that are not co-localized, a cation exchange chromatography column typically used to isolate ^{213}Bi from the ^{225}Ac parent was imaged. Described by Morgenstern *et al* [49], this procedure uses AG MP-50 cation exchange resin, loaded with ^{225}Ac in 4 M HNO_3. ^{225}Ac binds to the resin, along with most of the ^{213}Bi. Once the ^{213}Bi and ^{225}Ac regain equilibrium, ^{213}Bi is eluted in a solution of 0.1 M NaI and 0.1 M HNO_3. ^{225}Ac remains bound to the resin as does ^{221}Fr.

For the imaging study, (0.30 $\pm$ 0.02) MBq of ^{225}Ac was loaded onto the resin (AG-MP 50 resin, column volume 100 μL), and the ^{213}Bi was eluted in a 200 μL volume that was left in the column, but outside the resin volume. After the elution, the ^{213}Bi is no longer in equilibrium with ^{225}Ac: in the resin a deficiency of ^{213}Bi exists relative to ^{225}Ac; in the eluate an excess of ^{213}Bi and no ^{225}Ac is present. The expected result is a decay of ^{213}Bi in the eluate, and a growth of ^{213}Bi in the resin as equilibrium is re-established.

Beginning at 20 minutes post-elution, a series of six 1-hour data acquisitions were performed at the interface between the resin and the eluate. After image reconstruction, the total amount of ^{221}Fr and ^{213}Bi within the resin and the eluate was evaluated as a function of time.

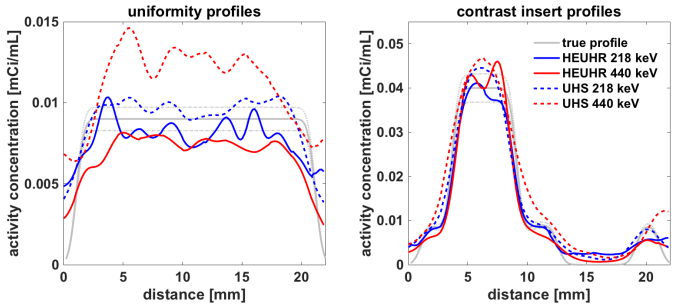

Figure 4.4: Profiles through contrast phantom images in the uniform region (a) and the contrast region (b). The ideal profile (solid grey) showing the known activity concentration and associated error (dashed grey) has been filtered with the same Gaussian filter applied to the images. Profiles from ^{221}Fr images are shown in blue, and profiles from ^{213}Bi images in red.

4.3 Results

4.3.1 Image contrast and noise

Table 4.2 contains contrast recovery and noise measurements acquired from the contrast phantom. Contrast recovery is highest for the HEUHR collimator, with contrast recovery values of 83-85% for the high activity concentration region, compared to 73-77% for the UHS collimator. However, contrast recovery between the cold and warm regions is reduced due to the non-zero background observed in the cold region and outside the phantom, a typical result caused by the difficulty of the image reconstruction to converge within low-activity regions.

For HEUHR images, the measured activity concentration within the hot region is within 9% of the expected values independently determined via gamma spectroscopy (Section 4.2.1). This error is reduced to 2% for the UHS images. However, measured activity concentrations in the low activity (warm) region differ from real values by less than 19%, with the exception of the UHS ^{213}Bi images in which an activity concentration 67% of the ideal value is measured. Profiles through the contrast inserts are shown in Fig. 4.4.

These observations are visually supported by images of the contrast phantom (Fig. 4.3). Each collimator appears visually to perform best in its nominal energy range. The HEUHR collimator can better distinguish the phantom from background in ^{213}Bi images, while the ^{221}Fr images ex-

hibit lower frequency noise and a higher background. In comparison, the UHS collimator produces ^{221}Fr images that better distinguish the phantom from background when compared to ^{213}Bi images.

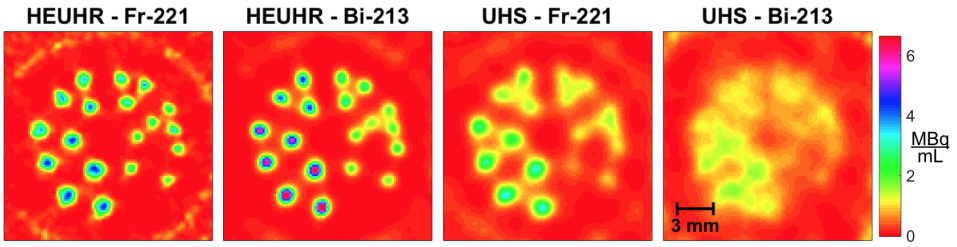

Figure 4.5: ^{221}Fr and ^{213}Bi images of the resolution phantom acquired with both the HEUHR and UHS collimators

Table 4.2: Image quality results from images of the contrast phantom, including the ideal values expected from a perfect image.

collimator	image	hot region mean [% of ideal value]	warm region mean [% of ideal value]	contrast recovery hot-warm [%]	contrast recovery warm-cold [%]	noise [%]	background variability [%]
HEUHR	**^{221}Fr**	91	89	84.5	66.5	15	7
	^{213}Bi	106	118.7	83	86.8	25	8
UHS	**^{221}Fr**	99	81.5	77	75.3	17	7
	^{213}Bi	102	67.0	73	68.7	29	15
ideal value		100	100	100	100	0	0

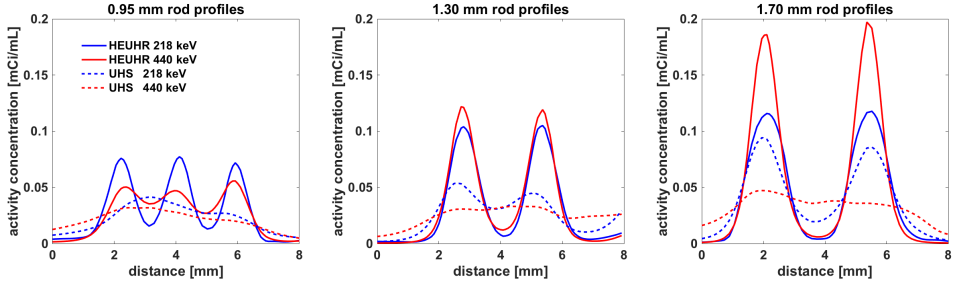

Figure 4.6: Profiles through rods of 0.95 mm diameter (left), 1.30 mm diameter (centre), and 1.70 mm diameter (right). The apparent activity within each rod can be compared to the known value of (0.13 ±0.01) mCi/mL. Profiles from ^{221}Fr images are shown in blue, and profiles from ^{213}Bi images in red.

4.3.2 Image resolution and limit of detection

Images of the resolution phantom are shown in Fig. 4.5. The HEUHR collimator clearly resolves all rods for both ^{221}Fr and ^{213}Bi images, while the UHS collimator resolves none of the rods in the ^{213}Bi images, and only some for ^{221}Fr. This is supported by inter-rod contrast measurements shown in Fig. 4.7 - the HEUHR collimator has inter-rod contrast values >35% for all rods in both ^{221}Fr and ^{213}Bi images while many UHS inter-rod contrast values are near or below zero, implying that more activity in the reconstructed image is seen between the rods than within them. The UHS collimator resolves rods only in ^{221}Fr images for diameters ≥1.3 mm. As the activity concentration is decreased (by reconstructing with fewer counts) the resolvability of rods remains unchanged above 0.23 MBq/mL.

While the rods may be resolvable, the activity concentration measured within them is not necessarily accurately estimated. Table 4.3 shows recovery coefficients for all resolved rods. RC values range between 0.55 and 0.97 for the largest rods and decrease with rod diameter. This is also seen in the profiles shown in Fig. 4.6. RC values change little for activity concentrations ≥0.23 MBq/mL.

4.3.3 Dynamic imaging of ^{221}Fr and ^{213}Bi distributions

SPECT and CT images of the cation exchange column after ^{213}Bi elution are shown in Fig. 4.8. While the ^{221}Fr images appear unchanged over time, changes in the ^{213}Bi activity distribution are visually apparent: a decreasing

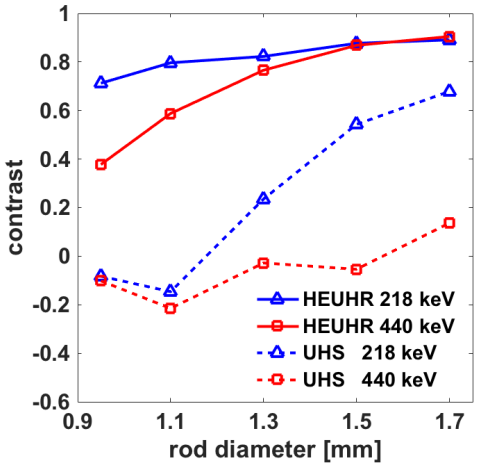

Figure 4.7: Inter-rod contrast measurements from the resolution phantom images.

Table 4.3: Recovery coefficients measured within resolvable rods of the resolution phantom. Omitted values denote rods that are not resolved (inter-rod contrast <0.2).

		rod diameter [mm]				
collimator	**image**	**0.95**	**1.10**	**1.30**	**1.50**	**1.70**
HEUHR	^{221}Fr	0.50	0.57	0.63	0.68	0.73
	^{213}Bi	0.37	0.49	0.69	0.86	0.97
UHS	^{221}Fr	-	-	0.31	0.44	0.55
	^{213}Bi	-	-	-	-	-

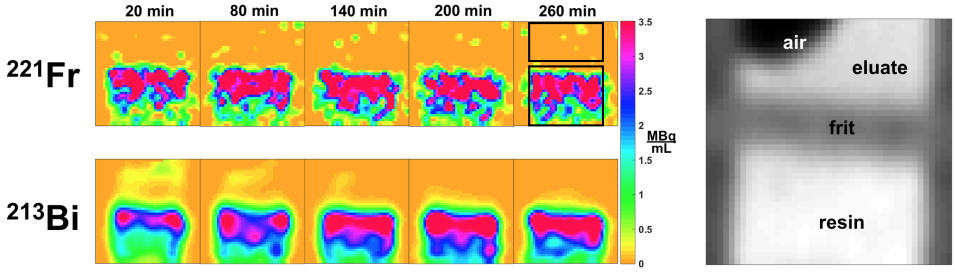

Figure 4.8: ^{221}Fr and ^{213}Bi SPECT images (left) of the cation exchange column acquired with the HEUHR collimator at multiple one-hour intervals after elution. Times for each image indicate the start time of the image frame. The CT image (right) corresponds to the same region of the phantom as the SPECT images. The black outlines in the ^{221}Fr SPECT image at $t = 260$ min indicate the boundaries of the volumes used to determine the total activities within the eluate and resin, plotted in Fig. 4.9. A non-uniform distribution of activity in the resin is also observed.

amount of ^{213}Bi in the eluate and an increasing amount in the resin.

The total activity within the resin and eluate over time is shown in Fig. 4.9. The curve fit to the ^{213}Bi resin activity measurements was calculated using the solutions to Equations 1 to 3, with the initial amount of ^{225}Ac and ^{221}Fr determined from the average of the last two ^{213}Bi data points, and the initial amount of ^{213}Bi determined by linear extrapolation of the first two points to $t = 0$. The shape of this curve agrees well with the remaining data points, and both ^{221}Fr and ^{213}Bi transient equilibrium values differ by only 5.5%. Within the eluate, an exponential fit to ^{213}Bi activities has a half-life of 39.8 min, with 95% confidence bounds of 31.3 and 54.6 min. Considering the small number of data points, this fit compares well to the ^{213}Bi half-life of 45.6 min.

4.4 Discussion

These results demonstrate the ability to quantitatively image the ^{225}Ac decay chain via simultaneous ^{221}Fr and ^{213}Bi SPECT. Given the results in in Sections 4.3.1 and 4.3.2, it is clear that a high-energy collimator such as the HEUHR is required to perform this technique. With the HEUHR collimator, spatial resolution of $\leq$0.85 mm and quantitative accuracy within 9% is achieved. Many of the imaging results of these phantom studies are also consistent with similar VECTor phantom studies in the literature. VECTor

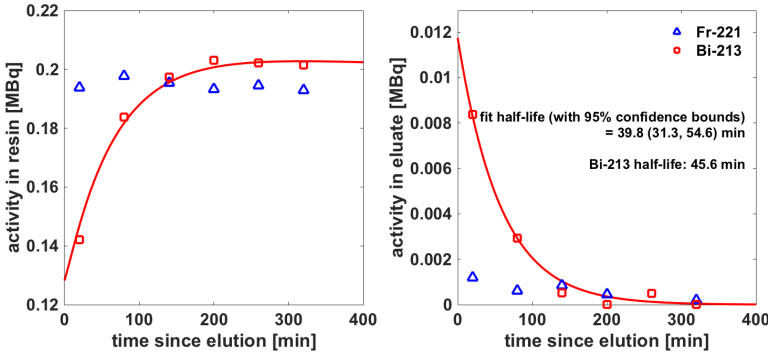

Figure 4.9: Plots of the total ^{221}Fr and ^{213}Bi activity within the resin (left) and the eluate (right) obtained from images of the cation exchange column. Background values (measured outside the column volume) have been subtracted.

studies using the UHS collimator, similar resolution phantoms and other low-energy single-photon emitters (^{99m}Tc) report resolution (1 mm) comparable to results for our low-energy single-photon emitter, ^{221}Fr images [182]. These isotopes have comparable energies (218 vs 140 keV). For the HEUHR collimator, other studies report resolvability for rods <0.55 mm with 140 keV and <0.75 mm for 511 keV, comparable to our results for ^{221}Fr and ^{213}Bi.

Studies by de Swart *et al* have characterized VECTor's ability to image ^{213}Bi using a similar high energy collimator but without the presence of ^{225}Ac or ^{221}Fr [179]. When using comparable amounts of activity, the authors report resolvability for rods ≥0.90 mm in ^{213}Bi images, as well as inter-rod contrast comparable to our HEUHR ^{213}Bi results (≥0.95 mm). The recovery coefficients within large volumes reported by de Swart *et al* are consistent with those given in Table 3 for ^{213}Bi and – accounting for the lower branching ratio – for ^{221}Fr as well.

The better performance of the tungsten HEUHR collimator is expected since – unlike the lead UHS collimator – it is designed for higher energies. With the UHS collimator, the higher energy (440 keV) ^{213}Bi photons (and the resulting scatter) are more capable of penetrating parts of the collimator than the lower energy (218 keV) ^{221}Fr photons. Not so for the HEUHR collimator, as illustrated in Table 4.1 by the number of counts acquired for each image: the average ratio of ^{213}Bi counts to ^{221}Fr counts is 1.75 for the HEUHR collimator and 3.13 for the UHS collimator - approximately 1.80 is expected, accounting for the relative branching ratios and detection

probabilities by the 9.5 mm thick NaI detector.

While a high energy collimator is needed to provide ^{221}Fr and ^{213}Bi images of acceptable quality, the HEUHR ^{213}Bi images in this study present artefacts not seen in other images. These ring-like artefacts are possibly a Gibbs artefact [190] or are possibly indicative of a slight system matrix inaccuracy. These artefacts can be seen in the profiles through the hot region of the HEUHR ^{213}Bi contrast image, shown in Fig. 4.4 and in the high-activity regions of the ^{213}Bi images in Fig. 4.8 (the ring-like artefact is viewed from the side in this figure). The cause of these artefacts is likely attributable to the fact that the system matrix provided by the manufacturer and used to reconstruct the images is calculated for 511 keV photons and does not perfectly reconstruct the 440 keV images. However, a similar effect is not observed for the ^{221}Fr (218 keV) images, for which a 140 keV system matrix is used.

Difficulties in obtaining enough ^{225}Ac is a challenge faced by other researchers involved in ^{225}Ac studies due to the cost and limited supply of this isotope. While other methods of supplying ^{225}Ac are under development, and TRIUMF expects to increase ^{225}Ac production in the near future, *in vivo* studies are not possible with the amount of ^{225}Ac presently available. Though increased activity would improve image quality, the long data acquisitions used here provide a total number of counts for image reconstruction (see Table 4.1) that is comparable to the number of counts for a typical *in vivo* study at our centre, usually $\sim 10^6$ to 10^7. Note that while the cation exchange column study only had 10^5 counts, this is compensated by the small image volume – only one bed position was used. More activity is needed for *in vivo* imaging due to the requirements to image a larger volume and reduce acquisition time to durations suitable for animal care. For mice, the number of bed positions may double and acquisition time may need to occur ten times faster. These factors combined suggest approximately 20 times more activity will be required to obtain *in vivo* images of comparable quality.

As seen in the contrast phantom image results, the accuracy of the images will also depend on the activity concentration (i.e. an *in vivo* image where all activity in concentrated in a small volume may not be directly compared to an image where the same amount of activity is spread out over a larger volume). Results from the resolution phantom images indicate activity concentrations $\geq$0.23 MBq/mL will result in acceptable image quality. This result implies that therapeutic amounts of ^{225}Ac (typically about 0.05 MBq/kg [29]) are likely not imageable in live subjects as a single VECTor bed position can only image a $\sim$1 mL volume. However, imaging with higher

activities ($\geq$10 MBq) could still provide a test of ^{225}Ac pharmaceutical performance by assessing the biodistribution of the decay chain in terms of percent uptake and retention in target and non-target organs. Imaging of ^{213}Bi-radiopharmaceutical biodistributions (without the presence of ^{225}Ac or ^{221}Fr) may be more feasible due to the higher ^{213}Bi maximum tolerable activity, as has been previously demonstrated [179].

These preliminary results demonstrate the feasibility of simultaneously imaging ^{221}Fr and ^{213}Bi activity distributions. While other microSPECT/CT systems could in principle perform this imaging technique, these results demonstrate a high-energy, high-performance collimator is needed to provide quantitative images of acceptable quality. The contrast phantom studies indicate that activity concentrations can be accurately determined within high activity regions of sufficient size, while resolution phantom studies show the ability to resolve mouse-organ-sized objects. The accuracy of ^{221}Fr activity concentration estimates indicates that down-scattering from ^{213}Bi does not affect the ability to quantitatively image ^{221}Fr, a result consistent with other studies that suggest the VECTor reconstruction software can correct for these effects [182]. While images will benefit from increased activity, this method is feasible and warrants further study *in vivo*.

This imaging technique shows potential to resolve a challenge commonly encountered in ^{225}Ac pharmaceutical research: easily assessing the biodistribution of ^{225}Ac progeny isotopes over time. Referring to the decay chain in Fig. 1.8, imaging of ^{221}Fr will indicate the location of alpha-emissions from ^{221}Fr as well as from ^{217}At, due to the latter's rapid decay. Similarly, ^{213}Bi images will be co-localized with alpha-emissions from both ^{213}Bi and ^{213}Po. Since ^{225}Ac itself cannot be directly imaged, the location of ^{225}Ac alpha-emissions could be determined by euthanizing the animal and repeating the imaging after the decay of any ^{221}Fr that is not co-localized with ^{225}Ac.

The information made available through this technique would be of significant importance to ^{225}Ac radiopharmaceutical development. Providing a complete picture of the ^{225}Ac decay chain's pharmacokinetics over time would measure the fraction of ^{225}Ac progeny isotopes maintained at the target site and could resolve persisting concerns within the field regarding the safety of serial alpha-emitting radionuclides like ^{225}Ac. As an example, in situations where an ^{225}Ac radiopharmaceutical is seen to result in renal toxicity due to ^{213}Bi, time-dependent biodistribution data made available by this technique could distinguish between: i) toxicity due to free ^{213}Bi that is co-injected with the radiopharmaceutical; toxicity due to ^{213}Bi that is generated by ^{225}Ac within the body before ^{225}Ac uptake at the tumour;

and iii) toxicity due to ^{213}Bi generated by ^{225}Ac at the tumour that has then migrated elsewhere. Given the short ^{213}Bi half-life, if either i) or ii) were the case then the toxic effects could be potentially reduced by administration of an agent that temporarily blocks ^{213}Bi uptake in the kidneys, increasing the amount of ^{225}Ac that could safely be administered. Ultimately, this technique could provide a useful test of new ^{225}Ac pharmaceuticals developed at TRIUMF or elsewhere, and help identify the pharmaceuticals best suited for therapeutic preclinical and clinical trials.

4.5 Summary

This chapter demonstrated that a microSPECT/CT system equipped with a high energy collimator is capable of simultaneously and quantitatively imaging dynamic ^{221}Fr and ^{213}Bi activity distributions resulting from the decay of ^{225}Ac.

However, larger quantities of ^{225}Ac are required for *in vivo* imaging. As described in Section 1.4, the inability of TRIUMF's ISAC Facility to reliably produce such quantities was the primary motivation for pivoting the focus of this thesis towards alternative ^{225}Ac production at TRIUMF's IPF, as detailed in Chapters 5, 6, and 7.

5 Thorium Target Design and Irradiation

5.1 Background

Of potential alternative accelerator-based ^{225}Ac-production methods (see Section 1.3), the proton-induced spallation of thorium at TRIUMF's 500 MeV Isotope Production Facility has potential to produce significant quantities of ^{225}Ac [1]. As discussed in detail in Chapter 7, the co-production of ^{225}Ra during the spallation process is also of interest, as ^{225}Ra can serve as a generator of additional ^{225}Ac.

To make ^{225}Ac via thorium spallation at TRIUMF, thorium targets are bombarded with 480 MeV protons at a beam current of up to 100 μA. During the irradiation the thorium is hermetically sealed within a target capsule. For safe and reliable operation it is crucial that this hermetic seal around the thorium is at all times able to withstand any thermally-induced mechanical stresses resulting from the large power deposition into the target from the proton beam (see Section 1.1.3), since such a "target failure" could enable the release of gaseous and volatile radionuclides co-produced within the thorium during the spallation process. Careful modelling and design of new targets must therefore be done to ensure safe and successful irradiations.

This chapter introduces the design of a new target system for ^{225}Ac production through proton-induced thorium spallation at the TRIUMF 500 MeV Isotope Production Facility (IPF). The input and assumption for the modeling are described and discussed, and modeling results and initial operational experiences are presented.

5.2 Materials and Methods

5.2.1 TRIUMF's 500 MeV Isotope Production Facility

TRIUMF's 500 MeV Isotope Production Facility (IPF) was first conceived in 1978, and modelled after a similar facility at Brookhaven National Laboratory [191]. Historically, IPF has been primarily used for the irradiation of molybdenum targets for the production $^{82}Sr/^{82}Rb$ generators, as well as occasional CsCl and KCl targets. However, the facility has received little use in recent years despite routinely receiving proton beam. IPF is located near the end of beamline 1A (BL1A), the main beamline of TRIUMF's 500 MeV cyclotron [192]. With the exception of TRIUMF's Thermal Neutron Facility [193] – which is downstream at the BL1A beam dump – the majority of BL1A users are located upstream from IPF and are not affected by its operations. Typical beam parameters for IPF are described in Section 5.2.2.

IPF consists of a 30 cm diameter, 8 m tall column of cooling water. The target station is located in the bottom of the water column at beam level. Above the water column, a shielded transfer hot cell is used to bring targets in or out of the facility and to move them in or out of the beam. Within the transfer cell, targets are inserted into one of six cassettes which are lowered into the cooling water column and down to target station by a chain drive. A total of 12 targets can be simultaneously irradiated at IPF – each cassette can hold a pair of up to 8 mm thick targets, separated by a 2.5 mm gap (see Figure 5.1b). When isotope production targets are not in use, helium gas targets are inserted to displace cooling water from the beam path, minimizing heat loads on the IPF cooling water heat exchanger. During irradiation, targets are submerged in the water column and housed in one of six cassettes through which recirculating cooling water is pumped (see Figures 5.1a and 5.1b). The cooling water flow of 114 L/min is routed through the station's 8 water circuits, six of which each feed individual cassettes. The two remaining water circuits are used for radial cooling of the target station's entrance and exit windows. Flow rates through individual cassettes are estimated to be between 7.2 and 23.4 L/min, depending on the location of the cassette. Cooling water temperature typically measures 25-28 °C at the target.

A typical IPF target is shown in Figure 5.1c: two Inconel® 600 windows (0.127 mm thickness) are welded to either side of a ring-shaped stainless steel target frame (10.1 cm diameter, 8.4 mm thickness), sealing within the 8.2 mm thick, 7.6 cm diameter puck of target material (ex. a puck of molyb-

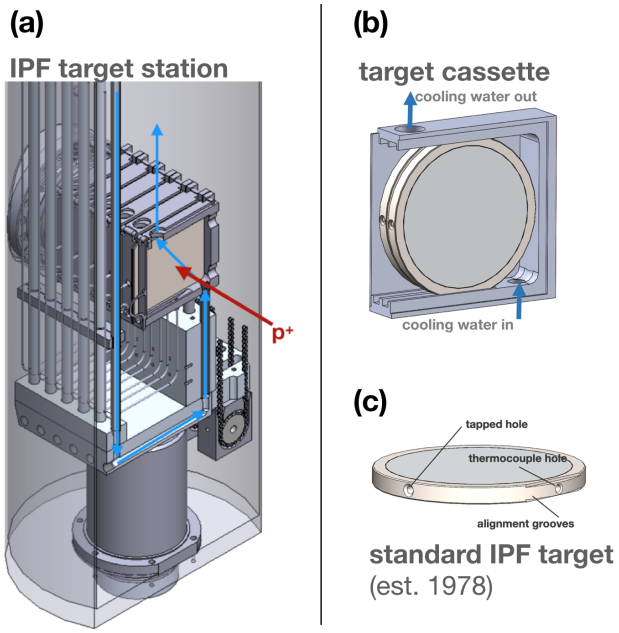

Figure 5.1: **a**) IPF target station at beam level, with six cassettes inserted into the beam. The arrows indicate cooling water flow direction. **(b)** An IPF cassette holding two targets. **(c)** A typical IPF target.

denum dioxide or potassium chloride salt) [191]). As shown in Figure 5.1, the targets interface with other IPF components in three ways: alignment grooves on the bottom of the frame fix the orientation of the target within the cassette; a thermocouple hole at the bottom of the target has a thermocouple inserted in it during irradiation to monitor target temperature; and a tapped hole in the side of the frame allows targets to be securely picked up and manipulated by a threaded rod. More details regarding the IPF facility and its targets are provided by Burgerjon *et al* [191].

5.2.2 Proton beam parameters

For 6-7 months per year, BL1A typically operates with 100-110 μA of 480 MeV protons at extraction from the TRIUMF main cyclotron, with the ability to increase this up to 170 μA. Before reaching IPF, beam losses occur due to two beryllium muon production targets (T1 and T2). Depending on the thickness of these targets, the proton beam reaching IPF can have an energy between 451 and 472 MeV and a current that is reduced by 15-40% to 60-94 μA under typical operating conditions. The beam profile at IPF is measured by a multi-wire scanner located 2 m before IPF. The Gaussian beam typically has a 2σ width between 25 and 35 mm in the horizontal and vertical directions, depending on the beam tune and thickness of the T1 and T2 targets.

Due to the variability in the beam conditions at IPF and the desire to design an ^{225}Ac production target that is compatible with all BL1A operating conditions, multiple operational cases are considered when modelling irradiations of the thorium targets. A symmetrical Gaussian beam shape is assumed, with 2σ beam widths between 15 and 40 mm. Currents between 60 and 120 μA are also considered. Beam energy is fixed at 454 MeV (the lowest estimated beam energy at IPF), since at 454-470 MeV a $<4\%$ change in beam energy negligibly affects isotope production rates and heat loads on the target as both cross-sections and stopping powers are relatively flat in this energy range [108, 118]

5.2.3 Thorium target

5.2.3.1 Design considerations

Since safe and reliable ^{225}Ac production requires the hermetic seal of the target to withstand any stresses caused by thermal changes in the target that result from the proton beam, the target design must also maximize

heat transfer from the thorium to the cooling water through the hermetic seal.

Post-irradiation processing of the target also requires that the thorium be dissolved. While a previous IPF thorium target prototype utilized ThO_2 [2], this is not suitable for routine ^{225}Ac production, due to the insoluble nature of ThO_2 [194]. Thorium metal was chosen as the target material as it can be readily dissolved post-irradiation. The metal also has other advantageous properties such as a high melting point and high density.

While the high density of thorium metal provides greater scaleability for maximizing ^{225}Ac production if simultaneous irradiation of larger thorium quantities are desired, current needs only require the irradiation of thin thorium foils <1 mm in thickness. Therefore, the 8 mm wide hermetic target casing used for decades at IPF had to be modified in this target design.

5.2.3.2 Mechanical assembly

The thorium target consists of an stainless steel 316 (SS316) outer frame that interfaces with IPF cassettes, and the thorium target material that is sealed within the frame by two Inconel® 718 windows (0.127 mm thickness). Currently, the thorium metal target material consists of a 60 mm diameter, 0.25 mm thick foil, purchased from IBI Labs (International Bio-Analytical Industries, Inc., Boca Raton, FL).

Sealing of the thorium within the target is done in two stages. First, the thorium is sealed within a target sub-assembly that consists of a thin inner welding ring (1 mm thick, 76 mm diameter), to which both windows are electron-beam (EB) welded (Figure 5.2a). The sub-assembly is then EB welded to the target frame (Figure 5.2b). A photo of the finished target is shown in Figure 5.2c.

Relevant material properties for the thorium, SS316, and Inconel® 718 components of the target assembly are shown in Table 5.1. Yield and ultimate strength values for Inconel® 718 were obtained from the materials certification provided by the manufacturer (American Special Metals, Coral Springs, FL). Material composition by mass for each target component is provided in Table 5.2.

All material properties used for modelling of the target were obtained either directly from the manufacturer, or the Knovel Engineering Data and Technical Reference Database [195]. Thorium material properties were also obtained from the ASM International databases [196].

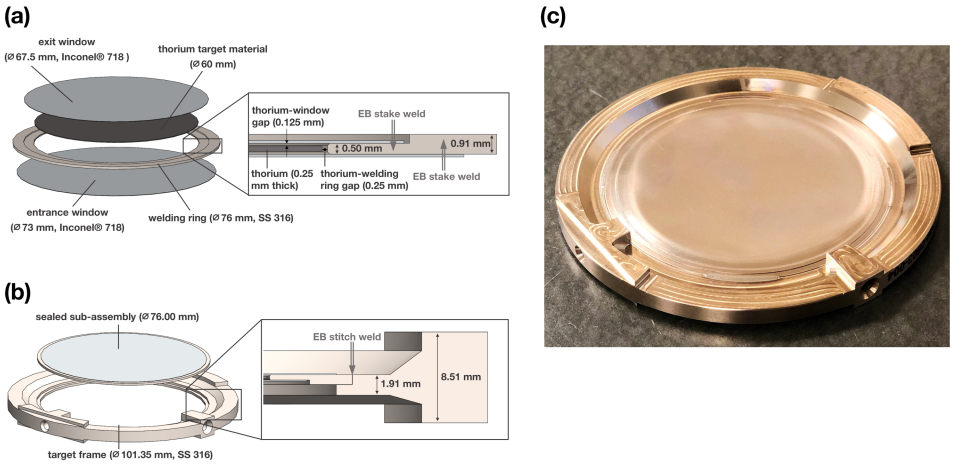

Figure 5.2: **a**) Target sub-assembly, including the thorium foil, welding ring, and entrance and exit windows. Note the location of EB welds that bind the windows to the welding ring, sealing the thorium within. **(b)** Welding of the sub-assembly to the target frame. **(c)** Photo of the thorium target. Note the inward deflection of the Inconel® 718 window.

Table 5.1: Base properties at room temperature for target components.

Property	**Inconel® 718**	**thorium**	**SS 316**
Density (g/cm^3)	8.19	11.72	8.0
Young's Modulus (GPa)	199	72.4	193
Thermal expansion (μm/mK)	13	11.1	16.3
Poisson's ratio	0.3	0.27	0.28
Yield strength (MPa)	460	144	290
Ultimate strength (MPa)	895	219	580
Melting Point (K)	1533	2028	1673
Thermal conductivity (W/m^{2}K)	11.1	13.86	14.6

Table 5.2: Elemental composition of alloys used in IPF targets. Values are from supplier certificates of analysis unless otherwise stated.

	Composition (% mass)								
Material	**Cu**	**Cr**	**Fe**	**Mn**	**Si**	**C**	**S**	**Mo**	**Ni**
Inconel® 718	0.3	17	23.6	0.35	0.35	0.08	0.015	3.3	55
SS 316	-	16	70	0.5	0.25	0.083	0.083	2	11
thorium	>99.5% by ICP-MS analysis								

5.2.3.3 Areal contact at thorium-window interface

Contact between the thorium foil and the target assembly window is an important factor when considering how effectively the target will be cooled during irradiation, as the majority of power deposited in the target assembly is expected to be removed to the cooling water via heat transfer over this barrier.

As shown in Figure 5.2a, before the thorium is sealed within the sub-assembly, a 0.125 mm gap exists between the thorium and each window. Sealing of the foil under the vacuum provided by the EB welding chamber results in a first mode deflection of the target windows: atmospheric pressure acts on the sealed, evacuated sub-assembly, forcing the windows to bend inwards (visible in Figure 5.2c). This ensures contact between the thorium and windows at the center of the target where heat loads from the proton beam are highest.

In order to measure the area for which the thorium and windows are in contact, the thickness of a manufactured sub-assembly was measured using a profilometer (Nanovea ST400). Shown in Figure 5.3, this indicates that the inner 49.8 mm of the thorium foil contacts the windows, as defined by the points where the windows stop deflecting inwards. These 49.8 mm represent 83.0% of the 60 mm thorium foil diameter, or 68.9% of the surface area. A second profile (not shown), made perpendicular to the one in Figure 9, also indicated 48.2 mm of contact (80.4% of the diameter).

For simulations of thorium target temperatures during irradiation, a conservative 45 mm wide contact region (75% of the diameter, and 56.3% of the surface area) is assumed. However, it should be noted that the amount of contact during the irradiation is expected to increase from measurements shown in Figure 5.3: while the profile measurement was done at atmosphere, additional pressure on the target windows will be present during irradiation

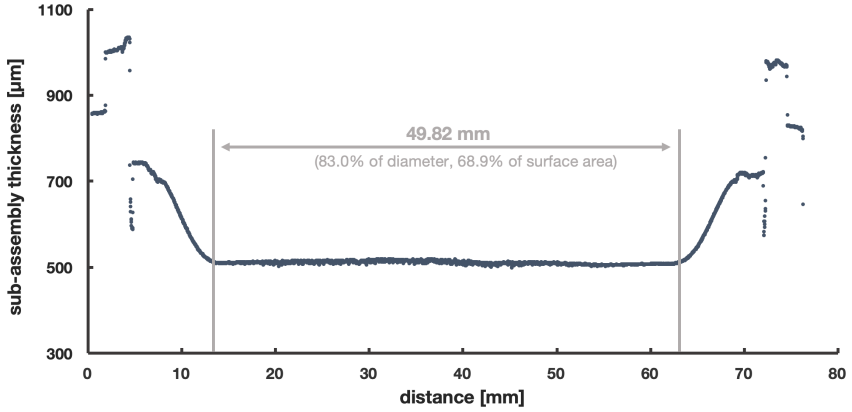

Figure 5.3: Plot of the thorium target sub-assembly thickness. Measurement of the inward deflection of the window, as also seen in Figure 5.2c, indicates the region for which the thorium and windows are in contact. The expected thickness in the centre of the sub-assembly (assuming contact of the thorium with both windows) is 504 μm.

due to the depth of the target in the cooling water column (8 m below the water surface).

5.2.3.4 Thermal contact resistance at thorium-window interface

In addition to the contact area between the thorium and windows, the thermal contact resistance at this interface is also an important factor when considering how effectively the target will be cooled during irradiation. The greatest predictors of contact resistance are contact pressure, surface roughness, hardness, and yield strength. Thorium is soft and has a polished finish, so the contact resistance would likely be small. While limited data exists for thorium contact resistance measurements, comparisons can be made to similar materials. Several copper and aluminum alloys have similar properties to that of thorium, however, since aluminum values for contact resistance are higher it is more conservative to compare the thorium to aluminum (6000 series). The aluminum alloy with the closest material properties to thorium is aluminum 6061-T4 (Table 5.3). Table 5.4 also shows approximated contact resistances for several comparable metals. The aluminum-aluminum contact resistance is the highest of the comparable metals at 0.0005 m^2K/W. Figure 11 shows a more detailed estimation of Aluminum 6061-T4 stress for the pressure range (0.1-0.2 MPa) the target will operate in. Since both sources

Table 5.3: Comparison of thorium to select aluminum and copper alloys in terms of material properties relevant to thermal contact resistance.

Material	Yield strength (MPa)	Brinell hardness
thorium	144	60-90
aluminum 6061-T4	146	65-89
aluminum 2024-T4	395	120-150
aluminum 7075-T6	503	150-191
copper 1010	305	105-123

Table 5.4: Thermal contact resistances for select materials under vacuum conditions.

Interface	Thermal contact resistance (m^2K/W)
iron-aluminum	0.00002
copper-copper	0.0001
aluminum-aluminum	0.00045
stainless-stainless	0.005
ceramic-ceramic	0.002

show a resistivity of below 0.001 m^2K/W the simulations will make the conservative approximation of 0.001 m^2K/W as the target contact resistance.

5.2.4 Thermomechanical modelling

5.2.4.1 Power deposition

Energy deposited by 454 MeV protons within each target component were simulated using SRIM [108] and results for each target component in MeV/proton are shown in Table 5.5. These values are then used to create power distribution profiles for each component that incorporate the beam's current and Gaussian profile. A MATLAB script is used to generate these profiles and output them as contours that can be imported directly into ANSYS CFX (version 19.0). ANSYS CFX then interpolates between these contours to determine the 3-dimensional power deposition distribution for each target component. Note that the beam is assumed to have a Gaussian

Table 5.5: Energy deposited in thorium target components by 454 MeV protons.

Component	Material	Thickness (mm)	Energy deposited (MeV/proton)
thorium foil	thorium	0.25	0.423
entrance window	Inconel® 718	0.127	0.21
exit window	Inconel® 718	0.127	0.21
target frame	SS 316	8.51	8.306
welding ring	SS 316	0.91	1.466

shape symmetrical in the x- and y-directions, with beam width specified by the 2σ-value of the Gaussian. Since beam current and width may change between individual IPF irradiations (see Section 5.2.2), multiple beam width and current values are considered.

5.2.4.2 Thermal modelling

ANSYS CFX simulations were used to model heat transport within the target during irradiation. Power deposition distributions and cooling water flow simulations were combined to model the thermal response of an irradiated and cooled target. Radiative heat transfer was excluded from the thermal simulations and only conductive heat flow was considered.

ANSYS CFX simulations used a κ-ϵ turbulence model to represent the mixed laminar and turbulent flow conditions present inside the target cassette. This model does not deal with issues of flow recovery, unconfined flows, flow separation or flow reattachment. While flow recovery, flow separation, and flow reattachment were observed in simulations, the flow rate is low enough for these effects to be negligible. Therefore, the κ-ϵ turbulence model is a robust, stable, and conservative model to use [197].

Properties of inlet cooling water flow across the targets were set to 28 °C, and a total flow rate of 0.120 L/s per cassette was used (corresponding to the lowest calculated value for mass flow rate through a given cassette, as detailed in Section 5.2.1). Due to the absence of flow measurements for individual cassettes, flow sensitivity checks were conducted to determine the effects of reduced flow on the simulation results.

The numerical accuracy of the solutions was determined based on the approach described by Celik *et al* [198]. The technique implements the iterative process of decreasing mesh size and solving the simulation until

temperature, heat transfer, and flow changes are negligible between mesh changes. The Grid Convergence Index is then used to estimate the rate of convergence of the solution and truncation errors. Based on this standard check, the maximum error in the simulated temperature results was 9 K for the target windows.

5.2.4.3 Mechanical modelling

To evaluate potential damage to the target during irradiation, stresses for the thorium foil and target windows were analyzed using a linear stress-strain model. Greater importance was placed on the integrity of the windows that provide a hermetic seal around the target during irradiation – damage to the thorium foil alone is not considered a target failure. Use of a linear model reduces computation time but limits the accuracy of results to cases where simulated stresses are below the yield stress of the materials. Therefore, when assessing the potential for target failure, the maximum stress in the target windows was, conservatively, compared to the yield stress of Inconel® 718.

To further reduce computation time, simulations also assumed temperature independence of material properties within the target assembly. This introduces an additional limitation: results will only be accurate within temperature ranges for which critical material properties are constant. For the Inconel® windows – the components critical when evaluating potential for target failure – this can be assumed between 0 and 600 °C. The most critical Inconel® 718 properties – the ultimate and yield strengths – drastically decrease above 600 °C . Note that other Inconel® 718 properties such as Young's modulus, Poisson's ratio, and thermal conductivity are also temperature dependent, but are mostly constant over the same 0 to 600 °C range. Due to its rare and radioactive nature, similar material property temperature-dependence data is challenging to find for thorium.

In addition to thermally-induced stresses in the target caused by the proton beam, the target also experiences stresses caused by atmospheric and hydrostatic pressures. Since the thorium is sealed within the sub-assembly under vacuum conditions, 0.1 MPa of atmospheric pressure is exerted on the Inconel® windows after the target is removed from the EB welding chamber. The windows experience an additional 0.1 MPa (0.2 MPa total) when submerged under 8 m of water in the IPF target station during irradiation.

In the centre of the target where the windows press against the thorium, this 0.2 MPa of stress is negligible compared to the stress caused by heat during irradiation (on order of 10^2 MPa). Higher stresses are experienced

near the edge of the window in the region where it deflects across the edge of the welding ring. Since accurate modelling of stresses at such boundaries is challenging, tests of the target's ability to withstand these pressures were conducted: after the target was placed in a helium pressure chamber at 0.5 MPa for 2 hours, no damage was observed. Based on this result, atmospheric and hydrostatic pressures were neglected when modelling the stresses in the thorium target during irradiation.

Mechanical simulation boundary conditions were selected on the perimeter of the thermal loading region to determine conservative worst case stresses. Similar to methods described in Section 5.2.4.2, various iterations of mesh size and type were completed to determine the grid independence of the mechanical solution before final simulations were completed.

5.2.5 Yield measurements

After test irradiations, the thorium foil was dissolved in 10 M HNO_3 + 12.5 mM HF and evaporated to a thorium nitrate salt before re-dissolution in 80.0 mL of 1 M HNO_3, in preparation for the radiochemical separation of ^{225}Ac from the target (see Chapter 7). A small portion (<100 μL) of the redissolved target was removed and analyzed by gamma ray spectroscopy with a N-type co-axial HPGe gamma spectrometer from Canberra fitted with a 0.5 mm beryllium window. The detector was calibrated (energy and efficiency) with a 20 mL ^{133}Ba and ^{152}Eu source. The dead time was less than 2%. Additional details regarding gamma spectroscopy methods can be found in Section 2.1.

The amount of ^{225}Ra produced was quantified using the 40 keV gamma line of ^{225}Ra, while the amount of ^{225}Ac produced was quantified using the 218 keV gamma line of ^{221}Fr (see Section 1.2.4).

5.3 Results and Discussion

5.3.1 Modelling and sensitivity analysis

Table 5.6 shows the power deposited by the proton beam in each target component and the total sum, accounting for different beam shapes and beam currents. The beam current was varied from 60 μA to 120 μA and the beam width from 15 mm to 40 mm to cover all realistic cases. While the total deposited power scales with the beam current as expected, variation due to the beam width are 23% for all beam currents. It should be noted that as the beam width increases, the total power deposited in the thorium

Table 5.6: Energy deposited in thorium target components by 454 MeV protons.

current (μA)	**width (mm)**	**power deposition in target (W)**					
		thorium	ent. window	exit window	welding ring	frame	total
60	15	25.42	12.63	12.63	0	0	50.68
	20	25.28	12.63	12.63	0.01	0.05	50.61
	25	24.59	12.63	12.63	0.01	0.88	50.75
	30	23.16	12.63	12.63	0.17	4.06	52.64
	35	21.21	12.63	12.63	0.27	10.04	56.78
	40	19.08	12.61	12.62	0.35	17.63	62.29
80	15	33.89	16.84	16.84	0	0	67.57
	20	33.71	16.84	16.84	0.02	0.07	67.48
	25	32.79	16.84	16.84	0.02	1.18	67.67
	30	30.88	16.84	16.84	0.22	5.41	70.19
	35	28.28	16.84	16.84	0.36	13.39	75.7
	40	25.44	16.82	16.83	0.46	23.5	83.05
100	15	42.36	21.05	21.05	0	0	84.46
	20	42.14	21.05	21.05	0.02	0.09	84.35
	25	40.99	21.05	21.05	0.02	1.47	84.58
	30	38.6	21.05	21.05	0.28	6.77	87.74
	35	35.36	21.05	21.05	0.45	16.74	94.63
	40	31.8	21.02	21.04	0.58	29.38	103.82
120	15	50.83	25.26	25.26	0	0	101.35
	20	50.57	25.26	25.26	0.03	0.11	101.22
	25	49.19	25.26	25.26	0.03	1.77	101.5
	30	46.32	25.26	25.26	0.33	8.12	105.29
	35	42.43	25.25	25.25	0.53	20.08	113.55
	40	38.16	25.22	25.25	0.69	35.26	124.58

foil decreases since some of the proton beam is, undesirably, no longer hitting the thorium but hits the welding ring and frame instead. As an example, the resulting temperature and thermally induced stress for a 100 μA, 20 mm beam are shown in Fig. 5.4, along with the cooling water flow profiles for a 0.12 L/s cassette flow. The maximum temperature and stress in the window follow roughly the beam shape.

To summarize, thermal results determined by ANSYS CFX for all beam parameters considered, are shown in Figure 5.5. Similarly, the resulting maximal stresses on the thorium foil and Inconel® windows are shown in Figure 5.6. As expected, increases in beam current and decreases in beam width result in higher maximum temperatures and stresses on the target windows. However, using safety factors defined relative to each material's yield strength, it can be seen that all beams of width >20 mm and <100 μA result in safety factors on the target window >1. Window temperatures also remain within the region of accuracy (<600 °C) as defined in Section 5.2.4.3. These limits are well within the range of typical beam parameters at IPF (Section 5.2.2), meaning that ^{225}Ac production at IPF can occur downstream of experimental users without any alterations to the beam or impact to other users of the beamline.

Some of the assumptions and input parameters to the thermomechanical simulations were simplified in order to reduce computation time. The temperature-independence of material properties, the linear stress-strain curves used for each material, and the mechanical simulation boundary conditions on the windows are examples that limit the accuracy of the simulations. However, these are balanced by conservative assumptions such as the thermal contact resistance value used for the thorium-inconel interface. Combined with conservative stress limits on the hermetic seal of the target (relative to the yield stress of Inconel® 718 as opposed to the much higher ultimate stress), these assumptions provide confidence that these targets can be irradiated safely under the simulated conditions.

To test the sensitivity of the window and thorium foil temperature on the achieved thermal contact resistance between the thorium foil and the window, simulations were carried out varying the resistance from 0.0005 m^2K/W to 0.003 m^2K/W. The window temperature, cooled by the cooling water, is almost unaffected even for a heat transfer resistance underestimated by a factor of three. The thorium foil temperature, however, raises from 442 K to 506 K, potentially causing damage to the thorium foil.

Similarly, we varied the water flow in the cassette holding the targets from the nominal 0.12 kg/s down to 0.006 kg/s. Although the temperatures of both the window and the thorium foil increase, even at a 95% reduction

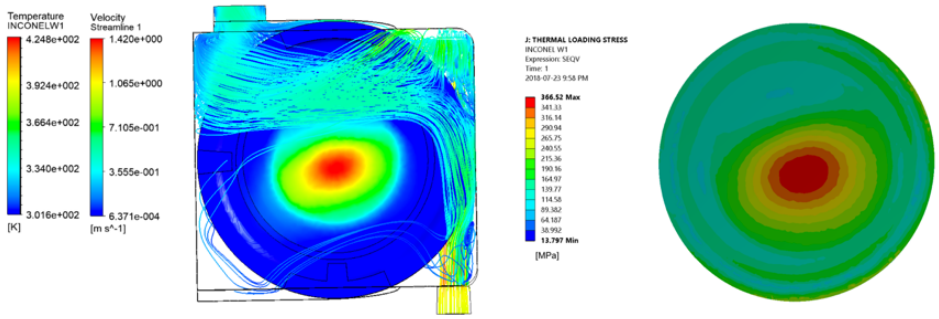

Figure 5.4: **a**) Example of simulated flow streamlines and temperatures; and **b**) stresses in the target entrance window for a 100 μA, 20 mm beam.

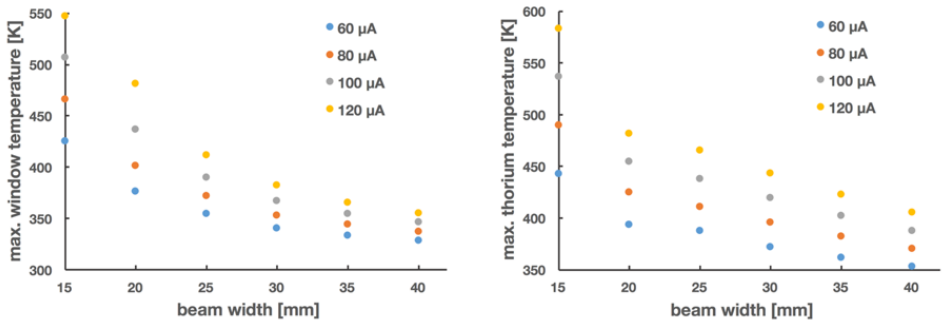

Figure 5.5: Maximum simulated temperatures within target window (left) and thorium foil (right) components during irradiations of varying beam current and width.

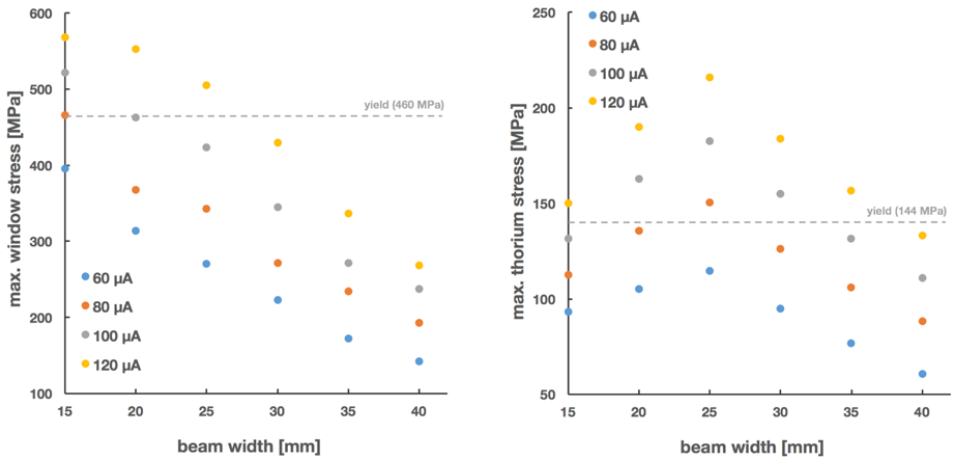

Figure 5.6: Maximum simulated stresses resulting from temperatures within window (left) and thorium (right) target components during irradiations. Note that increase in thorium foil stresses as beam width increases (from 15 to 25 mm) is due to deposition of heat in regions of the thorium that are not in contact with the window.

in water flow, the temperatures only increases by less than 15%. Note that a zero flow situation is interlocked by the target thermocouples, which would trip off the proton beam in the absence of cooling water flow.

5.3.2 Test irradiations

Two irradiations of this target design have been completed to date. Both targets were irradiated for 36.5 hours with an average beam current of 72.5 μA. Beam width was between 28-32 mm in the vertical and 30-35 mm in the horizontal directions.

After allowing targets to decay for 7 days, the thorium foil was removed from the target. In both cases, no damage, warping, or significant discoloration of the foil was observed.

The amount of ^{225}Ac and ^{225}Ra produced were measured via gamma spectroscopy. The decay corrected activity at EOB (average $\pm$ standard deviation) was (524 $\pm$ 21) MBq (14.2 mCi) and (86 $\pm$ 13) MBq (2.3 mCi) for ^{225}Ac and ^{225}Ra , respectively. These correspond to saturation yields of 72.5 MBq/μA for ^{225}Ac and 17.6 MBq/μA for ^{225}Ra.

While the ^{225}Ac quantities produced so far may be modest, significant scaleability exists for ^{225}Ac production at TRIUMF's IPF. An increase in

irradiation time to a full ^{225}Ac half-life (9.9 days), would increase production by a factor of at least 8. The simultaneous irradiation of 12 targets is also possible. Combined, these two factors alone suggest ^{225}Ac production at IPF could be readily scaled to at least 42 GBq (1.1 Ci) every 10 days, without requiring changes to the beam parameters or target design. Further increases in ^{225}Ac and ^{225}Ra yields could theoretically be achieved by increasing the proton beam current or the thickness of the 0.25 mm thick thorium foil (IPF targets can accommodate targets up to 8 mm thick), however, these would require a reassessment of the safety of such an irradiation – using the methodology presented herein – and a potential redesign of the target to prevent target failure.

The saturation yields for a 12-target irradiation would increase to 870 MBq/μA and 211 MBq/μA for ^{225}Ac and ^{225}Ra, respectively. Previous studies by others for the production of ^{225}Ac via ^{232}Th spallation have reported ^{225}Ac saturation yields of 444 MBq/μA at 90 MeV and 1140 MBq/μA at 192 MeV [138, 142]. However, these studies do not report yields for ^{225}Ra production, which is known to be smaller at the reported energies of irradiation [118, 130, 144]. The ^{225}Ra produced has the potential to not only provide approximately 0.8 MBq of ^{225}Ac per 1 MBq of ^{225}Ra [1], but also to provide generator-produced ^{225}Ac with significantly reduced ^{227}Ac impurities, a long-lived ($t_{1/2}$ = 21.8 y) alpha-emitting radioisotope with low regulatory restrictions on waste disposal and accidental intake [2].

5.4 Summary

A target system for accelerator-based production of ^{225}Ac from thorium metal at TRIUMF was presented and discussed. The thermomechanical response of the target to irradiation by the proton beam was thoroughly evaluated against conservative thresholds for target safety and the target was found to be compatible with the existing beam typically received at the irradiation facility.

The target system was tested in two irradiations with 72 μA of 450 MeV protons. After removal from the beam neither the target windows nor the thorium foil showed signs of warping, discoloration or any other signs of excessive heat or mechanical stress. With this system (524 $\pm$ 21) MBq of ^{225}Ac (14.2 mCi) and (86 $\pm$ 13) MBq of ^{225}Ra (2.3 mCi) was produced within a 36 hour irradiation, corresponding to saturation yields of 72.5 MBq/μA for ^{225}Ac and 17.6 MBq/μA for ^{225}Ra. It is estimated that the simultaneous irradiation of 12 targets over a 240 hour period could produce 42 GBq of

^{225}Ac and 7 GBq of ^{225}Ra without requiring any changes to the target or beam parameters – further scaleability exists if these parameters would also be changed.

6 Measured and Simulated ^{232}Th(p,x) Cross Sections

6.1 Background

Nuclear formation cross section data provides valuable information for validating nuclear physics models or predicting the amount of a radionuclide produced during an irradiation, which may have scientific, economic, or safety-related consequences. For complex geometries, high-energy irradiations with multiple reaction pathways, or in the absences of cross section data for a given activation product, incident particle energy, or target material, high-energy transport codes are often used to estimate residual nuclide production. Such codes combine various physics models with Monte Carlo methods to simulate the interactions of primary and secondary particles with targets and surrounding materials during an irradiation. Experimental results are essential for validating such codes for a given application.

FLUKA is one such high-energy transport code with applications in radiation shielding and facility design, dosimetry, detector and target design, medicine, and radionuclide production [128, 129]. A number of publications have demonstrated the accuracy of the results that FLUKA can provide in such applications [150–159]. One such application is the production of ^{225}Ac, a nuclide of currently heightened interest for use in targeted alpha therapy of metastatic disease [15–21, 25, 31, 32].

Most of the ∼63 GBq global annual ^{225}Ac supply comes from the decay of ^{229}Th ($t_{1/2}$ = 7600 y) generators, decaying through the ^{225}Ac parent isotope, ^{225}Ra ($t_{1/2}$ = 14.9 d) [1, 33, 35, 49, 103–105]. However, such ^{225}Ac generators are not abundant and the limited ^{225}Ac supply has resulted in many recent efforts to increase ^{225}Ac production via particle accelerators – most notably those of the US Department of Energy's Isotope Program [101, 104, 135, 138–140, 142, 199]. Of potential alternative accelerator-based ^{225}Ac-production methods, the proton-induced spallation of thorium at TRI-

UMF's 500 MeV Isotope Production Facility also has potential to produce significant quantities of ^{225}Ac [1, 5].

Irradiating materials with high-energy hadrons produces a plethora of radionuclides that must be considered when the production of a specific nuclide is concerned, and the case of as ^{225}Ac production from thorium spallation is no exception. In addition to ^{225}Ac itself, other Ac isotopes must also be considered as they cannot be chemically separated from the final ^{225}Ac product. Of particular concern is ^{227}Ac, which has a high radiotoxicity and 21.8 year half-life. ^{225}Ra production is also a radionuclide of interest, as it can be used to make spallation-produced ^{225}Ac with reduced ^{227}Ac content [2, 200]. Other spallation and fission products resulting from the irradiation must also be considered, since their quantities may dictate the associated safety, licensing, or transport regulations related to ^{225}Ac production.

This Chapter presents 38 cross section measurements relevant to ^{225}Ac production from the 438 MeV proton spallation of thorium. This selection of available data is compared to FLUKA simulations that estimate the production of the hundreds of co-produced nuclides. While other publications have reported cross sections for proton irradiation of thorium below 200 MeV and at 800 MeV [135, 138–140], to the best of my knowledge, the results reported herein are the first cross section measurements of thorium spallation near 438 MeV. Relevant concepts for nuclide production and cross sections are provided in Section 1.3.3.

6.2 Materials and Methods

6.2.1 Basic definitions and equations

The production of a radionuclide during the proton irradiation of a target material is described by the differential equation

$$\frac{dN}{dt} = \phi - \lambda N dt \tag{6.1}$$

which has the general solution

$$A(t) = \phi + Ce^{-\lambda t} \tag{6.2}$$

where ϕ is the constant production rate of the radionuclide decaying with decay constant λ and having a quantity of N nuclei or a radioactivity of $A = \lambda N$ at a given time t during the irradiation. The constant C is determined by $A(t = 0)$.

For a given irradiation, the amount of radioactivity at the end of bombardment (EOB) is described by

$$A_0 = \phi F(t) \tag{6.3}$$

where the time function $F(t)$ describes the nuclide's decay during irradiation, the irradiation profile, and $A(t = 0)$. In the most simple case of a continuous irradiation of duration Δt and $A(t = 0) = 0$, $F(t) = 1 - e^{-\lambda \Delta t}$ and

$$A_0 = \phi(1 - e^{-\lambda \Delta t}) \tag{6.4}$$

The production rate $\phi = \sigma N_T \Phi$ depends on the number of target nuclei, N_T, the proton flux, Φ, and the energy dependent formation cross section, $\sigma(E)$, which is characteristic of both the target and product nuclei.

If A_0 is determined, and if N_T and Φ are also well known, cross sections can then be calculated from Equation 6.4.

However, radionuclides are often produced both directly (described by the independent cross section σ^i) and indirectly after the decay of precursor nuclei co-produced during the irradiation (described by the cumulative cross section σ^c). For a daughter nuclide (d) with immediate precursor (parent) nuclei $(p_1, p_2, ..., p_n)$, these cross sections are related by

$$\sigma_d^c = \sigma_d^i + \sum_{i=1}^{n} \nu_i \sigma_{p_i}^c \tag{6.5}$$

where ν_i is the branching ratio with which parent p_i decays directly to (d) or (p_{i-1}).

When a radionuclide has no precursors, σ^i and σ^c are equivalent. Similarly, the contributions of individual parents to σ_d^c can be neglected if the parent is not produced during the irradiation or if $\nu_i \sigma_{p_i}^c \ll \sigma_d^i$.

One can also define the total mass cross section, which is the sum of independent cross sections for a given mass number. This value, also referred to as the total mass yield, is often used when comparing different nuclear physics models.

These definitions of σ^i and σ^c, as well as many of the equations below follow from the formulism presented by Titarenko *et al.* and used in similar publications [135, 201, 202]. Though conceptually similar to these publications, equations herein are presented differently due to differences in how A_0 is measured. Additional considerations are also presented later in this text for non-continuous irradiations and nuclei with multiple parents. The

latter must especially be considered for high Z (>83) targets such as thorium, which produce alpha-decaying nuclei and where product nuclei can have three or more parents with half-lives differing by orders of magnitude (ex. ^{225}Ac, ^{224}Ra).

As similarly described by Titarenko *et al.*, when measuring cross sections by the thin target activation method, two general situations arise depending on whether or not parent nuclei are present at the time of measurement.

Given an activity A measured at time t_m after EOB, a nuclide without precursors or with all its precursors decayed will decay with a pure exponential. In these situations, A_0 is determined by

$$A_0 = Ae^{\lambda t_m} \tag{6.6}$$

Equating Equations 6.4 and 6.6 determines the cross section from the measured value A and known values of Φ and N_T. However, unless the nuclide has no precursors, only σ^c is measurable since one cannot account for contributions from precursor decay. We consider a parent to have fully decayed after 10 half-lives (i.e. $t_m > 10 \ln 2/\lambda_{p_i}$)[9].

If a nuclide's precursor(s) have not fully decayed by t_m, parent contributions to the measured nuclide's decay rate must be accounted for when determining A_0. For a parent whose own precursors have decayed by t_m, the daughter activity at EOB, $A_0 \equiv D_0$ can be determined from the measured daughter activity, D, and measured parent activity, P, by replacing Equation 6.6 with:

$$D_0 = De^{\lambda_d t_m} - \frac{\nu P \lambda_d}{\lambda_d - \lambda_p}\left(\frac{e^{\lambda_d t_m}}{e^{\lambda_p t_m}} - 1\right) \tag{6.7}$$

Furthermore, Equation 6.4 must also be modified if Δt is not short enough (compared to the parent and daughter half-lives) for parent-daughter contributions during irradiation to be neglected. In such a situation, the amount of the parent remains described by Equations 6.1 and 6.4, while the daughter is described during the irradiation by

$$\frac{dN_d}{dt} = \nu\lambda_p N_p + \phi_d - \lambda_d N_d \tag{6.8}$$

which has the general solution

[9] One should also ensure that after 10 parent half-lives, the amount of parent remaining is negligible compared to the amount of the daughter being measured. If the parent is not measurable, this can be checked using FLUKA, which are at least accurate to an order of magnitude.

$$D_0 = \nu\phi_p - \frac{\nu\lambda_d\phi_p}{\lambda_d - \lambda_p}e^{-\lambda_p\Delta t} + \phi_d + Ce^{-\lambda_d\Delta t} \tag{6.9}$$

For $D(t=0) = P(t=0) = 0$, D_0 at EOB is thus given by

$$D_0 = \nu\phi_p\Bigg(1 + \Big(\frac{\lambda_d}{\lambda_d - \lambda_p} - 1\Big)e^{-\lambda_d\Delta t} - \frac{\lambda_d}{\lambda_d - \lambda_p}e^{-\lambda_p\Delta t}\Bigg) + \phi_d\Big(1 - e^{-\lambda_d\Delta t}\Big) \tag{6.10}$$

Combining Equations 6.7 and 6.10 with $\sigma_p^{i,c}$ determined from equations 6.4 and 6.6, allows one to determine σ_d^i. The determination of σ_d^c then follows from Equation 6.5.

When $\lambda_p > \lambda_d$, this approach is limited in situations where a parent contributes significantly to daughter production between EOB and t_m, resulting in an erroneously high measurement of the cross section. Titarenko *et al.* defines these as supracumulative cross sections, denoted σ^{c^*} [201, 202]. The maximum possible relative difference between σ^{c^*} and σ^c is given by

$$\frac{\sigma^{c^*} - \sigma^c}{\sigma^{c^*}} \leq \frac{\lambda_d}{\lambda_p - \lambda_d} \tag{6.11}$$

This difference is always positive since $\lambda_p > \lambda_d$. Equation 6.11 implies that the errors in the measurement of σ^c introduced by the supracumulative effects can be quite high. However, reported results often do not distinguish between σ^c and σ^{c^*} [201–203]. In such situations, care should be taken to try and account for parent decay between EOB and t_m or avoid reporting of the cross section altogether. The latter approach is taken in this work: the maximum potential error introduced herein to σ^c measurements, as determined by Equation 6.11 is <3.5% for ^{224}Ra and ^{127}Sb and <1.5% for all other nuclides.

A third situation can occur which must also be considered, where an activation product has multiple parents, only one of which is fully decayed by t_m. This is common for alpha-emitting nuclides produced from high Z (>83) targets such as thorium, notably including the three nuclides most relevant for ^{225}Ac production from ^{232}Th irradiation: ^{225}Ac, ^{225}Ra, and ^{227}Ac. In such situations the measured cross section is clearly not independent since indirect production through one parent is included. However, it may neither be fully cumulative with respect to all parent contributions.

When possible, the cross section – cumulative only with respect to the parent that has decayed by t_m – is determined from Equations 6.7 and 6.10 as previously described, along with the cumulative cross section for the still existing parent. The fully cumulative cross section for the daughter is then determined using Equation 6.5. If the existing parent's cross section cannot be determined or its contribution to the daughter's production neglected, σ^c for the daughter nuclide cannot be determined. Exceptions to this rule are made when the existing parent's contribution to the daughter nuclide's production occurs over an long timescale that is irrelevant for most applications (i.e. decades or millennia)[10]. While this determines a σ^c value relevant for practical applications and is similarly done by many other publications, it should be noted that this results in an underestimate of the true σ^c values as determined by Equation 6.5. Specific examples are provided Section 6.2.6.

6.2.2 Accounting for non-continuous irradiations

The non-continuous nature of the irradiation described in Section 6.2.3 requires that the time function of Equation 6.4 be modified to account for the multiple "beam-on" intervals separated by multiple "beam-off" intervals.

Assuming, as was the case, that all beam-on intervals use the same proton flux, we consider the situation where the target is irradiated with three beam-on intervals, Δt_1, Δt_3, and Δt_5, separated by beam-off intervals Δt_2 and Δt_4.

At time $t_1 = \Delta t_1$, a nuclides activity is described by

$$A(t_1) = \phi\big(1 - e^{-\lambda \Delta t_1}\big) \tag{6.12}$$

which is identical to Equation 6.4. By the end of the first beam-off interval at time $t_2 = \Delta t_1 + \Delta t_2$, the activity will have decayed to

$$A(t_2) = A(t_1) e^{-\lambda \Delta t_2} \tag{6.13}$$

Production after the second beam-on interval, at time $t_3 = \Delta t_1 + \Delta t_2 + \Delta t_3$, will be described by Equation 6.2, where the constant, C, is determined by the amount of activity at t_2 to be $C = \phi - A(t_2)$, therefore,

$$A(t_3) = \phi - \big(\phi - A(t_2)\big) e^{-\lambda \Delta t_3} \tag{6.14}$$

In a similar manner, the activity at times $t_4 = \Delta t_1 + \Delta t_2 + \Delta t_3 + \Delta t_4$ and $t_5 = t_4 + \Delta t_5$ is described by

[10] Distinctions between such semi-cumulative cross sections and fully cumulative cross sections do not appear to be made in the literature, including the EXFOR database [203].

$$A(t_4) = A(t_3)e^{\lambda\Delta t_4} \tag{6.15}$$

and

$$A(t_5) = \phi - \big(\phi - A(t_4)\big)e^{-\lambda\Delta t_5} \tag{6.16}$$

Combined, Equations 6.12 to 6.16 determine the activity at the end of the full irradiation profile, which simplifies to

$$A_0 = \phi\Big(1 - \Big[1 - \Big(1 - \big[1 - \big(1 - e^{-\lambda\Delta t_1}\big)e^{-\lambda\Delta t_2}\big] e^{-\lambda\Delta t_3}\Big)e^{-\lambda\Delta t_4}\Big]e^{-\lambda\Delta t_5}\Big) \tag{6.17}$$

The differences to Equation 6.4 introduced by the modified time function (Equation 6.17) can be significant if the nuclide's half-life is much longer lived than any of the beam-on or beam-off intervals. For example, ^{226}Ac ($t_{1/2}$ = 29.37 h) production is reduced by 41% when the correct time function is used (instead of Equation 6.4) to describe the irradiation in Section 6.2.3. In contrast, ^{227}Ac ($t_{1/2}$ = 21.8 y) is reduced by <0.01%.

If parent-daughter corrections are required during irradiation, the methodology in this appendix can also be used to modify the time function of Equation 6.10.

6.2.3 Thorium irradiations

Cross section data reported in this Chapter was derived from a 2018 irradiation conducted during the development of TRIUMF's ^{225}Ac production program [1, 2, 164, 200]. The thorium target consisted of a (0.25 ± 0.01) mm thick, (60.0 ± 0.1) mm diameter thorium-232 metal foil (>99.95% purity, as determined by ICP-MS) hermetically sealed within a (127 ± 6) μm thick Inconel 600 capsule. The use of the Inconel capsule ensures that any volatile or gaseous radionuclides produced in the thorium are not released into the cooling water in which the targets are submerged during irradiation. Furhter details of the thorium target design are described in Chapter 5 and have been reported elsewhere [5]. At 438 MeV the target is "thin", with <0.5 MeV proton energy lost over the foil thickness. As described in Section 6.2.5, the thin foil of the Inconel capsule can also be used as a beam monitor.

The irradiation was conducted at TRIUMF's 500 MeV Isotope Production Facility (IPF), located immediately in front of the TRIUMF cyclotron's

main beam dump [5, 191]. A detailed description of the IPF can be found in Chapter 5. The 500 MeV cyclotron currently operates at a typical extraction energy of 480 MeV, which is reduced to 454 MeV at IPF after passing through upstream muon production targets. The 454 MeV protons entering the IPF are further reduced to (438 ± 2) MeV at the location of the thorium foil after passing through target station components and cooling water. Measurements of the beam profile (approximately 1 m from the target) and current (approximately 10 m from the target) indicated an 65.2 μA Gaussian beam with full width at half max (FWHM) of 2.5 cm and 3.2 cm in the horizontal and vertical directions, respectively. The target was irradiated over the course of 72.9 hours to a nominal integrated current of 2640 μA*h (total beam-on time of 40.5 h) with the aim of producing approximately 555 MBq (15 mCi) of ^{225}Ac. Note that Equations 6.4 and 6.10 must be modified to account for the non-continuous nature of the irradiation (see Section 6.2.2).

After a 7-day cool-down period, the target was removed from the IPF and transferred to a radiochemistry lab where is was processed for ^{225}Ac extraction [200]. This 7-day decay period unfortunately limits the measurement of activation products to nuclides with half-lives on the order of 1 day or longer.

6.2.4 Gamma spectra acquisition and analysis

After removal from the target, the thorium foil was dissolved in 10 M HNO_3 + 12.5 mM HF, slowly evaporated to a dry thorium nitrate salt, and redissolved in a final (86.0 ± 0.2) mL volume of 1 M HNO_3. Aliquots of this solution were removed and analyzed by gamma ray spectroscopy. The preparation of gamma spectroscopy samples by dissolving the thorium was necessary to reduce radiation fields emanating from the samples, but unfortunately limits the analysis to non-volatile elements that are stable in aqueous solution (noble gases and halogens are excluded).

The detector used was a N-type co-axial HPGe gamma spectrometer from Canberra fitted with a 0.5 mm beryllium window. The detector's energy, width, and efficiency calibrations were performed using a ^{152}Eu and ^{133}Ba source. The geometry of the calibration source and all samples consisted of a 20.0 mL dilute HNO_3 solution in a scintillation vial positioned at a distance from the detector beyond which cascade-summing effects were shown to be negligible. More details regarding the gamma spectroscopy methods can be found in Section 2.1.

Spectra (dead time <0.6%) were acquired multiple times over a period 7

to 269 days after the end of irradiation, with different nuclides better quantified at different time points depending on the half-life. The resulting spectra (example in Figure 1) were extremely complex – containing on the order of 10^2 often-overlapping lines – and were therefore analyzed using the Genie 2000 software package (version 3.4, Canberra Industries). Gaussian curves were fitted by the user to all peaks (using the Genie 2000 Interactive Peak Fitting Tool) and compared against a gamma ray library representing the top 10^2 non-volatile, non-gaseous, gamma-emitting radionuclides estimated by FLUKA to be in the sample at the time of measurement. Only fitted peaks with >95% significance and a FWHM within 20% of the calibrated peak width were accepted. Decay correction during data acquisition was applied within Genie 2000 and is not included in the equations defined in Section 6.2.1.

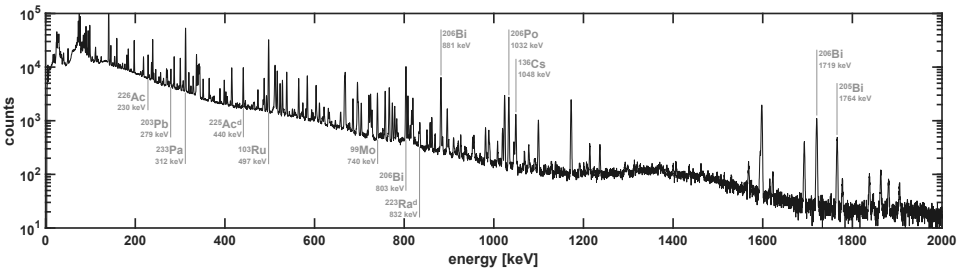

Figure 6.1: Gamma spectrum acquired of the irradiated thorium sample, 7.3 days after EOB, with select gamma lines from Table 6.1 labelled.

To prevent erroneous nuclide identification or quantification, the following acceptance criteria were used for the gamma spectroscopy results:

- Multiple gamma lines for an individual nuclide, each providing consistent individual measurements of the total radioactivity were required. The interference-corrected weighted mean of these results, as determined by Genie 2000, is then used to quantify the total radioactivity at the time of measurement.
- For nuclides providing only a single gamma ray line suitable for quantification, measurements at multiple time points were conducted to ensure the gamma line was decaying with the expected half-life.

Additional care was taken to ensure that gamma lines used for different nuclides in the library were sufficiently separated (>0.5 FWHM) to avoid false identification of a nuclide, especially with respect to mirror nuclei such as ^{111}In and ^{111}Ag.

Due to its important role in ^{225}Ac production, special attention was given to the quantification of ^{225}Ra. Due to the high slope of the efficiency curve in the low energy region (<100 keV), ^{225}Ra is challenging to accurately quantify via its single 40.0 keV emission, even when it is the only nuclide in the spectrum. Comparison of ^{225}Ra measurements at 40.0 keV (using a pure ^{225}Ra sample produced at TRIUMF's ISOL facility [3, 164]) to the measured grow-in of ^{221}Fr (218 keV) and ^{213}Bi (440 keV) was used to validate the efficiency calibration at 40.0 keV. Still, in the presence of all other thorium target activation production, ^{225}Ra detection becomes impossible due to the amount of low energy emissions (<100 keV) and scatter produced by other nuclides. Chemical separation of the dissolved thorium target was therefore performed before ^{225}Ra was measured using previously reported separation schemes [200]; the more easily detectable ^{223}Ra isotope was used to account for Ra losses during the process. The the amount of ^{225}Ra measured was then confirmed by monitoring the grow-in of ^{225}Ac.

Table 6.1 lists all 47 nuclides that were quantified from the gamma ray spectra, including all lines used for quantification. Section 6.2.6 describes how these values were used to determine cross sections for 38 of these nuclides.

6.2.5 Monitor reactions

The (127 ± 6) μm thick Inconel 600 foil used to hermetically seal the thorium during irradiation was also used to measure the proton flux. While they are non-standard monitor reactions [204], nickel spallation products from this nickel-chromium-iron alloy serve as a readily accessible beam monitor without requiring modification of the target design to accommodate additional monitor foils. The $^{\text{Nat}}$Ni(p,x)^{56}Co, $^{\text{Nat}}$Ni(p,x)^{57}Co, and $^{\text{Nat}}$Ni(p,x)^{60}Co reactions were chosen since these activation products have negligible interference from other target elements in the Inconel and are long-lived enough to be measured once the foil could be safely handled. Cumulative cross sections (37.15 ± 2.51) mb, (66.70 ± 5.69) mb, and (1.97 ± 0.30) mb for ^{56}Co, ^{57}Co, and ^{60}Co, respectively, were interpolated from available EXFOR data [144]. Table 6.2 shows the amount of these products at EOB, as measured by gamma spectroscopy (Section 6.2.4) at 270 d after EOB, and the corresponding current estimate derived using Equation 6.4. The weighted mean current estimate, (70.3 ± 4.4) μA, is larger than the nominal expected current (Section 6.2.3), 65.2 μA.

Table 6.1: Gamma spectroscopy data derived from analysis of the irradiation thorium samples, including the time of measurement (t_m) since end of irradiation, all gamma lines used in the analysis, and total radioactivity A in the entire thorium foil at the time of measurement.

nuclide	$t_{1/2}$ [d]	t_m [d]	energy [keV]	activity [Bq]	interference-corrected weighted mean [Bq]
^{233}Pa	27.0	46.3	311.90	(3.766 ± 0.168) x 10^8	(3.907 ± 0.168) x 10^8
			340.48	(4.118 ± 0.193) x 10^8	
			415.76	(4.234 ± 0.257) x 10^8	
^{230}Pa	17.4	46.3	454.92	(5.102 ± 1.154) x 10^6	(6.114 ± 0.512) x 10^6
			951.88	(6.299 ± 0.550) x 10^6	
^{228}Th^{d}	698.5	127.4	238.63	(1.875 ± 0.100) x 10^7	(1.882 ± 0.093) x 10^7
			240.99	(1.800 ± 0.389) x 10^7	
			583.19	(1.902 ± 0.125) x 10^7	
			727.33	(1.818 ± 0.284) x 10^7	
^{228}Ra^{d}	2098.8	269.4	338.02	(4.365 ± 0.820) x 10^5	(3.106 ± 0.287) x 10^5
			911.02	(2.742 ± 0.341) x 10^5	
			968.97	(4.104 ± 0.479) x 10^5	
^{227}Th	18.7	7.3	235.96	(2.348 ± 0.230) x 10^8	(2.310 ± 0.176) x 10^8
			256.23	(2.273 ± 0.229) x 10^8	
^{227}Ac^{d}	7946.8	269.4	351.07	(8.362 ± 0.802) x 10^5	(8.468 ± 0.506) x 10^5
			401.81	(1.033 ± 0.179) x 10^6	
			404.85	(9.283 ± 2.696) x 10^5	
^{226}Ac	1.2	7.3	185.60	(2.637 ± 1.323) x 10^7	(3.283 ± 0.268) x 10^7
			230.00	(3.317 ± 0.278) x 10^7	
			253.50	(3.015 ± 1.382) x 10^7	

^{225}Ra	14.9	7.3	40.00	(7.173 ± 0.430) x 10^7	(7.173 ± 0.430) x 10^7
^{225}Ac[d]	9.9	7.3	218.00	(3.347 ± 0.167) x 10^8	(3.354 ± 0.149) x 10^8
			440.45	(3.357 ± 0.155) x 10^8	
^{224}Ra[d]	3.7	7.3	238.63	(3.168 ± 0.153) x 10^8	(3.166 ± 0.139) x 10^8
			240.99	(3.033 ± 0.159) x 10^8	
			583.19	(3.289 ± 0.164) x 10^8	
^{223}Ra[d]	11.4	7.3	269.46	(2.010 ± 0.105) x 10^8	(2.157 ± 0.094) x 10^8
			271.23	(2.419 ± 0.099) x 10^8	
			351.07	(2.156 ± 0.126) x 10^8	
			401.81	(2.179 ± 0.181) x 10^8	
			404.85	(2.427 ± 0.100) x 10^8	
			427.08	(2.415 ± 0.307) x 10^8	
			832.01	(1.931 ± 0.301) x 10^8	
^{207}Bi	11515.8	269.4	569.70	(8.099 ± 0.412) x 10^5	(7.200 ± 0.353) x 10^5
			1063.66	(5.526 ± 0.417) x 10^5	
^{206}Bi	6.2	7.3	183.98	(3.287 ± 0.181) x 10^8	(2.662 ± 0.114) x 10^8
			516.18	(2.486 ± 0.124) x 10^8	
			803.10	(2.577 ± 0.127) x 10^8	
			881.01	(2.786 ± 0.135) x 10^8	
			895.12	(2.710 ± 0.134) x 10^8	
			1718.70	(2.635 ± 0.447) x 10^8	
^{206}Po	8.8	7.3	522.47	(3.393 ± 0.190) x 10^8	(2.953 ± 0.132) x 10^8
			807.38	(2.998 ± 0.160) x 10^8	
			980.23	(2.800 ± 0.159) x 10^8	
			1007.15	(2.520 ± 0.213) x 10^8	

			1032.26	$(2.904 \pm 0.129) \times 10^8$	
^{205}Bi	15.3	7.3	703.45	$(1.027 \pm 0.054) \times 10^8$	$(1.039 \pm 0.050) \times 10^8$
			987.66	$(1.052 \pm 0.060) \times 10^8$	
			1764.30	$(1.113 \pm 0.226) \times 10^8$	
^{203}Pb	2.2	7.3	279.20	$(4.019 \pm 0.189) \times 10^7$	$(4.019 \pm 0.189) \times 10^7$
			401.32	$(4.043 \pm 1.679) \times 10^7$	
^{201}Tl	3.0	7.3	135.34	$(5.016 \pm 1.728) \times 10^7$	$(3.207 \pm 0.480) \times 10^7$
			167.43	$(3.006 \pm 0.495) \times 10^7$	
^{144}Ce	284.9	269.4	133.51	$(3.077 \pm 1.261) \times 10^6$	$(3.077 \pm 0.174) \times 10^6$
^{141}Ce	32.5	127.4	145.44	$(6.379 \pm 0.401) \times 10^6$	$(6.379 \pm 0.401) \times 10^6$
^{140}Ba[d]	12.8	7.3	487.02	$(1.298 \pm 0.064) \times 10^8$	$(1.336 \pm 0.061) \times 10^8$
			815.77	$(1.411 \pm 0.074) \times 10^8$	
			925.19	$(1.286 \pm 0.101) \times 10^8$	
^{139}Ce	137.6	127.4	165.86	$(4.052 \pm 0.472) \times 10^6$	$(4.052 \pm 0.472) \times 10^6$
^{136}Cs	13.0	7.3	273.65	$(5.259 \pm 0.390) \times 10^7$	$(5.825 \pm 0.269) \times 10^7$
			818.51	$(5.942 \pm 0.287) \times 10^7$	
			1048.07	$(5.740 \pm 0.342) \times 10^7$	
^{134}Cs	753.8	46.3	604.72	$(1.936 \pm 0.186) \times 10^6$	$(1.968 \pm 0.153) \times 10^6$
			795.86	$(2.016 \pm 0.222) \times 10^6$	
^{132}Te[d]	3.2	7.3	228.16	$(5.891 \pm 0.347) \times 10^7$	$(5.993 \pm 0.266) \times 10^7$
			772.60	$(5.862 \pm 0.311) \times 10^7$	
			954.55	$(6.192 \pm 0.449) \times 10^7$	
^{131}Ba	11.5	7.3	123.80	$(3.014 \pm 0.206) \times 10^7$	$(2.807 \pm 0.184) \times 10^7$
			373.26	$(3.283 \pm 0.462) \times 10^7$	
^{127}Sb	3.9	7.3	252.40	$(1.168 \pm 0.113) \times 10^8$	$(1.096 \pm 0.051) \times 10^8$

			473.00	$(1.058 \pm 0.086) \times 10^8$	
^{126}Sb	12.4	46.3	414.70	$(1.285 \pm 0.117) \times 10^7$	$(1.309 \pm 0.064) \times 10^7$
			720.70	$(1.338 \pm 0.099) \times 10^7$	
			856.80	$(1.171 \pm 0.120) \times 10^7$	
^{125}Sn	9.6	7.3	822.48	$(8.590 \pm 2.558) \times 10^7$	$(6.190 \pm 0.679) \times 10^7$
			1067.10	$(6.109 \pm 0.762) \times 10^7$	
			1089.15	$(5.274 \pm 1.599) \times 10^7$	
			2002.13	$(9.867 \pm 5.005) \times 10^7$	
^{125}Sb	1006.9	269.4	380.45	$(3.692 \pm 0.673) \times 10^6$	$(3.496 \pm 0.150) \times 10^6$
			427.87	$(3.585 \pm 0.163) \times 10^6$	
			463.36	$(3.429 \pm 0.199) \times 10^6$	
			600.60	$(3.441 \pm 0.192) \times 10^6$	
			606.71	$(3.480 \pm 0.349) \times 10^6$	
^{124}Sb	60.2	46.3	713.78	$(3.604 \pm 0.887) \times 10^7$	$(3.989 \pm 0.452) \times 10^7$
			968.20	$(4.553 \pm 0.875) \times 10^7$	
			1690.97	$(3.899 \pm 0.604) \times 10^7$	
^{122}Sb	2.7	7.3	564.24	$(1.174 \pm 0.048) \times 10^8$	$(1.166 \pm 0.058) \times 10^8$
			692.65	$(8.912 \pm 2.009) \times 10^7$	
^{121m}Te^{d}	164.2	269.4	212.19	$(1.723 \pm 0.083) \times 10^6$	$(1.827 \pm 0.082) \times 10^6$
			507.39	$(2.394 \pm 0.179) \times 10^6$	
			573.13	$(1.965 \pm 0.110) \times 10^6$	
			1102.15	$(1.804 \pm 0.399) \times 10^6$	
^{121}Te	19.2	46.3	507.59	$(1.008 \pm 0.145) \times 10^7$	$(9.589 \pm 0.722) \times 10^6$
			573.14	$(9.727 \pm 0.817) \times 10^6$	
^{120m}Sb	5.8	46.3	197.30	$(1.861 \pm 0.227) \times 10^6$	$(1.409 \pm 0.129) \times 10^6$
			1023.30	$(1.127 \pm 0.212) \times 10^6$	

			1171.70	$(1.293 \pm 0.192) \times 10^6$	
^{115}Cd	2.2	7.3	260.90	$(2.671 \pm 0.293) \times 10^8$	$(2.488 \pm 0.121) \times 10^8$
			492.35	$(2.445 \pm 0.147) \times 10^8$	
			527.90	$(2.497 \pm 0.134) \times 10^8$	
^{114m}In	49.5	127.4	190.27	$(6.353 \pm 0.856) \times 10^6$	$(6.353 \pm 0.856) \times 10^6$
^{111}Ag	7.5	46.3	245.40	$(3.603 \pm 0.850) \times 10^7$	$(3.671 \pm 0.380) \times 10^7$
			342.13	$(3.685 \pm 0.413) \times 10^7$	
^{111}In	2.8	7.3	171.28	$(1.043 \pm 0.072) \times 10^7$	$(1.043 \pm 0.072) \times 10^7$
^{110m}Ag	249.8	46.3	657.76	$(1.022 \pm 0.058) \times 10^7$	$(9.648 \pm 0.494) \times 10^6$
			677.62	$(9.569 \pm 1.783) \times 10^6$	
			706.68	$(8.791 \pm 1.203) \times 10^6$	
			1384.29	$(8.928 \pm 0.618 \times 10^6$	
^{106}Ru[d]	371.8	269.4	621.93	$(2.300 \pm 0.127) \times 10^7$	$(2.300 \pm 0.127) \times 10^7$
^{105}Rh	1.5	7.3	306.10	$(3.389 \pm 0.164) \times 10^8$	$(2.015 \pm 0.093) \times 10^8$
			318.90	$(1.969 \pm 0.091) \times 10^8$	
^{103}Ru	39.2	46.3	497.08	$(2.330 \pm 0.113) \times 10^8$	$(2.295 \pm 0.106) \times 10^8$
			610.33	$(2.231 \pm 0.123) \times 10^8$	
^{99}Mo	2.7	7.3	181.07	$(5.140 \pm 0.283) \times 10^8$	$(5.236 \pm 0.244) \times 10^8$
			366.42	$(5.101 \pm 0.622) \times 10^8$	
			739.50	$(5.306 \pm 0.265) \times 10^8$	
^{95}Zr	64.0	46.3	724.19	$(1.074 \pm 0.054) \times 10^8$	$(1.011 \pm 0.046) \times 10^8$
			756.72	$(9.783 \pm 0.481) \times 10^7$	
^{95}Nb	35.0	46.3	765.80	$(1.168 \pm 0.057) \times 10^8$	$(1.168 \pm 0.057) \times 10^8$
^{88}Y	106.6	127.4	898.04	$(2.950 \pm 0.217) \times 10^6$	$(2.963 \pm 0.215) \times 10^6$
			1836.06	$(4.335 \pm 1.030) \times 10^6$	
^{83}Rb	86.2	269.4	529.59	$(5.463 \pm 0.577) \times 10^5$	$(5.624 \pm 0.520) \times 10^5$

	552.55	(4.018 ± 0.994) x 10^5

[d]Some or all gamma lines used for quantification belong to progeny nuclides in equilibrium.

Table 6.2: Results from gamma spectroscopy measurements of the Inconel foil used for beam monitor reaction and the resulting proton current estimates.

nuclide	$t_{1/2}$ [d]	energy [keV]	activity [Bq]	mean activity [Bq]	σ [mb]	current estimate [μA]
^{60}Co	1924.0	1173.2	(5.112 ± 0.134) x 10^5	(5.069 ± 0.114) x 10^5	37.15 ± 2.51	66.6 ± 5.9
		1332.5	(4.993 ± 0.166) x 10^5			
^{57}Co	271.8	122.1	(9.829 ± 0.355) x 10^8	(1.012 ± 0.026) x 10^8	66.70 ± 5.69	72.1 ± 7.5
		136.5	(1.033 ± 0.034) x 10^8			
		692.4	(1.044 ± 0.082) x 10^8			
^{56}Co	77.2	846.8	(1.829 ± 0.046) x 10^8	(1.834 ± 0.032) x 10^8	1.97 ± 0.30	84.0 ± 13.7
		1037.8	(1.838 ± 0.042) x 10^8			
		1238.3	(1.835 ± 0.042) x 10^8			

6.2.6 Cross sections calculations and uncertainties

Given the measured activities of activation products (Section 6.2.4), cross sections are determined by equating either Equations 6.4 and 6.6 or Equations 6.7 and 6.10. The choice of equations depends on whether or not the nuclide in question can be described as having all its precursors decayed at the time of measurement.

Independent cross sections, σ^i are determined from Equations 6.4 and 6.6 for nuclides that have no precursors. Typically, these are excited states such as ^{121m}Te, ^{120m}Sb, ^{114m}In, or ^{110m}Ag, but it also applies to ^{230}Pa. This case also applies if $\nu\sigma_p^c \ll \sigma_d^i$ such that $\sigma_d^i \cong \sigma_d^c$; an example is ^{226}Ac, whose parent ^{230}Pa has a 0.003% alpha decay.

If the nuclide in question has precursors which have decayed by t_m, then Equations 6.4 and 6.6 combine to determine the cumulative cross section, σ^c. The majority of cross sections reported herein fall into this category; examples include ^{228}Ra, ^{141}Ce, and ^{99}Mo, among others.

If a nuclide's parent is still present at t_m, then the parent nuclide's contribution to the daughter's production must either be accounted for or neglected, if justifiable. Examples of the latter are ^{136}Cs and ^{126}Sb, which have very long-lived parent nuclei ($t_{1/2} > 10^5$ y) which will not be produced with enough activity to significantly affect their daughter's decay curves. While ignoring such parent contributions means the measured cross section is not fully cumulative with respect to all parent contributions (as defined in Equation 6.5), it provides the cross section estimate that is most relevant for practical applications: if one wanted to estimate the amount of ^{126}Sb ($t_{1/2}$ = 12.35 d) produced during an irradiation, the timescale of interest is unlikely to include the distant future where ^{126}Sn ($t_{1/2}$ = 198 ky) decay contributes significantly to ^{126}Sb production[11]. Additional examples where contributions from a parent (satisfying $\lambda_p \ll \lambda_d$) are negligible include ^{225}Ra (negligible contributions from ^{229}Th), ^{227}Th, and ^{227}Ac.

When a parent exists at t_m and can't be neglected, its cumulative cross section must be determined from Equations 6.4 and 6.6, or neither σ_d^i nor σ_d^c can be reliably reported. Equations 6.7 and 6.10 are then used to determine the daughter's cross section, either independent or cumulative depending on the existence of other previously-decayed precursors. Examples of nuclides where such parent-daughter corrections were applied include ^{225}Ac, ^{224}Ra, ^{223}Ra, and ^{121}Te.

[11] Unless the parent's cross section is so much larger than the daughter's that it compensates for the much larger decay constant of the daughter.

When calculating cross sections, uncertainties in the gamma spectroscopy measurements – typically between 4 and 10% depending on the nuclide, including 2.4% from the efficiency calibration – were combined using the Gaussian law of error propagation with uncertainties from proton flux (6.2%), thorium foil thickness (4.0%), and nuclide decay constants.

6.2.7 Fluka simulations

Monte Carlo simulations were conducted using FLUKA (version 2011.2x.7) and the FLAIR interface (version 2.3-0) [128, 129, 205]. Details and description of the physics models used by FLUKA can be found in the Fluka Manual [128]. FLUKA is also introduced in Section 2.3.

All simulations used NEW-DEFAULTS default settings. PHYSICS settings included the new evaporation model with heavy fragment evaporation included, coalescence activated, and ion splitting disabled. Gamma ray interactions at all energies were included. Transport settings included pointwise low-energy neutron cross sections, a 0.0025 cm step size in thin target components (Inconel and thorium foils), 30 keV production and transport thresholds for (anti)electrons and photons, 100 keV transport threshold for protons, and full transport of all light and heavy ions linked to the DPMJET and RQMD event generators. The choice in the number of primaries used was determined by the maximum permissible run time on available clusters, provided that statistical error estimates were at least <1%.

FLUKA does not explicitly model isomeric state production, instead splitting residual nuclei equally between available ground or excited states. This must be considered when comparing results for nuclei that are affected by the modelling of isomeric state production. Activation products affected by isomeric state production include any excited states and ground states of nuclei with excited state for which the excited state is either long-lived enough to be present at t_m or if the excited state does not always decay directly to the ground state. For practical purposes, ground states with short-lived excited state precursors are not affected by isomeric state production[12], since any excited states decay quickly to the ground state.

The following subsections describe two FLUKA geometries used to model ^{232}Th(p,x) reactions.

[12] Provided $\nu = 1$

6.2.7.1 Thin foil simulations

To determine ^{232}Th(p,x) cross sections predicted by FLUKA, simulations were conducted of a proton beam incident on a 0.25 mm thick thorium foil under vacuum, using 4 billion primaries in an instantaneous irradiation[13].

With radioactive decay disabled, independent cross sections were determined from residual nuclei scoring and Equation 6.3, with $F(t) = 1$. Independent total mass cross sections were then determined (see Section 6.2.1), and cumulative mass cross sections for nuclides of interest were then determined using Equation 6.5.

6.2.7.2 Full target geometry simulations

Simulations of the entire measured cross section experiment were also conducted using 1.2 billion primaries. These simulations includes a more complete IPF target station and experimental thorium target geometry, the measured beam profile at the time of measurement, and the exact irradiation profile of the experimental irradiation, as described in Section 6.2.3. With radioactive decay enabled, radioactivation products were also scored after decay correction by FLUKA to the exact times of measurement (see Table 6.1). Cross sections were calculated from these activation results using the same methodology described in Section 6.2.6 for the measured cross sections.

This more complex simulation enables the comparison of measured and calculated cross sections under similar conditions. Simulating the measured cross section experiment in this way enables an estimation of any bias in the real cross section measurements that may be introduced by secondary particle interactions or transport originating from other components of the target station, which would not be included in the simplified simulations of Section 6.2.7.1.

As described in Section 6.3, the ratio, r, of the cross section determined by Section 6.2.7.2 divided by the cross section determined by Section 6.2.7.1, can be used to quantify this bias estimate.

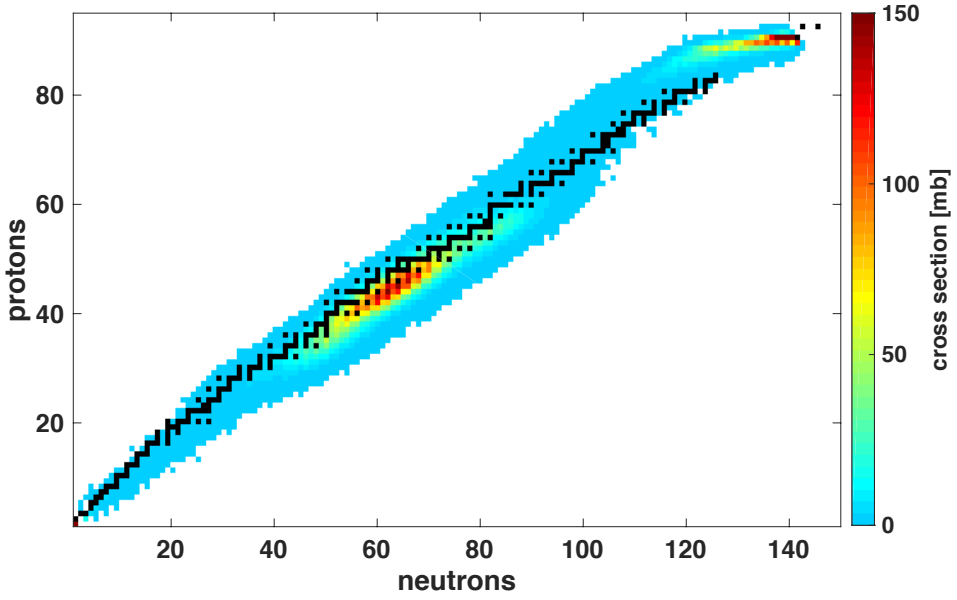

Figure 6.2: Independent cross sections for the 438 MeV proton irradiation of thorium determined via FLUKA, as described in Section 6.2.7.1.

6.3 Results and Discussion

Figure 6.2 shows independent cross sections for all nuclides, as determined via FLUKA. Visible are two distinct regions: spallation products (proton-heavy, Z>83) and fission products (neutron-heavy, Z approx. 30-60). As proton energy increases, the gap between these regions narrows.

Table 6.3 shows measured and calculated cross sections only for the specific nuclides that could be reliably measured in the gamma spectra and listed in Table 6.1. Figure 6.3a provides a comparison of the measured cross sections to the independent total mass yields calculated by FLUKA, as described in Section 6.2.7.1. As shown, mass numbers for which all contributions to the total mass yield can be measured show good agreement between the measured and calculated values.

While a direct comparison of measured and calculated nuclear formation cross-sections indicates the accuracy of models used in a simulation, in applications where simulations are used to predict the radioactive inven-

[13]Simulations were conducted at incident proton energies of 30, 40, 50, 60, 70, 80, 90, 100, 125, 150, 175, 200, 250, 300, 350, 400, 438, 500, 550, 600, 650, 700 750, 800, 900, and 1000 MeV.

tory resulting from a complex irradiation, a comparison of the measured and predicted radioactivities is of more practical relevance than a comparison of measured and predicted cross sections. For a given radionuclide of interest, the calculated radioactivity will depend not only on its formation cross section at the incident beam energy, but also on precursor nuclide cross section(s) and contributions from secondary hadrons and lower energy protons. Figure 6.3b compares the measured radioactivities in the thorium foil (Section 6.2.6) to the radioactivities calculated by FLUKA at the time of measurement (Section 6.2.7.2). This comparison include nuclides for which measured cross sections could not be determined due to the inability to account for parent nuclide contributions to the decay (^{206}Bi, ^{203}Pb, ^{201}Tl, ^{140}La, ^{125}Sb, ^{105}Rh, ^{95}Nb, and ^{88}Y) and nuclides formed predominantly by neutron capture (^{233}Pa). For 41 of these 47 nuclides, the calculated and measured radioactivities agree within a factor of 2. Excluding nuclides affected by metastable state production and neutron capture, 37 of the 38 remaining calculated and measured radioactivities agree within a factor of 2.

For individual nuclides, a comparison of calculated and measured cross sections is shown in Figure 6.3, alongside available values from the literature over the 0 to 1000 MeV range [144]. Again, the measured, calculated, and literature values generally agree within a factor of 2 or less for most nuclides. Measured and FLUKA-simulated cross sections especially agree for nuclides not affected by metastable state production. For nuclides related to ^{225}Ac production at 438 MeV, FLUKA appears to underestimate ^{225}Ra production while overestimating ^{225}Ac production, despite showing better agreement with measured values at lower energies. While no cross sections for proton irradiation of thorium near 438 MeV are reported in the literature, extrapolation from values reported at lower energies suggests that the measured values reported herein for 438 MeV are in reasonable agreement for all nuclides for which data is available, with the possible exception of ^{225}Ra. This potential discrepancy could possibly be attributed to the challenges of quantifying ^{225}Ra via gamma spectroscopy at 40.0 keV, despite the additional care taken in these measurements (see Section 6.2.4).

FLUKA-simulated cross sections alternatively calculated using the same geometry, irradiation and decay parameters, and methodology as the measured cross sections (Section 6.2.7.2) can be compared to the FLUKA cross sections of Table 6.3 and Figure 6.4 that were determined by the simulation of thin foil irradiations described in Section 6.2.7.1. As described in Section 6.2.7.2, this more complex simulation enables the comparison of measured and calculated cross sections under similar conditions and estimates any bias

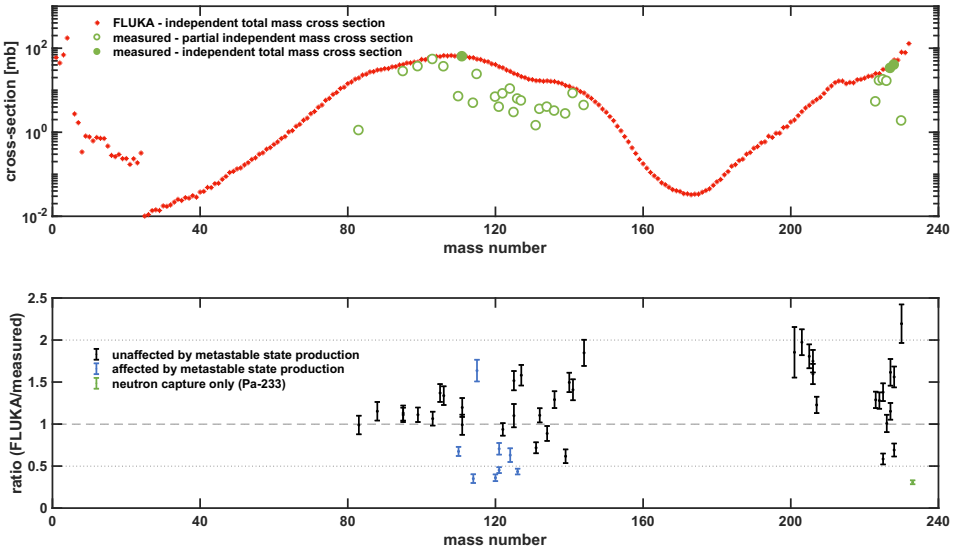

Figure 6.3: (a) Independent total mass cross sections determined by FLUKA (Section 6.2.7.1) are compared to measured mass cross sections. The total mass cross sections could only be determined for mass numbers 228, 227, and 111 – in other cases, cumulative cross sections for a given mass number could only be measured on one side of the line of stability and therefore represent only a partial contribution to the total independent mass cross section. Cumulative cross sections for ^{207}Bi, ^{206}Po, and ^{205}Bi are excluded since they are cumulative (not independent) with respect to the total mass, due to mass changes by alpha decay. (b) A comparison of measured (Section 6.2.6) and calculated (Section 6.2.7.2) radioactivities in the the irradiated target.

Table 6.3: Measured and calculated cross sections from the 438 MeV proton irradiation of thorium.

Nuclide	$t_{1/2}$ [d]	type[a]	cross section [mb]	
			measured	FLUKA
^{230}Pa	17.4	i	1.86 ± 0.23	3.02 ± 0.01
^{228}Th	697.7	c	38.18 ± 3.40	51.28 ± 0.06
^{228}Ra	2098.8	c	1.64 ± 0.19	1.05 ± 0.01
^{227}Th	18.7	c	15.55 ± 1.65	21.39 ± 0.04
^{227}Ac	7946.8	c	17.65 ± 1.68	18.51 ± 0.01
^{226}Ac	1.2	c	16.44 ± 1.81	15.01 ± 0.03
^{225}Ra	14.9	c	4.20 ± 0.40	2.41 ± 0.01
^{225}Ac	9.9	c	13.30 ± 1.21	19.32 ± 0.03
^{224}Ra	3.6	c	15.90 ± 1.40	17.98 ± 0.03
^{223}Ra	11.4	c	5.31 ± 0.39	5.01 ± 0.02
^{207}Bi	11515.8	c	21.59 ± 1.92	25.60 ± 0.03
^{206}Po	8.8	c	13.70 ± 1.19	23.10 ± 0.14
^{205}Bi	15.3	c	6.17 ± 0.54	17.36 ± 0.12
^{144}Ce	284.9	c	4.35 ± 0.40	6.77 ± 0.02
^{141}Ce	32.5	c	8.36 ± 0.81	9.92 ± 0.03
^{139}Ce	137.6	c	2.74 ± 0.38	1.63 ± 0.01
^{136}Cs	13.0	c	3.16 ± 0.28	3.63 ± 0.01
^{134}Cs	753.8	c	3.97 ± 0.43	3.21 ± 0.01
^{132}Te	3.2	c	3.53 ± 0.30	3.20 ± 0.01
^{131}Ba	11.5	c	1.44 ± 0.14	1.03 ± 0.01
^{127}Sb	3.9	c	5.59 ± 0.50	7.58 ± 0.02
^{126}Sb	12.4	c[b]	6.20 ± 0.55	2.40 ± 0.01
^{125}Sn	9.6	c[b]	2.95 ± 0.39	2.86 ± 0.01
^{124}Sb	60.2	c[b]	10.72 ± 1.45	6.29 ± 0.01
^{122}Sb	2.7	c	8.23 ± 0.73	7.35 ± 0.02
^{121}Te	19.2	c[b]	1.67 ± 0.24	1.52 ± 0.01
^{121m}Te	164.2	i[b]	2.42 ± 0.21	1.08 ± 0.01
^{120m}Sb	5.8	i[b]	6.87 ± 0.82	2.40 ± 0.01
^{115}Cd	2.2	c[b]	23.86 ± 2.11	36.63 ± 0.05
^{114m}In	49.5	i[b]	4.92 ± 0.76	1.65 ± 0.01
^{111}In	2.8	c	0.71 ± 0.07	0.84 ± 0.01
^{111}Ag	7.5	c	62.20 ± 7.92	57.03 ± 0.06
^{110m}Ag	249.8	i[b]	7.06 ± 0.63	4.64 ± 0.01
^{106}Ru	371.8	c	36.34 ± 3.35	45.00 ± 0.05
^{103}Ru	39.2	c	54.10 ± 4.72	53.87 ± 0.06

^{99}Mo	2.7	c	36.55 ± 3.19	37.78 ± 0.05
^{95}Zr	64.0	c	27.97 ± 2.43	28.29 ± 0.04
^{83}Rb	86.2	c	1.10 ± 0.13	1.05 ± 0.01

[a]Denotes cross section type: i = independent, c = cumulative. No supracumulative cross-sections are reported.
[b]Calculated cross sections for these nuclides will be affected by the incomplete modelling of isomeric state production in FLUKA.

in the measured cross sections introduced by secondary particle interactions. To compare these two methods, we define the ratio, r, of the cross section determined from the full geometry method (Section 6.2.7.2) divided by the cross section determined from the thin foil simulations (Section 6.2.7.1).

For 27 of the 38 nuclides with cross sections reported in Table 6.3 and Figure 6.4, the two different FLUKA estimates of the cross section are in good agreement ($r = 1.00 \pm 0.06$). Most (9 out of 11) of the remaining nuclides have $r > 1.06$ due to secondary proton or neutron interactions, the simualted energy spectra for which are shown in Figure 6.5. For spallation products ^{230}Pa, ^{228}Th, and ^{227}Th (r = 1.27, 1.09, and 1.11, respectively), the increased nuclide production when simulating the full target station geometry is due to lower energy (<438 MeV) secondary protons; neutron-only scoring of activation products in FLUKA indicate no neutron contributions to the production of these nuclei. Note that while the flux of secondary protons is only 3.7% of the total proton flux, Figure 6.4 illustrates that the cross sections for these nuclei are higher at energies below 438 MeV, and these protons thus contribute more than 3.7% to production of these nuclei; this is especially true for ^{230}Pa, the nuclide with greatest r. For fission products ^{144}Ce, ^{141}Ce, ^{136}Cs, ^{132}Te, ^{127}Sb, and ^{125}Sn (r =1.12, 1.12, 1.07, 1.15, 1.10, and 1.07, respectively) the increased production when simulating the full target station geometry is due production of the nuclide or its precursors via secondary neutron interactions. This is confirmed by neutron-only scoring of the activation products in FLUKA.

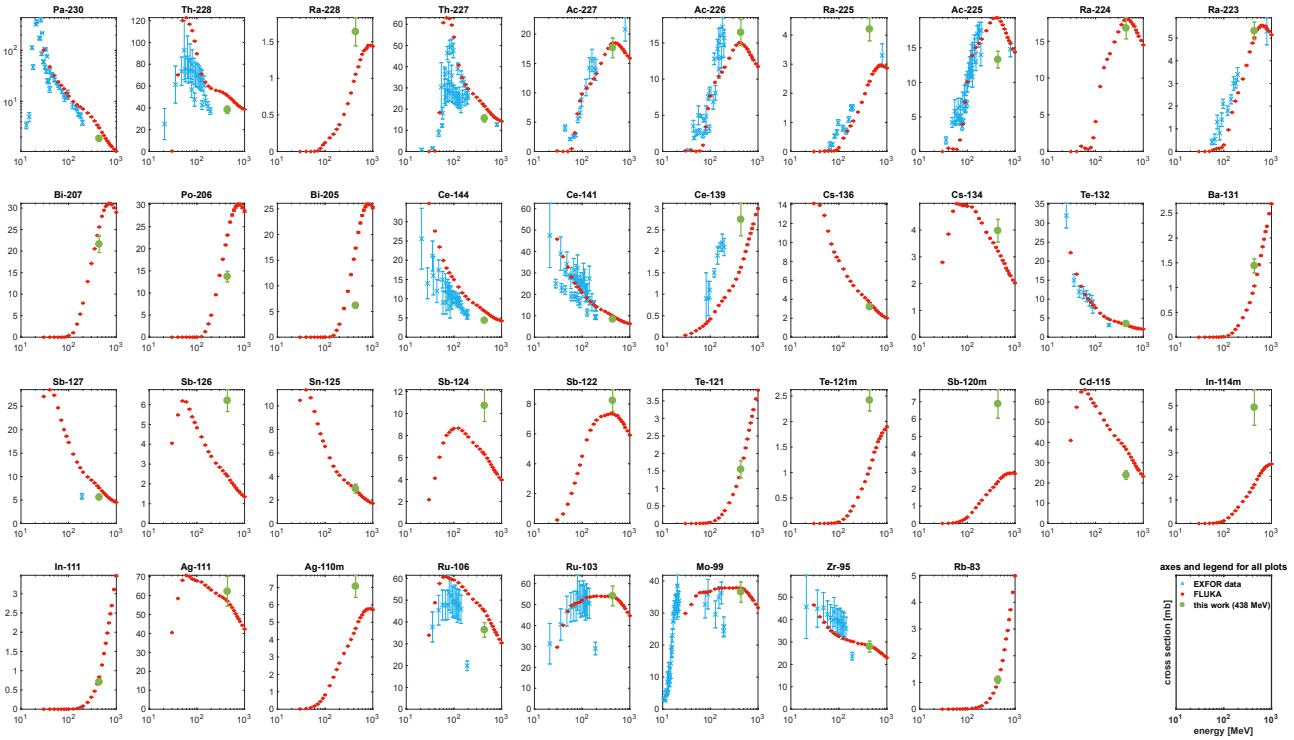

Figure 6.4: A comparison of cross sections determined in this work at 438 MeV, to literature (from the EXFOR database) and calculated values over the 0 to 1000 MeV range. The type of cross section (independent or cumulative) is indicated in Table 6.3. The axes label and legend for all plots is shown in the lower right.

With the exception of ^{230}Pa, these r values overall suggest that the secondary particle contributions to the production of nuclides in Table 6.3 and Figure 6.4 can be estimated to have a <15% effect on all the measured cross sections reported in this work; in most cases the effect is <6%. However, it should be acknowledged that no measured data regarding the energy spectra of secondary particles during the experiment is available, and in fact, measured ^{233}Pa production values – the only measured nuclide produced solely through neutron capture – suggest that the neutron flux may be underestimated by a factor of 3, as shown in Figure 6.3b. Only two nuclides have $r < 0.94$, ^{205}Bi ($r = 0.60$) and ^{121}Te ($r = 0.89$), the reasons for which is unknown.

The contribution of secondary protons and neutrons to nuclide production is further illustrated in Figure 6.6, with nuclides produced via neutron capture and neutron-induced fission the most prominent. Compared to Figure 6.2, the less symmetric fission yield from lower energy secondary particles contributes most to fission product production beyond the tails of the fission curve from the primary 438 MeV protons. While some of these nuclides are shown in Figure 6.6 to be almost entirely produced by secondary particles, they are also almost entirely short-lived precursors that have minor contributions to the reported cumulative cross sections.

6.4 Summary

Cross sections for the proton irradiation of thorium by 438 MeV protons have been reported for 38 spallation and high-energy fission product nuclei, along with comparisons to the FLUKA code. In general these cross sections agree within a factor of 2 with each other and with literature values extrapolated from 438 MeV to lower proton energies.

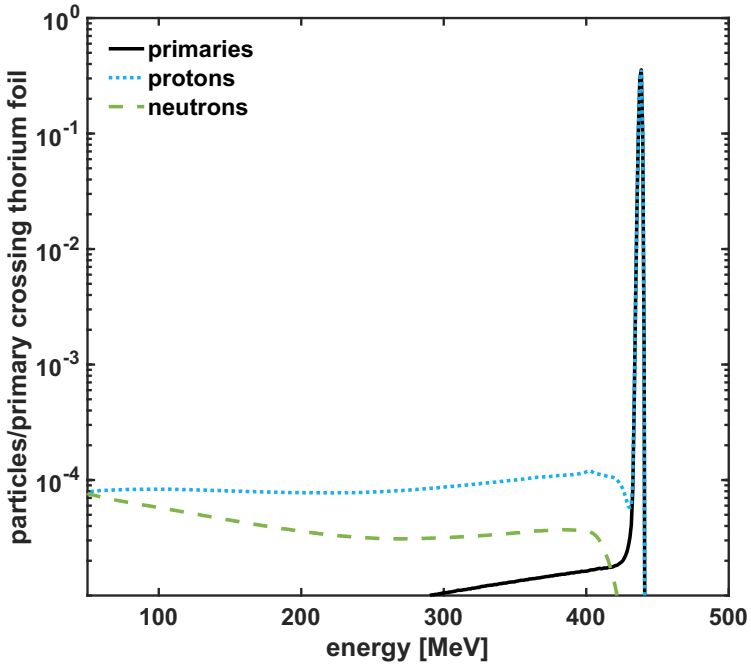

Figure 6.5: Energy spectra of primary protons, secondary protons, and secondary neutrons crossing the thorium foil in the FLUKA simulations of the IPF target during irradiation, as described in Section 6.2.7.2.

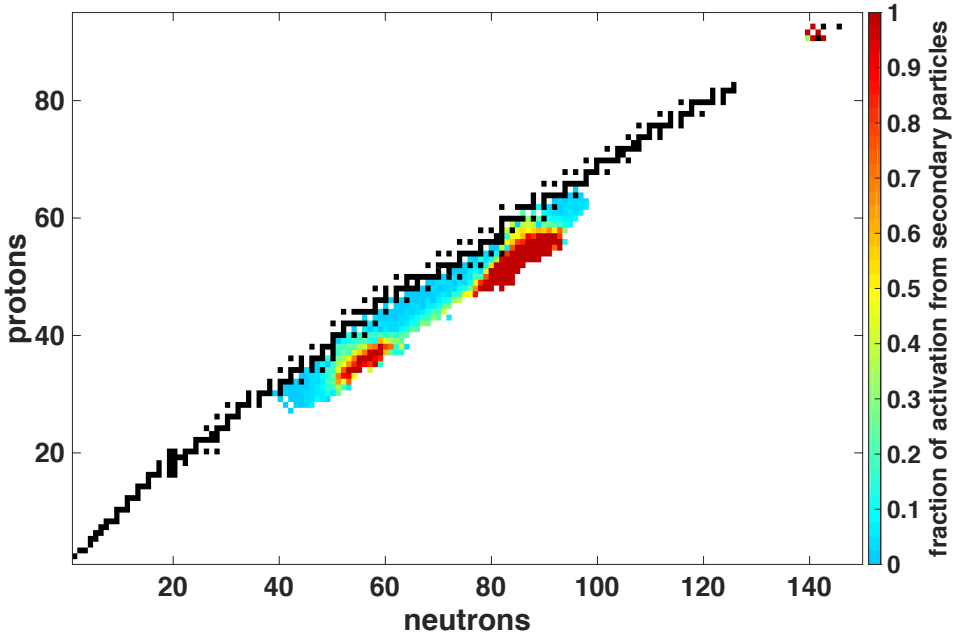

Figure 6.6: Relative contribution of secondary protons and neutrons to nuclide production during the thorium target irradiation, as estimated by FLUKA simulations described in Section 6.2.7.2.

7 ^{225}Ac Purification from Thorium Targets

7.1 Background

The high-energy (>70 MeV) proton irradiation of naturally enriched thorium (^{232}Th) is currently the most widely explored alternative ^{225}Ac production method [1, 33, 101, 104, 135–141, 143, 160]. While this approach may be capable of producing sufficient quantities of ^{225}Ac, the process co-produces hundreds of other radionuclides through spallation and high-energy fission reactions. Ac must therefore be separated from most other elements on the periodic table in order to obtain a radiochemically pure product, in addition to having to separate nanograms of Ac from tens of grams of Th target material. Multiple methods for extraction of Ac from proton irradiated thorium have been developed [104, 136, 143, 160, 206], though none have yet included an initial thorium de-bulking method that will reduce column sizes, processing times, and the large volumes of liquid radioactive waste that result. These advantages of thorium de-bulking are especially advantageous if a process is to be used with increasingly larger quantities of thorium in support of ^{225}Ac production scale-up.

Chemical purification methods are also not capable of separating ^{225}Ac from other Ac isotopes. ^{227}Ac ($t_{1/2}$ = 21.8 y) is one such isotope that is co-produced during thorium irradiations (at approximately 0.1-0.3% radioactivity relative to ^{225}Ac) whose presence may prevent the widespread use of thorium-spallation-derived ^{225}Ac. While recent research has shown that ^{227}Ac is likely not a concern from a patient dosimetry perspective [207, 208], the long half-life and multiple alpha-emissions of the ^{227}Ac decay chain result in restrictive regulatory limits for disposal of waste containing ^{227}Ac, which creates a significant economic burden on the manufacturers and users of ^{225}Ac-radiopharmaceuticals that contain ^{227}Ac. Low radiation protection limits for accidental internalization of ^{227}Ac within the body may also

require additional precautions for handling of ^{225}Ac-radiopharmaceuticals containing ^{227}Ac.

However, production of ^{227}Ac-free ^{225}Ac from the proton irradiation of thorium is possible, in principle [2], via the co-production of the ^{225}Ac parent nuclides, ^{225}Ra ($t_{1/2}$ = 14.9 d). The initial separation of Ac isotopes from the thorium and other spallation and fission products results in an Ac product that contains ^{225}Ac, ^{227}Ac, and shorter-lived isotopes such as ^{228}Ac ($t_{1/2}$ = 6.15 h), ^{226}Ac ($t_{1/2}$ = 29.37 h), and ^{224}Ac ($t_{1/2}$ = 2.78 h). This product is sometimes referred to as "first-pass ^{225}Ac" or "directly-produced ^{225}Ac", and is herein denoted as ^{227,225}Ac†. After the separation of ^{227,225}Ac†, Ra isotopes remain, including ^{225}Ra, ^{228}Ra ($t_{1/2}$ = 5.8 y), ^{226}Ra ($t_{1/2}$ = 1600 y), and ^{224}Ra ($t_{1/2}$ = 3.6 d). Of these, only ^{225}Ra and ^{228}Ra decay to Ac isotopes. After then waiting for ^{225}Ra decay to produce additional ^{225}Ac, repeating the Ra/Ac separation results in a second Ac product that could theoretically be ^{227}Ac-free. This product is sometimes referred to as "second-pass ^{225}Ac" or "generator-produced ^{225}Ac", and is herein denoted ^{225}Ac*.

Chapter 7 presents a chemical separation process for the production of both ^{227,225}Ac† and ^{225}Ac* products, using a novel precipitation-based thorium de-bulking method. The data presented will demonstrate how Ac is separated from most other elements and will compare the quality of TRIUMF's first two ^{227,225}Ac† and ^{225}Ac* production runs, demonstrating ^{225}Ac* production using an accelerator facility and chemical process that could be scaled to useful clinical or commercial quantities and with ^{227}Ac content low enough to be potentially considered ^{227}Ac-free from practical and regulatory perspectives.

7.2 Methods

7.2.1 Materials and reagents

All solvents and reagents were purchased from commercial suppliers and used as received. Trace metal grade HNO_3 (>99.999% basis) and Dowex 50WX8 resin (200-400 mesh, hydrogen form) was purchased from Sigma Aldrich. Anhydrous citric acid (ACS) was purchased from Anachemia (VWR Canada). DGA-normal resin (50-100 μm) was purchased from Eichrom. Deionized water (>18 MΩcm) was produced using a Millipore Direct-Q® 3UV water purifier.

7.2.2 Fluka simulations

FLUKA is a high-energy particle transport code that uses Monte Carlo methods and various physics models to simulate the interactions of particles with a user-defined environment. An introduction to FLUKA is provided in Section 2.3. In this Chapter, FLUKA was used to estimate the radioactive inventory of the thorium foil after proton irradiation. Validation studies demonstrating the accuracy of these simulations are described in Chapter 6.

All simulations were conducted using FLUKA (version 2011.2x.7) and the FLAIR interface (version 2.3-0) using the NEW-DEFAULTS default settings [128, 129, 205]. PHYSICS settings included the new evaporation model with heavy fragment evaporation included, coalescence activated, and ion splitting disabled. Gamma ray interactions at all energies were included. Transport settings included pointwise low-energy neutron cross sections, a 0.0025 cm step size in thin target components (Inconel and thorium foils), 30 keV production and transport thresholds for (anti)electrons and photons, 100 keV transport threshold for protons, and full transport of all light and heavy ions linked to the DPMJET and RQMD event generators. The choice in the number of primaries used was determined by the maximum permissible run time on available clusters, provided that statistical error estimates were at least <1%.

7.2.3 Gamma spectroscopy

The detector used was a N-type co-axial HPGe gamma spectrometer from Canberra fitted with a 0.5 mm beryllium window. The detector's energy, width, and efficiency calibrations were performed using a ^{152}Eu and ^{133}Ba source. The geometry of the calibration source and all samples consisted of a 20.0 mL dilute HNO_3 solution in a scintillation vial positioned at a distance from the detector beyond which cascade-summing effects were shown to be negligible. Dead time was kept below 1.5%. Further details regarding the gamma spectrometer and how it was setup and used are provided in Section 2.1.

Spectra were analyzed using the Genie 2000 software package (version 3.4, Canberra Industries) [145, 147]. Gaussian curves were manually fitted to all peaks and compared against gamma ray libraries built using data from the National Nuclear Data Center database [83]. Only fitted peaks with >95% significance and a full width at half maximum (FWHM) within 20% of the calibrated peak width were accepted. Decay correction before and during data acquisition was applied within Genie 2000.

Since thorium irradiated with 438 MeV protons contains on the order of 10^2 radionuclides, the resulting gamma spectra can be extremely complex. To prevent erroneous nuclide identification or quantification, multiple gamma lines for an individual nuclide each providing consistent individual measurements of the total radioactivity were required for positive identification of a nuclide[14]. The interference-corrected weighted mean of these results, as determined by Genie 2000, is then used to quantify the total radioactivity at the time of measurement. Additional care was taken to ensure that gamma lines used for different nuclides in the library were sufficiently separated (>0.5 FWHM) to avoid false identification of a nuclide.

Special attention was given to the quantification of ^{225}Ra due to the high slope of the efficiency curve in the low energy region (<100 keV) where ^{225}Ra emits its single 40.0 keV gamma ray. Comparison of ^{225}Ra measurements at 40.0 keV (using a pure ^{225}Ra sample produced at TRIUMF's ISOL facility [3, 164]) to the measured grow-in of ^{221}Fr (218 keV) and ^{213}Bi (440 keV) was used to validate the efficiency calibration at 40.0 keV. Still, in the presence of many other thorium target activation production, ^{225}Ra detection becomes challenging due to the amount of low energy emissions (<100 keV) and scatter produced by other nuclides. Due to its greater detectability, ^{223}Ra isotope were used to account for Ra losses during target processing.

Quantitative gamma spectroscopy measurements of ^{225}Ac were conducted after waiting at least 25 minutes for ^{221}Fr to reach equilibrium with ^{225}Ac, so that the ^{221}Fr nuclide's 218 keV gamma line could be used for ^{225}Ac quantification (see Section 1.2.4). In spectra containing many other potentially interfering nuclides, a waiting time of at least 6 hours was used so that ^{213}Bi equilibrium could also be reached; matching ^{221}Fr (218 keV) and ^{213}Bi (440 keV) activity values were then used as an indication of positive and accurate ^{225}Ac quantification.

Gamma spectroscopy detection limits for radionuclides of interest were determined using the ISO11929 algorithm available in Genie 2000 [147]. This algorithm is a Bayesian adaptation of the Currie method for determining detection limits [209, 210].

[14]Exception are made for nuclides – such as ^{225}Ra or ^{85}Sr – that only emit a single usable gamma ray signal. In such situations, the peak centroid must be within 0.2 keV of the expected peak energy, and have a FWHM that matches the calibrated peak width. Additional scrutiny is fairly placed on such results.

7.2.4 Process development using non-irradiated materials

Initial development tests focused on developing and optimizing the conditions for the precipitation, cation exchange, and extraction chromatography portions of the separation scheme shown in Figure 7.4, taking into consideration only the separation of Ac and Ra from bulk quantities of Th since tracers for the other spallation and fission products were not yet readily available. These tests can be done without additional Ac or Ra tracers by using the ^{228}Ac ($t_{1/2}$ = 6.15 h) and ^{224}Ra ($t_{1/2}$ = 3.66 d) radiotracers naturally present in the ^{232}Th decay chain[15]. While HPGe gamma spectroscopy (Section 7.2.3) is able to easily detect these radionuclides, ^{232}Th does not emit sufficient gamma rays to serve as a radiotracer that can measure the high degree of Th decontamination required by ^{225}Ac purification schemes. Therefore, a colorimetric assay for Th (Section 7.2.4.1) was initially employed, before ^{227}Th tracers became available from the first irradiated thorium target(Section 7.2.4.2). The final development tests done to generate the elution profiles shown in Figure 7.5 also included ^{225}Ra and ^{225}Ac tracers (Section 7.2.4.3).

An important distinction between these tests and the processing of irradiated thorium targets is that tests with non-irradiated material used thorium nitrate material as opposed to thorium metal. This was done due to the much higher cost of thorium metal. Since the thorium metal is evaporated to a nitrate salt after the dissolution anyway, the only expected differences between the processes of thorium nitrate material and thorium metal material are: 1) differences in impurities from two sources of stock materials; and 2) the absence of small quantities of HF that would otherwise be used in the dissolution of the metal.

The elution profiles of Figure 7.5 were obtained using n = 3 replicates of the following procedure. 20.0 g of thorium nitrate tetrahydrate (equivalent to 8.0 g of thorium metal) was dissolved in 80 mL of 1 M HNO_3 containing approximately 350 kBq of ^{225}Ra and ^{225}Ac tracers; a 0.5 mL colorimetry sample was removed, and a gamma spectroscopy measurement of the initial solution was performed.

The precipitation and filtration was performed as described in Section 7.3.2. Gamma spectroscopy measurements of ^{228,225}Ac and ^{225,224}Ra were performed on the diluted filtrate in order to quantify the Ac and Ra recovery from the precipitation; a 1 mL sample was removed to quantify the amount of thorium remaining in the filtrate via photometric determination (see Section

[15] Prompt counting of all samples is required due to the grow-in of ^{228}Ac from ^{228}Ra.

7.2.4.1). ^{227}Th and ^{223}Ra tracers (see Section 7.2.4.2) were then added.

The cation exchange column was then performed as described in Section 7.3.2. The load was collected in a single fraction; the citric and nitric acid washes were collected in 50 mL fractions; the Ra and Ac elution was collected in 10 mL fractions. All fraction were counted by gamma spectroscopy. After counting by gamma spectroscopy, the elution fractions were combined, a 0.5 mL colorimetry sample was removed, and the solution was diluted to 4 M HNO_3 for loading through the DGA column. 1 mL samples were also removed from all wash fractions for Th colorimetric assay.

The DGA column was then performed as described in Section 7.3.2. The DGA load was collected in 20 mL fractions, the wash in a single fraction, and the Ac elution in 1 mL fractions. All fraction were counted by gamma spectroscopy.

The timing of all gamma spectroscopy measurements was as prompt as possible (within minutes), such that parent-daughter decay corrections did not need to be applied for ^{228}Ra\$^{228}$Ac, ^{228}Th\$^{224}$Ra, ^{227}Th\$^{223}$Ra, or ^{225}Ra\$^{225}$Ac.

The average ± standard deviation for Th, Ra, and Ac content in each fraction (averaged over the multiple tracers and multiple replicates) is then plotted in Figure 7.5.

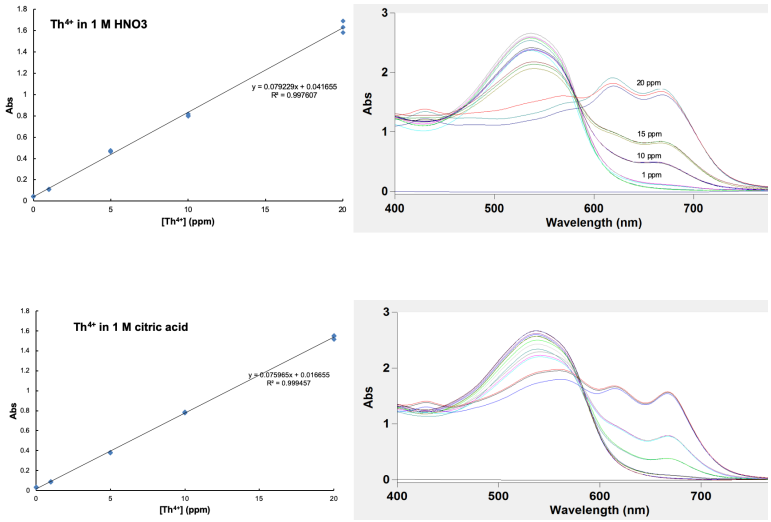

Figure 7.1: Calibration curves and UV-absorption spectra for thorium-arsenazo complexes in 1 M HNO_3 (top) and 1 M citric acid (bottom).

7.2.4.1 Thorium colorimetry measurements

Photometric determination of Th using the thorium-arsenazo complex has been previously reported [211]. Samples for Th assay were either nitric of citric acid from either the dissolution, precipitation, or cation exchange portions of the thorium target purification process (Figure 7.4). Aliquots of samples were diluted to 960 μL of either 1 M HNO_3 or 1 M citric acid; dilution factors varied between 10^0-10^3. The color reagent (Arsenazo-III, 2,7-Bis(2-arsonophenylazo)-1,8-dihydroxynaphthaline-3,6-disulfonic acid, purchased from Sigma Aldrich) was then added (40 μL, 25 mg/L), and the absorbance at 670 nm was then measured using a Cary 100 UV-Vis Spectrophotometer (Agilent Technologies).

Absorption spectra and calibration curves for both nitric and citric acid matrices are shown in Figure 7.1.

7.2.4.2 ^{227}Th and ^{223}Ra tracer production

The first thorium target irradiated and processed at TRIUMF was irradiated as described in Section 7.3.1, but allowed to decay for 5 months before being processed as described in Section 7.3.2. Detailed results from this initial target are excluded from this publication, however, (0.22 $\pm$ 0.04) MBq of ^{225}Ra and (0.23 $\pm$ 0.1) MBq of radiochemically pure[16] ^{227,225}Ac†were isolated from this irradiated target.

The ^{227,225}Ac† product from this initial target was kept for use as a ^{227}Ac/^{227}Th generator, with a total ^{227}Ac quantity of (382 $\pm$ 20) kBq, as measured by gamma spectroscopy of the ^{227}Th grow-in ($t_{1/2}$ = 18.68 d). The ^{227}Ac in 13 mL of 12 M HNO_3 was evaporated to dryness and redissolved in 5 mL of 8 M HNO_3. This solution was then passed through an anion exchange column containing 0.5 mL of DOWEX 1X8 resin (200-400) mesh conditioned with 4 mL of H_2O and 4 mL of 8 M HNO_3. The column was then washed with 2.5 mL of 8 M HNO_3 before the ^{227}Th was removed using 3.5 mL of 0.05 M HNO_3. The total amount of ^{227}Th obtained was (332 $\pm$ 12) kBq, at (99.1 $\pm$ 3.1)% chemical yield.

The ^{227}Th obtained was left to decay for at least 5 days, allowing for the grow-in of the additional ^{223}Ra tracer ($t_{1/2}$ = 11.4 d).

7.2.4.3 ^{225}Ra and ^{225}Ac tracer production

^{225}Ra and ^{225}Ac tracers were produced at TRIUMF's Isotope Separation

[16] All gamma spectrum peaks were identified as ^{228}Ac and ^{225}Ac peaks.

On-Line (ISOL) facility, as described in Chapter 3 and by Ramogida *et al* and Kunz *et al* [3, 164].

7.2.5 Process characterization using multi-element ICP-MS standards and radiotracers

To demonstrate the separation of Ac from the spallation and fission products present in the irradiated thorium targets, the fate of these other elements in the target purification process must be measured. To do this, multi-element ICP-MS standards were used as tracers. The target purification process (described in Section 7.3.2 and shown in Figure 7.4) was performed three separate times using three separate multi-elemental tracers:

a) 1.1 mL of 71A standard (10 ppm multi-element standard[17], 2% HNO_3, purchased from Inorganic Ventures) and 1.1 mL of a Y standard (10 ppm, 2% HNO_3)

b) 1.1 mL of a CMS-3 standard (10 ppm multi-element standard[18], 2% HNO_3 + trace HF, purchased from Inorganic Ventures)

c) A blank tracer, containing only 1.1 mL of 2% HNO_3

Each tracer was diluted to 260 mL of 0.5 M HNO_3, and 20 mL of this solution was then removed so that the initial amount of each tracer could be measured by ICP-MS. The remaining solution was then processed through the cation and extraction chromatography parts of the target purification process. Samples ($\leq$20 mL) were removed from the cation column load, citric wash, nitric wash, cation column elution, DGA column load, DGA column wash, Ac elution, and Ln elution. All nitric acid samples were then slowly evaporated in an acid-washed Teflon beaker and then redissolved in 2% HNO_3 containing 10 ppb In as an internal standard for analysis by ICP-MS.

Prior to analysis, the total dissolved solids in the citric wash and nitric wash were reduced. To do this, the pH of the citric wash sample was adjusted to pH 1.00 $\pm$ 0.05 using concentrated HNO_3; the pH of the nitric wash was not adjusted. The samples were then passed at 1 mL/min through a cation exchange column containing 2 mL of Dowex 50X8 (200-400 mesh) resin

[17] Contains 10 ppm for each of: Al, As, Ba, Be, Cd, Ca, Ce, Cr, Co, Cu, Dy, Er, Eu, Gd, Ga, Ho, Fe, La, Pb, Lu, Mg, Mn, Nd, Ni, P, K, Pr, Rb, Sm, Se, Ag, Na, Sr, S, Tl, Th, Tm, U, V, Yb, Zn, Cs, B

[18] Contains 10 ppm for each of: Ge, Hf, Mo, Nb, Ta, Sn, Ti, W, Zr

preconditioned with 20 mL of H_2O followed by 20 mL of 8 M HNO_3, then 20 mL of 1 M citric acid (pH 1.00) for the citric wash sample or 20 mL of 0.5 M HNO_3 for the nitric wash sample. The column was then washed (2 mL/min) with 120 mL of 0.1 M HNO_3 to remove residual citric acid before eluting the metals at 1 mL/min with 80 mL of 8 M HNO_3. The fractions were free of detectable citric acid and were evaporated and redissolved in 2% HNO_3 + 10 ppb In as previously described. This citric acid removal procedure was also performed using known quantities of the ICP-MS tracers listed above, so that recovery factors for individual elements could be determined.

Thorium dissolution and precipitation stages of the $^{227,225}Ac^{\dagger}$ purification process were omitted from this experiment, to avoid loss or contamination of the tracers during the dissolution or precipitation. All disposables, vials, pipette tips, columns, graduated cylinders, etc., used that came into contact with these samples were acid washed to remove trace metal contaminants prior to use. All nitric acids were prepared using Environmental Grade HNO_3 obtained from VWR. Trace metals were removed from the citric acid solution using 10 g of Chelex-100 (Bio-Rad) per 100 mL and stirred for 1 h prior to filtration.

ICP-MS analysis of these samples was provided by the University of British Columbia's Pacific Centre for Isotopic and Geochemical Research. The background amount of each element analyzed (averaged over 2 blank runs) was subtracted from the total amount measured in each fraction. Measured recovery factors for the citric acid removal process (above) were taken into account.

7.2.6 ICP-MS measurements of $^{227,225}Ac^{\dagger}$ and $^{225}Ac^{*}$

Aliquots (0.1-0.5 mL) of $^{227,225}Ac^{\dagger}$ and $^{225}Ac^{*}$ products were diluted to 10 mL using trace metal grade 1 M HNO_3. ICP-MS measurements of these radioactive samples were provided by the Analytical Chemistry Branch at Canadian Nuclear Laboratories (Chalk River, ON). The analysis provided included measurement of common stable impurities[19] as well as mass numbers A=120 through A=244, which provides a sensitive measurement (<1 pg/mL) of ^{227}Ac content.

Blank samples containing 10 mL of trace metal grade 1 M HNO_3 were also prepared, and the amount of stable impurities in these samples was subtracted from the amount seen in the ^{225}Ac samples, to provide the net

[19]Be, Ca, Sc, Ti, Cr, Mn, Fe, Co, Ni, Cu, Zn, Ga, Sr, Y, Zr, Nb, Mo, Sn, Ba, W, Pb, Th, and U

quantity of impurities in the $^{227,225}Ac^{\dagger}$ and $^{225}Ac^{*}$ product.

7.2.7 Radiolabelling tests with $^{227,225}Ac^{\dagger}$ and $^{225}Ac^{*}$

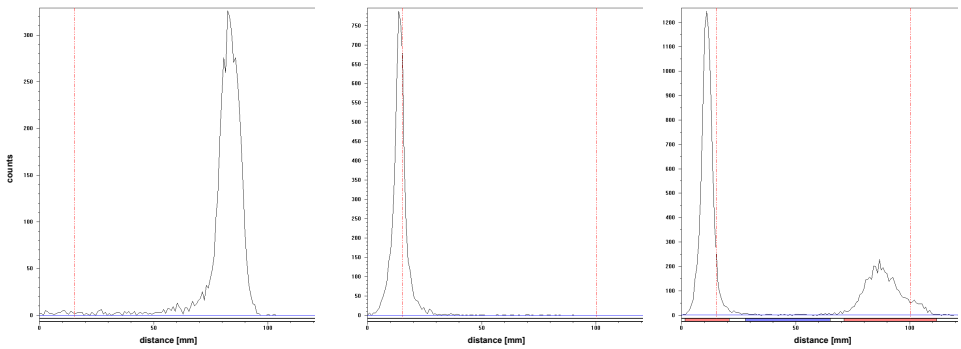

Figure 7.2: Example TLC trace data including a negative control (left) showing no ^{225}Ac labelling, a positive control (centre) showing complete ^{225}Ac labelling, and an example of a TLC indicating partial labelling (right), including the regions used for peak areas and background subtraction.

The ability to label disease-targeting biomolecules is an essential requirement of a quality radionuclide product. Two macrocyclic ligands were chosen to demonstrate the radiolabelling abilities of the $^{227,225}Ac^{\dagger}$ and $^{225}Ac^{*}$ products: DOTA, the most widely used ^{225}Ac ligand, and macropa, which is capable of labelling ^{225}Ac at low concentrations [3, 162, 212, 213].

$^{227,225}Ac^{\dagger}$ and $^{225}Ac^{*}$ products (13 mL 12 M HNO_3) were evaporated to dryness and redissolved in 0.05 M HNO_3. 3 μL aliquots of these ^{225}Ac solutions – each containing 40-45 kBq of ^{225}Ac – were added to 100 μL solutions of 1 M NH_4OAc (pH 7) containing DOTA or macropa at concentrations between 10^{-4} and 10^{-8} M. Macropa labelling was conducted at ambient temperature; DOTA labelling was conducted at 85 °C. All reactions were left for 30 minutes before a 5 μL aliquot was removed and spotted onto aluminum-backed ultrapure silica gel 60 with 250 μm thickness TLC plates (Fisher, 1 cm x 10 cm, with baseline at 15 mm). After drying, the plates were developed using a 0.4 M sodium citrate (pH 4) solution. ^{225}Ac-ligand complexes remain at the baseline under these conditions, while free ^{225}Ac moves with the solvent front. Plates were then counted on a BioScan 200 plate imaging scanner equipped with an Autochanger 1000 and analyzed using Win-Scan (version 2.2(11)).

Negative controls were performed alongside all labelling tests by adding

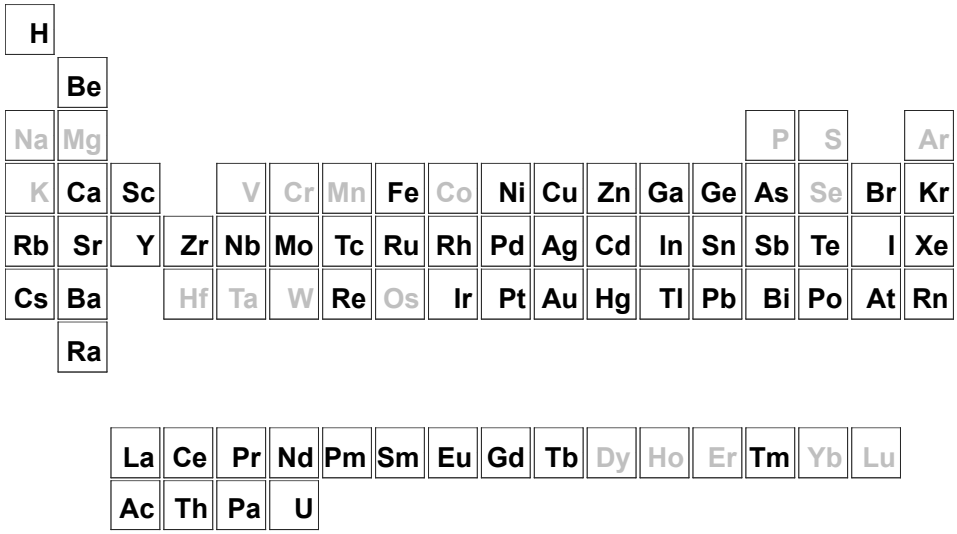

Figure 7.3: Elements with radioisotopes present inside the irradiated thorium at 1 week after the end of irradiation, and from which Ac must be separated in order produce a radiochemically pure product. Elements in gray have isotopes with activities <0.1% of the ^{225}Ac radioactivity, as estimated by FLUKA simulations (see Section 7.2.2). Elements in black have estimated activities >0.1% of the estimated ^{225}Ac radioactivity.

^{225}Ac to a ligand-free but otherwise identical solution of 1 M NH_4OAc (pH 7). Positive controls were performed using a radiolabelling solution containing 10^{-3} M of DOTA, heated to 85 °C for 60 min. Examples of TLC traces are shown in Figure 7.2.

7.3 Experimental

7.3.1 ^{225}Ra and ^{225}Ac production by thorium irradiation

Thorium foils (>99.95% purity, as determined by ICP-MS) of (0.25 ± 0.01) mm thickness and (60.0 ± 0.1) mm diameter were irradiated with (438 ± 2) MeV protons at TRIUMF's 500 MeV Isotope Production Facility (IPF), located immediately in front of the TRIUMF cyclotron's main beam dump [191]. Further details of the thorium target design have been reported elsewhere [5]. Targets were irradiated to a total integrated current of 2640 μA*h for a duration of 36-41 hours (total duration depended on the beam current), producing (521 ± 18) MBq of ^{225}Ac and (91 ± 14) MBq of ^{225}Ra at the end

of irradiation[20]. Targets were allowed to decay for at least 7 days before they were removed from the IPF and transferred to the radiochemistry lab.

While sufficient ^{225}Ra and ^{225}Ac quantities are produced in these irradiations, a plethora of many other radionuclides – including isotopes of most elements lighter than uranium – are also co-produced through nuclear spallation and fission reactions. Figure 7.3 provides a graphical representation of these elements, based on FLUKA simulations of the irradiations (see Section 7.2.2).

The consequence of this is that chemical processes used to extract ^{225}Ac from these targets must be capable of separating Ac from most other elements on the periodic table.

7.3.2 ^{227,225}Ac† and ^{225}Ac* purification

The chemical process used to purify ^{227,225}Ac† and ^{225}Ac* products from the irradiated thorium is shown in Figure 7.4. The irradiated thorium metal foils (mass ranging between 7.8 and 8.0 g) were placed in a borosilicate glass beaker and dissolved using up to 60 mL of 10 M HNO_3 + 12.5 mM HF while heating directly on a hot plate set to approximately 200 °C. The dissolutions began vigorously then settled once the bulk of the foil was dissolved, leaving behind a black powdery residue which dissolved more slowly; additional heat (hot plate set up to 300 °C), HF (up to 60 mL of 12.5 mM), or time (up to 4 h) was sometimes required to completely dissolve this residue. Within 2-4 hours, the thorium was fully dissolved, yielding a clear and colorless solution. Small (∼mg) amounts of a fine white solid often remained undissolved, hypothesized to be ThO_2 or ThF_4 [194]. Thorium can also be dissolved in hydrochloric or trichloroacetic acids [194].

The solution was then evaporated to a fully dried thorium nitrate salt, with care taken to ensure the salt does not overheat (< 150 °C) and oxidize to ThO_2 [214]. The salt was allowed to cool to ambient temperature then redissolved in 80.0 mL of 1 M HNO_3 (final volume (86 ± 2) mL).

The thorium was then selectively removed from the solution by precipitation as thorium peroxide [215–219]. Note that other precipitates [194], including thorium oxalate or thorium iodate, were also explored but were found to either be too difficult to filter or to result in greater co-precipitation of Ra or Ac than the thorium peroxide approach [219]. Another advantage of the thorium peroxide precipitation is that the precipitate can be easily

[20](As measured by gamma spectroscopy; average ± standard deviation), n = 3. Note that results from processing of only 2 targets are included later in the publication.

redissolved by a strong HNO_3 acid, allowing for easy clean up of this waste after process completion.

The thorium peroxide precipitation began by adding 56.0 mL of 30% H_2O_2 to the thorium nitrate solution. It is important that the H_2O_2 is added slowly (<10 mL/min) while rapidly stirring to ensure the formation of fine particulates that are easy to filter; rapid H_2O_2 addition results in a gelatinous precipitate. The precipitation was allowed to proceed for 2 hours at ambient temperature while stirring. Note that it is important to avoid heating during the precipitation as this was found to decrease the amount of Th removed from the solution. As previously reported [216, 220], increasing the H^+ concentration during the precipitation was also found to reduce the amount of thorium removed from the solution, while lower HNO_3 concentrations during the precipitation resulted in a more gelatinous precipitate that was harder to filter [194, 218], resulting in greater Ac and Ra losses. The precipitate was removed from the solution by slowly passing the white thorium peroxide slurry through a 10-15 μm glass filter. The precipitate was then washed with 140 mL of H_2O, which increases Ac and Ra recovery and simultaneously dilutes the filtrate to 0.25-0.5 M HNO_3 for loading onto the following cation exchange column.

When the filtering and washing of the precipitate is done well, this procedure was found (by n = 3 tests using non-irradiated materials; see Section 7.2.4) to remove >99.95% of the thorium from the solution, with (3.4 ± 0.4) mg of thorium remaining in the filtrate as determined by photometric measurements of the thorium-arsenazo complex (see Section 7.2.4.1). Though the procedure remained effective after transitioning to irradiated materials, it is not known if thorium decontamination still remained at >99.95% when irradiated materials were used. However, the Ra and Ac recoveries in the filtrate of (96.7 ± 7.9)% and (98.0 ± 2.7)%[21], respectively, did not differ measurably when irradiated materials were used.

The selectivity of this thorium peroxide precipitation was determined by gamma spectroscopy measurements of the filtrate and precipitate from tests with irradiated thorium, which suggested that only Zr, Nb, and Pa co-precipitated enough to remain predominantly in the precipitate: (120.1 ± 8.9)%[22], (112.5 ± 34.7)%, and (91.2 ± 6.1)% of initial ^{95}Zr, ^{95m}Nb, and ^{223}Pa quantities, respectively, were found in the precipitate; no detectable amounts were found in the filtrate. Uranium (^{233}U) is also expected to

[21] As measured using ^{225,224}Ra and ^{228,225}Ac radiotracers (Section 7.2.4).

[22] The >100% observation is possibly due to interference from other peaks that are present in the dissolved target solution, which were not present in the spectrum of the precipitate.

have been co-precipitated, but was not detectable in the gamma spectra at the time of measurement [221]. Co-precipitation of (10.1 ± 1.1)% of ^{103}Ru was also observed. Thorium peroxide precipitates are known to incorporate anions from the solution into their structure [216–218], which was also observed for radioactive halogen and semimetal species when the precipitation was conducted using irradiated materials: (74.2 ± 2.3)%, (55.6 ± 2.9)%, (93.5 ± 7.8)%, (76.9 ± 5.2)%, and (111.2 ± 7.2)% of ^{127,126,124,122,120m}Sb, ^{121m,121}Te, ^{131}I, ^{206}Bi, and ^{206}Po, respectively, was also observed to remain in the precipitate.

After the separation of Ra and Ac from the bulk thorium mass, ion exchange and extraction chromatography was used to separate Ra and Ac from the remaining trace Th and the many spallation and fission products shown in Figure 7.3. The chromatography scheme employed was similar to methods developed by others [104, 160, 206], but with minor changes enabled by the pre-removal of the bulk thorium mass by precipitation. The diluted filtrate (∼275 mL, ∼0.5 M HNO_3) was passed at 5 mL/min through a cation exchange column (16 mm diameter) containing 10 mL of Dowex 50X8 (200-400 mesh) resin preconditioned with 100 mL of H_2O followed by 100 mL of 10 M HNO_3 then 100 mL of 0.5 M HNO_3; under these conditions most radiometals present – including Th, Ra, and Ac – remain bound to the column. The column was then washed (5 mL/min) with 450 mL of 1 M citric acid (adjusted to pH 2.0-2.2 with ammonium hydroxide) that left Ra and Ac bound to the column while removing the residual Th (see Figure 7.5). The separation of Th from Ra and Ac using cation exchange resin in citric acid depends strongly on the pH [222], and a precise adjustment of the citric acid pH is required: higher pH values result in Ac being removed from the column while lower pH values result in thorium remaining on the column or requiring a larger wash volume.

The column was then washed (5 mL/min) with 50 mL of 0.5 M HNO_3 to remove residual citric acid before Ra and Ac were eluted at 1.5 mL/min from the column in 80 mL of 8 M HNO_3. This Ra and Ac fraction was then diluted with H_2O to 4 M HNO_3 and passed at 1 mL/min through a 0.2 mL DGA-normal (TODGA) extraction chromatography column (9 mm diameter) conditioned with 10 mL of H_2O followed by 10 mL of 4 M HNO_3. Under these conditions and in the absence of stable impurities that may saturate the DGA column, Ac and lanthanide (Ln) fission products will bind to the resin while Ra remains in the liquid phase. The column was then washed with 5 mL of 4 M HNO_3 before before Ac is eluted at 1 mL/min in 13 mL of 12 M HNO_3. Elution of Ac in high molarity HNO_3 allows for the separation from Ln [160], which are then removed from the column in 10

mL of 0.05 M HNO_3. At this stage, the process has produced the first-pass $^{227,225}Ac^{\dagger}$ product.

Results from radiotracer studies (using non-irradiated materials, as described in Section 7.2.4) used to characterize the behavior of Th, Ra, and Ac during this chromatography scheme are shown in Figure 7.5. Elution profiles show that Th, Ra, and Ac were well separated by the process; Ra and Ac chemical yields[23] were (97.2 ± 2.4)% and (99.7 ± 0.8)%, respectively, with no Th or Ra detectable in the Ac fraction.

When processing irradiated targets, similar Ra isolation yields of (98.3 ± 4.7)% (n = 2) were observed, however, Ac isolation yields were reduced to (44.0 ± 5.3)% (n = 2) due to saturation of the DGA column by stable impurities; this is elaborated on in Section 7.4. These yields correspond to isolated quantities of (65 ± 10) MBq for ^{225}Ra and (141 ± 9) MBq of $^{227,225}Ac^{\dagger}$, decay corrected to 7 days after the end of the 2640 μA*h (36-41 hour) irradiations.

The fate of other elements in the process is illustrated in Figure 7.6 and Table 7.1. This data was collected using stable tracers, supplemented by radiotracer data for Ac, Ra, Bi, Te, Sn, In, Rh, Ru, and Tc (see Section 7.2.5). The cation load fraction contained the majority of refractory metals and semimetals. Other transition metals appeared predominantly either in the citric acid wash fraction of the cation column or in the DGA load fraction after being eluted from the cation column along with Ra and Ac. Other alkaline earth metals appeared mostly with Ra in the DGA load fraction, but also increasingly appeared in the citric acid wash as their size decreases. Lanthanides showed two size dependent trends, with heavier lanthanides increasingly appearing in the citric acid wash fraction and lighter lanthanides appearing in the Ln elution. It is likely that the Ln elution was not complete, with most of the lighter La appearing in the Ln elution but most of the heavier Nd still remaining on the column. Ru appears to be the only element that was split more or less evenly between multiple fractions, and as previously mentioned, also appeared in similar quantities in the thorium peroxide precipitate.

The only element that appeared predominantly in the Ac elution was Ac. However, Table 7.1 shows that small fractions of other elements also appeared in this fraction, notably 3% of the initial quantity of La, 2% of the initial quantity of Sr, and approximately 0.1-1.0% of refractory metals. These results, including potential future remedies, are further discussed in Sections 7.3.3 and 7.4.

[23] average ± standard deviation, n = 3

As shown in Figure 7.4, the production of the second $^{225}Ac^{*}$ product occurred by taking the DGA load fraction, containing Ra isotopes, and immediately passing it through a larger 1.0 mL DGA-normal column in order to remove any residual ^{227}Ac. After waiting a period of 1-3 weeks[24] for the grow-in of ^{225}Ac, the DGA column was repeated to again separate Ac from Ra, providing the second-pass $^{225}Ac^{*}$ product. When decay corrected for a 7-day operational cycle of the generator, (21 ± 3) MBq of $^{225}Ac^{*}$ was isolated from the first $^{225}Ra/^{225}Ac^{*}$ separation from the generator that originally contained (65 ± 10) MBq of ^{225}Ra at 7 days after the end of the 2640 μA*h (36-41 hour) irradiations.

Table 7.1: Results (n = 1) for studies using stable multi-element ICP-MS standards as tracers for the column chromatography sections of the $^{227,225}Ac^{\dagger}$ purification process (see Section 7.2.5). Values represent the portion of each element found in each fraction of the process, after correcting for background quantities measured when no tracers were present. The bolded column represents the final $^{227,225}Ac^{\dagger}$ product.

element	**portion of initial tracer mass in each fraction [%]**						
	load	citric wash	nitric wash	DGA load	DGA wash	**Ac elution**	Ln elution
Be	0.19	55.63	33.36	6.60	0.02	**0.000 ± 0.000**	0.00
Al	10.44	135.82	9.89	0.00	0.00	**0.000 ± 0.183**	0.00
V	15.62	69.92	0.01	0.02	0.00	**0.000 ± 0.002**	0.00
Cr	0.00	5.48	0.00	102.44	2.07	**0.000 ± 0.031**	0.65
Mn	0.00	4.25	2.05	103.53	0.43	**0.000 ± 0.008**	0.02
Co	0.00	0.26	2.06	104.33	0.55	**0.000 ± 0.003**	0.00
Ni	0.10	33.26	41.16	71.75	0.49	**0.000 ± 0.036**	0.19
Cu	0.00	98.33	1.58	0.00	0.00	**0.058 ± 0.010**	0.12
Zn	0.00	0.00	14.52	81.42	1.15	**0.000 ± 0.056**	0.03
Ga	0.01	74.20	0.06	0.04	0.00	**0.000 ± 0.001**	2.30
As	92.79	45.54	2.04	0.08	0.00	**0.000 ± 0.001**	0.36
Se	52.72	80.76	1.85	0.16	0.02	**0.040 ± 0.073**	0.26
Rb	29.36	35.91	0.03	0.00	0.00	**0.000 ± 0.000**	0.00
Sr	0.00	11.62	9.00	95.11	4.83	**1.935 ± 0.054**	0.00
Y	0.29	111.67	12.12	0.00	0.08	**0.000 ± 0.003**	0.06
Ag	10.34	62.11	11.66	3.76	0.01	**0.000 ± 0.000**	0.00
Cd	0.03	0.00	0.37	100.45	0.52	**0.028 ± 0.004**	0.04
Cs	8.30	59.31	0.02	0.00	0.00	**0.000 ± 0.000**	0.00

[24]Note no consistent operational cycle for the generator has yet been applied.

Ba	0.19	3.97	2.71	102.50	0.00	**0.000 ± 0.001**	0.00
La	0.00	0.00	0.09	3.53	0.34	**2.995 ± 0.023**	75.24
Ce	0.00	0.08	0.08	0.25	0.01	**0.038 ± 0.001**	53.27
Pr	0.00	0.02	0.02	0.09	0.00	**0.004 ± 0.000**	30.77
Nd	0.00	3.19	1.22	0.06	0.00	**0.001 ± 0.000**	10.45
Sm	0.00	76.88	2.01	0.01	0.00	**0.000 ± 0.000**	0.03
Eu	0.00	83.10	0.87	0.02	0.00	**0.000 ± 0.000**	0.00
Gd	0.00	80.84	1.62	0.00	0.00	**0.001 ± 0.000**	0.14
Dy	0.00	85.36	0.53	0.00	0.00	**0.000 ± 0.000**	0.09
Ho	0.00	87.16	0.38	0.00	0.00	**0.000 ± 0.000**	0.00
Er	0.00	88.76	0.12	0.00	0.00	**0.000 ± 0.000**	0.02
Tm	0.00	89.64	0.03	0.00	0.00	**0.000 ± 0.000**	0.00
Yb	0.00	89.79	0.02	0.00	0.00	**0.000 ± 0.000**	0.00
Lu	0.00	90.46	0.01	0.00	0.00	**0.000 ± 0.000**	0.00
Tl	0.07	70.30	20.14	3.59	0.17	**0.180 ± 0.003**	0.18
Pb	2.77	0.00	1.53	127.00	3.17	**0.003 ± 0.004**	0.06
Th	6.69	91.26	0.12	0.79	0.10	**0.000 ± 0.000**	0.00
U	0.05	78.63	0.03	0.14	0.00	**0.007 ± 0.001**	0.02
Ti	19.72	93.21	15.42	0.08	0.00	**0.000 ± 0.000**	0.00
Ge	98.50	0.00	0.00	0.00	0.00	**0.000 ± 0.001**	0.00
Zr	7.73	115.78	8.09	1.83	0.23	**0.263 ± 0.020**	0.15
Nb	41.50	0.00	0.00	4.17	1.23	**0.677 ± 0.025**	0.63
Mo	97.72	0.61	2.12	0.77	0.20	**0.183 ± 0.009**	0.10
Sb	31.70	0.00	0.00	0.03	0.03	**0.011 ± 0.001**	0.02
Hf	5.52	65.92	1.31	1.16	0.19	**0.203 ± 0.013**	0.12
Ta	76.78	0.00	0.08	8.35	2.69	**0.257 ± 0.377**	1.81
W	618.89	0.00	0.05	6.84	2.41	**1.126 ± 0.051**	1.21

7.3.3 Comparison of $^{227,225}Ac^{\dagger}$ and $^{225}Ac^{*}$ products

The radionuclidic purity of both $^{227,225}Ac^{\dagger}$ and $^{225}Ac^{*}$ products, averaged over two production runs, is shown in Table 7.2. Results for $^{227,225}Ac^{\dagger}$, decay corrected to the end of processing (7 days after end of irradiation), were consistent with the results of Table 7.1, with small amounts of La (2.29% ^{140}La) and Sr (0.14% ^{85}Sr) isotopes present in the Ac fraction. While Table 7.1 suggest that small amounts of refractory metals (ex. tungsten) may also end up in the Ac fraction, radioisotopes of these elements are not co-produced in large quantities relative to ^{225}Ac or ^{225}Ra during thorium irradiations, as shown in Figure 7.3. The largest $^{227,225}Ac^{\dagger}$ radionuclide impurity was ^{226}Ac

($t_{1/2}$ = 29.37 h), at (5.83 ± 0.82)% of the total radioactivity. ^{227}Ac content in the in the ^{227,225}Ac† product measured (0.15 ± 0.04)% by ICP-MS (Section 7.2.6), which is similar to values reported by other labs producing ^{225}Ac from proton-induced spallation of thorium [136, 138–141, 143].

In comparison, ^{227}Ac in ^{225}Ac* was reduced to <7.5E-5% in both (n = 2) samples, in one sample measuring below the ICP-MS detection limit (<0.1 pg/mL, or <7.1E-5% of the ^{225}Ac activity). This measurement is supported by gamma spectroscopy measurements which show no detectable ^{227}Th ingrowth from ^{227}Ac after a 4 month decay period, supporting ^{227}Ac content of <5E-4%. ^{226}Ac content is similarly reduced in the ^{225}Ac* product. ^{228}Ac ($t_{1/2}$ = 6.14 h) impurities are expected to be present in both ^{227,225}Ac† and ^{225}Ac* products, but likely decayed before gamma spectroscopy measurements. While the total amount of ^{103,106}Ru and ^{85}Sr was similar for both ^{227,225}Ac† and ^{225}Ac*, the ∼4 times smaller quantity of ^{225}Ac* results in an increase of the percent impurities for these nuclides. The reduced ^{140}La ($t_{1/2}$ = 1.68 d) impurities present in ^{225}Ac* originated from the decay of ^{140}Ba ($t_{1/2}$ = 12.75 d) that follows Ra isotopes through the process and ends up in the ^{225}Ra/^{225}Ac generator (see Figure 7.6).

The chemical purity of the ^{227,225}Ac† and ^{225}Ac* products determined by ICP-MS measurements (Section 7.2.6) is shown in Figure 7.7. Most elements measure below 0.1 μg per MBq of ^{225}Ac, with Ca the only element that was consistently above 0.1 μg/MBq[25]. As previously mentioned, these elevated Ca levels were observed only when processing irradiated materials, and is discussed further in Section 7.4. While the calcium impurities are problematic due to their saturation of the DGA column, reducing the ^{227,225}Ac† chemical yields from the process, the amount of calcium and other stable impurities measured in the product did not appear to negatively affect radiolabelling capabilities of either the ^{227,225}Ac† or ^{225}Ac* products, with the exception of the one ^{227,225}Ac† product that contained >10 μg/MBq of stable calcium impurities.

Radiolabelling results for both ^{227,225}Ac† and ^{225}Ac* products with DOTA and macropa are shown in Figure 7.8. Radiolabelling yields for both DOTA and macropa using both radionuclide products was comparable to values reported in the literature for other sources of ^{225}Ac [3]. Macropa labelling yields[26] with both radionuclide products was >95% down to chelate concentrations of 10^{-6} M; DOTA labelling yields[27] with both products was

[25] Ba was above this threshold in 1 or 2 samples.

[26] At ambient temperature, 30 minute reaction time, pH 7

[27] At 85°C, 30 minute reaction time, pH 7

Table 7.2: Average (n = 2) radionuclidic purity of $^{227,225}Ac^{\dagger}$ and $^{225}Ac^{*}$ products, decay corrected to the times of final product purification. ^{227}Ac values were determined by ICP-MS (Section 7.2.6) while all other values were determined by gamma spectroscopy (Section 7.2.3).

	percent radioactivity [%]	
	$^{227,225}Ac^{\dagger}$	**$^{225}Ac^{*}$**
Ac-225	**93.04**	**98.82**
Ac-227	**0.15**	**<7.2E-5**
Ac-226	5.83	<0.01
La-140	2.29	0.01
Ru-106	<0.04	0.13
Ru-103	0.25	0.72
Sr-85	0.14	0.33
Th-227	<0.04	<0.17
Ra-226	<0.01	<0.06
Ra-225	<0.01	<0.05
Ra-224	<0.07	<0.02
Ra-223	<0.04	<0.14
Ce-141	<0.01	<0.03
Ba-140	<0.01	<0.04

>95% down to chelate concentrations of 10^{-4} M, with the exception of the one $^{227,225}Ac^{\dagger}$ product that contained >10 μg/MBq of stable calcium impurities (Figure 7.7).

7.4 Discussion

The chemical process presented in Section 7.3.2 produced two ^{225}Ac products that adequately labelled DOTA and macropa, however, no attempts have yet been made to optimize the process to improve the radionuclidic and chemical purity. Initial conditions for use of the cation and DGA columns were chosen based off of data from experiments with Th, Ra, and Ac alone (Figure 7.5) and did not yet consider other elements. Given that, the radiochemical purity observed for the first two production runs (Table 7.2) is encouraging, though improvements may need to be made to reduce the Sr, Ru, and La radioimpurities.

Given that Sr and Ru have distribution coefficients (K_d) with $\log(K_d)<1$ on DGA-normal resin in 4 M HNO_3 [169, 223], it is likely that simply increasing the volume of the DGA column wash may reduce the amount of these impurities in the ^{225}Ac products. If not, Sr-selective extraction resins [224], or anion exchanges resins for Ru removal [225] could be incorporated into the process as in-line filters for removal of these radioimpurities without expecting considerable Ac losses. Increasing the wash volume may also reduce stable impurities such as Pb, Ba, Zn, and Fe [223]. Optimizing the volume of the Ac elution (currently 13 mL of 12 M HNO_3) may also reduce the La impurities: as shown in Figure 7.5, this volume is larger than needed to elute >95% of Ac, and the La K_d under these conditions is known to be much larger than that for Ac [160, 169]. Changing the wash and Ac elution may also help reduce the Ca impurities, as Ac and Ca separation on DGA-normal resin in high molarity HNO_3 has also been previously demonstrated [226].

However, removing the source of Ca impurities is likely the best way to improve chemical purity. Since observing the saturation of the DGA-column by Ca during processing of irradiated thorium, a higher purity citric acid (Honeywell Fluka^{TM} Citric Acid monohydrate, TraceSELECT^{TM} $\geq$99.9998% metals basis) has been found to address this issue. Still, other sources of calcium are expected, due to the differences observed between the processing of irradiated and non-irradiated materials: these may include Ca impurities in the thorium metal or Ca leached from the processing equipment components (ex. glassware) due to the presence of HF during the

dissolution (see Section 7.2.4).

If these initial challenges to the chemical and radionuclidic purity can be resolved without reducing the ^{225}Ra or ^{225}Ac* radiochemical yields, then the methods presented herein may provide a new source of accelerator-produced ^{225}Ac with significantly reduced ^{227}Ac content compared to other ^{227,225}Ac† sources produced by irradiation of ^{232}Th. Irradiation of the existing target design (Section 7.3.1) for a full two weeks is expected to produce 566 MBq (15.3 mCi) of ^{225}Ra per target, once process losses (5%) and decay losses[28] (10%) are considered. Since each MBq of ^{225}Ra could produce approximately 0.9 MBq of ^{225}Ac*, assuming a 1 week operational cycle of the generator, the irradiation and processing of 1 target per week for 35 weeks per year[29] could produce approximately 17.8 GBq (0.5 Ci) per year of ^{225}Ac with reduced ^{227}Ac content. Since TRIUMF's IPF is capable of irradiating 12 targets simultaneously [5, 191], an additional 6-fold increase to the potential production quantities is also readily available. Additional increases could be achieved by increasing the thorium target thickness, though this would require a re-evaluation of the target's safety envelope [5].

While the ^{225}Ac* product may have reduced ^{227}Ac content, one clear disadvantage is the lower quantity produced: approximately 5-6 times more ^{225}Ac than ^{225}Ra was produced at the end of previous irradiations. Still, the ^{227,225}Ac† product may be useful as a parent nuclide in ^{225}Ac/^{213}Bi generators if the presence of ^{227}Ac prevents its direct use in ^{225}Ac-radiopharmaceuticals.

The targeted alpha therapy field has yet to establish an acceptable limit for ^{227}Ac, though this is crucial to any future production, quality control, and use of both ^{227,225}Ac† and ^{225}Ac*. If the source of ^{227}Ac concerns is waste disposal and the resulting costs, then an ^{227}Ac limit per patient dose (approximately 10 MBq of ^{225}Ac) equal to the exemption level for for ^{227}Ac disposal provides one potential limit to consider[30]. In Canada and under guideline exemption quantities recommended by the International Atomic Energy Agency (IAEA) [227–229], the ^{227}Ac exemption level is 1 kBq. This corresponds to a ^{227}Ac limit on the order of 0.01%, which is not met by ^{227,225}Ac† but is easily met by ^{225}Ac* (Table 7.2). In fact even our first attempts at ^{225}Ac* production demonstrate that at <7.5E-5% ^{227}Ac con-

[28] Assuming 2 days between the end of irradiation and the end of target processing

[29] TRIUMF's 500 MeV cyclotron typically operates only 8 months per year.

[30] The IAEA defines an exemption level as "*A value, established by a regulatory body and expressed in terms of activity concentration, total activity, dose rate or radiation energy, at or below which a source of radiation need not be subject to some or all aspects of regulatory control*" [227].

tent, a batch of 10^2 patient doses could contain ^{227}Ac below the exemption level and could be considered ^{227}Ac-free from regulatory and practical perspectives. While other jurisdictions may have more restrictive exemption levels that would necessitate additional improvements in the current ^{227}Ac impurities reported in Table 7.2, this work demonstrates that ^{225}Ac products with reduced ^{227}Ac content can be derived from the proton spallation of thorium. With an ^{227}Ac decontamination factor of >2000 from just the first two attempts at ^{225}Ac* production, it is conceivable that ^{225}Ac* products could meet ^{227}Ac limits that are ultimately accepted by the targeted alpha therapy field in the event that ^{227}Ac content in ^{227,225}Ac† products is determined to be too high.

7.5 Summary

A precipitation- and chromatography-based process for the separation of Ac from gram quantities of Th and trace quantities of most other elements was developed and demonstrated. This process has application in the production of ^{225}Ac from proton irradiated thorium.

When sufficient quantities of ^{225}Ra are also co-produced during thorium irradiation, this process is capable of producing an ^{225}Ac product (^{225}Ac*) with ^{227}Ac quantities >2000 times lower than other thorium-spallation-derived ^{225}Ac products (^{227,225}Ac†). The ^{227,225}Ac† product demonstrated similar or better quality when compared to the ^{225}Ac* product in terms of radiolabelling and chemical purity, and contained ^{227}Ac content low enough such that multiple patient doses of ^{225}Ac contained less than the IAEA recommended exemption level for ^{227}Ac, and could therefore be considered ^{227}Ac-free from a regulatory perspective.

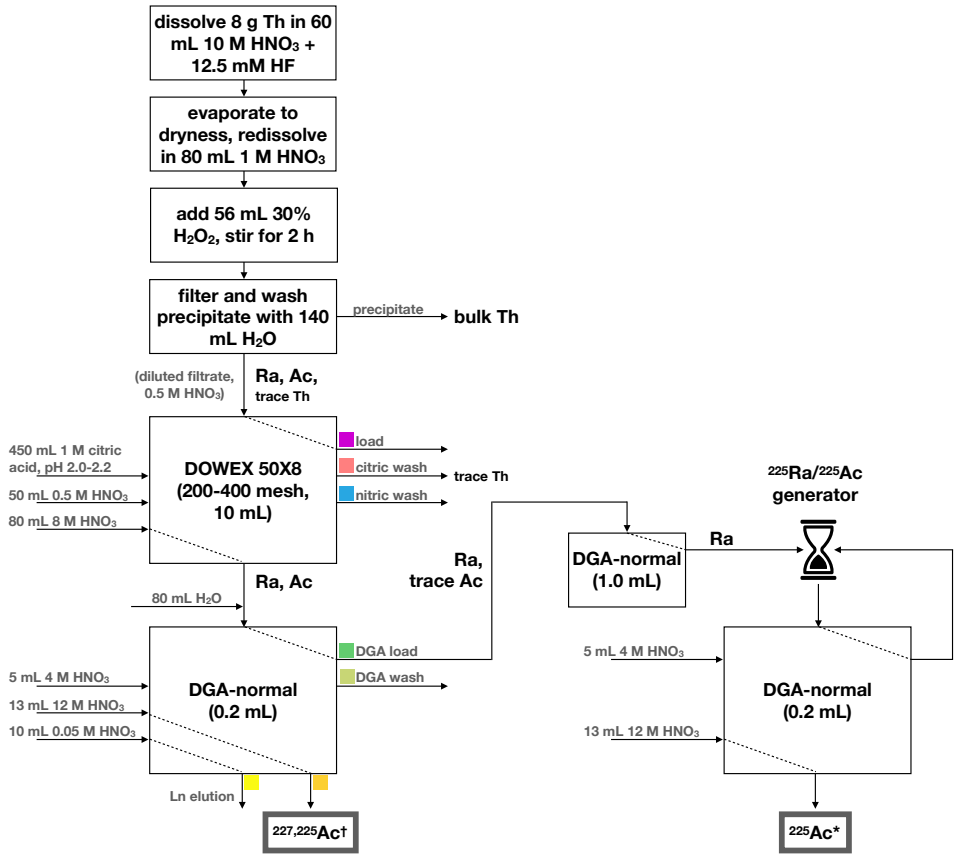

Figure 7.4: Flowchart describing the process used to produce $^{227,225}\mathrm{Ac}^{\dagger}$ and $^{225}\mathrm{Ac}^{*}$ products from thorium metal irradiated with high energy (>100 MeV) protons. Coloured squares correspond to the fractions shown in the Figure 7.6 legend.

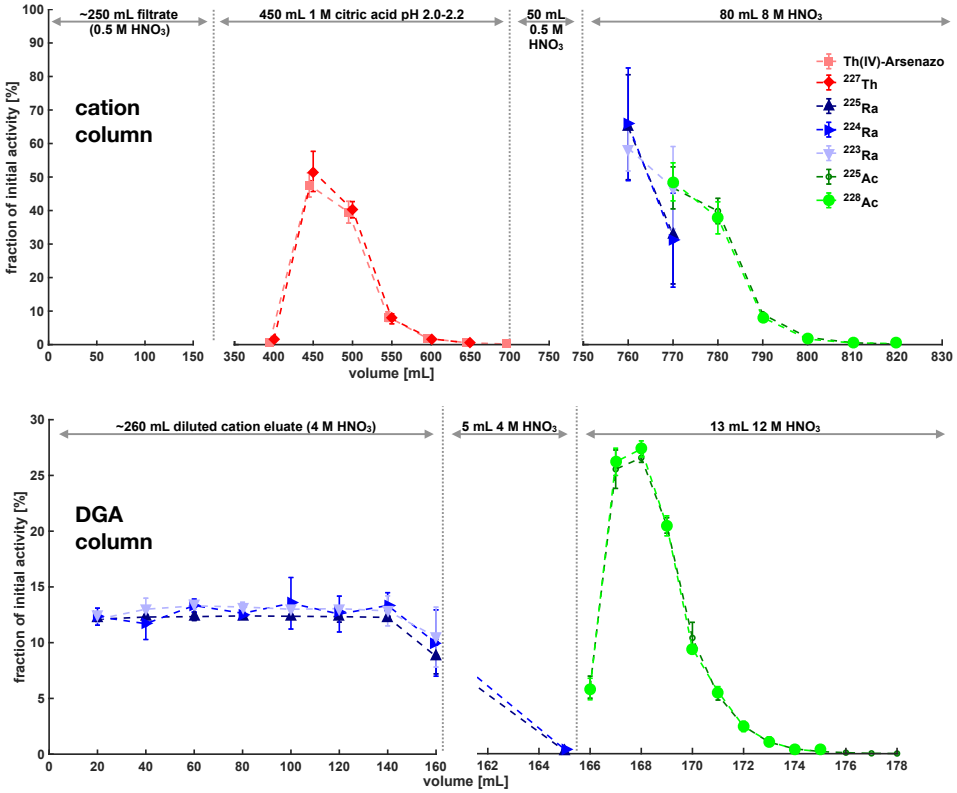

Figure 7.5: Elution profiles for Th, Ra, and Ac on the cation exchange column (top) and DGA-normal column (bottom) using thorium colorimetry, ^{227}Th, ^{225,224,223}Ra, and ^{228,225}Ac as tracers (see Section 7.2.4). Each data point represents the average ± standard deviation (n = 3) of independent elution profile measurements with the 7 individual tracers.

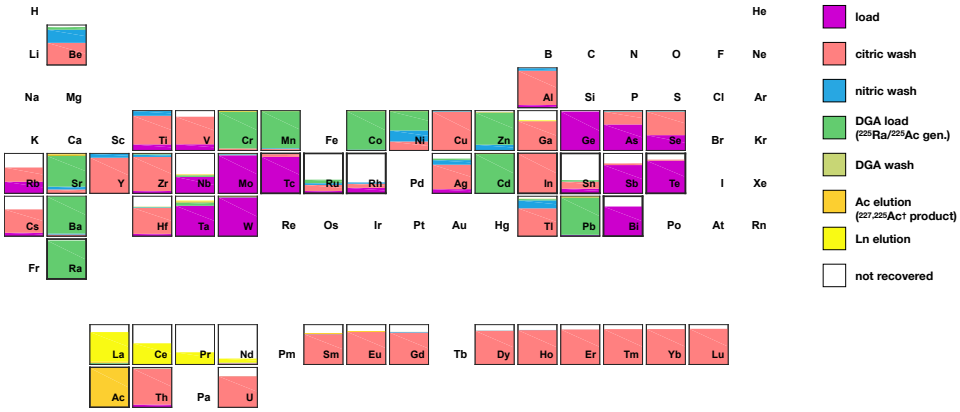

Figure 7.6: Results from tracer studies of the thorium processing scheme chromatography column steps. Elements with bold borders were evaluated using radiotracers (^{96}Tc, ^{103}Ru, ^{101m}Rh, ^{114m}In, ^{117m}Sn, ^{121m,121}Te, ^{205,206}Bi, ^{225,224,223}Ra, ^{228,225}Ac). All other elements were evaluated using multi-element ICP-MS standards as tracers. The area of each colour is proportional to the amount of the elemental tracer found in the fraction.

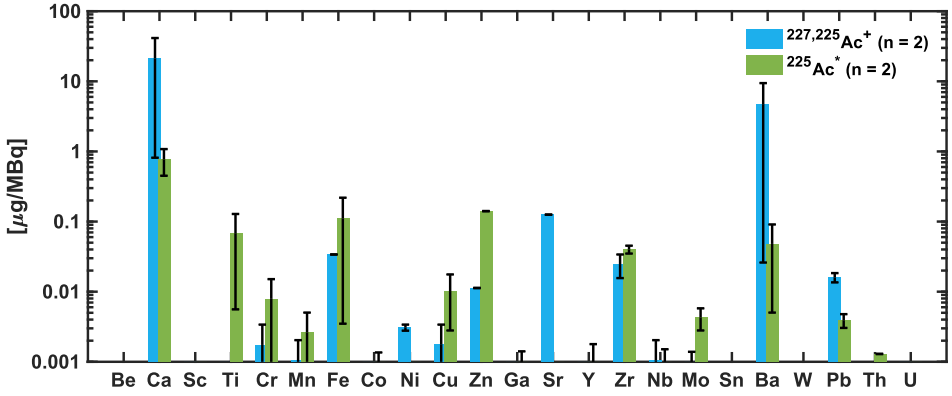

Figure 7.7: Average ± standard deviation (n = 2) stable elemental impurities in the ^{227,225}Ac† and ^{225}Ac* products, measured as described in Section 7.2.6.

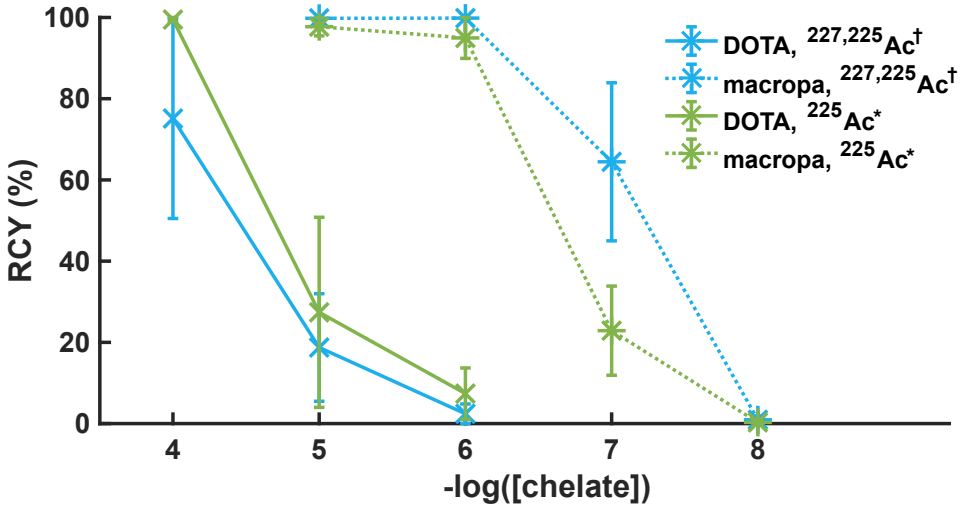

Figure 7.8: Concentration dependent radiolabelling studies with ^{227,225}Ac† and ^{225}Ac* products for both DOTA (85°C, 30 min, pH 7) and macropa (ambient temperature, 30 min, pH 7), as described in Section 7.2.7. Each data point represents the average ± standard deviation of n = 6 replicates (n = 3 replicates for each of the two ^{227,225}Ac† and ^{225}Ac* production runs).

8 Conclusion

Chapter 3 demonstrates how ^{225}Ac can be produced at TRIUMF's ISOL facility. Mass $A = 225$ ion beams containing up to 1.6×10^8 ions/s and up to 1.3×10^8 ions/s of ^{225}Ra and ^{225}Ac, respectively, were implanted into an aluminum target. Implantations produced up to 8.6 MBq of ^{225}Ra and up to 18 MBq of ^{225}Ac, which were separated using solid phase extraction DGA resin, resulting in a radiochemically pure ^{225}Ac product in >98% yield. Calcium, iron, copper, nickel and zinc were found in the ^{225}Ac product with amounts of (1392 ± 208), (203 ± 20), (47 ± 12), (19 ± 6), and (137 ± 21) ppb, respectively. This ^{225}Ac product was of suitable quantity and quality for use in preclinical ^{225}Ac-radiopharmaceutical development, as demonstrated by the number of publications that resulted from the ^{225}Ac production runs described in Table 3.1 [3, 4, 162, 163], including Chapter 4 of this thesis. However, due to demands for beam from other experiments, uranium carbide target reliability, and variations in the ^{225}Ac ion beam yield (between 10^6 and 10^8 ions/s), the ^{225}Ac available from ISAC is realistically limited to a few tens of MBq per year.

The significance of the work presented in Chapter 3 is therefore not in the amount of ^{225}Ac that can be produced, but in the ability to provide relatively small quantities of radioactivity with a limited amount of initial work. In contrast to conventional radionuclide production methods, no proton target (as in Chapter 5) or radiochemical separation strategy (as in Chapter 7) development is required for production of a new nuclide at ISAC. Instead one selects and tunes the beam to obtain a new mass from the mass separator. This versatility is a key strength of this nuclide production and isolation method. The experience with ^{225}Ac gained from using this initial ISOL-based production method motivated and made easier the production and handling of ^{225}Ac via the methods that were later developed using TRIUMF's IPF facility (see Chapters 5 to 7).

With larger-scale ^{225}Ac production from TRIUMF's IPF, future opportunities to produce novel medical radionuclides using ISAC-ISOL should

take advantage of this facility's versatility by studying other nuclides besides ^{225}Ac. This could include ^{226}Ac, which is an Ac isotope that, as described below, could potentially be directly imaged using its 230 keV gamma line.

Other future research efforts regarding ISAC implantations should consider the use of different implantation target materials for collection of the ion beam. While the aluminum targets used in this work have the advantage of being easy to manufacture and handle, the etching of the implanted radioactivity from the material adds large amounts of metal impurities to the ^{225}Ac radionuclide product, including Al and other trace metals found in aluminum materials, such as Ca, Fe, Ti, Zn, Zr, and Pb (see Table 3.2). While measurements of the resulting ^{225}Ac product radiolabeling capability suggest this did not negatively impact the usability of the ^{225}Ac produced from ISAC, this may not be the case for the collection of other radionuclides. Radiolabeling using nuclides with different chemical properties from Ac may be more adversely affected by the presence of these stable metal impurities, which can compete with the radiometal during radiolabeling reactions. In addition, the impurity profile of the radionuclide product will change when using different post-implantation radiochemical separation strategies required to purify radiometals other than Ac from Ra (a single DGA resin was used in Chapter 3 to separate ^{225}Ra and ^{225}Ac that were co-implanted). Removing the source of these metal impurities by using a non-metallic implantation target could improve the chemical purity of the radionuclides produced at ISAC. Potential alternative target materials could include thin high-purity salts used in radiolabeling buffers (ex. ammonium acetate) or ice, though the latter would likely require development of a cryogenically cooled implantation chamber.

Applications of the ISAC-produced ^{225}Ac include the ^{225}Ac decay chain imaging presented in Chapter 4 [4]. With respect to research questions outlined in Section 1.4, this work successfully demonstrated that VECTor can individually quantify distributions of ^{225}Ac progeny nuclides via simultaneous ^{221}Fr and ^{213}Bi SPECT and also characterized the performance of the instrumentation for creating such images, including assessment of image resolution, contrast recovery, and noise. A hotrod resolution phantom containing clusters of thin rods with diameters ranging between 0.85 and 1.70 mm was used to assess resolution. To demonstrate ability to simultaneously image dynamic ^{221}Fr and ^{213}Bi activity distributions, a phantom containing a ^{213}Bi generator from ^{225}Ac was imaged. These tests were performed with two collimators, a high-energy ultra-high resolution (HEUHR) collimator and an ultra-high sensitivity (UHS) collimator. Values consistent with activity concentrations determined independently via gamma spectroscopy

were observed in high activity regions of the images. In hotrod phantom images, the HEUHR collimator resolved all rods for both ^{221}Fr and ^{213}Bi images. With the UHS collimator, no rods were resolvable in ^{213}Bi images and only rods $\geq$1.3 mm were resolved in ^{221}Fr images. After eluting the ^{213}Bi generator, images accurately visualized the reestablishment of transient equilibrium of the ^{225}Ac decay chain. This work demonstrates the potential ability of evaluating the pharmacokinetics of the ^{225}Ac decay chain *in vivo*, but requires the use of a high-performance, high-energy collimator.

The ability to separately assess the biodistributions of each alpha emission in the ^{225}Ac decay chain and the resulting integrated dose to various tissues could significantly impact the *in vivo* assessment of ^{225}Ac-radiopharmaceuticals by enabling more detailed dosimetry. Determining the complete ^{221}Fr and ^{213}Bi biodistributions is challenging by *ex vivo* methods due to the short half-lives of ^{221}Fr ($t_{1/2}$ = 4.8 min) and ^{213}Bi ($t_{1/2}$ = 45.6 min). As discussed in Section 4.1, other imaging techniques are not able to provide such information. While other imaging modalities such as alpha-cameras [180] or Cherenkov imaging [181] have also been used to image the biodistributions of the ^{225}Ac decay chain or other alpha-emitting medical isotopes, quantitative SPECT has a distinct advantage over these methods in that photon energy discrimination can be used to distinguish between different components of the ^{225}Ac decay chain. The information made available through this technique could be of significant importance to ^{225}Ac radiopharmaceutical development. Providing a complete picture of the ^{225}Ac decay chain's pharmacokinetics over time would measure the fraction of ^{225}Ac progeny isotopes maintained at the target site and could resolve persisting concerns within the field regarding the safety of serial alpha emitting radionuclides such as ^{225}Ac [100].

However, until the use of this imaging technique can be demonstrated in a preclinical model, any suggested benefits to ^{225}Ac-radiopharmaceutical development remain hypothetical. As mentioned in Section 1.4, this was previously not pursued because of an inability to produce sufficient quantities of ^{225}Ac. New ^{225}Ac production methods at TRIUMF described in Chapters 5-7 now make such experiments possible.

However, even with access to greater quantities of ^{225}Ac this imaging technique may be limited by the fact that capturing ^{221}Fr and ^{213}Bi images requires the administration of ^{225}Ac quantities that are 2-3 orders of magnitude greater than the amount that would be used therapeutically. In fact, the amount of ^{225}Ac required with VECTor to image the ^{225}Ac decay chain's biodistribution in a mouse model (approximately 10 MBq or more) is comparable to a therapeutic ^{225}Ac dose in a human patient [25, 31, 32]. The

consequences of this are that not only may the biodistribution of imageable ^{225}Ac quantities differ from the biodistribution of therapeutic quantities – thereby reducing the image's utility for predicting biological outcomes – but also that an imageable ^{225}Ac quantity may be too toxic for an animal model to survive long enough to complete a SPECT scan. Nevertheless future research efforts should explore the ability of the VECTor system to image the ^{225}Ac decay chain *in vivo* and explore this unanswered question.

It should also be noted that, even if such preclinical imaging is able to provide more detailed dosimetry of ^{225}Ac-radiopharmaceuticals in preclinical models, the technique is unlikely to be applicable to dosimetry in human patients. Again, this is because capturing ^{221}Fr and ^{213}Bi images requires the administration of ^{225}Ac quantities that are 2-3 orders of magnitude greater than the amount that would be used therapeutically, making such a diagnostic image potentially harmful. Imaging to assess the ^{225}Ac decay chain's biodistribution and resulting dosimetry in patients prior to the administration of an ^{225}Ac-radiopharmaceutical may not be possible. Instead, such images must likely use other diagnostic radionuclides; this has been done already, for example, with ^{68}Ga and ^{111}In [25, 230]. This is in contrast to direct imaging with ^{213}Bi-radiopharmaceuticals, which generally have a $\sim 10^2$ times higher maximum tolerable dose [231] and are imageable in therapeutic quantities [179].

While diagnostic radionuclides such as ^{68}Ga and ^{111}In may provide a quantitative biodistribution that may be analogous to a subsequent ^{225}Ac-biodistribution, they would not be able to measure the fraction of ^{225}Ac progeny nuclides maintained at the target site or the fraction that provides dose to organs at risk. Additionally, the use of a non-Ac imaging isotope would create lingering questions about whether the biodistribution of the imaging radiopharmaceutical is still representative of the biodistribution of a chemically different ^{225}Ac-version of the radiopharmaceutical. ^{226}Ac is perhaps the only directly imageable SPECT nuclide (using its 230 keV gamma line), however, it similarly comes with technical challenges related to radionuclide production.

Despite these potential limitations of ^{225}Ac decay chain imaging, the desire to produce larger ^{225}Ac quantities to enable *in vivo* imaging experiments motivated a change in focus for this thesis away from ISOL-produced ^{225}Ac and towards the development of an alternative, larger-scale production methodology that is described by Chapters 5-7. While this does not diminish the successes of Chapters 3 and 4 – which achieved TRIUMF's first ^{225}Ac production and demonstrated the ability to simultaneously image multiple components of the ^{225}Ac decay chain – the ^{225}Ac production methods

described in Chapters 5-7 have greater potential to produce GBq quantities of ^{225}Ac, enabling studies not reasonable achievable using ISOL-produced ^{225}Ac.

Regarding research questions proposed in Section 1.4, Chapter 5 specifically demonstrates how a thorium target can be designed for irradiation at TRIUMF's IPF, which proton beam parameters can result in a safe irradiation, and how much ^{225}Ac and ^{225}Ra can be produced during irradiations. A new ^{225}Ac-production target system capable of withstanding the power deposited by the proton beam was designed and its performance simulated over a range of potential operating parameters (proton beam widths and intensities). Special attention was given to heat transfer and stress simulations within the target components during irradiation. Even with the application of conservative assumptions to the simulation inputs and with conservative thresholds for target safety, results show that all beams of width >20 mm and current <100 μA result in safety factors on the target windows >1. The target was successfully tested in two irradiations with a 72–73 μA proton beam for a duration of 36.5 h, demonstrating saturation yields of 72.5 MBq/μA and 17.6 MBq/μA for ^{225}Ac and ^{225}Ra, respectively.

The quantities that can be produced using these IPF targets are significant, both with respect to the amount available at TRIUMF and, potentially, the amount produced globally per year (approximately 63 GBq, see Section 1.3). It is estimated that the simultaneous irradiation of 12 targets over a 240 hour period could produce 42 GBq of ^{225}Ac and 7 GBq of ^{225}Ra without requiring any changes to the target or beam parameters. Further increases are possible if the proton current and target thickness are increased (as discussed below). Chapter 5 therefore provides the first demonstration of TRIUMF's capability as a potentially significant large-scale producer of ^{225}Ac. The methods and results of Chapter 5 may also be useful for target development projects at similar institutions or at other TRIUMF irradiation facilities.

While a strength of the work in Chapter 5 is that the modelling shows – even with very conservative assumptions – that these thorium targets can be safely irradiated, there are significant limitations to the methodologies that were applied. Due to the potential for production of hazardous alpha-emitting, volatile and gaseous radionuclides during the irradiation of thorium with high-energy protons, the work in Chapter 5 was motivated by the need to demonstrate confidence that these targets could be irradiated safely (see also Appendices C and D). While such work was required before the ^{225}Ac production research described in Chapters 6 and 7 could continue, these safety motivations meant that assumptions were made regarding the

input parameters of the models in Chapter 5, especially regarding unknown thermal properties of relevant materials (see Section 5.3).

These assumptions in the models' input parameters are a key limitation of the scientific work of Chapter 5, as is the absence of a comparison of the models to empirical data. These assumptions and their implications are discussed thoroughly in Section 5.3. Assumptions regarding the material properties of thorium can be credited in part to the radioactive nature of thorium and its designation as special nuclear material. Such factors make thorium a more logistically challenging material to study or use and therefore limit the amount of available data in the literature, relative to other non-radioactive or non-nuclear materials. For similar reasons, when conducting the work described in Chapter 5, it was not realistically possible to measure relevant thorium material properties because available equipment was located in facilities that lacked regulatory permission to possess or handle thorium. Procurement of devices – inside a sufficiently licensed facility – to measure the thermal conductivity of thorium and the thermal contact resistance of the thorium-Inconel interface of the IPF targets will improve the accuracy of the models presented in Chapter 5 and enable these models to be validated against quantitative data.

Such improvements to the thermomechanical models of the thorium targets during irradiation will be increasingly important if future efforts are undertaken to increase the thickness of the thorium irradiated in each target in support of increasing ^{225}Ac production. While the IPF target station has space for a 32-fold increase in thorium thickness, more thorium means more heat deposition within the target by the proton beam, meaning more heat that must be conducted through the thorium and across the thorium-Inconel interface. The assumptions used in Chapter 5 will therefore become increasingly prohibitive as the amount of thorium within the targets is increased.

Despite these limitations, the work of Chapter 5 resulted in the design and irradiation of a thorium target at TRIUMF's IPF, demonstrating the facility's ^{225}Ac production capability and enabling subsequent research regarding the separation of Ac from irradiated thorium targets that is presented in Chapter 7. Despite the limitations of the models that have been discussed, the work of Chapter 5 provides a strong foundation for any future thorium target design efforts, including the use of thermomechanical models based on empirical input data, provided such data becomes available in the future.

The thin nature of the thorium target design also enabled the cross section measurements described in Chapter 6. Thorium spallation cross

sections at proton energies of 438 MeV were determined to be (13.30 ± 1.21) mb and (4.2 ± 0.40) mb for ^{225}Ac and ^{225}Ra, respectively. A total of 36 other independent or cumulative cross sections for ^{232}Th(p,x) reactions at 438 MeV were also determined, including those relevant to ^{225}Ac production, such as ^{227}Ac and ^{226}Ac. These measurements contribute not only to the field of TAT but also to the body of known nuclear data by reporting nuclide formation cross sections that have not previously been measured (see Figure 6.4).

These 38 cross section measurements were also used to validate FLUKA simulations that enable the estimation of the production of the many other nuclides produced during the proton irradiation of thorium. While not the first study to do this, other reported FLUKA validation studies used different target materials or different proton energy ranges [150–159]. Determining that FLUKA is able to estimate the radioactive inventory of the irradiated thorium targets to within a factor of 2 is a valuable conclusion that permits FLUKA to be used in practical situations where knowledge of the radioactive inventory is required but is too onerous or is impossible to measure; examples include radiation safety analyses (see Appendices C and D) or radioactive shipping inventories. Since FLUKA is not the only Monte Carlo based high-energy particle transport code, future work could include a comparison with other codes (for example, GEANT4 [232, 233]) or with future versions of FLUKA itself. Future efforts could also consider repeating the cross sections reported in Chapter 6, as data from only a single irradiation was reported on in Chapter 6 due to the significant amount of effort required to analyze the gamma spectra (see Figure 6.1) and the long decay periods since EOB for these gamma spectroscopy samples shown in Table 6.1. However, any future repetitions of the work would be much easier now that gamma spectroscopy analysis methods for thorium spallation spectra are established.

Nevertheless, FLUKA is evidently a valuable tool for estimating the radionuclide inventory that results from the high-energy proton irradiation of thorium and, consequently, for estimating the requirements of radiochemical separation processes used to purify Ac from any irradiated thorium targets (see Figure 7.3). The radiochemical separation developed and characterized in Chapter 7 is one such process. The work of Chapter 7 accomplishes the goals set out in Section 1.4 by: demonstrating how existing radiochemical separation methods for isolation of Ac from proton irradiated IPF targets could be modified for use in TRIUMF's radiochemistry facilities; using ^{225}Ra produced during thorium irradiation to chemically isolate a generator-produced Ac product (^{225}Ac*) with fewer long-lived impurities (specifically, ^{227}Ac) than the directly-produced Ac product (^{227,225}Ac†); and by charac-

terizing and comparing the quality of these two Ac products.

Ac was separated from irradiated thorium and coproduced radioactive spallation and fission products using a thorium peroxide precipitation method followed by cation exchange and extraction chromatography. Stable and radioactive tracer studies demonstrated the ability of this method to separate Ac from most other elements, providing a directly produced Ac product ($^{227,225}Ac^{\dagger}$) with measured ^{227}Ac content of $(0.15 \pm 0.04)\%$. The second, indirectly produced Ac product ($^{225}Ac^{*}$) with ^{227}Ac content of $<7.5\times10^{-5}\%$ is obtained by repeating the final extraction chromatography step with the ^{225}Ra-containing fraction. The ^{225}Ra-derived $^{225}Ac^{*}$ showed similar or improved quality compared to the initial, directly-produced $^{227,225}Ac^{\dagger}$ product in terms of chemical purity and radiolabeling capability, the latter of which was comparable with other ^{225}Ac sources reported in the literature.

While the radiochemical process applied (see Figure 7.4) in Chapter 7 includes some process steps that are similar to other methods described in the literature [104], modifications and additional process steps were introduced that provide substantial benefit. The most considerable addition is the initial thorium peroxide precipitation, which has shown to be an effective and reliable method for thorium de-bulking without resulting in significant Ac or Ra losses (see Section 7.3.2). The removal of >95% of the thorium mass from the solution early in the process enables the use of smaller chromatography column(s) and fraction volumes in subsequent process steps, reducing the time needed for these steps and the quantity of radioactive waste that results. Additionally, the initial thorium de-bulking provides for a process that can be more easily applied to any future irradiations of targets containing larger quantities of thorium, as part of efforts to increase ^{225}Ac production. While various methods for Ac extraction from irradiated thorium exist in the literature [104, 136, 143, 160, 206], this is the first to include such an initial de-bulking method. The development of this thorium precipitation was additionally important when conducting thorium target processing at radiochemistry facilities at TRIUMF, since the reduction in chromatography column volumes and reagent volumes resulted in a reduced equipment footprint that was necessary in order to fit the process inside available hot cells.

While this thorium peroxide precipitation has shown to be a reliable and effective thorium de-bulking method, future research efforts should focus on exploring alternative precipitation methods and on deepening our understanding of the thorium peroxide precipitation chemistry. While other precipitates, including thorium oxalate and thorium iodate were briefly explored [219], they were found to either be too difficult to filter or to result

in greater co-precipitation of Ra or Ac than the thorium peroxide approach under the conditions tested. These other precipitates may be more effective under alternative conditions, and precipitations using other insoluble thorium compounds are yet to be studied [194]. Known advantages of the thorium peroxide approach are its compatibility with previous and subsequent process steps, the small (<5%) losses of Ac and Ra, and the ease of filtration. Additionally, the ability to easily redissolve the precipitate in a concentrated nitric acid substantially reduces the amount of handling required to dispose of any waste, an important consideration for chemical processes that must be conducted remotely inside a hot cell. However, these features of the thorium peroxide precipitation have been observed without a complete understanding of the chemistry involved in thorium peroxide formation or the structure of the thorium peroxide that results [215, 216]. Additionally, while actinides are generally known to form insoluble peroxides (the co-precipitation of uranium with thorium peroxide is previously reported [221], and the co-precipitation of protactinium with thorium peroxide was observed described in Section 7.3.2), the reasons why Ac was not observed to similarly co-precipitate with thorium peroxide remain unclear and could also be a focus of future research.

The subsequent process steps used to purify Ac from irradiated thorium targets include ion exchange and extraction chromatography. Chemically, these steps are similar to previously reported methods [104], though the thorium de-bulking enabled practical changes to the cation exchange process step that make it more reproducible and easier to carry out inside a hot cell. Specifically, by removing the bulk mass of thorium, the separation of Th from Ac and Ra on the cation exchange resin in a citric acid liquid phase can be done as a column wash, as opposed to a column loading step applied by other methods [104]. In practical terms, this means that pH adjustment of the citric acid (to within the narrow 2.0-2.2 range required for successful separation of Th from Ac and Ra) can be performed outside of the hot cell as preparation of an input reagent to the process, as opposed to within the hot cell as part of an additional process step. While the process overall resulted in $^{227,225}Ac^{\dagger}$ and $^{225}Ac^{*}$ products that demonstrated adequate radiolabelling capabilities (see Section 7.3.3), future research or development efforts may need to address the presence of other stable (ex. Ca^{2+}) or radioactive (ex. ^{140}La, $^{106,103}Ru$, and ^{85}Sr) impurities, as discussed in detail in Section 7.4.

Together, Chapters 5, 6, and 7 demonstrate the production of ^{225}Ac from a new source (TRIUMF's IPF). These production methods not only address the initial motivations for transitioning the work of this thesis away from ISAC-based production (see Section 1.4), but they also have a theo-

retical potential to provide ^{225}Ac in quantities that could markedly increase global ^{225}Ac supply. While ^{225}Ac can also be produced through long-lived ^{229}Th generators, increasing ^{229}Th availability is challenging since the grow-in of ^{229}Th ($t_{1/2}$ = 7340 y) from ^{233}U takes decades due to the long ^{229}Th half-life (see Section 1.3). Accelerator-based ^{225}Ac production is therefore advantageous for its scaleability. Accelerator-based methods involving ^{226}Ra irradiation are technically viable but, for reasons detailed in Section 1.3.4.4, have not been pursued to the same extent as ^{232}Th irradiation methods. While the proton spallation of thorium for ^{225}Ac production typically includes the co-production of ^{227}Ac, data reported in Chapter 6 demonstrates that at proton energies above approximately 100 MeV, ^{225}Ra production is sufficient to produce ^{225}Ac via ^{225}Ra/^{225}Ac generators. This reduces ^{227}Ac impurities, as shown in Chapter 7.

Together, Chapters 5, 6, and 7 are the first demonstration of ^{225}Ac* production technology using a thorium irradiation facility and chemical process that could be scaled to useful clinical or commercial quantities, while maintaining ^{227}Ac content low enough to be potentially considered ^{227}Ac-free from practical and regulatory perspectives. Irradiation of the existing target design (Chapter 5) for a full two weeks is expected to produce 566 MBq (15.3 mCi) of ^{225}Ra per target, once process losses (5%) and decay losses (10%) are considered (assuming 2 days between the end of irradiation and the end of target processing). Since each MBq of ^{225}Ra could produce approximately 0.9 MBq of ^{225}Ac*, assuming a 1 week operational cycle of the generator, the irradiation and processing of 1 target per week for 35 weeks per year (TRIUMF's 500 MeV cyclotron typically operates only 8 months per year) could produce approximately 17.8 GBq (0.5 Ci) per year of ^{225}Ac*. Since TRIUMF's IPF is capable of irradiating 12 targets simultaneously, an additional 6-fold increase to the potential production quantities is also readily available. This potential annual production of 53.4 GBq/y (3 Ci/y) of ^{225}Ac* would represent a 1.75-fold increase in the global availability of ^{225}Ac (see Section 1.3) and is readily available from the methods demonstrated in Chapters 5 through 7. Such a scale up of ^{225}Ac production beyond the relatively limited number of irradiations and processed targets described in this thesis has yet to be demonstrated and would likely require the establishment of engineered radiochemistry equipment, a robust quality control program, and (due to the number of long-lived radionuclides co-produced during thorium irradiation) a sustainable plan for radioactive waste management. Still, the work presented in this thesis provides the foundation for such an ^{225}Ac production paradigm should it be pursued in the future.

Bibliography

[1] A. K. H. Robertson, C. F. Ramogida, P. Schaffer, and V. Radchenko, "Development of ^{225}Ac Radiopharmaceuticals: TRIUMF Perspectives and Experiences," *Current Radiopharmaceuticals*, vol. 11, no. 3, pp. 156–172, 2018.

[2] A. K. H. Robertson, K. Ladouceur, M. Nozar, L. Moskven, C. F. Ramogida, J. D'Auria, V. Sossi, and P. Schaffer, "Design and Simulation of Thorium Target for Ac-225 Production," *AIP Conf. Proc.*, vol. 1845, no. 1, pp. 020019–1–020019–5, 2017.

[3] C. F. Ramogida, A. K. H. Robertson, U. Jermilova, C. Zhang, H. Yang, P. Kunz, J. Lassen, I. Bratanovic, V. Brown, L. Southcott, C. Rodríguez-Rodríguez, V. Radchenko, F. Bénard, C. Orvig, and P. Schaffer, "Evaluation of polydentate picolinic acid chelating ligands and an α-melanocyte-stimulating hormone derivative for targeted alpha therapy using ISOL-produced 225Ac," *EJNMMI Radiopharm. Chem.*, vol. 4, no. 1, 2019.

[4] A. K. H. Robertson, C. Ramogida, C. Rodriguez-Rodriguez, S. Blinder, P. Kunz, V. Sossi, and P. Schaffer, "Multi-isotope SPECT imaging of the ^{225}Ac decay chain: feasibility studies," *Physics in Medicine and Biology*, vol. 62, pp. 4406–4420, 2017.

[5] A. K. H. Robertson, A. Lobbezoo, L. Moskven, P. Schaffer, and C. Hoehr, "Design of a Thorium Metal Target for ^{225}Ac Production at TRIUMF," *Instruments*, vol. 3, no. 1, pp. 20–26, 2019.

[6] A. K. H. Robertson, P. Kunz, C. Hoehr, and P. Schaffer, "Nuclide production cross sections from irradiation of thorium by 438 mev protons and a comparison to fluka and geant4 simulations," *Phys. Rev. C*, vol. 102, p. 044613, Oct 2020.

[7] A. K. H. Robertson, B. L. McNeil, H. Yang, D. Gendron, R. Perron, V. Radchenko, S. Zeisler, P. Causey, and P. Schaffer, "^{232}Th-Spallation-Produced ^{225}Ac with Reduced ^{227}Ac Content," *Inorganic Chemistry*, vol. 59, no. 17, pp. 12156–12165, 2020.

[8] J. Strosberg, G. El-Haddad, E. Wolin, A. Hendifar, J. Yao, B. Chasen, E. Mittra, P. L. Kunz, M. H. Kulke, H. Jacene, D. Bushnell, T. M. O'Dorisio, R. P. Baum, H. R. Kulkarni, M. Caplin, R. Lebtahi, T. Hobday, E. Delpassand, E. Van Cutsem, A. Benson, R. Srirajaskanthan, M. Pavel, J. Mora, J. Berlin, E. Grande, N. Reed, E. Seregni, K. Öberg, M. Lopera Sierra, P. Santoro, T. Thevenet, J. L. Erion, P. Ruszniewski, D. Kwekkeboom, and E. Krenning, "Phase 3 Trial of 177Lu-Dotatate for Midgut Neuroendocrine Tumors," *N. Engl. J. Med.*, vol. 376, no. 2, pp. 125–135, 2017.

[9] T. E. Witzig, L. I. Gordon, F. Cabanillas, M. S. Czuczman, C. Emmanouilides, R. Joyce, B. L. Pohlman, N. L. Bartlett, G. A. Wiseman, N. Padre, A. J. Grillo-López, P. Multani, and C. A. White, "Randomized controlled trial of yttrium-90-labeled ibritumomab tiuxetan radioimmunotherapy versus rituximab immunotherapy for patients with relapsed or refractory low-grade, follicular, or transformed B-cell non-Hodgkin's lymphoma," *J. Clin. Oncol.*, vol. 20, no. 10, pp. 2453–2463, 2002.

[10] M. S. Kaminski, A. D. Zelenetz, O. W. Press, M. Saleh, J. Leonard, L. Fehrenbacher, T. A. Lister, R. J. Stagg, G. F. Tidmarsh, S. Kroll, R. L. Wahl, S. J. Knox, and J. M. Vose, "Pivotal study of iodine I-131 tositumomab for chemotherapy-refractory low-grade or transformed low-grade B-cell non-Hodgkin's lymphomas," *J. Clin. Oncol.*, vol. 19, no. 19, pp. 3918–3928, 2001.

[11] S. Poty, L. C. Francesconi, M. R. Mcdevitt, M. J. Morris, and S. Jason, "α-Emitters for Radiotherapy: Basic Radiochemistry to Clinical Studies – Part 1," *J. Nucl. Med.*, vol. 59, no. 6, pp. 1–27, 2018.

[12] S. Poty, L. C. Francesconi, M. R. McDevitt, M. J. Morris, and J. S. Lewis, "α-Emitters for Radiotherapy: From Basic Radiochemistry to Clinical Studies—Part 2," *J. Nucl. Med.*, vol. 59, no. 7, pp. 1020–1027, 2018.

[13] H. Song, R. F. Hobbs, R. Vajravelu, D. L. Huso, C. Esaias, A. Morgenstern, and G. Sgouros, "Radioimmunotherapy of breast cancer

metastases with alpha-particle-emitter 225Ac: comparing efficacy with 213Bi, 90Y," *Cancer Res.*, vol. 69, no. 23, pp. 8941–8948, 2009.

[14] F. Graf, J. Fahrer, S. Maus, A. Morgenstern, F. Bruchertseifer, S. Venkatachalam, C. Fottner, M. M. Weber, J. Huelsenbeck, M. Schreckenberger, B. Kaina, and M. Miederer, "DNA double strand breaks as predictor of efficacy of the alpha-particle emitter Ac-225 and the electron emitter Lu-177 for somatostatin receptor targeted radiotherapy," *PLoS ONE*, vol. 9, no. 2, 2014.

[15] Y. S. Kim and M. W. Brechbiel, "An overview of targeted alpha therapy," *Tumor Biology*, vol. 33, no. 3, pp. 573–590, 2012.

[16] M. R. McDevitt, G. Sgouros, R. D. Finn, J. L. Humm, J. G. Jurcic, S. M. Larson, and D. A. Scheinberg, "Radioimmunotherapy with alpha-emitting nuclides," *European journal of nuclear medicine*, vol. 25, no. 9, pp. 1341–1351, 1998.

[17] O. Couturier, S. Supiot, M. Degraef-Mougin, A. Faivre-Chauvet, T. Carlier, J.-F. Chatal, F. Davodeau, and M. Cherel, "Cancer radioimmunotherapy with alpha-emitting nuclides.," *European journal of nuclear medicine and molecular imaging*, vol. 32, no. 5, pp. 601–614, 2005.

[18] D. A. Mulford, D. A. Scheinberg, and J. G. Jurcic, "The promise of targeted alpha-particle therapy.," *Journal of Nuclear Medicine*, vol. 46 Suppl 1, pp. 199S–204S, 2005.

[19] M. W. Brechbiel, "Targeted alpha-therapy: past, present, future?," *Dalton Transactions*, no. 43, pp. 4918–28, 2007.

[20] K. E. Baidoo, K. Yong, and M. W. Brechbiel, "Molecular pathways: Targeted alpha-Particle radiation therapy," *Clinical Cancer Research*, vol. 19, no. 3, pp. 530–537, 2013.

[21] J. Elgqvist, S. Frost, J.-P. Pouget, and P. Albertsson, "The potential and hurdles of targeted alpha therapy - clinical trials and beyond.," *Frontiers in oncology*, vol. 3, p. 324, 2014.

[22] U. Haberkorn, F. Giesel, A. Morgenstern, and C. Kratochwil, "The future of radioligand therapy: α, β, or Both?," *J. Nucl. Med.*, vol. 58, no. 7, pp. 1017–1018, 2017.

[23] C. Parker, S. Nilsson D Heinrich, S. I. Helle, J. M. O'Sullivan, S. D. Fosså, A. Chodacki, P. Wiechno, J. Logue, M. Seke, A. Widmark, D. C. Johannessen, P. Hoskin, D. Bottomley, N. D. James, A. Solberg, I. Syndikus, J. Kliment, S. Wedel, S. Boehmer, M. Dall'Oglio, L. Franzén, R. Coleman, N. J. Vogelzang, C. G. O'Bryan-Tear, K. Staudacher, J. Garcia-Vargas, M. Shan, S. Bruland, and O. Sartor, "Alpha emitter radium-223 and survival in metastatic prostate cancer," *N. Engl. J. Med.*, vol. 369, no. 3, pp. 213–223, 2013.

[24] O. Sartor, R. Coleman, S. Nilsson, D. Heinrich, S. I. Helle, J. M. O'Sullivan, S. D. Fosså, A. Chodacki, P. Wiechno, J. Logue, A. Widmark, D. C. Johannessen, P. Hoskin, N. D. James, A. Solberg, I. Syndikus, N. J. Vogelzang, C. G. O'Bryan-Tear, M. Shan, Ø. S. Bruland, and C. Parker, "Effect of radium-223 dichloride on symptomatic skeletal events in patients with castration-resistant prostate cancer and bone metastases: Results from a phase 3, double-blind, randomised trial," *Lancet Oncol.*, vol. 15, no. 7, pp. 738–746, 2014.

[25] C. Kratochwil, F. Bruchertseifer, F. L. Giesel, M. Weis, F. A. Verburg, F. Mottaghy, K. Kopka, C. Apostolidis, U. Haberkorn, and A. Morgenstern, "225Ac-PSMA-617 for PSMA-Targeted -Radiation Therapy of Metastatic Castration-Resistant Prostate Cancer," *Journal of Nuclear Medicine*, vol. 57, no. 12, pp. 1941–1944, 2016.

[26] D. Blöcher, "DNA double-Strand break repair determines the RBE of αparticles," *Int. J. Radiat. Biol.*, vol. 54, no. 5, pp. 761–771, 1988.

[27] J. P. Pouget, I. Navarro-Teulon, M. Bardies, N. Chouin, G. Cartron, A. Pelegrin, and D. Azria, "Clinical radioimmunotherapy-the role of radiobiology," *Nat. Rev. Clin. Oncol.*, vol. 8, no. 12, pp. 720–734, 2011.

[28] M. R. McDevitt, D. Ma, L. T. Lai, J. Simon, P. Borchardt, R. K. Frank, K. Wu, V. Pellegrini, M. J. Curcio, M. Miederer, N. H. Bander, and D. a. Scheinberg, "Tumor Therapy with Targeted Atomic Nanogenerators," *Science*, vol. 294, no. 5546, pp. 1537–1540, 2001.

[29] J. G. Jurcic and T. L. Rosenblat, "Targeted alpha-particle immunotherapy for acute myeloid leukemia.," in *2014 Am. Soc. Clin. Oncol. Educ. B.*, pp. e126–31, Alexandria, VA: American Society of Clinical Oncology, 2014.

[30] J. G. Jurcic, M. Levy, J. Park, F. Ravandi, A. Perl, J. Pagel, B. D. Smith, J. Orozco, E. Estey, H. Kantarjian, D. Scheinberg, L. Finn,

S. Khan, G. Hildebrandt, M. Craig, E. Atallah, I. Molina, D. Cicic, G. Bergonio, and M. Berger, "Trial in Progress: A Phase I/II Study of Lintuzumab-Ac225 in Older Patients with Untreated Acute Myeloid Leukemia," in *Clinical Lymphoma, Myeloma & Leukemia*, vol. 17, p. S277, 2017.

[31] C. Kratochwil, F. Bruchertseifer, H. Rathke, M. Hohenfellner, F. L. Giesel, U. Haberkorn, and A. Morgenstern, "Targeted α-Therapy of Metastatic Castration-Resistant Prostate Cancer with 225 Ac-PSMA-617: Swimmer-Plot Analysis Suggests Efficacy Regarding Duration of Tumor Control," *J. Nucl. Med.*, vol. 59, no. 5, pp. 795–802, 2018.

[32] M. Sathekge, F. Bruchertseifer, O. Knoesen, F. Reyneke, I. Lawal, T. Lengana, C. Davis, J. Mahapane, C. Corbett, M. Vorster, and A. Morgenstern, "225Ac-PSMA-617 in chemotherapy-naive patients with advanced prostate cancer: a pilot study," *Eur. J. Nucl. Med. Mol. Imaging*, pp. 129–138, 2019.

[33] J. W. Engle, "The production of Ac-225," *Curr. Radiopharm.*, vol. 11, no. 3, pp. 173–179, 2018.

[34] NSAC Isotopes Subcommittee, "Meeting Isotope Needs and Capturing Opportunities for the Future: The 2015 Long Range Plan for the DOE-NP Isotope Program," tech. rep., US Department of Energy, 2015.

[35] R. A. Aliev, S. V. Ermolaev, A. N. Vasiliev, V. S. Ostapenko, E. V. Lapshina, B. L. Zhuikov, N. V. Zakharov, V. V. Pozdeev, V. M. Kokhanyuk, B. F. Myasoedov, and S. N. Kalmykov, "Isolation of Medicine-Applicable Actinium-225 from Thorium Targets Irradiated by Medium-Energy Protons," *Solvent Extraction and Ion Exchange*, vol. 32, no. 5, pp. 468–477, 2014.

[36] C. Apostolidis, R. Molinet, G. Rasmussen, and A. Morgenstern, "Production of Ac-225 from Th-229 for targeted alpha therapy," *Anal. Chem.*, vol. 77, no. 19, pp. 6288–6291, 2005.

[37] R. A. Boll, D. Malkemus, and S. Mirzadeh, "Production of actinium-225 for alpha particle mediated radioimmunotherapy," *Appl. Radiat. Isot.*, vol. 62, no. 5, pp. 667–679, 2005.

[38] M. W. Geerlings, F. M. Kaspersen, C. Apostolidis, and R. van der Hout, "The feasibility of 225Ac as a source of alpha-particles in radioimmunotherapy," *Nucl. Med. Commun.*, vol. 14, pp. 121–125, 1993.

[39] R. Alvarez, "Managing the Uranium-233 Stockpile of the United States," *Sci. Glob. Secur.*, vol. 21, no. 1, pp. 53–69, 2013.

[40] A. A. Kotovskii, N. A. Nerozin, I. V. Prokofev, V. V. Shapovalov, Y. A. Yakovshchits, A. S. Bolonkin, and A. V. Dunin, "Isolation of actinium-225 for medical purposes," *Radiochemistry*, vol. 57, no. 3, pp. 285–291, 2015.

[41] W. C. Rontgen, "Uber eine neue Art von Strahlen," *Sitzungsberichte der physikalisch-medicinischen Gesellschaft zu Wurzburg*, vol. 30, pp. 132–141, 1895.

[42] J. Slater, "From X-Rays to Ion Beams: A Short History of Radiation Therapy," in *Ion Beam Therapy* (U. Linz, ed.), ch. 1, pp. 3–16, Springer, 2012.

[43] J. D. Watson and F. H. C. Crick, "Molecular Structure of Nucleic Acids: A Structure for Deoxyribose Nucleic Acid," *Nature*, vol. 171, no. 4356, pp. 737–738, 1953.

[44] F. Knapp and A. Dash, *Radiopharmaceuticals for Therapy*. New Dheli: Springer, 1 ed., 2016.

[45] E. B. Podgorsak, *Radiation Physics for Medical Physicists*. Springer, 1 ed., 2006.

[46] S. Hertz and A. Roberts, "Radioactive Iodine in the Study of Thyroid Physiology: VII. The Use of Radioactive Iodine Therapy in Hyperthyroidism," *Journal of the American Medical Association*, vol. 131, no. 2, pp. 81–86, 1946.

[47] S. M. Seidlin and I. Rossman, "Radioiodine therapy of metastases from carcinoma of the thyroid; a 6-year progress report.," *The Journal of clinical endocrinology and metabolism*, vol. 9, no. 11, 1949.

[48] V. Frantellizzi, L. Cosma, G. Brunotti, A. Pani, A. Spanu, S. Nuvoli, F. De Cristofaro, L. Civitelli, and G. De Vincentis, "Target Alpha Therapy with Thorium-227," *Cancer Biotherapy and Radiopharmaceuticals*, vol. 35, no. 2, 2020.

[49] A. Morgenstern, "Bismuth-213 and actinium-225 generator performance and evolving therapeutic applications of two generator-derived alpha-emitting radioisotopes," *Curr. Radiopharm.*, vol. 5, no. 3, pp. 221–227, 2012.

[50] C. Kratochwil, F. L. Giesel, F. Bruchertseifer, W. Mier, C. Apostolidis, R. Boll, K. Murphy, U. Haberkorn, and A. Morgenstern, "213Bi-DOTATOC receptor-targeted alpha-radionuclide therapy induces remission in neuroendocrine tumours refractory to beta radiation: a first-in-human experience.," *Eur. J. Nucl. Med. Mol. Imaging*, vol. 41, no. 11, pp. 2106–19, 2014.

[51] M. E. Autenrieth, C. Seidl, F. Bruchertseifer, T. Horn, F. Kurtz, B. Feuerecker, C. D'Alessandria, C. Pfob, S. Nekolla, C. Apostolidis, S. Mirzadeh, J. E. Gschwend, M. Schwaiger, K. Scheidhauer, and A. Morgenstern, "Treatment of carcinoma in situ of the urinary bladder with an alpha-emitter immunoconjugate targeting the epidermal growth factor receptor: a pilot study," *European Journal of Nuclear Medicine and Molecular Imaging*, vol. 45, no. 8, pp. 1364–1371, 2018.

[52] J. G. Jurcic, S. M. Larson, G. Sgouros, M. R. McDevitt, R. D. Finn, C. R. Divgi, A. M. Ballangrud, K. A. Hamacher, D. Ma, J. L. Humm, M. W. Brechbiel, R. Molinet, and D. A. Scheinberg, "Targeted alpha particle immunotherapy for myeloid leukemia.," *Blood*, vol. 100, no. 4, pp. 1233–9, 2002.

[53] T. L. Rosenblat, M. R. McDevitt, D. A. Mulford, N. Pandit-Taskar, C. R. Divgi, K. S. Panageas, M. L. Heaney, S. Chanel, A. Morgenstern, G. Sgouros, S. M. Larson, D. A. Scheinberg, and J. G. Jurcic, "Sequential cytarabine and α-particle immunotherapy with bismuth-213-lintuzumab (HuM195) for acute myeloid leukemia," *Clinical Cancer Research*, vol. 16, no. 21, pp. 5303–5311, 2010.

[54] S. Kneifel, D. Cordier, S. Good, M. C. Ionescu, A. Ghaffari, S. Hofer, M. Kretzschmar, M. Tolnay, C. Apostolidis, B. Waser, M. Arnold, J. Mueller-Brand, H. R. Maecke, J. C. Reubi, and A. Merlo, "Local targeting of malignant gliomas by the diffusible peptidic vector 1,4,7,10-tetraazacyclododecane-1-glutaric acid-4,7,10-triacetic acid-substance P," *Clinical Cancer Research*, vol. 12, no. 12, pp. 3843–3850, 2006.

[55] D. Cordier, F. Forrer, F. Bruchertseifer, A. Morgenstern, C. Apostolidis, S. Good, J. Müller-Brand, H. Mäcke, J. C. Reubi, and A. Merlo, "Targeted alpha-radionuclide therapy of functionally critically located gliomas with 213Bi-DOTA-[Thi8,Met(O2)11]-substance P: a pilot trial.," *Eur. J. Nucl. Med. Mol. Imaging*, vol. 37, no. 7, pp. 1335–44, 2010.

[56] B. J. Allen, C. Raja, S. Rizvi, Y. Li, W. Tsui, P. Graham, J. F. Thompson, R. A. Reisfeld, J. Kearsley, A. Morgenstern, and C. Apostolidis, "Intralesional targeted alpha therapy for metastatic melanoma," *Cancer Biology and Therapy*, vol. 4, no. 12, pp. 1318–1324, 2005.

[57] C. Raja, P. Graham, S. M. Abbas Rizvi, E. Song, H. Goldsmith, J. Thompson, A. Bosserhoff, A. Morgenstern, C. Apostolidis, J. Kearsley, R. Reisfeld, and B. J. Allen, "Interim analysis of toxicity and response in phase 1 trial of systemic targeted alpha therapy for metastatic melanoma," *Cancer Biology and Therapy*, vol. 6, no. 6, pp. 846–852, 2007.

[58] B. Allen, A. Singla, S. Rizvi, P. Graham, F. Bruchertseifer, C. Apostolidis, and A. Morgenstern, "Analysis of patient survival in a Phase I trial of systemic targeted α-therapy for metastatic melanoma," *Immunotherapy*, vol. 3, no. 9, pp. 1041–50, 2011.

[59] J. C. dos Santos, M. Schäfer, U. Bauder-Wüst, W. Lehnert, K. Leotta, A. Morgenstern, K. Kopka, U. Haberkorn, W. Mier, and C. Kratochwil, "Development and dosimetry of ^{203}Pb/^{212}Pb-labelled PSMA ligands: bringing "the lead" into PSMA-targeted alpha therapy?," *European Journal of Nuclear Medicine and Molecular Imaging*, 2018.

[60] R. F. Meredith, J. Torgue, M. T. Azure, S. Shen, S. Saddekni, E. Banaga, R. Carlise, P. Bunch, D. Yoder, and R. Alvarez, "Pharmacokinetics and Imaging of ^{212}Pb-TCMC-trastuzumab After Intraperitoneal Administration in Ovarian Cancer Patients," *Cancer Biotherapy & Radiopharmaceuticals*, vol. 29, no. 1, 2014.

[61] R. Meredith, J. Torgue, S. Shen, D. Fisher, E. Banaga, P. Bunch, D. Morgan, J. Fan, and J. M. Straughn, "Dose Escalation and Dosimetry of First-In-Human α-Radioimmunotherapy With ^{212}Pb-TCMC-trastuzumab," *Journal of nuclear medicine : official publication, Society of Nuclear Medicine*, vol. 55, no. 10, 2014.

[62] M. R. Zalutsky, D. A. Reardon, G. Akabani, R. E. Coleman, H. Friedman, H. S. Friedman, R. E. Mclendon, T. Z. Wong, and D. Bigner, "Clinical Experience with alpha-Particle-Emitting 211At: Treatment of Recurrent Brain Tumor Patients with 211At-Labeled Chimeric Antitenascin Monoclonal Anitbody 81C6," *Journal of Nuclear Medicine*, vol. 49, no. 1, pp. 30–38, 2008.

[63] H. Andersson, E. Cederkrantz, T. Back, C. Divgi, J. Elgqvist, J. Himmelman, G. Horvath, L. Jacobsson, H. Jensen, S. Lindegren, S. Palm, and R. Hultborn, "Intraperitoneal alpha-Particle Radioimmunotherapy of Ovarian cancer Patients: Pharmacokinetics and Dosimetry of ^{211}At-MX35 F(ab')2 - A Phase I Study," *Journal of Nuclear Medicine*, vol. 50, no. 7, pp. 1153–1160, 2009.

[64] E. Cederkrantz, H. Andersson, P. Bernhardt, T. Bäck, R. Hultborn, L. Jacobsson, H. Jensen, S. Lindegren, M. Ljungberg, T. Magnander, S. Palm, and P. Albertsson, "Absorbed Doses and Risk Estimates of 211At-MX35 F(ab')2 in Intraperitoneal Therapy of Ovarian Cancer Patients," *International Journal of Radiation Oncology Biology Physics*, vol. 93, no. 3, pp. 569–576, 2015.

[65] S. Lindegren, P. Albertsson, T. Bäck, H. Jensen, S. Palm, and E. Aneheim, "Realizing Clinical Trials with Astatine-211: The Chemistry Infrastructure," *Cancer Biotherapy and Radiopharmaceuticals*, vol. 35, no. 2, pp. 1–12, 2020.

[66] C. Kratochwil, F. Bruchertseifer, F. Giesel, C. Apostolidis, U. Haberkorn, and A. Morgenstern, "Ac-225-DOTATOC - dose finding for alpha particle emitter based radionuclide therapy of neuroendocrine tumors," in *The Journal of Nuclear Medicine*, vol. 56, p. 1232, 2015.

[67] J. Kunikowska and L. Królicki, "Targeted α-Emitter Therapy of Neuroendocrine Tumors," *Seminars in Nuclear Medicine*, vol. 50, no. 2, pp. 171–176, 2020.

[68] L. Krolicki, F. Bruchertseifer, J. Kunikowska, H. Koziara, B. Królicki, M. Jakuciński, D. Pawlak, C. Apostolidis, S. Mirzadeh, R. Rola, A. Merlo, and A. Morgenstern, "Prolonged survival in secondary glioblastoma following local injection of targeted alpha therapy with 213Bi-substance P analogue," *European Journal of Nuclear Medicine and Molecular Imaging*, pp. 1–9, 2018.

[69] L. Królicki, J. Kunikowska, F. Bruchertseifer, H. Koziara, B. Królicki, M. Jakuciński, D. Pawlak, R. Rola, A. Morgenstern, E. Rosiak, and A. Merlo, "225Ac- and 213Bi-Substance P Analogues for Glioma Therapy," *Seminars in Nuclear Medicine*, vol. 50, no. 2, pp. 141–151, 2020.

[70] J. G. Jurcic, F. Ravandi, J. M. Pagel, J. H. Park, B. D. Smith, M. Y. Levy, E. H. Estey, A. E. Perl, H. Kantarjian, D. Earle, D. Cicic, and D. A. Scheinberg, "Phase I Trial of Targeted Alpha-Particle Immunotherapy with Actinium-225 (^{225}Ac)-Lintuzumab (Anti-CD33) and Low-Dose Cytarabine (LDAC) in Older Patients with Untreated Acute Myeloid Leukemia (AML)," in *Blood*, vol. 126, pp. 3794–3794, 2015.

[71] J. G. Jurcic, M. Y. Levy, J. H. Park, F. Ravandi, A. E. Perl, J. M. Pagel, B. D. Smith, E. H. Estey, H. Kantarjian, D. Cicic, and D. A. Scheinberg, "Phase I Trial of Targeted Alpha-Particle Therapy with Actinium-225 (^{225}Ac)-Lintuzumab and Low-Dose Cytarabine (LDAC) in Patients Age 60 or Older with Untreated Acute Myeloid Leukemia (AML)," in *Blood*, vol. 128, pp. 4050–4050, 2016.

[72] E. Atallah, M. Berger, J. Jurcic, G. Roboz, W. Tse, R. Mawad, D. Rizzieri, K. Begna, J. Orozco, M. Craig, M. Yair Levy, L. Finn, K. Sharif, A. Perl, and J. Park, "A Phase 2 Study of Actinium-225 (225Ac)-lintuzumab in Older Patients with Untreated Acute Myeloid Leukemia (AML)," *Journal of Medical Imaging and Radiation Sciences*, vol. 50, no. 1, p. S37, 2019.

[73] J. G. Jurcic, "Targeted Alpha-Particle Therapy for Hematologic Malignancies," *Seminars in Nuclear Medicine*, vol. 50, no. 2, pp. 152–161, 2020.

[74] B. Feuerecker, K. Knorr, A. Beheshti, C. Seidl, C. D'Alessandria, F. Bruchertseifer, R. Tauber, M. Retz, W. Weber, A. Morgenstern, and M. Eiber, "Safety and Efficacy of Ac-225-PSMA-617 in mCRPC after Failure of Lu-177-PSMA," *Journal of Medical Imaging and Radiation Sciences*, vol. 50, no. 1, pp. S20–S21, 2019.

[75] M. M. Sathekge, F. Bruchertseifer, I. O. Lawal, M. Vorster, O. Knoesen, T. Lengana, T. G. Boshomane, K. K. Mokoala, and A. Morgenstern, "Treatment of brain metastases of castration-resistant prostate cancer with 225Ac-PSMA-617," *European Journal of Nuclear Medicine and Molecular Imaging*, vol. 46, no. 8, pp. 1756–1757, 2019.

[76] M. Sathekge, F. Bruchertseifer, M. Vorster, I. O. Lawal, O. Knoesen, J. Mahapane, C. Davis, F. Reyneke, A. Maes, C. Kratochwil, T. Lengana, F. L. Giesel, C. Van de Wiele, and A. Morgenstern, "Predictors of Overall and Disease-Free Survival in Metastatic Castration-

Resistant Prostate Cancer Patients Receiving ^{225}Ac-PSMA-617 Radioligand Therapy," *Journal of Nuclear Medicine*, vol. 61, no. 1, pp. 62–69, 2020.

[77] C. Kratochwil, U. Haberkorn, and F. L. Giesel, "225Ac-PSMA-617 for Therapy of Prostate Cancer," *Seminars in Nuclear Medicine*, vol. 50, no. 2, pp. 133–140, 2020.

[78] A. Morgenstern, C. Apostolidis, and F. Bruchertseifer, "Supply and Clinical Application of Actinium-225 and Bismuth-213," *Seminars in Nuclear Medicine*, vol. 50, no. 2, pp. 119–123, 2020.

[79] C. Bal, M. Yadav, S. Ballal, M. Tripathi, and R. Sahoo, "Clinical experience of ^{225}Ac-PSMA-617 targeted alpha therapy in metastatic castration resistant prostate cancer patients: safety and efficacy results," in *Journal of Nuclear Medicine*, vol. 60, pp. 462–462, 2019.

[80] F. Khreish, N. Ebert, M. Ries, S. Maus, F. Rosar, H. Bohnenberger, T. Stemler, M. Saar, M. Bartholomä, and S. Ezziddin, "^{225}Ac-PSMA-617/^{177}Lu-PSMA-617 tandem therapy of metastatic castration-resistant prostate cancer: pilot experience," *European Journal of Nuclear Medicine and Molecular Imaging*, vol. 47, no. 3, pp. 721–728, 2020.

[81] T. Langbein, H. Kulkarni, A. Singh, C. Schuchardt, J. Zhang, and R. Baum, "Combined PRLT using Ac-225 and Lu-177 labeled PSMA-617 (TANDEM-PRLT) in end-stage metastatic prostate cancer: a concept to reduce salivary gland toxicity?," in *Journal of Nuclear Medicine*, vol. 60, pp. 77–77, 2019.

[82] H. Kulkarni, J. Zhang, T. Langbein, C. Schuchardt, A. Singh, D. Mueller, and R. Baum, "Radioligand therapy using combination of Ac-225 and Lu-177 labelled PSMA ligands for progressive end-stage metastatic prostate cancer: effective trade-off between response and toxicity," in *Journal of Nuclear Medicine*, vol. 60, pp. 464–464, 2019.

[83] National Nuclear Data Center, "Decay Radiation Search." https://www.nndc.bnl.gov/nudat2/indx_dec.jsp.

[84] H. Bateman, "The solution of a system of differential equations occurring in the theory of radioactive transformations," *Proc. Cambridge Pholosophical Soc. Math. Phys. Sci.*, vol. 15, pp. 426–427, 1910.

[85] S. Pommé, M. Marouli, G. Suliman, H. Dikmen, R. Van Ammel, V. Jobbágy, A. Dirican, H. Stroh, J. Paepen, F. Bruchertseifer, C. Apostolidis, and A. Morgenstern, "Measurement of the 225Ac half-life," *Appl. Radiat. Isot.*, vol. 70, no. 11, pp. 2608–2614, 2012.

[86] A. C. English, T. E. Cranshaw, J. A. Demers, J. A. Harvey, E. P. Hincks, J. V. Jelley, and A. N. May, "The (4n + 1) Radioactive Series," *Phys. Rev.*, vol. 72, pp. 253–254, 1947.

[87] F. Hagemann, L. I. Katzin, M. H. Studier, G. T. Seaborg, and A. Ghiorso, "The 4n + 1 radioactive series: The decay products of U233," *Phys. Rev.*, vol. 79, no. 3, pp. 435–443, 1950.

[88] R. Bonetti, C. Chiesa, A. Guglielmetti, R. Matheoud, C. Migliorino, A. L. Pasinetti, and H. L. Ravn, "Nuclear structure effects in the exotic decay of ^{225}Ac via ^{14}C emission," *Nucl. Physics, Sect. A*, vol. 562, no. 1, pp. 32–40, 1993.

[89] A. Guglielmetti, R. Bonetti, G. Ardisson, V. Barci, T. Giles, M. Hussonnois, J. F. Le Du, C. Le Naour, V. L. Mikheev, A. L. Pasinetti, H. L. Ravn, S. P. Tretyakova, and D. Trubert, "New measurement of exotic decay of ^{225}Ac by ^{14}C emission," *Eur. Phys. J. A*, vol. 386, pp. 383–386, 2001.

[90] A. K. Jain, S. Singh, S. Kumar, and J. K. Tuli, "Nuclear Data Sheets for A = 221," *Nucl. Data Sheets*, vol. 108, no. 4, pp. 883–922, 2007.

[91] F. G. Kondev, E. A. McCutchan, B. Singh, K. Banerjee, S. Bhattacharya, A. Chakraborty, S. Garg, N. Jovancevic, S. Kumar, S. K. Rathi, T. Roy, J. Lee, and R. Shearman, "Nuclear Data Sheets for A=217," *Nucl. Data Sheets*, vol. 147, pp. 382–458, 2018.

[92] G. Suliman, S. Pommé, M. Marouli, R. Van Ammel, H. Stroh, V. Jobbágy, J. Paepen, A. Dirican, F. Bruchertseifer, C. Apostolidis, and A. Morgenstern, "Half-lives of 221Fr, 217At, 213Bi, 213Po and 209Pb from the 225Ac decay series," *Appl. Radiat. Isot.*, vol. 77, pp. 32–37, 2013.

[93] H. B. Jeppesen, J. Byskov-Nielsen, P. Wright, J. G. Correia, L. M. Fraile, H. O. Fynbo, K. Johnston, and K. Riisager, "Alpha-decay half-life of 221Fr in different environments," *Eur. Phys. J. A*, vol. 32, no. 1, pp. 31–34, 2007.

[94] M. S. Basunia, "Nuclear Data Sheets for A = 213," *Nucl. Data Sheets*, vol. 108, no. 3, pp. 633–680, 2007.

[95] J. Chen and F. G. Kondev, "Nuclear Data Sheets for A = 209," *Nucl. Data Sheets*, vol. 126, pp. 373–546, 2015.

[96] M. Marouli, G. Suliman, S. Pommé, R. V. Ammel, V. Jobbágy, H. Stroh, H. Dikmen, J. Paepen, A. Dirican, F. Bruchertseifer, C. Apostolidis, and A. Morgenstern, "Decay data measurements on 213Bi using recoil atoms," *Appl. Radiat. Isot.*, vol. 74, pp. 123–127, 2013.

[97] A. K. Jain, R. Raut, and J. K. Tuli, "Nuclear Data Sheets for A = 225," *Nucl. Data Sheets*, vol. 110, no. 6, pp. 1409–1472, 2009.

[98] C. F. Liang, P. Paris, and R. K. Sheline, "α decay of 225Ra," *Phys. Rev. C*, vol. 62, no. 4, pp. 473031–473033, 2000.

[99] H. W. Kirby and M. L. Salutsky, "The Radiochemistry of Radium," *NAS-NRC Nucl. Sci. Ser.*, 1964.

[100] R. de Kruijff, H. Wolterbeek, and A. Denkova, "A Critical Review of Alpha Radionuclide Therapy: How to Deal with Recoiling Daughters?," *Pharmaceuticals*, vol. 8, no. 2, pp. 321–336, 2015.

[101] NorthStar Medical Radioisotopes, "Production of Actinium-225 via high Energy proton Induced Spallation of Thorium-232," tech. rep., NorthStar Medical Radioisotopes, 2011.

[102] R. Perron, D. Gendron, and P. W. Causey, "Construction of a thorium/actinium generator at the Canadian Nuclear Laboratories," *Applied Radiation and Isotopes*, vol. 164, no. March, p. 109262, 2020.

[103] B. L. Zhuikov, "Successes and problems in the development of medical radioisotope production in Russia," *Physics-Uspekhi*, vol. 59, no. 5, pp. 481–486, 2016.

[104] V. Radchenko, J. W. Engle, J. J. Wilson, J. R. Maassen, F. M. Nortier, W. A. Taylor, E. R. Birnbaum, L. A. Hudston, K. D. John, and M. E. Fassbender, "Application of ion exchange and extraction chromatography to the separation of actinium from proton-irradiated thorium metal for analytical purposes.," *J. Chromatogr. A*, vol. 1380, pp. 55–63, 2015.

[105] International Atomic Energy Agency, "Technicial Meeting on Alpha emitting radionuclides and radiopharmaceuticals for therapy," tech. rep., International Atomic Energy Agency, Vienna, 2013.

[106] J. Dilling, R. Kruecken, and L. Merminga, eds., *ISAC and ARIEL: The TRIUMF Radioactive Beam Facilities and the Scientific Program.* Dordrecht: Springer, 2014.

[107] R. Laxdal, A. Morton, and P. Schaffer, "Radioactive Ion Beams and Radiopharmaceuticals," *Rev. Accel. Sci. Technol.*, vol. 6, pp. 37–57, 2013.

[108] J. F. Ziegler, M. Ziegler, and J. Biersack, "SRIM: The stopping and range of ions in matter (2010)," *Nucl. Instruments Methods Phys. Res. Sect. B Beam Interact. with Mater. Atoms*, vol. 268, no. 11, pp. 1818–1823, 2010.

[109] R. dos Santos Augusto, L. Buehler, Z. Lawson, S. Marzari, M. Stachura, and T. Stora, "CERN-MEDICIS (Medical Isotopes Collected from ISOLDE): A New Facility," *Appl. Sci.*, vol. 4, no. 2, pp. 265–281, 2014.

[110] F. H. Garcia, "Calculation of rates for radioactive isotope beam production at TRIUMF," Master's thesis, Simon Fraser University, 2016.

[111] C. W. Forsberg and L. C. Lewis, "Uses For Uranium-233 : What Should Be Kept for Future Needs?," Tech. Rep. 208, Oak Ridge National Lab, Oak Ridge, TN, 1999.

[112] E. Rutherford, "Collision of α particles with light atoms . IV. An anomalous effect in nitrogen," *The London, Edinburgh, and Dublin Philosophical Magazine and Journal of Science*, vol. 37, no. 222, pp. 581–587, 1919.

[113] H. P. Schieck, *Nuclear Reactions: An Introduction.* Heidelberg: Springer, 2014.

[114] J. Konya and N. M. Nagy, "Nuclear Reactions," in *Nucl. Radiochem.*, vol. 2, Elsevier, 2012.

[115] W. D. Loveland, D. J. Morrissey, and G. T. Seaborg, *Modern Nuclear Chemistry*, vol. 69. Hoboken, NJ: Wiley, 2 ed., 2017.

[116] D. Filges and F. Goldenbaum, *Hanbook of Spallation Research*. Weinheim, Germany: Wiley, 2009.

[117] I. A. E. Agency, "IAEA-TECDOC-1340: Manual for reactor produced radioisotopes," tech. rep., International Atomic Energy Agency, Vienna, 2003.

[118] M. Chadwick, M. Herman, P. Obložinský, M. Dunn, Y. Danon, A. Kahler, D. Smith, B. Pritychenko, G. Arbanas, R. Arcilla, R. Brewer, D. Brown, R. Capote, A. Carlson, Y. Cho, H. Derrien, K. Guber, G. Hale, S. Hoblit, S. Holloway, T. Johnson, T. Kawano, B. Kiedrowski, H. Kim, S. Kunieda, N. Larson, L. Leal, J. Lestone, R. Little, E. McCutchan, R. MacFarlane, M. MacInnes, C. Mattoon, R. McKnight, S. Mughabghab, G. Nobre, G. Palmiotti, A. Palumbo, M. Pigni, V. Pronyaev, R. Sayer, A. Sonzogni, N. Summers, P. Talou, I. Thompson, A. Trkov, R. Vogt, S. van der Marck, A. Wallner, M. White, D. Wiarda, and P. Young, "ENDF/B-VII.1 Nuclear Data for Science and Technology: Cross Sections, Covariances, Fission Product Yields and Decay Data," *Nucl. Data Sheets*, vol. 112, no. 12, pp. 2887–2996, 2011.

[119] W. M. Stacey, *Nuclear Reactor Physics*. Weinheim, Germany: Wiley-VCH, 2nd ed., 2007.

[120] S. Hogle, R. A. Boll, K. Murphy, D. Denton, A. Owens, T. J. Haverlock, M. Garland, and S. Mirzadeh, "Reactor production of Thorium-229," *Appl. Radiat. Isot.*, vol. 114, pp. 19–27, 2016.

[121] R. A. Kuznetsov, P. S. Butkalyuk, V. A. Tarasov, A. Y. Baranov, I. L. Butkalyuk, E. G. Romanov, V. N. Kupriyanov, and E. V. Kazakova, "Yields of activation products in ^{226}Ra irradiation in the high-flux SM reactor," *Radiochemistry*, vol. 54, no. 4, pp. 383–387, 2012.

[122] G. Melville, H. Meriarty, P. Metcalfe, T. Knittel, and B. J. Allen, "Production of Ac-225 for cancer therapy by photon-induced transmutation of Ra-226," *Appl. Radiat. Isot.*, vol. 65, no. 9, pp. 1014–1022, 2007.

[123] P. D. Vansant, "Medical Isotope Production of Actinium-225 By Linear Accelerator Photon Irradiation of Radium-226," Master's thesis, Virginia Polytechnic Institute and State University, 2013.

[124] G. Melville and B. J Allen, "Cyclotron and linac production of Ac-225," *Appl. Radiat. Isot.*, vol. 67, no. 4, pp. 549–555, 2009.

[125] J. Lesrel, J. Arianer, M. Arianer, O. Bajeat, J.-m. Buhour, H. Bzyl, F. Carrey, M. Chabot, T. Corbin, H. Croizet, J. Curaudeau, F. Doizon, M. Ducourtieu, J.-m. Dufour, D. Grialou, C. Joly, M. Kaminski, H. Lefort, B. Lesellier, G. Magneney, L. Mottet, C. Planat, M. Raynaud, Y. Richard, A. Said, A. Semsoum, F. Taquin, C. Vogel, G. Bienvenu, J.-n. Cayla, and M. D. Lal, "Commissioning of the Alto 50 Mev Electron Linac," in *Proc. EPAC 2006*, (Edinburgh, Scotland), pp. 3–5, 2006.

[126] C. Apostolidis, R. Molinet, J. McGinley, K. Abbas, J. Möllenbeck, and A. Morgenstern, "Cyclotron production of Ac-225 for targeted alpha therapy.," *Appl. Radiat. Isot.*, vol. 62, no. 3, pp. 383–7, 2005.

[127] P. Schaffer, F. Bénard, A. Bernstein, K. Buckley, A. Celler, N. Cockburn, J. Corsaut, M. Dodd, C. Economou, T. Eriksson, M. Frontera, V. Hanemaayer, B. Hook, J. Klug, M. Kovacs, F. Prato, S. McDiarmid, T. Ruth, C. Shanks, J. Valliant, S. Zeisler, U. Zetterberg, and P. Zavodszky, "Direct Production of 99mTc via 100Mo(p,2n) on Small Medical Cyclotrons," *Phys. Procedia*, vol. 66, pp. 383–395, 2015.

[128] A. Ferrari, P. R. Sala, A. Fasso, and J. Ranft, "FLUKA: a multi-particle transport code," tech. rep., CERN, Geneva, 2005.

[129] T. Böhlen, F. Cerutti, M. Chin, A. Fassò, A. Ferrari, P. Ortega, A. Mairani, P. Sala, G. Smirnov, and V. Vlachoudis, "The FLUKA Code: Developments and Challenges for High Energy and Medical Applications," *Nucl. Data Sheets*, vol. 120, pp. 211–214, 2014.

[130] International Atomic Energy Agency, "Evaluated Nuclear Data File (ENDF)." https://www-nds.iaea.org/exfor/endf.htm.

[131] C. U. Jost, J. R. Griswold, S. H. Bruffey, S. Mirzadeh, D. W. Stracener, and C. L. Williams, "Measurement of cross sections for the 232Th(P,4n) 229Pa reaction at low proton energies," *AIP Conf. Proc.*, vol. 1525, pp. 520–524, 2013.

[132] IAEA, "IAEA-TECDOC-620: Nature and magnitude of the problem of spent radiation sources," tech. rep., IAEA, Vienna, 1991.

[133] IAEA, "IAEA-TECDOC-886: Conditioning and interim storage of spent radium sources IAEA-TECDOC-886," tech. rep., International Atomic Energy Agency, Vienna, 1996.

[134] M. Englert, L. Krall, and R. C. Ewing, "Is nuclear fission a sustainable source of energy?," *MRS Bull.*, vol. 37, no. 04, pp. 417–424, 2012.

[135] J. W. Engle, S. G. Mashnik, J. W. Weidner, L. E. Wolfsberg, M. E. Fassbender, K. Jackman, A. Couture, L. J. Bitteker, J. L. Ullmann, M. S. Gulley, C. Pillai, K. D. John, E. R. Birnbaum, and F. M. Nortier, "Cross sections from proton irradiation of thorium at 800 MeV," *Phys. Rev. C - Nucl. Phys.*, vol. 88, no. 1, 2013.

[136] S. V. Ermolaev, B. L. Zhuikov, V. M. Kokhanyuk, V. L. Matushko, S. N. Kalmykov, R. A. Aliev, I. G. Tananaev, and B. F. Myasoedov, "Production of actinium, thorium and radium isotopes from natural thorium irradiated with protons up to 141 MeV," *Radiochim. Acta*, vol. 100, no. 4, pp. 223–229, 2012.

[137] D. V. Filosofov, A. V. Rakhimov, G. A. Bozhikov, D. V. Karaivanov, N. A. Lebedev, Y. V. Norseev, and I. I. Sadikov, "Isolation of radionuclides from thorium targets irradiated with 300-MeV protons," *Radiochemistry*, vol. 55, no. 4, pp. 410–417, 2013.

[138] J. Griswold, D. Medvedev, J. Engle, R. Copping, J. Fitzsimmons, V. Radchenko, J. Cooley, M. Fassbender, D. Denton, K. Murphy, A. Owens, E. Birnbaum, K. John, F. Nortier, D. Stracener, L. Heilbronn, L. Mausner, and S. Mirzadeh, "Large scale accelerator production of ^{225}Ac: Effective cross sections for 78-192 MeV protons incident on ^{232}Th targets," *Appl. Radiat. Isot.*, vol. 118, no. September, pp. 366–374, 2016.

[139] J. W. Weidner, S. G. Mashnik, K. D. John, B. Ballard, E. R. Birnbaum, L. J. Bitteker, A. Couture, M. E. Fassbender, G. S. Goff, R. Gritzo, F. M. Hemez, W. Runde, J. L. Ullmann, L. E. Wolfsberg, and F. M. Nortier, "^{225}Ac and ^{223}Ra production via 800 MeV proton irradiation of natural thorium targets," *Appl. Radiat. Isot.*, vol. 70, no. 11, pp. 2590–5, 2012.

[140] J. W. Weidner, S. G. Mashnik, K. D. John, F. Hemez, B. Ballard, H. Bach, E. R. Birnbaum, L. J. Bitteker, A. Couture, D. Dry, M. E. Fassbender, M. S. Gulley, K. R. Jackman, J. L. Ullmann, L. E. Wolfsberg, and F. M. Nortier, "Proton-induced cross sections relevant to production of ^{225}Ac and ^{223}Ra in natural thorium targets below 200 MeV," *Appl. Radiat. Isot.*, vol. 70, no. 11, pp. 2602–7, 2012.

[141] B. L. Zhuikov, S. N. Kalmykov, S. V. Ermolaev, R. A. Aliev, V. M. Kokhanyuk, V. L. Matushko, I. G. Taranaev, and B. F. Myasoedov, "Production of 225Ac and 223 Ra by irradiation of Th with accelerated protons," *Radiokhimiya*, vol. 53, no. 1, pp. 73–80, 2011.

[142] J. R. Griswold, *Actinium-225 Production via Proton Irradiation of Thorium-232*. PhD thesis, Univeristy of Tennessee, Knoxville, 2016.

[143] R. A. Aliev, S. V. Ermolaev, A. N. Vasiliev, V. S. Ostapenko, E. V. Lapshina, B. L. Zhuikov, N. V. Zakharov, V. V. Pozdeev, V. M. Kokhanyuk, B. F. Myasoedov, and S. N. Kalmykov, "Isolation of Medicine-Applicable Actinium-225 from Thorium Targets Irradiated by Medium-Energy Protons," *Solvent Extr. Ion Exch.*, vol. 32, no. 5, pp. 468–477, 2014.

[144] National Nuclear Data Center, "Experimental Nuclear Reaction Data (EXFOR)." https://www.nndc.bnl.gov/exfor/exfor.htm.

[145] Canberra Industries, *Genie 2000 Customization Tools Manual v3.4*. Meriden, CT: Canberra Industries, 2013.

[146] Canberra Industries, *Genie 2000 Coincidence Summing Library*. Meriden, CT: Canberra Industries, 2008.

[147] Canberra Industries, *Genie 2000 Operations Manual v3.4*. Meriden, CT: Canberra Industries, 2013.

[148] W. Russ, R. Venkataraman, and F. Bronson, "Validation testing of the genie 2000 Cascade Summing Correction," *J. Radioanal. Nucl. Chem.*, vol. 264, no. 1, pp. 193–197, 2005.

[149] H. Zhu, K. Morris, W. Mueller, M. Field, R. Venkataraman, J. Lamontagne, F. Bronson, and A. Berlizov, "Validation of true coincidence summing correction in Genie 2000 V3.2," *J. Radioanal. Nucl. Chem.*, vol. 282, no. 1, pp. 205–209, 2009.

[150] M. Felcini and A. Ferrari, "Validation of FLUKA calculated cross-sections for radioisotope production in proton-on-target collisions at proton energies around 1 GeV," tech. rep., CERN, 2006.

[151] G. Battistoni, F. Broggi, M. Brugger, M. Campanella, M. Carboni, A. Empl, A. Fassò, E. Gadioli, F. Cerutti, A. Ferrari, A. Ferrari, S. Muraro, K. Parodi, V. Patera, M. Pelliccioni, L. Pinsky,

J. Ranft, S. Roesler, P. R. Sala, M. Santana, L. Sarchiapone, M. Sioli, G. Smirnov, F. Sommerer, C. Theis, S. Trovati, R. Villari, H. Vincke, H. Vincke, V. Vlachoudis, J. Vollaire, and N. Zapp, "The Application of the Monte Carlo Code FLUKA in Radiation Protection Studies for the Large Hadron Collider," *Nucl. Sci. Technol.*, vol. 2, pp. 358–364, 2011.

[152] F. Cerutti, A. Empl, A. Fedynitch, A. Ferrari, R. G. Alia, P. R. Sala, G. Smirnov, and V. Vlachoudis, "Nuclear model developments in FLUKA for present and future applications," in *EPJ Web Conf. - ND106*, vol. 146, 2017.

[153] E. Iliopoulou, P. Bamidis, M. Brugger, and R. Froeschl, "Measurements and FLUKA Simulations of Bismuth , Aluminium and Indium Activation at the upgraded CERN Shielding Benchmark Facility," in *IOP Conf. Ser. J. Phys. - ARIA*, vol. 1046, pp. 1–14, 2018.

[154] M. Brugger, H. Khater, S. Mayer, A. Prinz, S. Roesler, L. Ulrici, H. Vincke, and M. Park, "Benchmark Studies of Induced Radioactivity Produced in LHC Materials, Part I: Specific Activities," *Radiat. Prot. Dosimetry*, vol. 116, no. 1, pp. 6–11, 2005.

[155] M. Brugger, H. Khater, S. Mayer, A. Prinz, S. Roesler, L. Ulrici, and H. Vincke, "Benchmark Studies of Induced Radioactivity Produced in LHC Materials, Part II: Remanent Dose Rates," *Radiat. Prot. Dosimetry*, vol. 116, no. 1, pp. 12–15, 2005.

[156] M. Brugger, A. Ferrari, S. Ã. Roesler, and L. Ulrici, "Validation of the FLUKA Monte Carlo code for predicting induced radioactivity at high-energy accelerators," *Nucl. Instruments methods Phys. Res. A*, vol. 562, pp. 814–818, 2006.

[157] M. Brugger, A. Ferrari, I. Istituto, and F. Nucleare, "Calculation of radionuclide production cross sections with FLUKA and their application in high energy hadron collider studies," in *Int. Conf. Nucl. Data Sci. Technol.*, 2007.

[158] A. Ferrari, D. Kiselev, T. Koi, M. Wohlmuther, and J.-C. Davide, "Po-production in lead: A benchmark between Geant4, FLUKA and MCNPX," *arXiv*, 2018.

[159] A. Infantino, E. Oehlke, D. Mostacci, P. Schaffer, M. Trinczek, and C. Hoehr, "Nuclear Instruments and Methods in Physics Research B

Assessment of the production of medical isotopes using the Monte Carlo code FLUKA : Simulations against experimental measurements," *Nucl. INSTRUMENTS METHODS Phys.*, vol. 366, pp. 117–123, 2016.

[160] V. Radchenko, T. Mastren, C. A. L. Meyer, A. S. Ivanov, V. S. Bryantsev, R. Copping, D. Denton, J. W. Engle, J. R. Griswold, K. Murphy, J. J. Wilson, A. Owens, L. Wyant, E. R. Birnbaum, J. Fitzsimmons, D. Medvedev, C. S. Cutler, L. F. Mausner, M. F. Nortier, K. D. John, S. Mirzadeh, and M. E. Fassbender, "Radiometric evaluation of diglycolamide resins for the chromatographic separation of actinium from fission product lanthanides," *Talanta*, vol. 175, pp. 318–324, 2017.

[161] N. N. Mirashi, S. Chaudhury, and S. K. Aggarwal, "Dissolution of sintered thorium dioxide in phosphoric acid using autoclave and microwave methods with detection by gamma spectrometry," *Microchem. J.*, vol. 94, no. 1, pp. 24–27, 2010.

[162] N. A. Thiele, V. Brown, J. M. Kelly, A. Amor-Coarasa, U. Jermilova, S. N. MacMillan, A. Nikolopoulou, S. Ponnala, C. F. Ramogida, A. K. H. Robertson, C. Rodríguez-Rodríguez, P. Schaffer, C. Williams Jr., J. W. Babich, V. Radchenko, and J. J. Wilson, "An Eighteen-Membered Macrocyclic Ligand for Actinium-225 Targeted Alpha Therapy," *Angew. Chemie*, vol. 56, no. 46, 2017.

[163] P. Comba, U. Jermilova, C. Orvig, B. O. Patrick, C. F. Ramogida, K. Rück, C. Schneider, and M. Starke, "Octadentate picolinic acid-based bispidine ligand for radiometal ions," *Chemistry - A European Journal*, 2017.

[164] P. Kunz, C. Andreoiu, J. R. Crawford, J. Even, F. H. Garcia, L. Lambert, J. Lassen, V. Radchenko, C. F. Ramogida, A. K. H. Robertson, T. J. Ruth, and P. Schaffer, "Medical isotopes from ISAC actinide targets," *Prog. Nucl. Sci. Technol.*, vol. 5, pp. 4–7, 2018.

[165] P. Kunz, C. Andreoui, V. Brown, M. Vervantes, J. Even, F. H. Garcia, A. Gottberg, J. Lassen, V. Radchenko, C. F. Ramogida, A. K. H. Robertson, P. Schaffer, and R. Sothilingam, "Medical isotope colletion from ISAC targets," *EPJ Web Conf.*, vol. 229, no. 06003, pp. 1–5, 2020.

[166] J. R. Crawford, H. Yang, P. Kunz, S. Wilbur, P. Schaf-Fer, T. J. Ruth, C. Jason, Y. Hua, K. Peter, S. Paul, R. Thomas, D. S. Wilbur,

and P. Schaffer, "Development of a preclinical At generator system for targeted alpha therapy research with ^{211}At," *Nucl. Med. Biol.*, vol. 48, pp. 31–35, 2017.

[167] J. R. Crawford, P. Kunz, H. Yang, P. Schaffer, and T. J. Ruth, "^{211}Rn/^{211}At and ^{209}At production with intense mass separated Fr ion beams for preclinical ^{211}At-based α-therapy research," *Appl. Radiat. Isot.*, vol. 122, pp. 222–228, 2017.

[168] B. Zielinska, C. Apostolidis, F. Bruchertseifer, and A. Morgenstern, "An Improved Method for the Production of Ac-225/Bi-213 from Th-229 for Targeted Alpha Therapy," *Solvent Extraction and Ion Exchange*, vol. 25, no. 3, pp. 339–349, 2007.

[169] E. P. Horwitz, D. R. McAlister, A. H. Bond, and R. E. Barrans, "Novel Extraction of Chromatographic Resins Based on Tetralkyldiglycolamides: Characterization and Potential Applications," *Solvent Extr. Ion Exch.*, vol. 23, pp. 319–344, 2005.

[170] E. T. Clarke and A. E. Martell, "Stabilities of trivalent metal ion complexes of the tetraacetate derivatives of 12-, 13- and 14-membered tetraazamacrocycles," *Inorganica Chimica Acta*, vol. 190, no. 1, pp. 37–46, 1991.

[171] Y. Kim and M. W. Brechbiel, "An overview of targeted alpha therapy," *Tumour Biol.*, vol. 33, no. 3, pp. 573–90, 2012.

[172] M. Miederer, D. A. Scheinberg, and M. R. McDevitt, "Realizing the potential of the Actinium-225 radionuclide generator in targeted alpha particle therapy applications.," *Adv. Drug Deliv. Rev.*, vol. 60, no. 12, pp. 1371–82, 2008.

[173] J. Woodward, S. J. Kennel, A. Stuckey, D. Osborne, J. Wall, A. J. Rondinone, R. F. Standaert, and S. Mirzadeh, "LaPO4 nanoparticles doped with actinium-225 that partially sequester daughter radionuclides.," *Bioconjug. Chem.*, vol. 22, no. 4, pp. 766–76, 2011.

[174] S. Sofou, B. J. Kappel, J. S. Jaggi, M. R. McDevitt, D. A. Scheinberg, and G. Sgouros, "Enhanced retention of the alpha-particle-emitting daughters of Actinium-225 by liposome carriers.," *Bioconjug. Chem.*, vol. 18, no. 6, pp. 2061–7, 2015.

[175] S. Sofou, J. L. Thomas, H.-y. Lin, M. R. McDevitt, D. A. Scheinberg, and G. Sgouros, "Engineered liposomes for potential alpha-particle therapy of metastatic cancer.," *J. Nucl. Med.*, vol. 45, no. 2, pp. 253–60, 2004.

[176] M. F. McLaughlin, J. Woodward, R. a. Boll, J. S. Wall, A. J. Rondinone, S. J. Kennel, S. Mirzadeh, and J. D. Robertson, "Gold Coated Lanthanide Phosphate Nanoparticles for Targeted Alpha Generator Radiotherapy," *PLoS ONE*, vol. 8, no. 1, pp. 2–9, 2013.

[177] J. S. Jaggi, S. V. Seshan, M. R. McDevitt, K. LaPerle, G. Sgouros, and D. A. Scheinberg, "Renal tubulointerstitial changes after internal irradiation with alpha-particle-emitting actinium daughters.," *J. Am. Soc. Nephrol.*, vol. 16, no. 9, pp. 2677–89, 2005.

[178] M. Miederer, M. R. McDevitt, G. Sgouros, K. Kramer, N.-K. V. Cheung, and D. A. Scheinberg, "Pharmacokinetics, dosimetry, and toxicity of the targetable atomic generator, ^{225}Ac-HuM195, in nonhuman primates.," *J. Nucl. Med.*, vol. 45, no. 1, pp. 129–37, 2004.

[179] J. de Swart, H. S. Chan, M. C. Goorden, A. Morgenstern, F. Bruchertseifer, F. J. Beekman, M. de Jong, and M. W. Konijnenberg, "Utilizing High-Energy γ-Photons for High-Resolution ^{213}Bi SPECT in Mice.," *J. Nucl. Med.*, vol. 57, no. 3, pp. 486–92, 2016.

[180] T. Back and L. Jacobsson, "The Alpha-Camera: A Quantitative Digital Autoradiography Technique Using a Charge-Coupled Device for Ex Vivo High-Resolution Bioimaging of Alpha-Particles," *J. Nucl. Med.*, vol. 51, no. 10, pp. 1616–1623, 2010.

[181] D. N. Pandya, R. Hantgan, M. M. Budzevich, N. D. Kock, D. L. Morse, I. Batista, A. Mintz, K. C. Li, and T. J. Wadas, "Preliminary therapy evaluation of 225Ac-DOTA-c (RGDyK) demonstrates that Cerenkov radiation derived from 225Ac daughter decay can be detected by optical imaging for in vivo tumor visualization," *Theranostics*, vol. 6, no. 5, pp. 698–709, 2016.

[182] M. C. Goorden, F. van der Have, R. Kreuger, R. M. Ramakers, B. Vastenhouw, J. P. H. Burbach, J. Booij, C. F. M. Molthoff, and F. J. Beekman, "VECTor: A Preclinical Imaging System for Simultaneous Submillimeter SPECT and PET," *J. Nucl. Med.*, vol. 54, no. 2, pp. 306–312, 2012.

[183] O. Ivashchenko, F. van der Have, M. C. Goorden, R. M. Ramakers, and F. J. Beekman, "Ultra-High-Sensitivity Submillimeter Mouse SPECT," *J. Nucl. Med.*, vol. 56, no. 3, pp. 470–475, 2015.

[184] K. Miwa, M. Inubushi, Y. Takeuchi, T. Katafuchi, M. Koizumi, T. Saga, and M. Sasaki, "Performance characteristics of a novel clustered multi-pinhole technology for simultaneous high-resolution SPECT/PET.," *Ann. Nucl. Med.*, pp. 460–466, 2015.

[185] W. Branderhorst, B. Vastenhouw, and F. J. Beekman, "Pixel-based subsets for rapid multi-pinhole SPECT reconstruction.," *Phys. Med. Biol.*, vol. 55, no. 7, pp. 2023–34, 2010.

[186] A. A. Harteveld, A. P. W. Meeuwis, J. A. Disselhorst, C. H. Slump, W. J. G. Oyen, O. C. Boerman, and E. P. Visser, "Using the NEMA NU 4 PET image quality phantom in multipinhole small-animal SPECT.," *J. Nucl. Med.*, vol. 52, no. 10, pp. 1646–53, 2011.

[187] National Electrical Manufacturers Association, *NEMA Standards Publication NU 2-2007: Performance Measurements of Positron Emission Tomographs*. Rosslyn, VA: National Electrical Manufacturers Association, 2007.

[188] S. Tong, A. M. Alessio, and P. E. Kinahan, "Noise and signal properties in PSF-based fully 3D PET image reconstruction: an experimental evaluation," *Phys. Med. Biol.*, vol. 55, no. 5, p. 1453, 2010.

[189] M. D. Walker, M. C. Goorden, K. Dinelle, R. M. Ramakers, S. Blinder, M. Shirmohammad, F. van der Have, F. J. Beekman, and V. Sossi, "Performance Assessment of a Preclinical PET Scanner with Pinhole Collimation by Comparison to a Coincidence-Based Small-Animal PET Scanner.," *J. Nucl. Med.*, vol. 55, no. 8, pp. 1368–1374, 2014.

[190] D. L. Snyder, M. I. Miller, L. J. Thomas, and D. G. Politte, "Noise and Edge Artifacts in Maximum-Likelihood Reconstructions for Emission Tomography," *IEEE Trans. Med. Imaging*, vol. 6, no. 3, pp. 228–238, 1987.

[191] J. J. Burgerjon, B. D. Pate, R. E. Blaby, E. G. Page, J. Lenz, and B. T. Trevitt, "The TRIUMF 500 MeV, 100 uA Isotope Production Facility," in *Proc. 27th Conf. Remote Syst. Technol.*, (San Francisco), 1979.

[192] I. Bylinskii and M. K. Craddock, "The TRIUMF 500 MeV cyclotron: The driver accelerator," *Hyperfine Interact.*, vol. 225, no. 1-3, pp. 9–16, 2013.

[193] E. W. Blackmore, P. E. Dodd, and M. R. Shaneyfelt, "Improved capabilities for proton and neutron irradiations at TRIUMF," *IEEE Radiation Effects Data Workshop*, pp. 149–155, 2003.

[194] E. K. Hyde, *The Radiochemistry of Thorium*, vol. NAS-NS 300. Berkeley, California: Subcommittee on Radiochemistry, National Academy of Sciences–National Research Council, 1960.

[195] Knovel, "Knovel Engineering Technical Reference Information Database." https://app.knovel.com/web/.

[196] ASMI, *Properties and selection: Nonferrous alloys and special-purpose materials*, vol. 2. ASM International, 1991.

[197] B. Mohammadi and O. Pironneau, *Analysis of the K-epsilon turbulence model*. Wiley, 1994.

[198] I. B. Celik, U. Ghia, P. J. Roache, J. C. Freitas, H. Coleman, and P. E. Raad, "Procedure for Estimation and Reporting of Uncertainty Due to Discretization in CFD Applications," *Journal of Fluids Engineering*, vol. 130, no. 7, 2008.

[199] C. Cutler and L. Mausner, "Energetic protons boost BNL isotope production TRIUMF targets alpha therapy," *Cern Cour.*, vol. 56, no. 8, pp. 32–35, 2016.

[200] A. Robertson, C. Hoehr, A. Lobbezoo, L. Moskven, V. Radchenko, H. Yang, S. Zeisler, and P. Schaffer, "Ac-225 Production using TRIUMF's 500 MeV Cyclotron," *J. Med. Imaging Radiat. Sci.*, vol. 50, no. 1, p. S18, 2019.

[201] Y. E. Titarenko, O. V. Shvedov, V. F. Batyaev, E. I. Karpikhin, V. M. Zhivun, A. B. Koldobsky, and R. D. Mulambetov, "Cross sections for nuclide production in 1 GeV proton-irradiated 208Pb," *Phys. Rev. C*, vol. 65, no. 6, pp. 064610–1—-064610–19, 2002.

[202] Y. E. Titarenko, V. F. Batyaev, M. A. Butko, D. V. Dikarev, S. N. Florya, K. V. Pavlov, A. Y. Titarenko, R. S. Tikhonov, V. M. Zhivun, A. V. Ignatyuk, S. G. Mashnik, A. Boudard, S. Leray, J. David,

J. Cugnon, D. Mancusi, Y. Yariv, H. Kumawat, K. Nishihara, N. Matsuda, G. Mank, and W. Gudowski, "Verification of high-energy transport codes on the basis of activation data," *Phys. Rev. C*, vol. 84, no. 6, pp. 064612–1—-064612–19, 2011.

[203] N. Otsuka, "IAEA-NDS-208: LEXFOR (EXFOR Compiler's Manual)," tech. rep., International Atomic Energy Agency, Vienna, 2011.

[204] A. Hermanne, A. V. Ignatyuk, R. Capote, B. V. Carlson, J. W. Engle, M. A. Kellett, and T. Kib, "Reference Cross Sections for Charged-particle Monitor Reactions," *Nucl. Data Sheets*, vol. 148, pp. 338–382, 2018.

[205] V. Vlachoudis, "FLAIR: A powerful but user friendly graphical interface for FLUKA," in *Proc. Int. Conf. Math. Comput. Methods, React. Phys. (M&C 2009)*, (Saratoga Springs, NY), 2009.

[206] T. Mastren, V. Radchenko, A. Owens, R. Copping, R. Boll, J. Griswold, S. Mirzadeh, L. Wyant, M. Brugh, J. Engle, F. Nortier, E. Birnbaum, K. John, and M. Fassbender, "Simultaneous Separation of Actinium and Radium Isotopes from a Proton Irradiated Thorium Matrix," *Sci. Rep.*, vol. 7, no. 1, pp. 2–8, 2017.

[207] G. Sgouros, E. Frey, B. He, N. Ray, and D. Ludwig, "Dosimetric Impact of Ac-227 in Accelerator-Produced Ac-225," in *J. Med. Imaging Radiat. Sci.*, vol. 50, pp. S37–S38, 2019.

[208] Z. Jiang, E. Revskaya, D. R. Fisher, and E. Dadachova, "In vivo Evaluation of Free and Chelated Accelerator-produced Actinium- 225 – Radiation Dosimetry and Toxicity Results," *Curr. Radiopharm.*, vol. 11, no. 3, pp. 215–222, 2018.

[209] L. A. Currie, "Limits for Qualitative Detection and Quantitative Determination Application to Radiochemistry," *Anal. Chem.*, vol. 40, no. 3, pp. 586–593, 1968.

[210] IAEA, "IAEA/AQ/48: Determination and Interpretation of Characteristic Limits for Radioactivity Measurements," Tech. Rep. 48, IAEA, Vienna, Austria, 2017.

[211] S. Savvin, "Analytical use of arsenazo III: Determination of thorium, zirconium, uranium and rare earth elements," *Talanta*, vol. 8, no. 9, pp. 673–685, 1961.

[212] C. F. Ramogida and C. Orvig, "Tumour targeting with radiometals for diagnosis and therapy," *Chemical Communications*, vol. 49, pp. 4720–39, 2013.

[213] E. W. Price and C. Orvig, "Matching chelators to radiometals for radiopharmaceuticals.," *Chem. Soc. Rev.*, vol. 43, no. 1, pp. 260–90, 2014.

[214] Y. Harada, Y. Baskin, and J. H. Handwerk, "American Ceramic Society," *J. Am. Ceram. Soc.*, vol. 45, no. 6, 1962.

[215] S. S. Galley, C. E. Van Alstine, L. Maron, and T. E. Albrecht-Schmitt, "Understanding the Scarcity of Thorium Peroxide Clusters," *Inorg. Chem.*, vol. 56, no. 21, pp. 12692–12694, 2017.

[216] R. A. Hasty and J. E. Boggs, "Formation and Properties of Thorium Peroxide," *J. Less-Common Met.*, vol. 7, pp. 447–452, 1964.

[217] R. A. Hasty and J. E. Boggs, "Isotopic exchange study on thorium peroxide," *J. Inorg. Nucl. Chem.*, vol. 33, pp. 874–876, 1971.

[218] G. L. Johnson, M. J. Kelly, and D. R. Cuneo, "Reactions of aqueous thorium nitrate solutions with hydrogen peroxide," *J. Inorg. Nucl. Chem.*, vol. 27, no. 8, pp. 1787–1791, 1965.

[219] A. K. H. Robertson, H. Yang, S. Zeisler, and P. Schaffer, "PCT/CA2019/050370 Systems, Apparatus and Methods for Separating Actinium, Radium, and Thorium," 2019.

[220] D. R. McTaggart and J. C. Mailen, "Coprecipitation of Thorium and Uranium Peroxides From Acid Solutions," tech. rep., Oak Ridge National Laboratory, Oak Ridge, TN, 1981.

[221] J. E. Gindler, "The Radiochemistry of Uranium," tech. rep., U.S. Atomic Energy Commission, 1962.

[222] V. Tsoupko-Sitnikov, Y. Norseev, and V. Khalkin, "Generator of actinium-225," in *J. Radioanal. Nucl. Chem.*, pp. 75–83, 1996.

[223] A. Pourmand and N. Dauphas, "Distribution coefficients of 60 elements on TODGA resin: Application to Ca, Lu, Hf, U and Th isotope geochemistry," *Talanta*, vol. 81, no. 3, pp. 741–753, 2010.

[224] E. Philip Horwitz, R. Chiarizia, and M. L. Dietz, "A Novel Strontium-Selective Extraction Chromatographic Resin," *Solvent Extr. Ion Exch.*, vol. 10, no. 2, pp. 313–336, 1992.

[225] L. R. Bunney, N. E. Ballou, J. Pascual, and S. Foti, "Anion Exchange Behavior of Several Metal Ions in Hydrochloric, Nitric, and Sulfuric Acid Solutions," *Anal. Chem.*, vol. 31, no. 3, 1959.

[226] D. McAlister, R. Perron, D. Gendron, P. Causey, E. Philip Horwitz, and J. T. Harvey, "Selective Separation of Radium and Actinium from Bulk Thorium Target Material," in *J. Med. Imaging Radiat. Sci.*, vol. 50, pp. S14–S15, 2019.

[227] IAEA, "Radiation protection and safety of radiation sources: international basic safety standards general safety," tech. rep., IAEA, Vienna, Austria, 2014.

[228] IAEA, "IAEA-TECDOC-1679: Exemption from Regulatory Control of Goods Containing Small Amounts of Radioactive Material," tech. rep., IAEA, Vienna, Austria, 2012.

[229] G. of Canada, "Nuclear Substances and Radiation Devices Regulations," 2015.

[230] V. R. Solomon, E. Alizadeh, W. Bernhard, S. V. Hartimath, W. Hill, R. Chekol, K. M. Barreto, C. R. Geyer, and H. Fonge, "^{111}In- and ^{225}Ac-Labeled Cixutumumab for Imaging and α-Particle Radiotherapy of IGF-1R Positive Triple-Negative Breast Cancer," *Molecular Pharmaceutics*, vol. 16, no. 12, pp. 4807–4816, 2019.

[231] C. Kratochwil, K. Schmidt, A. Afshar-Oromieh, F. Bruchertseifer, H. Rathke, A. Morgenstern, U. Haberkorn, and F. L. Giesel, "Targeted alpha therapy of mCRPC: Dosimetry estimate of ^{213}Bismuth-PSMA-617," *European Journal of Nuclear Medicine and Molecular Imaging*, vol. 45, no. 1, pp. 31–37, 2018.

[232] S. Agostinelli, J. Allison, K. Amako, J. Apostolakis, H. Araujo, P. Arce, M. Asai, D. Axen, S. Banerjee, G. Barrand, F. Behner, L. Bellagamba, J. Boudreau, L. Broglia, A. Brunengo, H. Burkhardt, S. Chauvie, J. Chuma, R. Chytracek, G. Cooperman, G. Cosmo, P. Degtyarenko, A. Dell'Acqua, G. Depaola, D. Dietrich, R. Enami, A. Feliciello, C. Ferguson, H. Fesefeldt, G. Folger, F. Foppiano, A. Forti, S. Garelli, S. Giani, R. Giannitrapani, D. Gibin, J. J. Gomez

Cadenas, I. Gonzalez, G. Gracia Abril, G. Greeniaus, W. Greiner, V. Grichine, A. Grossheim, S. Guatelli, P. Gumplinger, R. Hamatsu, K. Hashimoto, H. Hasui, A. Heikkinen, A. Howard, V. Ivanchenko, A. Johnson, F. W. Jones, J. Kallenbach, N. Kanaya, M. Kawabata, Y. Kawabata, M. Kawaguti, S. Kelner, P. Kent, A. Kimura, T. Kodama, R. Kokoulin, M. Kossov, H. Kurashige, E. Lamanna, T. Lampen, V. Lara, V. Lefebure, F. Lei, M. Liendl, W. Lockman, F. Longo, S. Magni, M. Maire, E. Medernach, K. Minamimoto, P. Mora de Freitas, Y. Morita, K. Murakami, M. Nagamatu, R. Nartallo, P. Nieminen, T. Nishimura, K. Ohtsubo, M. Okamura, S. O'Neale, Y. Oohata, K. Paech, J. Perl, A. Pfeiffer, M. G. Pia, F. Ranjard, A. Rybin, S. Sadilov, E. di Salvo, G. Santin, T. Sasaki, N. Savvas, Y. Sawada, S. Scherer, S. Sei, V. Sirotenko, D. Smith, N. Starkov, H. Stoecker, J. Sulkimo, M. Takahata, S. Tanaka, E. Tcherniaev, E. Safai Tehrani, M. Tropeano, P. Truscott, H. Uno, L. Urban, P. Urban, M. Verderi, A. Walkden, W. Wander, H. Weber, J. P. Wellisch, T. Wenaus, D. C. Williams, D. Wright, T. Yamada, H. Yoshida, and D. Zschiesche, "GEANT4 - A simulation toolkit," *Nuclear Instruments and Methods in Physics Research, Section A: Accelerators, Spectrometers, Detectors and Associated Equipment*, vol. 506, no. 3, pp. 250–303, 2003.

[233] J. Allison, K. Amako, J. Apostolakis, P. Arce, M. Asai, T. Aso, E. Bagli, A. Bagulya, S. Banerjee, G. Barrand, B. R. Beck, A. G. Bogdanov, D. Brandt, J. M. Brown, H. Burkhardt, P. Canal, D. Cano-Ott, S. Chauvie, K. Cho, G. A. Cirrone, G. Cooperman, M. A. Cortés-Giraldo, G. Cosmo, G. Cuttone, G. Depaola, L. Desorgher, X. Dong, A. Dotti, V. D. Elvira, G. Folger, Z. Francis, A. Galoyan, L. Garnier, M. Gayer, K. L. Genser, V. M. Grichine, S. Guatelli, P. Guèye, P. Gumplinger, A. S. Howard, I. Hřivnáčová, S. Hwang, S. Incerti, A. Ivanchenko, V. N. Ivanchenko, F. W. Jones, S. Y. Jun, P. Kaitaniemi, N. Karakatsanis, M. Karamitrosi, M. Kelsey, A. Kimura, T. Koi, H. Kurashige, A. Lechner, S. B. Lee, F. Longo, M. Maire, D. Mancusi, A. Mantero, E. Mendoza, B. Morgan, K. Murakami, T. Nikitina, L. Pandola, P. Paprocki, J. Perl, I. Petrović, M. G. Pia, W. Pokorski, J. M. Quesada, M. Raine, M. A. Reis, A. Ribon, A. Ristić Fira, F. Romano, G. Russo, G. Santin, T. Sasaki, D. Sawkey, J. I. Shin, I. I. Strakovsky, A. Taborda, S. Tanaka, B. Tomé, T. Toshito, H. N. Tran, P. R. Truscott, L. Urban, V. Uzhinsky, J. M. Verbeke, M. Verderi, B. L. Wendt, H. Wenzel, D. H. Wright, D. M. Wright, T. Yamashita, J. Yarba, and H. Yoshida, "Recent develop-

ments in GEANT4," *Nuclear Instruments and Methods in Physics Research, Section A: Accelerators, Spectrometers, Detectors and Associated Equipment*, vol. 835, pp. 186–225, 2016.

A Additional Details on Gamma Spectroscopy Calibrations

A.1 Pulse Shape Timing Effects on Energy Resolution

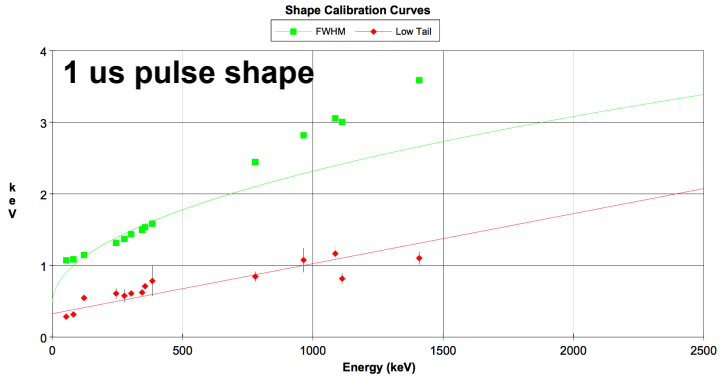

Datasource: C:\GENIE2K\CAMFILES\Andrew\cal_Eu152Ba133_20160922_short2.CNF
Energy = -3.665e-002 keV + 5.006e-001*Ch + 5.332e-007*Ch^2 - 1.574e-010*Ch^3
FWHM = 4.733e-001 keV + 5.827e-002*E^1/2
Lo Tail = 3.243e-001 keV + 6.992e-004*E

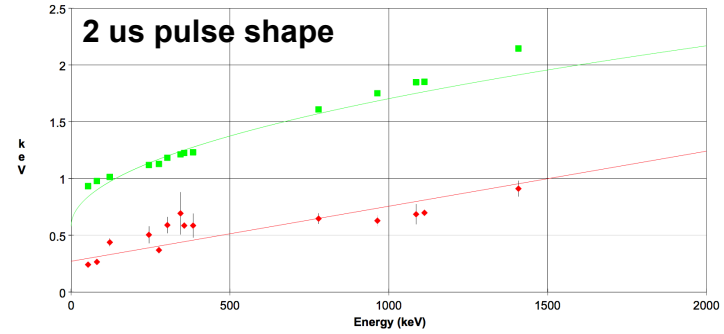

Datasource: C:\GENIE2K\CAMFILES\Andrew\cal_Eu152Ba133_20160922_2us.CNF
Energy = 5.079e-001 keV + 4.766e-001*Ch + 7.394e-007*Ch^2 - 1.433e-010*Ch^3
FWHM = 5.788e-001 keV + 3.554e-002*E^1/2
Lo Tail = 2.700e-001 keV + 4.850e-004*E

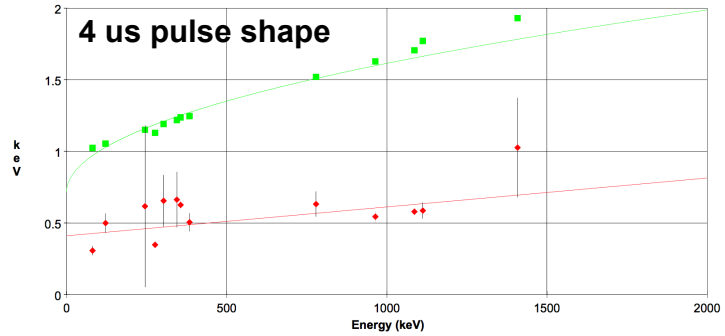

Datasource: C:\GENIE2K\CAMFILES\Andrew\cal_Eu152Ba133_20160922_4us.CNF
Energy = 1.339e+000 keV + 4.817e-001*Ch + 1.002e-006*Ch^2 - 1.796e-010*Ch^3
FWHM = 7.135e-001 keV + 2.847e-002*E^1/2
Lo Tail = 4.096e-001 keV + 2.019e-004*E

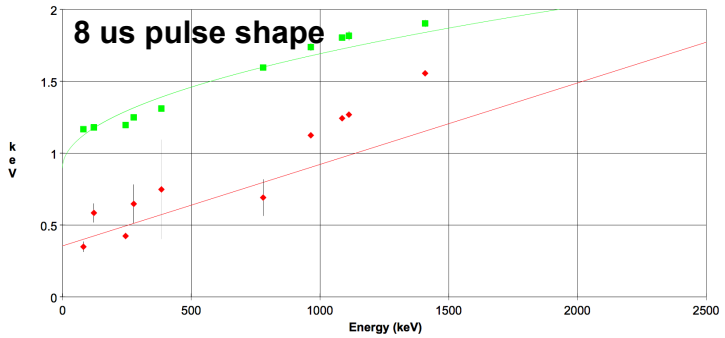

Datasource: C:\GENIE2K\CAMFILES\Andrew\cal_Eu152Ba133_20160922_8us.CNF
Energy = 3.706e+000 keV + 5.385e-001*Ch + 3.357e-006*Ch^2 - 6.831e-010*Ch^3
FWHM = 8.971e-001 keV + 2.511e-002*E^1/2
Lo Tail = 3.540e-001 keV + 5.669e-004*E

A.2 Fits to Peaks used in Energy and Shape Calibrations

Datasource : C:\GENIE2K\CAMFILES\Detector Maintenance\cal R01107b_P0-02.CNF
Sample ID : cal P0 20160925 Iterations : 9
Sample Date : 2016-09-25 6:54:00 PM Chi-square : 4.08
Fit Engine : Sum / Non-Linear LSQ Fit Region Start : 51.881 keV
Bkgnd Type : Step Region End : 54.323 keV

Nbr	Energy	Centroid	Area	%Error	FWHM	Ratio
1	53.112	217.04	158817.45	0.97	0.794	1.07

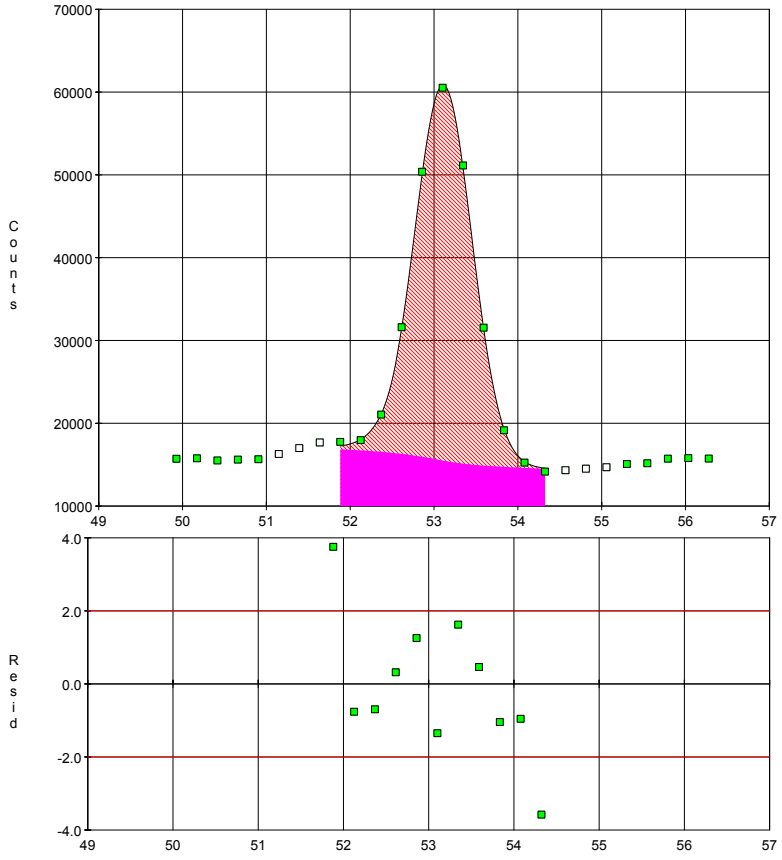

Datasource : C:\GENIE2K\CAMFILES\Detector Maintenance\cal R01107b_P0-02.CNF
Sample ID : cal P0 20160925 Iterations : 11
Sample Date : 2016-09-25 6:54:00 PM Chi-square : 12.30
Fit Engine : Sum / Non-Linear LSQ Fit Region Start : 78.504 keV
Bkgnd Type : Step Region End : 82.412 keV

Nbr	Energy	Centroid	Area	%Error	FWHM	Ratio
1	79.577	325.40	227298.39	0.52	0.836	1.05
2	80.993	331.19	2849221.75	0.19	0.839	1.05

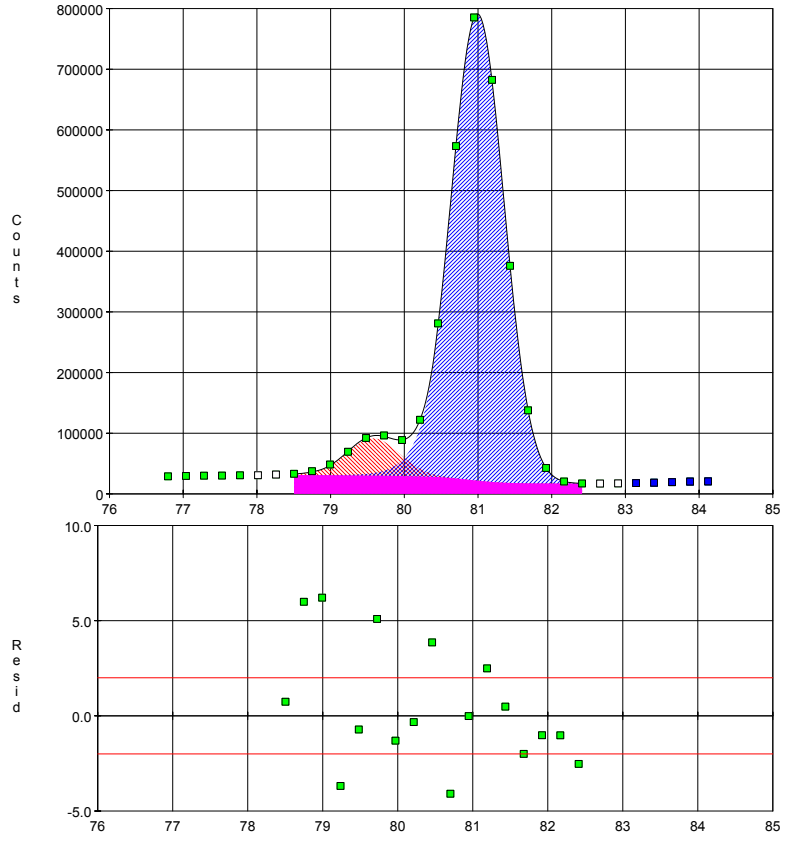

Datasource : C:\GENIE2K\CAMFILES\Detector Maintenance\cal R01107b_P0-02.CNF
Sample ID : cal P0 20160925 Iterations : 25
Sample Date : 2016-09-25 6:54:00 PM Chi-square : 1.55
Fit Engine : Sum / Non-Linear LSQ Fit Region Start : 120.516 keV
Bkgnd Type : Step Region End : 124.180 keV

Nbr	Energy	Centroid	Area	%Error	FWHM	Ratio
1	121.809	498.29	2194664.25	0.14	0.881	1.01
2	123.077	503.48	23429.91	1.77	0.883	1.01

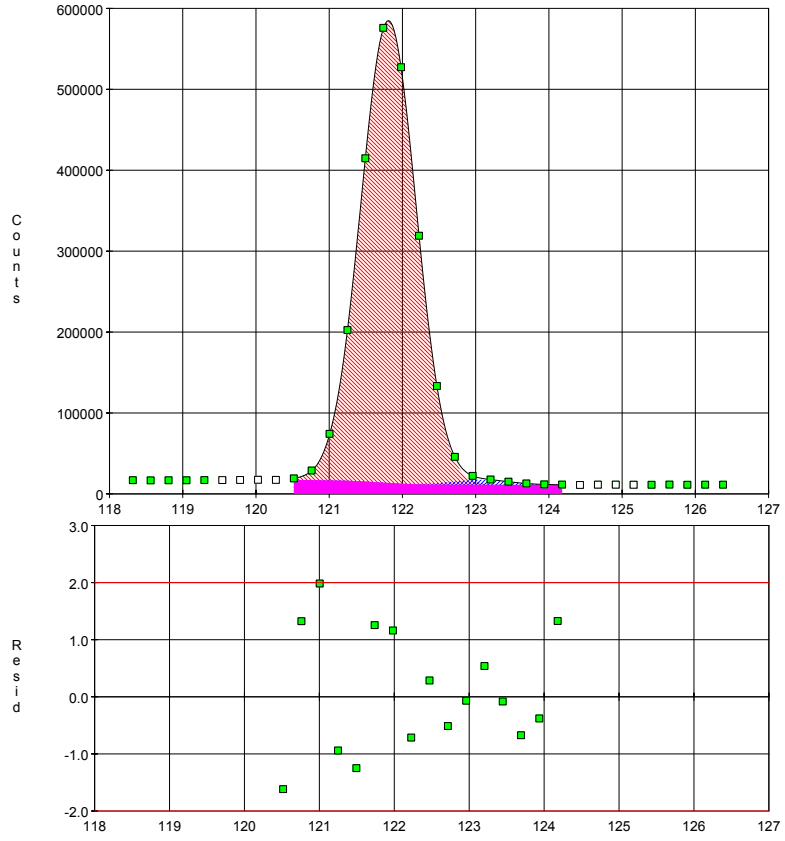

Datasource : C:\GENIE2K\CAMFILES\Detector Maintenance\cal R01107b_P0-02.CNF
Sample ID : cal P0 20160925 Iterations : 10
Sample Date : 2016-09-25 6:54:00 PM Chi-square : 1.23
Fit Engine : Sum / Non-Linear LSQ Fit Region Start : 274.913 keV
Bkgnd Type : Step Region End : 278.089 keV

Nbr	Energy	Centroid	Area	%Error	FWHM	Ratio
1	276.420	1131.17	248665.17	0.52	1.049	0.98

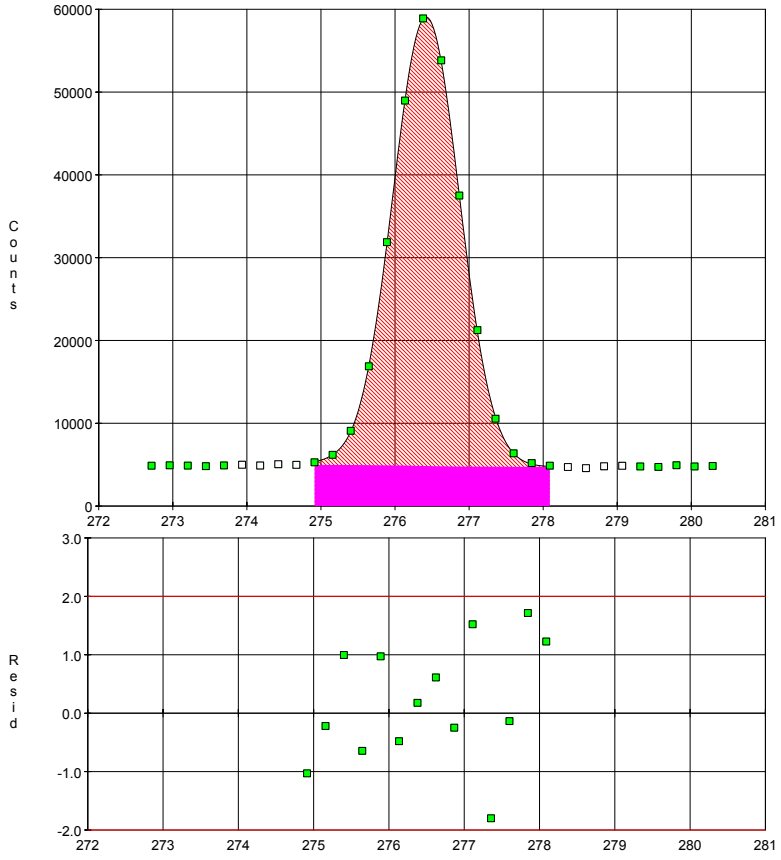

Datasource : C:\GENIE2K\CAMFILES\Detector Maintenance\cal R01107b_P0-02.CNF
Sample ID : cal P0 20160925 Iterations : 12
Sample Date : 2016-09-25 6:54:00 PM Chi-square : 2.21
Fit Engine : Sum / Non-Linear LSQ Fit Region Start : 301.300 keV
Bkgnd Type : Step Region End : 304.477 keV

Nbr	Energy	Centroid	Area	%Error	FWHM	Ratio
1	302.876	1239.45	602191.25	0.25	1.069	0.97

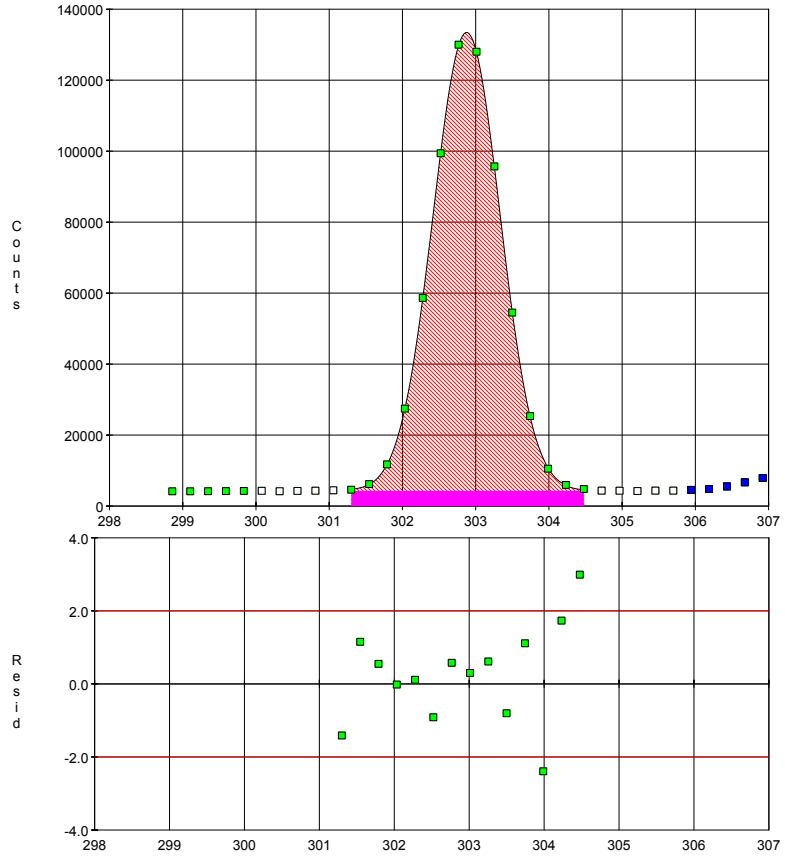

```
Datasource  : C:\GENIE2K\CAMFILES\Detector Maintenance\cal R01107b_P0-02.CNF
Sample ID   : cal P0 20160925               Iterations   : 13
Sample Date : 2016-09-25  6:54:00 PM        Chi-square   : 7.35
Fit Engine  : Sum / Non-Linear LSQ Fit      Region Start : 354.322 keV
Bkgnd Type  : Step                          Region End   : 357.499 keV

Nbr      Energy  Centroid        Area  %Error     FWHM    Ratio
  1     356.035   1457.01  1797139.38    0.11    1.127     0.98
```

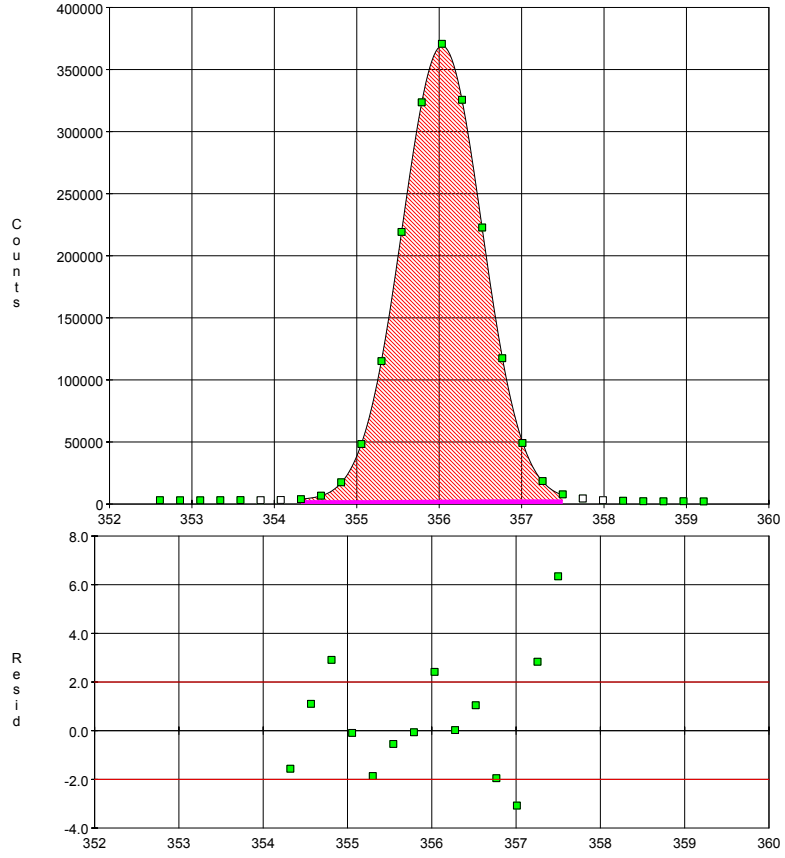

Datasource : C:\GENIE2K\CAMFILES\Detector Maintenance\cal R01107b_P0-02.CNF
Sample ID : cal P0 20160925 Iterations : 11
Sample Date : 2016-09-25 6:54:00 PM Chi-square : 3.83
Fit Engine : Sum / Non-Linear LSQ Fit Region Start : 776.854 keV
Bkgnd Type : Step Region End : 781.253 keV

Nbr	Energy	Centroid	Area	%Error	FWHM	Ratio
1	779.010	3187.82	182302.28	0.49	1.535	1.04

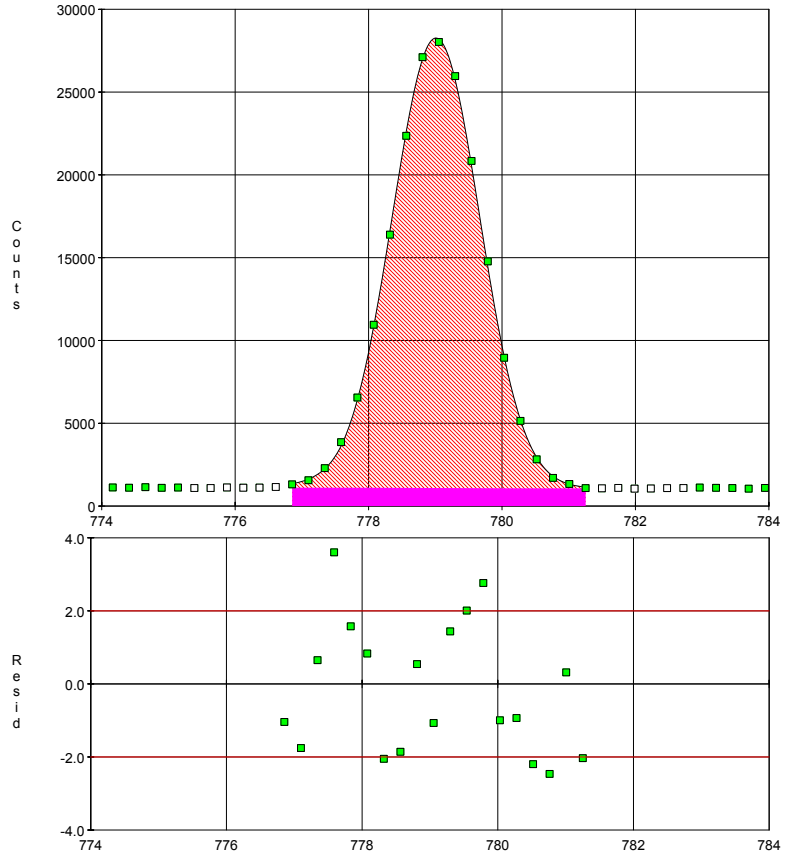

Datasource : C:\GENIE2K\CAMFILES\Detector Maintenance\cal R01107b_P0-02.CNF
Sample ID : cal P0 20160925 Iterations : 11
Sample Date : 2016-09-25 6:54:00 PM Chi-square : 1.22
Fit Engine : Sum / Non-Linear LSQ Fit Region Start : 1083.297 keV
Bkgnd Type : Step Region End : 1091.848 keV

Nbr	Energy	Centroid	Area	%Error	FWHM	Ratio
1	1085.84	4443.43	109234.41	0.66	1.814	1.09
2	1089.76	4459.48	18329.62	1.01	1.816	1.09

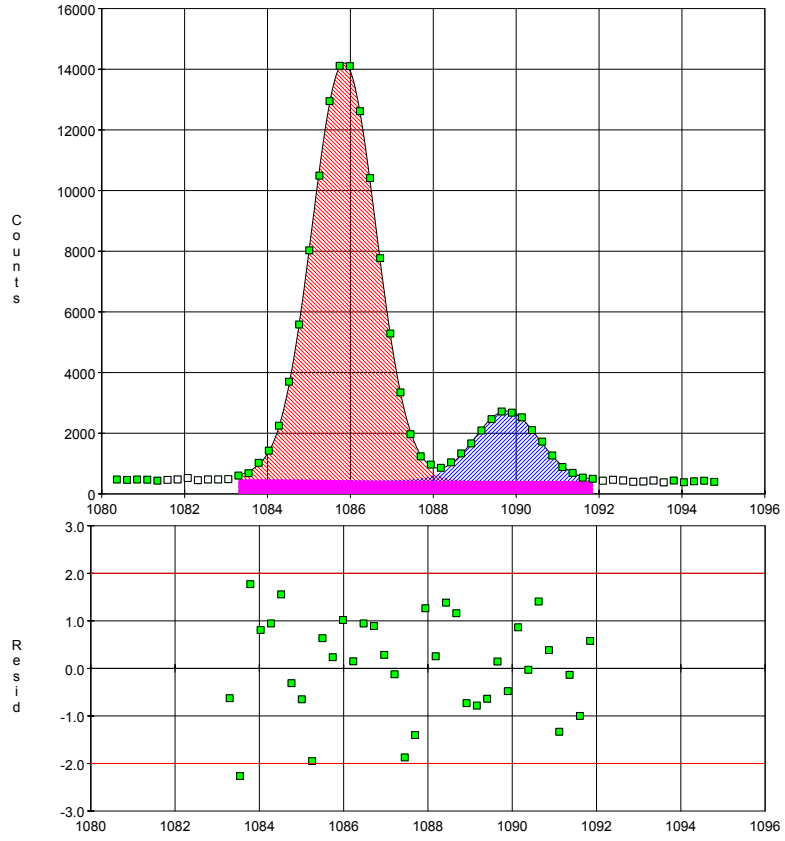

Datasource : C:\GENIE2K\CAMFILES\Detector Maintenance\cal R01107b_P0-02.CNF
Sample ID : cal P0 20160925 Iterations : 11
Sample Date : 2016-09-25 6:54:00 PM Chi-square : 3.25
Fit Engine : Sum / Non-Linear LSQ Fit Region Start : 1405.022 keV
Bkgnd Type : Step Region End : 1411.128 keV

Nbr	Energy	Centroid	Area	%Error	FWHM	Ratio
1	1408.06	5762.45	151396.52	0.42	2.101	1.15

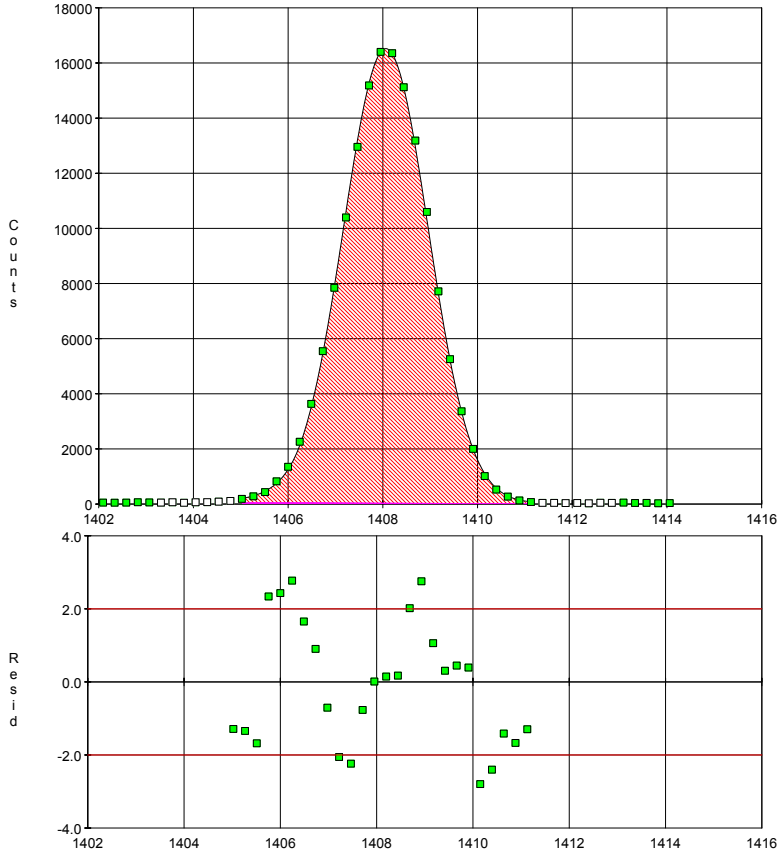

A.3 Peak Width Values Based on Linear Calibration Curve

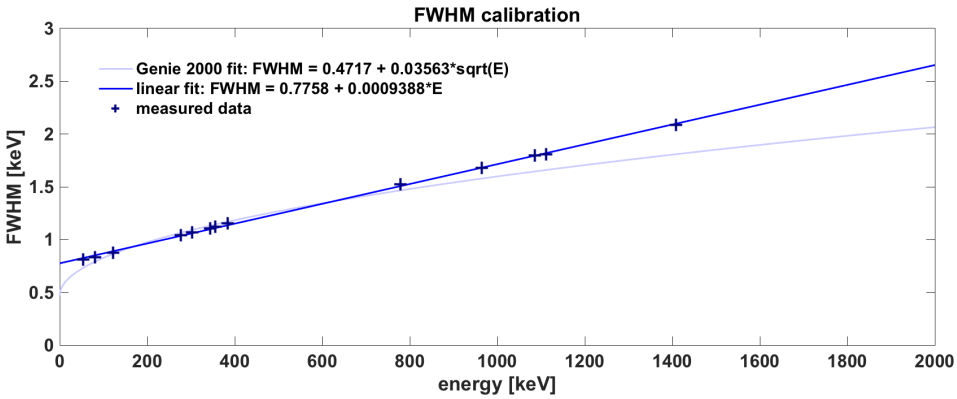

Peak Width Values Based on Linear Calibration Curve

Energy [keV]	FWHM [keV]	Energy [keV]	FWHM [keV]	Energy [keV]	FWHM [keV]	Energy [keV]	FWHM [keV]
0	0.776	500	1.245	1000	1.714	1500	2.183
20	0.795	520	1.264	1020	1.733	1520	2.202
40	0.813	540	1.282	1040	1.751	1540	2.220
60	0.832	560	1.301	1060	1.770	1560	2.239
80	0.851	580	1.320	1080	1.789	1580	2.258
100	0.870	600	1.339	1100	1.808	1600	2.277
120	0.888	620	1.357	1120	1.826	1620	2.295
140	0.907	640	1.376	1140	1.845	1640	2.314
160	0.926	660	1.395	1160	1.864	1660	2.333
180	0.945	680	1.414	1180	1.883	1680	2.352
200	0.963	700	1.432	1200	1.901	1700	2.370
220	0.982	720	1.451	1220	1.920	1720	2.389
240	1.001	740	1.470	1240	1.939	1740	2.408
260	1.020	760	1.489	1260	1.958	1760	2.427
280	1.038	780	1.507	1280	1.976	1780	2.445
300	1.057	800	1.526	1300	1.995	1800	2.464
320	1.076	820	1.545	1320	2.014	1820	2.483
340	1.095	840	1.564	1340	2.033	1840	2.502
360	1.113	860	1.582	1360	2.051	1860	2.520
380	1.132	880	1.601	1380	2.070	1880	2.539
400	1.151	900	1.620	1400	2.089	1900	2.558
420	1.170	920	1.639	1420	2.108	1920	2.577
440	1.189	940	1.658	1440	2.127	1940	2.596
460	1.207	960	1.676	1460	2.145	1960	2.614
480	1.226	980	1.695	1480	2.164	1980	2.633

A.4 Library Used for Background Analysis

```
Library Listing Report           2016-12-20 10:42:24 PM          Page  1

  *************************************************************************
  *****           L I B R A R Y   L I S T I N G   R E P O R T          *****
  *************************************************************************


       Filename: C:\GENIE2K\LIBRARIES\BACKGROUND.NLB

       Nuclide Library Description:
```

Nuclide Name	Half-Life (Seconds)	Energy (keV)	Energy Uncert. (keV)	Yield (%)	Yield Uncert.(Abs.+-)
K-40	3.938E+016	1460.822	0.006	10.6600	0.1800
Tl-208	1.832E+002	10.600	0.050	2.7500	0.1200
		72.805	0.001	2.0100	0.0600
		74.969	3.350	0.0900	0.0600
		84.450	0.005	0.4040	0.0110
		84.938	0.001	0.7760	0.0120
		87.300	0.050	0.2830	0.0080
		510.770	0.100	22.6000	0.2000
		583.187	0.002	85.0000	0.3000
		763.130	0.080	1.7900	0.3000
		860.557	0.004	12.5000	0.1000
		927.600	0.200	0.1250	0.0110
Pb-210	7.006E+008	10.800	0.050	22.7000	0.1000
		46.539	0.001	4.2500	0.0400
Tl-210	7.800E+001	296.000	3.000	79.0000	10.0000
		799.600	0.300	98.9600	0.0050
Bi-212	1.500E+003	727.330	0.009	6.6700	0.0900
		785.370	0.080	1.1020	0.0130
		893.408	0.005	0.3780	0.0190
		952.120	0.011	0.1700	0.0300
		1078.620	0.100	0.5640	0.0190
		1620.500	0.100	1.4700	0.0300
Pb-212	3.830E+004	10.800	0.050	14.3000	0.6000
		74.815	0.001	10.2800	0.2500
		77.107	0.001	17.1000	0.4000
		86.830	0.005	2.0700	0.0500
		87.349	0.001	3.9700	0.0900
		89.784	0.001	1.4600	0.0300
		115.183	0.005	0.5960	0.0090
		238.632	0.002	43.6000	0.5000
		300.087	0.001	3.3000	0.0400
Bi-214	1.194E+003	11.100	0.050	0.7700	0.0300
		76.863	0.001	0.5450	0.0150
		79.290	0.005	0.9070	0.0230
		89.256	0.001	0.1100	0.0030
		92.317	0.001	0.0777	0.0020
		273.800	0.050	0.1280	0.0070
		280.970	0.040	0.0670	0.0070
		333.370	0.050	0.0650	0.0040
		348.920	0.060	0.1040	0.0120
		351.900	0.500	0.0700	0.0100
		386.780	0.050	0.2950	0.0050
		388.890	0.050	0.4020	0.0100

Nuclide Library Description:

Nuclide Name	Half-Life (Seconds)	Energy (keV)	Energy Uncert. (keV)	Yield (%)	Yield Uncert.(Abs.+-)
Bi-214	1.194E+003	394.050	0.080	0.0126	0.0009
		396.020	0.060	0.0260	0.0040
		405.720	0.020	0.1690	0.0060
		454.790	0.020	0.2920	0.0040
		469.770	0.040	0.1320	0.0050
		609.320	0.005	45.4900	0.1600
		665.447	0.009	1.5310	0.0060
		703.110	0.040	0.4720	0.0090
		719.870	0.030	0.3920	0.0080
		752.850	0.030	0.1280	0.0070
		768.360	0.005	4.8940	0.0110
		786.350	0.140	0.3200	0.0400
		806.180	0.009	1.2640	0.0050
		821.180	0.030	0.1610	0.0080
		826.450	0.100	0.1170	0.0130
		934.056	0.006	3.1070	0.0100
		964.080	0.030	0.3650	0.0100
		1051.960	0.030	0.3130	0.0070
		1069.960	0.070	0.2720	0.0090
		1120.292	0.006	14.9200	0.0300
		1133.660	0.030	0.2512	0.0010
		1155.210	0.008	1.6330	0.0060
		1207.680	0.030	0.4510	0.0100
		1238.122	0.007	5.8340	0.0150
		1280.976	0.010	1.4340	0.0060
		1303.750	0.070	0.1070	0.0050
		1377.669	0.008	3.9880	0.0110
		1385.310	0.013	0.7930	0.0050
		1401.515	0.012	1.3300	0.0050
		1407.988	0.011	2.3940	0.0070
		1509.210	0.010	2.1300	0.0100
		1661.274	0.016	1.0470	0.0060
		1729.595	0.011	2.8780	0.0080
		1764.491	0.010	15.3000	0.0300
		1847.429	0.013	2.0250	0.0090
Pb-214	1.608E+003	10.800	0.050	12.0000	0.6000
		53.228	0.002	1.0750	0.0070
		74.815	0.001	5.8000	0.3000
		77.107	0.001	9.7000	0.5000
		86.830	0.005	1.1700	0.0600
		87.349	0.001	2.2400	0.1100
		89.784	0.001	0.8200	0.0400
		118.170	0.005	0.0940	0.0005
		196.190	0.050	0.0670	0.0080
		205.680	0.090	0.0114	0.0013
		241.995	0.002	7.2510	0.0160
		258.860	0.030	0.5310	0.0040
		274.800	0.040	0.3550	0.0100
		295.223	0.002	18.4200	0.0400
		298.760	0.005	0.0260	0.0050
		305.260	0.030	0.0312	0.0021
		314.330	0.070	0.0780	0.0060

Nuclide Library Description:

Nuclide Name	Half-Life (Seconds)	Energy (keV)	Energy Uncert. (keV)	Yield (%)	Yield Uncert.(Abs.+-)
Pb-214	1.608E+003	323.840	0.040	0.0290	0.0030
		351.932	0.002	35.6000	0.0700
		462.020	0.060	0.2120	0.0050
		480.432	0.020	0.3370	0.0040
		487.140	0.060	0.4320	0.0050
		511.000	0.009	0.0330	0.0090
		533.660	0.020	0.1810	0.0060
		538.420	0.080	0.0200	0.0030
		543.830	0.070	0.0440	0.0040
		580.140	0.030	0.3700	0.0040
		785.960	0.080	1.0600	0.0300
		839.070	0.080	0.5830	0.0080
Rn-218	3.500E-002	609.310	0.060	0.1240	0.0070
Th-231	9.187E+004	13.300	0.050	59.0000	15.0000
		25.640	0.020	14.1000	0.9000
		84.214	0.001	6.6000	0.4000
Th-234	2.082E+006	13.300	0.050	7.1000	0.5000
		63.290	0.020	3.7000	4.0000
		92.380	0.010	2.1300	0.2000
		92.800	0.020	2.1000	0.2000
		112.810	0.050	0.2100	0.0230
U-234	7.747E+012	120.900	0.020	0.0350	0.0050
U-235	2.221E+016	13.000	0.050	27.0000	4.0000
		19.550	0.050	63.0000	0.0500
		89.957	0.001	3.4300	0.0900
		93.350	0.005	5.5400	0.1400
		105.604	0.001	1.3100	0.0030
		143.760	0.020	0.2000	0.0020
		185.715	0.005	57.0000	0.6000
		202.120	0.010	1.0800	0.0230
		205.316	0.010	5.0200	0.0600

* = key line

TOTALS: 13 Nuclides 126 Energy Lines

A.5 Isotopes in the Genie 2000 v3.2 Cascade Summing Library

AC-228	CD-109†	EU-156	IN-114M2†	ND-149	RA-224*	SC-47*	TL-200
AG-108	CD-109M*	F-20*	IN-115M*	NI-65	RA-226*	SE-75	TL-200M
AG-108M	CD-109M2	FE-52*	IN-115M2*	NP-237	RA-228	SE-77M*	TL-201
AG-109M*	CD-111M	FE-52M	IN-116	NP-239	RB-83	SM-153	TL-201M
AG-110	CD-115	FE-59	IN-116M	OS-185	RB-86*	SM-153M	TL-202
AG-110M	CD-115M	GA-67	IN-116M2*	OS-191*	RB-86M*	SN-113†	TL-208
AG-111*	CE-137	GA-72	IN-117	OS-191M*	RB-88	SN-113M*	TL-210
AG-111M	CE-137M	GD-151	IN-117M*	OS-193	RE-186	SN-117M	TM-168
AL-26	CE-139	GD-153	IR-192	PA-231	RE-186M	SN-123*	TM-170
AL-28*	CE-139M*	GD-153M	IR-194	PA-233	RE-188	SN-123M*	U-0
AM-241*	CE-141*	GD-153M2	IR-194M	PA-234	RE-188M	SN-125	U-235*
AM-243*	CE-143	GD-159*	IR-194M2	PA-234M	RH-101	SN-125M	U-237
AS-74	CE-144*	GD-159M	K-42	PB-203	RH-101M	SR-85	U-238
AS-76	CF-249*	GE-75*	KR-87	PB-203M*	RH-102	SR-85M	U-238M*
AU-195	CF-251†	GE-75M	KR-88	PB-203M2	RH-102M	SR-87M*	U-239*
AU-195M*	CL-38	GE-77	LA-140	PB-210*	RH-102M2*	TA-182	V-48
AU-196	CL-38M*	GE-77M*	LU-172	PB-212*	RH-105*	TA-182M2	W-187
AU-196M*	CM-243	HF-175	LU-172M*	PB-214	RH-106	TB-158	XE-127
AU-196M2	CM-245	HF-180M*	LU-172M2*	PD-109*	RH-106M	TB-158M*	XE-127M
AU-198*	CO-56	HF-180M2	LU-173	PD-109M*	RH-99	TB-158M2	Y-88
AU-198M	CO-57	HF-181	LU-174	PD-111	RH-99M	TB-160	Y-88M
AU-199*	CO-58	HG-197	LU-174M	PD-111M	RU-103*	TC-95	Y-90*
AU-199M*	CO-58M*	HG-197M	LU-176	PM-143	RU-103M*	TC-95M	Y-90M
BA-131	CO-60	HG-203*	LU-176M	PM-144	RU-105	TC-98	YB-169
BA-131M	CO-60M	I-123	MN-52	PM-145	RU-97	TC-99*	YB-169M*
BA-133	CR-51*	I-125	MN-52M*	PM-146	S-37*	TC-99M*	YB-175
BA-133M	CS-134	I-126	MN-56	PM-148	SB-122	TE-127	YB-177
BA-135M*	CS-134M	I-131	MO-99	PM-148M	SB-122M	TE-127M	YB-177M
BA-137M*	CS-136	I-132	NA-22	PM-149*	SB-122M2*	TE-129	ZN-65*
BA-139*	CU-64*	I-132M	NA-24	PM-151	SB-124	TE-129M	ZN-69*
BA-140	DY-165	I-133	NB-92	PR-142	SB-124M*	TE-131	ZN-69M*
BI-207	DY-165M	I-133M	NB-92M	PR-144	SB-124M2	TE-131M	ZR-95*
BI-207M	ER-167M*	I-134	NB-94	PR-144M	SB-125	TE-132	ZR-97
BI-212	ER-171	I-134M	NB-94M*	PT-188	SB-126	TE-132M	
BI-214	EU-152	I-135	NB-95*	PT-191	SB-126M	TH-0	
BR-77	EU-152M	IN-111	NB-95M	PT-191M*	SB-127	TH-228	
BR-77M*	EU-152M2*	IN-111M*	NB-95M2*	PT-197	SC-44	TH-231	
BR-82	EU-154	IN-113M*	NB-97*	PT-197M	SC-44M	TH-232	
BR-82M	EU-154M	IN-114	NB-97M*	PU-239	SC-46	TH-234*	
CA-47	EU-155	IN-114M	ND-147	RA-0	SC-46M*	TI-44	

A.6 Library Used for Peak-to-Total Calibration

Library Listing Report 2017-01-09 5:38:44 PM Page 1

****

***** L I B R A R Y L I S T I N G R E P O R T *****

****

Filename: C:\GENIE2K\CAMFILES\PTCAL.NLB

Nuclide Library Description:

Nuclide Name	Half-Life (Seconds)	Energy (keV)	Energy Uncert. (keV)	Yield (%)	Yield Uncert.(Abs.+-)
MN-54	2.702E+007	834.827*	0.000	99.9750	0.0050
CO-57	2.341E+007	122.063*	0.000	85.5100	0.1800
		136.476	0.000	10.6000	0.1800
CU-64	4.572E+004	511.000*	0.000	35.2000	0.4000
		1345.770	0.060	0.4750	0.0110
ZN-65	2.112E+007	511.000	0.000	200.0000	0.0000
		1115.520*	0.000	50.7500	0.1000
ZR-89	2.823E+005	511.000	0.000	45.5000	0.5000
		909.150*	0.150	99.0400	0.0050
CD-109	4.009E+007	88.032*	0.000	3.7200	0.1100
SN-113	9.945E+006	255.120	0.000	1.9300	0.1000
		391.688*	0.000	64.9000	0.7000
TE-123m	1.364E+010	159.000*	0.000	0.0000	0.0000
CS-137	9.521E+008	661.650*	0.000	85.1200	0.2300
HG-203	4.026E+006	279.190*	0.000	77.3000	0.8000
RA-225	1.287E+006	40.000*	1.000	30.0000	0.0500
AM-241	1.364E+010	59.537*	0.001	35.9000	0.4000

* = key line

TOTALS: 12 Nuclides 17 Energy Lines

A.7 Fits to Peaks used in the Efficiency Calibration

The data presented in this section was acquired as described in Section 2.1.5.

```
Datasource  : C:\GENIE2K\CAMFILES\Detector Maintenance\cal R01107a_P5-01.CNF
Sample ID   : cal 20mL far                  Iterations   : 14
Sample Date : 2016-09-22  8:15:00 PM        Chi-square   : 2.19
Fit Engine  : Sum / Non-Linear LSQ Fit      Region Start : 29.675 keV
Bkgnd Type  : Step                          Region End   : 32.117 keV

Nbr      Energy  Centroid        Area  %Error     FWHM    Ratio
  1      30.424    124.07   604438.13    2.06    0.796     1.19
  2      30.810    125.65  1275426.75    1.34    0.797     1.19
```

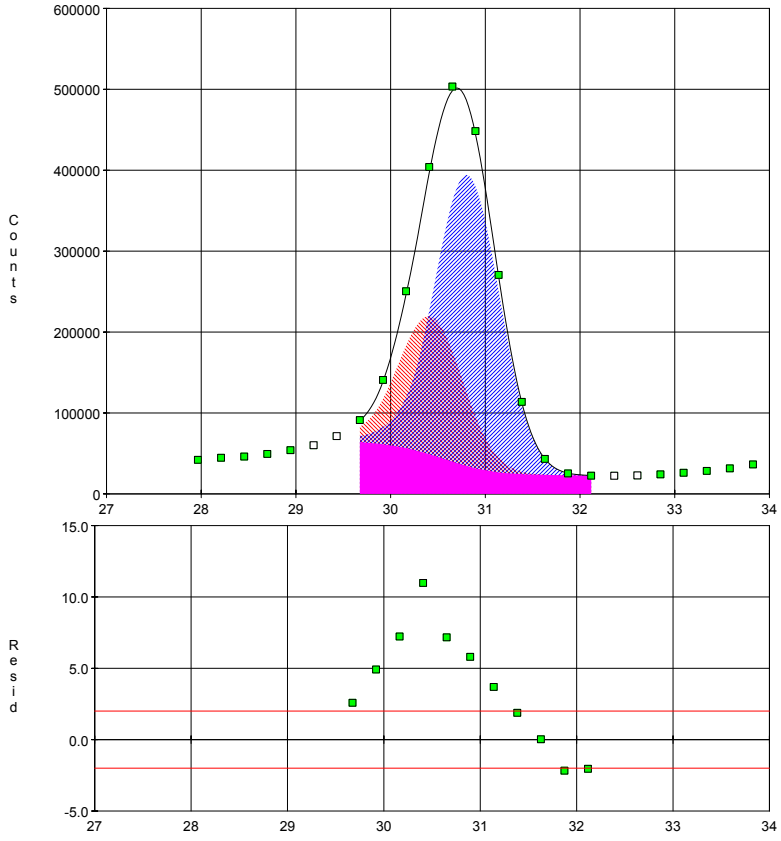

Datasource : C:\GENIE2K\CAMFILES\Detector Maintenance\cal R01107a_P5-01.CNF
Sample ID : cal 20mL far Iterations : 10
Sample Date : 2016-09-22 8:15:00 PM Chi-square : 12.64
Fit Engine : Sum / Non-Linear LSQ Fit Region Start : 38.222 keV
Bkgnd Type : Step Region End : 41.397 keV

Nbr	Energy	Centroid	Area	%Error	FWHM	Ratio
1	39.426	160.93	507707.16	0.63	0.816	1.17
2	40.011	163.32	963352.38	0.51	0.818	1.17

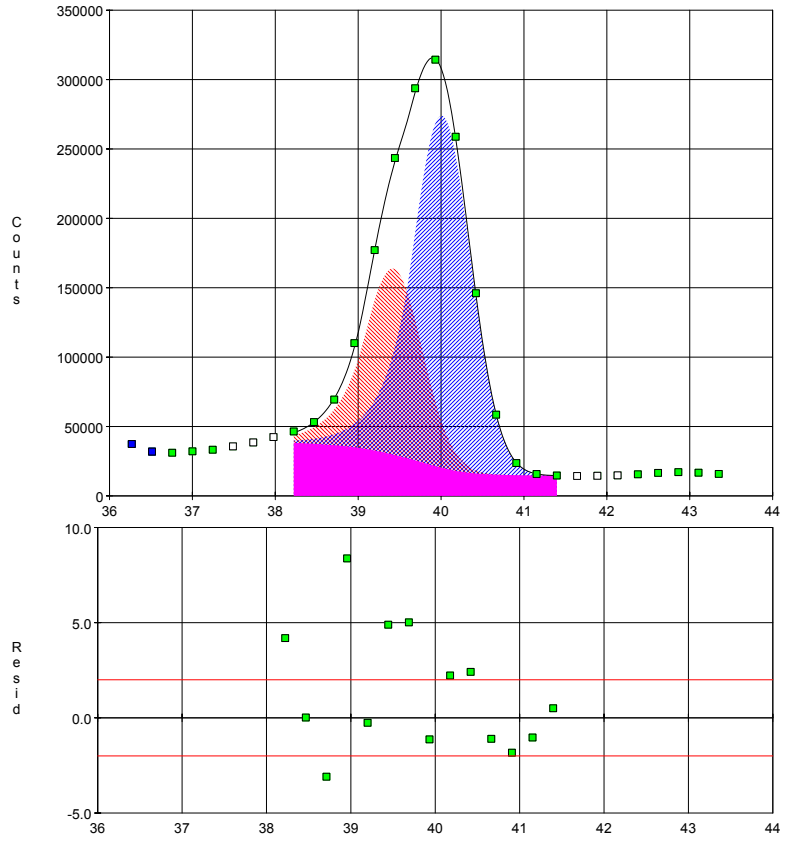

Datasource : C:\GENIE2K\CAMFILES\Detector Maintenance\cal R01107a_P5-01.CNF
Sample ID : cal 20mL far
Sample Date : 2016-09-22 8:15:00 PM
Fit Engine : Sum / Non-Linear LSQ Fit
Bkgnd Type : Step

Iterations : 9
Chi-square : 2.56
Region Start : 51.654 keV
Region End : 54.584 keV

Nbr	Energy	Centroid	Area	%Error	FWHM	Ratio
1	53.100	216.92	59922.52	1.69	0.810	1.11

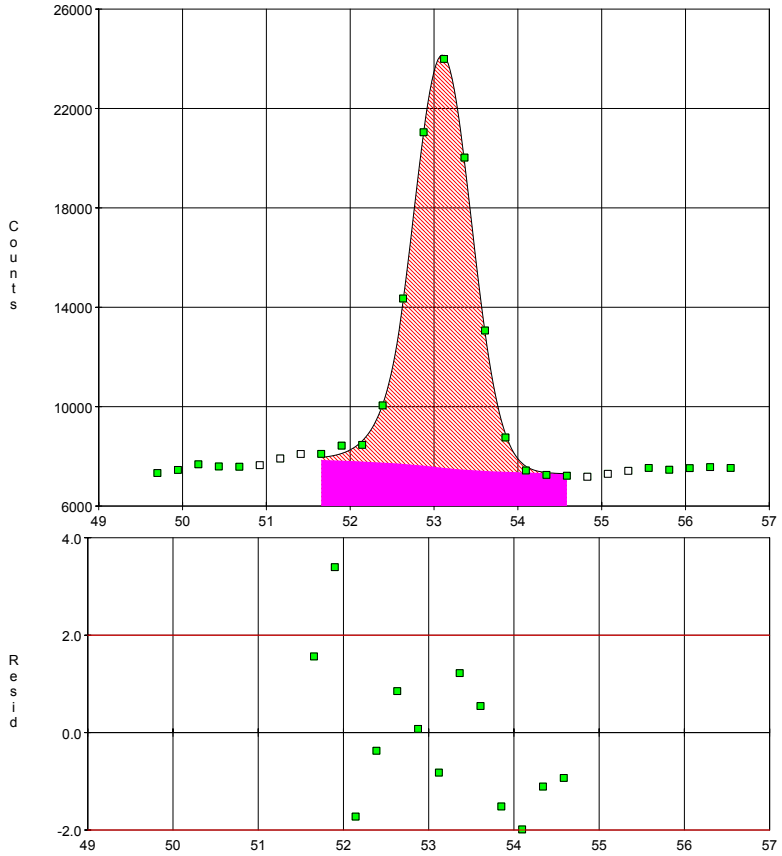

Datasource : C:\GENIE2K\CAMFILES\Detector Maintenance\cal R01107a_P5-01.CNF
Sample ID : cal 20mL far Iterations : 2
Sample Date : 2016-09-22 8:15:00 PM Chi-square : 4.47
Fit Engine : VMS Standard Peak Search Fit Region Start : 78.518 keV
Bkgnd Type : Step Region End : 82.670 keV

Nbr	Energy	Centroid	Area	%Error	FWHM	Ratio
1	79.609	325.47	77969.36	1.44	0.857	1.09
2	80.988	331.11	947035.56	0.13	0.830	1.05

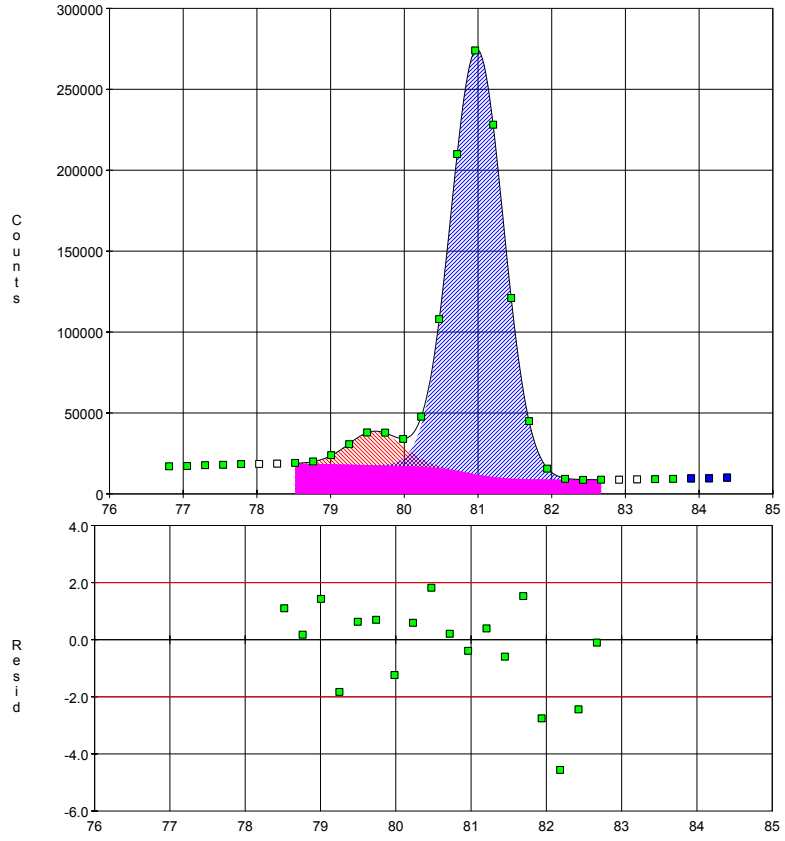

Datasource : C:\GENIE2K\CAMFILES\Detector Maintenance\cal R01107a_P5-01.CNF
Sample ID : cal 20mL far Iterations : 20
Sample Date : 2016-09-22 8:15:00 PM Chi-square : 16.17
Fit Engine : Sum / Non-Linear LSQ Fit Region Start : 120.528 keV
Bkgnd Type : Step Region End : 123.703 keV

Nbr	Energy	Centroid	Area	%Error	FWHM	Ratio
1	121.797	498.20	786961.00	0.30	0.865	1.00
2	122.928	502.83	9598.58	3.67	0.867	1.00

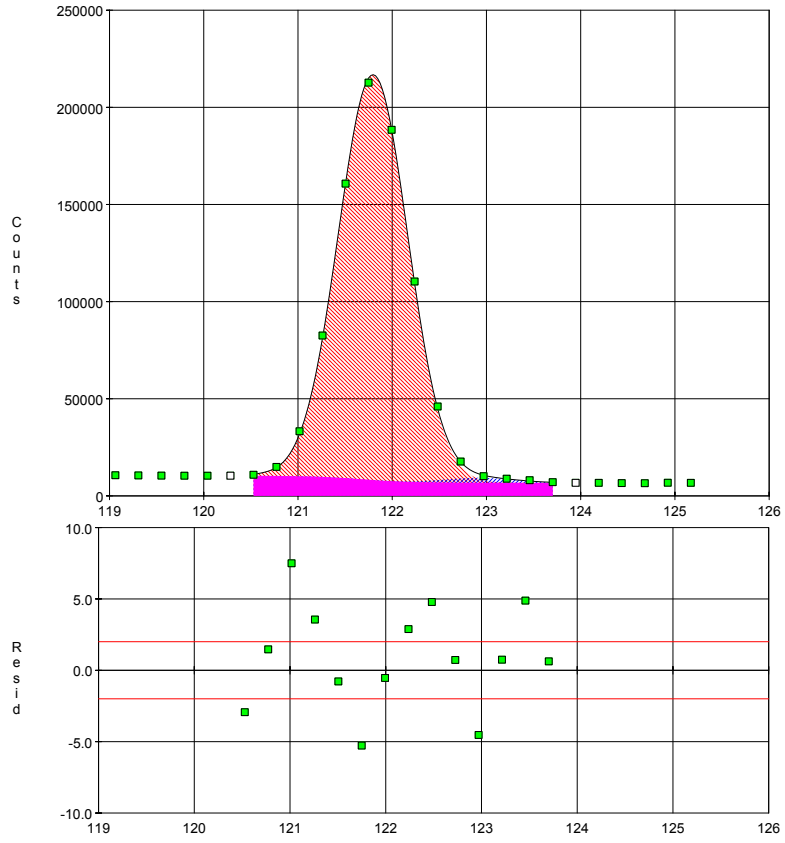

Datasource : C:\GENIE2K\CAMFILES\Detector Maintenance\cal R01107a_P5-01.CNF
Sample ID : cal 20mL far Iterations : 1
Sample Date : 2016-09-22 8:15:00 PM Chi-square : 5.60
Fit Engine : VMS Standard Peak Search Fit Region Start : 243.154 keV
Bkgnd Type : Step Region End : 246.330 keV

Nbr	Energy	Centroid	Area	%Error	FWHM	Ratio
1	244.716	1001.37	127079.59	0.54	1.029	1.00

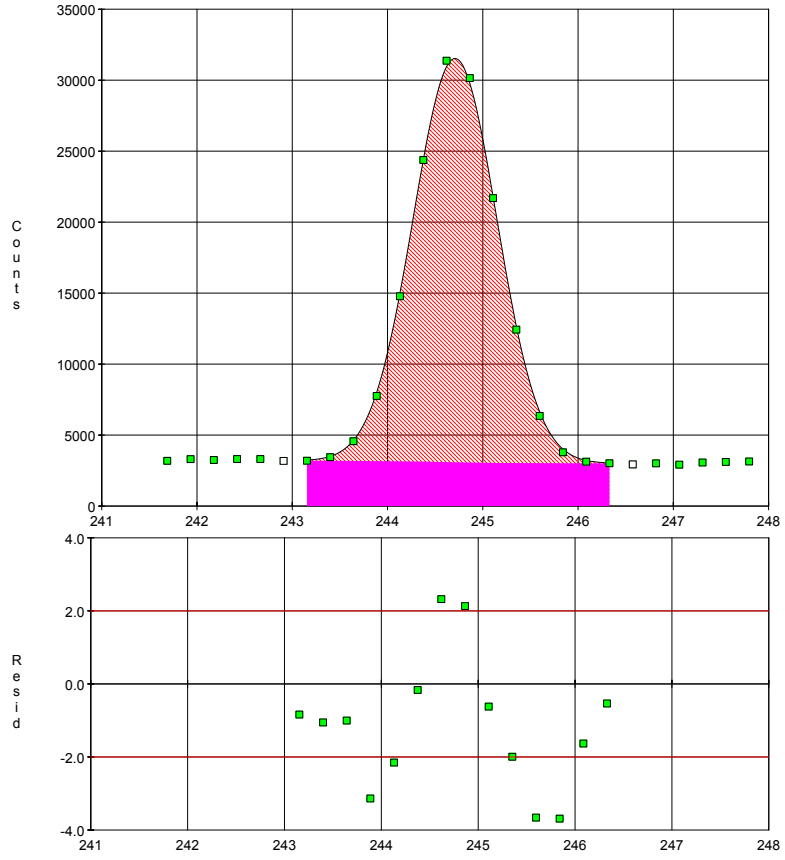

Datasource : C:\GENIE2K\CAMFILES\Detector Maintenance\cal R01107a_P5-01.CNF
Sample ID : cal 20mL far Iterations : 12
Sample Date : 2016-09-22 8:15:00 PM Chi-square : 1.30
Fit Engine : Sum / Non-Linear LSQ Fit Region Start : 300.811 keV
Bkgnd Type : Step Region End : 304.475 keV

Nbr	Energy	Centroid	Area	%Error	FWHM	Ratio
1	302.850	1239.35	246015.23	0.42	1.068	0.98

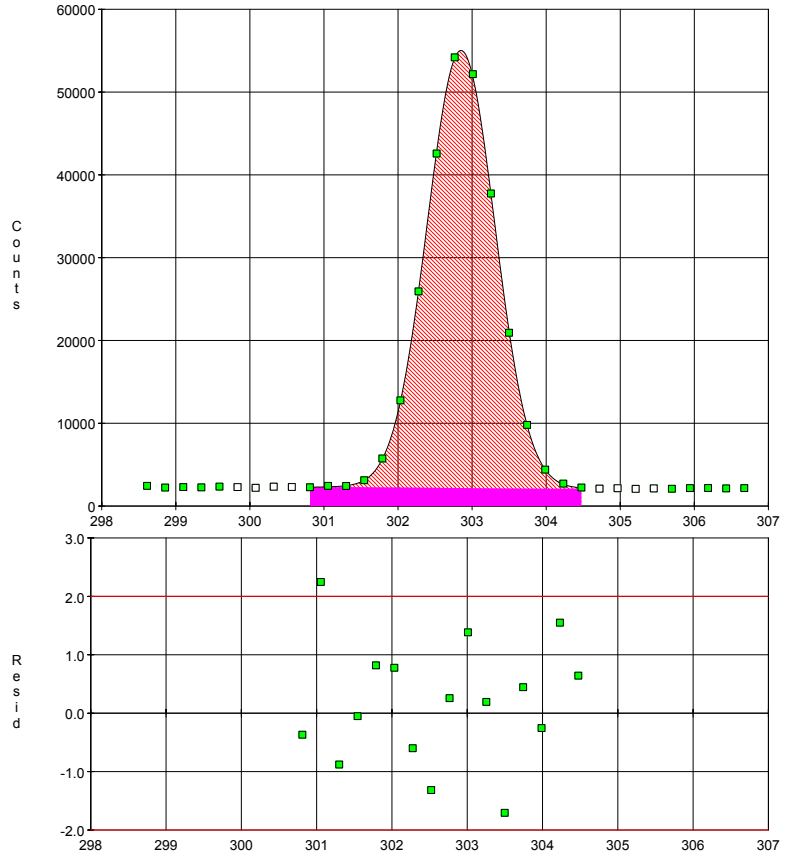

Datasource : C:\GENIE2K\CAMFILES\Detector Maintenance\cal R01107a_P5-01.CNF
Sample ID : cal 20mL far Iterations : 12
Sample Date : 2016-09-22 8:15:00 PM Chi-square : 2.95
Fit Engine : Sum / Non-Linear LSQ Fit Region Start : 342.590 keV
Bkgnd Type : Step Region End : 346.011 keV

Nbr	Energy	Centroid	Area	%Error	FWHM	Ratio
1	344.276	1408.90	311955.56	0.34	1.108	0.98

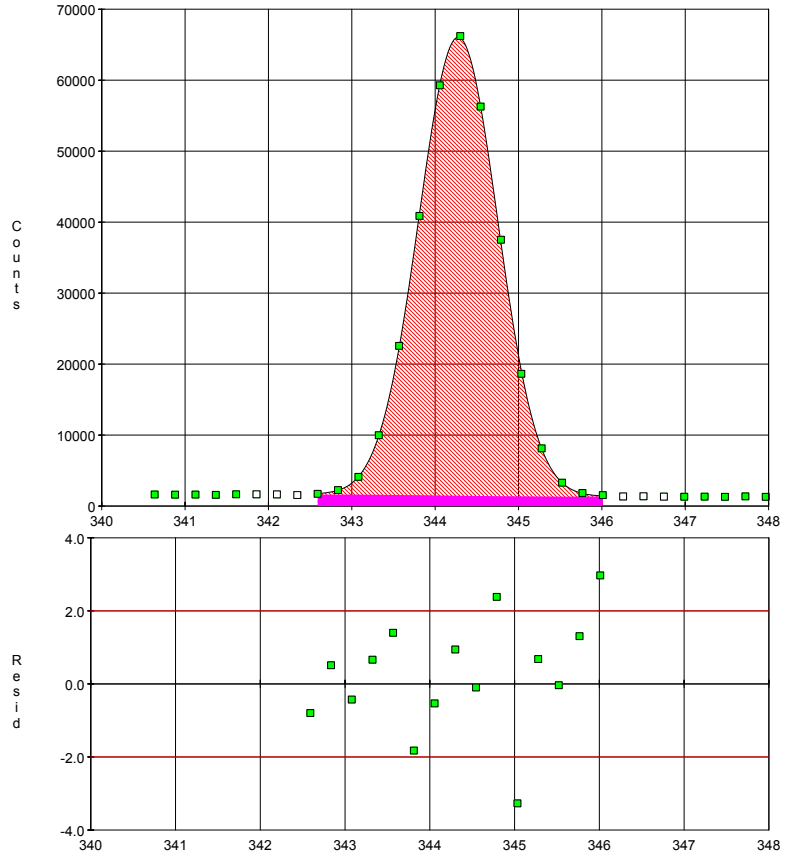

Datasource : C:\GENIE2K\CAMFILES\Detector Maintenance\cal R01107a_P5-01.CNF
Sample ID : cal 20mL far Iterations : 13
Sample Date : 2016-09-22 8:15:00 PM Chi-square : 1.72
Fit Engine : Sum / Non-Linear LSQ Fit Region Start : 354.074 keV
Bkgnd Type : Step Region End : 357.983 keV

Nbr	Energy	Centroid	Area	%Error	FWHM	Ratio
1	356.010	1456.92	699148.38	0.17	1.120	0.98

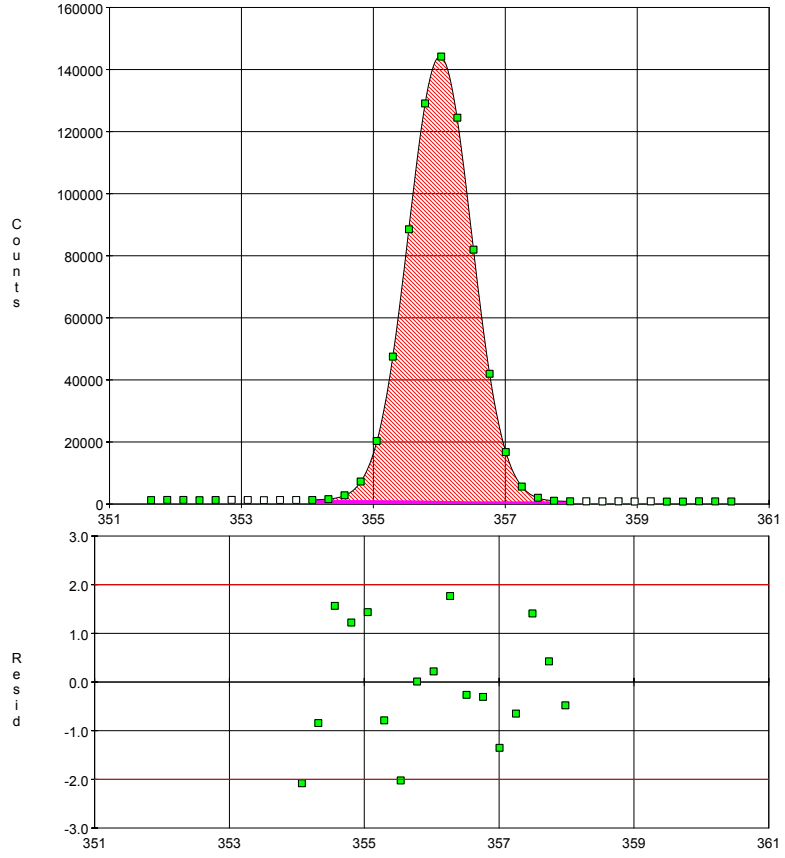

Datasource : C:\GENIE2K\CAMFILES\Detector Maintenance\cal R01107a_P5-01.CNF
Sample ID : cal 20mL far Iterations : 10
Sample Date : 2016-09-22 8:15:00 PM Chi-square : 1.84
Fit Engine : Sum / Non-Linear LSQ Fit Region Start : 381.928 keV
Bkgnd Type : Step Region End : 385.349 keV

Nbr	Energy	Centroid	Area	%Error	FWHM	Ratio
1	383.835	1570.80	92059.26	0.64	1.134	0.97

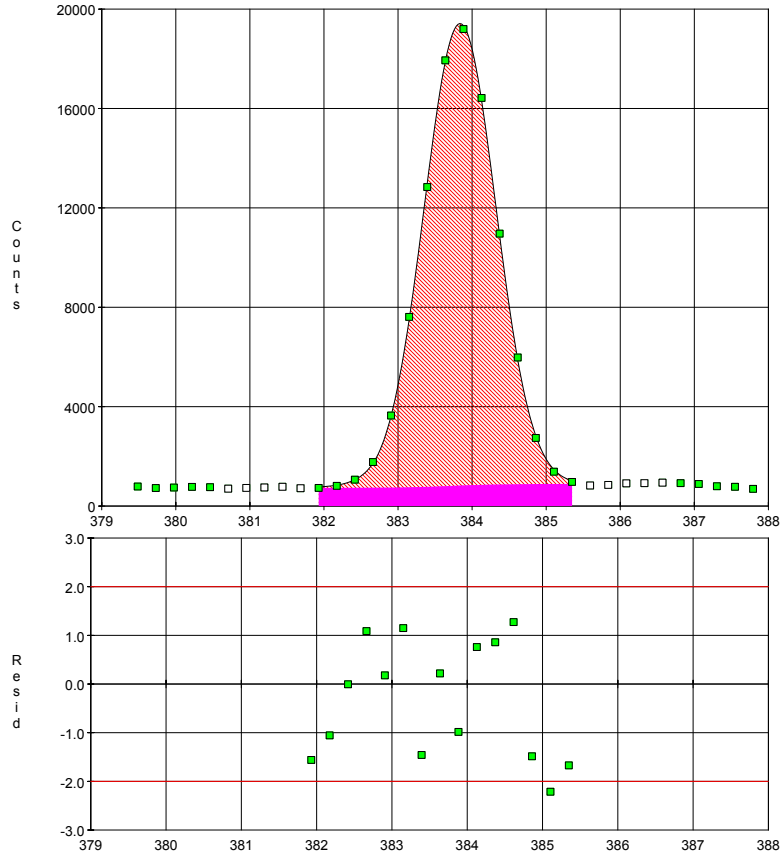

```
Datasource  : C:\GENIE2K\CAMFILES\Detector Maintenance\cal R01107a_P5-01.CNF
Sample ID   : cal 20mL far                  Iterations   : 1
Sample Date : 2016-09-22  8:15:00 PM       Chi-square   : 2.60
Fit Engine  : VMS Standard Peak Search Fit  Region Start : 409.051 keV
Bkgnd Type  : Step                         Region End   : 412.960 keV

Nbr      Energy  Centroid        Area  %Error     FWHM    Ratio
  1     411.147   1682.44    21809.62    1.00    1.194     1.00
```

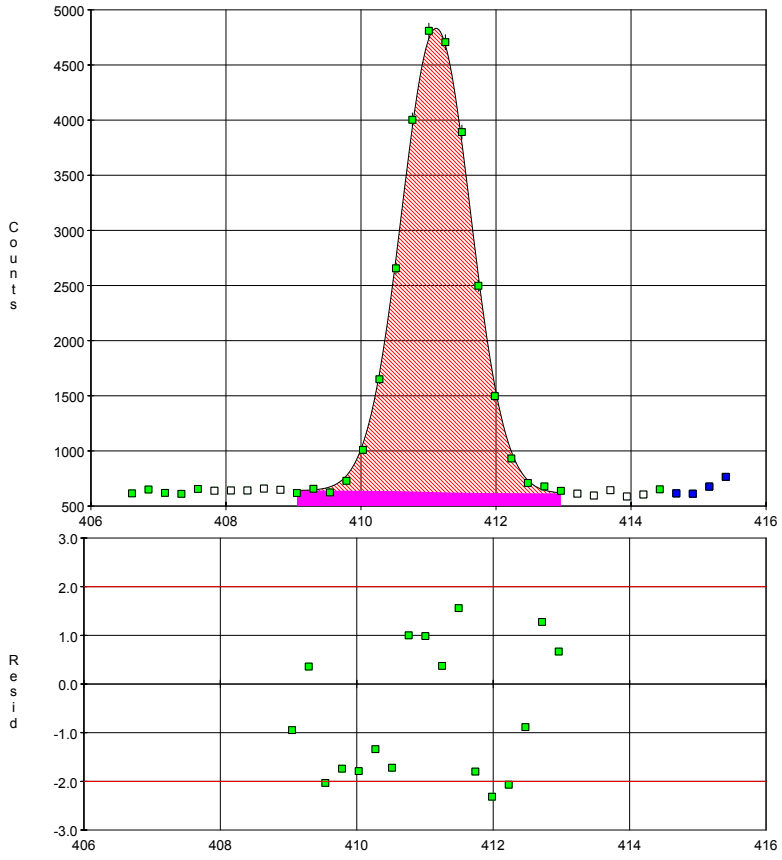

Datasource : C:\GENIE2K\CAMFILES\Detector Maintenance\cal R01107a_P5-01.CNF
Sample ID : cal 20mL far
Sample Date : 2016-09-22 8:15:00 PM
Fit Engine : Sum / Non-Linear LSQ Fit
Bkgnd Type : Step

Iterations : 10
Chi-square : 2.16
Region Start : 776.350 keV
Region End : 781.238 keV

Nbr	Energy	Centroid	Area	%Error	FWHM	Ratio
1	778.959	3187.68	66625.45	0.80	1.528	1.04

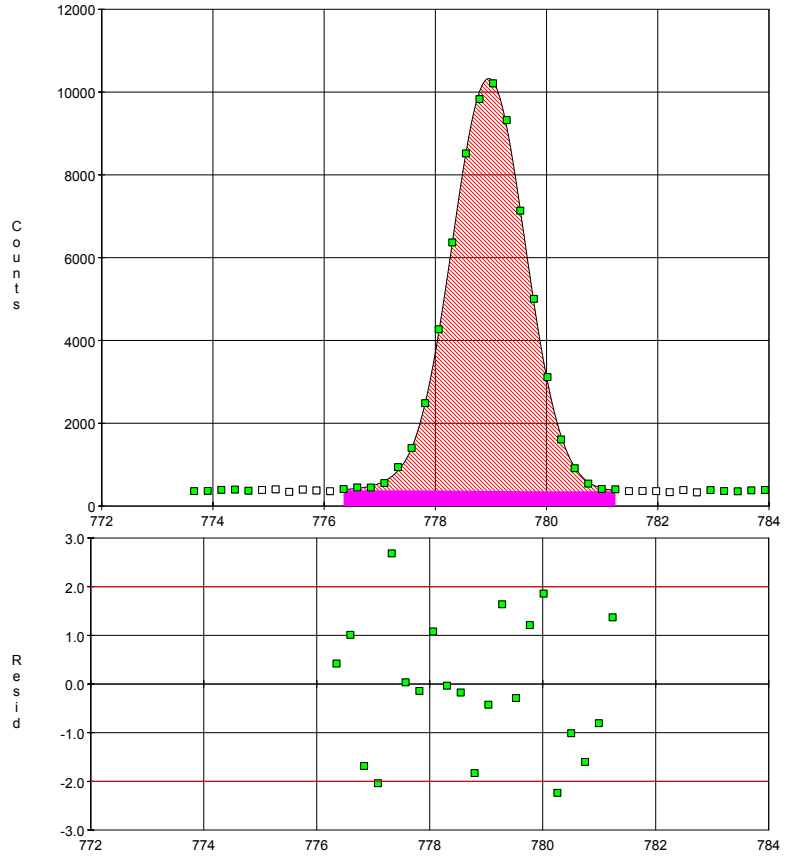

Datasource : C:\GENIE2K\CAMFILES\Detector Maintenance\cal R01107a_P5-01.CNF
Sample ID : cal 20mL far
Sample Date : 2016-09-22 8:15:00 PM
Fit Engine : Sum / Non-Linear LSQ Fit
Bkgnd Type : Step

Iterations : 12
Chi-square : 1.25
Region Start : 864.818 keV
Region End : 869.951 keV

Nbr	Energy	Centroid	Area	%Error	FWHM	Ratio
1	867.456	3549.79	19807.60	2.17	1.619	1.06

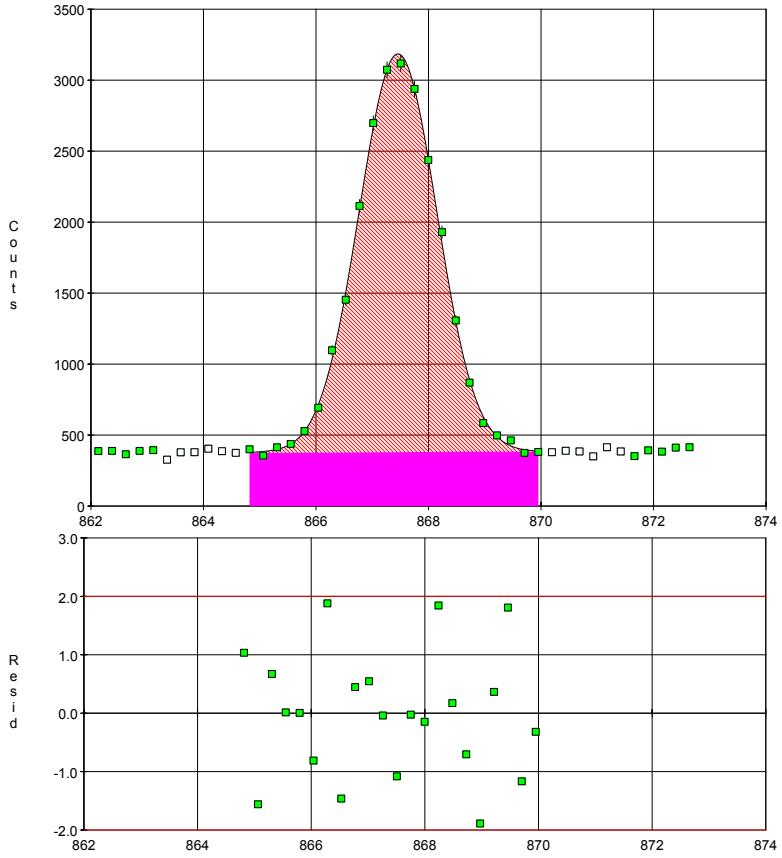

Datasource : C:\GENIE2K\CAMFILES\Detector Maintenance\cal R01107a_P5-01.CNF
Sample ID : cal 20mL far
Sample Date : 2016-09-22 8:15:00 PM
Fit Engine : Sum / Non-Linear LSQ Fit
Bkgnd Type : Step

Iterations : 11
Chi-square : 1.23
Region Start : 1082.064 keV
Region End : 1092.572 keV

Nbr	Energy	Centroid	Area	%Error	FWHM	Ratio
1	1085.80	4443.30	38682.43	0.92	1.802	1.09
2	1089.71	4459.32	6634.42	1.59	1.804	1.09

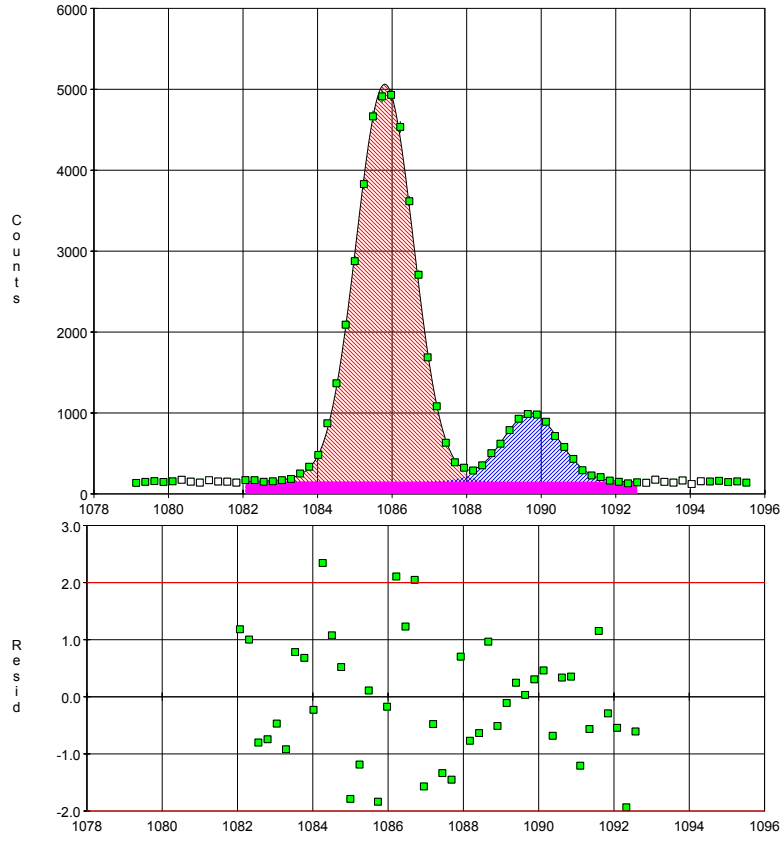

```
Datasource  : C:\GENIE2K\CAMFILES\Detector Maintenance\cal R01107a_P5-01.CNF
Sample ID   : cal 20mL far                  Iterations   : 10
Sample Date : 2016-09-22  8:15:00 PM       Chi-square   : 1.47
Fit Engine  : Sum / Non-Linear LSQ Fit     Region Start : 1108.943 keV
Bkgnd Type  : Step                         Region End   : 1115.051 keV

Nbr      Energy  Centroid        Area  %Error     FWHM    Ratio
  1     1112.05   4550.75    50832.14    0.92    1.806     1.09
```

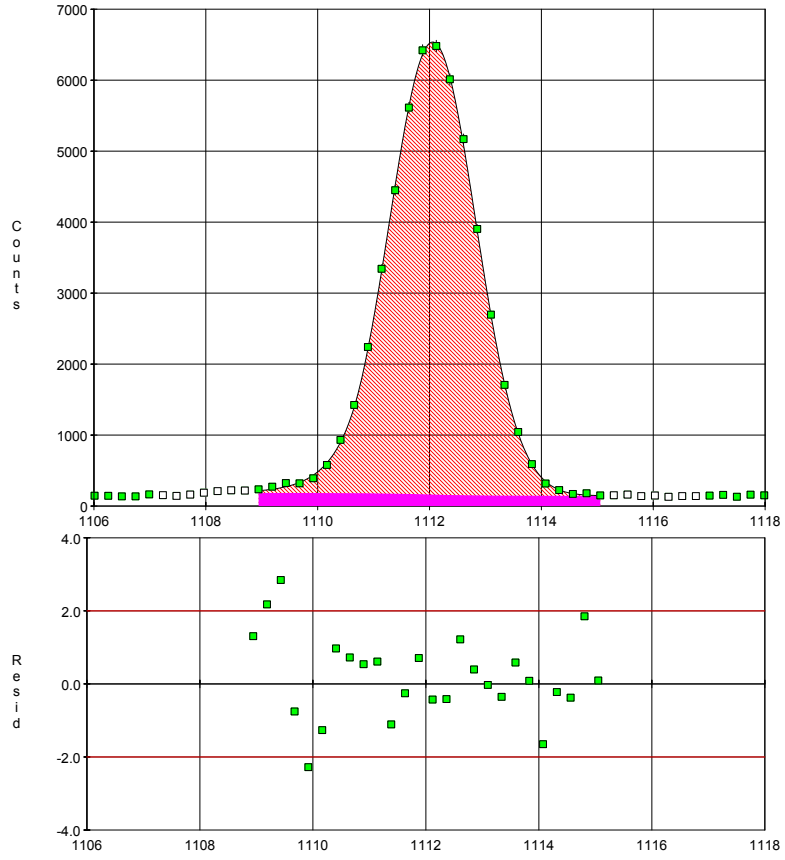

Datasource : C:\GENIE2K\CAMFILES\Detector Maintenance\cal R01107a_P5-01.CNF
Sample ID : cal 20mL far
Sample Date : 2016-09-22 8:15:00 PM
Fit Engine : Sum / Non-Linear LSQ Fit
Bkgnd Type : Step

Iterations : 12
Chi-square : 0.77
Region Start : 1296.334 keV
Region End : 1302.441 keV

Nbr	Energy	Centroid	Area	%Error	FWHM	Ratio
1	1299.15	5316.55	5420.52	3.10	1.990	1.13

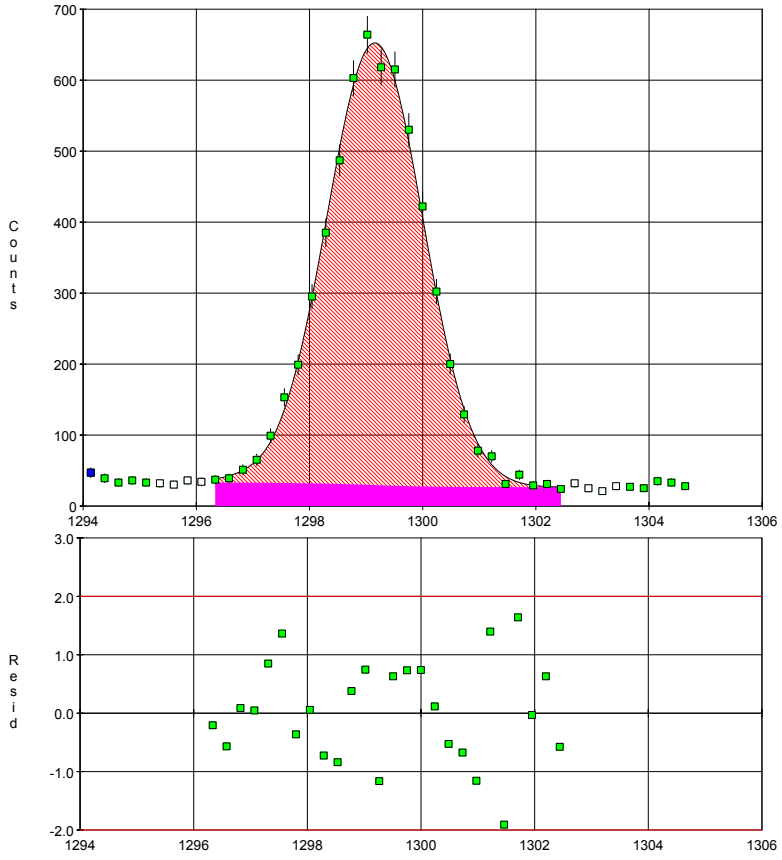

Datasource : C:\GENIE2K\CAMFILES\Detector Maintenance\cal R01107a_P5-01.CNF
Sample ID : cal 20mL far
Sample Date : 2016-09-22 8:15:00 PM
Fit Engine : Sum / Non-Linear LSQ Fit
Bkgnd Type : Step

Iterations : 10
Chi-square : 2.78
Region Start : 1404.786 keV
Region End : 1411.625 keV

Nbr	Energy	Centroid	Area	%Error	FWHM	Ratio
1	1408.02	5762.28	62844.36	0.59	2.083	1.15

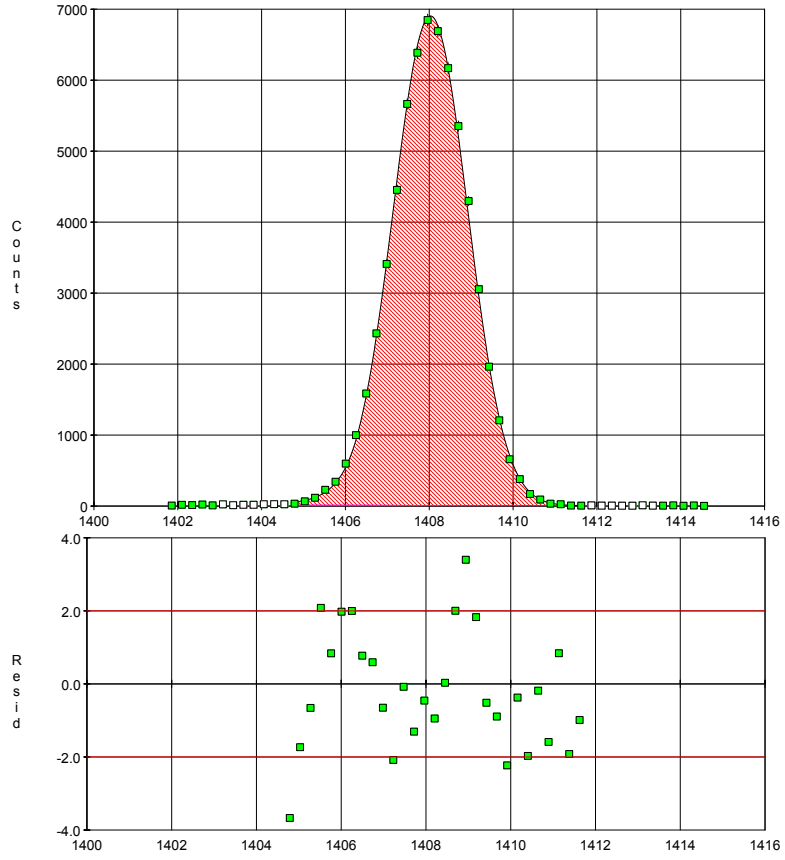

A.8 List of ^{133}Ba and ^{152}Eu Calibration Sources

R-#	Description	Activity
R-01106	Stock ^{133}Ba solution, (5.108 ± 3%) kBq/mL on 2016-06-01	(102.3 ± 3.1) kBq at time of purchase
R-01107	Stock ^{152}Eu solution, (5.157 ± 3%) kBq/mL on 2016-06-01	(103.4 ± 3.1) kBq at time of purchase
R-01107a	20 mL vial containing 20 mL volume	(30.05 ± 0.90) kBq of ^{133}Ba (30.23 ± 0.91) kBq of ^{152}Eu
R-01107b	20 mL vial containing 20 mL volume	(1.505 ± 0.045) kBq of ^{133}Ba (1.515 ± 0.045) kBq of ^{152}Eu
R-01107c	HPLC vial containing 1.5 mL volume	(1.507 ± 0.045) kBq of ^{133}Ba (1.520 ± 0.046) kBq of ^{152}Eu

Table A.1: List of calibration sources belonging to TRIUMF Life Sciences group used for the calibration of the detector. All activity values refer to the activity on 2016-06-01.

B Alpha Spectroscopy Procedures

TRIUMF Document-174953

Quantitative Alpha Spectroscopy of ^{225}Ac: Standard Operating Procedure

Document Type: Operating Procedures

Release: 1 **Release Date:** 2019-10-07

Author(s): Brooke McNeil, Andrew Robertson

	Name:	Approval Record
Author:	Brooke McNeil	
Approved By:	Andrew Robertson	

History of Changes

Release Number	Date	Description of Changes	Author(s)
1	2019-10-07	Initial Release	Brooke McNeil, Andrew Robertson

Keywords: Alpha spectrometer, microprecipitation, cerium fluoride, ^{225}Ac, HF

Distribution List: Brooke McNeil, Andrew Robertson, Paul Schaffer, Valery Radchenko, Caterina Ramogida, Vicky Hannemaayer, Hua Yang

1 Scope

The following document describes how to perform microprecipitation to determine ^{225}Ac activity on the ORTEC alpha spectrometer. Microprecipitation is a common method used to allow for the measurement of actinides by alpha spectrometry. In the microprecipitation method, a stable carrier, with a mass of tens to hundreds of micrograms, is added so that the insoluble carrier precipitate, which is cerium fluoride in the following described method, aids the precipitated analyte, present in much smaller quantities (mBq to Bq), to be captured by the filter rather than be lost in vacuum filtration. Microprecipitation is useful for alpha spectroscopy as the sample layer formed is thin, which prevents self-absorption of alpha particles in the sample material.

2 Safety

2.1 PPE requirements

Personal protective equipment necessary for the purification procedure includes:

- Lab coat
- Safety glasses
- Gloves (Double, thick nitrile) and sleeve protectors
- Fume hood

2.2 Training requirements

Required training:

- Chemical Safety
- Lab Safety
- WHMIS
- Advanced Radiation Protection
- HF Handling
- Alpha Radiation

Workers must be designated as a Nuclear Energy Worker and must have completed forty hours of supervised training prior to handling ^{225}Ac.

2.3 Safety Requirements

This procedure involves the use of concentrated hydrofluoric acid. Consults SDS and HF handling SOP prior to performing this procedure.

3 Materials

3.1 Apparatus

- Falcon tubes (15 mL)
- Tweezers
- Transfer pipets
- Heat lamp
- Funnel apparatus
- Clamp
- Vacuum flask
- Vacuum
- Double sided tape
- Resolve filter – 0.1 µm 25 mm polypropylene (Eichrom part: RF-100-25PP01)

3.2 Reagents and Solutions

All reagents should be made using MilliQ water.

- 500 µg/mL Ce carrier (3.570 mM cerium nitrate hexahydrate)
- 80% ethanol
- 100% ethanol
- Hydrofluoric acid (49%)
- 0.05 M HNO_3

4 Microprecipitation Procedure[1]

1. To a solution of ^{225}Ac, using 0.05 M HNO_3, dilute such that the concentration is 1-10 Bq/µL.

2. To a 15 mL Falcon tube, add 100 µL of the ^{225}Ac solution and then make the volume up to 10 mL with 0.05 M HNO_3.

3. Add 200 µL of the cerium carrier solution (100 µg Ce) and 1 mL of concentrated (49%) hydrofluoric acid to the tube.

4. Vortex and allow the solution to mix for at least 30 minutes before filtering.

5. Set up the vacuum apparatus as shown below in Figure 1.

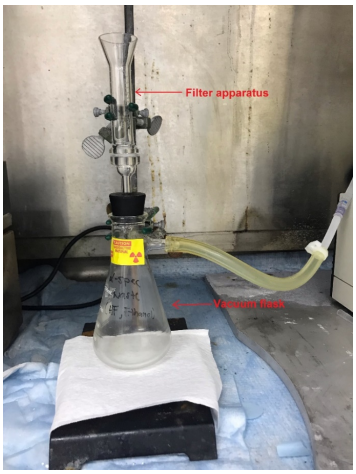

Fig. 1. Vacuum apparatus set up for microprecipitation

[1]For information on assaying other elements, refer to the Eichrom procedure, "Rare Earth Fluoride Microprecipitation", Method No. SPA01.

6. Place a Resolve filter (White filter located between two blue protective sheets) onto the filter apparatus and lower the funnel apparatus and use a clamp to secure the two apparatuses.

7. Apply vacuum (10 in. Hg) and use a transfer pipet to add 5 mL of 80% ethanol to condition the filter and allow all of the solution to pass through the filter.

8. Use a transfer pipet to add 3 mL of MilliQ water to the filter and allow all of the solution to pass through.

9. While continuously mixing the sample solution with the transfer pipet, add the sample to the filter. Once all of the sample has passed through, add 5 mL of MilliQ water to the used Falcon tube and then add to the filter. Allow the entire solution to pass through the filter.

10. Wash the sides of the funnel apparatus with 5 mL of MilliQ water followed by 3 mL of anhydrous ethanol once the solution has completely passed through. Run the vacuum for an additional 2 minutes to allow the filter to further try.

11. Turn off the vacuum and use tweezers to remove the filter from the filter apparatus. Place the filter in a dish and put under the heat lamp for approximately 3 minutes or until it is dry which can be observed by it turning from a dull grey to bright white in colour. Once dry, remove from heat to prevent overheating and wrinkling of the filter.

12. Allow the sample to reach transient equilibrium (At least overnight) before measuring on the alpha spectrometer.

5 Measurement on the Alpha Spectrometer

The following instructions are based on the ORTEC Soloist Alpha Spectrometer and for use with the Alpha Acquisition and Analysis Software. Figure 2 shows the set-up of the alpha spectrometer.

Fig. 2. ORTEC Soloist Alpha Spectrometer

The main components of the alpha spectrometer include the detector, vacuum chamber (Figure 3), pulser control, and vacuum control.

1. Plug in the vacuum and turn the vacuum control dial to vent (Setting shown in Figure 2).

2. Open the vacuum chamber door, which is shown below in Figure 3.

Fig. 3. Vacuum Chamber

3. Attach the filter, using double sided tape, to the sample holder, shown in Figure 4, and insert the sample holder into the second last slot from the detector, which is the gold cylinder shown at the top of the chamber in Figure 3.

Fig. 4. Sample Holder

5. Close the vacuum chamber door and ensure it is sealed. If it is not sealing, apply vacuum grease around the O ring using a KimWipe and wipe away any excess. Turn the vacuum control dial to pump.

6. Allow the sample to be pumped down for at least one minute.

7. In the alpha spectrometer software (Alpha Analysis and Acquisition), enter in the sample details by clicking the  icon, as shown in Figure 5 below.

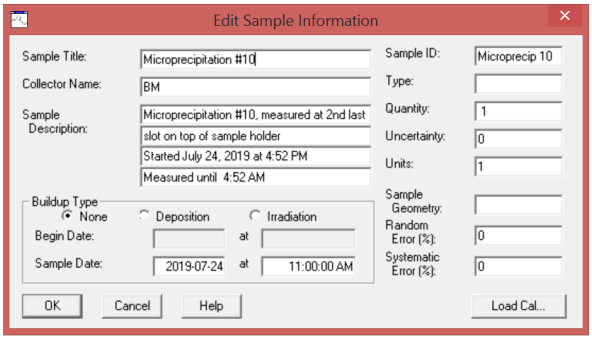

Fig. 5. Example Sample Information for a Microprecipitation Sample

8. To load the correct calibration files in the sample info, click “Load Cal”, found in the right bottom corner in Figure 5, and select “alpha_P09.CAL” and the efficiency calibration box to select this file for the efficiency calibration, as shown below in Figure 6, and then click load. To load the energy calibration, select “alpha_enerCal_temp.CAL” and the energy calibration box and then click load.

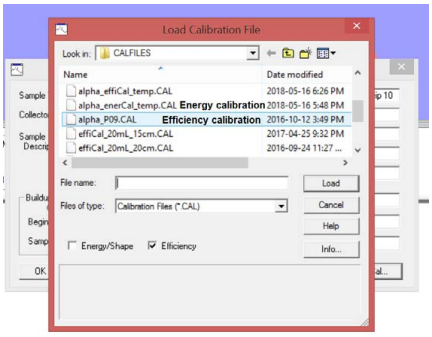

Fig. 6. Alpha spectrometer calibration files

9. To edit the counting time, click on the icon and enter the desired counting time.

10. Under acquire, click start to begin counting the sample and allow to count for the desired amount of time. An alpha spectrum for the Ac-225 decay chain should appear as shown below in Figure 7.

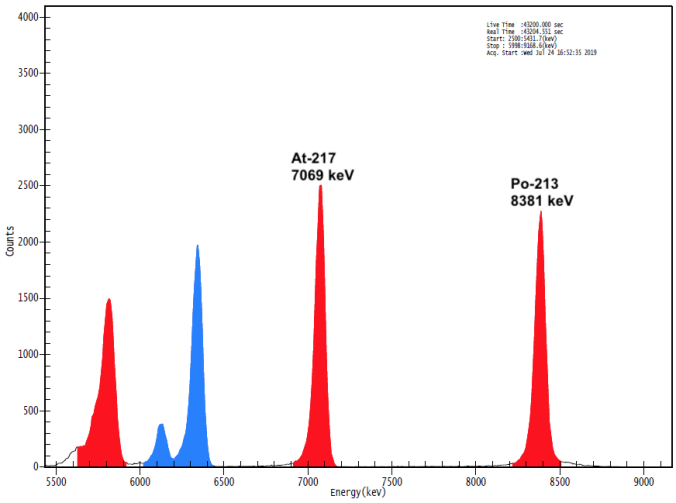

Fig. 7. Alpha Spectrum of ^{225}Ac Decay Chain

11. Once the sample has finished counting, click “Analyze” and then select “Execute Sequence” and then select “Ac-225 ALPHA”, as shown below in Figure 8.

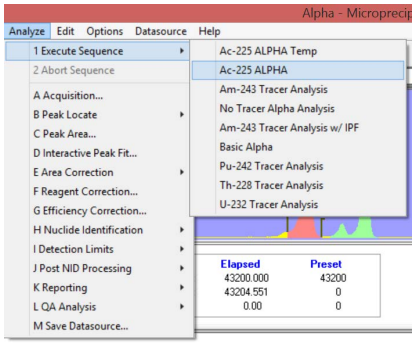

Fig. 8. Analysis of Alpha Spectrometer Data

12. The analysis sequence will generator a report that identifies the radionuclides and their activity in the sample.

13. The final amount of ^{225}Ac in the sample, assuming transient equilibrium of the decay chain during the measurement, is calculated by taking the output value for the ^{217}At peak and multiplying by the filtration efficiency of (53.0 $\pm$ 3.8)%. See Section 6 for more details on how this efficiency was determined.

6 Analysis sequence

The Ac-225 ALPHA analysis sequence settings are shown in Figures 9 to 14.

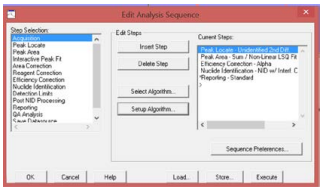

Fig. 9. Analysis sequence steps

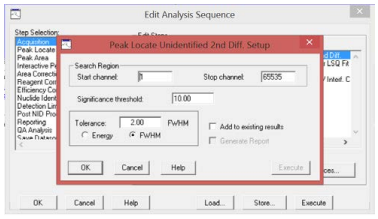

Fig. 10. Peak Locate Unidentified Second Difference settings

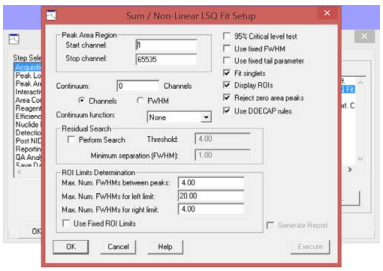

Fig. 11. Sum/Non-Linear LSQ Fit Settings

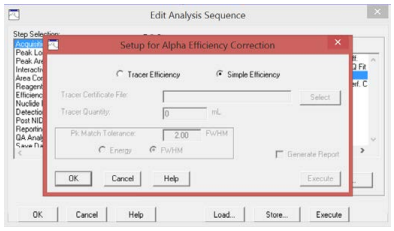

Fig. 12. Efficiency Correction Alpha Settings

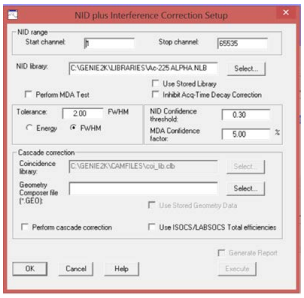

Fig. 13. Nuclide Identification – NID with Interference Correction Settings

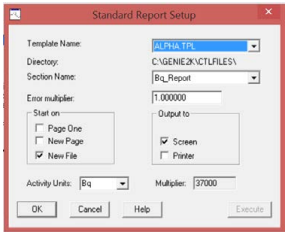

Fig. 14. Standard Report Settings

7 Analysis and Microprecipitation Efficiency

To determine the efficiency of the microprecipitation method, the gamma spectrometer was used to determine the activity present initially in the sample solution and the activity found in the wash. The analysis sequence used was "Ac-225 and Ra-225." It was determined that the initial activity in the sample solution was (146.5 $\pm$ 5.5) Bq (via ^{221}Fr) and thus if the microprecipitation method was 100% efficient, approximately (146.5 $\pm$ 5.5) Bq would be expected to be found in the alpha sample.

When the filters were counted in the alpha spectrometer until the activity uncertainty reached below 5% and the "Ac-225 ALPHA" analysis sequence with

the previously mentioned calibration settings were used, it was determined that the average (n =10) measured activity in the microprecipitation sample was (80.9 ± 3.2) Bq of ^{217}At and (85.2 ± 4.0) Bq of ^{213}Po.

To determine if it was an issue of microprecipitation efficiency or alpha spectrometer calibration settings, the wash fractions of the microprecipitation procedure were collected and counted on the gamma spectrometer. It was determined that the activity in the wash was (68.9 ± 0.3) Bq, which corresponds to (47.0 ± 3.8)% of the initial activity and thus the microprecipitation efficiency was (53.0 ± 3.8)%.

C Safety Analysis Report for Irradiation of Thorium Targets

Safety Report

L124: Irradiation of Thorium Targets at the TRIUMF 500 MeV Isotope Production Facility

authored by Andrew K. H. Robertson

August 27, 2018

CONTENTS

1 IDENTIFICATION

Experiment L124: Irradiation of Thorium Targets at the TRIUMF 500 MeV Isotope Production Facility

The experiment spokespersons Andrew Robertson, Keith Ladouceur, Cornelia Hoehr, and Paul Schaffer. The experiment safety coordinator is Andrew Robertson. The experimental users are Andrew Robertson and Louis Moskven.

Andrew Robertson TRIUMF Life Sciences
4004 Wesbrook Mall, Vancouver BC
arobertson@triumf.ca
604 222 1047 ext. 6733 (office)
778 228 7471 (cell)

2 INTRODUCTION

2.1 Background

Targeted alpha therapy (TAT) shows high potential as an effective treatment option for small tumours and metastases [1]. Actinium-225 ($t_{1/2}$ = 9.92 d) is a promising TAT radionuclide, which can be used directly in combination with biomolecules or as a generator source of the shorter TAT radionuclide, bismuth-213 ($t_{1/2}$ = 45.6 min). Development of ^{225}Ac and ^{213}Bi radiopharmaceuticals has progressed slowly due to the limited availability and the resulting high cost of these isotopes. Global annual ^{225}Ac production is approximately 63 GBq (1.7 Ci) [2–6].

2.2 Scope

In coordination with L125 [7], experiment L124 aims to develop regular production and processing of clinically relevant quantities of ^{225}Ac (100 mCi, or 3.7 GBq) and ^{213}Bi and potentially other valuable medical radionuclides at TRIUMF using irradiation facilities at the 500 MeV Isotope Production Facility (IPF) on beamline 1A (BL1A) and processing facilities in the MHESA RCR1 lab. While the scope of L125, *Isolation of Medical Isotopes from Irradiated Thorium Metal Targets*, concerns the processing of medical isotopes from irradiated thorium targets, this experiment covers the target fabrication and irradiation at IPF. In other terms, L124 begins when the radioactive thorium metal is added to the target during its manufacture and ends when the irradiated target leaves the IPF hotcell.

These experiments are distinct so as to separate the safety review process for each stage of the project. In this manner, safety approval for irradiating thorium targets for possible shipment and processing off-site will be independent of safety approval for processing the targets on site.

2.3 Experimental Objectives

1. Produce clinically relevant quantities of actinium-225 (100 mCi, or 3.7 GBq)[1] from thorium metal irradiated with high energy (>450 MeV) protons

2.4 Impact Statement

This project leverages unique TRIUMF infrastructure to produce understudied and sought-after isotopes with potential to significantly aid the treatment of aggressive cancers. However, much remains to be understood about the chemistry and biology needed to attach ^{225}Ac or ^{213}Bi to biomolecules that specifically target and treat cancer. As a result, the use of ^{225}Ac and ^{213}Bi in TAT is an area of research that has great interest.

1 While the long-term experimental objective is to produce 100 mC (3.7 GBq) i of ^{225}Ac per irradiation, the first irradiation described in this review is for the production of ~12 mCi (440 MBq) of ^{225}Ac.

This work therefore has high translational potential, with the ability to enable other experiments at TRIUMF and other institutions that are otherwise be impractical due to the high cost and limited availability of ^{225}Ac and ^{213}Bi (current cost is a minimum purchase of 20 mCi (740 MBq) of ^{225}Ac for $35000). As such, this effort is expected to enable new collaborations between TRIUMF and other TAT research centres. A recent survey of experimenters in the TAT field suggests that demand for ^{225}Ac from researchers within Canada is at minimum 5.6 GBq (150 mCi) per month and growing.

The knowledge and experience with thorium target irradiation, target processing, and waste management that will be developed through L124 and L125 will directly support any future efforts at TRIUMF to scale up production to commercial quantities, as well as the future larger-scale ^{225}Ac production at ARIEL.

2.5 Previous L124 Irradiations

The first irradiation under the purview of L124 occurred in December 2016, and involved the irradiation of a thorium oxide test target receiving 2.5 µAh of beam. This irradiation was done in single-user mode and with T1 and T2 removed from BL1A. While not ideal for post-irradiation processing of the target, thorium oxide foils from the ISAC Target Group were incorporated into an IPF target. Since no other thorium sources were readily available at the time, the irradiation of this target was the most expedient way to demonstrate IPF's ability to produce ^{225}Ac from spallation of thorium. As such, the thorium oxide target was also sealed in a way that prevented the removal of the thorium post-irradiation. However, crude gamma spectroscopy measurements of the irradiated target indicated that the December 2016 irradiation met its objective of demonstrating the feasibility of ^{225}Ac production via proton spallation of thorium at IPF.

The next two L124 irradiations used a thorium metal design (see Document-148097*L124 Thorium Metal Target for IPF, Release 3*. Both targets were successfully irradiated (one in December 2017 and another in May 2018) with 2640 µAh of beam at typical BL1A high-current operating conditions (~100 µA). No damage to the target capsule or the thorium target material was observed after these irradiations.

3 DESCRIPTION

3.1 Location of Experiment

Manufacturing of the non-thorium components of the target capsule will take place in the TRIUMF Machine Shop, without any thorium present. Since this portion of the manufacturing is standard work for the Machine Shop, it is covered by their internal safety standards and practices and not by this safety review.

Preparation of the thorium foils will occur inside a glovebox in the RCR1 (MHESA B1 level).

Sealing of the thorium foils within the target capsule will be conducted in the TRIUMF Machine Shop. Post-manufacturing tests of the target will also be conducted in ATG workspaces.

Irradiation of the targets will then take place at the 500 MeV Isotope Production Facility (IPF) located near the end of BL1A, as shown in Fig. 1. After irradiation, the targets will remain in the IPF hotcell for one week to permit the decay of short-lived radioisotopes.

3.2 The 500 MeV Isotope Production Facility

Irradiation of the targets will occur at IPF, located near the end of BL1A (Fig. 1). Immediately upstream from the Thermal Neutron Facility (TNF), IPF is the second-last facility before the BL1A beam dump. The description and safety report of this facility is primarily contained in the Document-563, *TRIUMF Safety Report v.3 (2011)* [8], with further descriptions in earlier reports [9, 10]. The IPF was first conceptualized in 1978 (Fig. 2) [9].

Targets are inserted into the IPF hotcell by way of a shielded flask [11]. Within the target irradiation station there is space for six target cassettes; each cassette can hold a pair of targets. Independent chain

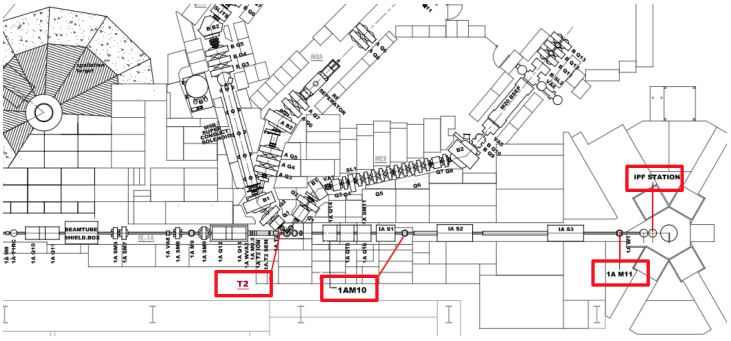

Figure 1: Beamline 1A layout with key beam diagnostic and target locations noted.

drives are used to insert and remove individual cassettes from the beam line. This can be performed whether the beam is on or off. The cassettes can be placed in three positions: in the proton beam, a "parked" position just above the beam, or in the IPF hotcell. The operators of the facility have considerable experience inserting and removing targets, including molybdenum targets, the more recent KCl targets [12], and the December 2016 L124 test thorium oxide target (see Section 2.5). As the target capsules for the thorium targets are nearly identical, there will be no difference in the handling procedures.

When cassettes are lowered into the proton beam, they are submerged in a volume of water and re-circulated water is injected into each cassette to cool the outer surface of the targets directly (see Fig. 3). The water also flows through an ion exchange resin to remove metal ions from the water. A minimum of four targets must be located in the beamline for the safety interlock conditions to be met. In the case where fewer than four targets are scheduled for irradiation, the remaining cassette spaces are filled with helium targets. As a single thorium target will be run during this irradiation, three helium targets will be inserted to meet the interlock requirements (helium targets are used to reduce the energy deposited into the cooling water, as each helium target in the beam occupies a volume that would otherwise be occupied by cooling water).

Thermocouples are used to measure the outer temperature of the target capsule and the temperature of the cooling water; the resistivity of the cooling water is also monitored. Protect monitors are used to monitor beam position, however, information on the beam profile at full current is not available since the nearest profile monitor, 1AM11 (Fig. 1), can only take $<$10 µA. Similarly, accurate current measurements at IPF cannot be obtained as the nearest current monitor, 1AM10 (Fig. 1), is located just after T2, roughly 15 m from IPF. Therefore, beam losses between T2 and IPF are not accounted for by 1AM10 readings.

3.3 Target Design and Manufacture

The target material consists of a thorium metal foil (60 mm diameter, 0.25 mm thickness, or 0.293 g/cm^2) supplied by IBI Labs (Boca Raton, Florida). The supplied foils currently have a significant oxide layer that will be removed before the targets are fabricated. The thorium metal foil is hermetically sealed within a target capsule consisting of a steel, ring-shaped body and 0.13 mm thick Inconel®-718 entrance and exit windows[2]. The outer dimensions of the target are approximately 10 cm diameter and 1 cm thickness. A schematic of the target is shown in Fig. 4. The target body is shaped to centre the thorium foil radially within the target and to also press it against the entrance window, facilitating improved cooling of the thorium foil via conduction through the window. Windows are attached to

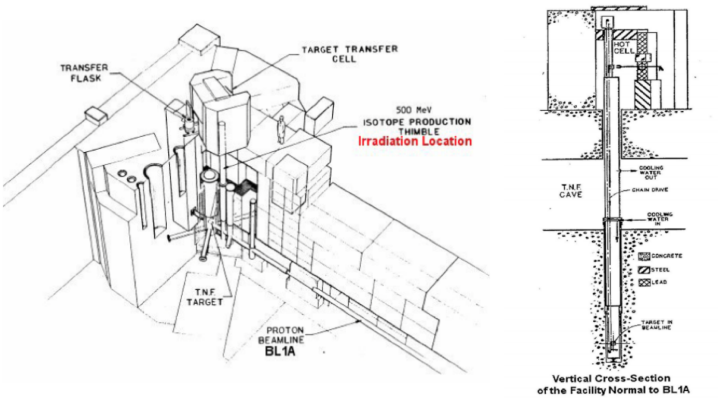

Figure 2: Diagrams of the 500 MeV Isotope Production Facility (IPF) [9].

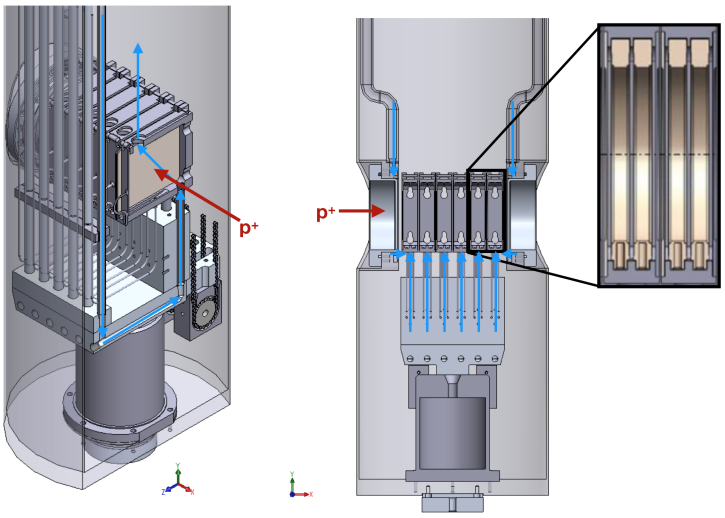

Figure 3: Diagrams of the IPF target station, with 6 cassettes at beam level. Inset image shows two targets per cassette. Blue arrows indicate cooling water flow; red arrows indicate proton beam direction [13].

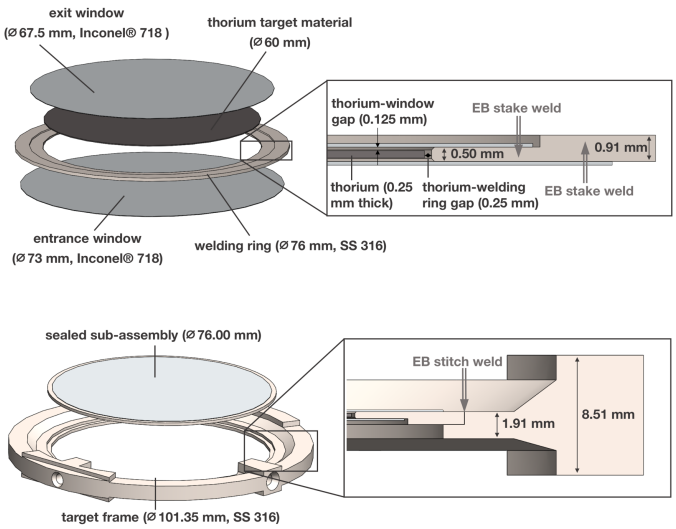

Figure 4: L124 target design.

the target body by electron-beam welding, the process of which also seals the thorium within the target capsule.

Sealing of the target with an electron-beam weld – which is conducted under vacuum – will ensure that the interior volume of the fabricated target is under vacuum.

After manufacturing, leak tests of the target will be conducted following standard ATG procedures for leak testing IPF targets.

Detailed description and analysis of the target design, manufacturing, and post-manufacture testing can be found in the design note, *L124 Thorium Metal Target for IPF* (Document-148097) [13].

3.4 Target Irradiation Parameters

The target will be irradiated at IPF under typical high-current BL1A beam parameters (480 MeV, ~100 µA at extraction or ~450 MeV, ~85 µA at IPF[3]) so that use of IPF can occur independent of the needs of other BL1A users. While the experiment ultimately aims to produce 3.7 GBq (100 mCi) quantities of ^{225}Ac, for this first initial production run the duration of the irradiation will be chosen such that approximately 440 MBq (12 mCi) of ^{225}Ac will remain in the target at 1 week after end of bombardment (EOB); this duration will be 2640 µA*h of beam on target. After the irradiation, the target will be removed from the beam and left inside the parked position within the IPF water column until they reach thermal equilibrium with the cooling water. After checking for signs of target failure (Section 3.2) and after taking and analyzing (via gamma spectroscopy) a sample of the IPF cooling water, the target will be raised to the IPF hotcell, where it will remain until one week after EOB, permitting the decay of short-lived radioisotopes before targets are removed from the IPF hotcell.

2 The composition of Inconel®-718 is as follows: 50.00-55.00% Ni, 17.00-21.00% Cr, 4.75-5.50% Nb, 2.80-3.30% Mo, 0.65-1.15% Ti, <1.00% Co, 0.20-0.80% Al, <0.35% Mn, <0.35% Si, <0.30%Cu, <0.08% C, <0.015% S, <0.015% P, <0.006% B, Fe remainder [14].

3 Beam losses between the cyclotron and IPF are approximately 15% with the short 12 mm T2 target [15]

During the initial irradiation of a new target design, commissioning tests on the target will be performed as described in *Commissioning Plan for Irradiation of L124 Thorium Metal Targets at IPF (Document-148095)* [16].

3.5 Target Failure Modes

As defined in *L124 Thorium Metal Target for IPF* (Document-148097) [13], an IPF target is classified as failed if the hermetic seal encapsulating the thorium foil is lost, or if the target body, entrance, or exit window is compromised before, during, or after irradiation. The thorium foil is not a safety-critical component from a failure modes perspective, so long as failure of this component does not result in failure of target windows or target body. Melting of the thorium would be considered among the worst failure paths, as temperatures would be well above safe limits for the Inconel windows of the target assembly. Excessive deformation, cracking, or pin-hole formation in the thorium foil is of limited danger to the target assembly.

4 DEFINITION OF HAZARDS

The hazards associated with this experiment are radiological hazards.

4.1 Methods Used for Estimation of Radiation Hazards

Estimates of the radioisotope inventory of the irradiated thorium targets were obtained using FLUKA simulations [17]. These simulations were performed by Andrew Robertson with guidance from Mina Nozar. The simulated radioactive inventory and resulting dose estimates presented in this document were based off of a 454 MeV, 55 μA, 48 hour irradiation, which produces 440 MBq (12 mCi) of ^{225}Ac one week after EOB. A Gaussian beam profile was used with a FWHM of 3.18 cm and 3.25 cm in the x and y directions, respectively; beam direction was set along the z-axis. The geometry included the target, as described in Section 3.3, as well as the cassettes, cooling water, and entrance window for the IPF target station. `NEW-DEFAULTS` default settings were used. Physics and transport settings were set to enable nuclear coalescence and evaporation, photonuclear interactions, and low-energy neutron transport and cross-sections. Production and transport thresholds were set to 30 keV for electrons, positrons, and gammas. A 100 keV proton energy transport threshold was also set. A 0.001 cm maximum step size was set for charged particles in the thorium foil; a 0.005 cm maximum was set for other regions. A total of 800 million primary particles were simulated. Note that the accuracy of these FLUKA simulations is limited due to the limited understanding of the beam parameters at the end of BL1A, since the nearest diagnostics are many metres upstream.

Given the estimated radioisotope inventory, dose rate estimates of the target were calculated using an Excel-based calculator developed by the TRIUMF Radiation Protection Group (RPG) that calculates gamma radiation dose rates – both with or without shielding – from a given isotope assuming a point source geometry. Comparison with dose rates determined via FLUKA simulation show these methods agree within <10% for unshielded dose rates at 1 m from the target.

Similar simulations and calculations conducted as part of L124 in 2016 using a thorium oxide test target were within 20% of all measurements of ^{225}Ac radioactivity and dose rate at 1 m from the target. This supports the reliability of these FLUKA simulations and dose calculations for approximating the radiation hazards associated with this experiment.

While some changes to the target design have been made since the FLUKA simulations were run, the changes are expected to negligibly affect the isotope inventory and resulting dose rates since the total mass and approximate radial distribution of thorium and steel (the components producing >99% of the dose rate from the target) has changed by <1%.

Internal and external dose estimates resulting from the worst-case release of volatile radioisotopes were calculated as described in TRIUMF Safety Analysis Reports (SARs) for ISAC targets: *Actinide Target Safety Analysis Report (Document-12972)* and *Actinide Target SAR Addendum for Thorium Oxide (Document-110961)* [18,19]. These documents contain dose estimates resulting from a worst-case release

of volatile radioisotopes from ISAC actinide targets. These calculations assume all volatile radioactive isotopes within the target become uniformly distributed within a sphere of 15 m radius and that a worker wearing no respiratory protection is located at the centre of the sphere for a duration of 30 minutes. This scenario ("Scenario C" described in Document-110961) assumes that all the radioactive air released through the ventilation systems is somehow drawn into an office building. Decay of short-lived isotopes and the dispersion of these radioactive gasses during the 30 minute exposure is neglected. It should be noted that this is an extremely conservative model.

Off-site dose estimates to members of the public resulting from a worst case release of volatile and gaseous radioisotopes were also calculated using the methods described the ISAC actinide target SARs [18, 19].

While *Actinide Target Safety Analysis Report (Document-12972)* and *Actinide Target SAR Addendum for Thorium Oxide (Document-110961)* guide the methodology for on-site and off-site airborne dose estimates described in this document, the following modifications were made to these methods to incorporate additional information gained in the years following their publication:

1. The ISAC SARs used a 1 minute half-life cut-off of for isotopes used in the calculations. However, ^{220}Rn ($t_{1/2} = 55.6$ s) has since been shown to be a real potential airborne dose hazard [20]. Dose calculations herein include ^{220}Rn. This results in a <1% change to the dose estimates.

2. TRIUMF is currently in the process of updating its Derived Release Limits (DRLs) – annual limits for radioactivity released into the environment – and defining Single-event Derived Release Limits (SDRLs) – limits for a single accidental release of radioactivity into the environment. The old SDRLs used in the ISAC actinide target SARs are considered outdated. SDRLs used in this document to estimate the off-site dose to members of the public resulting from a worst case release of radioisotopes were provided by RPG [21]. These SDRLs are listed in Appendix A.

3. When considering airborne radiation hazards resulting from an accidental release of radioactivity, one must consider which elements have the potential to become airborne. In the ISAC actinide target SARs, the volatile elements with potential to become airborne are: hydrogen, chlorine, argon, selenium, bromine, krypton, iodine, xenon, radon, and polonium [18, 19]. Using a conservative approach, the ISAC actinide target SARs also assume a 100% release of these isotopes. Dose calculations in this document closely follow this definition of relevant isotopes, but with extra attention paid to the chemical form and potential volatility of polonium isotopes, which results in polonium being excluded entirely from airborne dose calculations. Further details are provided in Section 4.1.1.

All values for Annual Limits on Intake (ALI) used in this document were obtained from the *Actinide Target SAR Addendum for Thorium Oxide* (Document-110961), unless otherwise specified [19].

4.1.1 *Assessment of Potential Release of Polonium Isotopes*

Relevant Literature

Polonium is known to be a potentially volatile isotope, however, the potential for polonium to become airborne depends greatly on its chemical and physical form. When calculating airborne dose estimates, the ISAC actinide target SARs conservatively assume polonium isotopes to be 100% volatile [18, 19]. However, making the same assumptions for this report results in estimated airborne on-site and off-site worst case doses that are, respectively, 92.7% and 99.8% attributable to polonium isotopes. Therefore, special consideration is made in this document regarding the potential of polonium to be volatile at various stages of the experiment so that more realistic dose estimates can be made.

As a hazardous radioactive (and most often alpha-emitting) element with no stable isotopes, the chemistry of polonium has not been extensively studied. Polonium is most commonly studied in the context of radiation protection and in its use as an environmental tracer, in both cases typically as naturally occuring ^{210}Po from ^{238}U decay [22]. Human-made polonium is typically only produced in milligram quantities or less. It's chemical properties are known to be very similar to tellurium, and tellurium is often used as an analogue for predicting polonium's chemical behaviour when information on polonium itself is not directly available [23–25]. It should be noted that tellurium is not treated

as volatile in the ISAC actinide target SARs, though polonium's even lighter homolog, selenium, is [18, 19].

Polonium is known to easily and spontaneously deposit onto other metal surfaces, and this characteristic is routinely exploited to easily prepare ^{210}Po alpha spectroscopy samples [22, 23, 26, 27]. When kept below 100 °C, the deposited polonium is not volatile and remains on the metal surface [22]. Above 100 ° the volatility increases, with 90% of the polonium being lost at 300 °C [22].

This non-volatility of trace polonium metal quantities is in contrast to the known volatility of solid polonium metal samples. This is because samples of purified solid polonium metal of measurable mass (i.e. >trace amounts) are: 1) only ever produced in µg-mg quantities, having a high surface area to volume ratio; and 2) such samples are self-heating due to the energy deposited from their own alpha decay [23]. This self-heating effect is so intense (140 W/g) that solid polonium samples prepared in non-trace quantities can easily become much hotter than their surroundings, resulting in a 50% loss of the material over a three day period [28].

Inorganic polonium compounds are not volatile in aqueous solutions; the element is soluble in acids, and at near neutral pH forms colloids and permanently sticks to the surfaces of containers [22,23,25,27]. In room temperature aqueous solutions, polonium can potentially become volatile via incorporation into volatile organic compounds (ex. via a bacteria) [22, 29, 30]. The only volatile inorganic polonium compounds are halides (ex. polonium tetrachloride) [22, 23, 27], though these are soluble in water and are thus only volatile in solid form.

Polonium-containing particulates also have the potential to disperse polonium in air. The most notable example of this occurred in 1957 at a fire in the Windscale nuclear reactor (Cumbria, UK) – which at the time was producing ^{210}Po via bismuth irradiation – resulting in the release of 8.8 TBq of ^{210}Po into the environment [26, 31]. The released polonium was found to be contained within bismuth particles of 1 µm mean diameter [31].

To summarize the above information, polonium has the potential to become airborne if in one of the following forms:

1. A solid or liquid heated above 100 °C
2. A purified solid metal of measurable mass (i.e. >trace quantities)
3. A solid halide compound
4. A volatile organic compound
5. A fine particulate

Assessment of Polonium Volatility During L124 Irradiation

In the context of L124, *Irradiation of Thorium Targets at the TRIUMF 500 MeV Isotope Production Facility*, airborne dose estimates concern the release of volatile and gaseous radioisotopes into the air resulting from a target failure during irradiation. Both on-site doses (dose to a TRIUMF worker) and off-site doses (dose to a member of the public) are estimated. For polonium to become a contributing element to these doses it would have to go through the following steps:

1. Leave the target thorium material, in which the polonium is produced
2. Leave the cooling water package in which the targets are submerged at a 10 m depth
3. Leave the ventilation systems on the target station, including the ducting and HEPA filters

The following analyzes polonium's potential volatility in each of these three steps.

Step 1

Polonium is likely to be volatile as the thorium is expected to reach temperatures above 500 °C ("Form 1"). However, note that in the event of a target failure, water will enter the target capsule, lowering the temperature of the thorium.

Step 2

Polonium is not volatile in this situation as the cooling water remains below 50 °C – any trace quantities of polonium that leave the thorium foil after a target failure will remain in the cooling water system.

Most likely, this polonium will be trapped by the ion exchange resin on the water package or will deposit itself on interior surfaces of the water package.

"Form 1" is discounted because of the temperature of the water. The cooling water temperature is monitored during irradiation and elevated temperatures result in a beam trip.

"Form 2" is entirely impossible.

"Form 3" is discounted. While halogens including fluorine, chlorine, bromine, iodine, and astatine are co-produced in the thorium during the irradiation, these are soluble in the cooling water and are not expected to be released. This is supported anecdotally by target failures at the BL2C target station: while krypton radioisotopes have been shown to leave both the failed target and the cooling water package, the bromine isotopes that are retained in the water column [32].

"Form 4" is discounted because no biological organisms capable of incorporating polonium into volatile organic compound can be conceived to exist inside the cooling water that is cycled at high velocity through both the proton beam and the ion exchange resin.

"Form 5" is discounted because fine particulates will not become airborne when wet. Furthermore, combustion of a target immersed in water is inconceivable.

Step 3

Polonium that leaves the cooling water system is unlikely to be volatile in significant quantities this situation. Inorganic polonium that somehow leaves the cooling water would be expected to deposit itself on the interior surfaces of the ducting. This is supported by observations at ISAC in which polonium – brought into the ventilation system via its parent isotope, radon – sticks to the interior surfaces of the ducting [33].

However, it is conceivable that water vapour from the cooling water condenses on some surfaces above the water, and ultimately evaporates to leave behind polonium halide salts. However, considering that polonium concentrations in the cooling water will be below picomolar levels, vaporization of the cooling water will occur at a much slower rate than at which polonium will be trapped in the ion exchange resin or irreversibly deposit itself onto the surfaces of the cooling water system.

"Form 1" is discounted as the temperature of air or vapours inside the ventilation would not be expected to rise above 100 °C (see Step 2).

"Form 2" is again considered impossible.

"Form 3" is considered conceivable but extremely unlikely to occur in significant quantities.

"Form 4" is discounted, for reasons similar as in Step 2: one would not expect biological organisms inhabiting the ventilation system that could incorporate polonium into organic molecules.

"Form 5" is discounted as particulates would be expected to be trapped in the HEPA filters.

Conclusion

For the above reasons, in the context of L124 polonium is not be considered as volatile and can be excluded from airborne dose estimates.

4.2 Radiation Hazards

The thorium metal used as a target material is naturally radioactive, even before it is irradiated. While the metal itself does not pose a significant contamination hazard, the oxide layer on the metal's surface does.

The irradiation of thorium is expected to produce significant quantities of hazardous radioisotopes. The simulated radioactive inventory present within the thorium foil at EOB is shown in Appendix B. This inventory includes gamma-, beta-, and alpha-emitting isotopes. Some of these isotopes are also volatile halogens, noble gases, and elements that are potentially volatile depending on their chemical form (the definition of the relevant volatile and gaseous isotopes used in this document is provided in Section 4.1). As such, the irradiated thorium presents significant external and internal radiation hazards, including airborne radiation hazards.

Table 1 lists the activity at EOB and the ALI of the non-radon alpha-emitting radionuclides with half-lives >1 hour produced in the target. The selection of isotopes for this table was copied from *Actinide Target SAR Addendum for Thorium Oxide* [19].

Table 1: Activity and ALI of the non-radon alpha-emitting radionuclides produced within the thorium foil with and present at EOB and with half-lifes >1 hour. These ALI values were obtained from the *Actinide Target SAR Addendum for Thorium Oxide* (Document-110961) [19]. Information on quantities of other isotopes, including radons and those with half-lifes <1 hour can be found in Appendices B and C.

Nuclide	ALI [Bq]	Activity [Bq]	A/ALI
Po-204	7.41E+05	2.47E+09	3.33E+03
Po-205	2.25E+08	2.12E+09	9.42E+00
Po-206	4.20E+06	7.10E+08	1.69E+02
Po-207	1.33E+08	3.51E+09	2.64E+01
Po-208	8.33E+03	7.62E+06	9.15E+02
Po-209	8.33E+03	2.37E+05	2.85E+01
Po-210	9.09E+03	5.31E+07	5.84E+03
At-207	1.05E+07	3.12E+09	2.97E+02
At-209	1.68E+06	4.90E+09	2.92E+03
At-211	1.82E+05	4.70E+09	2.58E+04
Ra-223	3.51E+03	1.51E+08	4.30E+04
Ra-224	4.17E+03	1.37E+09	3.29E+05
Ra-226	9.09E+03	1.99E+03	2.19E-01
Ac-224	2.02E+05	4.02E+09	1.99E+04
Ac-225	3.08E+03	6.73E+08	2.19E+05
Ac-226	2.00E+04	2.70E+09	1.35E+05
Ac-227	4.26E+02	8.45E+05	1.98E+03
Th-227	2.63E+03	4.41E+08	1.68E+05
Th-228	6.25E+02	2.71E+07	4.34E+04
Pa-228	3.92E+05	1.77E+08	4.52E+02
Pa-229	5.26E+04	1.95E+08	3.71E+03
Pa-230	3.51E+04	7.64E+07	2.18E+03
U-230	1.67E+03	2.12E+05	1.27E+02
U-232	7.69E+02	5.67E+03	7.37E+00
		Total:	**1.01E+06**

The non-thorium components of the target capsule will also become radioactive. However, these isotopes are non-volatile and are not alpha-emitters. These components of the target present significant external radiation hazards as well as surface contamination hazards.

Dose estimates and worst-case release estimates for different stages in the experiment are provided in Section 5.

5 SAFETY MEASURES

5.1 Preparation of Thorium Foils

5.1.1 *Procedure and Safety Measures*

The foils currently contain an oxide layer that is loosely bound to the thorium metal. Since the presence of the oxide during the post-irradiation dissolution of the foil is problematic, the oxide layer will be removed from the foils using an abrasive (ex. steel wool, or similar) before they are placed in the targets. The steel wool will be kept wet during this process to minimize the dispersion of particulates that are removed. This work will be performed inside a glove box in the RCR1 lab, in order to contain the resulting contamination. The interior of the glove box will additionally be covered with plastic to reduce contamination of the glovebox interior. Afterwards, any resulting loose contamination will be cleaned up. Workers performing this work will wear a respirator and disposable full-body "tank" suit. The prepared foils will be checked for removable contamination; only foils that do not have any removable contamination will be brought to the machine shop from RCR1.

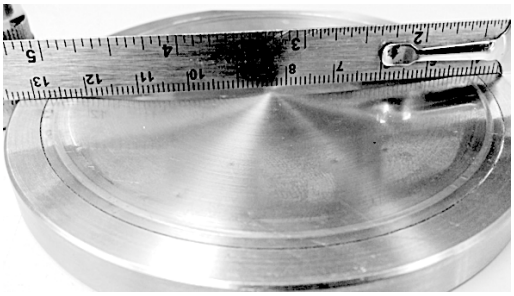

Figure 5: Image showing the inward deformation of IPF target windows for targets that are sealed under vacuum by an electron-beam weld.

Prepared foils may be stored in the ISAC target lab glove box, which provides inert atmosphere environment to prevent further oxidization. This lab already regularly handles and stores actinides (thorium and uranium).

5.1.2 *Gamma Radiation Exposure During Foil Preparation*

As the measured dose rate at 0.5 m from a single thorium foil is <2 μSv/h, the dose accrued while preparing the foils is considered negligible.

5.1.3 *Contamination of Workers During Foil Preparation*

The ALI for ^{232}Th is 120 mg for inhalation and 23 g for ingestion [34], while a single foil is <8.5 g. Additionally, since the thorium metal is non-dispersible, the airborne contamination is low. The use of wet steel wool will minimize dispersion of the thorium oxide that is removed. Given that the work will be conducted in a sealed glove box and that full PPE, including respirators, will be worn when decontaminating the glove box, the potential for internalizing harmful quantities of thorium is considered low.

5.2 Target Manufacture and Testing

5.2.1 *Procedure and Safety Measures*

After welding of the exit window to the target body, the thorium foil will be removed from a sealed plastic bag and placed between the target body and the entrance window. The thorium will then be sealed within the target by electron-beam welding of the entrance window to the target body.

Sealing of the target under vacuum in the electron-beam welder will result in the fabricated target capsule's interior also being under vacuum. This results in the thin entrance and exit windows deforming inwards, as shown in Fig. 5. Since the windows will not remain deformed if vacuum is lost inside the target, this deformation provides a visual check of the integrity of the target seal. Targets will also be leaked checked by placing them in a pressure vessel that is filled with helium gas to 30 psi for 24 hours. Any leaks in the hermetic seal of the target will result in helium penetration into the target capsule, and a loss of the the inward deformation of the windows.

Swell testing of the targets will also be performed by heating them to 350 °C for 25 minutes. Targets that swell by >1.14 mm fail the swell test.

Additional details of the target manufacturing and testing process can be found in the Engineering Note, *L124 Thorium Metal Target for IPF* (Document-148097) [13].

Table 2: Room temperature material properties of thorium and Inconel-718 relevant to results of thermal and stress simulations [36,37].

Material	Melting Point [K]	Yield Stress [MPa]	Ultimate Stress [MPa]
Inconel 718	1533	460	895
Thorium	2028	144	219

5.2.2 *Gamma Radiation Exposure During Target Manufacture and Testing*

As the measured dose rate at 0.5 m from a single thorium foil is <2 μSv/h at 1 m, the dose accrued while sealing the thorium foil within the target and testing the target is considered negligible.

5.2.3 *Contamination of Workers During Target Manufacture and Testing*

The ALI for ^{232}Th is 120 mg for inhalation and 23 g for ingestion [34], while a single foil is <8.5 g. Additionally, since the thorium metal is a durable and non-volatile metal, the potential for removable contamination – particularly airborne contamination – is considered extremely low. Given that the foils will be already checked for removable contamination, the PPE described in Section 5.2.1 is sufficient to prevent workers from being contaminated by ^{232}Th during sealing of the thorium within the target capsule.

5.3 Target Irradiation

5.3.1 *Summary of Thermal and Stress Analysis of Target During Irradiation*

Full details of this analysis can be found in the target's Engineering Note, *L124 Thorium Metal Target for IPF (Document-148097)*, with additional information found in the Design Reviews, *L124 Design Review 2017-11-09 (Document-148946)* [13,35]. A summary of the analysis and conclusions are provided herein.

All combinations of the following parameters were studied in multiple thermal and stress simulations:

- Given that BL1A typically operates at extracted currents of ~100-110 μA, with beam losses of 15% [15] simulations of on-target beam currents of 60, 80, 100, and 120 μA were studied.
- Since beam profile affects the volumetric heat load deposited in the target, Gaussian beam profiles with 15, 20, 25, 30 35, and 40 mm FWHM were simulated. As the beam is expected to be tuned to approximately a 20 mm FWHM at IPF, the 15 mm case is considered extreme.

Material properties of thorium and Inconel-718 relevant to the thermal and stress results are shown in Table 2.

While comprehensive results of the thermal and stress analysis can be found in *L124 Thorium Metal Target for IPF (Document-148097)*, Figure 6 provides a summary of the most important results relevant to the potential for target failure: the stress experienced by the target windows during irradiation. This analysis conservatively uses the yield stress (as opposed to the ultimate tensile stress) as a benchmark for the safety of the target. Irradiation conditions for which the maximum stress experienced by the window are below the yield stress of Inconel 718 are considered highly unlikely to fail.

These results suggest irradiation conditions that maintain a minimum width of 20 mm FWHM and a maximum current of 100 μA on target will not result in target failure

While damage to the thorium foil is possible, it is important to emphasize that none of the simulated cases – regardless of beam width, current, fractional contact, or thermal resistivity – result in stresses to the windows that could cause a target failure (as defined in Section 3.5).

5.3.2 *Procedure and Safety Measures*

The thorium target will be lowered into the proton beam and irradiated as described in Section 3.4. During the irradiation, monitoring devices described in Section 3.2 will be used to monitor the target and beam. The controls system implemented at IPF (Fig. 7) will cause the proton beam to trip off if all

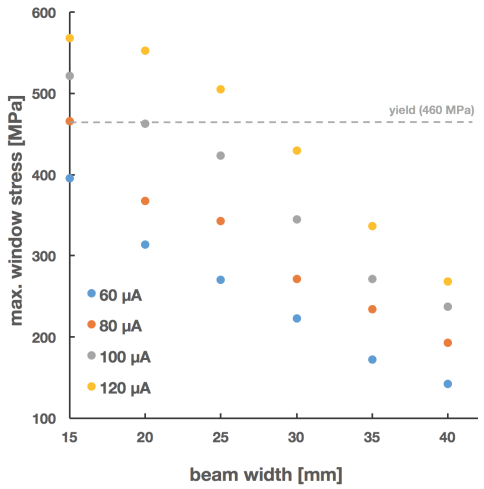

Figure 6: Maximum simulated stress values experienced by the target window during irradiations by proton beams of various widths and currents.

conditions for an acceptable target irradiation are not met. However, these checks are only applied at the start of the irradiation (using 1AM11) and are not actively monitored during the irradiation, since 1AM11 can handle only up to 10 µA. Correct beam profile (minimum 20 mm FWHM) will be ensured by the beam tune. Correct beam position will be ensured by beam collimators after T1 and T2 and IPF protect monitors, and a poor beam position that results in the beam hitting the outer ring of the target would result in heating of the target capsule that would be detected by the thermocouple attached to the target (beam is tripped when this thermocouple reaches 100 °C). Acceptable beam current will occur by ensuring that the current read by 1AM10 does not exceed 100 µA. An 80 µA current limit will be applied for the initial irradiation of new target designs.

Additionally, radiation monitors on the IPF hotcell exhaust stack and cooling water resistivity monitors will be used to detect a potential target failure, with a sudden increase in both stack exhaust radioactivity and cooling water resistivity indicating a target failure. However, it should be noted that these methods may not reliably detect a non-catastrophic (small) leak.

5.3.3 *Worst-Case Release Estimates Resulting from Target Failure*

The greatest potential hazard associated with this experiment is the release of volatile and gaseous alpha-emitting isotopes from within the target capsule during the irradiation, resulting from a failure of the capsule's hermetic seal (Section 3.5). While it must be considered, it is unlikely to occur given the post-manufacturing tests of the target (Section 5.2.1), the results of the thermal analysis (Section 5.3.1), and a long history of safely irradiating similar targets at IPF.

Calculations of the the maximum credible on-site dose to a TRIUMF worker and the maximum credible off-site dose to a member of the public were performed as described in Section 4.1 using the simulated radioisotope inventory of the target at EOB (listed in Appendix B). Details of these calculations can be found in Appendix C. Due to the state of the nuclear ventilation at IPF, and the lack of charcoal filtration on the exhaust stack, these calculations assume that none of the volatile or gaseous isotopes present within the thorium are filtered before leaving the IPF exhaust stack.

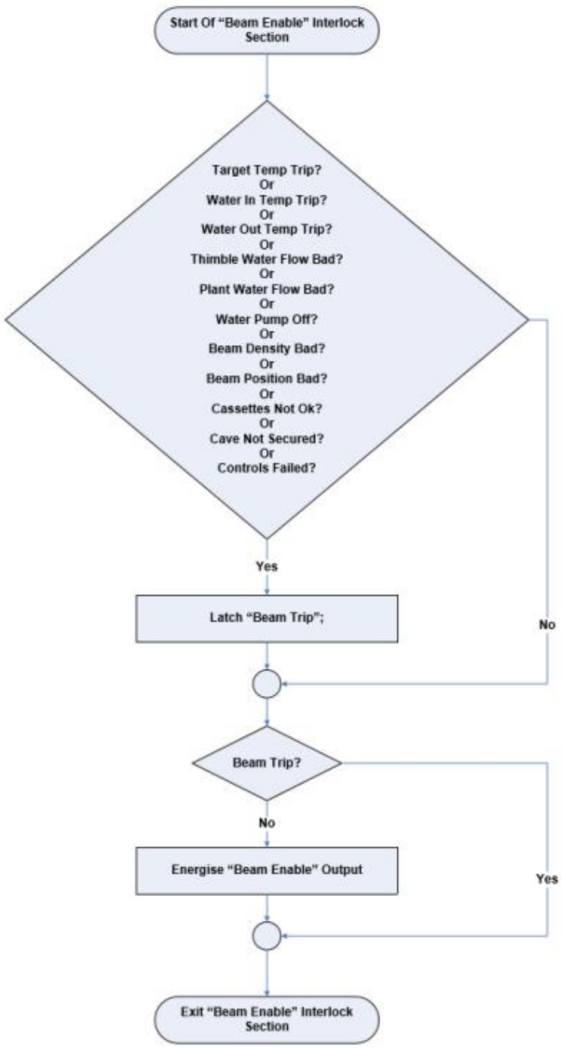

Figure 7: IPF Safety Flow Chart overview.

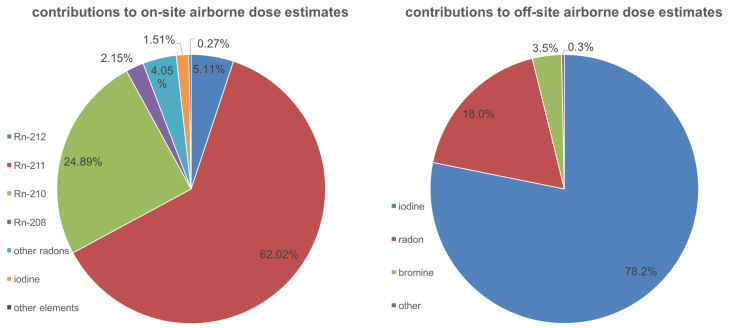

Figure 8: Breakdown of maximum credible on-site (left) and off-site (right) doses resulting from an L124 target failure.

The calculated maximum credible dose to a worker at the TRIUMF site resulting from a target failure is 13.68 mSv (0.04 mSv external dose, 13.64 mSv inhalation dose). Radon isotopes contribute the most (98% of total) to this dose estimate, 62% and 25% of which is attributed to ^{211}Rn and ^{210}Rn, respectively (Fig. 8).

Following methods described in Section 4.1, the associated maximum credible off-site dose is 25 µSv, which is dominated (78.2% of total) by iodine isotopes (Fig. 8).

Both the on- and off-site doses can be compared to the maximum credible releases determined via similar methods for the ISAC thorium target: 15 mSv on-site and 0.84 mSv off-site[4].

While these values represent the maximum possible dose, realistic doses resulting from an L124 target failure are expected to be lower for the following reasons:

1. These calculations assume that none of the volatile or gaseous isotopes remain trapped inside the 0.25 mm thick thorium metal foil in which they are produced.
2. A target failure during irradiation would occur at the target station, which sits under 9 m of cooling water. Experience from target failures at the beamline 2C Solid Target Facility (STF) has shown that the water column will trap and limit the release of volatile halogen isotopes [32], which in this case contribute 84.5% to the off-site dose.
3. Methods for calculating maximum credible on-site doses (Section 4.1) use a very conservative approach.

5.4 Target Removal from Beam

5.4.1 *Procedure and Safety Measures*

The IPF chain drive used to insert and remove targets from the beam is operated remotely. At EOB, targets will be raised to the parked position and left there, still within the IPF water column, until they reach thermal equilibrium with the cooling water and signs of a target failure have been checked. In addition to signs of a target failure described in Section 3.2, a sample of the IPF cooling water will taken and analyzed by RPG (via gamma spectroscopy) before targets are raised from the parked position into the IPF hotcell.

Once the target is raised to the hotcell level the target will be visually checked for signs of target failure before being placed inside a transfer flask located within the hotcell, which will provide additional

4 Charcoal filters on the ISAC exhaust stack are assumed to remove 99.5% of the polonium, iodine, bromine, and selenium isotopes. This assumption is not made for IPF releases since charcoal filters are not present on that stack.

radiation shielding. The target will remain in the flask and inside the IPF hotcell until one week after EOB, at which point it will be removed from the IPF hotcell and transferred to Experiment L125 [7].

5.4.2 *External Radiation Exposure to Workers at IPF*

During manipulation of the targets within the IPF hotcell, the hotcell operator is exposed gamma radiation emitted from the target through the 12" thick hot cell lead glass window. Operators will wear dosimeters during this work (the area in front of the IPF hotcell is a direct-reading-dosimeter-required area).

Exposure to these radiation fields occurs for less than 10 minutes, at least one hour after end of beam (due to the time taken to analyze the water sample). At EOB, the simulated dose rate at 1 m from the target is 128.8 mSv/h without shielding. However, assuming at least 10 cm of lead shielding provided by the IPF hotcell, the expected dose rate will be below 0.53 mSv/h. While the actual dose rate would be expected to be lower due to decay of many short-lived isotopes during the hour the target is in the parked position[5], a maximum 10-minute duration in a maximum 0.53 mSv/h field will result in 0.09 mSv of dose to the hotcell operator. As a comparison, the gamma dose to personnel from IPF molybdenum targets is 1.3 mSv/h while operating the hotcell. The typical dose to an operator during a molybdenum target transfer is 0.07 mSv (an average of a three minute exposure at 1.3 mSv/h).

6 DEFINITION OF RESPONSIBILITIES

Andrew Robertson is the experimental safety coordinator.

The Applied Technology Group (ATG) has overall responsibility for operation of the 500 MeV Isotope Production Facility. This includes target manufacture, preparation, and quality assurance, as well as the insertion and removal of targets from the beamline, and sampling of the IPF cooling water.

RPG and Operators in the 500 MeV Control Room are responsible for monitoring ventilation stacks from the IPF during the experiment and for collecting any required air samples from these stacks. RPG also has responsibility for analyzing the cooling water sample.

The TRIUMF Cyclotron Operations group is responsible for delivering the proton beam to the IPF and for monitoring the safe operating conditions of the beam and targets. Specifically, this includes the responsibility of ensuring that the beam is tuned such that the beam profile is not too narrow (minimum 20 mm FWHM), and ensuring that the current on the nearest upstream monitor from IPF (1AM10) does not exceed 95 μA during the irradiation.

6.1 Thorium Inventory Management

The ^{232}Th that makes up the target material is a controlled nuclear substance, the inventory of which TRIUMF reports in detail to the Canadian Nuclear Safety Commission (CNSC). Only thorium that has been exempted from restrictions on its modification will be used in the experiment. The spokespersons are also responsible for ensuring that items containing thorium are appropriately labelled, that the quantity of thorium therein is recorded, and for reporting on a monthly basis to the Radioactive Materials Coordinator any changes to the location, mass, chemical form, or physical form of any thorium materials.

7 DECOMMISSIONING AND DISPOSAL

At the end of the post-irradiation cool-down of the target in the IPF hotcell, the targets will be transferred to Experiment L125. Therefore, disposal and decommissioning related to the combined L124 and L125 project is covered by the L125 Safety Report and is not included herein [7].

5 At 8 hours after EOB, the simulated dose rate at 1 m from the target is 24.5 mSv/h without shielding, and 90 μSv/h with 10 cm of lead shielding.

REFERENCES

[1] Clemens Kratochwil, Frank Bruchertseifer, Frederik L Giesel, Mirjam Weis, Frederik A Verburg, Felix Mottaghy, Klaus Kopka, Christos Apostolidis, Uwe Haberkorn, and Alfred Morgenstern. 225Ac-PSMA-617 for PSMA targeting alpha-radiation therapy of patients with metastatic castration-resistant prostate cancer. *J. Nucl. Med.*, 57(12):1941–4, jul 2016.

[2] B L Zhuikov. Successes and problems in the development of medical radioisotope production in Russia. *Physics-Uspekhi*, 59(5):481–486, 2016.

[3] V Radchenko, J W Engle, J J Wilson, J R Maassen, F M Nortier, W A Taylor, E R Birnbaum, L A Hudston, K D John, and M E Fassbender. Application of ion exchange and extraction chromatography to the separation of actinium from proton-irradiated thorium metal for analytical purposes. *J. Chromatogr. A*, 1380:55–63, feb 2015.

[4] R. A. Aliev, S. V. Ermolaev, A. N. Vasiliev, V. S. Ostapenko, E. V. Lapshina, B. L. Zhuikov, N. V. Zakharov, V. V. Pozdeev, V. M. Kokhanyuk, B. F. Myasoedov, and S. N. Kalmykov. Isolation of Medicine-Applicable Actinium-225 from Thorium Targets Irradiated by Medium-Energy Protons. *Solvent Extr. Ion Exch.*, 32(5):468–477, 2014.

[5] Alfred Morgenstern. Bismuth-213 and actinium-225–generator performance and evolving therapeutic applications of two generator-derived alpha-emitting radioisotopes. *Curr. Radiopharm.*, 5(3):221–227, 2012.

[6] International Atomic Energy Agency. Technicial Meeting on Alpha emitting radionuclides and radiopharmaceuticals for therapy. Technical report, International Atomic Energy Agency, Vienna, 2013.

[7] Andrew K. H. Robertson. Safety Report for L125: Isolation of Medical Isotopes from Irradiated Thorium Metal Targets (Document-148963). Technical report, TRIUMF, Vancouver, Canada, 2017.

[8] L Moritz. TRIUMF Safety Report (Document-563). Technical report, TRIUMF, Vancouver, 2011.

[9] J. J. Burgerjon and R. Thomas. Irradiation Facility for Isotope Production Concept #2 (Document-95666). Technical report, TRIUMF, Vancouver, 1978.

[10] J. J. Burgerjon, B. D. Pate, R. E. Blaby, E. G. Page, J. Lenz, and B. T. Trevitt. The TRIUMF 500 MeV, 100 uA Isotope Production Facility. In *Proc. 27th Conf. Remote Syst. Technol.*, San Francisco, 1979.

[11] Rene van den Elzen. TRIUMF ATG Target Change Procedure for the 500 MeV Irradiation Facility (ATG-PRO-OPR-500-001). Technical report, TRIUMF, Vancouver, 2006.

[12] Ewart Blackmore. Safety Report for the Irradiation of Potassium Chloride Targets in the TRIUMF 500 MeV Isotope Production Facility (Document-65086). Technical report, TRIUMF, Vancouver, 2012.

[13] L. Moskven and AKH. Robertson. L124 Thorium Metal Target for IPF (Document-148097). Technical report, TRIUMF, Vancouver, Canada, 2017.

[14] Inconel 718, Alloy 718, UNS No7718 - MEGA MEX.

[15] Yuri Bylinsky. personal communication.

[16] Andrew K H Robertson. Commissioning Plan for Irradiation of L124 Thorium Metal Targets at IPF (Document-148095). Technical report, TRIUMF, Vancouver, Canada, 2017.

[17] A. Ferrari, P. R. Sala, A. Fasso, and J. Ranft. FLUKA: a multi-particle transport code. Technical report, CERN, Geneva, 2005.

[18] A Trudel and J Mildenberger. Actinide Target Safety Analysis Report (Document-12972). Technical report, TRIUMF, Vancouver, Canada, 2011.

[19] J Mildenberger and A Trudel. Actinide Target SAR Addendum for Thorium Oxide (Document-110961). Technical report, TRIUMF, Vancouver, Canada, 2014.

[20] J Mildenberger. Rn-220 from ISAC target pits (Document-130951). Technical report, TRIUMF, Vancouver, Canada, 2016.

[21] Joe Mildenberger. personal communication.

[22] K. Murray Matthews, Chang Kyu Kim, and Paul Martin. Determination of 210Po in environmental materials: A review of analytical methodology. *Appl. Radiat. Isot.*, 65(3):267–279, 2007.

[23] K. W. Bagnall. The Chemistry of Polonium. *Adv. Inorg. Chem. Radiochem.*, 4:197–229, 1962.

[24] E. Wiberg and N. Wiberg. *Inorganic Chemistry*. Academic Press, Berlin, 2001.

[25] N. Hussain, T. G. Ferdelman, T. M. Church, and George W. Luther. Bio-volatilization of polonium: Results from laboratory analyses. *Aquat. Geochemistry*, 1(2):175–188, 1995.

[26] R. Wilson, K. Araj, A. O. Allen, P. Auer, D. G. Boulware, F. Finlayson, S. Goren, C. Ice, L. Lidofsky, A. L. Sessoms, M. L. Shoaf, I. Spiewak, and T. Tombrello. Report to the American Physical Society of the sudy group on radionuclide release from severe accidents at nuclear power plants. *Rev. Mod. Phys.*, 57(3), 1985.

[27] P. E. Figgins. The Radiochemistry of Polonium. Technical report, Mound Laboratory, US Atomic Energy Commission, Miamisburg, OH, 1961.

[28] Polonium: Los Alamos National Laboratory.

[29] Noriyuki Momoshima, L. I Xiang Song, Susumu Osaki, and Yonezo Maeda. Formation and emission of volatile polonium compound by microbial activity and polonium methylation with methylcobalamin. *Environ. Sci. Technol.*, 35(14):2956–2960, 2001.

[30] H Mabuchi. On the volatility of some polonium compounds. *J. Inorg. Nucl. Chem.*, 25(1955):657–660, 1963.

[31] M. J. Crick and G. S. Linsley. An assessment of the radiological impact of the Windscale reactor fire, October 1957. *Int. J. Radiat. Biol.*, 46(5):479–506, 1984.

[32] A Trudel. Worst Case Emissions Analysis Report (Document-55017). Technical report, TRIUMF, Vancouver, Canada, 2015.

[33] J. Mildenberger and A. Trudel. Actinide Target 2uA Irradiation Report (Document-34296). Technical report, TRIUMF, Vancouver, Canada, 2011.

[34] International Commission on Radiological Protection. ICRP Publication 68: Dose Coefficients for Intakes of Radionuclides by Workers. *Ann. ICRP*, 24(4), 1994.

[35] Anders Mjos. L124 Design Review 2017-11-09 (Document-148946). Technical report, TRIUMF, Vancouver, Canada, 2017.

[36] Volume 2 ASM International Handbook. Properties and selection: Nonferrous alloys and special-purpose materials. In *ASM Met. Handb.*, volume 2, page 1300. 1990.

[37] Special Metals Corporation. Inconel 718 Alloy, 2007.

A SINGLE-EVENT DERIVED RELEASE LIMITS USED FOR OFF-SITE DOSE ESTIMATES

Nuclide	SDRL [TBq]	Nuclide	SDRL [TBq]	Nuclide	SDRL [TBq]	Nuclide	SDRL [TBq]
H-3	2.00E+03	FE-55	3.01E-01	KR-75	5.10E+02	SN-113	1.44E-01
BE-7	9.23E-01	FE-52	3.42E+00	KR-76	4.67E+02	SB-122	4.37E-01
C-11	2.68E+02	FE-59	3.44E-02	KR-77	2.19E+02	SB-124	2.00E-02
C-14	1.69E+02	CO-55	1.41E+00	KR-79	7.78E+02	SB-125	7.09E-03
N-13	4.02E+02	CO-56	1.01E-02	KR-81	3.51E+04	TE-121	2.29E-01
O-14	5.78E+02	CO-57	8.39E-02	KR-83M	6.89E+06	TE-121M	3.93E-02
O-15	1.18E+03	CO-58	3.80E-02	KR-85	7.87E+04	TE-123M	6.11E-02
F-17	1.73E+03	CO-60	7.16E-04	KR-85M	1.31E+03	TE-132	1.68E-01
F-18	3.56E+01	CO-61	2.11E+02	KR-87	2.62E+02	I-120	3.04E+01
NE-24	1.42E+03	NI-56	2.21E-01	KR-88	8.17E+01	I-120M	2.45E+01
NA-22	1.57E-03	NI-57	7.69E-01	KR-89	4.54E+02	I-121	1.34E+02
NA-24	1.22E+00	CU-64	1.63E+01	RB-81	2.35E+01	I-122	6.38E+02
MG-28	8.76E-01	CU-67	2.07E-01	RB-82M	4.05E+00	I-123	2.47E+01
AI-26	3.47E-05	ZN-65	1.57E-02	RB-83	4.29E-02	I-124	9.14E-02
SI-31	1.29E+02	GA-67	2.61E+00	RB-84	4.52E-02	I-125	3.72E-02
P-32	8.70E-02	GA-68	5.50E+01	RB-86	6.78E-02	I-126	2.08E-02
P-33	6.74E-01	GE-68	9.29E-02	RB-88	2.43E+02	I-128	1.02E+03
S-35	9.71E-01	GE-75	4.71E+02	RB-89	1.01E+02	I-129	3.05E-03
CL-34M	5.60E+01	AS-71	1.08E+00	SR-82	2.98E-02	I-130	2.51E+00
CL-36	7.43E-03	AS-72	6.99E-01	SR-85	7.29E-02	I-131	3.41E-02
CL-38	6.48E+01	AS-73	4.22E-01	SR-85M	2.67E+02	I-132	2.43E+01
CL-39	4.79E+01	AS-74	1.01E-01	SR-89	5.28E-02	I-132M	1.05E+02
AR-37	7.38E+07	AS-76	1.09E+00	Y-88	1.10E-02	I-133	9.31E-01
AR-39	1.03E+06	SE-73	7.61E+00	ZR-88	7.88E-02	I-134	4.92E+01
AR-41	1.59E+02	SE-73M	3.39E+02	ZR-89	4.93E-01	I-135	7.70E+00
AR-42	1.18E+03	SE-75	3.31E-02	ZR-95	4.79E-02	XE-118	1.99E+03
AR-43	3.44E+02	SE-79	2.37E-02	ZR-97	1.49E+00	XE-119	4.33E+02
AR-44	1.24E+02	SE-81	2.83E+03	NB-95	8.84E-02	XE-120	1.86E+02
K-43	2.68E+00	SE-81M	6.79E+02	NB-95M	1.08E+00	XE-121	1.26E+02
K-44	6.83E+01	SE-83	6.38E+01	NB-97	7.59E+01	XE-122	1.73E+02
CA-45	1.60E-01	SE-84	1.65E+03	MO-99	1.43E+00	XE-123	3.05E+02
CA-47	2.63E-01	BR-74	3.19E+01	TC-96	2.20E-01	XE-125	3.29E+02
SC-43	1.39E+01	BR-75	3.27E+01	TC-99M	8.19E+01	XE-127	7.50E+02
SC-44	7.26E+00	BR-76	1.54E+00	RU-103	9.74E-02	XE-129M	8.85E+03
SC-44M	3.90E-01	BR-77	3.37E+00	PD-100	8.87E-01	XE-131M	2.41E+04
SC-46	1.65E-02	BR-80	1.50E+03	PD-103	9.94E-01	XE-133	6.01E+03
SC-47	1.12E+00	BR-80M	8.85E+01	AG-105	1.10E-01	XE-133M	7.40E+03
TI-44	1.76E-03	BR-82	6.97E-01	AG-108M	9.13E-05	XE-135	8.04E+02
V-48	4.72E-02	BR-83	3.97E+02	AG-110M	4.40E-03	XE-135M	7.74E+02
CR-51	2.14E+00	BR-84	6.41E+01	AG-111	2.77E-01	XE-137	3.82E+03
MN-52	1.18E-01	BR-85	9.85E+03	CD-109	6.06E-02	XE-138	1.68E+02
MN-54	1.19E-02	BR-87	8.18E+02	IN-111	1.57E+00	CS-127	2.68E+01
MN-56	1.43E+01	KR-74	3.25E+02	IN-114M	2.93E-02	CS-129	6.96E+00

Nuclide	SDRL [TBq]
CS-130	4.28E+00
CS-131	4.80E+00
CS-132	4.90E-01
CS-134	2.30E-03
CS-137	1.79E-02
CS-138	4.65E+01
BA-128	6.44E-01
BA-131	3.24E-01
BA-137M	6.36E-04
Eu-152	6.67E-04
TA-182	1.77E-02
Re-182	3.99E+00
Re-182	3.40E-01
Re-184	6.33E-02
RE-184M	3.12E-02
RE-186	4.15E-01
AU-195	1.49E-01
AU-198	6.69E-01
AU-199	1.53E+00
HG-197	3.24E+00
HG-199M	6.72E+01
HG-203	1.40E-01
TL-200	2.01E+00
TL-201	5.46E+00
TL-202	3.40E-01
PB-203	2.65E+00
PB-212	4.52E-01
BI-203	2.31E+00
BI-205	9.53E-02
BI-207	2.12E-04
BI-210	3.66E-01
BI-212	3.69E+00
PO-203	5.79E+01
PO-204	1.00E+00
PO-205	2.46E+01
PO-206	3.12E-01
PO-207	9.00E+00
PO-208	1.18E-04
PO-209	1.08E-04
PO-210	9.05E-05
PO-211	2.05E+05
PO-212M	9.41E+10
PO-218	1.34E+01
RN-206	1.55E+02

Nuclide	SDRL [TBq]
RN-207	3.25E+02
RN-208	3.00E+01
RN-209	5.80E+01
RN-210	3.01E+02
RN-211	1.44E+01
RN-212	4.79E+01
RN-220	3.06E+02
RN-221	1.99E-03
RN-222	3.47E+00
RN-223	4.52E+01
RA-223	1.73E-03
RA-224	7.06E-03
RA-225	1.33E-03
RA-226	4.36E-04
RA-228	9.33E-05
AC-225	8.85E-03
AC-227	6.42E-05
AC-228	8.77E-01
TH-227	1.45E-02
TH-228	8.70E-04
TH-232	3.63E-04
U-234	3.82E-03
U-235	5.13E-04
U-238	4.26E-03
NP-237	9.53E-04
PU-238	6.63E-04
PU-239	6.10E-04
PU-240	6.08E-04
PU-241	3.27E-02
PU-242	6.34E-04
AM-241	6.35E-04

B RADIOACTIVE INVENTORY OF THORIUM FOIL AT EOB

Nuclide	Z	A	Activity [Bq]	+- [%]
U-233	92	233	5.34E+00	0.54
U-232	92	232	5.47E+03	4.01
U-230	92	230	2.12E+05	2.06
Pa-233	91	233	4.48E+08	0.51
Pa-232	91	232	1.68E+08	4.03
Pa-231	91	231	1.14E+03	0.44
Pa-230	91	230	7.64E+07	2.06
Pa-229	91	229	1.95E+08	3.54
Pa-228	91	228	1.77E+08	4.53
Pa-227	91	227	4.59E+07	9.45
Pa-226	91	226	3.26E+07	12.45
Pa-225	91	225	3.86E+06	32.66
Pa-224	91	224	2.57E+06	40.31
Pa-223	91	223	1.29E+06	57.44
Th-233	90	233	9.03E+09	0.51
Th-231	90	231	1.51E+10	0.44
Th-230	90	230	1.07E+03	0.46
Th-229	90	229	7.32E+03	0.59
Th-228	90	228	2.71E+07	0.57
Th-227	90	227	4.41E+08	0.79
Th-226	90	226	6.33E+09	0.69
Th-225	90	225	2.93E+09	1.16
Th-224	90	224	1.54E+09	1.77
Th-223	90	223	9.54E+08	2.14
Th-222	90	222	4.14E+08	3.38
Th-221	90	221	2.03E+08	4.66
Th-220	90	220	1.39E+08	6
Th-219	90	219	9.35E+07	6.8
Th-218	90	218	7.38E+07	7.82
Th-217	90	217	4.81E+07	10.02
Th-216	90	216	4.06E+07	10.65
Th-216m	90	216	2.06E+07	10.65
Th-215	90	215	2.53E+07	12.44
Th-214	90	214	6.01E+06	25.84
Ac-232	89	232	2.83E+07	11.79
Ac-231	89	231	4.83E+09	0.91
Ac-230	89	230	2.86E+09	1.24
Ac-229	89	229	4.65E+09	1.05
Ac-228	89	228	3.36E+09	1.14
Ac-227	89	227	8.45E+05	0.88

Nuclide	Z	A	Activity [Bq]	+- [%]
Ac-226	89	226	2.70E+09	1
Ac-225	89	225	6.73E+08	0.87
Ac-224	89	224	4.02E+09	1.11
Ac-223	89	223	4.51E+09	0.98
Ac-222	89	222	1.98E+09	1.09
Ac-222m	89	222	1.78E+09	1.11
Ac-221	89	221	3.58E+09	1.07
Ac-220	89	220	2.46E+09	1.27
Ac-219	89	219	2.34E+09	1.4
Ac-218	89	218	1.46E+09	1.71
Ac-217	89	217	1.15E+09	1.93
Ac-216	89	216	3.04E+08	2.81
Ac-216m	89	216	3.04E+08	2.81
Ac-215	89	215	7.25E+08	2.4
Ac-214	89	214	4.40E+08	2.89
Ac-213	89	213	2.22E+08	4.17
Ac-212	89	212	5.28E+07	8.83
Ac-211	89	211	6.87E+06	24.04
Ac-210	89	210	1.72E+06	49.62
Ra-230	88	230	6.82E+07	7.74
Ra-229	88	229	1.36E+08	5.73
Ra-228	88	228	1.73E+05	4.1
Ra-227	88	227	3.27E+08	3.08
Ra-226	88	226	1.99E+03	2.02
Ra-225	88	225	5.49E+07	2.61
Ra-224	88	224	1.37E+09	0.93
Ra-223	88	223	1.51E+08	1.67
Ra-222	88	222	8.00E+09	0.63
Ra-221	88	221	4.06E+09	0.93
Ra-220	88	220	3.63E+09	1.18
Ra-219	88	219	2.65E+09	1.18
Ra-218	88	218	2.82E+09	1.18
Ra-217	88	217	2.16E+09	1.32
Ra-216	88	216	2.54E+09	1.31
Ra-215	88	215	1.95E+09	1.65
Ra-214	88	214	2.51E+09	1.38
Ra-213	88	213	2.01E+09	1.51
Ra-213m	88	213	9.85E+08	1.51
Ra-212	88	212	1.82E+09	1.49
Ra-211	88	211	1.07E+09	1.92

Ra-210	88	210	7.35E+08	2.47
Ra-209	88	209	2.50E+08	4.18
Ra-208	88	208	5.71E+07	8.14
Ra-207	88	207	3.96E+06	34
Ra-207m	88	207	2.15E+06	34
Fr-228	87	228	8.58E+05	70.53
Fr-227	87	227	8.15E+06	21.88
Fr-226	87	226	8.58E+06	21.27
Fr-225	87	225	2.23E+07	13.97
Fr-224	87	224	3.95E+07	10.99
Fr-223	87	223	6.31E+07	8.49
Fr-222	87	222	8.77E+07	6.39
Fr-221	87	221	8.22E+08	1.12
Fr-220	87	220	5.22E+08	1.84
Fr-219	87	219	4.75E+09	0.95
Fr-218	87	218	3.64E+09	1.07
Fr-218m	87	218	1.38E+08	3.64
Fr-217	87	217	4.05E+09	0.93
Fr-216	87	216	2.96E+09	1.22
Fr-215	87	215	2.96E+09	1.17
Fr-214	87	214	1.85E+09	1.45
Fr-214m	87	214	3.93E+08	2.1
Fr-213	87	213	2.85E+09	1.17
Fr-212	87	212	1.91E+09	1.46
Fr-211	87	211	1.94E+09	1.49
Fr-210	87	210	1.31E+09	1.67
Fr-209	87	209	1.05E+09	1.88
Fr-208	87	208	5.30E+08	2.9
Fr-207	87	207	3.13E+08	3.51
Fr-206	87	206	4.63E+07	6.53
Fr-206m	87	206	4.46E+07	6.53
Fr-205	87	205	1.33E+07	17.77
Fr-204	87	204	8.58E+05	70.53
Rn-224	86	224	1.72E+06	49.62
Rn-223	86	223	8.58E+05	70.53
Rn-222	86	222	9.14E+05	37.21
Rn-221	86	221	8.15E+06	25.41
Rn-220	86	220	1.38E+09	0.93
Rn-219	86	219	1.64E+08	2.19
Rn-218	86	218	8.04E+09	0.62
Rn-217	86	217	4.09E+09	0.93
Rn-216	86	216	3.69E+09	1.17

Rn-215	86	215	2.73E+09	1.16
Rn-214	86	214	2.87E+09	1.17
Rn-214m	86	214	5.24E+07	4.73
Rn-214n	86	214	5.24E+07	4.73
Rn-213	86	213	2.43E+09	1.25
Rn-212	86	212	4.09E+09	0.95
Rn-211	86	211	2.54E+09	1.27
Rn-210	86	210	3.64E+09	1.02
Rn-209	86	209	2.35E+09	1.25
Rn-208	86	208	2.36E+09	1.35
Rn-207	86	207	1.66E+09	1.52
Rn-206	86	206	1.38E+09	1.77
Rn-205	86	205	6.43E+08	2.58
Rn-204	86	204	3.63E+08	3.08
Rn-203	86	203	6.45E+07	5.72
Rn-203m	86	203	6.05E+07	5.89
Rn-202	86	202	4.76E+07	8.63
Rn-201	86	201	1.07E+06	44.27
Rn-201m	86	201	1.07E+06	44.27
Rn-200	86	200	8.58E+05	70.53
At-218	85	218	8.58E+05	70.52
At-217	85	217	8.22E+08	1.12
At-216	85	216	5.24E+08	1.84
At-215	85	215	4.75E+09	0.95
At-214	85	214	3.78E+09	1.07
At-214m	85	214	2.43E+06	23.26
At-214n	85	214	2.43E+06	23.26
At-213	85	213	4.06E+09	0.93
At-212	85	212	2.97E+09	1.22
At-212m	85	212	1.57E+07	11.68
At-211	85	211	4.70E+09	0.85
At-210	85	210	2.43E+09	1.26
At-209	85	209	4.90E+09	0.95
At-208	85	208	1.88E+09	1.04
At-207	85	207	3.12E+09	1.08
At-206	85	206	1.59E+09	1.32
At-205	85	205	1.80E+09	1.44
At-204	85	204	8.72E+08	1.89
At-204m	85	204	1.39E+08	3.42
At-203	85	203	6.44E+08	2.47
At-202	85	202	2.77E+08	3.72
At-202m	85	202	9.25E+07	4.64

At-201	85	201	1.31E+08	5.29
At-200	85	200	3.93E+07	10.59
At-200m	85	200	2.15E+07	10.8
At-199	85	199	9.01E+06	21.77
Po-218	84	218	9.13E+05	37.21
Po-217	84	217	1.79E+06	25.41
Po-216	84	216	1.38E+09	0.93
Po-215	84	215	1.64E+08	2.2
Po-214	84	214	8.04E+09	0.62
Po-213	84	213	4.88E+09	0.82
Po-212	84	212	4.62E+09	0.95
Po-211	84	211	5.49E+09	0.74
Po-211m	84	211	1.72E+06	34.73
Po-210	84	210	5.31E+07	0.8
Po-209	84	209	2.37E+05	0.7
Po-208	84	208	7.62E+06	0.79
Po-207	84	207	3.51E+09	0.93
Po-207m	84	207	1.61E+07	12.46
Po-206	84	206	7.10E+08	0.87
Po-205	84	205	2.12E+09	1.18
Po-204	84	204	2.47E+09	1.1
Po-203	84	203	9.55E+08	1.48
Po-203m	84	203	8.09E+07	4.92
Po-202	84	202	1.33E+09	1.61
Po-201	84	201	3.35E+08	2.4
Po-201m	84	201	1.07E+08	4.46
Po-200	84	200	4.87E+08	2.54
Po-199	84	199	1.53E+08	4.22
Po-199m	84	199	6.01E+07	6.08
Po-198	84	198	1.37E+08	5.59
Po-197	84	197	1.58E+07	12.68
Po-197m	84	197	1.39E+07	13.61
Po-196	84	196	1.24E+07	19.79
Bi-214	83	214	1.75E+06	39.08
Bi-213	83	213	8.09E+08	1.15
Bi-212	83	212	1.45E+09	1.08
Bi-211	83	211	4.91E+09	0.91
Bi-210	83	210	9.14E+08	1.07
Bi-208	83	208	3.08E+01	1.22
Bi-208m	83	208	8.58E+05	49.62
Bi-207	83	207	4.76E+05	0.76
Bi-206	83	206	6.98E+07	1

Bi-205	83	205	1.88E+08	1.1
Bi-204	83	204	2.29E+09	1.1
Bi-204m	83	204	9.01E+06	16.04
Bi-203	83	203	1.17E+09	1.24
Bi-203m	83	203	1.52E+07	11.8
Bi-202	83	202	1.36E+09	1.61
Bi-201	83	201	6.03E+08	1.88
Bi-201m	83	201	2.98E+07	8.48
Bi-200	83	200	5.07E+08	2.23
Bi-200m	83	200	2.63E+07	7.68
Bi-200n	83	200	2.63E+07	7.68
Bi-199	83	199	4.27E+08	2.17
Bi-199m	83	199	5.62E+07	6.16
Bi-198	83	198	1.81E+08	3.61
Bi-198m	83	198	5.32E+07	5.87
Bi-197	83	197	1.51E+08	3.75
Bi-197m	83	197	4.72E+07	6.18
Bi-196	83	196	5.08E+07	7.19
Bi-196m	83	196	2.77E+07	8.79
Bi-195	83	195	2.79E+07	9.1
Bi-195m	83	195	1.97E+07	9.6
Bi-194	83	194	5.58E+06	16.13
Bi-194m	83	194	5.58E+06	16.13
Bi-194n	83	194	5.58E+06	16.13
Bi-193	83	193	3.43E+06	24.04
Bi-193m	83	193	3.43E+06	24.04
Bi-192	83	192	8.58E+05	49.62
Bi-192m	83	192	8.58E+05	49.62
Pb-214	82	214	9.02E+05	37.21
Pb-213	82	213	1.70E+06	25.41
Pb-212	82	212	9.66E+08	0.94
Pb-211	82	211	1.61E+08	2.22
Pb-210	82	210	1.20E+06	0.67
Pb-209	82	209	4.84E+09	0.83
Pb-207m	82	207	4.43E+05	0.76
Pb-204m	82	204	8.58E+05	49.62
Pb-203	82	203	4.09E+08	1.23
Pb-203m	82	203	1.14E+06	34.73
Pb-203n	82	203	1.14E+06	34.73
Pb-202	82	202	9.27E+01	1.58
Pb-202m	82	202	5.58E+06	19.13
Pb-201	82	201	6.18E+08	1.93

Pb-201m	82	201	4.93E+06	20.61
Pb-200	82	200	4.46E+08	2.24
Pb-199	82	199	5.07E+08	2.28
Pb-199m	82	199	1.22E+07	13.93
Pb-198	82	198	2.57E+08	3.28
Pb-197	82	197	2.09E+08	3.21
Pb-197m	82	197	2.34E+07	9.72
Pb-196	82	196	2.36E+08	3.44
Pb-195	82	195	1.20E+08	3.91
Pb-195m	82	195	3.69E+07	7.33
Pb-194	82	194	2.16E+08	4.29
Pb-193	82	193	3.96E+07	7.88
Pb-193m	82	193	1.74E+07	11.08
Pb-192	82	192	4.95E+07	9.98
Pb-191	82	191	4.65E+06	21.91
Pb-191m	82	191	4.29E+06	22.42
Pb-190	82	190	5.58E+06	26.89
Tl-210	81	210	3.50E+02	39.09
Tl-209	81	209	1.69E+07	1.15
Tl-208	81	208	5.21E+08	1.08
Tl-207	81	207	4.90E+09	0.91
Tl-206	81	206	1.19E+03	1.07
Tl-202	81	202	2.81E+05	36.19
Tl-201	81	201	1.66E+08	1.95
Tl-201m	81	201	8.58E+05	49.62
Tl-200	81	200	2.28E+08	2.23
Tl-200m	81	200	6.44E+05	57.44
Tl-199	81	199	5.08E+08	2.32
Tl-199m	81	199	3.86E+06	22.54
Tl-198	81	198	2.60E+08	3.31
Tl-198m	81	198	1.57E+06	29.38
Tl-198n	81	198	1.57E+06	29.38
Tl-197	81	197	2.47E+08	3.35
Tl-197m	81	197	9.65E+06	14.59
Tl-196	81	196	2.44E+08	3.37
Tl-196m	81	196	8.37E+06	16.93
Tl-195	81	195	1.80E+08	4.26
Tl-195m	81	195	1.18E+07	13.87
Tl-194	81	194	2.29E+08	4.16
Tl-194m	81	194	1.35E+07	13.04
Tl-193	81	193	1.25E+08	5.12
Tl-193m	81	193	2.40E+07	9.61

Tl-192	81	192	6.63E+07	7.94
Tl-192m	81	192	1.67E+07	10.87
Tl-191	81	191	3.37E+07	7.76
Tl-191m	81	191	1.82E+07	10.34
Tl-190	81	190	1.61E+07	12.14
Tl-190m	81	190	1.05E+07	13.42
Tl-189	81	189	1.06E+07	14.92
Tl-189m	81	189	6.65E+06	18.35
Tl-188	81	188	2.16E+06	29.46
Tl-188m	81	188	1.93E+06	32.66
Tl-187	81	187	1.14E+06	49.62
Tl-187m	81	187	8.58E+05	49.62
Hg-199m	80	199	6.44E+05	57.44
Hg-197	80	197	9.34E+07	3.36
Hg-197m	80	197	1.13E+06	37.22
Hg-195	80	195	1.80E+08	4.21
Hg-195m	80	195	3.19E+06	19.42
Hg-194	80	194	1.87E+03	4.01
Hg-193	80	193	1.69E+08	4.27
Hg-193m	80	193	1.33E+07	11.39
Hg-192	80	192	1.10E+08	6.4
Hg-191	80	191	6.65E+07	6.64
Hg-191m	80	191	1.46E+07	11.88
Hg-190	80	190	6.13E+07	7.83
Hg-189	80	189	2.88E+07	10.72
Hg-189m	80	189	1.18E+07	12.07
Hg-188	80	188	3.28E+07	11.04
Hg-187	80	187	6.37E+06	20.19
Hg-187m	80	187	4.93E+06	22.38
Hg-186	80	186	1.21E+07	18.22
Hg-185	80	185	1.65E+06	44.25
Hg-185m	80	185	1.07E+06	44.27
Hg-184	80	184	8.58E+05	70.53
Au-197m	79	197	4.29E+05	70.53
Au-196m	79	196	5.72E+05	49.62
Au-196n	79	196	5.54E+05	49.62
Au-196	79	196	3.14E+05	49.62
Au-195	79	195	9.51E+05	4.2
Au-195m	79	195	6.44E+05	57.44
Au-194	79	194	1.50E+06	40.29
Au-193	79	193	1.30E+08	4.62
Au-193m	79	193	1.93E+06	32.66

Au-192	79	192	1.15E+08	6.21
Au-191	79	191	9.02E+07	6.1
Au-191m	79	191	4.72E+06	21.17
Au-190	79	190	7.42E+07	7.45
Au-190m	79	190	6.44E+06	17.52
Au-189	79	189	4.83E+07	8.62
Au-189m	79	189	7.72E+06	16.6
Au-188	79	188	4.66E+07	9.02
Au-187	79	187	2.67E+07	12.49
Au-187m	79	187	7.72E+06	15.13
Au-186	79	186	2.58E+07	13.35
Au-185	79	185	8.27E+06	19.36
Au-185m	79	185	6.22E+06	19.8
Au-184	79	184	3.42E+06	34.73
Au-183	79	183	3.29E+06	34.14
Au-182	79	182	8.58E+05	70.53
Pt-193	78	193	4.92E+03	4.61
Pt-193m	78	193	1.18E+05	70.53
Pt-191	78	191	2.74E+07	6.81
Pt-189	78	189	5.80E+07	8.12
Pt-188	78	188	7.63E+06	7.93
Pt-187	78	187	3.88E+07	10.47
Pt-186	78	186	3.82E+07	10.64
Pt-185	78	185	2.15E+07	13.68
Pt-185m	78	185	6.87E+06	17.96
Pt-184	78	184	1.89E+07	14.82
Pt-184m	78	184	7.72E+06	16.12
Pt-183	78	183	6.50E+06	21.62
Pt-183m	78	183	3.22E+06	24.9
Pt-182	78	182	9.87E+06	20.6
Pt-181	78	181	3.53E+06	33.73
Pt-180	78	180	8.60E+05	69.75
Ir-190m	77	190	4.29E+05	57.44
Ir-190n	77	190	4.29E+05	57.44
Ir-190	77	190	9.62E+04	57.44
Ir-189	77	189	4.23E+06	8
Ir-189m	77	189	2.86E+05	70.53
Ir-189n	77	189	2.86E+05	70.53
Ir-188	77	188	2.89E+06	13.52
Ir-187	77	187	3.95E+07	10.17
Ir-186	77	186	3.32E+07	10.4
Ir-186m	77	186	1.07E+06	44.27

Ir-185	77	185	2.83E+07	11.85
Ir-184	77	184	2.66E+07	13.41
Ir-183	77	183	1.74E+07	15.56
Ir-182	77	182	1.59E+07	16.73
Ir-181	77	181	1.08E+07	19.42
Ir-180	77	180	3.43E+06	34.67
Ir-179	77	179	1.30E+06	56.91
Ir-178	77	178	3.26E+02	70.53
Os-185	76	185	2.79E+05	11.95
Os-183	76	183	1.78E+07	14.53
Os-183m	76	183	1.66E+06	34.73
Os-182	76	182	1.67E+07	14.1
Os-181	76	181	1.32E+07	16.67
Os-181m	76	181	2.36E+06	29.38
Os-180	76	180	1.07E+07	20.39
Os-179	76	179	4.30E+06	30.81
Os-178	76	178	2.58E+06	40.27
Os-177	76	177	1.69E+06	49.57
Os-176	76	176	8.68E+05	69.71
Re-183	75	183	2.62E+05	14.17
Re-182	75	182	4.53E+06	13.9
Re-181	75	181	1.45E+07	16.31
Re-180	75	180	1.29E+07	18.75
Re-179	75	179	7.74E+06	22.51
Re-178	75	178	5.15E+06	28.05
Re-177	75	177	4.70E+06	29.37
Re-176	75	176	3.01E+06	37.09
Re-174	75	174	1.29E+06	57.44
Re-173	75	173	8.82E+05	68.63
W-181	74	181	9.96E+04	16.36
W-179	74	179	8.16E+06	21.85
W-178	74	178	4.51E+05	24.71
W-177	74	177	5.56E+06	26.88
W-176	74	176	6.02E+06	25.79
W-175	74	175	3.00E+06	37.22
W-174	74	174	3.43E+06	34.73
W-173	74	173	2.60E+06	39.93
W-172	74	172	2.15E+06	52.57
Ta-179	73	179	1.77E+04	21.24
Ta-178	73	178	4.49E+05	24.71
Ta-177	73	177	2.71E+06	24.9
Ta-176	73	176	7.14E+06	23.22

Ta-175	73	175	5.75E+06	27.75
Ta-174	73	174	5.15E+06	28.06
Ta-173	73	173	3.46E+06	38.71
Ta-172	73	172	5.15E+06	30.44
Ta-171	73	171	1.29E+06	57.44
Ta-170	73	170	8.58E+05	70.53
Ta-169	73	169	8.58E+05	70.53
Hf-175	72	175	9.82E+04	25.71
Hf-173	72	173	3.45E+06	31.86
Hf-172	72	172	1.37E+04	25.6
Hf-171	72	171	2.81E+06	37.22
Hf-170	72	170	1.88E+06	44.27
Hf-169	72	169	2.15E+06	44.27
Lu-173	71	173	6.61E+03	31.43
Lu-172	71	172	4.02E+05	44.12
Lu-172m	71	172	1.07E+06	44.27
Lu-171	71	171	7.09E+05	27.47
Lu-171m	71	171	1.29E+06	40.31
Lu-170	71	170	2.39E+06	27.54
Lu-170m	71	170	1.72E+06	34.73
Lu-169	71	169	2.94E+06	29.38
Lu-169m	71	169	1.29E+06	40.31
Lu-168	71	168	1.33E+06	46.35
Lu-168m	71	168	8.58E+05	49.62
Lu-167	71	167	8.58E+05	70.53
Lu-166	71	166	9.27E+05	49.62
Lu-166m	71	166	5.72E+05	49.62
Lu-166n	71	166	5.72E+05	49.62
Lu-165	71	165	8.58E+05	49.62
Lu-165m	71	165	8.58E+05	49.62
Yb-169	70	169	1.63E+05	31.62
Yb-169m	70	169	1.07E+06	52.57
Yb-167	70	167	3.86E+06	32.66
Yb-166	70	166	2.48E+06	26.89
Yb-165	70	165	4.29E+06	30.9
Yb-164	70	164	3.00E+06	37.22
Yb-163	70	163	2.15E+06	44.27
Tm-170	69	170	1.38E+04	57.44
Tm-168	69	168	3.17E+04	44.27
Tm-167	69	167	1.07E+06	22.54
Tm-166	69	166	4.96E+06	25.3
Tm-165	69	165	4.30E+06	24.9

Tm-164	69	164	5.71E+06	25.88
Tm-164m	69	164	1.50E+06	37.22
Tm-163	69	163	6.87E+06	27.11
Tm-162	69	162	3.12E+06	34.73
Tm-162m	69	162	1.72E+06	34.73
Tm-161	69	161	1.29E+06	57.44
Tm-160	69	160	8.26E+05	70.59
Tm-159	69	159	8.58E+05	70.53
Er-167m	68	167	9.87E+04	70.53
Er-165	68	165	6.61E+06	21.74
Er-163	68	163	9.87E+06	21.51
Er-161	68	161	6.44E+06	26.63
Er-160	68	160	4.13E+06	27.75
Er-159	68	159	3.43E+06	34.73
Er-158	68	158	3.86E+06	32.66
Er-155	68	155	8.58E+05	70.53
Ho-167	67	167	8.58E+05	70.53
Ho-166	67	166	3.70E+05	60.64
Ho-166m	67	166	1.36E+00	70.53
Ho-164	67	164	1.29E+06	57.44
Ho-164m	67	164	6.44E+05	57.44
Ho-163	67	163	1.11E+01	18.15
Ho-163m	67	163	2.15E+06	34
Ho-162	67	162	3.48E+06	30.9
Ho-162m	67	162	2.15E+06	30.9
Ho-161	67	161	1.63E+07	15.56
Ho-161m	67	161	4.93E+06	19.67
Ho-160	67	160	8.27E+06	19.59
Ho-160n	67	160	1.57E+06	29.38
Ho-160m	67	160	1.57E+06	29.38
Ho-159	67	159	1.03E+07	20.94
Ho-159m	67	159	3.43E+06	25.62
Ho-158	67	158	5.16E+06	26.51
Ho-158m	67	158	7.15E+05	44.27
Ho-158n	67	158	7.15E+05	44.27
Ho-157	67	157	4.29E+06	30.9
Ho-156	67	156	2.57E+06	40.31
Ho-155	67	155	3.00E+06	37.22
Ho-154	67	154	4.29E+05	70.53
Ho-154m	67	154	4.29E+05	70.53
Dy-165	66	165	1.69E+06	49.62
Dy-165m	66	165	1.17E+06	51.37

Dy-159	66	159	1.41E+05	17.38
Dy-157	66	157	1.39E+07	17.6
Dy-157m	66	157	4.93E+06	20.61
Dy-155	66	155	8.06E+06	21.73
Dy-153	66	153	3.84E+06	32.66
Dy-152	66	152	3.43E+06	34.73
Tb-165	65	165	8.58E+05	70.53
Tb-164	65	164	8.58E+05	70.53
Tb-163	65	163	3.43E+06	34.73
Tb-162	65	162	1.03E+07	19.2
Tb-161	65	161	2.58E+06	16.52
Tb-160	65	160	9.78E+04	28.06
Tb-158m	65	158	5.15E+06	20.08
Tb-158	65	158	2.17E+02	20.08
Tb-157	65	157	8.07E+02	13.01
Tb-156n	65	156	4.00E+06	18.97
Tb-156m	65	156	2.98E+06	18.97
Tb-156	65	156	1.73E+06	18.97
Tb-155	65	155	4.64E+06	13.35
Tb-154m	65	154	2.50E+06	26.35
Tb-154	65	154	2.41E+06	26.35
Tb-154n	65	154	1.98E+06	26.35
Tb-153	65	153	7.21E+06	15.85
Tb-152	65	152	7.41E+06	20.18
Tb-152m	65	152	3.00E+06	25.84
Tb-151	65	151	6.90E+06	21.67
Tb-151m	65	151	3.22E+06	26.63
Tb-150	65	150	3.00E+06	25.84
Tb-150m	65	150	2.57E+06	28.06
Tb-149	65	149	4.29E+05	70.45
Tb-149m	65	149	4.29E+05	70.53
Gd-163	64	163	2.15E+06	44.27
Gd-162	64	162	7.29E+06	23.26
Gd-161	64	161	9.87E+06	19.67
Gd-159	64	159	2.14E+07	12.28
Gd-153	64	153	1.08E+05	13.25
Gd-151	64	151	1.66E+05	16.85
Gd-149	64	149	1.28E+06	23.12
Gd-148	64	148	3.50E+02	24.03
Gd-147	64	147	2.26E+06	32.45
Gd-146	64	146	4.86E+04	49.62
Eu-162	63	162	2.15E+06	44.27

Eu-161	63	161	2.15E+06	44.27
Eu-160	63	160	1.09E+07	19.65
Eu-159	63	159	2.15E+07	13.82
Eu-158	63	158	4.46E+07	9.54
Eu-157	63	157	6.47E+07	7.53
Eu-156	63	156	8.25E+06	5.36
Eu-155	63	155	1.39E+05	4.77
Eu-154m	63	154	9.01E+06	14.94
Eu-154	63	154	7.87E+03	14.94
Eu-152n	63	152	5.44E+06	16
Eu-152m	63	152	5.28E+06	16
Eu-152	63	152	2.98E+03	16
Eu-150m	63	150	7.35E+06	15.83
Eu-150	63	150	8.42E+02	15.83
Eu-149	63	149	3.20E+05	14.97
Eu-148	63	148	3.88E+05	17.06
Eu-147	63	147	8.17E+05	16.19
Eu-146	63	146	2.58E+06	21.46
Eu-145	63	145	1.35E+06	26.37
Eu-144	63	144	3.00E+06	37.22
Sm-160	62	160	4.72E+06	32.09
Sm-159	62	159	1.07E+07	19.59
Sm-158	62	158	2.45E+07	12.77
Sm-157	62	157	5.49E+07	8.5
Sm-156	62	156	9.81E+07	5.79
Sm-155	62	155	1.46E+08	5.1
Sm-153	62	153	1.59E+08	3.78
Sm-151	62	151	1.12E+04	2.95
Sm-145	62	145	8.67E+04	13.87
Sm-143	62	143	1.07E+07	19.59
Sm-143m	62	143	3.43E+06	20.08
Sm-143n	62	143	3.43E+06	20.08
Sm-142	62	142	4.29E+06	30.9
Sm-141	62	141	1.08E+06	44.27
Sm-141m	62	141	1.07E+06	44.27
Pm-158	61	158	8.58E+06	21.27
Pm-157	61	157	2.19E+07	13.84
Pm-156	61	156	4.57E+07	9.1
Pm-155	61	155	9.93E+07	5.97
Pm-154	61	154	1.22E+08	5.25
Pm-154m	61	154	4.12E+07	6.92
Pm-153	61	153	2.64E+08	4.27

Pm-152	61	152	3.08E+08	3.57
Pm-152m	61	152	3.53E+07	6.23
Pm-152n	61	152	3.53E+07	6.23
Pm-151	61	151	3.81E+08	2.98
Pm-150	61	150	9.23E+07	6.79
Pm-149	61	149	3.93E+08	2.36
Pm-148	61	148	7.48E+06	7.7
Pm-148m	61	148	1.08E+06	7.7
Pm-147	61	147	2.19E+05	3.83
Pm-146	61	146	4.21E+04	7.83
Pm-145	61	145	1.33E+04	8
Pm-144	61	144	1.85E+05	9.27
Pm-143	61	143	3.20E+05	8.61
Pm-142	61	142	3.26E+07	10.64
Pm-141	61	141	2.23E+07	14.99
Pm-140	61	140	4.51E+06	24.71
Pm-140m	61	140	4.08E+06	25.41
Pm-139	61	139	3.00E+06	37.22
Pm-139m	61	139	1.29E+06	40.31
Pm-138	61	138	8.58E+05	57.44
Pm-138m	61	138	4.29E+05	57.44
Pm-138n	61	138	4.29E+05	57.44
Nd-156	60	156	1.22E+07	18.68
Nd-155	60	155	2.51E+07	12.95
Nd-154	60	154	8.09E+07	7.46
Nd-153	60	153	1.29E+08	5.91
Nd-152	60	152	2.73E+08	3.93
Nd-151	60	151	4.16E+08	3.36
Nd-149	60	149	7.84E+08	2.5
Nd-147	60	147	1.56E+08	1.69
Nd-141	60	141	7.94E+07	7.39
Nd-141m	60	141	2.85E+07	8.87
Nd-140	60	140	2.21E+07	8.54
Nd-139m	60	139	1.50E+07	12.11
Nd-139	60	139	1.98E+07	12.5
Nd-138	60	138	2.10E+07	13.1
Nd-137	60	137	8.15E+06	21.88
Nd-137m	60	137	3.86E+06	22.54
Nd-136	60	136	3.43E+06	34.73
Nd-135	60	135	4.29E+05	70.53
Nd-135m	60	135	4.29E+05	70.53
Pr-154	59	154	1.39E+07	16.48

Pr-153	59	153	4.24E+07	9.59
Pr-152	59	152	9.11E+07	6.96
Pr-151	59	151	2.32E+08	4.59
Pr-150	59	150	3.50E+08	3.07
Pr-149	59	149	5.85E+08	2.97
Pr-148	59	148	6.51E+08	2.38
Pr-148m	59	148	1.85E+08	3.59
Pr-147	59	147	1.16E+09	1.9
Pr-146	59	146	1.42E+09	1.62
Pr-145	59	145	1.76E+09	1.45
Pr-144	59	144	2.55E+08	3.78
Pr-144m	59	144	1.23E+08	3.92
Pr-143	59	143	1.01E+08	1.35
Pr-142	59	142	1.27E+08	5.46
Pr-142m	59	142	7.70E+07	5.46
Pr-140	59	140	1.38E+08	5.17
Pr-139	59	139	1.36E+08	6.14
Pr-138	59	138	4.93E+07	7.1
Pr-138m	59	138	2.83E+07	8.28
Pr-137	59	137	4.59E+07	9.99
Pr-136	59	136	2.66E+07	13.6
Pr-135	59	135	1.20E+07	18.97
Pr-134	59	134	2.79E+06	29.01
Pr-134m	59	134	2.36E+06	29.38
Pr-133	59	133	1.29E+06	57.44
Ce-152	58	152	1.46E+07	16.99
Ce-151	58	151	3.78E+07	10.76
Ce-150	58	150	1.20E+08	5.75
Ce-149	58	149	2.02E+08	4.46
Ce-148	58	148	4.67E+08	2.77
Ce-147	58	147	6.68E+08	2.38
Ce-146	58	146	1.08E+09	1.95
Ce-145	58	145	1.37E+09	1.73
Ce-144	58	144	9.21E+06	1.44
Ce-143	58	143	1.37E+09	1.28
Ce-141	58	141	1.03E+08	1.22
Ce-139	58	139	3.44E+06	3.69
Ce-139m	58	139	1.14E+08	4.48
Ce-138m	58	138	1.21E+08	4.2
Ce-137	58	137	1.50E+08	4.67
Ce-137m	58	137	4.47E+07	5.15
Ce-135	58	135	6.98E+07	7.15

Ce-135m	58	135	3.52E+07	7.82
Ce-134	58	134	2.05E+07	9.03
Ce-133m	58	133	1.26E+07	12.9
Ce-133	58	133	1.39E+07	13.26
Ce-132	58	132	1.03E+07	21.75
Ce-131	58	131	2.79E+06	29.01
Ce-131m	58	131	2.36E+06	29.38
La-150	57	150	1.13E+07	20.83
La-149	57	149	5.60E+07	8.31
La-148	57	148	1.03E+08	5.65
La-147	57	147	2.82E+08	3.73
La-146	57	146	2.46E+08	3.38
La-146m	57	146	1.53E+08	3.7
La-145	57	145	8.18E+08	2.15
La-144	57	144	1.09E+09	1.89
La-143	57	143	1.62E+09	1.52
La-142	57	142	2.03E+09	1.5
La-141	57	141	2.42E+09	1.25
La-140	57	140	4.43E+08	2.24
La-137	57	137	3.16E+01	2.63
La-136	57	136	2.78E+08	3.9
La-136m	57	136	1.39E+08	3.9
La-135	57	135	2.54E+08	3.58
La-134	57	134	1.75E+08	5.2
La-133	57	133	1.51E+08	5.06
La-132	57	132	6.50E+07	8.07
La-132m	57	132	3.11E+07	8.63
La-131	57	131	4.25E+07	9.71
La-130	57	130	1.85E+07	14.7
La-129	57	129	7.29E+06	26.08
La-129m	57	129	3.65E+06	26.08
Ba-149	56	149	3.40E+06	33.73
Ba-148	56	148	1.94E+07	14.6
Ba-147	56	147	4.93E+07	8.62
Ba-146	56	146	1.08E+08	6.18
Ba-145	56	145	2.00E+08	4.19
Ba-144	56	144	4.68E+08	2.7
Ba-143	56	143	6.24E+08	2.53
Ba-142	56	142	1.17E+09	1.93
Ba-141	56	141	1.45E+09	1.57
Ba-140	56	140	2.21E+08	1.35
Ba-139	56	139	2.28E+09	1.4

Ba-137m	56	137	4.52E+08	2.24
Ba-136m	56	136	4.24E+08	2.41
Ba-135m	56	135	1.69E+08	2.75
Ba-133	56	133	1.23E+05	3.26
Ba-133m	56	133	9.13E+07	3.93
Ba-131	56	131	2.54E+07	4.2
Ba-131m	56	131	9.44E+07	4.72
Ba-130m	56	130	7.55E+07	5.07
Ba-129m	56	129	3.43E+07	7.52
Ba-129	56	129	4.16E+07	7.87
Ba-128	56	128	1.53E+07	10.82
Ba-127	56	127	1.37E+07	19.03
Ba-126	56	126	4.29E+06	34
Cs-147	55	147	2.99E+06	35.87
Cs-146	55	146	7.12E+06	24.58
Cs-145	55	145	3.40E+07	10.11
Cs-144	55	144	4.36E+07	6.21
Cs-144m	55	144	3.90E+07	6.22
Cs-143	55	143	2.03E+08	3.92
Cs-142	55	142	3.48E+08	3.08
Cs-141	55	141	6.39E+08	2.43
Cs-140	55	140	8.63E+08	2.12
Cs-139	55	139	1.32E+09	1.74
Cs-138	55	138	1.54E+09	1.63
Cs-138m	55	138	4.80E+08	2.18
Cs-137	55	137	3.22E+05	1.17
Cs-136m	55	136	6.72E+08	1.84
Cs-136	55	136	1.01E+08	1.84
Cs-135	55	135	4.50E+00	1.12
Cs-135m	55	135	6.48E+08	1.91
Cs-134m	55	134	4.01E+08	2.23
Cs-134	55	134	1.41E+06	2.23
Cs-132	55	132	1.14E+08	2.84
Cs-131	55	131	7.63E+07	2.76
Cs-130	55	130	3.67E+08	3.48
Cs-130m	55	130	1.83E+08	3.48
Cs-129	55	129	2.75E+08	3.25
Cs-128	55	128	2.02E+08	4.31
Cs-127	55	127	1.49E+08	5.42
Cs-126	55	126	6.05E+07	7.84
Cs-125	55	125	2.70E+07	12.03
Cs-124	55	124	4.72E+06	29.38

Cs-124m	55	124	2.36E+06	29.38
Cs-123	55	123	2.15E+06	44.27
Cs-123m	55	123	1.07E+06	44.27
Xe-144	54	144	4.61E+06	25.01
Xe-143	54	143	1.27E+07	15.42
Xe-142	54	142	6.46E+07	6.62
Xe-141	54	141	1.14E+08	5.07
Xe-140	54	140	2.56E+08	3.68
Xe-139	54	139	3.21E+08	3
Xe-138	54	138	6.71E+08	2.37
Xe-137	54	137	7.86E+08	2.24
Xe-135	54	135	2.10E+09	1.34
Xe-135m	54	135	7.94E+08	1.51
Xe-134m	54	134	8.27E+08	1.48
Xe-133	54	133	3.83E+08	1.16
Xe-133m	54	133	2.83E+08	1.88
Xe-132m	54	132	6.48E+08	1.87
Xe-131m	54	131	4.80E+07	2.07
Xe-129m	54	129	5.01E+07	2.76
Xe-127	54	127	2.11E+07	2.87
Xe-127m	54	127	2.22E+08	3.51
Xe-125	54	125	1.80E+08	4.12
Xe-125m	54	125	9.14E+07	4.54
Xe-123	54	123	4.81E+07	9.18
Xe-122	54	122	1.74E+07	14.39
Xe-121	54	121	6.87E+06	25.62
Xe-120	54	120	8.58E+05	70.53
I-142	53	142	8.24E+05	49.68
I-141	53	141	9.22E+06	18.12
I-140	53	140	2.83E+07	10.47
I-139	53	139	7.64E+07	5.67
I-138	53	138	1.40E+08	4.9
I-137	53	137	2.25E+08	4.54
I-136	53	136	2.36E+08	3.27
I-136m	53	136	1.59E+08	3.39
I-135	53	135	8.78E+08	2.08
I-134	53	134	1.22E+09	2.02
I-134m	53	134	4.88E+08	2.25
I-133	53	133	1.45E+09	1.46
I-133m	53	133	7.00E+08	1.71
I-132	53	132	1.37E+09	1.67
I-132m	53	132	5.73E+08	2.02

I-131	53	131	3.78E+08	1.18
I-130	53	130	1.02E+09	1.86
I-130m	53	130	5.94E+08	1.86
I-128	53	128	1.09E+09	1.78
I-126	53	126	8.81E+07	2.05
I-125	53	125	2.19E+07	1.98
I-124	53	124	1.31E+08	3.44
I-123	53	123	3.87E+08	3.31
I-122	53	122	1.65E+08	5.34
I-121	53	121	9.23E+07	7.6
I-120m	53	120	1.03E+07	14.54
I-120	53	120	1.12E+07	15.24
I-119	53	119	8.58E+06	23.51
Te-138	52	138	1.40E+07	13.13
Te-137	52	137	2.19E+07	10.89
Te-136	52	136	1.04E+08	5.14
Te-135	52	135	1.28E+08	5.17
Te-134	52	134	3.32E+08	3.61
Te-133	52	133	2.89E+08	2.59
Te-133m	52	133	2.25E+08	2.71
Te-132	52	132	3.25E+08	2.17
Te-131	52	131	7.43E+08	2.02
Te-131m	52	131	2.76E+08	2.15
Te-129	52	129	1.41E+09	1.53
Te-129m	52	129	2.62E+07	1.77
Te-127	52	127	1.06E+09	1.3
Te-127m	52	127	9.41E+06	1.68
Te-125m	52	125	1.68E+07	1.73
Te-123m	52	123	5.79E+06	2.11
Te-121	52	121	2.52E+07	2.94
Te-121m	52	121	2.07E+06	3.1
Te-119	52	119	7.35E+07	5.28
Te-119m	52	119	1.93E+07	5.54
Te-118	52	118	1.57E+07	7.48
Te-117	52	117	1.72E+07	15.85
Te-117m	52	117	8.58E+06	15.85
Te-116	52	116	6.44E+06	24.9
Sb-136	51	136	3.92E+06	23.24
Sb-135	51	135	2.05E+07	12.04
Sb-134m	51	134	3.39E+07	7.25
Sb-134	51	134	1.62E+07	9.28
Sb-133	51	133	1.14E+08	5.19

Sb-133m	51	133	6.95E+07	5.52
Sb-133n	51	133	3.47E+07	5.52
Sb-132m	51	132	1.14E+08	4.29
Sb-132	51	132	6.33E+07	5.44
Sb-131	51	131	3.15E+08	3.37
Sb-130	51	130	2.30E+08	3.02
Sb-130m	51	130	2.23E+08	3.07
Sb-129	51	129	5.26E+08	2.25
Sb-129m	51	129	3.95E+08	2.35
Sb-128m	51	128	7.73E+08	2.03
Sb-128	51	128	4.56E+08	2.08
Sb-127	51	127	6.22E+08	1.4
Sb-126m	51	126	1.00E+09	1.68
Sb-126n	51	126	5.02E+08	1.68
Sb-126	51	126	6.75E+07	1.68
Sb-125	51	125	4.35E+06	1.08
Sb-124m	51	124	1.26E+09	1.61
Sb-124n	51	124	6.28E+08	1.61
Sb-124	51	124	3.56E+07	1.61
Sb-122m	51	122	8.66E+08	1.56
Sb-122	51	122	6.95E+08	1.56
Sb-120	51	120	5.43E+08	2.21
Sb-120m	51	120	1.16E+08	2.21
Sb-119	51	119	5.91E+08	1.92
Sb-118	51	118	2.33E+08	2.99
Sb-118m	51	118	2.17E+08	3.15
Sb-117	51	117	3.12E+08	3.79
Sb-116	51	116	5.66E+07	6.28
Sb-116m	51	116	5.02E+07	6.58
Sb-115	51	115	4.16E+07	10.23
Sb-114	51	114	1.20E+07	18.28
Sn-134	50	134	2.41E+06	28.09
Sn-133	50	133	9.67E+06	15.02
Sn-132	50	132	3.50E+07	8.53
Sn-131m	50	131	2.74E+07	8.86
Sn-131	50	131	1.89E+07	9.72
Sn-130m	50	130	4.73E+07	6.11
Sn-130	50	130	3.67E+07	6.88
Sn-129	50	129	7.25E+07	5.67
Sn-129m	50	129	5.90E+07	5.74
Sn-128	50	128	3.33E+08	3.56
Sn-128m	50	128	1.59E+08	3.68

Sn-127	50	127	2.56E+08	2.71
Sn-127m	50	127	2.74E+08	2.88
Sn-126	50	126	4.33E+01	1.97
Sn-125	50	125	1.05E+08	1.59
Sn-125m	50	125	8.16E+08	1.61
Sn-123m	50	123	2.71E+09	1.21
Sn-123	50	123	1.05E+07	1.48
Sn-121	50	121	3.64E+09	0.83
Sn-121m	50	121	1.01E+05	1.11
Sn-119m	50	119	4.94E+06	1.27
Sn-117m	50	117	6.02E+07	1.8
Sn-113	50	113	9.72E+05	7.14
Sn-113m	50	113	4.25E+07	7.2
Sn-111	50	111	7.29E+06	23.26
Sn-110	50	110	1.72E+06	49.62
In-132	49	132	1.02E+06	44.31
In-131m	49	131	2.09E+06	27.81
In-131	49	131	6.41E+05	36.37
In-131n	49	131	6.35E+05	36.37
In-130n	49	130	3.72E+06	20.8
In-130m	49	130	3.71E+06	20.8
In-130	49	130	1.84E+06	27.5
In-129m	49	129	1.00E+07	14.75
In-129	49	129	7.29E+06	16.74
In-128m	49	128	1.95E+07	10.08
In-128	49	128	1.87E+07	10.28
In-127m	49	127	5.63E+07	5.65
In-127	49	127	5.38E+07	5.82
In-126m	49	126	1.26E+08	4.43
In-126	49	126	9.13E+07	4.84
In-125	49	125	2.71E+08	2.91
In-125m	49	125	2.41E+08	2.96
In-124	49	124	5.06E+08	2.17
In-124m	49	124	3.24E+08	2.35
In-123	49	123	9.89E+08	1.65
In-123m	49	123	8.03E+08	1.67
In-122	49	122	1.39E+09	1.53
In-122m	49	122	5.42E+08	1.6
In-122n	49	122	5.42E+08	1.6
In-121m	49	121	2.00E+09	0.99
In-121	49	121	2.25E+09	1
In-120	49	120	3.71E+09	0.92

In-120m	49	120	9.12E+08	1.22
In-120n	49	120	9.12E+08	1.22
In-119m	49	119	3.69E+09	0.79
In-119	49	119	3.95E+09	0.8
In-118	49	118	7.06E+09	0.8
In-118m	49	118	2.01E+09	1.14
In-118n	49	118	1.01E+09	1.14
In-117	49	117	7.88E+09	0.57
In-117m	49	117	5.28E+09	0.57
In-116m	49	116	1.47E+09	1.41
In-116	49	116	7.35E+08	1.41
In-116n	49	116	7.35E+08	1.41
In-115m	49	115	4.75E+09	0.53
In-114	49	114	7.54E+08	1.88
In-114n	49	114	3.72E+08	1.88
In-114m	49	114	1.03E+07	1.88
In-113m	49	113	3.95E+08	2.21
In-112	49	112	3.17E+08	3.93
In-112m	49	112	1.59E+08	3.93
In-111	49	111	6.53E+07	5.05
In-111m	49	111	8.02E+07	5.2
In-110	49	110	2.68E+07	8.59
In-110m	49	110	2.51E+07	8.59
In-109	49	109	2.32E+07	14.07
In-109m	49	109	7.72E+06	14.07
In-109n	49	109	7.72E+06	14.07
In-108	49	108	1.50E+06	42.38
In-108m	49	108	1.07E+06	44.27
Cd-128	48	128	2.36E+06	39.09
Cd-127	48	127	6.58E+06	22.53
Cd-126	48	126	3.27E+07	10.48
Cd-125	48	125	2.20E+07	9.15
Cd-125m	48	125	2.20E+07	9.15
Cd-124	48	124	1.83E+08	5.02
Cd-123	48	123	2.31E+08	3.81
Cd-123m	48	123	1.22E+08	4.08
Cd-122	48	122	8.49E+08	2.37
Cd-121	48	121	7.41E+08	1.97
Cd-121m	48	121	4.57E+08	2.18
Cd-120	48	120	2.80E+09	1.17
Cd-119	48	119	1.81E+09	1.04
Cd-119m	48	119	1.66E+09	1.04

Cd-118	48	118	6.05E+09	0.9
Cd-117	48	117	3.79E+09	0.68
Cd-117m	48	117	3.35E+09	0.69
Cd-115	48	115	4.16E+09	0.58
Cd-115m	48	115	5.98E+07	0.92
Cd-113m	48	113	3.49E+05	1.2
Cd-111m	48	111	5.14E+08	2.08
Cd-109	48	109	7.96E+05	3.95
Cd-109m	48	109	8.20E+07	4.12
Cd-109n	48	109	8.20E+07	4.12
Cd-107	48	107	2.47E+07	14.17
Cd-105	48	105	1.29E+06	57.44
Ag-124	47	124	1.31E+07	17.86
Ag-123	47	123	4.78E+07	9.29
Ag-122	47	122	4.44E+07	6.52
Ag-122m	47	122	4.64E+07	6.57
Ag-121	47	121	2.85E+08	3.81
Ag-120	47	120	4.30E+08	2.61
Ag-120m	47	120	2.54E+08	2.7
Ag-119	47	119	7.35E+08	1.77
Ag-119m	47	119	5.87E+08	1.85
Ag-118	47	118	1.38E+09	1.41
Ag-118m	47	118	9.78E+08	1.41
Ag-117	47	117	2.02E+09	0.94
Ag-117m	47	117	1.91E+09	0.94
Ag-116	47	116	3.64E+09	1.01
Ag-116m	47	116	1.54E+09	1.23
Ag-115	47	115	5.30E+09	0.71
Ag-115m	47	115	2.97E+09	0.74
Ag-114	47	114	9.23E+09	0.71
Ag-113	47	113	1.03E+10	0.64
Ag-113m	47	113	3.56E+09	0.75
Ag-112	47	112	1.10E+10	0.56
Ag-111	47	111	2.32E+09	0.58
Ag-111m	47	111	1.21E+10	0.59
Ag-110	47	110	1.04E+09	1.49
Ag-110m	47	110	5.78E+06	1.49
Ag-109m	47	109	1.35E+10	0.5
Ag-108	47	108	3.89E+08	2.14
Ag-108m	47	108	3.53E+03	2.14
Ag-107m	47	107	2.53E+08	3.09
Ag-106	47	106	6.76E+07	5.54

Ag-106m	47	106	1.02E+07	5.54
Ag-105	47	105	2.06E+06	8.83
Ag-105m	47	105	3.07E+07	8.89
Ag-104	47	104	9.15E+06	17.41
Ag-104m	47	104	6.87E+06	17.41
Ag-103	47	103	1.72E+06	49.62
Ag-103m	47	103	8.58E+05	49.62
Pd-120	46	120	8.43E+07	7.01
Pd-119	46	119	1.48E+08	5.2
Pd-118	46	118	4.82E+08	2.99
Pd-117	46	117	7.66E+08	2.43
Pd-117m	46	117	3.12E+08	2.65
Pd-116	46	116	2.00E+09	1.56
Pd-115	46	115	1.80E+09	1.35
Pd-115m	46	115	9.51E+08	1.43
Pd-114	46	114	5.20E+09	0.9
Pd-113	46	113	5.18E+09	0.86
Pd-113m	46	113	1.22E+09	1.08
Pd-113n	46	113	1.22E+09	1.08
Pd-112	46	112	7.68E+09	0.64
Pd-111	46	111	9.87E+09	0.66
Pd-111m	46	111	2.13E+09	0.98
Pd-109	46	109	1.27E+10	0.51
Pd-109m	46	109	1.73E+09	1
Pd-107	46	107	8.96E+00	0.56
Pd-107m	46	107	9.13E+08	1.5
Pd-103	46	103	8.27E+06	6.51
Pd-101	46	101	7.57E+06	23.88
Pd-100	46	100	5.45E+05	49.62
Rh-117	45	117	1.41E+08	5.59
Rh-116	45	116	1.24E+08	4.12
Rh-116m	45	116	1.24E+08	4.12
Rh-115	45	115	7.76E+08	2.5
Rh-114	45	114	6.95E+08	1.99
Rh-114m	45	114	4.94E+08	2.05
Rh-113	45	113	2.74E+09	1.21
Rh-112	45	112	2.40E+09	1.14
Rh-112m	45	112	1.31E+09	1.43
Rh-111	45	111	6.18E+09	0.87
Rh-110m	45	110	5.57E+09	0.81
Rh-110	45	110	2.27E+09	0.99
Rh-109	45	109	1.04E+10	0.6

Rh-109m	45	109	4.50E+09	0.65
Rh-108	45	108	9.59E+09	0.65
Rh-108m	45	108	2.28E+09	1.09
Rh-107	45	107	1.37E+10	0.6
Rh-106	45	106	1.64E+09	1.19
Rh-106m	45	106	1.60E+09	1.22
Rh-105	45	105	8.20E+09	0.58
Rh-105m	45	105	4.71E+09	0.6
Rh-104	45	104	1.44E+09	1.68
Rh-104m	45	104	7.22E+08	1.68
Rh-103m	45	103	9.52E+08	1.18
Rh-102	45	102	1.26E+06	3.23
Rh-102m	45	102	2.47E+05	3.23
Rh-101	45	101	1.16E+05	5.29
Rh-101m	45	101	2.58E+07	5.47
Rh-100	45	100	3.39E+07	9.3
Rh-100m	45	100	2.12E+07	9.39
Rh-99m	45	99	7.50E+06	18.31
Rh-99	45	99	6.20E+05	18.31
Rh-98	45	98	1.72E+06	44.62
Rh-98m	45	98	8.58E+05	49.62
Ru-115	44	115	6.24E+07	8.17
Ru-114	44	114	2.01E+08	4.62
Ru-113	44	113	3.44E+08	3.69
Ru-112	44	112	1.08E+09	1.87
Ru-111	44	111	1.57E+09	1.63
Ru-110	44	110	3.30E+09	1.25
Ru-109	44	109	2.90E+09	1.02
Ru-109m	44	109	1.45E+09	1.22
Ru-108	44	108	7.31E+09	0.76
Ru-107	44	107	8.34E+09	0.78
Ru-106	44	106	4.18E+07	0.62
Ru-105	44	105	1.16E+10	0.63
Ru-103	44	103	4.53E+08	0.62
Ru-103m	44	103	1.33E+09	1.33
Ru-101m	44	101	5.41E+08	2
Ru-97	44	97	7.17E+06	15.17
Tc-115	43	115	6.44E+06	26.63
Tc-113	43	113	4.89E+07	10.81
Tc-112	43	112	9.66E+07	6.5
Tc-111	43	111	3.17E+08	3.64
Tc-110	43	110	5.58E+08	2.81

Tc-109	43	109	1.44E+09	1.81
Tc-108	43	108	1.97E+09	1.39
Tc-107	43	107	3.93E+09	1.17
Tc-106	43	106	4.93E+09	0.94
Tc-105	43	105	7.47E+09	0.78
Tc-104	43	104	8.54E+09	0.73
Tc-103	43	103	1.04E+10	0.69
Tc-102	43	102	9.60E+09	0.61
Tc-102m	43	102	1.91E+09	1.12
Tc-101	43	101	1.15E+10	0.6
Tc-100	43	100	2.19E+09	1.44
Tc-99m	43	99	3.53E+09	0.62
Tc-99	43	99	5.41E+01	0.79
Tc-97m	43	97	3.15E+06	3.44
Tc-96m	43	96	6.39E+07	5.85
Tc-96	43	96	3.46E+07	5.85
Tc-95m	43	95	5.50E+05	9.51
Tc-95	43	95	2.02E+07	9.57
Tc-94m	43	94	5.79E+06	19.42
Tc-94	43	94	5.79E+06	19.42
Tc-93	43	93	1.52E+06	49.62
Tc-93m	43	93	8.58E+05	49.62
Mo-110	42	110	6.82E+07	7.83
Mo-109	42	109	1.14E+08	6.79
Mo-108	42	108	3.83E+08	3.3
Mo-107	42	107	6.62E+08	2.66
Mo-106	42	106	1.60E+09	1.69
Mo-105	42	105	2.18E+09	1.34
Mo-104	42	104	4.22E+09	0.95
Mo-103	42	103	4.97E+09	1
Mo-102	42	102	7.65E+09	0.73
Mo-101	42	101	7.69E+09	0.69
Mo-99	42	99	3.64E+09	0.71
Mo-93	42	93	6.88E+01	7.9
Mo-93m	42	93	3.92E+07	7.98
Mo-91	42	91	1.29E+06	49.62
Mo-91m	42	91	8.58E+05	49.62
Nb-107	41	107	9.48E+07	6.5
Nb-106	41	106	1.58E+08	5.01
Nb-105	41	105	4.81E+08	3.01
Nb-104m	41	104	3.72E+08	2.29
Nb-104	41	104	4.77E+08	2.31

Nb-103	41	103	1.82E+09	1.58
Nb-102	41	102	1.55E+09	1.36
Nb-102m	41	102	9.83E+08	1.49
Nb-101	41	101	4.07E+09	1.03
Nb-100	41	100	3.46E+09	1.1
Nb-100m	41	100	1.55E+09	1.18
Nb-99	41	99	3.41E+09	0.84
Nb-99m	41	99	2.79E+09	0.85
Nb-98	41	98	5.33E+09	0.9
Nb-98m	41	98	1.74E+09	1.14
Nb-97	41	97	7.88E+09	0.63
Nb-97m	41	97	5.73E+09	0.65
Nb-96	41	96	2.06E+09	1.07
Nb-95	41	95	5.30E+07	1.28
Nb-95m	41	95	3.55E+08	1.35
Nb-94m	41	94	5.90E+08	2
Nb-94	41	94	2.20E+02	2
Nb-93m	41	93	8.63E+04	2.4
Nb-92m	41	92	1.84E+07	3.97
Nb-91m	41	91	1.51E+06	5.27
Nb-91	41	91	3.89E+02	5.28
Nb-90	41	90	1.62E+07	14.16
Nb-90m	41	90	9.01E+06	14.16
Nb-89	41	89	6.44E+05	57.44
Nb-89m	41	89	6.44E+05	57.44
Zr-104	40	104	1.07E+08	6.81
Zr-103	40	103	2.01E+08	4.5
Zr-102	40	102	5.63E+08	2.85
Zr-101	40	101	8.90E+08	2.09
Zr-100	40	100	1.91E+09	1.75
Zr-99	40	99	2.23E+09	1.42
Zr-98	40	98	3.59E+09	1.15
Zr-97	40	97	3.96E+09	0.93
Zr-95	40	95	1.49E+08	0.83
Zr-93	40	93	1.54E+01	0.77
Zr-90m	40	90	2.87E+08	2.85
Zr-89	40	89	4.25E+07	5.9
Zr-89m	40	89	6.29E+07	5.92
Zr-88	40	88	6.15E+05	11
Zr-87	40	87	3.00E+06	37.22
Zr-87m	40	87	1.50E+06	37.22
Zr-86	40	86	2.60E+06	37.22

Y-102	39	102	3.43E+07	7.63
Y-102m	39	102	3.01E+07	7.91
Y-101	39	101	1.55E+08	5.11
Y-100	39	100	1.87E+08	3.78
Y-100m	39	100	1.44E+08	3.85
Y-99	39	99	6.96E+08	2.39
Y-98m	39	98	5.02E+08	2.07
Y-98	39	98	5.73E+08	2.11
Y-97	39	97	1.16E+09	1.53
Y-97m	39	97	5.50E+08	1.55
Y-97n	39	97	4.84E+08	1.7
Y-96	39	96	1.65E+09	1.41
Y-96m	39	96	8.80E+08	1.56
Y-95	39	95	3.90E+09	1.15
Y-94	39	94	4.98E+09	0.86
Y-93	39	93	5.73E+09	0.83
Y-93m	39	93	2.56E+09	0.85
Y-92	39	92	6.86E+09	0.74
Y-91m	39	91	3.50E+09	0.74
Y-91	39	91	1.33E+08	0.75
Y-90m	39	90	6.91E+08	1.77
Y-90	39	90	5.38E+08	1.77
Y-89m	39	89	6.28E+08	1.64
Y-88	39	88	5.07E+06	3.41
Y-87	39	87	4.79E+07	4.87
Y-87m	39	87	7.65E+07	4.92
Y-86	39	86	3.93E+07	9.42
Y-86m	39	86	2.10E+07	9.6
Y-85	39	85	3.86E+06	25.14
Y-85m	39	85	3.86E+06	25.14
Y-84	39	84	8.58E+05	49.62
Y-84m	39	84	8.58E+05	49.62
Y-83	39	83	6.01E+05	70.53
Y-83m	39	83	4.29E+05	70.53
Sr-102	38	102	4.49E+06	29.8
Sr-101	38	101	5.02E+06	29.88
Sr-100	38	100	4.36E+07	9.28
Sr-99	38	99	7.50E+07	6.86
Sr-98	38	98	2.31E+08	4.45
Sr-97	38	97	3.33E+08	3.51
Sr-96	38	96	7.85E+08	2.24
Sr-95	38	95	1.15E+09	1.94

Sr-94	38	94	2.22E+09	1.18
Sr-93	38	93	2.94E+09	1.19
Sr-92	38	92	4.39E+09	0.94
Sr-91	38	91	4.78E+09	0.9
Sr-90	38	90	7.89E+05	0.87
Sr-89	38	89	1.68E+08	0.86
Sr-87m	38	87	4.36E+08	2.01
Sr-85	38	85	3.27E+06	5.32
Sr-85m	38	85	8.05E+07	5.43
Sr-83	38	83	1.02E+07	16.74
Sr-83m	38	83	7.51E+06	16.92
Sr-82	38	82	1.36E+05	40.31
Rb-100	37	100	3.86E+06	32.66
Rb-99	37	99	9.01E+06	21.77
Rb-98	37	98	8.88E+06	14.14
Rb-98m	37	98	8.88E+06	14.14
Rb-97	37	97	5.67E+07	8.09
Rb-96	37	96	9.50E+07	6.31
Rb-95	37	95	3.18E+08	4.05
Rb-94	37	94	5.12E+08	2.54
Rb-93	37	93	1.12E+09	1.94
Rb-92	37	92	1.76E+09	1.53
Rb-91	37	91	2.73E+09	1.18
Rb-90	37	90	2.32E+09	1.17
Rb-90m	37	90	1.14E+09	1.32
Rb-89	37	89	4.46E+09	0.94
Rb-88	37	88	5.07E+09	0.93
Rb-86m	37	86	6.80E+08	1.78
Rb-86	37	86	9.75E+07	1.78
Rb-84m	37	84	2.00E+08	3.16
Rb-84	37	84	1.65E+07	3.16
Rb-83	37	83	3.27E+06	4.17
Rb-83m	37	83	9.96E+07	4.21
Rb-82	37	82	2.58E+07	9.64
Rb-82m	37	82	2.54E+07	9.69
Rb-81	37	81	2.03E+07	14.24
Rb-81m	37	81	1.03E+07	14.24
Rb-80	37	80	3.00E+06	42.38
Rb-79	37	79	8.58E+05	70.53
Kr-95	36	95	2.14E+07	13.93
Kr-94	36	94	9.22E+07	6.6
Kr-93	36	93	1.52E+08	4.99

Kr-92	36	92	5.04E+08	2.73
Kr-91	36	91	8.28E+08	2.19
Kr-90	36	90	1.53E+09	1.75
Kr-89	36	89	2.18E+09	1.17
Kr-88	36	88	3.20E+09	1.16
Kr-87	36	87	3.61E+09	1.1
Kr-85m	36	85	4.21E+09	0.92
Kr-85	36	85	5.30E+05	1.08
Kr-83m	36	83	4.29E+09	0.93
Kr-81	36	81	3.53E+00	4.19
Kr-81m	36	81	9.76E+07	4.5
Kr-79	36	79	1.42E+07	12.23
Kr-79m	36	79	1.12E+07	12.57
Br-94	35	94	4.93E+06	28.37
Br-93	35	93	2.86E+07	11.12
Br-92	35	92	4.74E+07	9.64
Br-91	35	91	1.77E+08	4.33
Br-90	35	90	3.17E+08	3.76
Br-89	35	89	7.90E+08	2.13
Br-88	35	88	1.18E+09	1.81
Br-87	35	87	1.91E+09	1.45
Br-86	35	86	2.45E+09	1.3
Br-85	35	85	3.51E+09	1.06
Br-84	35	84	3.19E+09	1.13
Br-84m	35	84	7.43E+08	1.77
Br-83	35	83	3.96E+09	0.96
Br-82	35	82	5.62E+08	2.23
Br-82m	35	82	4.67E+08	2.23
Br-80	35	80	3.68E+08	3.65
Br-80m	35	80	1.84E+08	3.65
Br-79m	35	79	1.23E+08	3.96
Br-78	35	78	9.14E+07	6.59
Br-77m	35	77	1.63E+07	10.97
Br-77	35	77	1.46E+07	11
Br-76	35	76	4.48E+06	28.06
Br-76m	35	76	2.57E+06	28.06
Se-91	34	91	9.57E+06	20.34
Se-89	34	89	9.25E+07	6.6
Se-88	34	88	2.49E+08	4.16
Se-87	34	87	4.46E+08	3.06
Se-86	34	86	1.05E+09	2.04
Se-85	34	85	1.20E+09	1.6

Se-84	34	84	2.45E+09	1.4
Se-83m	34	83	1.41E+09	1.21
Se-83	34	83	9.53E+08	1.26
Se-81	34	81	2.85E+09	1.36
Se-81m	34	81	5.26E+08	2.04
Se-79m	34	79	2.32E+09	1.32
Se-79	34	79	1.51E+01	1.32
Se-77m	34	77	1.05E+08	4.35
Se-75	34	75	4.74E+05	10.23
As-87	33	87	7.91E+07	7.93
As-86	33	86	1.49E+08	5.28
As-85	33	85	3.80E+08	3.29
As-84	33	84	3.00E+08	2.98
As-84m	33	84	2.25E+08	3.02
As-83	33	83	1.15E+09	1.77
As-82	33	82	9.34E+08	1.84
As-82m	33	82	4.64E+08	2.26
As-81	33	81	1.84E+09	1.71
As-80	33	80	1.99E+09	1.4
As-79	33	79	2.08E+09	1.4
As-78	33	78	2.12E+09	1.47
As-77	33	77	1.05E+09	1.51
As-76	33	76	2.23E+08	3.71
As-74	33	74	7.83E+06	6.39
As-73	33	73	7.92E+05	10
As-72	33	72	7.74E+06	19.59
As-71	33	71	2.06E+06	28.06
As-69	33	69	8.58E+05	70.53
Ge-85	32	85	2.38E+07	13.86
Ge-84	32	84	8.81E+07	6.67
Ge-83	32	83	1.41E+08	5.3
Ge-82	32	82	4.75E+08	2.98
Ge-81	32	81	2.69E+08	2.97
Ge-81m	32	81	2.55E+08	3.01
Ge-80	32	80	1.01E+09	2.11
Ge-79	32	79	6.88E+08	2.06
Ge-79m	32	79	3.33E+08	2.47
Ge-78	32	78	1.47E+09	1.72
Ge-77m	32	77	1.01E+09	1.9
Ge-77	32	77	4.92E+08	2.05
Ge-75	32	75	1.19E+09	1.83
Ge-75m	32	75	2.02E+08	3.09

Ge-73m	32	73	9.11E+08	2.07
Ge-71	32	71	7.09E+06	8.3
Ge-71m	32	71	3.05E+07	8.45
Ge-69	32	69	4.92E+06	21.27
Ge-68	32	68	4.38E+03	70.53
Ga-84	31	84	2.36E+06	41.17
Ga-83	31	83	1.39E+07	16.31
Ga-82	31	82	3.30E+07	11.85
Ga-81	31	81	1.22E+08	5.68
Ga-80	31	80	1.65E+08	5.24
Ga-79	31	79	3.80E+08	3.44
Ga-78	31	78	4.94E+08	3
Ga-77	31	77	6.99E+08	2.47
Ga-76	31	76	7.36E+08	2.34
Ga-75	31	75	8.00E+08	2.22
Ga-74	31	74	5.93E+08	2.46
Ga-74m	31	74	5.03E+08	2.46
Ga-73	31	73	8.32E+08	2.24
Ga-72	31	72	4.04E+08	2.74
Ga-70	31	70	1.18E+08	5.8
Ga-68	31	68	2.75E+07	11.88
Ga-67	31	67	2.53E+06	23.26
Ga-66	31	66	3.33E+06	34.73
Zn-81	30	81	4.29E+06	34
Zn-80	30	80	1.63E+07	15.1
Zn-79	30	79	3.89E+07	10.88
Zn-78	30	78	9.71E+07	7.05
Zn-77	30	77	9.93E+07	6.18
Zn-77m	30	77	5.71E+07	6.5
Zn-76	30	76	2.91E+08	3.58
Zn-75	30	75	2.57E+08	4.15
Zn-74	30	74	4.22E+08	3.16
Zn-73	30	73	3.48E+08	3.5
Zn-73m	30	73	1.20E+08	4.62
Zn-72	30	72	2.71E+08	2.88
Zn-71	30	71	3.34E+08	3.31
Zn-71m	30	71	9.52E+07	5.12
Zn-69	30	69	3.92E+08	3.37
Zn-69m	30	69	6.10E+07	5.31
Zn-65	30	65	4.86E+04	21.27
Zn-63	30	63	8.58E+05	70.53
Cu-79	29	79	3.00E+06	37.22

Cu-78	29	78	3.44E+06	34.64
Cu-77	29	77	1.37E+07	17.29
Cu-76	29	76	2.58E+07	12.94
Cu-75	29	75	6.11E+07	8.86
Cu-74	29	74	7.74E+07	7.34
Cu-73	29	73	1.67E+08	5.27
Cu-72	29	72	1.56E+08	5.73
Cu-71	29	71	2.39E+08	3.96
Cu-70	29	70	1.50E+08	4.91
Cu-70m	29	70	6.93E+07	5.72
Cu-69	29	69	2.65E+08	4.06
Cu-68	29	68	2.53E+08	4.33
Cu-68m	29	68	6.33E+07	5.98
Cu-67	29	67	1.12E+08	3.95
Cu-66	29	66	1.53E+08	4.58
Cu-64	29	64	3.42E+07	10.49
Cu-62	29	62	6.42E+06	24.9
Cu-61	29	61	2.15E+06	44.27
Ni-74	28	74	9.84E+06	19.94
Ni-73	28	73	1.46E+07	17.25
Ni-72	28	72	3.52E+07	10.54
Ni-71	28	71	4.87E+07	9.09
Ni-70	28	70	8.11E+07	7.4
Ni-69	28	69	8.07E+07	7.22
Ni-68	28	68	1.37E+08	5.75
Ni-67	28	67	1.30E+08	5.84
Ni-66	28	66	6.91E+07	5.46
Ni-65	28	65	1.43E+08	5.24
Ni-63	28	63	5.58E+03	5.7
Co-71	27	71	7.93E+06	23.94
Co-70	27	70	6.87E+06	27.11
Co-69	27	69	1.93E+07	14.92
Co-68	27	68	2.15E+07	15.47
Co-67	27	67	3.82E+07	10.41
Co-66	27	66	3.61E+07	10.45
Co-65	27	65	6.14E+07	7.77
Co-64	27	64	8.41E+07	7.65
Co-63	27	63	9.44E+07	6.25
Co-62	27	62	6.81E+07	7.24
Co-62m	27	62	2.57E+07	9.07
Co-61	27	61	1.04E+08	6.7
Co-60m	27	60	1.50E+07	12.28

Co-60	27	60	2.16E+04	12.28
Co-58m	27	58	4.80E+06	21.51
Co-58	27	58	1.66E+05	21.51
Co-57	27	57	1.53E+04	37.22
Fe-68	26	68	3.43E+06	34.73
Fe-67	26	67	3.86E+06	32.66
Fe-66	26	66	8.15E+06	24.29
Fe-65	26	65	8.15E+06	23.12
Fe-64	26	64	2.62E+07	13.79
Fe-63	26	63	2.32E+07	13.57
Fe-62	26	62	4.21E+07	10.23
Fe-61	26	61	4.98E+07	9.34
Fe-59	26	59	2.00E+06	8.71
Fe-55	26	55	4.18E+03	42.38
Mn-65	25	65	1.72E+06	49.62
Mn-64	25	64	2.57E+06	40.31
Mn-63	25	63	4.29E+06	30.9
Mn-62	25	62	9.01E+06	22.79
Mn-61	25	61	1.33E+07	18.35
Mn-60	25	60	1.07E+07	16.59
Mn-60m	25	60	7.29E+06	17.75
Mn-59	25	59	2.70E+07	13.23
Mn-58	25	58	2.70E+07	11.1
Mn-58m	25	58	1.33E+07	11.97
Mn-57	25	57	3.56E+07	10.15
Mn-56	25	56	4.98E+07	9.5
Mn-54	25	54	3.80E+04	22.42
Mn-52m	25	52	4.29E+05	70.53
Mn-52	25	52	9.59E+04	70.53
Cr-62	24	62	1.29E+06	57.44
Cr-61	24	61	1.29E+06	57.44
Cr-60	24	60	2.57E+06	40.31
Cr-59	24	59	7.29E+06	23.26
Cr-58	24	58	1.37E+07	17.41
Cr-57	24	57	7.72E+06	23.88
Cr-56	24	56	3.00E+07	11.94
Cr-55	24	55	2.70E+07	11.6
Cr-51	24	51	1.47E+05	37.22
Cr-49	24	49	2.57E+06	40.31
V-56	23	56	3.86E+06	32.66
V-55	23	55	1.20E+07	18.28
V-54	23	54	1.54E+07	15.63
V-53	23	53	1.67E+07	15.29
V-52	23	52	2.45E+07	13.93
V-49	23	49	2.96E+04	24.7
V-48	23	48	2.14E+05	40.31
Ti-54	22	54	2.15E+06	44.27
Ti-53	22	53	3.86E+06	32.66
Ti-52	22	52	8.15E+06	21.88
Ti-51	22	51	1.54E+07	17.51
Ti-45	22	45	1.29E+06	57.44
Sc-51	21	51	3.00E+06	37.22
Sc-50	21	50	5.51E+06	29.01
Sc-50m	21	50	2.57E+06	30.44
Sc-49	21	49	1.54E+07	17.06
Sc-48	21	48	4.58E+06	21.27
Sc-47	21	47	3.42E+06	20.67
Sc-46m	21	46	8.58E+05	49.62
Sc-46	21	46	2.82E+04	49.62
Sc-45m	21	45	1.72E+06	34.73
Sc-44	21	44	1.49E+06	44.27
Sc-44m	21	44	4.65E+05	44.27
Sc-43	21	43	1.72E+06	49.62
Ca-47	20	47	1.92E+06	23.24
Ca-45	20	45	6.85E+04	27.51
K-47	19	47	1.72E+06	49.62
K-46	19	46	3.43E+06	34.73
K-45	19	45	3.00E+06	37.22
K-44	19	44	4.72E+06	29.38
K-43	19	43	5.32E+06	24.04
K-42	19	42	4.00E+06	33.99
Ar-44	18	44	1.72E+06	49.62
Ar-43	18	43	2.57E+06	40.31
Ar-42	18	42	5.45E+02	29.38
Ar-41	18	41	6.44E+06	24.9
Ar-39	18	39	9.53E+01	28.51
Ar-37	18	37	2.50E+05	28.26
Cl-42	17	42	1.29E+06	57.44
Cl-41	17	41	3.86E+06	32.66
Cl-40	17	40	3.86E+06	32.66
Cl-39	17	39	4.29E+06	34
Cl-38	17	38	5.58E+06	26.89
Cl-38m	17	38	1.93E+06	32.66
Cl-34	17	34	6.20E+05	70.53

Cl-34m	17	34	4.29E+05	70.53
S-40	16	40	8.58E+05	70.53
S-39	16	39	8.58E+05	70.53
S-38	16	38	1.72E+06	49.62
S-37	16	37	3.00E+06	37.22
S-35	16	35	1.35E+05	22.42
P-37	15	37	1.72E+06	49.62
P-35	15	35	3.00E+06	37.22
P-34	15	34	5.15E+06	28.06
P-33	15	33	3.16E+05	27.82
P-32	15	32	2.38E+05	40.31
P-30	15	30	3.86E+06	32.66
Si-35	14	35	8.58E+05	70.53
Si-34	14	34	2.15E+06	44.27
Si-33	14	33	7.85E+05	70.84
Si-32	14	32	4.90E+01	42.9
Si-31	14	31	2.15E+06	44.27
Al-31	13	31	1.29E+06	57.44
Al-30	13	30	1.29E+06	57.44
Al-29	13	29	1.72E+06	49.62
Al-28	13	28	1.80E+06	44.49
Mg-29	12	29	8.58E+05	70.53
Mg-28	12	28	1.37E+06	49.62
Mg-27	12	27	1.72E+06	49.62
Na-27	11	27	8.58E+05	70.53
Na-25	11	25	2.57E+06	40.31
Na-24	11	24	6.35E+07	7.45
Na-24m	11	24	1.42E+07	12.73
Na-22	11	22	2.50E+03	49.62
Ne-25	10	25	1.29E+06	57.44
Ne-24	10	24	4.29E+07	9.08
Ne-23	10	23	3.73E+07	10.88
F-22	9	22	2.15E+07	14.94
F-21	9	21	2.49E+07	13.07
F-20	9	20	3.86E+07	10.18
F-18	9	18	8.58E+05	70.53
O-22	8	22	8.58E+05	70.53
O-21	8	21	9.01E+06	21.77
O-20	8	20	2.27E+07	13.76
O-19	8	19	3.99E+07	10.1
O-15	8	15	8.58E+05	70.53
N-18	7	18	8.15E+06	23.12

N-17	7	17	3.09E+07	12.61
N-16	7	16	4.16E+07	9.69
N-13	7	13	2.15E+06	44.27
C-16	6	16	7.72E+06	22.54
C-15	6	15	3.69E+07	11.12
C-14	6	14	9.56E+01	5.3
C-11	6	11	1.33E+07	17.17
C-10	6	10	1.72E+06	49.62
B-14	5	14	2.15E+06	44.27
B-13	5	13	2.27E+07	13.5
B-12	5	12	4.07E+07	10.01
B-8	5	8	1.72E+06	49.62
Be-12	4	12	3.86E+06	32.66
Be-11	4	11	1.33E+07	17.77
Be-8	4	8	8.65E+07	6.53
Be-7	4	7	1.20E+06	9.8
Li-9	3	9	1.67E+07	16.54
Li-8	3	8	7.65E+07	7.22
He-8	2	8	4.72E+06	29.38
He-6	2	6	4.73E+08	3.05
H-3	1	3	6.41E+06	0.41

C AIRBORNE DOSE CALCULATIONS

Summary				
Nuclide	On-Site External Dose [mSv]	On-Site Internal Dose [mSv]	Off-Site Dose - No Filtration [mSv]	Off-Site Dose - With HC1 Stack Filtration [mSv]
H	3.38E-11	1.01E-06	3.20E-09	3.20E-09
Cl	1.20E-05	6.29E-06	1.76E-07	8.78E-10
Ar	1.25E-05	0.00E+00	6.18E-08	6.18E-08
Se	2.67E-03	2.23E-03	1.82E-05	9.11E-08
Br	1.09E-02	8.94E-03	8.78E-04	4.39E-06
Kr	1.04E-02	0.00E+00	5.78E-05	5.78E-05
I	9.13E-03	1.98E-01	1.95E-02	9.77E-05
Xe	1.22E-03	0.00E+00	7.82E-06	7.82E-06
Rn	8.67E-03	1.34E+01	4.50E-03	4.50E-03
Total [mSv]	**0.0430**	**13.6323**	**0.0250**	**0.0047**
	13.6753			

Filtration Parameters	
Elements filtered	Filter efficiency (99.5% HC stack and 99.5% filtration in HC
Po, Cl, Se, Br, I	0.999975

On-Site Exposure Parameters			
Exposure Time for External and Internal On-Site Dose [s]	Radius of Cloud for External On-Site Dose [m]	Radius of Cloud for Internal On-Site Dose [m]	Inhalation Rate [L/min]
1800	30	15	12

Nuclide	A	Z	Activity (Bq)	DCFA (Sv/Bq s/m3)	External Dose from Airbourne Cloud (mSv)	DCFI_a (Sv/Bq)	Inhalation Dose (mSv)	SDRL (Bq/mSv)	Maximum Offsite Dose - Unfiltered (mSv)	Maximum Offsite Dose - Filtered (mSv)
Gaseous and Volatile Alpha Isotopes										
Rn-223	223	86	8.58E+05	6.09E-15	8.32E-08	1.20E-07	2.62E-03	4.52E+13	1.90E-08	1.90E-08
Rn-222	222	86	9.14E+05	1.91E-17	2.78E-10	7.09E-06	1.65E-01	3.47E+12	2.63E-07	2.63E-07
Rn-221	221	86	8.15E+06	5.55E-15	7.20E-07	3.64E-07	7.56E-02	1.99E+09	4.09E-03	4.09E-03
Rn-220	220	86	1.38E+09	1.85E-17	4.07E-07	9.20E-10	3.23E-02	3.06E+14	4.51E-06	4.51E-06
Rn-212	212	86	4.09E+09	0.00E+00	0.00E+00	6.71E-09	6.99E-01	4.79E+13	8.54E-05	8.54E-05
Rn-211	211	86	2.54E+09	9.44E-14	3.82E-03	1.31E-07	8.48E+00	1.44E+13	1.76E-04	1.76E-04
Rn-210	210	86	3.64E+09	2.79E-15	1.62E-04	3.67E-08	3.40E+00	3.01E+14	1.21E-05	1.21E-05
Rn-209	209	86	2.35E+09	4.76E-14	1.78E-03	1.71E-09	1.02E-01	5.80E+13	4.05E-05	4.05E-05
Rn-208	208	86	2.36E+09	1.10E-14	4.13E-04	4.89E-09	2.94E-01	3.00E+13	7.86E-05	7.86E-05
Rn-207	207	86	1.66E+09	3.96E-14	1.05E-03	2.30E-09	9.73E-02	3.25E+14	5.11E-06	5.11E-06
Rn-206	206	86	1.38E+09	6.57E-14	1.44E-03	2.10E-09	7.38E-02	1.55E+14	8.88E-06	8.88E-06
				Total Rn Dose:	**8.67E-03**	**Total Rn Dose:**	**1.34E+01**	**Total Rn Dose:**	**4.50E-03**	**4.50E-03**
Gaseous and Volatile Non-Alpha Isotopes										
H-3	3	1	6.41E+06	3.31E-19	3.38E-11	6.2E-12	1.01E-06	2.00E+15	3.20E-09	3.20E-09
				Total H Dose:	**3.38E-11**	**Total H Dose:**	**1.01E-06**	**Total H Dose:**	**3.20E-09**	**3.20E-09**
Cl-36	36	17	7.04E-02	2.23E-17	2.50E-17	3.3E-10	5.92E-13	7.43E+09	9.48E-12	2.37E-16
Cl-38	38	17	5.58E+06	7.87E-14	6.99E-06	2.5E-11	3.55E-06	6.48E+13	8.61E-08	2.15E-12
Cl-39	39	17	4.29E+06	7.29E-14	4.98E-06	2.5E-11	2.73E-06	4.79E+13	8.96E-08	2.24E-12
				Total Cl Dose:	**1.20E-05**	**Total Cl Dose:**	**6.29E-06**	**Total Cl Dose:**	**1.76E-07**	**4.39E-12**
Ar-41	41	18	6.44E+06	6.5E-14	6.67E-06	0	0.00E+00	1.59E+14	4.05E-08	4.05E-08

Ar-42	42	18	5.45E+02	9E-18	7.81E-14	0	0.00E+00	1.18E+15	4.62E-13	4.62E-13
Ar-43	43	18	2.57E+06	7.69E-14	3.15E-06	0	0.00E+00	3.44E+14	7.46E-09	7.46E-09
Ar-44	44	18	1.72E+06	9.82E-14	2.69E-06	0	0.00E+00	1.24E+14	1.39E-08	1.39E-08
				Total Ar Dose:	**1.25E-05**	**Total Ar Dose:**	**0.00E+00**	**Total Ar Dose:**	**6.18E-08**	**6.18E-08**
Se-73m	73	34	2.15E+05	1.17E-14	4.01E-08	9.2E-12	5.04E-08	3.39E+14	6.33E-10	1.58E-14
Se-81	81	34	2.85E+09	5.24E-16	2.38E-05	8E-12	5.81E-04	2.83E+15	1.01E-06	2.51E-11
Se-81m	81	34	5.26E+08	6.18E-16	5.18E-06	1.6E-11	2.14E-04	6.79E+14	7.75E-07	1.94E-11
Se-83	83	34	9.53E+08	1.21E-13	1.84E-03	1.8E-11	4.37E-04	6.38E+13	1.49E-05	3.74E-10
Se-84	84	34	2.45E+09	2.07E-14	8.08E-04	1.6E-11	9.99E-04	1.65E+15	1.49E-06	3.71E-11
				Total Se Dose:	**2.67E-03**	**Total Se Dose:**	**2.23E-03**	**Total Se Dose:**	**1.82E-05**	**4.55E-10**
Br-75	75	35	0.00E+00	5.84E-14	0.00E+00	2.9E-11	0.00E+00	3.27E+13	0.00E+00	0.00E+00
Br-76	76	35	4.48E+06	1.34E-13	9.56E-06	2.4E-10	2.74E-05	1.54E+12	2.90E-06	7.25E-11
Br-77	77	35	1.46E+07	1.51E-14	3.51E-06	6.2E-11	2.31E-05	3.37E+12	4.33E-06	1.08E-10
Br-80	80	35	3.68E+08	3.85E-15	2.26E-05	5.9E-12	5.53E-05	1.50E+15	2.46E-07	6.15E-12
Br-80m	80	35	1.84E+08	3.11E-16	9.11E-07	3.3E-11	1.55E-04	8.85E+13	2.08E-06	5.20E-11
Br-82	82	35	5.62E+08	1.3E-13	1.16E-03	3.5E-10	5.01E-03	6.97E+11	8.06E-04	2.02E-08
Br-83	83	35	3.96E+09	3.82E-16	2.41E-05	1.6E-11	1.61E-03	3.97E+14	9.99E-06	2.50E-10
Br-84	84	35	3.19E+09	9.41E-14	4.78E-03	2.2E-11	1.79E-03	6.41E+13	4.98E-05	1.24E-09
Br-85	85	35	3.51E+09	2.74E-15	1.53E-04	2.9E-12	2.59E-04	9.85E+15	3.56E-07	8.91E-12
Br-87	87	35	1.91E+09	1.57E-13	4.78E-03	1.5E-13	7.30E-06	8.18E+14	2.33E-06	5.84E-11
				Total Br Dose:	**1.09E-02**	**Total Br Dose:**	**8.94E-03**	**Total Br Dose:**	**8.78E-04**	**2.20E-08**
Kr-77	77	36	4.29E+05	4.86E-14	3.32E-07	0	0.00E+00	2.19E+14	1.96E-09	1.96E-09
Kr-79	79	36	1.42E+07	1.21E-14	2.74E-06	0	0.00E+00	7.78E+14	1.82E-08	1.82E-08
Kr-81	81	36	3.53E+00	2.67E-16	1.50E-14	0	0.00E+00	3.51E+16	1.01E-16	1.01E-16
Kr-83m	83	36	4.29E+09	1.5E-18	1.02E-07	0	0.00E+00	6.89E+18	6.23E-10	6.23E-10
Kr-87	87	36	3.61E+09	4.12E-14	2.37E-03	0	0.00E+00	2.62E+14	1.38E-05	1.38E-05
Kr-88	88	36	3.20E+09	1.02E-13	5.20E-03	0	0.00E+00	8.17E+13	3.92E-05	3.92E-05
Kr-89	89	36	2.18E+09	8.1E-14	2.81E-03	0	0.00E+00	4.54E+14	4.80E-06	4.80E-06
				Total Kr Dose:	**1.04E-02**	**Total Kr Dose:**	**0.00E+00**	**Total Kr Dose:**	**5.78E-05**	**5.78E-05**
I-120	120	53	1.12E+07	1.38E-13	2.46E-05	1E-10	2.85E-05	3.04E+13	3.68E-07	9.21E-12
I-121	121	53	9.23E+07	1.94E-14	2.85E-05	2.7E-11	6.35E-05	1.34E+14	6.86E-07	1.72E-11
I-122	122	53	1.65E+08	4.56E-14	1.20E-04	0	0.00E+00	6.38E+14	2.58E-07	6.46E-12
I-123	123	53	3.87E+08	7.28E-15	4.49E-05	7.4E-11	7.30E-04	2.47E+13	1.57E-05	3.91E-10
I-124	124	53	1.31E+08	5.38E-14	1.12E-04	4.4E-09	1.47E-02	9.14E+10	1.43E-03	3.58E-08
I-125	125	53	2.19E+07	5.22E-16	1.82E-07	5.1E-09	2.85E-03	3.72E+10	5.88E-04	1.47E-08
I-126	126	53	8.81E+07	2.15E-14	3.02E-05	9.8E-09	2.20E-02	2.08E+10	4.24E-03	1.06E-07
I-128	128	53	1.09E+09	4.16E-15	7.22E-05	1.3E-11	3.61E-04	1.02E+15	1.07E-06	2.67E-11
I-129	129	53	6.67E-01	3.8E-16	4.04E-15	0.000000036	6.12E-10	3.05E+09	2.18E-10	5.46E-15
I-130	130	53	1.02E+09	1.04E-13	1.69E-03	6.7E-10	1.74E-02	2.51E+12	4.07E-04	1.02E-08
I-131	131	53	3.78E+08	1.82E-14	1.10E-04	7.4E-09	7.13E-02	3.41E+10	1.11E-02	2.77E-07
I-132	132	53	1.37E+09	1.12E-13	2.44E-03	9.4E-11	3.28E-03	2.43E+13	5.65E-05	1.41E-09
I-132m	132	53	5.73E+08	1.53E-14	1.40E-04	7.9E-11	1.15E-03	1.05E+14	5.45E-06	1.36E-10
I-133	133	53	1.45E+09	2.94E-14	6.79E-04	1.5E-09	5.54E-02	9.31E+11	1.56E-03	3.89E-08
I-134	134	53	1.22E+09	1.3E-13	2.53E-03	4.5E-11	1.40E-03	4.92E+13	2.48E-05	6.20E-10
I-135	135	53	8.78E+08	7.98E-14	1.12E-03	3.2E-10	7.16E-03	7.70E+12	1.14E-04	2.85E-09
				Total I Dose:	**9.13E-03**	**Total I Dose:**	**1.98E-01**	**Total I Dose:**	**1.95E-02**	**4.89E-07**
Xe-120	120	54	8.58E+05	1.94E-14	2.65E-07	0	0.00E+00	1.86E+14	4.61E-09	4.61E-09
Xe-121	121	54	6.87E+06	9.14E-14	1.00E-05	0	0.00E+00	1.26E+14	5.44E-08	5.44E-08
Xe-122	122	54	1.74E+07	2.46E-15	6.82E-07	0	0.00E+00	1.73E+14	1.01E-07	1.01E-07
Xe-123	123	54	4.81E+07	3.03E-14	2.32E-05	0	0.00E+00	3.05E+14	1.58E-07	1.58E-07
Xe-125	125	54	1.80E+08	1.19E-14	3.41E-05	0	0.00E+00	3.29E+14	5.46E-07	5.46E-07
Xe-127	127	54	2.11E+07	1.25E-14	4.20E-06	0	0.00E+00	7.50E+14	2.81E-08	2.81E-08
Xe-129m	129	54	5.01E+07	1.06E-15	8.46E-07	0	0.00E+00	8.85E+15	5.66E-09	5.66E-09
Xe-131m	131	54	4.80E+07	3.89E-16	2.97E-07	0	0.00E+00	2.41E+16	1.99E-09	1.99E-09
Xe-133	133	54	3.83E+08	1.56E-15	9.51E-06	0	0.00E+00	6.01E+15	6.37E-08	6.37E-08
Xe-133m	133	54	2.83E+08	1.27E-15	5.72E-06	0	0.00E+00	7.40E+15	3.82E-08	3.82E-08
Xe-135	135	54	2.10E+09	1.19E-14	3.98E-04	0	0.00E+00	8.04E+14	2.61E-06	2.61E-06
Xe-137	137	54	7.86E+08	9.46E-15	1.18E-04	0	0.00E+00	3.82E+15	2.06E-07	2.06E-07
Xe-138	138	54	6.71E+08	5.77E-14	6.17E-04	0	0.00E+00	1.68E+14	4.00E-06	4.00E-06
				Total Xe Dose:	**1.22E-03**	**Total Xe Dose:**	**0.00E+00**	**Total Xe Dose:**	**7.82E-06**	**7.82E-06**

D Safety Analysis Report for Chemical Processing of Thorium Targets

Safety Report

L125: Isolation of Medical Isotopes from Irradiated Thorium Metal Targets

authored by Andrew K. H. Robertson

July 26, 2019

CONTENTS

1 IDENTIFICATION

Experiment L125: Isolation of Medical Isotopes from Irradiated Thorium Metal Targets

The experiment spokespersons are Andrew Robertson and Paul Schaffer. The experiment safety coordinator is Andrew Robertson. Vicky Hanemaayer is the RCR1 Lab Manager. The experimental users with access to all aspects of L125 are exclusively limited to Andrew Robertson and Hua Yang. Additional users of the ^{212}Pb generator include Brooke McNeil, Tom Kostelnik, Neil Weatherall, Isabel Rodrigo, and Lily Southcott. Stefan Zeisler and Ellard Portman are assisting with ^{225}Ac production runs and upgrades of the L125 hot cell equipment.

Andrew Robertson TRIUMF Life Sciences
4004 Wesbrook Mall, Vancouver BC
arobertson@triumf.ca
604 222 1047 ext. 6733 (office)
778 228 7471 (cell)

2 INTRODUCTION

Summary of changes in this version

Appendix G has been added, which describes a modified process for L125 in which targets are irradiated at IPF to an integrated current of 360 µA*h and thorium foils are shipped from the TRIUMF site. This 360 µA*h irradiation represents 13.6% of the 2640 µA*h irradiation that is assumed in all other sections of this document.

No other changes have been made.

Background

Targeted alpha therapy (TAT) shows high potential as an effective treatment option for small tumours and metastases [1]. Actinium-225 ($t_{1/2}$ = 9.92 d) is a promising TAT radionuclide, which can be used directly in combination with biomolecules or as generator source of the shorter TAT radionuclide, bismuth-213 ($t_{1/2}$ = 45.6 min). Development of ^{225}Ac and ^{213}Bi radiopharmaceuticals has progressed slowly due to the limited availability and the resulting high cost of these isotopes. Global annual ^{225}Ac production is approximately 63 GBq (1.7 Ci) [2–6].

Scope

In coordination with L124 [7], experiment L125 aims to develop regular production and processing of clinically relevant quantities of ^{225}Ac (100 mCi, or 3.7 GBq) and ^{213}Bi and potentially other valuable medical radionuclides at TRIUMF using irradiation facilities at the BL1A Isotope Production Facility (IPF) and processing facilities in the MHESA RCR1 lab. While the scope of L124, *Irradiation of Thorium Targets at the TRIUMF 500 MeV Isotope Production Facility,* will be limited to the production of ^{225}Ac (including target fabrication and irradiation at IPF), L125 will encompass the post-irradiation processing of the targets (including target transfer to RCR1, target opening, and processing of targets in the RCR1 hot cell). In other terms, L125 begins when targets leave the IPF hot cell.

These experiments are distinct so as to separate the safety review process for each stage of the project. In this manner, safety approval for irradiating thorium targets for possible shipment and

processing off-site will be independent of safety approval for processing the targets on site. While multiple isotopes of interest (e.g. ^{223}Ra, ^{224}Ra, ^{212}Bi, ^{212}Pb) will be produced in the target, ^{225}Ac and ^{213}Bi are the isotopes of present focus.

From the perspective of the safety report, the scope of L125 also includes the applications of L125-produced isotopes that will occur at the TRIUMF site. A description of experiments using L125-produced isotopes that occur off-site is not included in this report.

Current Experimental Objectives

1. Establish methods for the isolation of clinically relevant quantities of actinium (100 mCi, or 3.7 GBq)[1] and radium isotopes from thorium metal irradiated with high energy protons, using and improving upon published methods
2. Quantify ^{225}Ac production yields and the presence of any radioactive or stable impurities in the final isolated ^{225}Ac product
3. Test ability to use this ^{225}Ac as generators of ^{213}Bi
4. Test abilities of ^{225}Ac and ^{213}Bi products for radiolabeling of common ^{225}Ac or ^{213}Bi biomolecules
5. Collect relevant safety data and establish protocols for ^{225}Ac and ^{213}Bi production that will guide TRIUMF's proposed future larger-scale ^{225}Ac production and processing efforts (including commercially on BL1A or at ARIEL under the recently awarded CFI grant)

Impact Statement

This project leverages unique TRIUMF infrastructure to produce understudied and sought-after isotopes with potential to significantly aid the treatment of aggressive cancers. However, much remains to be understood about the chemistry and biology needed to attach ^{225}Ac or ^{213}Bi to biomolecules that specifically target and treat cancer. As a result, the use of ^{225}Ac and ^{213}Bi in TAT is an area of research that has great interest.

This work therefore has high translational potential, with the ability to enable other experiments at TRIUMF and other institutions that are otherwise impractical due to the high cost and limited availability of ^{225}Ac and ^{213}Bi (current cost is a minimum purchase of 0.75 GBq (20 mCi) of ^{225}Ac for $35000). As such, this effort is expected to enable new collaborations between TRIUMF and other TAT research centres. A recent survey of experimenters in the TAT field suggests that demand for ^{225}Ac from researchers within Canada is at minimum 5.6 GBq (150 mCi) per month and growing.

The knowledge and experience with thorium target irradiation, target processing, and waste management that will be developed through L124 and L125 will directly support any future efforts at TRIUMF to scale up production to commercial quantities, as well as the future larger-scale ^{225}Ac production at ARIEL.

3 DESCRIPTION

3.1 Location of Experiment

The experiment will begin at the BL1A IPF hot cell, located in TRIUMF's Meson Hall. The irradiated target will be removed from the rear of this hot cell within a lead flask and then transported to the RCR1 lab, located on the B1 level of TRIUMF's MHESA building. The target will then be placed inside hot cell #1 (HC1), one of the RCR1 lab's four hot cells. The remainder of the experiment will take place within HC1, except for some samples that must be brought to the QC room on the Radiochemistry Annex (RCA1) ground floor for analysis, and except for some samples that may be shipped off site.

1 While the long-term experimental objective is to produce 100 mCi (3.7 GBq) of ^{225}Ac per irradiation, the first irradiation described in this review is for the production of ~12 mCi (440 MBq) of ^{225}Ac.

Table 1: Possible modes in which RCR1 hot cells can be operated.

Hot Cell Mode	Shielded Glovebox Mode	Glovebox Mode	Fume Hood Mode
		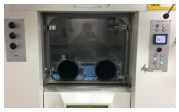	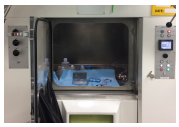
Full shielding with all doors closed. Actions inside hot cell performed only with manipulators.	Ports open so that arms can be inserted in glovebox mode while the torso is still fully shielded. Actions inside the hot cell performed by hand, using thick rubber gloves.	Glovebox mode without any shielding provided by the hot cell doors. Actions inside the hot cell performed by hand, using thick rubber gloves.	Front door of hot cell opened such that it can be used in a manner similar to a fume hood. No shielding of the body. Actions inside the hot cell performed by hand while wearing disposable gloves and sleeves.

HC1 has four different modes in which it can be used that offer varying levels of radiation shielding, contamination control, and airflow control. These modes, defined in Table 1, are referred to throughout this document.

3.2 Overview of Experimental Procedures

This subsection provides a brief overview of the experimental procedures. A more detailed description of each stage of the experiment is provided Sections 3.3 through 3.7.

Targets containing 8.3 g of Th (>99.5% purity) metal hermetically sealed within an Inconel® capsule will be irradiated at IPF and allowed to cool for at least one week before removal of the target from the IPF hot cell. Irradiation conditions will use typical high-current BL1A beam parameters (480 MeV, ~100 µA at extraction or ~450 MeV, ~85 µA at IPF) so that use of IPF can occur independent of the needs of other BL1A users. While the experiment ultimately aims to produce 3.7 GBq (100 mCi) quantities, for this first initial production run the duration of the irradiation will be chosen such that approximately 440 MBq (12 mCi) of ^{225}Ac will remain in the target at 1 week after end of bombardment (EOB). This duration is expected to be 2600 µA*h. Additional details of the initial irradiation can be found in *Commissioning Plan for Irradiation of L124 Thorium Metal Targets at IPF (Document-148095)* [8].

Targets will be transferred from the IPF hot cell to RCR1 hot cell #1 (HC1) using a custom transfer flask. Once inside HC1, the hermetic seal of the target will be broken, the thorium metal removed and dissolved in concentrated acids. Chemical processing of the irradiated targets using two or more chromatography columns will then be performed using a semi-automated system consisting of remotely controlled pumps and valves. After processing, solutions containing isolated ^{225}Ac isotopes will be removed from the hot cell and transferred to a fume hood (or a second hot cell operated in fume hood mode) for radiolabelling experiments.

3.3 Target Design

The target material consists of a thorium metal foil (60 mm diameter, 0.25 mm thickness, or 0.293 g/cm^2) supplied by IBI Labs (Boca Raton, Florida). The supplied foils currently have a significant oxide layer that will be removed before the targets are fabricated. The thorium metal foil is hermetically sealed within a target capsule consisting of a steel, ring-shaped body and 0.13 mm thick Inconel®-718 entrance and exit windows[2]. The outer dimensions of the target are approximately 10 cm diameter and 1 cm thickness. Design iterations of the L124 thorium targets are shown in Fig. 1. The target

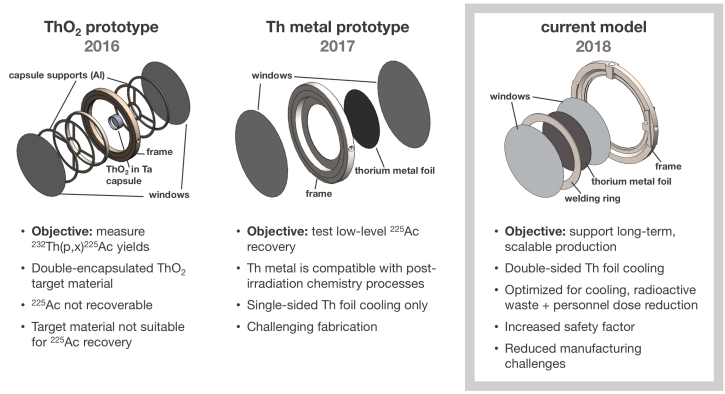

Figure 1: Exterior (left) and cross-sectional view (right) the target showing the outer capsule and target interior and thorium foil.

body is shaped to centre the thorium foil radially within the target and to also press it against the entrance window, facilitating improved cooling of the thorium foil via conduction through the window. Windows are attached to the target body by electron-beam welding, the process of which also seals the thorium within the target capsule.

Sealing of the target with an electron-beam weld – which is conducted under vacuum – will ensure that the interior volume of the fabricated target is under vacuum. After manufacturing, leak tests of the target will be conducted following standard ATG procedures for leak testing IPF targets.

The design review process for the first thorium metal prototype target has been completed [10, 11], and two successful irradiations of this target have been completed. Design and safety approval of the new thorium metal target is currently underway. For the most up-to-date and complete information on L124 target, the reader is referred to the design note, *L124 Thorium Metal Target for IPF* (Document-148097) [12].

3.4 Target Transfer

After irradiation, the target will remain inside the IPF hot cell for one week to allow shorter-lived isotopes to decay before transferring the target to the RCR1 hot cell. This limits the external radiation dose that will be received by workers conducting the target transfer.

The custom transfer flask designed for this experiment is shown in Fig. 2. A new flask was required for this project as load limits on the MHESA elevator (1800 kg) prevented use of the flask previously used to transfer hot targets from the IPF hot cell to Nordion hot cells (2250 kg). The new transfer flask (214 kg) and the IPF hot cell interface such that the flask lid can be opened and closed from within the hot cell. As such, the targets are removed from the IPF hot cell within a sealed flask. The flask will then be craned onto a cart near the doorway between the Meson Hall and the MHESA building. The cart will then be brought to the RCR1 lab.

With the flask positioned in front of the HC1 port door, a small hoist will be used to lift the flask lid, exposing the target that is sitting on a shelf attached to the bottom of the flask lid (as shown in Fig. 2). The target (approximately 250 g) will then be lifted manually by means of an long pole (>1 m length) into the HC1 port. Once the HC1 port door is closed, the target is behind the shielding of the hot cell.

2 The composition of Inconel®-718 is as follows: 50.00-55.00% Ni, 17.00-21.00% Cr, 4.75-5.50% Nb, 2.80-3.30% Mo, 0.65-1.15% Ti, <1.00% Co, 0.20-0.80% Al, <0.35% Mn, <0.35% Si, <0.30%Cu, <0.08% C, <0.015% S, <0.015% P, <0.006% B, Fe remainder [9].

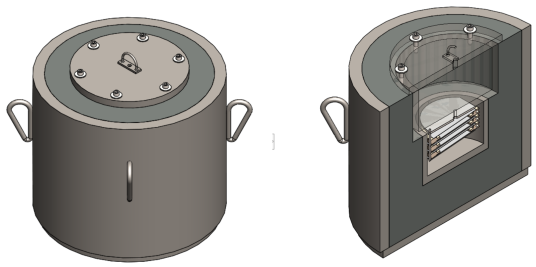

Figure 2: Drawing of the transfer flask, which includes space for up to two targets that sit on shelves attached to the bottom of the flask lid. The flask has at least 7 cm of lead and 3 cm of steel shielding in all directions.

More details on the transfer flask design can be found in *L125 Target Transfer Flask (Document-148098)* and *L125 Target Transfer Flask Requirements (Document-148102)* [13, 14]. The design review process for this flask has been completed [10, 11].

3.5 Opening of Target Capsule

Using the hot cell manipulators, the target will be inserted into a semi-automated device that will remotely open the target capsule and remove the thorium foil. Shown in Fig. 3, this device uses blades from pipe cutters to cut through the target window so that the thorium foil can be removed. A design review of the target opener has been completed [15].

3.6 Processing of Irradiated Target

Modifications of previously published methods will be employed for dissolution of irradiated thorium metal and subsequent purification of actinium and radium isotopes, mostly notably techniques described by Radchenko *et al* [3, 16]. Similar methods requiring the use of different resins, acids, or acid concentrations may also be employed, since such minor changes do not pose any additional safety considerations.

Using the manipulators, the thorium foil will be placed inside a 500 mL beaker. A solution of 10 M HNO_3 and 12.5 mM HF[3](approximately 60 mL) will be added to the beaker and heated to <90 °C. This has been shown to dissolve similar amounts of thorium within 30 minutes. The solution containing the dissolved target will then be evaporated to dryness and redissolved in 80.0 mL of 1 M HNO_3, to which 56 mL of H_2O_2 will be added to precipitate out bulk thorium as thorium peroxide. The chalky mixture will then be passed through a filter to remove the precipitate (which is later redissolved in 10 M HNO_3). The filtrate will then be washed with water, diluting the filtrate to appoximately 0.5 M HNO_3, which is then passed through a cation exchange column (roughly 10 mL DOWEX 50x8, 100-200 mesh). Under these conditions, elements such as Ra, Ac, and Th will be absorbed onto the resin. The resin is then washed with 450 mL of 1 M citric acid (pH 2.0-2.2) to remove trace thorium quantities, as well as other spallation products. The resin is then washed with an additional 50 mL of 0.5 M HNO_3. Ra and Ac are then eluted from the resin using 60 mL of 8 M HNO_3, which is passed through a column containing 2 mL of DOWEX1X8 resin (200-400 mesh) which will filter out remaining trace Th quantities. The solution is then diluted to approximately 4 M HNO_3 and loaded onto a column containing 200 mg of DGA resin. Under loading conditions, Ra and Ba will pass through the column without sorption and actinium and lanthanides will be retained on the column. The column will be washed with 5 mL of 4 M HNO_3 to remove residual radium and barium impurities. Actinium will be

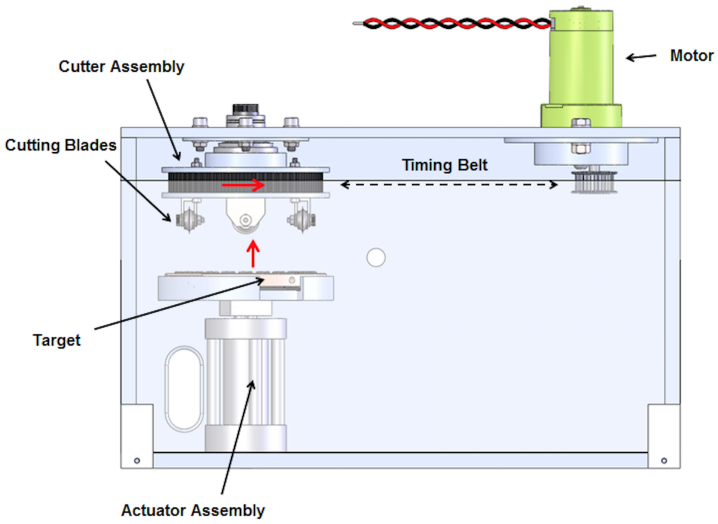

Figure 3: Design of target opener.

separated from lanthanides by eluting with 10-12 M HNO_3 (5-20 mL) from DGA column. A flowchart of this separation process is shown in Fig. 4.

3.7 Testing of ^{225}Ac Products

Small aliquots of each solution produced during target processing will be removed from the hot cell so that their composition can be determined using gamma spectroscopy, alpha spectroscopy, or inductively coupled plasma mass spectrometry (ICP-MS). Products containing ^{225}Ac will also be removed in small quantities to test the ability of the ^{225}Ac product for labelling with chelates or biomolecules relevant to the TAT field. In general, these reactions involve combining ^{225}Ac and the chelate in a buffer solution (total volume $<$ 1 mL), with heating below 80 °C. The radiolabeling yield of these reactions is then tested using iTLC plates, where 1-10 µL of the labelled product is placed on the plate before a mobile phase is added. The plates are then counted on a plate reader in the RCA1 QC room. The RCR1 HPLC may also be used to characterize radiolabeling reaction products, provided that no organic solvents are used (see Section 7). The use of TLC plates and HPLC for characterization of ^{225}Ac-radiolabeled biomolecules is already approved as part of experiment L122 [17].

As the ^{225}Ac progeny isotope ^{213}Bi ($t_{1/2}$ = 45.6 min) is itself a TAT isotope of interest, a ^{213}Bi generator from the ^{225}Ac fraction may also be produced. In a manner similar to the chromatography described in Section 3.6, the solution containing ^{225}Ac will be loaded onto an ion exchange (AG-MP 50) resin (100-200 mesh, hydrogen form) in 4 M HNO_3, binding ^{225}Ac to the resin. The column is then washed with additional 4 M HNO_3 before ^{213}Bi is eluted by passing a solution containing 0.1 M NaI/0.1 M HCl through the resin [5]. Other similar methods using different resins or acids may be applied.

Use of the solution containing isolated Ra isotopes will be used as a second source of ^{225}Ac. Beginning >17.5 days after initial thorium target purification, the entire solution (<50 mL) will be once

3 A small amount of fluoride is required to catalyze the dissolution.

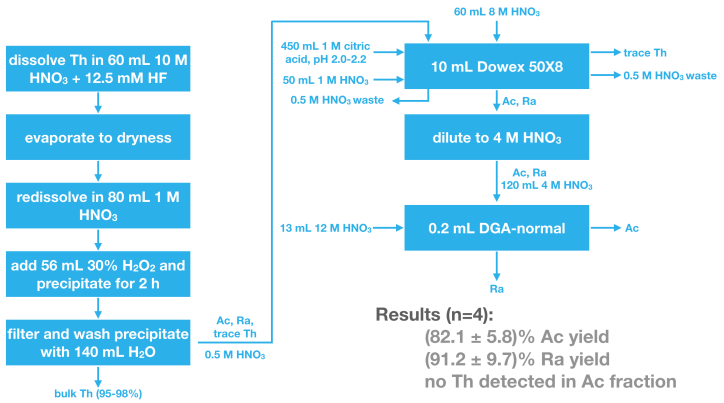

Figure 4: Flowchart describing the thorium target dissolution and ^{225}Ac purification process. Yield results for tests using non-irradiated thorium are shown.

again passed through the a DGA column (as described in Section 3.6) to separate out ^{225}Ac produced via the decay of ^{225}Ra, this time without the need to remove other spallation products.

Radiopharmaceuticals labelled with clinically relevant quantities of ^{225}Ac (~37 MBq) or preclinically relevant quantities of ^{213}Bi (~440 MBq) may also be produced.

Finally, aliquots of the dissolved target solution (after evaporation of HCl and HF acids and conversion to citric acid) may also be taken such that new chromatography methods for the purification of medical isotopes from irradiated thorium metal can be tested.

3.8 ^{212}Pb Generator and Applications

In addition to ^{225}Ac, spallation of ^{232}Th also results in production of significant ^{228}Th quantities. As illustrated by the decay scheme in Figure 5, ^{228}Th ($t_{1/2}$ = 1.91 y) is a parent isotope of the medical isotope ^{212}Pb ($t_{1/2}$ = 10.64 h). Therefore, isolation of thorium isotopes from L125 targets presents the opportunity to develop a long-lived generator of ^{212}Pb, ensuring a reliable supply of this isotope for research. Fortunately, the selective precipitation of thorium employed by the revised ^{225}Ac purification process thus also provides a source of ^{212}Pb. If repurposed as part of ^{212}Pb generators, this thorium fraction would otherwise be long-lived radioactive waste.

Thorium hydroxide precipitates isolated as part of ^{225}Ac purification will be redissolved in 10 M nitric acid and allowed to decay for a period of at least 4 months. At this point, the thorium solution will be evaporated to dryness and redissolved in 40 to 100 mL of 1 M nitric acid, forming the ^{228}Th generator solution. ^{212}Pb will be periodically isolated from the generator stock by passing the solution through a column containing 30-200 mg of Pb extraction resin (purchased from Eichrom). This resin is known to be a highly selective extractor of lead [18], a fact already demonstrated by other TRIUMF experiments (L128). After the ^{212}Pb binds to the resin, the resin will be washed with approximately 2 mL of 1 M nitric acid. ^{212}Pb will then be eluted from the resin using a variety of potential aqueous solvents, such as 0.15 M ammonium acetate.

The isolated ^{212}Pb will then be used in radiolabelling or *in vivo* studies, which are already described in detail in Section 3.7.

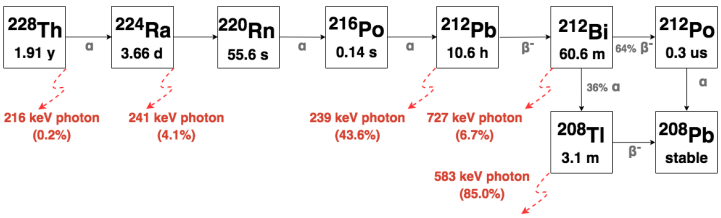

Figure 5: ^{228}Th decay scheme. Emissions useful for identification and quantification of isotopes are shown in red.

4 DEFINITION OF HAZARDS

4.1 Methods Used for Estimation of Radiation Hazards

Estimates of the radioisotope inventory of the irradiated thorium targets were obtained using FLUKA simulations. These simulations were performed by Andrew Robertson with guidance from Mina Nozar.

Given the estimated radioisotope inventory, dose rate estimates of the target were calculated using an Excel-based calculator developed by the TRIUMF Radiation Protection Group (RPG) that calculates gamma radiation dose rates – both with or without shielding – from a given isotope assuming a point source geometry. Comparison with dose rates determined via FLUKA simulation show these methods agree within <10% for unshielded dose rates at 1 m from the target. Note that the accuracy of these FLUKA simulations is limited due to the limited understanding beam parameters at the end of BL1A, since the nearest diagnostics are many metres upstream. Simulated radioactivity values and resulting dose estimates presented in this document were based off of a 454 MeV, 55 μA, 48 hour irradiation, which produces 432 MBq of ^{225}Ac one week after EOB.

Similar simulations and calculations conducted as part of L124 in 2016 using a thorium oxide test target were within 20% of all measurements of ^{225}Ac radioactivity and dose rate at 1 m from the target. This supports the reliability of these FLUKA simulations and dose calculations for approximating the radiation hazards associated with this experiment.

While some changes to the target design have been made since the FLUKA simulations were run, the changes are expected to negligibly affect the isotope inventory and resulting dose rates since the total mass and approximate radial distribution of thorium and steel (the components producing >99% of the dose from the target) has changed by <1%.

Internal and external dose estimates resulting from the worst case release of volatile radioisotopes were calculated as described in TRIUMF Safety Analysis Reports (SARs) for ISAC targets: *Actinide Target Safety Analysis Report* (Document-12972) and *Actinide Target SAR Addendum for Thorium Oxide* (Document-110961) [19, 20]. These documents contain dose estimates resulting from a worst case release of volatile radioisotopes from ISAC actinide targets. These calculations assume all volatile radioactive isotopes within the target become uniformly distributed within a sphere of 15 m radius and that a worker wearing no respiratory protection is located at the centre of the sphere for a duration of 30 minutes. This scenario ("Scenario C" described in Document-110961) assumes that all the radioactive air released through the ventilation systems is somehow drawn into an office building. Decay of short-lived isotopes during the 30 minute exposure time is neglected as is the dispersion of these radioactive gasses during this time. It should be noted that this is an extremely conservative model.

Off-site dose estimates to members of the public resulting from a worst case release of volatile radioisotopes were also calculated using the methods described the ISAC actinide target SARs [19, 20]. When considering airborne radiation doses resulting from an accidental release of radioactivity, one

must consider which elements have the potential to become airborne. In the ISAC actinide target SARs, the volatile elements with potential to become airborne are: hydrogen, chlorine, argon, selenium, bromine, krypton, iodine, xenon, radon, and polonium. This document uses the same definition of potentially volatile or gaseous isotopes. Note that while the *L124 Safety Report (Document-148928)* does not treat polonium as volatile [7], this report does. This is because of the potential for polonium to be in a volatile chemical or physical form during some L125 activities.

While *Actinide Target Safety Analysis Report* (Document-12972) and *Actinide Target SAR Addendum for Thorium Oxide* (Document-110961) guide the methodology for on-site and off-site airborne dose estimates described in this document, the following modifications were made to these methods to incorporate additional information gained in the years following their publication:

1. The ISAC SARs used a 1 minute half-life cut-off of for isotopes used in the calculations. However, ^{220}Rn ($t_{1/2} = 55.6$ s) has since been shown to be a real potential airborne dose hazard [21]. Dose calculations herein include ^{220}Rn. This results in a $<1\%$ change to the dose estimates.

2. TRIUMF is currently in the process of updating its Derived Release Limits (DRLs) – annual limits for radioactivity released into the environment – and defining Single-event Derived Release Limits (SDRLs) – limits for a single accidental release of radioactivity into the environment. The old SDRLs used in the ISAC actinide target SARs are considered outdated. SDRLs used in this document to estimate the off-site dose to members of the public resulting from a worst case release of radioisotopes were provided by RPG [22]. These SDRLs are listed in Appendix A.

All values for Annual Limits on Intake (ALI) used in this document were obtained from the *Actinide Target SAR Addendum for Thorium Oxide* (Document-110961), unless otherwise specified [20].

4.2 Radiation Hazards

Table 2: Activity and ALI of the non-radon alpha-emitting radionuclides produced within the thorium foil and present one week after EOB. These ALI values were obtained from the *Actinide Target SAR Addendum for Thorium Oxide* (Document-110961) [20].

Nuclide	ALI [Bq]	Activity [Bq]	A/ALI
Po-204	7.41E+05	0	0.00E+00
Po-205	2.25E+08	0	0.00E+00
Po-206	4.20E+06	4.35E+08	1.03E+02
Po-207	1.33E+08	3.97E+05	2.99E-03
Po-208	8.33E+03	7.81E+06	9.37E+02
Po-209	8.33E+03	2.66E+05	3.20E+01
Po-210	9.09E+03	7.72E+07	8.50E+03
At-207	1.05E+07	0	0.00E+00
At-209	1.68E+06	0	0.00E+00
At-211	1.82E+05	1.26E+06	6.92E+00
Ra-223	3.51E+03	2.32E+08	6.61E+04
Ra-224	4.17E+03	4.18E+08	1.00E+05
Ra-226	9.09E+03	2.93E+03	3.23E-01
Ac-224	2.02E+05	1.89E+04	9.37E-02
Ac-225	3.08E+03	4.32E+08	1.40E+05
Ac-226	2.00E+04	5.14E+07	2.57E+03
Ac-227	4.26E+02	8.46E+05	1.99E+03
Th-227	2.63E+03	3.40E+08	1.29E+05
Th-228	6.25E+02	2.83E+07	4.53E+04
Pa-228	3.92E+05	8.88E+05	2.26E+00
Pa-229	5.26E+04	7.67E+06	1.46E+02
Pa-230	3.51E+04	5.78E+07	1.65E+03
U-230	1.67E+03	1.33E+06	7.94E+02
U-232	7.69E+02	1.40E+04	1.82E+01
	Total:		**4.98E+05**

The irradiation of the thorium metal targets is expected to produce significant quantities of hazardous radioisotopes. The simulated radioactive composition of isotopes present within the thorium foil at one week after EOB is shown in Appendix B. This inventory includes gamma-, beta-, and alpha-emitting isotopes. Some of these isotopes are also volatile halogens, noble gases, and elements that are potentially volatile depending on their chemical form (the definition of the relevant volatile and gaseous isotopes used in this document is provided in Section 4.1). As such, the irradiated thorium presents significant external and internal radiation hazards, including airborne radiation hazards.

Table 2 lists the activity at EOB + 1 week and the ALI of the non-radon alpha-emitting radionuclides with half-lives >1 hour. The selection of isotopes for this table was copied from *Actinide Target SAR Addendum for Thorium Oxide (Document-110961)* [20].

The non-thorium components of the target capsule will also become radioactive. However, these isotopes are non-volatile and are not alpha-emitters. These components of the target present significant external radiation hazards as well as surface contamination hazards.

Dose estimates and worst-case release estimates for different stages in the experiment are provided in Section 5.

4.3 Chemical Hazards

The strong acids used in various stages of the experiment are corrosive, with potential to cause chemical burns if they come in contact with skin.

The use of small quantities of dilute HF or $(NH_4)_2SiF_6$ are particularly hazardous. Small quantities of HF are potentially fatal if they come in contact with the skin. $(NH_4)_2SiF_6$ is potentially fatal if inhaled or ingested.

4.4 Industrial Hazards

Lifting hazards are mainly associated with the movement of the transfer flask by the Meson Hall crane.

Fire hazards are associated with the accumulation of flammable waste inside the hot cell (ex. disposable gloves).

5 SAFETY MEASURES

5.1 Summary of Radiation Safety Measures

Standard safety practices associated with working in TRIUMF radiochemistry labs will be followed, including wearing proper PPE, routinely monitoring oneself for contamination, and routinely swiping the floor. In addition, additional zone control near HC1 will be employed: additional tacky mats will be placed on the surrounding HC1, the area will be marked off with tape, and a pancake probe and alpha contamination monitor will be available at the boundary of this zone, along with additional PPE and decontamination supplies.

Safety measures specific to this experiment will also be followed. Table 3 summarizes the radiation related risks and hazards for each task discussed in Sections 5.3 through 5.7. For each of these tasks the maximum credible estimated risk after considering all planned safety measures is compared with an existing similar or greater radiation hazard at TRIUMF.

Table 3: Task-based risk and dose summary.

Task	Hazard or Risk	Maximum Credible Estimate Given All Safety Measures	Example of Comparable or Larger Existing Risk
Target Transfer from IPF to HC1 (Section 5.3)	External Whole Body Dose	23 µSv	<500 µSv daily dose guideline
	Internal Dose or Contamination	Minimal risk given PPE and exposure only to metal activation contaminants on target outer surface	Contamination from handling of irradiated metals is a common hazard at TRIUMF
	Accidental Release of Volatile Radioisotopes	668 µSv on-site, 5 µSv off-site	Off-site dose from accidental release from an ISAC U or Th target is 150 µSv or 836 µSv, respectively [20]
Target Opening and Thorium Dissolution (Section 5.5.4)	External Dose	<2 µSv/h - performed in hot cell mode	Dose rate outside HC_4 after ^{99m}Tc target irradiation
	Internal Dose or Contamination	None – performed in hot cell mode	n/a
	Expected Release of Volatile Radioisotopes	58 µSv on-site, 0.02 µSv off-site	After filtration this dose is mostly due to radon isotopes. This can be compared to the release of xenon isotopes by medical isotope production at Nordion, which in 2016 contributed a total off-site dose of 1.46 uSv when calculated using methods listed in Section 4.1 and using measured values stated in the *TRIUMF 2016 Annual Compliance Report* (Table 9-3) [23].
Ac and Ra Purification (Section 5.5)	External Dose	<2 µSv/h - performed in hot cell mode	Dose rate outside HC_4 after ^{99m}Tc target irradiation
	Internal Dose or Contamination	None – performed in hot cell mode	n/a

	Release of Volatile Radioisotopes	None – any volatile isotopes are expected to be released during the target opening or thorium dissolution	n/a
Sampling of Purification Products (Section 5.7)	External Whole Body Dose	<3.5 µSv/h	Dose rates from these samples are much lower than from other samples that TRIUMF radiochemists routinely manipulate by hand (ex. 2.8 mSv/h at 1 m from C-11 produced during experiment L4 [24])
	External Extremity Dose	Not estimated	See above cell
	Internal Dose or Contamination	Handling <5000 ALI of non-volatile alpha-emitting isotopes in aqueous form while operating the hot cell in fume hood mode	Handling of up to 16000 ALI of non-volatile alpha-emitting isotopes in aqueous form is approved for experiment L122
Handling of ^{225}Ra \ ^{225}Ac and ^{225}Ac \ ^{213}Bi Generators (Section 5.7)	External Whole Body Dose	<15 µSv/h	Dose rates from these samples are much lower than from other samples that TRIUMF radiochemists routinely manipulate by hand (ex. 2.8 mSv/h at 1 m from C-11 produced during experiment L4 [24])
	External Extremity Dose	Not estimated	See above cell
	Internal Dose or Contamination	None – handling of this material, representing 29000 ALI, is performed in glovebox mode	n/a

Radiolabeling Studies with ^{225}Ac or ^{213}Bi (Section 5.7)	External Whole Body Dose	<3.5 µSv/h	These studies are already approved and performed as part of experiment L112. The additional presence of ^{227}Ac in this experiment increases the ALI of a sample containing ^{225}Ac by ~1%
	External Extremity Dose	Not estimated	See above cell
	Internal Dose or Contamination	< ALI of Ac isotopes	See above cell
Preparation of Radiopharmaceuticals Containing Clinically Relevant Quantities of ^{225}Ac or ^{213}Bi (Section 5.7)	External Whole Body Dose	<15 µSv/h	These studies are already approved and performed as part of experiment L112, with the exception of handling up to 400 MBq of ^{213}Bi. However, 400 MBq of ^{213}Bi represents only 40 ALI. Compared to L112, the additional presence of ^{227}Ac in this experiment increases the ALI of a sample containing ^{225}Ac by ~1%
	External Extremity Dose	Not estimated	See above cell
	Internal Dose or Contamination	40 ALI for ^{213}Bi , 12000 ALI for ^{225}Ac with contaminants	See above cell
Testing of New Purification Methods (Section 5.7)	External Whole Body Dose	<2.6µSv/h	Dose rates from these samples are much lower than from those that TRIUMF radiochemists routinely manipulate by hand (ex. 2.8 mSv/h at 1 m from C-11 produced during experiment L4 [24])
	External Extremity Dose	Not estimated	See above
	Internal Dose or Contamination	None – performed in glovebox mode	n/a

Waste Disposal (Section 7)	External Whole Body Dose	<2.6µSv/h	Dose rates from these samples are much lower than from those that TRIUMF radiochemists routinely manipulate by hand (ex. 2.8 mSv/h at 1 m from C-11 produced during experiment L4 [24])
	External Extremity Dose	Not estimated	See above
	Internal Dose or Contamination	None – performed in glovebox mode	n/a

5.2 Target Irradiation

Target irradiation will be conducted under the purview of L124 [7]. A comprehensive discussion of safety concerns related to target irradiation is therefore outside the scope of this safety report. However, a brief description of the irradiation is provided herein.

Targets will be irradiated at IPF under typical high-current BL1A beam parameters (480 MeV, ~100 μA at extraction or ~450 MeV, ~85 μA at IPF). The duration of the irradiation will be chosen such that approximately 440 MBq (12 mCi) of ^{225}Ac will exist in the target at 1 week after end of bombardment (EOB). After removal from beam, targets will be raised from the beam level and into the IPF hot cell where they will be left for at least one week before transfer to RCR1. This cooldown period allows short-lived isotopes to decay such that the dose rate from the target can be reduced before the target transfer occurs. During this cool-down period, radiation fields from the target will be contained by the IPF hot cell shielding. Monitoring of the integrity of the target capsule during this period will be done using the hot cell stack monitors, which may detect airborne contamination that would result from the release of volatile radioisotopes from inside the target capsule. Visual confirmation of the target capsule's integrity will also be done; the windows on the target will be deformed inwards as long as vacuum is maintained inside the target.

5.3 Target Transfer

5.3.1 *Procedure and Safety Measures*

The transfer of targets from the IPF hot cell to the RCR1 hot cell will be governed by an active TRIUMF Work Permit at the time of the transfer. The planned work will be reviewed and approved by RPG personnel before being conducted.

Targets will be removed from the IPF hot cell one week after EOB. Only one target will be transferred at a time. At one week after EOB, the target is expected to present an external gamma radiation field of 3.52 mSv/h at 1 m without shielding. The target will be removed from the IPF hot cell within a shielded transfer flask (see Section 3.4). This flask contains a minimum of 7 cm of lead and 3 cm of steel shielding in all directions, reducing the external dose rate to an estimated 0.03 mSv/h at 1 m. Note that this dose rate estimate – determined via FLUKA – matches measurements of dose rates from previous target irradiations. After removal from the IPF hot cell, the outer surface of the flask will be swiped for loose contamination and decontaminated if necessary.

The Meson Hall crane will be used to lift the 214 kg flask from the IPF hot cell area and place it on a cart located in the Meson Hall Extension. The flask will then be pushed to the MHESA building and transferred to the RCR1 lab on the B1 level via the MHESA elevator (1800 kg capacity).

Once in RCR1, the flask will be opened and the target inserted into the hot cell access port. PPE for this part of the work will include a disposable full-body suit, elbow sleeves, cover shoes, gloves, and a respirator. Plastic sheeting will be placed on the floor and nearby surfaces to help contain the spread of any contamination present inside the flask or on the surface of the target. The flask lid will be lifted using a hoist until the target can be picked up by a >1 m pole and immediately inserted into the hot cell access port, at which point radiation fields will be reduced by 10 cm of lead shielding to below 5 μSv/h. Fig. 6 shows the the hand- or drill-powered hoist that is used to lift the flask lid and also shows how the pole securely attaches to the target such that it can be reliably picked up without dropping. Once the target is behind shielding, the area will be checked for contamination and decontaminated if necessary. A high-volume air sample will also be taken to check for airborne contamination. Note that after the first two L125 target transfers (April and May 2018), no removable contamination was found on surfaces other than the inside of the transfer flask (<10 kcpm).

5.3.2 *Gamma Radiation Exposure During Target Transfer*

During the transport of the flask to the RCR1 lab the target is contained in the flask and the resulting 0.03 mSv/h field at 1 m will result in a dose of 0.003 mSv assuming a minimum distance from the target of 1 m and an estimated exposure time of 5 minutes during the transfer of the flask to RCR1.

During the transfer of the target from the flask and into the RCR1 hot cell, the target is not behind any shielding. This portion of the job is expected to expose two workers to gamma radiation fields

of 3.52 mSv/h (at 1 m from the target) for a duration of 30 seconds, resulting in a dose of 0.03 mSv per worker. Note that this estimate is higher than personnel doses measured during the first two L125 target transfers (April and May 2018).

5.3.3 *Contamination of Workers During Target Transfer*

The exterior surface of the target is expected to be contaminated with metal activation products produced in the steel or Inconel® components of the target. Such contaminated metals are routinely encountered at TRIUMF. However, since workers will be wearing full PPE (including tank suit, gloves, and shoe covers) and will not be directly contacting the target, the risk of contaminating personnel is minimal. Contaminants from the thorium foil will be contained within the capsule.

5.3.4 *Possibility of Target Capsule Rupture During Target Transfer*

While alpha-emitting and volatile radioisotopes are expected to be sealed inside the target during the target transfer, rupture of the target hermetic seal during the transfer has the potential to release volatile radioisotopes into the surrounding air. Of these, the most hazardous are the alpha-emitting isotopes. During the transfer the target is not contained within a nuclear ventilation system and any release of volatile radioisotopes during this time would not be contained.

The release of all volatile isotopes within the target would be most hazardous during the portion of the transfer occurring in RCR1 when the target is lifted from the flask into the hot cell. At this point, the target is contained in neither the flask nor the hot cell. The risk of a target rupture releasing volatile radioisotopes will be minimized by the following factors:

- the interior of the target capsule is below atmospheric pressure
- the target securely attaches to the extendable pole shown in Fig. 6
- this portion of the target transfer will be rehearsed with cold targets

However, given a rupture of the hermetic seal of the target capsule in RCR1, dose calculations described in Section 4.1 suggest that the release of all volatile isotopes within the target during that time could expose a worker to an external dose of 0.23 mSv and an internal dose (due to inhalation of radioactive isotopes) of 66.8 mSv[4]. However, this dose will be reduced due to three factors:

- All workers in RCR1 at the time of the target transfer will be wearing respirators that provide a protection factor of 10
- The target is expected to be outside of both the flask and the RCR1 hot cell for less than one minute, after which an air sample will be immediately taken. If significant levels of airborne contamination were detected, all workers would immediately leave RCR1, having only been exposed to the airborne radioactivity for under 3 minutes. This provides a reduction factor of 10 since calculations described in Section 4.1 assume a 30 minute exposure.
- While this document assumes polonium to be a volatile isotope, it is unlikely to be volatile in this circumstance and it is known to stick to metal surfaces below 100 °C, meaning it is very unlikely to leave the thorium foil and target capsule.

These factors combine to reduce the maximum external dose by a factor of 10 to 23 µSv and reduce the maximum internal dose by a factor of 100 to 668 µSv.

Following the methods of Section 4.1, the maximum off-site dose to a member of the public due the release of volatile isotopes during the target transfer in RCR1 is 0.92 mSv, assuming that none of this air is filtered. However, ventilation for the RCR1 lab is controlled by the fume hood, which draws air out of RCR1. The charcoal and HEPA filters on this stack filter out 99.5% of bromine, selenium, iodine, and polonium isotopes [20], which reduces this maximum possible dose to 5 µSv.

A breakdown of the airborne dose estimates by isotope is shown in Appendix C. Section 5.1 provides a comparison of the dose estimates in this section to dose estimates from similar hazards existing at TRIUMF.

4 The calculation described in Section 4.1 was modified to account for the actual volume of RCR1. A 400 m^3 volume was used instead of the standard 15 m radius sphere.

Figure 6: Photos showing how the flask lid will be raised and the targets pickup up when the target is moved from the transfer flask and into HC1. Note that the flask pictured is not the one that will be used, however, the hoist and extendable pole will interface with the actual flask and targets in the same manner.

5.4 Opening of the Target Capsule

5.4.1 *Procedure and Safety Measures*

After the target capsule has been opened, as described in Section 3.5, the thorium foil will be removed. The remaining components of the target capsule will be placed behind a lead bunker (walls >7.5 cm thickness) at the back of HC1. This removes the largest contribution to the external radiation field emanating from the entire target (3.52 mSv/h at 1 m), as the dose rate from the thorium foil alone is expected to be only 0.86 mSv/h at 1 m. The target capsule will be allowed to decay for at least 6 months (or until radiation fields have been sufficiently reduced) before it is removed from the hot cell and given to RPG for disposal (see Section 7.1). One year after EOB, the target body is expected to emit a dose rate of 33 μ Sv/h at 1 m.

5.4.2 *External Doses to Workers During Opening of the Target Capsule*

This work will be conducted within the RCR1 hot cell shielding. The resulting dose rate outside of the hot cell is expected to be less than 5 μSv/h before the components of the target body are placed in the shielding bunker. After the target body is placed behind shielding the dose rate outside of the hot cell is expected to be less than 2 μSv/h.

5.4.3 *Contamination of Workers During Opening of Target Capsule*

This work will be conducted within the RCR1 HC1 hot cell, operated in hot cell mode. All work will be carried out using the manipulators or remotely controlled systems. Therefore, there is no risk of contamination of personnel during this portion of the experiment.

5.4.4 *Release of Volatile or Gaseous Isotopes During Opening of Target Capsule*

The opening of the target capsule is not expected to result in the release of volatile radioisotopes that were produced within the thorium during the irradiation, as these isotopes will remain trapped within

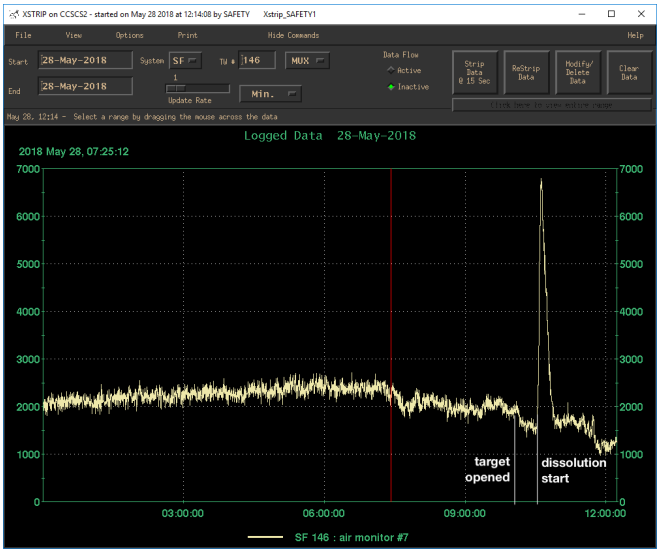

Figure 7: Stack monitor readings during processing of first thorium metal target at 1 week after EOB.

the thorium metal. This is supported by RCR1 stack radiation monitor readings during the processing of the first two L124/L125 metal targets, shown in Figure 7. However, the release of volatile and gaseous isotopes is expected to occur during target dissolution and evaporation (see Section 5.5.4.

The release of these volatile isotopes will be further controlled by use of an additional air containment and filtration system that will be built inside HC1. While initially designed to trap and filter air during both the target opening and the dissolution, results from the first runs (Figure 7) indicate this is only necessary during the dissolution. Additionally, due to the large volume of the target opener, providing sufficient air flow to trap any gases released during target opening is challenging. Therefore, trapping and filtering air during opening of the target is not necessary and is no longer done. The updated internal air containment system is described in Section 5.5.4.

5.5 Dissolution of Thorium Foil

5.5.1 *Procedure and Safety Measures*

The irradiated thorium foil will be placed in a 500 mL beaker for the dissolution, which is capped with a large custom stopper, shown in Fig. 9. This stopper contains three ports: one for airflow into the beaker from the hot cell, a second for airflow out of the beaker, and a third for remotely adding the acids used for the dissolution. As described in Section 3.6, the solution of dissolved thorium will also be evaporated to near dryness after the dissolution.

Shown in Fig. 8, a system for trapping acidic vapours as well as volatile or gaseous radioactive isotopes is employed during the dissolution and evaporation. This systems pumps air out of the beaker and through a liquid trap, a soda lime column for neutralization of any acidic vapour, then a filter consisting of activated charcoal and tellurium. This filter is expected to further reduce the release of chlorine, bromine, selenium, iodine, and polonium isotopes by an additional 99.5%. Work at TRIUMF

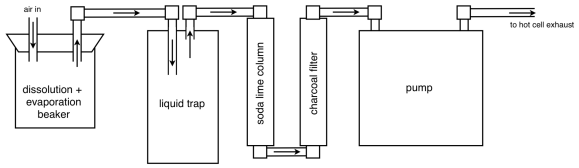

Figure 8: Diagram of system that will be employed to capture and filter acidic and radioactive gases that may be released during opening of the target capsule and dissolution of the thorium foil. Blue arrows indicate direction of airflow. Not shown: manipulator-controlled valves, flow indicators.

and elsewhere has shown that tellurium is an effective trap for polonium isotopes, the element that contributes the most to airborne dose estimates [25]. This will allow any volatile radioisotopes trapped within the thorium and released during the dissolution to be captured and filtered before the air is released through the hot cell stack.

Contamination surveys conducted during the first two L125 runs show that this system effectively prevents the release of volatile and gaseous isotopes into the hot cell, as very little contamination was found on surfaces inside the hot cell after the run (<200 cpm on swipes of surfaces) or on liquid samples removed from the hot cell during the run (<1000 cpm on swipes, mostly due to the contents of the samples themselves). Measurements conducted using air sampling filters during the first two L125 runs also show that the charcoal filter traps >99.5% of volatile halogen isotopes (based off of gamma spectroscopy measurements that quantified the amount of ^{125}I or ^{131}I on sampling filters upstream and downstream of the charcoal filter) before they are released into the hot cell stack. With this data acquired, these sampling filters have now been removed, as they are highly susceptible to corrosion and are prone to leaking, reducing the efficiency of the rest of the air containment system.

After dissolution and evaporation, the thorium nitrate salts are redissolved in approximately 80 mL of 1 M HNO_3. This solution is then removed from the beaker by using the manipulators to insert a thin tubing line in through the larger air inlet. This is necessary as the tubing is only rated for concentrated acids at temperatures below 50 °C and therefore cannot be in contact with the solutions during the dissolution or evaporation.

5.5.2 *External Doses to Workers During Thorium Dissolution*

This work will be conducted within the RCR1 hot cell shielding. The resulting dose rate outside of the hot cell is expected to be less than 2 μSv/h.

5.5.3 *Contamination of Workers During Thorium Dissolution*

This work will be conducted within the RCR1 HC1 hot cell, operated with the shielding doors closed. All work will be carried out using the manipulators or remotely controlled systems. Therefore, there is no risk of contamination of personnel during this portion of the experiment.

5.5.4 *Release of Volatile or Gaseous Isotopes During Thorium Dissolution*

Volatile and gaseous isotopes within the target are expected to be released during the dissolution and evaporation. Calculations of the dose resulting from the release of these isotopes assume the entire volatile inventory (as defined in Section 4.1).

Isotopes of these elements with half-lives greater than 50 seconds are listed in Appendix C along with the estimated maximum amount released. This selection of isotopes is identical to those used in the *Actinide Target SAR Addendum for Thorium Oxide*, with the addition of ^{220}Rn [20]. Without any mitigation, this release is estimated to result in a maximum on-site internal dose of 1.80 mSv (calculated as defined in Section 4.1). However, the presence of charcoal and HEPA filters on the hot cell exhaust nominally filters out 99.5% of chlorine, bromine, selenium, iodine, and polonium

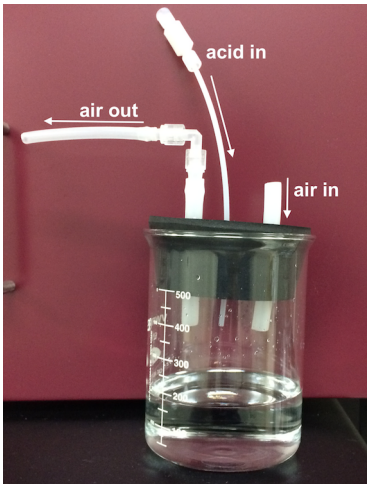

Figure 9: Image of the beaker (with stopper) that will be used for the thorium dissolution and evaporation. Note that an ETFE stopper is used instead of the rubber stopper shown.

isotopes [20], which reduces this maximum possible dose to 0.06 mSv. The off-site dose to members of the public from this release is estimated at 0.92 mSv without accounting for the hot cell stack filters and 4.6 µSv when filtration is considered. Calculation details and a breakdown of these airborne dose estimates by isotope are shown in Appendix C. Assuming the air containment system captures all of the radioactive isotopes within the target and that the filters remove airborne contaminants with the expected 99.5% efficiency, this results in lower the maximum expected on-site internal dose to 0.05 mSv and the off-site dose to members of the public to 0.02 µSv. Details of these calculations can be found in Appendix C. After filtration, polonium isotopes dominate the dose contribution.

It is also important to keep in mind that these calculations are conservative and are in practice expected to be lower for reasons that include:

- As shown in Appendix C, the isotope that contributes >99% to unfiltered airborne internal radiation doses both on- and off-site is ^{206}Po. However, polonium is known to not be 100% volatile and despite the production of large quantities of Po isotopes during ISAC actinide target irradiation, no measurable release of Po isotopes through ISAC stacks has been detected [20]
- The alpha-emitting volatile isotopes are radon isotopes and while methods defined in Section 4.1 and the *Actinide Target SAR Addendum for Thorium Oxide* Report [20] assume that radon isotopes are not filtered, work both within and outside of TRIUMF has demonstrated that charcoal filters can trap radon to some extent [21, 26].

During target dissolution, the hot cell stack can also be monitored by existing radiation detectors monitored in the Main Control Room. It is also possible to make arrangements with RPG to sample and analyze the air released from the hot cell stack using existing RPG systems. This will ensure that actual releases can be quantified.

Section 5.1 provides a comparison of the dose estimates in this section to dose estimates from similar hazards existing at TRIUMF.

5.6 Purification of ^{225}Ac and ^{225}Ra from Dissolved Thorium

5.6.1 *Procedures and Safety Measures*

Chemical separation of actinium and radium isotopes from the dissolved thorium target requires the use of multiple chromatography columns. First attempts will use the columns and procedure described in Section 3.6, but other columns or similar chemical procedures may also be explored. However, the general methods and tools used to perform this process while minimizing the spread of contamination will not change.

The isolation of actinium and radium isotopes will be done within the hot cell with the shielding doors closed. A system of pumps and valves that can be controlled from outside the hot cell will be used to pass the necessary solutions through the required steps of the process. The same system is used to control the dissolution and evaporation steps described in Section 5.5.1. The components of this system are described in Table 4. To perform the procedure described in Section 3.6, 20 valves and 5 pumps are planned. A schematic of this setup is shown in Appendix D.

This procedure will first be tested with thorium metal that has not been irradiated. If available, a small amount (<1 MBq) of ^{225}Ac and ^{225}Ra will be added to the initial solution of dissolved thorium as tracers. The results of these tests will be documented.

5.6.2 *External Doses to Workers During Chemical Processing*

This work will be conducted within the RCR1 hot cell shielding. The resulting dose rate outside of the hot cell is expected to be less than 2 μSv/h.

5.6.3 *Contamination of Workers During Chemical Processing*

This work will be conducted within the RCR1 HC1 hot cell, operated with the shielding doors closed. All work will be carried out using the manipulators or remotely controlled systems. Therefore, there is no risk of contamination of personnel during this portion of the experiment.

5.6.4 *Release of Volatile or Gaseous Isotopes During Chemical Processing*

All volatile radioisotopes produced in the thorium metal are expected to have already been released during the dissolution and evaporation steps. Following this single release of volatile and gaseous isotopes, the continuous production of any alpha-emitting volatile or gaseous isotopes listed in Appendix C from a long-lived parent isotope will be limited to the progeny of ^{226}Ra, ^{222}Rn ($t_{1/2}$ = 3.8 d), of which a maximum of 3 kBq is expected and the progeny of ^{228}Th, ^{220}Rn, of which 28.3 MBq is expected. However, after processing of the target, the container containing these isotopes will be kept sealed. Therefore, a continuous release of ^{226}Ra or ^{228}Th progeny through the hot cell ventilation is not expected.

Since the solution of isolated radium isotopes will act as a secondary generator of ^{225}Ac via ^{225}Ra ($t_{1/2}$ = 14.9 d), the container will be opened approximately every 17.5 days to remove additional quantities of ^{225}Ac. This could be expected to release a maximum of 3 kBq of ^{222}Rn every 17.5 days.

5.6.5 *Contamination Control During Chemical Processing*

While performing the chemical process within a hot cell protects workers from contamination, measures will still be taken to prevent the hot cell from becoming contaminated. The semi-automated system using components shown in Fig. 4 as well as those employed for the dissolution and evaporation (Section 5.5.1) are expected to contain radioactive liquids within sealed containers or tubing, as has been demonstrated during the first two L125 runs. Personnel conducting the purification will visually monitor the system via the hot cell window throughout the process for any unexpected leaks of radioactive liquids and will immediately turn off all pumps if one is observed.

As a secondary measure of contamination control, all components and containers involved in opening, dissolving, and processing the thorium target will be placed on spill trays lined with absorbent paper to prevent any liquid spills or leaks from irreparably contaminating the hot cell surfaces. This applies to all work described in this document that includes the handling of radioactive liquids.

Table 4: Components of semi-automated system for controlling thorium target processing.

Containers 	Containers used to hold stock acid solutions, radioactive solutions, waste products, and desired ^{225}Ac or ^{225}Ra products will glass solvent containers (50 - 500 mL) compatible with GL45 solvent caps. These containers will be reused between separate production runs. plastic containers are compatible with all acids used in the experiment.
Container Seals 	Solvent caps with inlets for tubing are employed to provide a tight seal on each container. These caps are equipped with inlet and outlet air valves to prevent pressure build up when liquid is pumped in or out of a container. designed to provide tight seals epta caps are used to seal all nalgene and Falcon tube containers. The only containers that don't use these caps are the glass beakers used for the dissolution and evaporation stages, described in Section 5.5.1 – these are sealed with the large stoppers shown in Fig. 9.
Valves 	Pinch valves will be used to open and close tubing to and from different solutions at various stages in the process. The image to the left shows the valve in the default closed state. The valve opens with the application of a 24 VDC potential. The use of pinch valves prevents acid or alpha-radiation damage to the pinch valve, since the valve only contacts the outer surface of the tubing.
Pumps 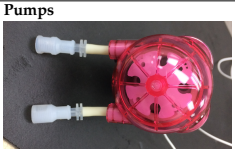	Peristaltic pumps will be used to pump solutions at different stages of the process. Pump speed is controlled between approximately 2 and 16 mL/min by varying the input voltage between 8 and 24V. The state of pinch valves upstream or downstream will determine to and from where liquids will be pumped.
Tubing and Fittings 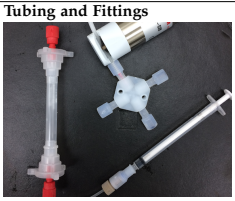	Tubing used will be either ETFE tubing or BioChem CFlex tubing, both of which are compatible with all solvents and other components used in the setup. Fitting components that contact the solvents are all ETFE plastic and compatible.
Controls 	A control box consisting of switches dedicated to each pump and valve will be used to control the processing of the thorium targets. These switches, located outside the hot cell, are directly wired to each pump and valve through the built-in hot cell wire ports. The controls are further wired such that no pump can be turned on unless at least one upstream and downstream valve is open, this prevents the buildup of pressure within the flexible tubing.

Table 5: Comparison of directly- and indirectly-produced ^{225}Ac products by both yield and contaminants. Isolation of Ra and Ac isotopes 1 week after EOB gives the directly-produced ^{225}Ac product. Allowing the Ra fraction to sit for 17.5 days and then once again separating Ra and Ac isotopes provides the indirectly-produced ^{225}Ac product via ^{225}Ra decay.

	Directly-Produced ^{225}Ac	**Indirectly-Produced ^{225}Ac**
^{225}Ac [MBq]	**432**	**17**
^{228}Ac/^{225}Ac [%]	0.040	0.974
^{227}Ac/^{225}Ac [%]	0.196	3.2×10^{-13}
^{226}Ac/^{225}Ac [%]	11.900	0.000

At least one of the manipulators is expected to become contaminated by typical metal activation products on the outer surface of the target when it is picked up before opening the target and removing the thorium. Contamination of the manipulators by thorium spallation products will be minimized by using a suction tube to pick up the foil (thus avoiding direct manipulation of the foil with a manipulator) and placing it the dissolution beaker. However, some contamination to the manipulators from thorium spallation products may be unavoidable.

Again, contamination surveys after the first two L125 runs show that contamination control measures in place are effective, as very little contamination was found on surfaces inside the hot cell after the run (<200 cpm on swipes, mostly radon progeny) or on liquid samples removed from the hot cell during the run (<1000 cpm on swipes, mostly due to the contents of the samples themselves).

5.7 Testing of ^{225}Ac Products

5.7.1 *Radioactive Composition of ^{225}Ac Products*

The purification of Ac and Ra isotopes from the irradiated thorium will result in two ^{225}Ac products: directly-produced ^{225}Ac isolated in the Ac fraction one week after EOB, and indirectly-produced ^{225}Ac extracted 17.5 days later from the isolated Ra isotopes after the decay of ^{225}Ra to ^{225}Ac [27]. Since these two products are expected to contain different radioactive contaminants, it is scientifically crucial to the experiment that both are assessed for their utility as a supply for ^{225}Ac-radiopharmaceuticals. The most notable difference is in the amount of ^{227}Ac co-produced. Concern exists within the TAT field that the presence of ^{227}Ac – a long-lived ($t_{1/2}$ = 21.8 y) and toxic alpha-emitter – may prevent the regulatory approval of an ^{225}Ac-radiopharmaceutical. For this experiment, ^{227}Ac is also challenging from a waste management perspective.

Table 5 contains details regarding the anticipated quantities of Ac contaminants in each ^{225}Ac product. These values were determined using the FLUKA simulation results and modelling of the purification process that assumes perfect chemistry (i.e. no breakthrough of ^{227}Ac into the initially isolated Ra fraction, for example). The directly-produced ^{225}Ac product is expected to contain ~0.2% ^{227}Ac by activity at EOB + 1 week and a total of 1.45×10^{5} ALI of Ac isotopes.

While the indirectly-produced ^{225}Ac is expected to have a ~25 times lower yield, it is also expected to be ^{227}Ac-free, and contain 5.8×10^{3} ALI of Ac isotopes.

5.7.2 *Procedures and Safety Measures*

Sampling of Purification Products

To gather information about the process of purifying ^{225}Ac and ^{225}Ra from the thorium, it is necessary to remove samples of all solutions produced during the ^{225}Ac purification process so that their composition can be determined by gamma spectroscopy, alpha spectroscopy, and ICP-MS. To do this, lead brick shielding will be employed inside the hot cell such that a worker can put their hands inside the front area of the hot cell (in either glove box or fume hood mode) without exposing the worker to high whole body or extremity (hand) doses. A diagram of this shielding setup is shown in Fig. 11. Two sliding doors made of 10 cm of lead and capable of being opened and closed by the manipulators will be built. With these shielding doors open, the semi-automated purification process can be visually monitored through the shielding of the hot cell door. With these shielding doors closed, the hot cell

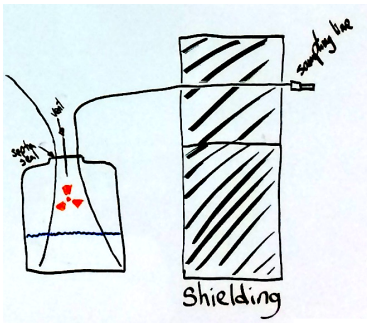

Figure 10: Diagram illustrating how radioactive solutions will be sampled from behind shielding. Pre-positioned sampling lines with syringe fittings will be used to remove up to 100 µL (<1% of total volume) of a radioactive solution. Increased shielding and distance to the bulk volume of radioactive liquid will reduce worker's hand dose during the process.

front door can be lowered to permit use of the hot cell in fume hood or glove box mode without exposing the worker to the high radiation fields from the purification products. The 10 cm of lead shielding is expected to lower the dose rate from the purification products from 820 µSv/h to 2.5 µSv/h at 1 m (at the front of the hot cell).

Sampling lines pre-positioned in each container will allow small aliquots of the highly radioactive solutions to be sampled from behind this shielding. The diagram of this is shown in Fig. 10. The syringe adapter on the end of the sampling line will allow up to 100 µL (<0.1% of radioactive inventory) of a radioactive solution to be removed. These adapters will be plugged when not in use. The 100 µL sample will then be transferred to a vial and diluted to a concentration suitable for gamma spectroscopy, alpha spectroscopy, or ICP-MS measurements. The collection and dilution of these samples will be conducted in fume hood mode. All samples removed from the hot cell will first be swiped for removable contamination. A conservative maximum possible dose rate expected from a 100 µL sample of any of the purification products is 1 µSv/h at 1 m without shielding. Using values from Table 2, a <100 µL sample of any of the purification products would contain $<4.98\times10^{3}$ ALI.

Secondary Production of ^{225}Ac from Isolated Radium Isotopes

Use of the solution containing isolated Ra isotopes will be used as a second source of ^{225}Ac. Beginning >17.5 days after initial thorium target purification, the entire solution (<50 mL) will be passed through an extraction chromatography column to purify additional ^{225}Ac quantities. The anticipated radioactive composition of this solution at the time this task will be performed and the resulting dose rate from each isotope is shown in the table of Appendix E, including Ra isotopes and their decay products in equilibrium as well as barium (Ba) isotopes that are known to follow Ra isotopes through the thorium purification process [3]. This inventory represents a total of 2.9×10^{4} ALI. The total expected dose rate at 1 m from this vial is 8.18 µSv/h. Since this dose rate is well below the dose rate of high activity solutions routinely handled by hand by TRIUMF's radiochemists, this work will not be semi-automated but will be done in the hot cell by hand. However, due to the relatively large volumes of liquid anticipated (<50 mL) and the presence of long-lived alpha-emitting isotopes such as ^{226}Ra, this work will be performed in glovebox mode.

^{225}Ac Radiolabeling Test Reactions

Small aliquots (<100 µL containing <200 kBq of ^{225}Ac and <72 ALI of Ac isotopes) of the two isolated ^{225}Ac products will also be used to perform radiolabeling experiments. These simple reactions

are described in Section 3.7 and will be performed inside the hot cell in fume hood mode, as will preparation of iTLC plates. These plates will then be sealed with parafilm before they are checked for removable contamination and transferred to the RCA1 QC room for readout. This process of labeling biomolecules with similar amounts of ^{225}Ac in RCR1 hot cells and measuring the resulting iTLC plates on the QC room plate reader has already been subject to safety review under L122 and has been performed many dozens of times [17]. The RCR1 HPLC may also be used to characterize radiolabeling reaction products, provided that no organic solvents are used (see Section 7).

The additional presence of ^{227}Ac does not significantly increase the hazards associated with this work. As can be seen in Table 2, in terms of ALIs, ^{225}Ac is produced at two orders of magnitude more than ^{227}Ac. However, the presence of ^{227}Ac does significantly increase waste management issues, which are described in Section 7.

Preparation of an ^{225}Ac Generator of ^{213}Bi

As the ^{225}Ac progeny isotope ^{213}Bi ($t_{1/2} = 45.6$ min) is itself a TAT isotope of interest, a ^{213}Bi generator from the directly-produced ^{225}Ac fraction may also be produced. This work may involve the entirety of the directly produced ^{225}Ac (<440 MBq in <30 mL, $<1.45\times10^5$ ALI), which will be loaded onto an ion exchange (AG-MP 50) resin. Once loaded, Ac isotopes (dominantly ^{225}Ac and ^{227}Ac) will remain on the resin, within which ^{213}Bi is continuously produced and can be removed as needed. The anticipated radioactive composition of this loading solution at the time this task will be performed and the resulting dose rate from each isotope is shown in the table F, including Ac isotopes and their decay products in equilibrium. The total expected dose rate at 1 m from this vial is 11.11 µSv/h. Since this dose rate is well below the dose rate of high activity solutions routinely handled by hand by TRIUMF's radiochemists, this work will not be semi-automated but will be done in the hot cell by hand. However, due to the presence of hazardous amounts of ^{227}Ac , the loading of the column will be performed in glovebox mode. Since ^{227}Ac will remain bound to the column throughout the lifetime of the generator's use, eluting of the generator will be done within the hot cell, operating in fume hood mode.

Alone, ^{213}Bi has an ALI of 1.11×10^7 Bq [28]. Radiolabelling of the collected ^{213}Bi (<440 MBq, <40 ALI) may also be performed in the hot cell by hand, operating in fume hood mode. This would produce ^{213}Bi-radiopharmaceuticals with activities great enough for preclinical trials.

Preparation of Clinically Relevant Quantities of ^{225}Ac-Radiopharmaceuticals

A clinical dose of ^{225}Ac-TAT requires approximately 37 MBq (1 mCi) of ^{225}Ac in the final radiolabeled product. Preparation of such compounds may also be conducted within the hot cell and is already approved as part of L122 [17]. When using the directly-produced ^{225}Ac, the work will be done in glovebox mode due to the presence of ^{227}Ac. When using the indirectly-produced (and ^{227}Ac-free) ^{225}Ac product, this work will be conducted in fume hood mode. L122 is already approved to handle up to 37 MBq of ^{225}Ac in solution (without ^{227}Ac) within the RCR1 hot cells in fume hood mode [17].

Low-Level Testing of Other Irradiated Thorium Purification Methods

Since the investigation of novel processes for purification of ^{225}Ac from irradiation thorium is also of interest, small samples (<10 µL and <0.01% of the target's total radioactive inventory) of the dissolved target solution (after evaporation of HCl and HF acids and conversion to citric acid) may also be taken such that new chromatography methods can be tested. These tests will be conducted with the hot cell operating in fume hood mode. The dose rate expected from 0.01% of the thorium target is <0.1 µSv/h.

Similarly, the purification method that will be implemented for full processing of the irradiated target will be practiced before introducing the irradiated target into the hot cell. This tests will use readily available tracers of key isotopes as tracers for the elements that must be separated. These tracers will include <2 MBq ^{225}Ra and ^{225}Ac from CNL, <2 MBq ^{89}Zr from the TR13, <2 MBq ^{177}Lu from BC Caner Agency (originally purchased from ITG), and potentially ^{227}Th sourced from the US DOE. Additionally, since limited thorium metal is available for such tests, in some cases, thorium nitrate already available at TRIUMF may be used in place of non-irradiated thorium metal. The uses of these tracers does not change the hazard assessment and safety precautions outlined in previous

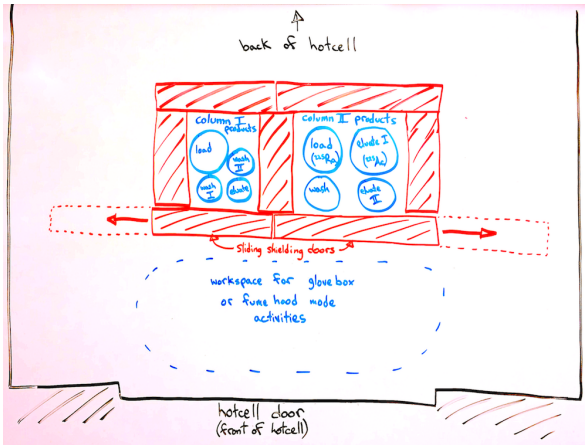

Figure 11: Aerial view of hot cell setup, illustrating how shielding will be used to surround containers of radioactive liquids produced during the purification process. Two sliding lead doors capable of being opened and closed by the manipulators will be built. With these shielding doors open, the semi-automated purification process can be visually monitored through the shielding of the hot cell door. With these shielding doors closed, the hot cell front door can be lowered to permit use of the hot cell in fume hood or glove box mode without exposing the worker to the high radiation fields from the purification products.

parts of this document since the anticipated co-production of these isotopes in the irradiated targets has already been considered.

Summary of Activities Performed Outside the Hot Cell

With a few exceptions, all work described in Section 5.7 will be conducted in HC1, operating in glovebox mode or fume hood mode, as indicated. Activities performed in fume hood mode maybe also be conducted in HC2, in which ^{225}Ac samples are already regularly handled in fume hood mode as part of L122 [17].

However, some samples must be removed from the hot cell entirely for analysis, since the required equipment is located outside the hot cell. This includes:

- Vials containing liquid samples for gamma spectroscopy will be removed from the hot cell and counted in the RCR1 HPGe detector.
- Samples prepared for alpha spectroscopy will be removed from the hot cell and counted on the alpha spectroscopy detector in RCR1. These samples consist of a small metal disk on top of which a drop of a radioactive solution has been evaporated. Due to the sensitivity of the alpha spectroscopy detector, the total activity of these samples will be on the order of 10^2 Bq.
- As described in Section 3.7, TLC plates spotted with a drop of a solution from the purified ^{225}Ac products and developed inside an RCR1 hot cell, will be sealed in a plastic bag and removed from the hot cell. These plates typically contain 10^2-10^4 Bq. These samples will be brought to the RCA1 QC room, where the TLC plate reader is located. Plates will remain inside a plastic bag while they are counted.

- Vials containing liquid samples of radiolabeling reaction products may be removed from the hot cell and analyzed on the RCR1 HPLC.
- Vials containing samples prepared for ICP-MS will be removed from the hot cell and shipped off-site for analysis.
- Prepared ^{225}Ac-radiopharmaceuticals will be removed from the hot cell and shipped off-site for animal studies.

All samples removed from the hot cell will be in a sealed container (ex. vial or plastic bag) with an exterior surface verified (via swipes) to be free of removable contamination. Alpha spectroscopy samples must be removed from their container before being placed in the detector.

5.7.3 *External Doses to Workers During Testing of ^{225}Ac Products*

Whole Body Dose Estimates

With the exception of the operation of ^{225}Ra\$^{225}$Ac and ^{225}Ac\$^{213}$Bi generators, all tasks described in Section 5.7 involve handling samples having dose rates of <1.2 µSv/h at 1 m without shielding. The worker's body may be closer to the samples during the work, increasing the dose rate to <5 µSv/h if a 0.5 m distance is assumed, plus an additional 2.5 µSv/h from other contents of the hot cell (behind the shielding shown in Fig. **??**). Since it is unlikely a worker will spend more than 4 hours in one day within 0.5 m from these samples, an estimated upper limit of dose received conducting these tasks is 30 µSv per day.

While the dose rates are higher for the operation of ^{225}Ra\$^{225}$Ac and ^{225}Ac\$^{213}$Bi generators (8.18 and 11.11 µSv/h at 1 m, respectively), these tasks take less time. If an upper limit of one hour spent by a worker at 0.5 m from the generator is assumed, doses of up to 33 µSv for the elution of the ^{225}Ra-^{225}Ac generator and 47 µSv for the ^{225}Ac-^{213}Bi generator can be expected, including the additional 2.5 µSv/h from other contents of the hot cell.

Extremity Dose Estimates

The radioactive samples described in Section 5.7 that will be manipulated by hand present dose rates well below those of other materials frequently handled by TRIUMF's radiochemists. Therefore, no significant extremity doses are expected. Wherever possible, workers will use shielding (ex. lead pigs) and distance (ex. tools such as tongs) to limit the dose received by their hands.

5.7.4 *Risk of Contamination During Testing of ^{225}Ac Products*

Workers performing tasks described in Section 5.7 with the hot cell operated in glovebox mode will wear a lab coat, safety glasses, cover shoes, hydrophobic elbow sleeves, and gloves. Since all unsealed radioactive samples containing long-lived alpha-emitters such as ^{227}Ac or ^{226}Ra that are handled in fume hood mode are also <100 µL in volume, the risk of an accident resulting in the spill of activity out of the hot cell or the penetration of activity through the worker's PPE is reduced. Using values from Table 2, a <100 µL sample of any of the purification products would contain $<4.98\times10^{3}$ ALI. Given the handling of such small volumes, the ease of use gained by working in fume hood mode is expected to help reduce the spread of contamination within the hot cell, an important concern considering that some samples must leave the hot cell for analysis. While working in glovebox mode provides a higher level of protection to the worker from direct contamination, these thick glovebox gloves can be awkward and difficult to cover with disposable gloves. This contrasts with the use of fume hood mode, where a worker wearing multiple layers of disposable gloves can easily remove pairs of gloves when touching different surfaces, reducing the spread of contamination.

Whenever the hot cell front door will be opened for operations in fume hood mode, swipes of the front interior area of the hot cell will first be taken in glovebox mode. Surfaces swiped will also include the inner surface of the hot cell door and the hot cell gloves themselves.

Still, tasks described in Section 5.7 that involve handling larger volumes of radioactive solutions or larger quantities of ^{227}Ac will be performed in glovebox mode, the risk of contaminating a worker to these isotopes is controlled.

Protection of hot cell surfaces from contamination is described in Section 5.6.5.

A comparison of the contamination or internal dose hazard for this experiment with similar hazards from other TRIUMF experiments or activities is further provided in Section 5.1

Prior Experience Handling Liquid ^{225}Ac and ^{225}Ra Samples

The users of L125 (Andrew Robertson and Hua Yang), along with other TRIUMF workers, have previously handled liquid sources of both ^{225}Ac and ^{225}Ra isotopes in RCR1 hot cells under the purview of L122. L122 has safety approval to handle up to 37 MBq of ^{225}Ac and 37 MBq of ^{225}Ra (or a total of 1.2×10^4 ALI) [17]. Two years of experience during these experiments has shown that ^{225}Ac and ^{225}Ra contamination does not spread easily once in liquid form and at no point has contamination spread outside the hot cell or onto workers.

^{227}Ac Contamination

^{227}Ac is the isotope with the most restrictive ALI and is produced in significant quantities in this experiment. While ^{227}Ac, as an alpha-emitter with few gamma emissions, may present challenges in terms of direct detectability, any substances containing ^{227}Ac are also expected to contain ^{225}Ac, ^{226}Ac, and/or ^{228}Ac, which themselves are easily detectable by all contamination monitors, as are ^{227}Ac decay products ^{227}Th and ^{223}Ra. Though ^{227}Ac will outlive these isotopes, once ^{225}Ac has decayed there is no motivation to handle these substances. As shown in Table 2, nearly 100 times more ALIs of ^{225}Ac will be produced than ALIs of ^{227}Ac, and experiments involving similar ^{225}Ac quantities are already conducted in RCR1 hot cells in fume hood mode. Proposed tasks involving larger ^{225}Ac quantities will be performed in glovebox mode.

5.8 ^{212}Pb Generator and Applications

At 6 months after EOB, the ^{228}Th stock solution from the first L125 target (irradiated in December 2017 and processing in April 2018), has an external dose rate of 2.5 µSv/h at 1 m. The main contribution to this dose rate is a 2.61 MeV gamma emission (99.8% branching ratio) emitted by the ^{228}Th progeny ^{208}Tl. The radioactive inventory of this solution has been measured, and is shown in Table 6. In addition to this, the solution also contains approximately 8 g of natural thorium. In total, this inventory contains 1973 ALI of radioactivity if inhaled, and 35.43 ALI of activity if ingested. However, since ^{228}Th is a non-volatile metal in an aqueous solution, inhalation of ^{228}Th is not considered a credible exposure scenario.

To minimize handling of the generator stock solution, an automatic apparatus for loading the ^{212}Pb onto the extraction resin will be built. This apparatus will meet the following safety-related requirements:

1. retain the ^{228}Th solution in a closed loop, such that the user does not have to handle it by hand
2. for each use of the generator, the user is only required to exchange the single-use resin, and to wash and elute the resin using a syringe
3. a peristaltic pump for moving the solution through the resin will be placed downstream from resin, such that liquid is pulled through the resin, not pushed. This prevents build-up of back pressure and also prevents a spill in the event that the user does not properly attach the column
4. house the stock ^{228}Th solution within 3-5 cm of a steel shielding that is expected to reduce the external dose rate to below 1 µSv/h at 1 m

By using this apparatus, the user is only required to handle the ^{228}Th progeny isotopes, namely ^{212}Pb ($t_{1/2}$ = 10.6 h), which will decay within days in the event of any spills or generation of contaminated waste.

The generator apparatus will be placed on an acid resistant spill tray and absorbent spill paper will also be utilized. Due to the release of ^{220}Rn from the generator, the generator will be kept inside the RCR1 fume hood. Note that this does not introduce any new airborne radioactivity releases,

as the hazard assessment for this ^{220}Rn is already included in the hazard assessment for the ^{225}Ac purification.

Handling of the ^{212}Pb produced from the generator will expose the user to a dose rate of <2.5 µSv/h at 1 m. This activity will be handled in a fume hood or hot cell operating in fume hood mode. Small sealed quantities may be removed from the fume hood for analysis (ex. gamma spectroscopy, TLC plate reading etc.).

Table 6: Radionuclide inventory of ^{228}Th solution produced as by-product of the first processed L125 target

Nuclide	half-life	Activity [Bq]	$ALI_{ing.}$ [Bq]	$ALI_{inh.}$ [Bq]	$A/ALI_{ing.}$
Th-228*	1.91 y	9.78E+06	2.78E+05	5.00E+02	35.21
*including decay products (not listed)					
Th-227	18.7 d	3.37E+05	2.27E+06	2.00E+03	0.15
Ag-110m	250 d	4.20E+05	7.14E+06	1.67E+06	0.06
Se-75	120 d	1.37E+05	7.69E+06	1.54E+07	0.02
		Total:			**35.43**

5.9 Chemical Safety Measures

Chemical safety hazards described in Section 4.3 are commonly found in TRIUMF's radiochemistry labs. Equipment and spill kits required for dealing with chemicals spills are available in the lab. Workers have also completed chemical safety training and are aware of the location of SDS for the chemicals involved.

The use, handling, and storage of HF will be conducted in accordance with UBC Risk Management Services guideline for the handling of HF (UBCV-RMS-OHS-GDL 14-006)[5].

5.10 Industrial Safety Measures

Industrial hazards described in Section **??** are limited to the lifting of heavy objects, notably the transfer flask. Craning of the flask will be conducted by the Meson Hall crane operators, not the experimenters. The workers will wear safety boots when transporting heavy objects and will wear hard hats if near the Meson Hall crane while it's in use.

The accumulation of flammable material within the hot cell – notably disposable solid waste – will be limited to one bag (~12"x15") of disposables at a time.

6 DEFINITION OF RESPONSIBILITIES

Andrew Robertson is the experimental Safety Coordinator and is responsible for ensuring the overall safety of the experiment and that all actions taken comply with this safety report. Due to the presence of long-lived isotopes with low ALI values (ex. ^{227}Ac) and the level of care that must be taken to prevent contamination of surfaces inside the hot cell with these isotopes, Andrew Robertson and Hua Yang will be the only users of HC1 and this experiment and the ^{225}Ac materials it produces. Brooke McNeil will also be a user of the ^{228}Th-^{212}Pb generator and the resulting ^{212}Pb. Stefan Zeisler and Ellard Portman are assisting with ^{225}Ac production runs and upgrades of the L125 hot cell equipment.

Other groups outside of the Life Science Division also have specific responsibilities related to this experiment. As the Applied Technology Group (ATG) has ownership of the IPF, ATG Operators will be responsible for removing the transfer flask from IPF; Meson Hall Crane Operators will then be responsible for lifting the flask as necessary. RPG and Operators in the 500 MeV Control Room are responsible for monitoring stacks from the IPF, RCR1 fume hood, and HC1 during the experiment and for collecting any required air samples from these stacks. The L125 Safety Coordinator will coordinate with RPG regarding the timing of any required air sampling of the ventilation stacks. RPG is also

5 http://riskmanagement.sites.olt.ubc.ca/files/2016/05/UBCV-RMS-OHS-GDL-14-006-Handling-Hydrofluoric-Acid.pdf

responsible for receiving waste generated in this experiment that is prepared according to this safety approval.

6.1 Thorium Inventory Management

The ^{232}Th that makes up the target material is a controlled nuclear substance, the inventory of which TRIUMF reports in detail to the Canadian Nuclear Safety Commission (CNSC). Only thorium that has been exempted from restrictions on its modification will be used in the experiment. The spokespersons are also responsible for ensuring that items containing thorium are appropriately labelled, that the quantity of thorium therein is recorded, and for reporting on a monthly basis to the Radioactive Materials Coordinator any changes to the location, mass, chemical form, or physical form of any thorium materials.

7 DECOMMISSIONING AND DISPOSAL

In the scope of this experiment, less than 10 targets (including those irradiated since 2017) will be irradiated. It's anticipated this number is sufficient to develop TRIUMF's ^{225}Ac production processes that in the future could support routine (i.e. non-experimental) production.

7.1 Disposal of the Target Capsule

After the experiment, the target capsule will consist of activated and contaminated metal waste, primarily steel. This type of activated metal waste is common at TRIUMF. The target capsule will be allowed to decay inside HC1 for at least 6 months (or until radiation fields have been sufficiently reduced) before it is removed from the hot cell, sealed in an 8 mil plastic bag, and given to RPG for disposal, probably in the vault tunnel at the discretion of RPG. One year after EOB, the target body is expected to emit a dose rate of 33 µSv/h at 1 m.

7.2 Disposal of Liquid Waste

All liquid waste products are expected to be in the form of acidic aqueous solutions. No organic solvent waste containing radioisotopes will be generated, until a waste management stream for such materials at TRIUMF is defined by the RPG and the RCR1 Lab Manager. At the time that disposal of this waste will occur (at least two weeks after EOB), the dose rate from liquid waste products is expected to be approximately 600 µSv/h at 1 m without shielding (as determined by measurements of previous runs). The following procedure will be used prepare this waste for removal from RCR1:

1. Liquid waste will be pumped into a 1 L glass solvent bottle with a GL45 cap. These bottle caps are also compatible with caps that have inserts for tubing so that the bottle can be easily attached to any future waste processing (avoids having to pour liquid out the bottle).
2. The pH of the waste will be adjusted to between 4 and 10 by addition of NaOH.
3. The cap on the bottle will be closed and sealed with parafilm.
4. The bottle will be placed in a 4L pail (or similar), along with absorbent material capable of absorbing any liquids in the event of a spill.
5. All info (pH, volume, solvents, radioactive inventory, dose rate, and date) will be recorded on the outside of the pail and also in the RCR1 waste log. The waste log is kept by the RCR1 Lab Manager and documents waste transferred to RPG for temporary storage or disposal.
6. The user will prepare the waste, and the RCR1 Lab Manager will verify this was done correctly and then coordinate with RPG to transfer the waste into temporary storage.

Liquid waste will remain in temporary storage until it has decayed to the point that the external dose rate is low enough that the waste can be processed for final disposal without accruing significant personnel doses.

7.3 Disposal of Compactable Solid Waste

In order to minimize the volume of solid waste contaminated with long-lived isotopes with low disposability limits (most notably ^{227}Ac) [6]and in the spirit of sorting radioactive waste at the source [29], all solid waste produced by activities associated with this experiment will be segregated from other solid radioactive waste routinely produced in RCR1. Solid waste from L125 will be further separated into multiple streams including: 1) unlikely but potentially contaminated waste; 2) low-level contaminated waste; and 3) highly contaminated waste.

Solid waste produced by this experiment will include items such as empty containers, tubing, and fittings associated with the purification process, as well as other items such as pipette tips, disposable PPE (gloves and elbow sleeves), cleaning supplies (i.e. paper towels), and small 1.5 mL vials. This is waste that is typically produced in TRIUMF's radiochemistry labs. These items are bagged and given to RPG, who then characterizes each bag by total count rate [31, 32]. Bags of similar radioactivity level are then compacted into metal barrels. Each barrel is then assayed using gamma spectroscopy [33] and stored on site for decay until its radioactive contents are below the limit for which they can be disposed of via the landfill. This waste management program is described in *Radioactive Waste Management for the TRIUMF Site* (Document-5330) [34]. With the exception of the target capsule and the glass bottles, filter, and beakers required for the dissolution and storage of liquids produced during the purification process, all solid wastes associated with this work can be compacted. Disposal of this waste will occur in coordination with the RPG.

7.4 Decommissioning of the Experiment

Decommissioning of the experiment will involve removal of all equipment from inside the hot cell. Compactable items may be deposed of as described in Section 7.3, while non-compactable objects will be first swiped for removable contamination, decontaminated if possible, and then given to RPG for disposal. There is currently no anticipated timeline for the decommissioning of the experiment.

REFERENCES

[1] Clemens Kratochwil, Frank Bruchertseifer, Frederik L Giesel, Mirjam Weis, Frederik A Verburg, Felix Mottaghy, Klaus Kopka, Christos Apostolidis, Uwe Haberkorn, and Alfred Morgenstern. 225Ac-PSMA-617 for PSMA targeting alpha-radiation therapy of patients with metastatic castration-resistant prostate cancer. *J. Nucl. Med.*, 57(12):1941–4, jul 2016.

[2] B L Zhuikov. Successes and problems in the development of medical radioisotope production in Russia. *Physics-Uspekhi*, 59(5):481–486, 2016.

[3] V Radchenko, J W Engle, J J Wilson, J R Maassen, F M Nortier, W A Taylor, E R Birnbaum, L A Hudston, K D John, and M E Fassbender. Application of ion exchange and extraction chromatography to the separation of actinium from proton-irradiated thorium metal for analytical purposes. *J. Chromatogr. A*, 1380:55–63, feb 2015.

[4] R. A. Aliev, S. V. Ermolaev, A. N. Vasiliev, V. S. Ostapenko, E. V. Lapshina, B. L. Zhuikov, N. V. Zakharov, V. V. Pozdeev, V. M. Kokhanyuk, B. F. Myasoedov, and S. N. Kalmykov. Isolation of Medicine-Applicable Actinium-225 from Thorium Targets Irradiated by Medium-Energy Protons. *Solvent Extr. Ion Exch.*, 32(5):468–477, 2014.

6 ^{227}Ac is of particular concern since the criteria for disposal of waste containing ^{227}Ac via the landfill is limited to an activity concentration of $<$0.1 Bq/g or a total activity of $<$1 kBq [30]. A total of 0.85 MBq of ^{227}Ac is expected to be produced during this experiment.

[5] Alfred Morgenstern. Bismuth-213 and actinium-225–generator performance and evolving therapeutic applications of two generator-derived alpha-emitting radioisotopes. *Curr. Radiopharm.*, 5(3):221–227, 2012.

[6] International Atomic Energy Agency. Technicial Meeting on Alpha emitting radionuclides and radiopharmaceuticals for therapy. Technical report, International Atomic Energy Agency, Vienna, 2013.

[7] A. K. H. Robertson. Safety Report for L124: Irradiation of Thorium Targets at the TRIUMF 500 MeV Isotope Production Facility (Document-148928). Technical report, TRIUMF, Vancouver, Canada, 2017.

[8] Andrew K H Robertson. Commissioning Plan for Irradiation of L124 Thorium Metal Targets at IPF (Document-148095). Technical report, TRIUMF, Vancouver, Canada, 2017.

[9] Inconel 718, Alloy 718, UNS No7718 - MEGA MEX.

[10] Anders Mjos. L124 Design Review 2017-10-27 (Document-148948). Technical report, TRIUMF, Vancouver, Canada, 2017.

[11] Anders Mjos. L124 Design Review 2017-11-09 (Document-148946). Technical report, TRIUMF, Vancouver, Canada, 2017.

[12] L. Moskven and AKH. Robertson. L124 Thorium Metal Target for IPF (Document-148097). Technical report, TRIUMF, Vancouver, Canada, 2017.

[13] Andrew K H Robertson. L125 Target Transfer Flask Requirements (Document-148102). Technical report, TRIUMF, Vancouver, Canada, 2017.

[14] L. Moskven. L125 Target Transfer Flask (Document-148098). Technical report, TRIUMF, Vancouver, Canada, 2017.

[15] Sam Varah. Design Review of L214 Remote Thorium Target Opener (Document-146024). Technical report, TRIUMF, Vancouver, Canada, 2017.

[16] Valery Radchenko, Jonathan W. Engle, Justin J. Wilson, Joel R. Maassen, Meiring F. Nortier, Eva R. Birnbaum, Kevin D. John, and Michael E. Fassbender. Formation cross-sections and chromatographic separation of protactinium isotopes formed in proton-irradiated thorium metal. *Radiochim. Acta*, 104(5):291–304, 2016.

[17] C. F. Ramogida. Safety Report for L122: Alpha-emitter studies using the ISAC implantation station. Technical report, TRIUMF, Vancouver, Canada, 2017.

[18] E Philip Horwitz, Mark L Dietz, Susan Rhoads, Claudia Felinto, Noel I Gale, and Judith Houghton. A lead-selective extraction chromatographic resin and its application to the isolation of lead from geological samples. 292:263–273, 1994.

[19] A Trudel and J Mildenberger. Actinide Target Safety Analysis Report (Document-12972). Technical report, TRIUMF, Vancouver, Canada, 2011.

[20] J Mildenberger and A Trudel. Actinide Target SAR Addendum for Thorium Oxide (Document-110961). Technical report, TRIUMF, Vancouver, Canada, 2014.

[21] J Mildenberger. Rn-220 from ISAC target pits (Document-130951). Technical report, TRIUMF, Vancouver, Canada, 2016.

[22] Joe Mildenberger. personal communication.

[23] J Mildenberger and A. Trudel. Annual Compliance Report 2016. Technical Report February, TRIUMF, Vancouver, Canada, 2016.

[24] Trevor Uittenbosch. personal communication.

[25] Jason R Crawford, Hua Yang, Peter Kunz, Scott Wilbur, Paul Schaf-Fer, Thomas J Ruth, Crawford Jason, Yang Hua, Kunz Peter, Schaffer Paul, Ruth Thomas, D Scott Wilbur, and Paul Schaffer. Development of a preclinical At generator system for targeted alpha therapy research with 211 At. *Nucl. Med. Biol.*, 48:31–35, 2017.

[26] John P Greene, Jerry Nolen, and Sam Baker. Nickel-backed Bi targets for the production of 211At. *J. Radioanal. Nucl. Chem.*, pages 1–4, 2015.

[27] A. K. H. Robertson, K. Ladouceur, M. Nozar, L. Moskven, C. F. Ramogida, J. D'Auria, V. Sossi, and P. Schaffer. Design and Simulation of Thorium Target for Ac-225 Production. *AIP Conf. Proc.*, 1845(1):020019–1 —– 020019–5, 2017.

[28] United States Nuclear Regulatory Commission.

[29] M Kinakin. Sorting Radioactive Waste at the Source (Document-5816). Technical report, TRIUMF, Vancouver, Canada, 2012.

[30] Nuclear substances and radiation devices regulations (2000). Retrieved from the Justice Laws website: http://laws-lois.justice.gc.ca/eng/regulations/SOR-2000-207/.

[31] M Kinakin. Characterization of radioactive waste (Document-5815). Technical Report August, TRIUMF, Vancouver, 2012.

[32] J Mildenberger. Radioactive waste area sorting cave sensitivity. Technical report, TRIUMF, Vancouver, Canada, 2012.

[33] M Kinakin. Assaying Radioactive Waste (Document-8000). Technical report, TRIUMF, Vancouver, 2012.

[34] M Kinakin. Radioactive Waste Management for the TRIUMF Site (Document-5330). Technical report, TRIMF, Vancouver, 2016.

A SINGLE-EVENT DERIVED RELEASE LIMITS USED FOR OFF-SITE DOSE ESTIMATES

Nuclide	SDRL [TBq]	Nuclide	SDRL [TBq]	Nuclide	SDRL [TBq]	Nuclide	SDRL [TBq]
H-3	2.00E+03	FE-55	3.01E-01	KR-75	5.10E+02	SN-113	1.44E-01
BE-7	9.23E-01	FE-52	3.42E+00	KR-76	4.67E+02	SB-122	4.37E-01
C-11	2.68E+02	FE-59	3.44E-02	KR-77	2.19E+02	SB-124	2.00E-02
C-14	1.69E+02	CO-55	1.41E+00	KR-79	7.78E+02	SB-125	7.09E-03
N-13	4.02E+02	CO-56	1.01E-02	KR-81	3.51E+04	TE-121	2.29E-01
O-14	5.78E+02	CO-57	8.39E-02	KR-83M	6.89E+06	TE-121M	3.93E-02
O-15	1.18E+03	CO-58	3.80E-02	KR-85	7.87E+04	TE-123M	6.11E-02
F-17	1.73E+03	CO-60	7.16E-04	KR-85M	1.31E+03	TE-132	1.68E-01
F-18	3.56E+01	CO-61	2.11E+02	KR-87	2.62E+02	I-120	3.04E+01
NE-24	1.42E+03	NI-56	2.21E-01	KR-88	8.17E+01	I-120M	2.45E+01
NA-22	1.57E-03	NI-57	7.69E-01	KR-89	4.54E+02	I-121	1.34E+02
NA-24	1.22E+00	CU-64	1.63E+01	RB-81	2.35E+01	I-122	6.38E+02
MG-28	8.76E-01	CU-67	2.07E-01	RB-82M	4.05E+00	I-123	2.47E+01
AI-26	3.47E-05	ZN-65	1.57E-02	RB-83	4.29E-02	I-124	9.14E-02
SI-31	1.29E+02	GA-67	2.61E+00	RB-84	4.52E-02	I-125	3.72E-02
P-32	8.70E-02	GA-68	5.50E+01	RB-86	6.78E-02	I-126	2.08E-02
P-33	6.74E-01	GE-68	9.29E-02	RB-88	2.43E+02	I-128	1.02E+03
S-35	9.71E-01	GE-75	4.71E+02	RB-89	1.01E+02	I-129	3.05E-03
CL-34M	5.60E+01	AS-71	1.08E+00	SR-82	2.98E-02	I-130	2.51E+00
CL-36	7.43E-03	AS-72	6.99E-01	SR-85	7.29E-02	I-131	3.41E-02
CL-38	6.48E+01	AS-73	4.22E-01	SR-85M	2.67E+02	I-132	2.43E+01
CL-39	4.79E+01	AS-74	1.01E-01	SR-89	5.28E-02	I-132M	1.05E+02
AR-37	7.38E+07	AS-76	1.09E+00	Y-88	1.10E-02	I-133	9.31E-01
AR-39	1.03E+06	SE-73	7.61E+00	ZR-88	7.88E-02	I-134	4.92E+01
AR-41	1.59E+02	SE-73M	3.39E+02	ZR-89	4.93E-01	I-135	7.70E+00
AR-42	1.18E+03	SE-75	3.31E-02	ZR-95	4.79E-02	XE-118	1.99E+03
AR-43	3.44E+02	SE-79	2.37E-02	ZR-97	1.49E+00	XE-119	4.33E+02
AR-44	1.24E+02	SE-81	2.83E+03	NB-95	8.84E-02	XE-120	1.86E+02
K-43	2.68E+00	SE-81M	6.79E+02	NB-95M	1.08E+00	XE-121	1.26E+02
K-44	6.83E+01	SE-83	6.38E+01	NB-97	7.59E+01	XE-122	1.73E+02
CA-45	1.60E-01	SE-84	1.65E+03	MO-99	1.43E+00	XE-123	3.05E+02
CA-47	2.63E-01	BR-74	3.19E+01	TC-96	2.20E-01	XE-125	3.29E+02
SC-43	1.39E+01	BR-75	3.27E+01	TC-99M	8.19E+01	XE-127	7.50E+02
SC-44	7.26E+00	BR-76	1.54E+00	RU-103	9.74E-02	XE-129M	8.85E+03
SC-44M	3.90E-01	BR-77	3.37E+00	PD-100	8.87E-01	XE-131M	2.41E+04
SC-46	1.65E-02	BR-80	1.50E+03	PD-103	9.94E-01	XE-133	6.01E+03
SC-47	1.12E+00	BR-80M	8.85E+01	AG-105	1.10E-01	XE-133M	7.40E+03
TI-44	1.76E-03	BR-82	6.97E-01	AG-108M	9.13E-05	XE-135	8.04E+02
V-48	4.72E-02	BR-83	3.97E+02	AG-110M	4.40E-03	XE-135M	7.74E+02
CR-51	2.14E+00	BR-84	6.41E+01	AG-111	2.77E-01	XE-137	3.82E+03
MN-52	1.18E-01	BR-85	9.85E+03	CD-109	6.06E-02	XE-138	1.68E+02
MN-54	1.19E-02	BR-87	8.18E+02	IN-111	1.57E+00	CS-127	2.68E+01
MN-56	1.43E+01	KR-74	3.25E+02	IN-114M	2.93E-02	CS-129	6.96E+00

Nuclide	SDRL [TBq]
CS-130	4.28E+00
CS-131	4.80E+00
CS-132	4.90E-01
CS-134	2.30E-03
CS-137	1.79E-02
CS-138	4.65E+01
BA-128	6.44E-01
BA-131	3.24E-01
BA-137M	6.36E-04
Eu-152	6.67E-04
TA-182	1.77E-02
Re-182	3.99E+00
Re-182	3.40E-01
Re-184	6.33E-02
RE-184M	3.12E-02
RE-186	4.15E-01
AU-195	1.49E-01
AU-198	6.69E-01
AU-199	1.53E+00
HG-197	3.24E+00
HG-199M	6.72E+01
HG-203	1.40E-01
TL-200	2.01E+00
TL-201	5.46E+00
TL-202	3.40E-01
PB-203	2.65E+00
PB-212	4.52E-01
BI-203	2.31E+00
BI-205	9.53E-02
BI-207	2.12E-04
BI-210	3.66E-01
BI-212	3.69E+00
PO-203	5.79E+01
PO-204	1.00E+00
PO-205	2.46E+01
PO-206	3.12E-01
PO-207	9.00E+00
PO-208	1.18E-04
PO-209	1.08E-04
PO-210	9.05E-05
PO-211	2.05E+05
PO-212M	9.41E+10
PO-218	1.34E+01
RN-206	1.55E+02

Nuclide	SDRL [TBq]
RN-207	3.25E+02
RN-208	3.00E+01
RN-209	5.80E+01
RN-210	3.01E+02
RN-211	1.44E+01
RN-212	4.79E+01
RN-220	3.06E+02
RN-221	1.99E-03
RN-222	3.47E+00
RN-223	4.52E+01
RA-223	1.73E-03
RA-224	7.06E-03
RA-225	1.33E-03
RA-226	4.36E-04
RA-228	9.33E-05
AC-225	8.85E-03
AC-227	6.42E-05
AC-228	8.77E-01
TH-227	1.45E-02
TH-228	8.70E-04
TH-232	3.63E-04
U-234	3.82E-03
U-235	5.13E-04
U-238	4.26E-03
NP-237	9.53E-04
PU-238	6.63E-04
PU-239	6.10E-04
PU-240	6.08E-04
PU-241	3.27E-02
PU-242	6.34E-04
AM-241	6.35E-04

B RADIOACTIVE INVENTORY OF THORIUM FOIL 7 DAYS AFTER EOB

Nuclide	Z	A	Activity [Bq]	+- [%]
U-233	92	233	3.99E+01	0.51
U-232	92	232	1.40E+04	4.02
U-230	92	230	1.33E+06	2.06
Pa-233	91	233	3.78E+08	0.51
Pa-232	91	232	4.15E+06	4.03
Pa-231	91	231	2.47E+03	0.43
Pa-230	91	230	5.78E+07	2.06
Pa-229	91	229	7.67E+06	3.54
Pa-228	91	228	8.88E+05	4.53
Th-231	90	231	1.58E+08	0.44
Th-230	90	230	1.08E+03	0.46
Th-229	90	229	7.50E+03	0.58
Th-228	90	228	2.83E+07	0.57
Th-227	90	227	3.40E+08	0.79
Th-226	90	226	4.48E+07	0.98
Th-224	90	224	2.98E+02	4.53
Ac-228	89	228	1.72E+05	4.1
Ac-227	89	227	8.46E+05	0.87
Ac-226	89	226	5.14E+07	1
Ac-225	89	225	4.32E+08	0.84
Ac-224	89	224	1.89E+04	4.53
Ra-228	88	228	1.72E+05	4.1
Ra-226	88	226	2.93E+03	1.45
Ra-225	88	225	3.96E+07	2.61
Ra-224	88	224	4.18E+08	0.89
Ra-223	88	223	2.32E+08	0.89
Ra-222	88	222	4.48E+07	0.98
Ra-221	88	221	4.32E+05	0.84
Ra-220	88	220	3.04E+02	4.53
Fr-223	87	223	1.17E+04	0.87
Fr-222	87	222	3.11E+03	1
Fr-221	87	221	4.32E+08	0.84
Fr-220	87	220	1.70E+03	4.53
Rn-222	86	222	2.59E+05	36.92
Rn-220	86	220	4.18E+08	0.89
Rn-219	86	219	2.32E+08	0.89
Rn-218	86	218	4.48E+07	0.98
Rn-217	86	217	4.75E+05	0.84
Rn-216	86	216	3.04E+02	4.53
Rn-211	86	211	8.75E+05	1.27
At-218	85	218	5.18E+01	36.92
At-217	85	217	4.32E+08	0.84
At-216	85	216	1.69E+03	4.53
At-215	85	215	5.33E+02	0.89
At-211	85	211	1.26E+06	1.27
At-210	85	210	1.42E+03	1.24
At-209	85	209	2.29E+00	0.95
Po-218	84	218	2.59E+05	36.92
Po-216	84	216	4.18E+08	0.89
Po-215	84	215	2.32E+08	0.89
Po-214	84	214	4.50E+07	0.99
Po-213	84	213	4.25E+08	0.84
Po-212	84	212	3.05E+08	0.9
Po-211	84	211	1.38E+06	0.77
Po-210	84	210	7.72E+07	0.68
Po-209	84	209	2.66E+05	0.71
Po-208	84	208	7.81E+06	0.79
Po-207	84	207	3.97E+05	1.27
Po-206	84	206	4.35E+08	0.87
Bi-214	83	214	2.61E+05	36.93
Bi-213	83	213	4.33E+08	0.84
Bi-212	83	212	4.77E+08	0.9
Bi-211	83	211	2.32E+08	0.89
Bi-210	83	210	3.48E+08	1.06
Bi-208	83	208	3.08E+01	1.22
Bi-207	83	207	6.98E+05	0.75
Bi-206	83	206	3.18E+08	0.87
Bi-205	83	205	1.48E+08	1.09
Bi-204	83	204	1.09E+05	1.1
Bi-203	83	203	6.43E+04	1.21
Pb-214	82	214	2.60E+05	36.92
Pb-212	82	212	4.71E+08	0.89
Pb-211	82	211	2.32E+08	0.89
Pb-210	82	210	1.55E+06	0.6
Pb-209	82	209	4.39E+08	0.84
Pb-207m	82	207	6.49E+05	0.75
Pb-203	82	203	8.30E+07	1.22
Pb-202	82	202	1.08E+02	1.48
Pb-201	82	201	3.01E+03	1.9
Pb-200	82	200	2.08E+06	2.22
Tl-210	81	210	5.23E+01	36.93
Tl-209	81	209	9.05E+06	0.84
Tl-208	81	208	1.71E+08	0.9
Tl-207	81	207	2.31E+08	0.89
Tl-206	81	206	4.53E+02	1.06
Tl-202	81	202	1.93E+05	35.39
Tl-201	81	201	5.63E+07	1.93
Tl-200	81	200	1.82E+07	2.22
Tl-199	81	199	1.04E+02	2.29
Hg-197	80	197	1.74E+07	3.38
Hg-197m	80	197	8.48E+03	37.22
Hg-195	80	195	1.40E+05	19.2
Hg-195m	80	195	1.94E+05	19.42
Hg-194	80	194	1.90E+03	4
Hg-193	80	193	7.22E+01	11.39
Hg-193m	80	193	6.90E+02	11.39
Au-196	79	196	1.61E+05	49.62
Au-196n	79	196	3.38E+00	49.62
Au-195	79	195	1.40E+06	4.21
Au-194	79	194	7.20E+04	39.26
Au-193	79	193	2.83E+05	4.52
Pt-193	78	193	1.21E+04	4.47
Pt-193m	78	193	3.83E+04	70.53
Pt-191	78	191	6.15E+06	6.61
Pt-189	78	189	1.35E+03	8.11
Pt-188	78	188	4.77E+06	7.93
Ir-190	77	190	6.50E+04	57.44
Ir-189	77	189	4.42E+06	8.01

Ir-188	77	188	5.36E+06	7.91
Ir-187	77	187	7.81E+02	10.17
Ir-186	77	186	3.54E+04	10.43
Ir-185	77	185	9.40E+03	11.88
Os-185	76	185	4.51E+05	11.87
Os-183	76	183	2.57E+03	14.41
Os-183m	76	183	1.29E+01	34.73
Os-182	76	182	8.67E+04	14.11
Re-183	75	183	3.93E+05	14.15
Re-182	75	182	2.13E+06	14
Re-181	75	181	4.54E+04	16.25
W-181	74	181	1.99E+05	16.3
W-178	74	178	3.62E+05	24.7
Ta-179	73	179	1.81E+04	21.24
Ta-178	73	178	3.63E+05	24.7
Ta-177	73	177	3.78E+05	24.89
Ta-176	73	176	5.54E+00	23.42
Ta-175	73	175	9.05E+01	27.76
Hf-175	72	175	1.26E+05	25.62
Hf-173	72	173	2.88E+04	32.17
Hf-172	72	172	1.38E+04	25.62
Hf-171	72	171	1.89E+02	37.23
Hf-170	72	170	1.31E+03	44.27
Lu-173	71	173	1.42E+04	30.3
Lu-172	71	172	2.02E+05	42.53
Lu-171	71	171	4.96E+05	26.9
Lu-170	71	170	2.93E+05	27.47
Lu-169	71	169	9.65E+04	29.38
Yb-169	70	169	2.53E+05	25.58
Yb-166	70	166	3.18E+05	26.89
Tm-170	69	170	1.33E+04	57.44
Tm-168	69	168	3.01E+04	44.27
Tm-167	69	167	6.37E+05	22.54
Tm-166	69	166	3.68E+05	26.89
Tm-165	69	165	9.00E+04	24.9
Er-165	68	165	1.37E+05	24.89
Er-160	68	160	7.03E+04	27.75
Ho-166m	67	166	1.36E+00	70.53
Ho-163	67	163	1.18E+01	18.11
Ho-160	67	160	7.14E+04	27.75
Dy-159	66	159	1.39E+05	17.39
Dy-157	66	157	8.61E+00	17.6
Dy-155	66	155	7.18E+01	21.53
Tb-161	65	161	1.28E+06	16.52
Tb-160	65	160	9.14E+04	28.06
Tb-158	65	158	2.17E+02	20.08
Tb-157	65	157	9.38E+02	13.01
Tb-156	65	156	1.01E+06	18.97
Tb-156m	65	156	2.52E+04	18.97
Tb-155	65	155	2.14E+06	13.24
Tb-154	65	154	1.36E+04	26.35
Tb-154m	65	154	1.04E+01	26.35
Tb-154n	65	154	1.17E+04	26.35
Tb-153	65	153	9.69E+05	15.67
Tb-152	65	152	1.03E+04	20.34
Tb-151	65	151	9.38E+03	21.55

Gd-159	64	159	4.10E+04	12.28
Gd-153	64	153	1.70E+05	11.38
Gd-151	64	151	2.00E+05	16.18
Gd-149	64	149	7.68E+05	23.08
Gd-148	64	148	3.50E+02	24.03
Gd-147	64	147	1.06E+05	32.45
Gd-146	64	146	4.39E+04	49.62
Eu-157	63	157	3.04E+04	7.53
Eu-156	63	156	7.88E+06	5.27
Eu-155	63	155	1.40E+05	4.77
Eu-154	63	154	7.95E+03	14.94
Eu-152	63	152	3.05E+03	16
Eu-152m	63	152	1.86E+01	16
Eu-150	63	150	8.42E+02	15.83
Eu-150m	63	150	8.23E+02	15.83
Eu-149	63	149	3.55E+05	13.28
Eu-148	63	148	3.55E+05	17.06
Eu-147	63	147	7.91E+05	15.84
Eu-146	63	146	9.26E+05	20.93
Eu-145	63	145	5.99E+05	26.33
Sm-156	62	156	4.09E+02	5.79
Sm-153	62	153	1.29E+07	3.78
Sm-151	62	151	2.48E+04	2.85
Sm-145	62	145	9.86E+04	13.02
Pm-151	61	151	6.36E+06	2.98
Pm-149	61	149	4.68E+07	2.37
Pm-148	61	148	3.06E+06	7.7
Pm-148m	61	148	9.64E+05	7.7
Pm-147	61	147	8.59E+05	1.75
Pm-146	61	146	4.20E+04	7.83
Pm-145	61	145	1.33E+04	7.97
Pm-144	61	144	1.82E+05	9.27
Pm-143	61	143	3.14E+05	8.61
Nd-147	60	147	1.01E+08	1.69
Nd-140	60	140	5.25E+06	8.54
Pr-145	59	145	6.26E+00	1.45
Pr-144	59	144	9.06E+06	1.44
Pr-144m	59	144	1.36E+05	1.44
Pr-143	59	143	1.75E+08	1.21
Pr-142	59	142	2.89E+05	5.46
Pr-140	59	140	5.25E+06	8.54
Ce-144	58	144	9.06E+06	1.44
Ce-143	58	143	4.07E+07	1.28
Ce-141	58	141	9.94E+07	1.22
Ce-139	58	139	3.52E+06	3.69
Ce-137	58	137	2.03E+06	5.15
Ce-137m	58	137	1.51E+06	5.15
Ce-135	58	135	9.73E+04	7.15
Ce-134	58	134	4.43E+06	9.03
La-140	57	140	1.84E+08	1.23
La-137	57	137	3.71E+01	2.54
La-135	57	135	1.45E+06	4.65
La-134	57	134	4.44E+06	9.03
Ba-140	56	140	1.51E+08	1.35
Ba-137m	56	137	3.05E+05	1.17
Ba-136m	56	136	7.80E+06	1.84

Ba-135m	56	135	2.92E+06	2.75
Ba-133	56	133	1.67E+05	3.27
Ba-133m	56	133	4.57E+06	3.93
Ba-131	56	131	1.70E+07	4.2
Ba-128	56	128	2.08E+06	10.82
Cs-137	55	137	3.22E+05	1.17
Cs-136	55	136	6.97E+07	1.84
Cs-135	55	135	5.77E+00	1.07
Cs-134	55	134	1.47E+06	2.23
Cs-132	55	132	5.41E+07	2.84
Cs-131	55	131	5.44E+07	2.5
Cs-129	55	129	7.41E+06	3.24
Cs-128	55	128	2.08E+06	10.82
Cs-127	55	127	1.21E+00	5.43
Xe-135	54	135	1.28E+04	1.54
Xe-135m	54	135	2.84E+00	2.08
Xe-133	54	133	3.24E+08	1.14
Xe-133m	54	133	3.38E+07	1.72
Xe-131m	54	131	3.31E+07	2
Xe-129m	54	129	2.90E+07	2.76
Xe-127	54	127	1.94E+07	2.82
Xe-125	54	125	1.85E+05	4.11
Xe-122	54	122	5.29E+04	14.39
I-135	53	135	1.76E+01	2.08
I-133	53	133	5.44E+06	1.46
I-132	53	132	7.37E+07	2.17
I-131	53	131	2.35E+08	1.17
I-130	53	130	8.30E+04	1.86
I-126	53	126	6.09E+07	2.05
I-125	53	125	2.21E+07	1.92
I-124	53	124	4.11E+07	3.44
I-123	53	123	6.13E+04	3.33
I-122	53	122	5.31E+04	14.39
Te-132	52	132	7.15E+07	2.17
Te-131	52	131	1.28E+06	2.15
Te-131m	52	131	5.70E+06	2.15
Te-129	52	129	1.48E+07	1.74
Te-129m	52	129	2.32E+07	1.74
Te-127	52	127	1.75E+08	1.34
Te-127m	52	127	1.17E+07	1.38
Te-125m	52	125	1.55E+07	1.72
Te-123m	52	123	5.56E+06	2.11
Te-121	52	121	1.97E+07	2.97
Te-121m	52	121	2.00E+06	3.1
Te-119	52	119	5.22E+04	5.28
Te-119m	52	119	6.87E+06	5.54
Te-118	52	118	6.98E+06	7.48
Sb-128	51	128	1.12E+03	2.07
Sb-127	51	127	1.78E+08	1.4
Sb-126	51	126	4.58E+07	1.68
Sb-126m	51	126	4.33E+01	1.97
Sb-125	51	125	4.73E+06	1.06
Sb-124	51	124	3.30E+07	1.61
Sb-122	51	122	1.15E+08	1.56
Sb-120m	51	120	5.00E+07	2.21
Sb-119	51	119	3.95E+07	2.18

Sb-118	51	118	6.98E+06	7.48
Sn-126	50	126	4.33E+01	1.97
Sn-125	50	125	6.32E+07	1.59
Sn-123	50	123	1.01E+07	1.48
Sn-121	50	121	4.93E+07	0.83
Sn-121m	50	121	1.01E+05	1.11
Sn-119m	50	119	4.86E+06	1.27
Sn-117m	50	117	4.23E+07	1.8
Sn-113	50	113	9.37E+05	7.14
In-115m	49	115	5.18E+08	0.58
In-114	49	114	8.90E+06	1.88
In-114m	49	114	9.31E+06	1.88
In-113m	49	113	9.37E+05	7.14
In-111	49	111	1.16E+07	5.05
Cd-115	48	115	4.74E+08	0.58
Cd-115m	48	115	5.37E+07	0.92
Cd-113m	48	113	3.56E+05	1.18
Cd-111m	48	111	5.88E+06	5.05
Cd-109	48	109	7.97E+05	3.95
Ag-113	47	113	3.95E+00	0.64
Ag-112	47	112	3.55E+07	0.64
Ag-111	47	111	1.26E+09	0.58
Ag-111m	47	111	1.33E+00	0.98
Ag-110	47	110	7.71E+04	1.49
Ag-110m	47	110	5.67E+06	1.49
Ag-109m	47	109	3.39E+06	1.01
Ag-108	47	108	3.07E+02	2.14
Ag-108m	47	108	3.53E+03	2.14
Ag-106m	47	106	5.76E+06	5.54
Ag-105	47	105	1.84E+06	8.83
Pd-112	46	112	3.02E+07	0.64
Pd-111	46	111	1.07E+00	0.98
Pd-111m	46	111	1.36E+00	0.98
Pd-109	46	109	2.59E+06	0.51
Pd-107	46	107	9.06E+00	0.56
Pd-103	46	103	6.22E+06	6.51
Pd-101	46	101	8.10E+00	23.88
Pd-100	46	100	1.43E+05	49.62
Rh-106	45	106	4.12E+07	0.62
Rh-105	45	105	3.68E+08	0.58
Rh-103m	45	103	4.06E+08	0.61
Rh-102	45	102	1.23E+06	3.23
Rh-102m	45	102	2.45E+05	3.23
Rh-101	45	101	1.22E+05	5.3
Rh-101m	45	101	8.42E+06	5.47
Rh-100	45	100	3.11E+05	29.77
Rh-99	45	99	4.59E+05	18.31
Ru-106	44	106	4.12E+07	0.62
Ru-103	44	103	4.00E+08	0.62
Ru-97	44	97	1.35E+06	15.17
Tc-99	43	99	1.71E+02	0.62
Tc-99m	43	99	5.99E+08	0.71
Tc-97m	43	97	2.98E+06	3.44
Tc-96	43	96	1.13E+07	5.85
Tc-95	43	95	7.97E+04	9.54
Tc-95m	43	95	5.08E+05	9.51

Mo-99	42	99	6.22E+08	0.71
Mo-93	42	93	7.66E+01	7.9
Mo-93m	42	93	1.62E+00	7.98
Nb-97	41	97	4.34E+06	0.93
Nb-97m	41	97	3.82E+06	0.93
Nb-96	41	96	1.41E+07	1.07
Nb-95	41	95	8.82E+07	1.05
Nb-95m	41	95	9.36E+07	1.33
Nb-94	41	94	2.20E+02	2
Nb-93m	41	93	8.62E+04	2.4
Nb-92m	41	92	1.14E+07	3.97
Nb-91	41	91	4.15E+02	5.27
Nb-91m	41	91	1.40E+06	5.27
Nb-90	41	90	5.56E+03	14.16
Zr-97	40	97	4.03E+06	0.93
Zr-95	40	95	1.39E+08	0.83
Zr-93	40	93	1.98E+01	0.75
Zr-89	40	89	9.65E+06	5.91
Zr-88	40	88	5.81E+05	11
Zr-86	40	86	2.24E+03	37.22
Y-93	39	93	6.21E+04	0.83
Y-91	39	91	1.54E+08	0.74
Y-91m	39	91	1.47E+04	0.9
Y-90	39	90	9.41E+07	1.75
Y-89m	39	89	9.65E+06	5.9
Y-88	39	88	4.87E+06	3.39
Y-87	39	87	1.47E+07	4.87
Y-87m	39	87	1.26E+04	4.92
Y-86	39	86	2.70E+04	18.52
Sr-91	38	91	2.68E+04	0.9
Sr-90	38	90	7.90E+05	0.87
Sr-89	38	89	1.54E+08	0.86
Sr-85	38	85	3.10E+06	5.32
Sr-83	38	83	2.80E+05	16.74
Sr-82	38	82	1.12E+05	40.31
Rb-86	37	86	7.52E+07	1.78
Rb-84	37	84	1.43E+07	3.16
Rb-83	37	83	3.24E+06	4.22
Rb-82	37	82	1.12E+05	40.31
Kr-85	36	85	5.72E+05	1.05
Kr-81	36	81	3.58E+00	4.17
Kr-79	36	79	5.12E+05	12.23
Br-82	35	82	2.08E+07	2.23
Br-77	35	77	1.90E+06	11
Br-76	35	76	3.38E+03	28.06
Se-79	34	79	1.52E+01	1.32
Se-77m	34	77	1.33E+05	1.51
Se-75	34	75	4.55E+05	10.23
As-77	33	77	6.22E+07	1.51
As-76	33	76	2.67E+06	3.71
As-74	33	74	5.96E+06	6.39
As-73	33	73	7.47E+05	9.98
As-72	33	72	8.79E+04	19.59
As-71	33	71	3.45E+05	28.06
Ge-77	32	77	1.65E+04	2.05
Ge-71	32	71	4.95E+06	8.06
Ge-69	32	69	2.50E+05	21.27
Ge-68	32	68	4.30E+03	70.53
Ga-72	31	72	3.18E+07	2.88
Ga-68	31	68	4.31E+03	70.53
Ga-67	31	67	5.71E+05	23.26
Ga-66	31	66	1.62E+01	34.91
Zn-72	30	72	2.21E+07	2.88
Zn-69	30	69	1.38E+04	5.31
Zn-69m	30	69	1.29E+04	5.31
Zn-65	30	65	4.76E+04	21.27
Cu-67	29	67	1.71E+07	3.95
Cu-66	29	66	8.20E+06	5.46
Cu-64	29	64	3.57E+03	10.49
Ni-66	28	66	8.19E+06	5.46
Ni-63	28	63	5.58E+03	5.7
Co-60	27	60	2.16E+04	12.28
Co-58	27	58	1.79E+05	21.51
Co-58m	27	58	1.43E+01	21.51
Co-57	27	57	1.50E+04	37.22
Fe-59	26	59	1.79E+06	8.71
Fe-55	26	55	4.16E+03	42.38
Mn-54	25	54	3.74E+04	22.42
Mn-52	25	52	4.03E+04	70.53
Cr-51	24	51	1.23E+05	37.22
V-49	23	49	2.94E+04	24.71
V-48	23	48	1.58E+05	40.31
Sc-48	21	48	3.18E+05	21.27
Sc-47	21	47	1.60E+06	16.9
Sc-46	21	46	2.66E+04	49.62
Sc-44	21	44	6.75E+04	44.25
Sc-44m	21	44	6.37E+04	44.27
Ca-47	20	47	6.60E+05	23.24
Ca-45	20	45	6.67E+04	27.52
K-43	19	43	2.88E+04	24.04
K-42	19	42	8.69E+02	21.83
Ar-42	18	42	5.45E+02	29.38
Ar-39	18	39	9.69E+01	28.52
Ar-37	18	37	2.17E+05	28.26
S-35	16	35	1.28E+05	22.42
P-33	15	33	2.61E+05	27.82
P-32	15	32	1.70E+05	40.3
Si-32	14	32	4.90E+01	42.9
Al-28	13	28	5.22E+03	49.62
Mg-28	12	28	5.21E+03	49.62
Na-24	11	24	2.65E+04	7.45
Na-22	11	22	2.49E+03	49.62
C-14	6	14	9.56E+01	5.3
Be-7	4	7	1.10E+06	9.8
H-3	1	3	6.40E+06	0.41

C AIRBORNE DOSE CALCULATIONS

Summary					
Nuclide	On-Site External Dose [mSv]	On-Site Internal Dose [mSv]	Off-Site Dose - No Filtration [mSv]	Off-Site Dose - With HC1 Stack Filtration [mSv]	Off-Site Dose - With Additional Filtration in HC [mSv]
H	3.13E-11	9.38E-07	2.97E-09	2.97E-09	2.97E-09
Cl	2.31E-17	5.46E-13	8.75E-12	4.37E-14	2.19E-16
Ar	7.38E-14	0.00E+00	4.36E-13	4.36E-13	4.36E-13
Se	1.40E-58	3.43E-57	5.93E-60	2.97E-62	1.48E-64
Br	5.36E-05	2.32E-04	3.75E-05	1.88E-07	9.38E-10
Kr	9.92E-08	0.00E+00	6.61E-10	6.61E-10	6.61E-10
I	2.77E-04	7.00E-02	1.12E-02	5.62E-05	2.81E-07
Xe	1.40E-05	0.00E+00	9.46E-08	9.46E-08	9.46E-08
Rn	2.06E-06	5.78E-02	1.52E-06	1.52E-06	1.52E-06
Po	4.32E-04	1.67E+00	9.12E-01	4.56E-03	2.28E-05
Total [mSv]	**0.001**	**1.803**	**0.92**	**0.00462**	**0.00002**
	1.804				

Filtration Parameters	
Elements filtered	Filter efficiency (99.5% HC stack and 99.5% filtration in HC
Po, Cl, Se, Br, I	0.999975

On-Site Exposure Parameters			
Exposure Time for External and Internal On-Site Dose [s]	Radius of Cloud for External On-Site Dose [m]	Radius of Cloud for Internal On-Site Dose [m]	Inhalation Rate [L/min]
1800	30	15	12

Nuclide	A	Z	Activity (Bq)	DCFA (Sv/Bq s/m3)	External Dose from Airbourne Cloud (mSv)	DCFI_a (Sv/Bq)	Inhalation Dose (mSv)	SDRL (Bq/mSv)	Maximum Offsite Dose - Unfiltered (mSv)	Maximum Offsite Dose - Filtered (mSv)
Gaseous and Volatile Alpha Isotopes										
Rn-223	223	86	0.00E+00	6.09E-15	0.00E+00	1.20E-07	0.00E+00	4.52E+13	0.00E+00	0.00E+00
Rn-222	222	86	2.42E+05	1.91E-17	7.36E-11	7.09E-06	4.37E-02	3.47E+12	6.97E-08	6.97E-08
Rn-221	221	86	0.00E+00	5.55E-15	0.00E+00	3.64E-07	0.00E+00	1.99E+09	0.00E+00	0.00E+00
Rn-220	220	86	4.18E+08	1.85E-17	1.23E-07	9.20E-10	9.80E-03	3.06E+14	1.37E-06	1.37E-06
Rn-212	212	86	0.00E+00	0.00E+00	0.00E+00	6.71E-09	0.00E+00	4.79E+13	0.00E+00	0.00E+00
Rn-211	211	86	1.29E+06	9.44E-14	1.94E-06	1.31E-07	4.30E-03	1.44E+13	8.94E-08	8.94E-08
Rn-210	210	86	6.27E-12	2.79E-15	2.78E-25	3.67E-08	5.86E-21	3.01E+14	2.08E-26	2.08E-26
Rn-209	209	86	0.00E+00	4.76E-14	0.00E+00	1.71E-09	0.00E+00	5.80E+13	0.00E+00	0.00E+00
Rn-208	208	86	0.00E+00	1.10E-14	0.00E+00	4.89E-09	0.00E+00	3.00E+13	0.00E+00	0.00E+00
Rn-207	207	86	0.00E+00	3.96E-14	0.00E+00	2.30E-09	0.00E+00	3.25E+14	0.00E+00	0.00E+00
Rn-206	206	86	0.00E+00	6.57E-14	0.00E+00	2.10E-09	0.00E+00	1.55E+14	0.00E+00	0.00E+00
				Total Rn Dose:	**2.06E-06**	**Total Rn Dose:**	**5.78E-02**	**Total Rn Dose:**	**1.52E-06**	**1.52E-06**
Po-218	218	84	2.42E+05	4.48E-19	1.73E-12	8.40E-09	5.18E-05	1.34E+13	1.81E-08	4.52E-13
Po-212	212	84	3.36E+08	0.00E+00	0.00E+00	5.20E-18	4.45E-11			
Po-211	211	84	1.71E+06	3.81E-16	1.03E-08	7.60E-12	3.30E-07	2.05E+17	8.34E-12	2.08E-16
Po-210	210	84	7.62E+07	4.16E-19	5.05E-10	6.10E-07	1.18E+00	9.05E+07	8.42E-01	2.11E-05
Po-209	209	84	2.64E+05	2.20E-16	9.24E-10	2.40E-06	1.61E-02	1.08E+08	2.45E-03	6.11E-08
Po-208	208	84	7.75E+06	0.00E+00	0.00E+00	2.40E-06	4.74E-01	1.18E+08	6.59E-02	1.65E-06
Po-207	207	84	5.85E+05	6.50E-14	6.06E-07	5.80E-11	8.65E-07	9.00E+12	6.50E-08	1.63E-12
Po-206	206	84	4.54E+08	5.97E-14	4.32E-04	1.10E-11	1.27E-04	3.12E+11	1.46E-03	3.64E-08
Po-205	205	84	2.02E-21	7.80E-14	2.51E-33	3.30E-11	1.70E-33	2.46E+13	8.23E-35	2.06E-39
Po-204	204	84	2.52E-05	5.68E-14	2.28E-17	2.70E-08	1.74E-14	1.00E+12	2.52E-17	6.30E-22
				Total Po Dose:	**4.32E-04**	**Total Po Dose:**	**1.67E+00**	**Total Po Dose:**	**9.12E-01**	**2.28E-05**
Gaseous and Volatile Non-Alpha Isotopes										
H-3	3	1	5.94E+06	3.31E-19	3.13E-11	6.2E-12	9.38E-07	2.00E+15	2.97E-09	2.97E-09

			Total H Dose:	**3.13E-11**	**Total H Dose:**	**9.38E-07**	**Total H Dose:**	**2.97E-09**	**2.97E-09**
Cl-36	36	17	6.50E-02	2.23E-17	2.31E-17	3.3E-10	5.46E-13	7.43E+09	8.75E-12	2.19E-16
Cl-38	38	17	1.53E-11	7.87E-14	1.92E-23	2.5E-11	9.77E-24	6.48E+13	2.37E-25	5.92E-30
Cl-39	39	17	0.00E+00	7.29E-14	0.00E+00	2.5E-11	0.00E+00	4.79E+13	0.00E+00	0.00E+00
				Total Cl Dose:	**2.31E-17**	**Total Cl Dose:**	**5.46E-13**	**Total Cl Dose:**	**8.75E-12**	**2.19E-16**
Ar-41	41	18	1.83E-21	6.5E-14	1.89E-33	0	0.00E+00	1.59E+14	1.15E-35	1.15E-35
Ar-42	42	18	5.15E+02	9E-18	7.38E-14	0	0.00E+00	1.18E+15	4.36E-13	4.36E-13
Ar-43	43	18	0.00E+00	7.69E-14	0.00E+00	0	0.00E+00	3.44E+14	0.00E+00	0.00E+00
Ar-44	44	18	0.00E+00	9.82E-14	0.00E+00	0	0.00E+00	1.24E+14	0.00E+00	0.00E+00
				Total Ar Dose:	**7.38E-14**	**Total Ar Dose:**	**0.00E+00**	**Total Ar Dose:**	**4.36E-13**	**4.36E-13**
Se-73m	73	34	0.00E+00	1.17E-14	0.00E+00	9.2E-12	0.00E+00	3.39E+14	0.00E+00	0.00E+00
Se-81	81	34	1.68E-44	5.24E-16	1.40E-58	8E-12	3.43E-57	2.83E+15	5.93E-60	1.48E-64
Se-81m	81	34	0.00E+00	6.18E-16	0.00E+00	1.6E-11	0.00E+00	6.79E+14	0.00E+00	0.00E+00
Se-83	83	34	0.00E+00	1.21E-13	0.00E+00	1.8E-11	0.00E+00	6.38E+13	0.00E+00	0.00E+00
Se-84	84	34	0.00E+00	2.07E-14	0.00E+00	1.6E-11	0.00E+00	1.65E+15	0.00E+00	0.00E+00
				Total Se Dose:	**1.40E-58**	**Total Se Dose:**	**3.43E-57**	**Total Se Dose:**	**5.93E-60**	**1.48E-64**
Br-75	75	35	3.58E-26	5.84E-14	3.33E-38	2.9E-11	2.65E-38	3.27E+13	1.10E-39	2.74E-44
Br-76	76	35	4.98E+03	1.34E-13	1.06E-08	2.4E-10	3.04E-08	1.54E+12	3.22E-09	8.06E-14
Br-77	77	35	2.71E+06	1.51E-14	6.51E-07	6.2E-11	4.28E-06	3.37E+12	8.03E-07	2.01E-11
Br-80	80	35	1.44E-03	3.85E-15	8.84E-17	5.9E-12	2.17E-16	1.50E+15	9.64E-19	2.41E-23
Br-80m	80	35	1.35E-03	3.11E-16	6.67E-18	3.3E-11	1.13E-15	8.85E+13	1.52E-17	3.80E-22
Br-82	82	35	2.56E+07	1.3E-13	5.30E-05	3.5E-10	2.28E-04	6.97E+11	3.67E-05	9.17E-10
Br-83	83	35	7.12E-12	3.82E-16	4.33E-26	1.6E-11	2.90E-24	3.97E+14	1.80E-26	4.49E-31
Br-84	84	35	0.00E+00	9.41E-14	0.00E+00	2.2E-11	0.00E+00	6.41E+13	0.00E+00	0.00E+00
Br-85	85	35	0.00E+00	2.74E-15	0.00E+00	2.9E-12	0.00E+00	9.85E+15	0.00E+00	0.00E+00
Br-87	87	35	0.00E+00	1.57E-13	0.00E+00	1.5E-13	0.00E+00	8.18E+14	0.00E+00	0.00E+00
				Total Br Dose:	**5.36E-05**	**Total Br Dose:**	**2.32E-04**	**Total Br Dose:**	**3.75E-05**	**9.38E-10**
Kr-77	77	36	2.82E-35	4.86E-14	2.18E-47	0	0.00E+00	2.19E+14	1.29E-49	1.29E-49
Kr-79	79	36	5.15E+05	1.21E-14	9.92E-08	0	0.00E+00	7.78E+14	6.61E-10	6.61E-10
Kr-81	81	36	3.59E+00	2.67E-16	1.53E-14	0	0.00E+00	3.51E+16	1.02E-16	1.02E-16
Kr-83m	83	36	3.00E-11	1.5E-18	7.16E-28	0	0.00E+00	6.89E+18	4.35E-30	4.35E-30
Kr-87	87	36	1.23E-30	4.12E-14	8.06E-43	0	0.00E+00	2.62E+14	4.70E-45	4.70E-45
Kr-88	88	36	1.00E-08	1.02E-13	1.63E-20	0	0.00E+00	8.17E+13	1.23E-22	1.23E-22
Kr-89	89	36	0.00E+00	8.1E-14	0.00E+00	0	0.00E+00	4.54E+14	0.00E+00	0.00E+00
				Total Kr Dose:	**9.92E-08**	**Total Kr Dose:**	**0.00E+00**	**Total Kr Dose:**	**6.61E-10**	**6.61E-10**
I-120	120	53	8.87E-31	1.38E-13	1.95E-42	1E-10	2.26E-42	3.04E+13	2.92E-44	7.30E-49
I-121	121	53	2.99E-16	1.94E-14	9.23E-29	2.7E-11	2.06E-28	1.34E+14	2.22E-30	5.55E-35
I-122	122	53	6.79E+04	4.56E-14	4.93E-08	0	0.00E+00	6.38E+14	1.06E-10	2.66E-15
I-123	123	53	9.38E+04	7.28E-15	1.09E-08	7.4E-11	1.77E-07	2.47E+13	3.79E-09	9.48E-14
I-124	124	53	4.61E+07	5.38E-14	3.95E-05	4.4E-09	5.17E-03	9.14E+10	5.04E-04	1.26E-08
I-125	125	53	2.24E+07	5.22E-16	1.86E-07	5.1E-09	2.91E-03	3.72E+10	6.02E-04	1.50E-08
I-126	126	53	6.08E+07	2.15E-14	2.08E-05	9.8E-09	1.52E-02	2.08E+10	2.93E-03	7.32E-08
I-128	128	53	0.00E+00	4.16E-15	0.00E+00	1.3E-11	0.00E+00	1.02E+15	0.00E+00	0.00E+00
I-129	129	53	7.22E-01	3.8E-16	4.37E-15	0.000000036	6.62E-10	3.05E+09	2.36E-10	5.91E-15
I-130	130	53	1.32E+05	1.04E-13	2.19E-07	6.7E-10	2.26E-06	2.51E+12	5.27E-08	1.32E-12
I-131	131	53	2.45E+08	1.82E-14	7.11E-05	7.4E-09	4.63E-02	3.41E+10	7.20E-03	1.80E-07
I-132	132	53	7.95E+07	1.12E-13	1.42E-04	9.4E-11	1.90E-04	2.43E+13	3.28E-06	8.19E-11
I-132m	132	53	4.09E-28	1.53E-14	9.97E-41	7.9E-11	8.24E-40	1.05E+14	3.89E-42	9.73E-47
I-133	133	53	7.54E+06	2.94E-14	3.53E-06	1.5E-09	2.88E-04	9.31E+11	8.10E-06	2.03E-10
I-134	134	53	0.00E+00	1.3E-13	0.00E+00	4.5E-11	0.00E+00	4.92E+13	0.00E+00	0.00E+00
I-135	135	53	3.27E+01	7.98E-14	4.15E-11	3.2E-10	2.66E-10	7.70E+12	4.24E-12	1.06E-16
				Total I Dose:	**2.77E-04**	**Total I Dose:**	**7.00E-02**	**Total I Dose:**	**1.12E-02**	**2.81E-07**
Xe-120	120	54	0.00E+00	1.94E-14	0.00E+00	0	0.00E+00	1.86E+14	0.00E+00	0.00E+00
Xe-121	121	54	0.00E+00	9.14E-14	0.00E+00	0	0.00E+00	1.26E+14	0.00E+00	0.00E+00
Xe-122	122	54	6.77E+04	2.46E-15	2.65E-09	0	0.00E+00	1.73E+14	3.92E-10	3.92E-10
Xe-123	123	54	3.97E-17	3.03E-14	1.91E-29	0	0.00E+00	3.05E+14	1.30E-31	1.30E-31
Xe-125	125	54	2.64E+05	1.19E-14	5.01E-08	0	0.00E+00	3.29E+14	8.03E-10	8.03E-10
Xe-127	127	54	1.93E+07	1.25E-14	3.84E-06	0	0.00E+00	7.50E+14	2.57E-08	2.57E-08
Xe-129m	129	54	3.04E+07	1.06E-15	5.14E-07	0	0.00E+00	8.85E+15	3.44E-09	3.44E-09
Xe-131m	131	54	3.36E+07	3.89E-16	2.08E-07	0	0.00E+00	2.41E+16	1.39E-09	1.39E-09
Xe-133	133	54	3.46E+08	1.56E-15	8.59E-06	0	0.00E+00	6.01E+15	5.75E-08	5.75E-08
Xe-133m	133	54	3.95E+07	1.27E-15	7.99E-07	0	0.00E+00	7.40E+15	5.33E-09	5.33E-09
Xe-135	135	54	2.20E+04	1.19E-14	4.16E-09	0	0.00E+00	8.04E+14	2.73E-11	2.73E-11
Xe-137	137	54	0.00E+00	9.46E-15	0.00E+00	0	0.00E+00	3.82E+15	0.00E+00	0.00E+00
Xe-138	138	54	0.00E+00	5.77E-14	0.00E+00	0	0.00E+00	1.68E+14	0.00E+00	0.00E+00
				Total Xe Dose:	**1.40E-05**	**Total Xe Dose:**	**0.00E+00**	**Total Xe Dose:**	**9.46E-08**	**9.46E-08**

D SEMI-AUTOMATED CHEMISTRY SYSTEM FLOWCHART

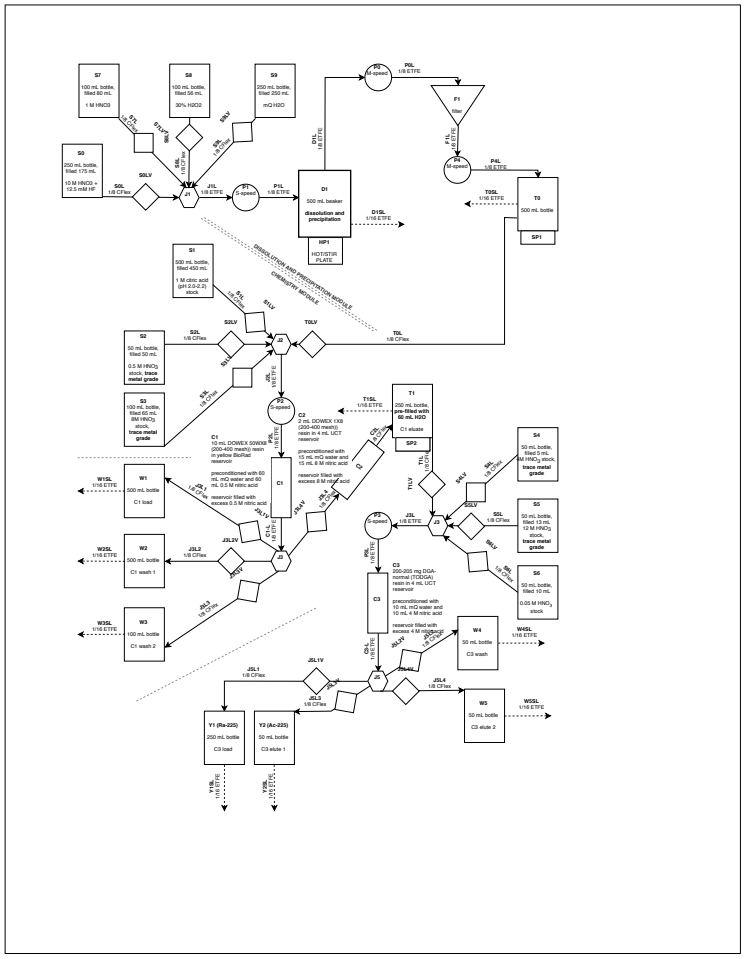

E CONTENTS OF THE SOLUTION CONTAINING ISOLATED RADIUM ISOTOPES 24.5 DAYS AFTER EOB

Table 7: Anticipated radioactive contents of the isolated solution of Ra isotopes at EOB + 1 week. This list includes Ba isotopes that are expected to follow Ra through the initial purification, as well as all Ra decay chains in equilibrium.

Nuclide	Activity [Bq]	Dose Rate at 1 m (unshielded) [μSv/h]
Ba-128	1.41E+04	0.00
Ba-131	5.93E+06	0.49
Ba-133	1.67E+05	0.01
Ba-133m	2.57E+03	0.00
Ba-135m	9.29E+01	0.00
Ba-140	5.82E+07	1.54
Ra-223	8.00E+07	1.37
Rn-219	8.00E+07	0.66
Po-215	8.00E+07	0.00
Pb-211	8.00E+07	0.72
Bi-211	8.00E+07	0.54
Tl-207	8.00E+07	0.03
Ra-224	1.52E+07	0.02
Rn-220	1.52E+07	0.00
Po-216	1.52E+07	0.00
Bi-212	1.52E+07	0.21
Po-212	9.73E+06	0.09
Tl-208	5.47E+06	2.18
Ra-225	1.76E+07	0.06
Ac-225	7.80E+06	0.01
Fr-221	7.80E+06	0.03
At-217	7.80E+06	0.00
Bi-213	7.80E+06	0.14
Tl-209	1.95E+05	0.05
Ra-226	2.93E+03	0.00
Rn-222	2.93E+03	0.00
Po-218	2.93E+03	0.00
Pb-214	2.93E+03	0.00
Bi-214	2.93E+03	0.00
Po-214	2.93E+03	0.00
Pb-210	2.93E+03	0.00
Bi-210	2.93E+03	0.00
Po-210	2.93E+03	0.00
Ra-228	1.71E+05	0.00
Total		**8.18**

F CONTENTS OF THE SOLUTION CONTAINING ISOLATED ACTINIUM ISOTOPES 7 DAYS AFTER EOB

Table 8: Anticipated radioactive contents of the isolated solution of Ac isotopes at EOB + 1 week. Ac decay chains are assumed to be in equilibrium for the purpose of determining upper limits on dose rates.

Nuclide	Activity [Bq]	Dose Rate at 1 m (unshielded) [μSv/h]
Ac-225	4.32E+08	4.74E-01
Bi-213	4.33E+08	7.97E+00
Fr-221	4.32E+08	1.62E+00
At-217	4.32E+08	0.00E+00
Po-213	4.25E+08	0.00E+00
Ac-226	5.14E+07	8.71E-01
Po-214	4.50E+07	0.00E+00
Ra-222	4.48E+07	5.87E-02
Rn-218	4.48E+07	5.04E-03
Th-226	4.48E+07	4.22E-02
Ac-227	8.46E+05	0.00E+00
Th-227	8.34E+05	1.35E-02
Ra-223	8.34E+05	1.43E-02
Fr-223	1.18E+04	8.19E-05
Rn-219	8.34E+05	6.93E-03
Pb-211	8.34E+05	7.55E-03
Bi-211	8.34E+05	5.61E-03
Tl-207	8.34E+05	2.83E-04
Ac-228	1.72E+05	1.96E-02
Ac-224	1.89E+04	5.30E-04
Total		**11.11**

G MODIFIED L125 PROCESS FOR SHIPMENT OF IRRADIATED THORIUM

This amendment to the L125 safety analysis describes an alternative process where irradiated thorium foils are shipped off the TRIUMF site for chemical processing at collaborating institutions. All safety aspects of this document will be followed, with the exception of the modifications described below. In general, since the level of the irradiation will be approximately 13.6% of the total 2640 μA*h irradiation described elsewhere in this document, the safety case described in this appendix is considered to be less hazardous and in most cases personnel will receive lower doses and be exposed to lower radiation hazards.

Thorium targets will be irradiated at IPF to a total of 360 μA*h and allowed to decay for 7 days, as required by the L124 SAR [7]. Targets will then be transferred to HC1 in RCR1 as described in Section 3.4 and opened as described in Section 3.5.

From within the hot cell, the thorium foil will then be placed inside a plastic bag and removed through the hot cell's side port. Using forceps to reduce hand dose, this bag will then be sealed within a second bag which will be swiped for loose contamination and placed inside a pig containing 11 mm of lead shielding. During this portion of the work, the foil is estimated to emit a dose rate of 484 μSv/h at 0.5 m without shielding. One worker will be exposed to this radiation field for less than 2 minutes, for a total whole body dose of <16 μSv. The hand dose is estimated to be <400 μSv.

One day later (at least 8 days after EOB), the Type A container containing the thorium foil will be shipped off site. The total ratio of A/A2 shipping values is calculated by FLUKA at this time point to be 0.751.

When using the Croft ("yellow can") Type A shipping container, which contains 1.1 cm of lead shielding, there will be a total of 1.9 cm of lead shielding (including the pig that is also inside the container). The estimated dose rate on the outside of the package is estimated to be 24 μSv/h at 1 m and approximately 1553 μSv/h on the surface of the package (which has a diameter of 25 cm). Additional shielding will be provided by 0.6 cm of steel within the container, which is not included in the shielding calculations.

A TRIUMF Radioactive Material Shipping Permit will be obtained in coordination with RPG, and all Transportation of Dangerous Goods (TDG) paperwork at the time of shipment will be completed by someone with valid TDG certification.